Dynamical Subgrid-scale Parameterizations for Quasigeostrophic Flows using Direct Numerical Simulations

Meelis Juma Zidikheri

A thesis submitted for the degree of
Doctor of Philosophy of
The Australian National University

December, 2007

Declaration

This thesis is an account of research undertaken between March 2004 and December 2007 at CSIRO Marine and Atmospheric Research, Aspendale Laboratories, Victoria, Australia, and at The Department of Theoretical Physics, Research School of Physical Sciences and Engineering, The Australian National University, Canberra, Australia.

Except where acknowledged in the customary manner, the material presented in this thesis is, to the best of my knowledge, original and has not been submitted in whole or part for a degree at any other university.

Meelis Juma Zidikheri
December, 2007

Acknowledgements

I would like to thank my principal supervisor, Jorgen Frederiksen, for his continued support during my PhD candidature. Jorgen has been closely involved in all aspects of the research presented here, and he has invested a considerable amount of his time towards my training; I would like to express my gratitude to him for that. I would also like to thank the following people who have contributed in one way or another to the completion of my thesis: Rowena Ball and Bob Dewar, my supervisors at ANU, for their encouragement and making me feel welcome during my visits to Canberra; Terry O'Kane, formerly of CSIRO Marine and Atmospheric Research, for illuminating discussions and assistance with computational work, particularly during the early stages of my candidature; Steve Kepert, formerly of CSIRO Marine and Atmospheric Research, for assistance with computational work; Stacey Osbrough, of CSIRO Marine and Atmospheric Research, for assistance with some of the diagrams produced in this thesis; and staff at the CSIRO/Bureau of Meteorology High Performance Computing and Communications Centre (HPCCC), for assistance with computing issues, particularly Robert Bell and Aaron McDonough. I would also like to thank my family for their support: my mum, Reet; my sister, Asha; and my girlfriend, Kelly. Additionally, I would like to express my gratitude posthumously to my father, Ali Juma Zidikheri. As well as human resources, I have benefitted from material resources. I would like to thank the following organizations for their support: The Research School of Physical Sciences and Engineering of the Australian National University, for funding my PhD scholarship; CSIRO Complex Systems Science, for funding my supplementary scholarship; CSIRO Marine and Atmospheric Research, for providing me with a room and access to facilities; and the Australian Research Council, through the *Discovery Projects* funding scheme (Project No. DP0343765), for travel support to Canberra.

Preface

Chapter 1 is an introduction to the main ideas in this thesis. Chapters 2 and 3 (and Appendices C and D) contain descriptions of key concepts of geophysical fluid dynamics and turbulence that are used in this thesis. Many, but not all, of the concepts can be found in standards textbooks on these subjects; I have relied heavily on the textbooks by Salmon (1998) and Vallis (2006). The spectral form of the two-level QG equation in Section 2.7 and its related DIA closure expression in Section 3.3.3 originate from unpublished work by Jorgen Frederiksen. The aforementioned chapters and appendices are not meant to serve as a conventional literature review; rather, they are pedagogical in nature. Chapter 4 is a description of research on multiple equilibria and mode reduction in barotropic atmospheric flows that I have carried out under the supervision of Jorgen Frederiksen. A large portion of the material in Section 4.1 has been published, with me as the principal author (see Zidikheri et al., 2007). The numerical model that I use for the direct numerical simulation in Chapter 4 was developed at CSIRO Marine and Atmospheric Research by Jorgen Frederiksen, Anthony Davies, Robert Bell, and Terence O'Kane, with additional problem-specific code written by me. The FORTRAN code for implementing Brent's Principal Axis algorithm has been written, and kindly been made available online, by John Burkardt. Chapter 5 is a literature review of the Subgrid-scale Parameterization problem. Chapters 6, 7, 8, and 9 are descriptions of research that I have carried out under the supervision of Jorgen Frederiksen on applying Frederiksen and Kepert's (2006) subgrid-scale parameterization methodology to atmospheric and oceanic baroclinic flows. Appendices A and B are descriptions of material that can be found in research literature. Appendices E and F are descriptions of the numerical models used to generate the results of Chapters 6, 7, and 8. These models have been developed at CSIRO Marine and Atmospheric Research by Jorgen Frederiksen, Robert Bell, and Steve Kepert, with additional problem-specific code written by me. Appendix G contains a straightforward algebraic manipulation. Appendices H and I (and parts of Chapter 8) contain results that have been displayed using code written by Stacey Osbrough at CSIRO Marine and Atmospheric Research.

Abstract

In this thesis, parameterizations of non-linear interactions in quasigeostrophic (QG) flows for severely truncated models (STM) and Large Eddy Simulations (LES) are studied. Firstly, using Direct Numerical Simulations (DNS), atmospheric barotropic flows over topography are examined, and it is established that such flows exhibit multiple equilibrium states for a wide range of parameters. A STM is then constructed, consisting of the large scale zonal flow and a topographic mode. It is shown that, qualitatively, this system behaves similarly to the DNS as far as the interaction between the zonal flow and topography is concerned, and, in particular, exhibits multiple equilibrium states. By fitting the analytical form of the topographic stationary wave amplitude, obtained from the STM, to the results obtained from DNS, renormalized dissipation and rotation parameters are obtained. The usage of renormalized parameters in the STM results in better quantitative agreement with the DNS.

In the second type of problem, subgrid-scale parameterizations in LES are investigated with both atmospheric and oceanic parameters. This is in the context of two-level QG flows on the sphere, mostly, but not exclusively, employing a spherical harmonic triangular truncation at wavenumber 63 (T63) or higher. The methodology that is used is spectral, and is motivated by the stochastic representation of statistical closure theory, with the 'damping' and forcing covariance, representing backscatter, determined from the statistics of DNS. The damping and forcing covariance are formulated as 2×2 matrices for each wavenumber. As well as the transient subgrid tendency, the mean subgrid tendency is needed in the LES when the energy injection region is unresolved; this is also calculated from the statistics of the DNS. For comparison, a deterministic parameterization scheme consisting of 2×2 'damping' parameters, which are calculated from the statistics of DNS, has been constructed. The main difference between atmospheric and oceanic flows, in this thesis, is that the atmospheric LES completely resolves the deformation scale, the energy and enstrophy injection region, and the truncation scale is spectrally distant from it, being well in the enstrophy cascade inertial range. In oceanic flows, however, the truncation scale is in the vicinity of the injection scale, at least for the parameters chosen, and is therefore not in an inertial range. A lower resolution oceanic LES at T15 is also examined, in which case the injection region is not resolved at all.

For atmospheric flows, it is found that, at T63, the matrix parameters are practically diagonal so that stratified atmospheric flows at these resolutions may be treated as uncoupled layers as far as subgrid-scale parameterizations are concerned. It is also found that the damping parameters are relatively independent of the (vertical) level, but the backscatter parameters are proportional to the subgrid flux in a given level. The stochastic and deterministic parameterization schemes give comparably good results relative to the DNS. For oceanic flows, it is found that the full matrix structure of the parameters must be used. Furthermore, it is found that there is a strong injection of barotropic energy from the subgrid scales, due to the unresolved, or partially resolved, baroclinic instability injection scales. It is found that the deterministic parameterization is too numerically unstable to be of use in the LES, and instead the stochastic parameterization must be used

to obtain good agreement with the DNS. The subgrid tendency of the ensemble mean flow is also needed in some problems, and is found to reduce the available potential energy of the flow.

Contents

Chapter 1

Introduction

This thesis will be concerned mainly with mode reduction in large scale atmospheric and oceanic flows. The need for systematic mode reduction, also known as subgrid-scale parameterization, arises because such flows are turbulent, which implies that they involve coupled motions on very wide ranges of space and time scales. For example, in the atmosphere, the largest scales of motion are in the order of 10000 km while the smallest scales might be in the order of 1 cm (Holton, 1992). The range of time scales is similarly vast. The difficulty, of course, is that these motions are not independent; motions on very different space and times scale can and do interact. Given this, then any computation of motion at a particular scale, say the large scale, needs to involve some parameterization of the small scale motions, if as it often turns out be, it is impossible to compute the latter. One cannot simply study a particular scale of motion in isolation as can be done in many other problems in physics. To illustrate these ideas better we use a toy model of fluid motion as follows.

The acceleration of a particle with velocity $u(x,t)$ at position x and time t is just $a = \frac{\partial u(x,t)}{\partial t}$. However, if the particle is a parcel of fluid in motion, then if the position x is measured relative to a frame moving with the fluid, we have

$$a = \frac{d}{dt}u(x(t),t) = \frac{\partial u}{\partial t} + \frac{\partial x}{\partial t}\frac{\partial u}{\partial x} = \frac{\partial u}{\partial t} + u\frac{\partial u}{\partial x}, \tag{1.1}$$

which follows from the fact that the reference frame is moving so $x = x(t)$ and the chain rule for partial derivatives. It sufficient for our arguments to assume that the fluid is not accelerating, so

$$\frac{\partial u}{\partial t} + u\frac{\partial u}{\partial x} = 0 \tag{1.2}$$

is a heuristic equation for fluid motion. Now assume that the motion consists of a time-independent part, $\overline{u}$, and a transient part, u'. Hence,

$$u(x,t) = \overline{u} + u'(x,t). \tag{1.3}$$

It is also convenient to assume that $\overline{u}$ is uniform in space as well. Then with this caveat, after substituting Eq. 1.3 in Eq. 1.2, we have the evolution equation for the transients (perturbations):

$$\frac{\partial u'}{\partial t} + \overline{u}\frac{\partial u'}{\partial x} + u'\frac{\partial u'}{\partial x} = 0. \tag{1.4}$$

In the absence of the $u'\frac{\partial u'}{\partial x}$ term, this equation is linear in u'. The trial solution $u'(x,t) = \exp\left[i(kx + \omega t)\right]$ yields the frequency $\omega = -k\overline{u}$, which implies that u' is always stable; that is, it does not grow exponentially with time. However, the model that

we are working with is very simplistic. In more realistic problems, flow instabilities, such as barotropic, baroclinic, and topographic instabilities for atmospheric and oceanic flows exist, so the frequency will in such problems have an imaginary component, making the solution unstable for some flow parameters. The instability will also typically have a peak at some wavenumber. In this toy model, the 'missing' instabilities can be represented by a transient forcing, $f(t)$, in the equation of motion, Eq. 1.2. Hence,

$$\frac{\partial u'}{\partial t} + \overline{u}\frac{\partial u'}{\partial x} + u'\frac{\partial u'}{\partial x} = f. \tag{1.5}$$

It is illuminating to expand u' in terms of waves with wavenumbers k, with corresponding length scales $\lambda = \frac{1}{k}$. Hence,

$$u'(x,t) = \sum_k u_k(t)\exp(ikx). \tag{1.6}$$

Here, u_k is the amplitude of the wave with wavenumber k. The flow, u', will be real if $u_k^* = u_{-k}$. Similarly,

$$f(x,t) = \sum_k f_k(t)\exp(ikx). \tag{1.7}$$

Substituting Eqs. 1.6 and 1.7 in Eq. 1.5, we have

$$\frac{\partial u_k}{\partial t} = \sum_p \sum_q A_{kpq} u_p u_q - ik\overline{u}u_k + f_k. \tag{1.8}$$

Here, A_{kpq} are interaction coefficients which depend on the wavenumbers k, p, and q.

Now, imagine that the instability is initially confined to a single wavenumber k. In the absence of the non-linear terms, the amplitude u_k would grow without bound. However consider a mode with wavenumber k', where $k' \neq k$; the evolution equation for this mode is

$$\frac{\partial u_{k'}}{\partial t} = \sum_p \sum_q A_{k'pq} u_p u_q - ik\overline{u}u_{k'}. \tag{1.9}$$

The amplitude $u_{k'}$ will grow because when either p or $q = k$, the non-linear term $u_k u_q$ (or $u_p u_k$) will be large because the mode with wavenumber k grows exponentially due to an instability. Non-linear interactions, then, cause other modes, with wavenumbers $k' \neq k$, to grow. In physical space, this corresponds to a motion of a particular scale, initially growing due to a (linear) instability of the flow, breaking up into motions of other scales. In three-dimensional fluids, these motions are generally of smaller scales, but in two-dimensional fluids, with atmospheric and oceanic fluids being examples thereof, it is possible for motions of larger scales to be generated as well. This phenomenon, whereby a fluid motion of a certain scale generates, via non-linear interactions, motions at numerous other scales, is understood to be turbulence, as far as this thesis is concerned. Clearly, an analytical solution is out of the question for such problems. However, numerical solutions are also problematic because one would have to resolve the smallest scales of motion, since all scales are coupled. This is out of reach of current computational technology for many problems of interest, including atmospheric and oceanic flows. In any case, even if such computational capabilities were to be available, they would be of no use for solving real-world problems in a deterministic sense, since it is not conceivably possible to measure the initial conditions of a physical system, such as the atmosphere or oceans, with such

precision. Instead, one can only hope to obtain flow statistics. The equations of motion of turbulent flows are thus inherently stochastic.

Flow statistics are impossible to compute directly from equations of type (1.8) since the tendency $\frac{\partial \langle u_k \rangle}{\partial t}$ would involve a second-order moment $\langle u_p u_q \rangle$, and the tendency for the second order moment would consequently involve the third order moments, and ad infinitum. This is called the closure problem of turbulence, and attempts to close the hierarchy of equations by additional assumptions regarding the flow statistics are called closure theories of turbulence. One can also use phenomenology to deduce some qualitative features of the flow statistics. So for example, in a two-dimensional fluid, the energy and enstrophy, which are flow statistics, are both conserved. This constrains the transfers of energy and enstrophy to be towards the large scales and small scales, respectively.

In many cases, one is interested in particular scales of motion, but has to carry around the computationally burdensome other scales. So, using our toy model as an example, we might be interested in looking at the interaction of a particular scale of motion with amplitude u_k with the background flow $\overline{u}$:

$$\frac{\partial u_k}{\partial t} = -ik\overline{u}u_k + f_k. \tag{1.10}$$

This is a severely truncated, or reduced, model since we have ignored modes with wavenumbers other than k. In some simple cases, one might be able to obtain an analytic solution to this problem. However, the neglected non-linear terms will have an effect on the flow, and these interactions have to be parameterized in some way. One way of doing this is to run a sufficiently high resolution simulation, with the non-linear terms included, and try to fit the analytic solution of the reduced-order model to the results of the higher resolution simulation by redefining some flow parameters. This is the first type of problem that we shall examine in this thesis (in Chapter 4) in relation to a barotropic (depth independent) atmospheric flow over topography.

The second type of problem involves choosing a cutoff wavenumber k_* in the flow, and, for wavenumbers $k \leq k_*$, parameterizing the interactions with wavenumbers $k > k_*$. This is called subgrid-scale parameterization, and is needed to run simulations truncated at wavenumber k_*. Thus, we have

$$\frac{\partial u_k}{\partial t} = \sum_{p \leq k_*} \sum_{q \leq k_*} A_{kpq} u_p u_q + g(u_k) - ik\overline{u}u_k + f_k. \tag{1.11}$$

Here, $g(u_k)$ is a function of the resolved scale amplitudes u_k which parameterizes non-linear interactions involving at least one wavenumber greater than k_*. The simplest choice for this function is

$$g(u_k) = a_k u_k + b_k. \tag{1.12}$$

This form is justified by phenomenology and closure theories of turbulence. The parameters a_k, if negative, are to be regarded as damping parameters, and b_k are random forcing functions. The parameters a_k and b_k are calculated from the statistics of a high resolution simulation, with wavenumbers $k \leq k_*$ resolved. Generally, for reasons to be explained in latter parts of this thesis, it is sufficient to have the resolution of the high resolution simulation corresponding to a maximum wavenumber $2k_*$.

In large scale atmospheric problems, the main sources of instability are usually well resolved. This means that the most significant amplitudes of the forcing function, f_k, in Eq. 1.8 are resolved. In oceanic problems, on the other hand, baroclinic instability

is responsible for the formation of mesoscale eddies of size in the order of 50 km, which are hard to resolve in complex models. Hence, the most significant amplitudes of the forcing, f_k, in Eq. 1.8 are not resolved in oceanic problems. If baroclinic instability is the only source of instability in the problem, and if k_* is sufficiently small, then in fact the amplitudes f_k that are resolved are relatively insignificant. Hence, in this respect, the oceanic problem is different to the atmospheric problem, and, for reasons to be discussed in the latter parts of thesis, is thus harder to parameterize. It should be noted that the toy model that we have presented here is just for illustrative purposes. In the rest of this thesis, we work with fairly realistic atmospheric and oceanic models, namely, the quasigeostrophic (QG) equations of motion. The outline for the rest of this thesis is as follows.

In Chapter 2, we introduce the QG equations of motion used in this study. We also show how the QG equations may be linearized to predict various atmospheric and oceanic motions such as Rossby waves, stationary topographic waves, and baroclinic instability. In Chapter 3, we look at turbulence, with a focus on QG turbulence. In the first part, we look at the phenomenology of QG turbulence, which leads to the prediction of various atmospheric and oceanic phenomena such as the inverse cascade, zonalization of flows, eddy-induced drag, and barotropization. In the second part, we examine closure theories of turbulence, with an emphasis on the Direct Interaction Approximation (DIA). This will help to justify the form of the subgrid-scale parameterizations used in this thesis.

In Chapter 4, we look at the tendency of barotropic flows over topography to generate multiple equilibrium states, which is thought to be related to the atmospheric phenomenon known as Blocking. A significant portion of this chapter is focussed on establishing the ubiquity of multiple equilibria in flows of various complexities; this includes severely truncated models (STM) and Direct Numerical Simulations (DNS) of the equations of motion. We also explore how to parameterize the non-linear interactions in a STM so that it is in better agreement with DNS.

In Chapter 5, we review the literature on subgrid-scale parameterizations, including advective-diffusive tensor subgrid-scale parameterizations and self-consistently calculated subgrid-scale parameterizations. By the latter we mean parameters calculated from the statistics of high resolution simulations, whether by closure methods or by DNS. We also introduce the methodology for subgrid-scale parameterizations used in this study, which is an extension of that outlined by Frederiksen and Kepert (2006). Finally, we attempt to relate Frederiksen and Kepert's self-consistent DNS methodology to the advective-diffusive tensor methodology, and show that the latter is deficient in some respects.

In Chapters 6, 7, and 8, we examine subgrid-scale parameterizations for a variety of atmospheric and oceanic QG flows. In Chapter 6, we look at the equivalent layer problem. This is a highly symmetrical problem where the flow statistics in both layers are the same. It enables us to look at some aspects of the subgrid-scale parameterization problem without the complications induced by rotation and different forcing coefficients in the two layers. In Chapter 7, we introduce differential rotation and different forcing coefficients in the two layers. However, the forcing is of a very simple form, being confined to the largest scale only. The inclusion of rotation and different forcing coefficients in the vertical makes this problem closer to realistic atmospheric and oceanic flows.

In Chapter 8, we introduce zonal jets in the problem. This corresponds to mean forcing on a range of large scales, hence complicating the mean-transient interactions in the problem, but also raising the level of realism. The jets in the atmosphere correspond to mid-latitude jet streams, and in the ocean they are exemplified by the Atlantic Circumpo-

lar Current, which flows around the globe in the vicinity of 60^oS. In Chapter 9, we briefly summarize the main results of this thesis and discuss their implications.

Chapter 2

Fundamentals of Quasigeostrophic Dynamics

2.1 Introduction

In this chapter we introduce the basic equations and dynamics of quasigeostrophic (QG) flows that will be used throughout this thesis. Starting from the three-dimensional quasigeostrophic potential vorticity (QGPV) equations, we show how the two-level QGPV equations may be obtained for the ocean and atmosphere; we also discuss the inclusion of topography as a bottom boundary condition. The concept of barotropic and baroclinic modes is introduced. We discuss the wavenumber (spectral) representation of the equations of motion. The generalized beta-plane equations for barotropic flows over topography, which are the primary equations in the study of multiple equilibria in Chapter 4, are introduced. Finally, we discuss the dynamics of the linearized equations of motion, from which we deduce various atmospheric and oceanic motions such Rossby waves, extratropical storms, and mesoscale eddies.

2.2 The Quasigeostrophic Potential Vorticity Equation

The equations of motion of the atmosphere and oceans are a set non-linear partial differential equations derived from the momentum, thermodynamic, continuity, and state equations. These sets of equations are very complex, and are challenging even for the most powerful computers in operation to date. Moreover, the equations contain motions that are not of interest to Meteorologists and Oceanographers such as sound waves. To overcome the the latter problem, approximations such as the hydrostatic approximation, which assumes vertical balance, and the Boussinesq Approximation, which assumes that density is nearly constant in the ocean, are used to simplify the basic equations of motion so that they only retain motions of interest. These are the primitive equations. The primitive equations are still very challenging computationally; it is only with the advent of fast electronic computers that they have been routinely used to simulate atmospheric and oceanic flows. Prior to that, simpler sets of equations have been used to analyze atmospheric and oceanic motions; the most widely used of these are the Quasigeostrophic Potential Vorticity (QGPV) equations. They are derived based on the assumption of approximate geostrophic balance (balance between the pressure gradient and the Coriolis force), which is a good approximation for mid-latitude synoptic-scale motions. The QGPV equations are useful for analyzing various extratropical motions such as Rossby waves in both the atmosphere and oceans, cyclones in the atmosphere, and mesoscale eddies in

the ocean. The QGPV equations are also useful for the purposes of studying large scale atmospheric and oceanic turbulence as they are relatively simple in structure, yet they retain the quadratic non-linearity of the basic equations of motion (Haltiner and Williams, 1980; Washington and Parkinson, 1986; Marshall et al., 1997). The form of the QGPV equation that we use is as given by Salmon (1998):

$$\frac{\partial q}{\partial t} + J(\psi, q) = 0, \tag{2.1}$$

where $q = q(x, y, z, t)$ is the three-dimensional quasigeostrophic potential vorticity:

$$q = \nabla^2\psi + f + \frac{\partial}{\partial z}\left(\frac{f_0^2}{N^2}\frac{\partial\psi}{\partial z}\right). \tag{2.2}$$

Here, ψ is the streamfunction; f is the Coriolis parameter as a function of latitude, which appears in the QGPV equation because of differential rotation; f_0 is the value of the Coriolis parameter at a fixed mid-latitude location (where the quasi-geostrophic approximation is valid); and N is the Brunt-Vaisala (buoyancy) frequency, whose square is

$$N^2(z) = -\frac{g}{\rho_0}\frac{\partial\bar{\rho}}{\partial z}, \tag{2.3}$$

which appears in the QGPV equation due to stratification. In Eq. 2.3, $\bar{\rho}$ is the depth-dependent part of the density field; ρ_0 is the constant part of the density field, and it assumed (Salmon, 1998) that $\bar{\rho} \ll \rho_0$; g is the acceleration due to gravity. The Jacobian operator is

$$J(\psi, q) = \frac{\partial\psi}{\partial x}\frac{\partial q}{\partial y} - \frac{\partial\psi}{\partial y}\frac{\partial q}{\partial x} = \mathbf{u}\cdot\nabla q, \tag{2.4}$$

since the wind $\mathbf{u} = (u, v, 0)$ is the horizontal wind, whose components are related to the streamfunction as

$$u = -\frac{\partial\psi}{\partial y} \tag{2.5}$$

and

$$v = \frac{\partial\psi}{\partial x}. \tag{2.6}$$

In Cartesian geometry, the beta-plane approximation is used so that

$$f = f_0 + \beta y. \tag{2.7}$$

β is determined by expanding

$$f = 2\Omega\sin\phi \tag{2.8}$$

in Taylor series to first order; here, Ω is the angular velocity of the Earth and ϕ is the latitude. Additionally, the meridional coordinate $y = a\phi$, where a is the radius of the Earth so that

$$\beta = \frac{2\Omega\cos\phi_0}{a}. \tag{2.9}$$

It is, however, also possible to work in spherical geometry, and in that case, the global latitudinal variation of f as given by Eq. 2.8 is used in Eq. 2.1; this will be discussed further in subsequent chapters. In the QG approximation, the potential vorticity field, q, is advected by the horizontal velocity $\mathbf{u}$ only. However, the vertical velocity, w, is also

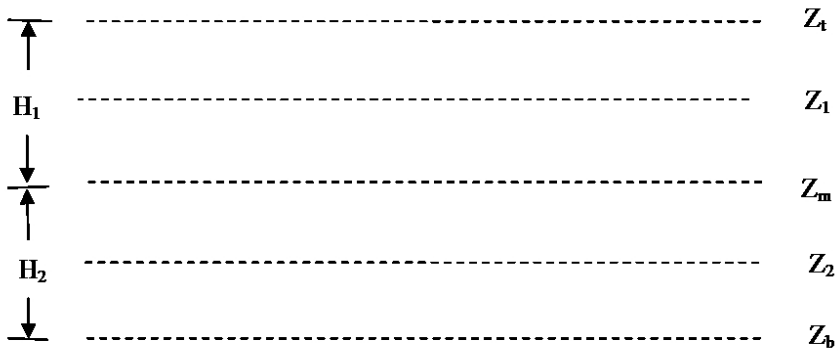

Figure 2.1: The quasigeostrophic two level model.

frequently needed, and it can be determined from

$$\frac{\partial}{\partial t}\left(\frac{\partial \psi}{\partial z}\right) + J\left(\psi, \frac{\partial \psi}{\partial z}\right) + w\frac{N^2}{f_0} = 0. \tag{2.10}$$

This is the quasigeostrophic form of the thermodynamic equation (Salmon, 1998).

2.3 The Oceanic Two Level Quasigeostrophic Equations

We can further simplify the three-dimensional QGPV equation by discretizing the vertical coordinates. The physical assumption is that the fluid is stratified into layers of different densities; that is, within each layer the density is uniform. We discretize the vertical coordinates by evaluating the three dimensional QGPV equations, Eq. 2.1, at levels 1 and 2, as shown in fig. 2.1. Levels 1 and 2 are defined to be the midpoints of layers 1 and 2, respectively. We also need to estimate vertical derivatives at levels 1 and 2, as implied by Eq. 2.2; this is done by taking finite differences. For example, at level 1 $\left.\frac{\partial \chi}{\partial z}\right|_{z=z_1} = \frac{\chi_t - \chi_m}{z_t - z_m}$, where χ is some variable with a z dependence. It is also assumed that $\frac{\partial \psi}{\partial z} = 0$ at the top and bottom boundaries. This is equivalent to assuming that the vertical velocity $w = 0$ at the boundaries. The potential vorticity, q, at levels 1 and 2 is then estimated to be

$$q_1 = \nabla^2 \psi_1 + f - F_1(\psi_1 - \psi_2) \tag{2.11}$$

and

$$q_2 = \nabla^2 \psi_2 + f + F_2(\psi_1 - \psi_2). \tag{2.12}$$

Here,

$$F_1 = \frac{2f_0^2}{N_m^2 H_1 (H_1 + H_2)} \tag{2.13}$$

and

$$F_2 = \frac{2f_0^2}{N_m^2 H_2 (H_1 + H_2)} \tag{2.14}$$

are the layer coupling constants. For simplicity, we shall set $H_1 = H_2 = H$ so that we are left with a single coupling constant

$$F_o = \frac{f_0^2}{N_m^2 H^2}. \tag{2.15}$$

This is a very crude model of the ocean, but is sufficient for our purposes. The two level QGPV equations for the ocean are then

$$\frac{\partial q_i}{\partial t} + J(\psi_i, q_i) = 0, \tag{2.16}$$

with

$$q_i = \nabla^2 \psi_i + f + (-1)^i F_o(\psi_1 - \psi_2), \tag{2.17}$$

and the index $i = 1, 2$. It is frequently more convenient to work with the definition of the potential vorticity without the rotation term; that is, the reduced potential vorticity

$$q_i^r = \nabla^2 \psi_i + (-1)^i F_o(\psi_1 - \psi_2). \tag{2.18}$$

The two level QGPV is then

$$\frac{\partial q_i^r}{\partial t} + J(\psi_i, q_i^r + f) = 0. \tag{2.19}$$

Since the variation in density is small compared to the constant part, ρ_0, we can estimate $\rho_0 \approx \rho_2$ in Eq. 2.3. Hence, the Brunt-Vaisala frequency (at the interface) can then be written

$$N_m^2 = \frac{g'}{H}, \tag{2.20}$$

where

$$g' = \frac{\rho_2 - \rho_1}{\rho_2} g \tag{2.21}$$

is the reduced gravity. We then have

$$F_o = \frac{f_0^2}{g' H}. \tag{2.22}$$

Typical oceanic values are $g' = 0.02$ ms^{-2}, $H = 1750$ m, $\Omega = 7.292 \times 10^{-5}$ s^{-1}, and the latitude, $\phi = 60^o$. This gives $F_o = 4.5 \times 10^{-10}$ m^{-2}. Now the internal radius of deformation, λ_i, is defined as

$$\lambda_i = \frac{1}{\sqrt{2F_o}}, \tag{2.23}$$

so with these values we get $\lambda_i \sim 30$ km.

2.4 The Atmospheric Two Level Quasigeostrophic Equations

Salmon (1998) shows that the atmospheric primitive equations may be cast in the same form as the oceanic primitive equations with appropriate redefinition of the variables. In

particular the vertical coordinate, z, is replaced by $\tilde{z}$, which satisfies

$$\frac{\partial \tilde{z}}{\partial p} = -\frac{R}{p}\left(\frac{p}{p_s}\right)^{\frac{R}{c_p}}. \tag{2.24}$$

Here, p is the pressure; p_s is the surface pressure (1000 mb); R is the gas constant; and c_p is the specific heat capacity of dry air at constant pressure. It is, however, more convenient to work with pressure as the vertical coordinate; that is, in the coordinate system (x, y, p, t). This can be done by transforming all the $\frac{\partial}{\partial z}$ vertical derivatives in Eq. 2.1 (with $z \to \tilde{z}$) into $\frac{\partial}{\partial p}$ vertical derivatives using the chain rule. The Brunt-Vaisala frequency is

$$N^2(\tilde{z}) = \frac{\partial \bar{\theta}}{\partial \tilde{z}} = \delta \frac{\partial \bar{\theta}}{\partial p}, \tag{2.25}$$

where $\bar{\theta}$ is the horizontally-averaged potential temperature; θ is defined as

$$\theta = T\left(\frac{p_s}{p}\right)^{\frac{R}{c_p}}, \tag{2.26}$$

with T being the temperature, and

$$\delta = \frac{\partial p}{\partial \tilde{z}} \tag{2.27}$$

is taken to be a constant in the lower atmosphere (Salmon, 1998). Using the definition of the potential temperature, Eq. 2.26, and the ideal gas relation, $p = \rho R T$, we find

$$\frac{\partial \bar{\theta}}{\partial p} = -\left(\frac{p_0}{p}\right)^{\frac{R}{c_p}} S(p), \tag{2.28}$$

where $S(p)$ is the static stability of the atmosphere defined as

$$S(p) = -\left(\frac{\partial \bar{T}}{\partial p} - \frac{R}{c_p}\frac{\bar{T}}{p}\right), \tag{2.29}$$

p_0 is the surface pressure, and $\bar{T}$ is the horizontally-averaged temperature. Hence the Brunt-Vaisala frequency in p-coordinates is

$$N^2(p) = \frac{\delta^2 R}{p} S(p). \tag{2.30}$$

The form of the *three-dimensional* atmospheric QGPV equation in p-coordinates is as given by Eq. 2.1 for z-coordinates; however, q, the three-dimensional potential vorticity is

$$q = \nabla^2 \psi + f + \frac{\partial}{\partial p}\left(\frac{f_0^2}{\frac{RS}{p}}\frac{\partial \psi}{\partial p}\right). \tag{2.31}$$

Eq. 2.31 can be discretized vertically in pressure coordinates in exactly the same way as the corresponding oceanic equations, described in the previous section. The resulting two level atmospheric QGPV equations have the form given in Eq. 2.16 with the *two-dimensional* quasigeostrophic potential vorticity

$$q_i = \nabla^2 \psi_i + f + (-1)^i F_a(\psi_1 - \psi_2). \tag{2.32}$$

The layer coupling constant

$$F_a = \frac{f_0^2}{R\Delta p S_m}. \tag{2.33}$$

Here Δp is the pressure difference between level 1 and 2; S_m is the static stability at mid-level. Typical atmospheric values are $\Delta p = 5\times10^4$ Pa (500 mb), $R = 287$ JK^{-1}, $S_m = 5\times10^{-4}$ KPa^{-1}, $\Omega = 7.292\times10^{-5}$ s^{-1}, and the latitude, $\phi = 60^o$. This gives $F_a = 2.2\times10^{-12}$ m^{-2}, and hence $\lambda_i \sim 500$ km. Note that this corresponds to a radius of deformation at least an order of magnitude greater than that in the ocean.

2.5 Two level Equations with Topography

Topography is an important ingredient in large scale atmospheric and oceanic dynamics. It generates stationary waves in the atmosphere and boundary currents in the ocean.

The topographic interaction can be included in the two level QGPV equations by imposing a non-zero vertical velocity at the bottom boundary. That is

$$w_b = \mathbf{u}\cdot\nabla\mathbf{\Delta} = J(\psi,\Delta). \tag{2.34}$$

Here, $\Delta = \Delta(x,y)$ is the bottom elevation. We can deduce the the corresponding boundary condition for $\frac{\partial\psi}{\partial z}$ from Eq. 2.10. This is

$$\left.\frac{\partial\psi}{\partial z}\right|_{z=z_b} = -\frac{N_b^2}{f_0}\Delta. \tag{2.35}$$

If we repeat the procedure described in Section 2.2 with Eq. 2.35 as the bottom boundary condition, we again obtain the two level QGPV equations with the form given by Eq. 2.1. The potential vorticities are given by

$$q_1 = \nabla^2\psi_1 + f - F(\psi_1 - \psi_2), \tag{2.36}$$

as before; however

$$q_2 = \nabla^2\psi_2 + f + F(\psi_1 - \psi_2) + h \tag{2.37}$$

has an additional topographic contribution. Here, h is defined as

$$h = f_0\frac{\Delta}{H}. \tag{2.38}$$

It is the contribution of the bottom topography to the quasigeostrophic potential vorticity. If we remove the rotation and topographic terms from the definition of potential vorticity, the two level QGPV equation with bottom topography is

$$\frac{\partial q_i^r}{\partial t} + J(\psi_i, q_i^r + f + h_i) = 0, \tag{2.39}$$

where $h_1 = 0$ and $h_2 = h$.

2.6 Barotropic and Baroclinic Modes

It is often convenient to work in terms of the variables

$$\psi = \frac{1}{2}(\psi_1 + \psi_2), \tag{2.40}$$

the barotropic streamfunction, and

$$\tau = \frac{1}{2}(\psi_1 - \psi_2), \tag{2.41}$$

the baroclinic streamfunction. The barotropic mode represents the vertically averaged part of the flow while the baroclinic mode represents the shear flow. In terms of these variables, Eq. 2.39 becomes

$$\frac{\partial}{\partial t}\nabla^2\psi + J(\psi, \nabla^2\psi + f + \frac{h}{2}) + J(\tau, \nabla^2\tau - \frac{h}{2}) = 0, \tag{2.42}$$

the barotropic vorticity equation, and

$$\frac{\partial}{\partial t}(\nabla^2\tau - k_i^2\tau) + J(\psi, \nabla^2\tau - k_i^2\tau - \frac{h}{2}) + J(\tau, \nabla^2\psi + f + \frac{h}{2}) = 0, \tag{2.43}$$

the baroclinic vorticity equation. Here,

$$k_i = \frac{1}{\lambda_i} \tag{2.44}$$

is the inverse of the internal radius of deformation, which is defined in Eq. 2.23. We call these equations the QGPV equations in barotropic-baroclinic (BTBC) space.

It is frequently useful to consider the barotropic vorticity equation on its own as a model for vertically-averaged atmospheric or oceanic flow. The baroclinic terms in Eq. 2.42 are then not explicitly included, so

$$\frac{\partial}{\partial t}\nabla^2\psi + J(\psi, \nabla^2\psi + f + h) = 0, \tag{2.45}$$

where we have set $\frac{h}{2} \rightarrow h$. However, we need to recognize that there is a source of barotropic energy not explicitly shown in Eq. 2.45 which has its origin in the coupling between the barotropic and baroclinic modes as implied by Eqs. 2.42 and 2.43. This is usually modelled by a stochastic forcing. In the absence of rotation and topography, the barotropic vorticity equation reduces to the two-dimensional vorticity equation. Therefore, the barotropic part of the flow behaves like a two-dimensional fluid. The baroclinic part reflects stratification effects.

2.7 The Spectral Equations

The wavenumber (spectral) representation is commonly used in atmospheric modelling. In general, this is not the case in oceanic modelling due to the presence of continents, which precludes periodic boundary conditions, making the spectral technique hard to implement. However, in both systems, turbulence is best studied in terms of the wavenumber representation as this enables one to lucidly analyze the interactions between different scales, a key property of turbulence. The Cartesian (planar) coordinate system offers the sim-

plest approach to the spectral technique, and so we shall base most of our discussion in this geometry. However, the numerical model that has been used for most of the work is spherical, and so we also discuss the spherical spectral equations in Appendix A.

If we can assume that the flow is doubly periodic, then we can expand the fields (such as ψ, q, and h), denoted in general by $\chi = \chi(x, y, t)$, as a complex Fourier series:

$$\chi(x, y, t) = \sum_{\mathbf{k}} \chi_{\mathbf{k}}(t) \exp(i\mathbf{k} \cdot \mathbf{x}). \tag{2.46}$$

Here $\mathbf{k} = (k_x, k_y)$ is a two-dimensional wavevector and $\chi_{\mathbf{k}}$ is the amplitude of the wave with wavevector $\mathbf{k}$. In what follows, we shall denote the magnitude of the wavevector $\mathbf{k}$ by the wavenumber k. In the sum, Eq. 2.46, for every wavevector $\mathbf{k}$, there is a corresponding wavevector $-\mathbf{k}$. It is straightforward to show that we require

$$\chi_{-\mathbf{k}} = \chi^*_{\mathbf{k}} \tag{2.47}$$

to ensure that the physical space fields, χ, are real. Upon using the expansion given by Eq. 2.46 in the barotropic vorticity equation, Eq. 2.45, and after some algebra (see, for example, Frederiksen (2003)), we obtain the spectral equation

$$\frac{\partial \zeta_{\mathbf{k}}}{\partial t} = \sum_{\mathbf{p}} \sum_{\mathbf{q}} \delta(\mathbf{k} + \mathbf{p} + \mathbf{q}) \left[K(\mathbf{k}, \mathbf{p}, \mathbf{q}) \zeta_{-\mathbf{p}} \zeta_{-\mathbf{q}} + A(\mathbf{k}, \mathbf{p}, \mathbf{q}) \zeta_{-\mathbf{p}} h_{-\mathbf{q}} \right] - i\omega_{\mathbf{k}} \zeta_{\mathbf{k}}. \tag{2.48}$$

Here,

$$\zeta_{\mathbf{k}} = -k^2 \psi_{\mathbf{k}}, \tag{2.49}$$

$$\omega_{\mathbf{k}} = -\frac{\beta k_x}{k^2}, \tag{2.50}$$

$$A(\mathbf{k}, \mathbf{p}, \mathbf{q}) = -\frac{(p_x q_y - p_y q_x)}{p^2} \tag{2.51}$$

and

$$\begin{aligned} K(\mathbf{k}, \mathbf{p}, \mathbf{q}) &= \frac{1}{2} \left[A(\mathbf{k}, \mathbf{p}, \mathbf{q}) + A(\mathbf{k}, \mathbf{q}, \mathbf{p}) \right] \\ &= \frac{1}{2} (p_x q_y - p_y q_x) \left[\frac{1}{q^2} - \frac{1}{p^2} \right]. \end{aligned} \tag{2.52}$$

The interaction coefficient $K(\mathbf{k}, \mathbf{p}, \mathbf{q})$ is symmetric with respect to $\mathbf{p} \leftrightarrow \mathbf{q}$ while no such symmetry exists for the interaction coefficient $A(\mathbf{k}, \mathbf{p}, \mathbf{q})$.

It is also possible to write the two-level equations, Eqs. 2.42 and 2.43, in the compact form (Frederiksen, 2007, unpublished manuscript):

$$\frac{\partial \zeta^a_{\mathbf{k}}}{\partial t} = \sum_{\mathbf{p}} \sum_{\mathbf{q}} \delta(\mathbf{k} + \mathbf{p} + \mathbf{q}) \left[K^{a\alpha\beta}(\mathbf{k}, \mathbf{p}, \mathbf{q}) \zeta^{\alpha}_{-\mathbf{p}} \zeta^{\beta}_{-\mathbf{q}} + A^{a\alpha\beta}(\mathbf{k}, \mathbf{p}, \mathbf{q}) \zeta^{\alpha}_{-\mathbf{p}} H^{\beta}_{-\mathbf{q}} \right] - i\omega^a_{\mathbf{k}} \zeta^a_{\mathbf{k}}. \tag{2.53}$$

Here, repeated *Greek* indices are summed over, and $a = 0, 1$. $\zeta^0_{\mathbf{k}} = -k^2 \psi_{\mathbf{k}}$; $\zeta^1_{\mathbf{k}} = -(k^2 + k_i^2)\tau_{\mathbf{k}}$; $H^0_{\mathbf{k}} = \frac{h_{\mathbf{k}}}{2}$; $H^1_{\mathbf{k}} = -\frac{h_{\mathbf{k}}}{2}$ $\omega^0_{\mathbf{k}} = -\frac{\beta k_x}{k^2}$; and $\omega^1_{\mathbf{k}} = -\frac{\beta k_x}{k^2 + k_i^2}$. The explicit forms of the

generalized interaction coefficients in Eq. 2.53 are given by

$$\begin{aligned}
K^{000}(\mathbf{k},\mathbf{p},\mathbf{q}) &= \frac{1}{2}\left(p_x q_y - p_y q_x\right)\left[\frac{1}{q^2} - \frac{1}{p^2}\right] \\
K^{011}(\mathbf{k},\mathbf{p},\mathbf{q}) &= \frac{1}{2}\left(p_x q_y - p_y q_x\right)\left[\frac{1}{q^2+k_i^2} - \frac{1}{p^2+k_i^2}\right] \\
K^{101}(\mathbf{k},\mathbf{p},\mathbf{q}) &= \frac{1}{2}\left(p_x q_y - p_y q_x\right)\left[\frac{1}{q^2+k_i^2} - \frac{1}{p^2}\right] \\
K^{110}(\mathbf{k},\mathbf{p},\mathbf{q}) &= \frac{1}{2}\left(p_x q_y - p_y q_x\right)\left[\frac{1}{q^2} - \frac{1}{p^2+k_i^2}\right] \\
K^{010}(\mathbf{k},\mathbf{p},\mathbf{q}) = K^{001}(\mathbf{k},\mathbf{p},\mathbf{q}) &= K^{100}(\mathbf{k},\mathbf{p},\mathbf{q}) = K^{111}(\mathbf{k},\mathbf{p},\mathbf{q}) = 0.
\end{aligned} \tag{2.54}$$

Additionally,

$$\begin{aligned}
A^{000}(\mathbf{k},\mathbf{p},\mathbf{q}) &= -\frac{(p_x q_y - p_y q_x)}{p^2} \\
A^{011}(\mathbf{k},\mathbf{p},\mathbf{q}) &= -\frac{(p_x q_y - p_y q_x)}{p^2+k_i^2} \\
A^{101}(\mathbf{k},\mathbf{p},\mathbf{q}) &= -\frac{(p_x q_y - p_y q_x)}{p^2} \\
A^{110}(\mathbf{k},\mathbf{p},\mathbf{q}) &= -\frac{(p_x q_y - p_y q_x)}{p^2+k_i^2} \\
A^{010}(\mathbf{k},\mathbf{p},\mathbf{q}) = A^{001}(\mathbf{k},\mathbf{p},\mathbf{q}) &= A^{100}(\mathbf{k},\mathbf{p},\mathbf{q}) = A^{111}(\mathbf{k},\mathbf{p},\mathbf{q}) = 0.
\end{aligned} \tag{2.55}$$

The crucial point is that the interaction coefficients $K^{a\alpha\beta}(\mathbf{k},\mathbf{p},\mathbf{q})$ are symmetric with respect to the exchange $\mathbf{p} \leftrightarrow \mathbf{q}$ and $\alpha \leftrightarrow \beta$ in this formulation. Hence, the two-level spectral equations are then isomorphic to the spectral barotropic vorticity equation (BVE), Eq. 2.48, and this means that many of the theoretical results, particularly the statistical closure theories (see Section 3.3), which have previously been formulated for the BVE, are also easily generalized to the two-level case.

2.8 Generalized Beta Plane Equations

The spectral representation in the previous section assumes periodic boundary conditions, and this means, implicitly, that there is no mean large scale flow. For the more general case, the mean zonal flow is split from the rest of the flow in the BVE, Eq. 2.45. These are the *standard* beta-plane equations. The *generalized* beta-plane equations were introduced by Frederiksen and O'Kane (2005):

$$\frac{\partial \zeta}{\partial t} + J(\psi - Uy, \zeta + h + \beta y + k_0^2 U y) \tag{2.56}$$

and

$$\frac{\partial U}{\partial t} = \frac{1}{S}\int_S h \frac{\partial \psi}{\partial x} dS, \tag{2.57}$$

where S is the area of the domain $S = [0, 2\pi] \times [0, 2\pi] = (2\pi)^2$. Here, the mean zonal flow, U, has been separated from the rest of the flow. ψ and $\zeta = \nabla^2\psi$ are the streamfunction and vorticity of the residual flow, which is the total flow minus the mean zonal flow. The generalized beta-plane equations have an extra $k_0^2 U y$ term. This term can be considered to be a modification of the βy term in the standard beta-plane equations. Its importance is structural (see Frederiken and O'Kane, 2005), rather than quantitative. The ratio $\frac{k_0^2 U}{\beta} = U$, and the dimensionless value of U for a typical dimensional U of 10 ms^{-1} in the atmosphere is given by $U = \frac{10}{a\Omega} \approx 0.02$. Hence the modification is small, being only about 2% of β. A more detailed discussion regarding the motivation for this extra term is given in Appendix B of this thesis.

2.9 Linear Instability Analysis

The QGPV equations generate Rossby waves (Rossby, 1939), which are observable as meanders of jet streams in the atmosphere and of currents in the ocean (Platzmann, 1968; Dickinson, 1978). Rossby waves arise as a result of the variation of the Coriolis parameter with latitude (β). They can also be generated by the spatial variation of topography; the resulting waves are then called topographic Rossby waves (Rossby, 1945; Veronis, 1966; Rhines, 1969). The topography also generates mean patterns known as stationary waves. The QGPV equations are unstable with respect to a form of instability called baroclinic instability (Charney, 1947; Eady, 1949). In the atmosphere, baroclinic instability is associated with synoptic storms, with length scales of around 1000 km. In the ocean, baroclinic instability is thought to be responsible for mesoscale eddies, of length scales around 50 km (Salmon, 1998). We will discuss Rossby waves and topographic Rossby waves by linearizing the generalized barotropic beta plane equations while baroclinic instability will be discussed by linearizing the two level equations, Eqs. 2.42 and 2.43, in the barotropic-baroclinic (BTBC) formulation.

2.9.1 Rossby Waves and Stationary Waves

Consider the generalized barotropic beta-plane equations written as

$$\frac{\partial \zeta}{\partial t} = -J(\psi - Uy, \zeta + h + \beta' y), \tag{2.58}$$

where $\beta' = \beta + k_0^2 U$. We can linearize this equation by assuming that the perturbations ψ and ζ are small, and hence $J(\psi, \zeta) = 0$. The term $J(-Uy, \beta' y) = 0$ by the definition of the Jacobian. Hence, we can write

$$\frac{\partial \zeta}{\partial t} = -\beta' \frac{\partial \psi}{\partial x} - \frac{\partial h}{\partial y}\frac{\partial \psi}{\partial x} + \frac{\partial h}{\partial x}\frac{\partial \psi}{\partial y} - U\frac{\partial \zeta}{\partial x} - U\frac{\partial h}{\partial x}. \tag{2.59}$$

Now, it is convenient to set $U = 0$, and assume that the topographic gradients are constants for reasons that will become apparent later. Hence, defining $\gamma = \frac{\partial h}{\partial x}$ and $\delta = \frac{\partial h}{\partial y}$, where γ and δ are constants, we have

$$\frac{\partial \zeta}{\partial t} = -\beta \frac{\partial \psi}{\partial x} - \delta \frac{\partial \psi}{\partial x} + \gamma \frac{\partial \psi}{\partial y}. \tag{2.60}$$

It can readily be verified that Eq. 2.60 has the solution $\zeta = \exp\left[i(\mathbf{k}\cdot x - \omega_{\mathbf{k}} t)\right]$ (strictly, we need $\zeta = \exp\left[i(\mathbf{k}\cdot x - \omega_{\mathbf{k}} t)\right] + \exp\left[-i(\mathbf{k}\cdot x - \omega_{\mathbf{k}} t)\right]$ to ensure a real solution, but we shall proceed with the complex solution for simplicity). If we substitute this solution in Eq. 2.60, we obtain an expression for the frequency

$$\omega_{\mathbf{k}} = \frac{\gamma k_y - \delta k_x - \beta k_x}{k^2}. \tag{2.61}$$

If no topography is present ($h = 0$), then

$$\omega_{\mathbf{k}} = -\frac{\beta k_x}{k^2}, \tag{2.62}$$

which is the dispersion relation for (beta) Rossby waves. Even without the beta effect ($\beta' = 0$), we obtain waves with dispersion relation

$$\omega_{\mathbf{k}} = \frac{\gamma k_y - \delta k_x}{k^2}. \tag{2.63}$$

These are topographic Rossby waves.

The case $U \neq 0$, $\gamma = \gamma(x, y)$, and $\delta = \delta(x, y)$ is more complicated as there is no plane wave solution. We can simplify matters somewhat by assuming that the topography has the same spatial variation as the solution ψ:

$$\psi(\mathbf{x}, t) = h(\mathbf{x})F(t). \tag{2.64}$$

Then $J(\psi, h) = F(t)J(h, h) = 0$. This removes topographic Rossby waves, so we have

$$\frac{\partial \zeta}{\partial t} = -\beta' \frac{\partial \psi}{\partial x} - U\frac{\partial \zeta}{\partial x} - U\frac{\partial h}{\partial x}. \tag{2.65}$$

Assuming that the solution is sinusoidal in space, but not necessarily in time, we have $\zeta = \zeta_{\mathbf{k}}(t)\exp i(\mathbf{k}\cdot\mathbf{x})$, $\psi = \psi_{\mathbf{k}}(t)\exp i(\mathbf{k}\cdot\mathbf{x})$, and $h = h_{\mathbf{k}}\exp i(\mathbf{k}\cdot\mathbf{x})$, where $\zeta_{\mathbf{k}} = -k^2\psi_{\mathbf{k}}$. Hence,

$$\frac{\partial \zeta_{\mathbf{k}}}{\partial t} = ik_x\frac{\beta'}{k^2}\zeta_{\mathbf{k}} - ik_x U\zeta_{\mathbf{k}} - ik_x U h_{\mathbf{k}}. \tag{2.66}$$

This equation has a non-trivial steady-state for $\zeta_{\mathbf{k}}$:

$$\zeta_{\mathbf{k}} = -\frac{h_{\mathbf{k}} U}{U - \frac{\beta'}{k^2}}, \tag{2.67}$$

or

$$\psi_{\mathbf{k}} = \frac{h_{\mathbf{k}} U}{k^2\left(U - \frac{\beta'}{k^2}\right)}. \tag{2.68}$$

This state is is usually referred to as a stationary wave. It exists even if $\beta = 0$, in which case

$$\psi_{\mathbf{k}} = \frac{h_{\mathbf{k}}}{k^2}. \tag{2.69}$$

Hence the streamfunction is proportional to, and in phase with, the topography in physical space. On the other hand, if $\beta' \neq 0$, there are two possibilities. If $U > \frac{\beta'}{k^2}$ then $\psi_{\mathbf{k}} = \frac{h_{\mathbf{k}} U}{k^2\left|U - \frac{\beta'}{k^2}\right|}$, and the streamfunction in phase with the topography. This is the supercritical

state. If $U < \frac{\beta'}{k^2}$ then $\psi_{\mathbf{k}} = -\frac{h_{\mathbf{k}} U}{k^2 \left| U - \frac{\beta'}{k^2} \right|}$, and the streamfunction is exactly out of phase with the topography. This is the subcritical state. If $U = \frac{\beta'}{k^2}$, then $\psi_{\mathbf{k}}$ has a singularity. However, physically, this is not a problem as dissipation always exists to remove the singularity. The inclusion of the Ekman damping term in the equations of motion is sufficient for this purpose; this will be discussed further in Section 4. The presence of dissipation will also mean that the stationary states are not exactly in or out of phase with the topography as implied here; however, there will still be a distinct phase difference between the subcritical and supercritical states. The inclusion of other topographic modes ($J(\psi, h) \neq 0$) will also alter the critical values of U.

2.9.2 Baroclinic Instability

In this analysis, we closely follow Salmon (1998). Here, we consider the two-level QGPV equations in BTBC form. We split the flow fields in terms of a time-independent mean and time-dependent transient parts:

$$\psi(x, y, t) = \bar{\psi}(x, y) + \psi'(x, y, t), \tag{2.70}$$

$$\tau(x, y, t) = \bar{\tau}(x, y) + \tau'(x, y, t). \tag{2.71}$$

The simplest choice for the mean quantities $\bar{\psi}$ and $\bar{\tau}$ is

$$\bar{\psi}(x, y) = 0, \tag{2.72}$$

$$\bar{\tau}(x, y) = -Uy. \tag{2.73}$$

Here U is a uniform large scale flow. Eqs. 2.72 and 2.73 represent a large scale mean flow U in the upper layer and a large scale mean flow $-U$ in the lower layer. We then substitute Eqs. 2.70 and 2.71, using the mean fields defined in Eqs. 2.72 and 2.73, in the QGPV equations 2.42 and 2.43. We then obtain

$$\frac{\partial}{\partial t} \nabla^2 \psi = -\beta \frac{\partial \psi}{\partial x} - U \nabla^2 \left(\frac{\partial \tau}{\partial x} \right), \tag{2.74}$$

$$\frac{\partial}{\partial t} (\nabla^2 \tau - k_i^2 \tau) = -\beta \frac{\partial \tau}{\partial x} - U \nabla^2 \left(\frac{\partial \psi}{\partial x} \right) - k_i^2 U \frac{\partial \psi}{\partial x}. \tag{2.75}$$

Here we have dropped the primes on the transient quantities ($\psi' \to \psi$ and $\tau' \to \tau$). We have also neglected any product of transient quantities; for example $J(\psi', \nabla^2 \psi')$, or $J(\psi', \nabla^2 \tau')$. This is called *linearization* as the resulting equations are linear in the prognostic variables (ψ and τ).

It is convenient to write Eqs. 2.74 and 2.75 in wavenumber space by expanding $\psi(x, y, t) = \sum_{\mathbf{k}} \psi_{\mathbf{k}}(t) \exp(i\mathbf{k} \cdot \mathbf{x})$ and $\tau(x, y, t) = \sum_{\mathbf{k}} \tau_{\mathbf{k}}(t) \exp(i\mathbf{k} \cdot \mathbf{x})$ so that

$$\frac{\partial}{\partial t} \mathbf{\Psi} = i \mathbf{W} \mathbf{\Psi}, \tag{2.76}$$

where

$$\mathbf{\Psi} = \begin{pmatrix} \psi_{\mathbf{k}} \\ \tau_{\mathbf{k}} \end{pmatrix} \tag{2.77}$$

and

$$\mathbf{W} = \begin{pmatrix} w_{\psi\psi} & w_{\psi\tau} \\ w_{\tau\psi} & w_{\tau\tau} \end{pmatrix}. \tag{2.78}$$

Here

$$w_{\psi\psi} = -\omega^0_{\mathbf{k}} = \frac{\beta k_x}{k^2}, \tag{2.79}$$

where $\omega^0_{\mathbf{k}}$ is the barotropic Rossby wave frequency;

$$w_{\tau\tau} = -\omega^1_{\mathbf{k}} = \frac{\beta k_x}{k^2 + k_i^2}, \tag{2.80}$$

where $\omega^1_{\mathbf{k}}$ is the baroclinic Rossby wave frequency;

$$w_{\psi\tau} = -k_x U; \tag{2.81}$$

and

$$w_{\tau\psi} = -k_x \left(\frac{k^2 - k_i^2}{k^2 + k_i^2} \right) U. \tag{2.82}$$

The general solution of Eq. 2.76 is

$$\mathbf{\Psi} = c_1 \mathbf{v_1} \exp(i\omega_1 t) + c_2 \mathbf{v_2} \exp(i\omega_2 t), \tag{2.83}$$

where ω_1 and ω_2 are eigenvalues of $\mathbf{W}$; $\mathbf{v_1}$ and $\mathbf{v_2}$ are eigenvectors of $\mathbf{W}$; and, c_1 and c_2 are arbitrary constants.

Note that in the absence of mean shear ($U = 0$), the matrix $\mathbf{W}$ is diagonal with its eigenvalues ω being simply (minus) the Rossby wave frequencies $\omega^0_{\mathbf{k}}$ and $\omega^1_{\mathbf{k}}$. Thus the solutions will be

$$\psi = c_1 \exp(-i\omega^0_{\mathbf{k}} t) \tag{2.84}$$

and

$$\tau = c_2 \exp(-i\omega^1_{\mathbf{k}} t). \tag{2.85}$$

These solutions correspond to barotropic and baroclinic Rossby waves respectively.

In the more general case with mean shear, the solution, Eq. 2.83, may be unstable if either of the eigenvalues of $\mathbf{W}$ have positive imaginary parts. This situation corresponds to an exponentially growing wave. These eigenvalues are determined by

$$\omega = \frac{1}{2} \left[(w_{\psi\psi} + w_{\tau\tau}) \pm \sqrt{(w_\psi - w_\tau)^2 + 4 w_{\psi\tau} w_{\tau\psi}} \right], \tag{2.86}$$

and they are imaginary if

$$(w_\psi - w_\tau)^2 < -4 w_{\psi\tau} w_{\tau\psi}. \tag{2.87}$$

This condition corresponds to

$$\beta^2 k_i^4 < 4U^2 k^4 (k_i^4 - k^4). \tag{2.88}$$

If $\beta = 0$, then all wavenumbers $k < k_i$ will be unstable. However, the presence of β means that for $k < k_i$, the instability of a certain wavenumber will also depend on the value of U, the magnitude of the mean shear. Hence for certain values of U, below the critical value $U_c = \frac{\beta^2}{k_i^4}$, there will be baroclinically-stable wavenumbers. Hence linear

theory predicts that β has a stabilizing effect; non-linear theory (see Section 3.2.6) also predicts a stabilizing effect due to β.

Given the instability condition, Eq. 2.88, the most unstable wavenumber is found by maximizing $Im(\omega)$ with respect to k_x and k_y. The result is given in Salmon's textbook (Salmon, 1998) as $\mathbf{k}_{max} = (0.644k_i, 0)$ for $\beta = 0$, and $\mathbf{k}_{max} = (0.841k_i, 0)$ for $\beta \neq 0$ and $U = U_c$. Hence the most unstable wavenumber in both cases is slightly larger than the radius of deformation scale. The most unstable wavenumber is closer to the deformation scale when the beta effect is present; that is, larger scale waves are more stable in that case. The presence of non-linearity, which has been ignored in this analysis, means that wavenumbers which are not very baroclinically unstable may be become destabilized through non-linear interactions. In fact, the most energetic transient waves can turn out to be of scale much larger in size than that implied by linear analysis alone, as we shall see in subsequent chapters, and as discussed, for example, by Gall (1976), Salmon (1980), and Hart (1981).

2.10 Summary

In this chapter, we have introduced the quasi-geostrophic equations, which are simplified equations that may be used to model mid-latitude synoptic-scale motions. We have introduced both the barotropic (depth-independent) equation and the stratified two-level equations. For the stratified equations, an important scale is the internal radius of deformation. The radius of deformation can be described as the minimum scale at which stratification effects are important; for the atmosphere, it was found to be an order of magnitude greater than that for the ocean. We have discussed the spectral representation of the quasi-geostrophic equations. We have also discussed the barotropic generalized beta-plane equations, which are isomorphic to the spherical (differentially rotating) equations. Finally, we performed linear analysis of both the barotropic generalized beta-plane equations with topography and the two-level (baroclinic) equations. From the former, we deduced the existence of Rossby waves and stationary topographic waves, and from the latter, we deduced the existence of baroclinic instability as well as baroclinic Rossby waves. In the next chapter, we shall look at these motions in the presence of turbulence, which arises from the non-linear terms that we have left out in the linear analysis.

Chapter 3

Quasigeostrophic Turbulence

3.1 Introduction

In the first part of this chapter, we shall examine the phenomenology of turbulence. We shall discuss and compare the phenomenologies of three-dimensional, two-dimensional, and quasigeostrophic turbulence (the large-scale turbulence of the atmosphere and ocean). We shall see that quasigeostrophic turbulence contains aspects of two-dimensional behaviour, but has additional features not described by purely two-dimensional dynamics, such as the barotropization of the flow. In the second part of this chapter, we shall examine the statistical theories of turbulence, the Direct Interaction Approximation (DIA) in particular. We shall see that the average effect of turbulent eddies can be described by additional eddy dissipation and stochastic backscatter parameters, which can be combined with the 'bare' dissipation and random forcing to form new 'renormalized' parameters.

3.2 Phenomenology of Turbulence

We shall start this section by introducing the evolution equations for energy and enstrophy in an incompressible fluid described by the Navier-Stokes equations. These equations, and the differences between the three-dimensional and two-dimensional versions, shall then motivate the discussion of three-dimensional and two-dimensional turbulence phenomenology. This is followed by a discussion of the power laws exhibited by the energy spectra in two-dimensional turbulence. Finally, we look at quasigeostrophic turbulence by extending the arguments used for two-dimensional turbulence.

3.2.1 The Energy Balance Equation

The energy balance equation can be derived from the Navier-Stokes equations for an incompressible fluid:

$$\frac{\partial \mathbf{v}}{\partial t} + \mathbf{v} \cdot \nabla \mathbf{v} = -\nabla p + \mathbf{f_v} + \nu \nabla^2 \mathbf{v} \tag{3.1}$$

$$\nabla \cdot \mathbf{v} = 0. \tag{3.2}$$

Here, incompressibility is taken to mean constant density, and we have set the density, $\rho = 1$ for convenience. $\mathbf{v} = (u, v, w)$ is the velocity of the fluid, p is its pressure, f_v is a forcing, and ν is the *molecular* viscosity (as opposed to eddy viscosity). The energy, E, is defined as

$$E = \frac{1}{2} \int_V \mathbf{v} \cdot \mathbf{v} dV. \tag{3.3}$$

Hence, to derive an energy equation for Eq. 3.1, we need to operate with $\mathbf{v}\cdot$ and integrate over the volume, V. Note that the fluid is assumed to be in a solid box so that $\mathbf{v}$ vanishes at the boundaries. After some algebra, we find that

$$\frac{\partial E}{\partial t} = E_s - 2\nu Z, \tag{3.4}$$

where

$$E_s = \int_V \mathbf{f_v} \cdot \mathbf{v} dV, \tag{3.5}$$

is the energy source from the forcing, and

$$Z = \frac{1}{2}\int_V \omega \cdot \omega dV, \tag{3.6}$$

is the enstrophy of the fluid.

3.2.2 The Enstrophy Balance Equation

The enstrophy $Z = \frac{1}{2}\int_V \omega \cdot \omega dV$ is defined in terms of the square of the vorticity, $\omega = \nabla \times \mathbf{v}$, just as the energy, $E = \frac{1}{2}\int_V \mathbf{v} \cdot \mathbf{v} dV$, is defined in terms of the square of the velocity, $\mathbf{v}$. Therefore, to develop an enstrophy equation analogous to the energy equation 3.4, we need to write the Navier-Stokes equation in terms of the vorticity. This is done by taking the curl of the momentum equation, Eq. 3.1. Upon using standard vector identities, including $\nabla \times \nabla p = 0$, which eliminates the pressure, it can be found that

$$\frac{\partial \omega}{\partial t} + \mathbf{v} \cdot \nabla \omega = \omega \cdot \nabla \mathbf{v} + \mathbf{f}_\omega + \nu \nabla^2 \omega \tag{3.7}$$

$$\nabla \cdot \omega = 0. \tag{3.8}$$

Here,

$$\mathbf{f}_\omega = \nabla \times \mathbf{f_v} \tag{3.9}$$

is the vorticity forcing. The first term on the right hand side is known as the vortex stretching term, and is effectively a source term.

The vorticity equations 3.7 and 3.8, in the absence of the vortex stretching term, are isomorphic to the velocity equations 3.1 and 3.2, and thus we can immediately write the enstrophy equation

$$\frac{\partial Z}{\partial t} = Z_s + Z_s' - 2\nu P. \tag{3.10}$$

Here

$$P = \frac{1}{2}\int_V (\nabla \times \omega) \cdot (\nabla \times \omega) dV, \tag{3.11}$$

is the palinstrophy,

$$Z_s = \int_V \mathbf{f}_\omega \cdot \omega dV \tag{3.12}$$

is the enstrophy input, and

$$Z_s' = \int_V \omega \cdot (\omega \cdot \nabla \mathbf{v}) dV \tag{3.13}$$

is the enstrophy production due to the vortex stretching term.

Now, in two dimensions, the vortex stretching term in Eq. 3.7 vanishes because

$\omega \cdot \nabla \mathbf{v} \equiv \omega_i \frac{\partial}{\partial x_i} v_j = \omega_3 \frac{\partial}{\partial x_3} v_3 = 0$ since the vorticity is in the vertical direction, and the vertical velocity is zero in two dimensions. The two-dimensional vorticity equation is thus

$$\frac{\partial \zeta}{\partial t} + \mathbf{u} \cdot \nabla \zeta = f_\zeta + \nu \nabla^2 \zeta. \tag{3.14}$$

Here, $\zeta = \omega \cdot \mathbf{k}$ and $\mathbf{u}$ are the two-dimensional vorticity and velocity respectively. In the absence of forcing and dissipation, the two dimensional vorticity equation becomes

$$\frac{D\zeta}{Dt} = 0. \tag{3.15}$$

Hence the inviscid two-dimensional vorticity equation conserves the vorticity of each fluid parcel.

Unlike the energy equation, which maintains the same form in two dimensions, the enstrophy equation in two dimensions is

$$\frac{\partial Z}{\partial t} = Z_s - 2\nu P \tag{3.16}$$

because of the absence of the vortex-stretching term. This is the underlying reason why the phenomenology of two-dimensional turbulence is different to the phenomenology of three-dimensional turbulence.

3.2.3 Three-Dimensional Turbulence

It is illuminating to write the variables in Eqs. 3.4 and 3.10 in dimensionless form. This enables one to judge the importance of the different terms for various flow parameters. Writing the dimensionless quantities with a tilde, we have $E = U^2 \tilde{E}$, $Z = \Omega^2 \tilde{Z}$, $P = \frac{\Omega^2}{L^2} \tilde{P}$, $E_s = U^2 \Omega \tilde{E}_s$, $Z_s = \Omega^3 \tilde{Z}_s$, $Z'_s = \Omega^3 \tilde{Z}'_s$ and $t = \frac{1}{\Omega} \tilde{t}$. Here L and U are length and velocity scales respectively. Equations 3.4 and 3.10 can then be written as

$$\frac{\partial \tilde{E}}{\partial \tilde{t}} = \tilde{E}_s - \left(\frac{1}{Re}\right) 2\tilde{Z}. \tag{3.17}$$

and

$$\frac{\partial \tilde{Z}}{\partial \tilde{t}} = \tilde{Z}_s + \tilde{Z'}_s - \left(\frac{1}{Re}\right) 2\tilde{P}. \tag{3.18}$$

Here, the Reynolds number of the flow is defined as

$$Re = \frac{UL}{\nu}. \tag{3.19}$$

Typical values, say for the ocean, are $U = 0.1$ ms^{-1}, $L = 1000$ km, and $\nu = 10^{-6}$ m^{2}s^{-1}, giving $Re \sim 10^{11}$. Thus, in general, geophysical flows are very high Reynolds number flows.

A naive scaling would then suggest that we can ignore the viscous term in Eq. 3.17 by taking the infinite Reynolds number (or zero viscosity) limit. However, this implies that there is no dissipation, and hence the energy will increase without bound due to the forcing, something that is not physical. A way out of this conundrum is provided by Eq. 3.18. This suggests that in the limit of vanishing viscosity, the enstrophy in three-dimensional turbulence can grow due to the vortex stretching term, even in the absence of an external forcing term. It can be shown then that the viscous energy dissipation

does not vanish, but instead tends to a non-zero constant value. Vortex stretching, then, is the mechanism by which three-dimensional high Reynolds number flows are able to dissipate energy. A large scale eddy gets stretched and breaks down into smaller eddies, which in turn break down in yet smaller eddies, a process that goes on until molecular dissipation wipes out the motion altogether. The energy transfer to small scales is usually assumed to occur as a cascade. This means that eddies of a particular size break down into slightly smaller eddies, and these in turn break into slightly even smaller eddies. In other words, the energy transfer is local in wavenumber space. This is the physical picture of three-dimensional turbulence (Tennekes, 1985; Frisch, 1995).

3.2.4 Two-Dimensional Turbulence

Geostrophic flows are quasi two-dimensional flows. This is because on a large scale the atmosphere and the oceans are very thin layers of fluid in which the horizontal motions are much greater than the vertical motions. The latter are suppressed because of the effects of rotation and stratification. These two effects will be considered in the next section; however, in this section, we consider the phenomenology of an idealized two-dimensional fluid.

As we saw in the previous section, the vortex stretching term vanishes in two dimensions. This means that there is no enstrophy production term in the absence of external forcing, and hence the viscous energy dissipation rate must vanish for high Reynolds-number two-dimensional flows. On the other hand, it can be shown that the enstrophy dissipation rate does not vanish; instead in the limit of vanishing viscosity there is sufficient production of palinstrophy to yield a non-zero enstrophy dissipation rate (Vallis, 1992). Hence we may guess that in two dimensional turbulence it is the enstrophy that is cascaded to smaller scales, and not the energy as in three-dimensional turbulence.

Another way to think about this is to consider the two-dimensional energy and enstrophy balance equations in the absence of forcing and dissipation:

$$\frac{\partial E}{\partial t} = 0 \tag{3.20}$$

and enstrophy

$$\frac{\partial Z}{\partial t} = 0 \tag{3.21}$$

Equations 3.20 and 3.21 imply that the energy and enstrophy are conserved in an inviscid and unforced two dimensional fluid. The simultaneous conservation of energy and enstrophy can be shown to lead to the prediction that enstrophy is cascaded downscale, which is consistent with the fact the viscous enstrophy dissipation rate is non-zero, and that energy is in turn cascaded upscale, which is consistent with the fact that the viscous energy dissipation rate is zero. Strictly, we need a large-scale sink of energy in Eq. 3.20 and a small-scale sink sink of enstrophy in Eq. 3.21 for this occur, but it is convenient to consider the inviscid equations in deducing the directions of the transfers. Historically, the prediction that energy is transferred upscale and enstrophy is transferred downscale was made by Fjortoft (Fjortoft, 1951), and is thus sometimes known as Fjortoft's theorem. A lucid argument for the direction of the cascades is given by Vallis (2006); this is discussed in Appendix C.

3.2.5 Energy Spectra in Two-dimensional Turbulence

Is it possible to make a more quantitative statement about the energy distribution in a turbulent flow? Kolmogorov attempted to do this, deducing a $k^{-\frac{5}{3}}$ power law for three-dimensional turbulence (see Frisch, 1996, for extensive discussion and references to Kolmogorov's original papers). The arguments that follow are of a similar nature, but adapted for two-dimensional turbulence. The power laws for two-dimensional turbulence were deduced by Kraichnan (1967), Leith (1968), and Batchelor (1969).

As we have seen from the previous section, the picture of two-dimensional turbulence is as follows. Energy is injected at some scale, taken to be an intermediate scale for simplicity of argument, and cascades *upscale* until it is removed by large scale dissipation. The key point in Kolmogorov's argument is that at some range of scales, in between the injection and dissipation scales, the so-called inertial range, the energy spectrum is independent of the details of the injection, such as anisotropy for example. Rather, the spectrum depends only on the flux, ε, and the wavenumber, k. This is reasonable if the transfers are largely local, so that the energy (enstrophy) gradually 'forgets' the details of the injection after several cascade 'steps'. With this assumption, it is also implied that the spectrum should be isotropic in the inertial range.

The power law for the energy spectrum is then deduced by dimensional arguments. The energy $E \sim U^2$ has dimensions of L^2T^{-2}. The flux, ε, which is the rate of energy injection, has units of L^2T^{-3}. The wavenumber, k, has units of L^{-1}. The energy spectrum, $E(k) = \frac{\partial E}{\partial k}$ has units of L^3T^{-2}. The energy spectrum is taken to be of the form $E(k) = C_e\varepsilon^x k^y$, where C_e is an undetermined constant. Dimensionally, we have $L^3T^{-2} = L^{2x-y}T^{-3x}$, from which we can deduce that $x = \frac{2}{3}$ and $y = \frac{5}{3}$. Hence, the inertial range energy spectrum for the inverse cascade should be of the form

$$E(k) = C_e\varepsilon^{\frac{2}{3}}k^{-\frac{5}{3}}. \tag{3.22}$$

For the forward enstrophy cascade the energy spectrum should depend on the enstrophy flux, η, and the wavenumber, k, if Kolmogorov's locality assumption is invoked once again. η, the rate of enstrophy injection, has dimensions of T^{-3} (since the enstrophy, $Z \sim \zeta^2$, and ζ has dimensions of T^{-1}). Using the same dimensional arguments as for the enstrophy cascade, we obtain

$$E(k) = C_z\eta^{\frac{2}{3}}k^{-3} \tag{3.23}$$

for the forward cascade in two-dimensional turbulence. In Eq. 3.23, C_z is an undetermined constant.

We should mention that the two-dimensional turbulence phenomenology has some difficulties associated with it, some of which are discussed by Vallis (1992, 2006). One problem of relevance concerns the prediction of eddy-turnover time. The eddy-turnover time, $\tau(k)$, is the time taken for an eddy of energy $E(k)$ to move a distance $\frac{1}{k}$. Dimensionally, we have

$$\tau(k) = \left[k^3E(k)\right]^{-\frac{1}{2}}. \tag{3.24}$$

For the energy cascade, substitution of Eq. 3.24 in Eq. 3.22 gives

$$\tau(k) = C_e\varepsilon^{-\frac{1}{3}}k^{-\frac{2}{3}} \tag{3.25}$$

while for the enstrophy cascade, substitution of Eq. 3.24 in Eq. 3.23 gives

$$\tau(k) = C_z \eta^{-\frac{1}{3}}. \tag{3.26}$$

Hence, the eddy-turnover time for the enstrophy cascade is independent of the wavenumber. This is paradoxical since it is expected that for there to be a steady-state, the small eddies need to 'spin' faster than the large eddies. This difficulty suggests that Kolmogorov's hypothesis may be significantly violated in two-dimensional turbulence. Improvements to the phenomenology to address this issue have been suggested by Kraichnan (1971).

3.2.6 Quasigeostrophic Turbulence

We are now in a position to discuss quasigeostrophic turbulence, which is the turbulence of large-scale atmospheric and oceanic motions. The continuously-stratified QGPV equation is

$$\frac{Dq}{Dt} = 0, \tag{3.27}$$

where

$$q = \nabla^2 \psi + f + \frac{\partial}{\partial z}\left(\frac{f_0^2}{N^2}\frac{\partial \psi}{\partial z}\right) \tag{3.28}$$

is the three-dimensional quasigeostrophic potential vorticity. If we compare Eqs 3.27 and 3.15, we immediately see that the QGPV equation is isomorphic to the two-dimensional vorticity equation. Furthermore, these equations are the same in the absence of rotation (f) and stratification (vertical derivative term). Two-dimensional turbulence phenomenology, therefore, paints a picture of geostrophic turbulence, but it is not a complete picture. In this section, we shall consider the effects of rotation and stratification separately.

Beta-Plane Turbulence

Two-dimensional turbulence on a beta plane creates large scale zonally elongated structures (Rhines, 1975; Vallis and Maltrud, 1993; Frederiksen et al., 1996). A lucid discussion of this phenomenon is given by Vallis (2006). Consider the barotropic vorticity equation on the beta-plane, without topography:

$$\frac{\partial \zeta}{\partial t} + J(\psi, \zeta + \beta y) = 0. \tag{3.29}$$

In spectral space, we have from Eq. 2.48 (in the absence of topography):

$$\frac{\partial \zeta_{\mathbf{k}}}{\partial t} = \sum_{\mathbf{p}} \sum_{\mathbf{q}} \delta(\mathbf{k} + \mathbf{p} + \mathbf{q}) K(\mathbf{k}, \mathbf{p}, \mathbf{q}) \zeta_{-\mathbf{p}} \zeta_{-\mathbf{q}} - i\omega_{\mathbf{k}} \zeta_{\mathbf{k}}, \tag{3.30}$$

where $\omega_{\mathbf{k}} = -\frac{\beta k_x}{k^2}$ is the Rossby-wave frequency. Now, in the absence of the non-linear terms, the solution to Eq. 3.30 will consist of Rossby waves; that is $\zeta_{\mathbf{k}}(t) = \exp i\omega_{\mathbf{k}} t$. On the other hand, as $k \to \infty$, we have $\omega_{\mathbf{k}} \to 0$, so the Rossby waves are confined to the large scales. We therefore expect that the small scales are dominated by turbulent eddies. If we assume, then, that at large scales Rossby waves dominate, and at small-scales, turbulence dominates, what is the scale at which they are equally important? A simple estimate of this is given by Vallis (2006). The time-scale of the Rossby waves is given by the inverse

Rossby-wave frequency

$$T_r = \frac{k}{\beta}. \tag{3.31}$$

The turbulence time-scale is estimated by

$$T_t = \frac{1}{Uk}, \tag{3.32}$$

which corresponds to a linearly-falling eddy turnover time. Equating Eqs. 3.31 and 3.32, we obtain the beta scale, also sometimes known as the Rhines scale:

$$L_\beta = \sqrt{\frac{U}{\beta}}, \tag{3.33}$$

where $L_\beta = \frac{1}{k_\beta}$. A typical value for β is 10^{-11} m^{-1}s^{-1}. For the atmosphere, $U \approx 10$ ms^{-1}, giving $L_\beta \approx 1000$ km, while for the ocean, $U \approx 0.1$ ms^{-1}, giving $L_\beta \approx 100$ km. These values are very rough estimates, but they do seem to imply that the Rhines scale is close to the radii of deformation of both the atmosphere and the ocean. The Rhines scale is usually interpreted as the scale where the inverse cascade of energy is arrested by the beta effect, although 'arrested' is misleading terminology as discussed further below.

The analysis above assumes that the Rossby wave frequency is isotropic. In reality, the Rossby wave frequency is highly anisotropic, and thus a better estimate for the time scale of the Rossby waves would be

$$T_r = \frac{k_x^2 + k_y^2}{\beta k_x}. \tag{3.34}$$

Equating this to Eq. 3.32, Vallis (2006) obtains

$$\begin{aligned} (k_x)_\beta &= \sqrt{\frac{\beta}{U}} \cos^{\frac{3}{2}} \theta \\ (k_y)_\beta &= \sqrt{\frac{\beta}{U}} \sin\theta \cos^{\frac{1}{2}} \theta, \end{aligned} \tag{3.35}$$

where $\theta = \arctan\left(\frac{k_y}{k_x}\right)$. Plotting k_y against k_x results in a 'dumb-bell' shape with center at the origin ($k_x = k_y = 0$). The inside of the dumbbell describes the region where Rossby waves dominate whereas the outside is dominated by turbulence. Energy injected at an intermediate scale, outside the dumbbell, will cascade upscale as demanded by the quasi two-dimensional nature of Eq. 3.29. Moreover, if there is not sufficient large-scale dissipation, energy will continue to cascade upscale in an anisotropic fashion. The flux of energy will 'avoid' the inside of the dumbbell, but can continue upscale (towards lower wavenumber) by going through the $k_x = 0$ (vertical) axis. In other words, the turbulence will create zonally-elongated structures. Sukoriansky et al. (2006) have questioned the existence of a spectral separation between large-scale Rossby waves and small-scale turbulence. This suggests a different interpretation of the Rhines scale; however, the creation of zonal jets by 'turbulence anisotropization' as described above remains undisputed.

Topographic Turbulence

The interaction between turbulence and large scale topography can create large scale mean fields, which arise spontaneously even if there are no mean fields initially. Bretherton and Haidvogel (1976) used numerical simulations to show that an initially random field over topography eventually becomes correlated with the topography. Salmon et al. (1976) used the methods of equilibrium statistical mechanics to show that a mean state proportional to the topography emerges in an inviscid unforced barotropic fluid. A more extensive review of the literature is given by Holloway (1986).

It is, however, possible to understand this phenomenon using more simplistic arguments as follows. Consider the form drag equation for barotropic flow over topography, Eq. 2.57, written as

$$\frac{\partial U}{\partial t} = T, \tag{3.36}$$

where

$$T = \frac{1}{S}\int_S hv dS \tag{3.37}$$

is the form drag on the zonal flow, U, defined as,

$$U = \frac{1}{S}\int_S u dS \tag{3.38}$$

and the meridional flow is defined as

$$V = \frac{1}{S}\int_S v dS. \tag{3.39}$$

Now, suppose initially there is no mean meridional circulation; that is $V = 0$. However, we imagine that turbulent (transient) eddies exist so that v is not zero everywhere. It is not hard to see then from the definition, Eq. 3.37, that $T = 0$ only if h has no spatial variation; otherwise, in general, $T \neq 0$ even if $V = 0$. Thus, the zonal flow will experience form drag even if there is no mean eddy field initially; this form drag is purely a result of the interactions between transient eddies and the topography.

Stratified Two-level Turbulence

We now consider the effects of stratification. The basic ideas originate from the works of Charney (1971), Rhines (1977), and Salmon (1978). The two-level QGPV equations have two quadratic invariants just like the two-dimensional vorticity equation. The quantities conserved are the *total* energy and *potential* enstrophy. The total energy is inherently a three-dimensional quantity as it contains the coupling between the two levels (the potential energy). This means that to extend the arguments for two-dimensional turbulence to QG turbulence, we must work in three-dimensional wavenumber space (which is nevertheless severely truncated in the vertical for the two-level problem). Hence, for example, analogously to the two-dimensional case, the energy is preferentially cascaded towards lower *three-dimensional* wavenumber, which implies not only larger scales, but also barotropization. This is because barotropic flow can be thought of as having a vertical wavenumber of zero. It turns out that there are three distinct regimes for QG phenomenology: scales near the deformation scale, scales larger than the deformation scale, and scales smaller than the deformation scale. These ideas are explored in more detail in Appendix D.

In summary, the phenomenology of quasigeostrophic turbulence is as follows. Solar

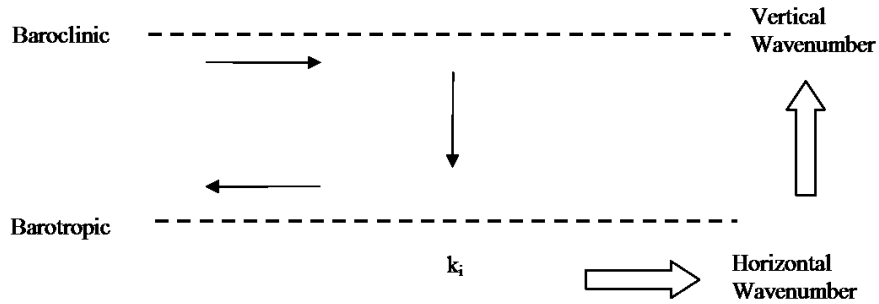

Figure 3.1: Energy transfers in two-layer quasigeostrophic turbulence (directions indicated by arrows).

heating in the atmosphere, or surface winds on the oceans, provides large-scale sources of baroclinic energy in the form of mean vertical gradients. This baroclinic energy may cascade downscale if there is a large-scale instability. However, the principal means by which baroclinic energy, in the form of transients, ends up at smaller scales is via baroclinic instability, which is a non-local interaction. Baroclinic instability is a process where the mean potential energy of the large scale flow is converted into transient kinetic energy. It can be shown using triad interaction arguments, similar to ones employed above, that baroclinic instability is a spectrally non-local process (Salmon, 1978; Salmon, 1998; Vallis, 2006). We can also anticipate this from the fact that baroclinic instability is deducible by linear analysis, where there is no possibility of local non-linear interactions. Both barotropic and baroclinic modes near the deformation scale are excited by this non-local interaction (see Eq. 2.83). Now, at these scales, the baroclinic triads 'mix' barotropic and baroclinic energies; however, because of the simultaneous conservation of total energy and potential enstrophy, baroclinic energy is preferentially cascaded towards the barotropic mode. Once barotropic, the energy cascades upscale via barotropic triad interactions, as in two-dimensional turbulence, until it is removed by large-scale drag, or forced to create large-scale zonally-elongated structures by the beta-effect. Fig. 3.1 shows, schematically, the direction of energy transfers in two-layer turbulence. Potential enstrophy (not shown) injected at the deformation scale by baroclinic instability will be cascaded to larger wavenumbers, for the same reason that energy is cascaded to lower wavenumbers, until it is dissipated. At large wavenumbers the flow is quasi two-dimensional (barotropic); the two layers behave as if they were uncoupled.

3.3 Statistical Closure Theories of Turbulence

3.3.1 Introduction

Consider the two-dimensional vorticity equation in spectral form:

$$\frac{\partial \zeta_{\mathbf{k}}(t)}{\partial t} = \sum_{\mathbf{p}} \sum_{\mathbf{q}} \delta(\mathbf{k}+\mathbf{p}+\mathbf{q}) K(\mathbf{k},\mathbf{p},\mathbf{q}) \zeta_{-\mathbf{p}}(t) \zeta_{-\mathbf{q}}(t). \tag{3.40}$$

The coupling between different space and time scales results in the flow described by this equation becoming chaotic in time; small perturbations to the initial conditions will result in an exponential deviation in time of the perturbed solutions. In principle, if we had access to precise information about the initial conditions, and had sufficient computing capabilities to resolve all scales of motion, then the solution is completely deterministic. In practice, this is obviously impossible, and hence $\zeta_{\mathbf{k}}(t)$ is a random variable. If we try to compute the statistics of $\zeta_{\mathbf{k}}(t)$, however, we run into the closure problem of turbulence, which is as follows. Imagine we have an ensemble of flows at $t = 0$, and we try to evaluate the statistical quantities associated with the ensemble, such as the first and second-order moments (mean and covariance, respectively) at some later time. Denoting ensemble averages by angular brackets, we have, for the first-order moment

$$\frac{\partial \langle \zeta_{\mathbf{k}}(t) \rangle}{\partial t} = \sum_{\mathbf{p}} \sum_{\mathbf{q}} \delta(\mathbf{k} + \mathbf{p} + \mathbf{q}) K(\mathbf{k}, \mathbf{p}, \mathbf{q}) \langle \zeta_{-\mathbf{p}}(t) \zeta_{-\mathbf{q}}(t) \rangle. \tag{3.41}$$

Hence to determine the first-order moment, we need the second-order moment. The equation for the second-order moment on the right hand side of Eq. 3.41 can be written as

$$\frac{\partial \langle \zeta_{-\mathbf{p}}(t) \zeta_{-\mathbf{q}}(t') \rangle}{\partial t} = \sum_{\mathbf{m}} \sum_{\mathbf{n}} \delta(\mathbf{p} + \mathbf{m} + \mathbf{n}) K(\mathbf{p}, \mathbf{m}, \mathbf{n}) \langle \zeta_{\mathbf{m}}(t) \zeta_{\mathbf{n}}(t) \zeta_{-\mathbf{q}}(t') \rangle. \tag{3.42}$$

Equations 3.41 and 3.42 are not closed as the latter contains the third-order moment $\langle \zeta_{\mathbf{m}}(t) \zeta_{\mathbf{n}}(t) \zeta_{-\mathbf{q}}(t') \rangle$. It is not hard to see then that in a turbulent flow, all the moments are coupled; for example, the centroid of the distribution (first-order moment) depends on the tails of the distribution (higher-order moments), and vice-versa. In practice, the statistical quantities of interest are the first and second moments. There is a vast body of work devoted to the problem of closing such as system of equations, usually at the second order. These are statistical closure theories of turbulence.

Now, if the statistics were Gaussian (also known as normal distribution or bell-curve), then we could close the hierarchy of equations because

$$\langle X_1 X_2 X_3 \rangle = 0 \tag{3.43}$$

and

$$\langle X_1 X_2 X_3 X_4 \rangle = \langle X_1 X_2 \rangle \langle X_3 X_4 \rangle + \langle X_1 X_3 \rangle \langle X_2 X_4 \rangle + \langle X_1 X_4 \rangle \langle X_2 X_3 \rangle \tag{3.44}$$

for a Gaussian random variable X. However, we know that the statistics of turbulent flow are not Gaussian. For example, since Eq. 3.42 is effectively an equation for enstrophy (with $-\mathbf{q} = \mathbf{p}$), which is also related to the energy, Gaussian statistics would imply that each mode conserves its enstrophy and energy, which is clearly not the case in turbulent flow; the transfer of energy and enstrophy across scales is a key property of turbulence. Nevertheless, this implies that quasi Gaussian statistics may be appropriate for describing 'weak turbulence', where there is very little transfer of energy among the modes. This is the approach taken (with a twist) in the Direct Interaction Approximation (DIA), originally developed by Kraichnan (1959). In the DIA, it is initially assumed that there is a small expansion parameter, λ, that controls the strength of turbulence, and that at the lowest order, the statistics are Gaussian. The closed equations are then 'renormalized'; this procedure involves a modification of the variables so that the equations have the same

form irrespective of the size of the expansion parameter. Another class of theories known as Quasi Normal Closures close the equations by assuming that at the fourth order the statistics are may be expressed in terms of second order moments as in Eq. 3.44. The third order moment, however, is not taken to be zero, but is solved in terms of the second order moments. The equations then become closed at the second order. A review of the literature is given by Lesieur (1997).

3.3.2 The Direct Interaction Approximation: Barotropic Vorticity Equation

Here, we follow the discussion of the DIA for the barotropic vorticity equation (BVE) given by Frederiksen (2003). The BVE with rotation, forcing, and dissipation can be written as

$$\frac{\partial \zeta_{\mathbf{k}}(t)}{\partial t} = \sum_{\mathbf{p}} \sum_{\mathbf{q}} \delta(\mathbf{k}+\mathbf{p}+\mathbf{q}) K(\mathbf{k},\mathbf{p},\mathbf{q}) \zeta_{-\mathbf{p}}(t) \zeta_{-\mathbf{q}}(t) - D^0_{\mathbf{k}} \zeta_{\mathbf{k}}(t) + f^0_{\mathbf{k}}(t). \tag{3.45}$$

Here $D^0_{\mathbf{k}}$ is an operator defined as

$$D^0_{\mathbf{k}} = \nu^0_{\mathbf{k}} k^2 + i\omega^0_{\mathbf{k}}, \tag{3.46}$$

where $\nu^0_{\mathbf{k}}$ is a wavenumber-dependent viscosity. $\omega^0_{\mathbf{k}}$ is the Rossby-wave frequency. $f^0_{\mathbf{k}}$ is a forcing, frequently taken to be random in nature; physically, it could correspond to an energy injection due to baroclinic instability, for example. It is assumed that the flow is homogeneous; that is

$$\langle \zeta_{\mathbf{k}}(t) \rangle = 0 \tag{3.47}$$

and

$$\langle \zeta_{\mathbf{k}}(t) \zeta_{-\mathbf{l}}(t') \rangle = \delta_{\mathbf{kl}} \langle \zeta_{\mathbf{k}}(t) \zeta_{-\mathbf{k}}(t') \rangle = \delta_{\mathbf{kl}} C_{\mathbf{k}}(t,t'). \tag{3.48}$$

Similar relations must also hold for the forcing function; that is

$$\langle f_{\mathbf{k}}(t) f_{-\mathbf{l}}(t') \rangle = \delta_{\mathbf{kl}} \langle f_{\mathbf{k}}(t) f_{-\mathbf{k}}(t') \rangle = \delta_{\mathbf{kl}} F^0_{\mathbf{k}}(t,t'). \tag{3.49}$$

Furthermore, the forcing is assumed to be white noise, so

$$\langle f_{\mathbf{k}}(t) f_{-\mathbf{k}}(t') \rangle = F^0_{\mathbf{k}}(t) \delta(t-t'). \tag{3.50}$$

The DIA closure equations for the covariance, $C_{\mathbf{k}}(t,t')$, are derived in detail by Frederiksen (2003) for the BVE:

$$\frac{\partial}{\partial t} C_{\mathbf{k}}(t,t') = -\int_{t_0}^{t} ds \left[D^0_{\mathbf{k}} \delta(t-s) + \eta_{\mathbf{k}}(t,s) \right] C_{-\mathbf{k}}(t',s) + \int_{t_0}^{t'} ds S_{\mathbf{k}}(t,s) R_{-\mathbf{k}}(t',s), \tag{3.51}$$

where the response function, $R_{\mathbf{k}}$, is defined as

$$R_{\mathbf{k}}(t,t') = \langle \frac{\delta \zeta_{\mathbf{k}}(t)}{\delta f_{\mathbf{k}}(t')} \rangle, \tag{3.52}$$

and satisfies the equation

$$\frac{\partial}{\partial t} R_{\mathbf{k}}(t,t') = -\int_{t'}^{t} ds \left[D^0_{\mathbf{k}} \delta(t-s) + \eta_{\mathbf{k}}(t,s) \right] R_{-\mathbf{k}}(t',s). \tag{3.53}$$

The terms represented by $\eta_{\mathbf{k}}$ and $S_{\mathbf{k}}$ modify the dissipation and noise covariance, respectively. They are given by

$$\eta_{\mathbf{k}}(t,s) = -4\sum_{\mathbf{p}}\sum_{\mathbf{q}} \delta(\mathbf{k}+\mathbf{p}+\mathbf{q})K(\mathbf{k},\mathbf{p},\mathbf{q})K(-\mathbf{p},-\mathbf{q},-\mathbf{k})R_{-\mathbf{p}}(t,s)C_{-\mathbf{q}}(t,s) \tag{3.54}$$

and

$$S_{\mathbf{k}}(t,s) = 2\sum_{\mathbf{p}}\sum_{\mathbf{q}} \delta(\mathbf{k}+\mathbf{p}+\mathbf{q})K(\mathbf{k},\mathbf{p},\mathbf{q})K(-\mathbf{k},-\mathbf{p},-\mathbf{q})C_{-\mathbf{p}}(t,s)C_{-\mathbf{q}}(t,s). \tag{3.55}$$

The equal-time covariance equation is

$$\frac{\partial}{\partial t}C_{\mathbf{k}}(t,t) = -2Re\int_{t_0}^{t} ds\left[D^0_{\mathbf{k}}\delta(t-s)+\eta_{\mathbf{k}}(t,s)\right]C_{-\mathbf{k}}(t,s)+2Re\int_{t_0}^{t} dsS_{\mathbf{k}}(t,s)R_{-\mathbf{k}}(t,s)+F^0_{\mathbf{k}}(t). \tag{3.56}$$

Note that the integrals persist in the equal-time relations. This is a consequence of the fact that the non-linearity results in coupling not just between different spatial scales, but also between different time scales. In other words, the flow has 'memory'. The covariance equation, Eq. 3.56, reveals something important about the role of non-linear interactions on the flow. This is that the non-linear interactions can act as an effective dissipation *and* as an effective forcing. Not only does turbulence smooth gradients, that is, it acts as an enhanced diffusion, it also injects noise into the system. If we write the the equal-time covariance equation, eq. 3.56, as

$$\frac{\partial}{\partial t}C_{\mathbf{k}}(t,t) = -2Re\int_{t_0}^{t} dsD^r_{\mathbf{k}}(t,s)C_{\mathbf{k}}(s,t)+F^r_{\mathbf{k}}, \tag{3.57}$$

where

$$D^r_{\mathbf{k}}(t,s) = D^0_{\mathbf{k}}\delta(t-s)+\eta_{\mathbf{k}}(t,s) \tag{3.58}$$

and

$$F^r_{\mathbf{k}}(t) = F^0_{\mathbf{k}}(t)+2Re\int_{t_0}^{t} dsS_{\mathbf{k}}(t,s)R_{-\mathbf{k}}(t,s), \tag{3.59}$$

then we can see that $\eta_{\mathbf{k}}$ renormalizes the dissipation, $D^0_{\mathbf{k}}$, while $2Re\int_{t_0}^{t} dsS_{\mathbf{k}}(t,s)R_{-\mathbf{k}}(t,s)$ renormalizes the noise covariance, $F^0_{\mathbf{k}}$. It can be shown (Frederiksen, 2003) that $S_{\mathbf{k}}$ is positive semi-definite, and hence $2Re\int_{t_0}^{t} dsS_{\mathbf{k}}(t,s)R_{-\mathbf{k}}(t,s)$ is also positive semi-definite, which justifies its identification with turbulent noise. $D^r_{\mathbf{k}}$ and $F^r_{\mathbf{k}}$ are called renormalized dissipation and noise covariance, respectively.

Renormalization, as outlined here, has analogies in other areas of Physics. Consider the example given by McComb (1990). Imagine an electron in a plasma. The Coulomb potential, V_0, at a distance, r, from the electron is given by $V_0 = \frac{q_0}{r}$, where q_0 is the 'true' or 'bare' charge of the electron. The electron is however 'screened' by a cloud of charges surrounding it, and it was shown by Debye and Huckel that the effective potential is instead $V_r = \frac{q_r}{r}$, where q_r is the effective, or renormalized, charge of the electron given by $q_r = q_0\exp\left(-\frac{r}{\lambda}\right)$; λ is a length scale dependent on parameters such as electron density. Note that the Coulomb (bare) potential describes a two-body problem (an electron and a test charge). In reality, in a plasma for example, the test charge interacts not only with the electron in question, but also with the cloud of charges surrounding the electron. So it is intrinsically a many-body problem. However, renormalization allows one to treat the

problem as a two-body problem by a suitable redefinition of quantities, the charge in this case. Note also that renormalization only allows one to include the average effects of the charged cloud on the electron, by the introduction of a length scale, but does not reproduce the many-body dynamics in detail. All of these features are generic to a renormalization procedure, and thus have analogies in turbulent fluid dynamics.

This motivates the description of the quantities $D^r_{\mathbf{k}}$ and $F^r_{\mathbf{k}}$ as renormalized quantities, and $D^0_{\mathbf{k}}$ and $F^0_{\mathbf{k}}$ as bare quantities, a terminology used throughout this thesis. $\eta_{\mathbf{k}}$ and $2Re\int_{t_0}^{t} dsS_{\mathbf{k}}(t,s)R_{-\mathbf{k}}(t,s)$ represent the average effects of the turbulent eddies on a particular mode of the flow, analogous to the effects of the charged cloud. They are called the eddy dissipation and stochastic backscatter, respectively. $D^0_{\mathbf{k}}$ and $F^0_{\mathbf{k}}$ are the dissipation and forcing covariance in the absence of turbulence, and $D^r_{\mathbf{k}}$ and $F^r_{\mathbf{k}}$ are the dissipation and forcing covariance and in the presence of turbulence. The renormalization of the DIA (see McComb (1990) or Frederiksen (2003)) is also done in the same spirit. If we imagine that a small expansion parameter, λ, exists, then the perturbation expansion in terms of λ can be truncated at second order, and the equation for the covariance, $C_{\mathbf{k}}$, can be written in terms of second-order moments only; these are the 'bare' equations. Even though there is no small expansion parameter in turbulent flow, renormalized equations can be written, with the variables redefined, so that they retain the same form as the bare equations. This was argued in heuristic terms by Kraichnan (1959); it was later justified by formal analyses (Wyld, 1961; Martin et al, 1972; Phythian, 1977; Jensen, 1981). As with all renormalization schemes, it only incorporates some of the average effects of the higher order terms, and is thus an approximation. The lack of the indirect interactions in this approximation is thought to be the reason why the DIA does not reproduce the correct phenomenological power laws ($k^{-\frac{5}{3}}$ and k^{-3} for the energy and enstrophy cascades, respectively) in the inertial ranges. It does, however, reproduce the statistics of direct numerical simulations quite well at large scales.

There are other closure schemes that have been devised that do reproduce the correct power laws, but they usually involve additional assumptions and arbitrary parameters. Furthermore, they can be derived from the DIA, so the DIA is in some sense the fundamental closure scheme. Two such closure schemes are the Regularized Direct Interaction Approximation (RDIA) and the Eddy-Damped Quasi-Normal Markovian (EDQNM) closures. The RDIA, based on ideas introduced by Kraichnan (1964), assumes that one of the effects of the higher order terms is to limit the interactions to be between similar scales of motion. The localness of the turbulent transfers is after all a fundamental assumption that the power laws are derived from. The RDIA limits the interaction to be between similar scales by modifying the interaction coefficients so that only modes close in wavenumber-space interact. With this modification, the closure reproduces the power laws quite well with a cutoff parameter corresponding to a range of interaction of about six wavenumbers for the case studied (Frederiksen and Davies, 2004). The EDQNM, originally formulated by Orszag (1970a) is in a class of closures called Markovian closures. This means that the integration over different time lags is not explicitly done as in the DIA, which makes it more computationally efficient, but it has an ad-hoc parameter that must be tuned to direct numerical simulations. The EDQNM then reproduces the correct power laws in the inertial ranges as well as being in good agreement with the DNS at other scales (Leith, 1971; Orszag, 1977).

3.3.3 Generalization to Stratified Turbulence

The DIA can be extended to inhomogeneous flows with mean fields and topography in barotropic flows (Frederiksen, 1999); this is called the Quasi-diagonal DIA (QDIA). Additionally, it is possible to generalize this closure methodology to the two-level (baroclinic) equations, written in compact form in Eq. 2.53 (Frederiksen, 2007, unpublished manuscript), and including dissipation and forcing. We only consider the equation for the equal-time covariance $C^{ab}_{\mathbf{k}}(t,t) = \langle \zeta^a_{\mathbf{k}}(t)\zeta^b_{-\mathbf{k}}(t)\rangle$, where superscripts denote vertical wavenumbers, and assume that the mean field is zero:

$$\frac{\partial}{\partial t}C^{ab}_{\mathbf{k}}(t,t) = -2Re\int_{t_0}^{t} ds\,[D^{a\alpha}_{\mathbf{k}}\delta(t-s) + \eta^{a\alpha}_{\mathbf{k}}(t,s)]\,C^{b\alpha}_{-\mathbf{k}}(t,s) + 2Re\int_{t_0}^{t} ds S^{a\alpha}_{\mathbf{k}}(t,s)R^{b\alpha}_{-\mathbf{k}}(t,s) + F^{ab}_{\mathbf{k}}(t), \tag{3.60}$$

where the response function $R^{ab}_{\mathbf{k}}$ satisfies

$$\frac{\partial}{\partial t}R^{ab}_{\mathbf{k}}(t,t') = -\int_{t'}^{t} ds\,[D^{a\alpha}_{\mathbf{k}}\delta(t-s) + \eta^{a\alpha}_{\mathbf{k}}(t,s)]\,R^{b\alpha}_{-\mathbf{k}}(t',s). \tag{3.61}$$

In Eqs. 3.60 and 3.61, the Greek indices are summed over; hence these equations are 2×2 *matrix* equations for each wavenumber. The assumption used in deriving these equations is that the flow is horizontally homogeneous, or quasi homogeneous if mean fields are present, but it is vertically inhomogeneous due to coupling in the vertical. The damping, $\eta^{ab}_{\mathbf{k}}$, and noise, $S^{ab}_{\mathbf{k}}$, coefficients are defined similarly to the corresponding barotropic coefficients, Eqs. 3.54 and 3.55, but they are matrices, rather than numbers, for each wavenumber. The bare dissipation operator is $D^{aa}_{\mathbf{k}} = \nu^a_{\mathbf{k}}k^2 + i\omega^a_{\mathbf{k}}$ with $D^{ab}_{\mathbf{k}} = 0$ if $a \neq b$, where $\nu^a_{\mathbf{k}}$ are viscosities, or hyperviscosities; $\omega^a_{\mathbf{k}}$ are Rossby wave frequencies. The bare noise covariance is $\langle f^a_{\mathbf{k}}(t)f^b_{-\mathbf{k}}(t')\rangle = F^{ab}_{\mathbf{k}}(t)\delta(t-t')$, where $f^a_{\mathbf{k}}(t)$ are random forcing functions acting on the two-level equations, Eq. 2.53, and assumed to represent white noise. Salmon (1978, 1980) and Hoyer and Sadourny (1982) used the EDQNM closure theory to construct similar sets of closed equations for their baroclinic models. Their results were consistent with the phenomenology of QG turbulence.

3.4 Summary

In this chapter, we examined the phenomenology of turbulence, specifically quasi-geostrophic turbulence, the turbulence of large scale atmospheric and oceanic flows. For two-layer quasi-geostrophic flows, it was found that the spectral transfers of energy and enstrophy are more transparent in the BTBC formulation of the two-layer equations as this brings out the isomorphism between two-dimensional turbulence and two-level stratified quasigeostrophic turbulence. In this formalism, there are two modes of transfer; one barotropic, the other baroclinic. The barotropic mode represents the depth-independent motion and is thus phenomenologically the same as two-dimensional turbulence; energy is cascaded upscale and enstrophy is cascaded downscale. The baroclinic mode, on the other hand, has three distinct spectral regimes. Near the deformation scale, the baroclinic mode tends to transfer energy to the large scales via the barotropic mode; that is, there is a conversion of baroclinic energy into barotropic energy. At scales smaller than the deformation scale, the baroclinic mode behaves just like the barotropic mode. And, at scales larger than the deformation scale, the baroclinic mode transfers energy *downscale*. Hence, the baroclinic mode reflects stratification effects, which are absent in the barotropic mode.

We also examined the effect of Rossby waves and topography on turbulence. Rossby waves create an anistropic inverse cascade, where the energy is preferentially cascaded towards the zonal ($m = 0$) modes. Bottom topography is responsible for the spontaneous appearance of a stationary state of the same pattern as the topography; this creates extra drag on the zonal flow, which would be absent without turbulent eddies. After examining phenomenology, we examined closure theories of turbulence, the DIA in particular. It was found that the effect of turbulent eddies is to create not only damping, but also an injection of noise into the system. For homogenous turbulence, explicit expressions for the damping and noise variance may be found from the DIA closure. We also discussed vertically-inhomogeneous turbulence, and concluded that the damping and noise parameters are matrices; this is due to the correlation (coupling) between vertical modes. In both homogeneous and inhomogeneous turbulence, the damping and noise parameters are in the form of time integrals; this reflects the correlation between different temporal scales.

Chapter 4

Multiple Equilibria and Atmospheric Blocking

In the first part of this chapter we investigate the dynamics of multiple equilibria in barotropic flow over topography. We find that a very severely truncated model (STM) consisting of just the zonal flow and the topographically-excited waves is able to simulate the qualitative features of the dynamics quite well. In the second part, we attempt to fit the analytical expression for the stationary wave amplitude, obtained from the STM, to the amplitude obtained from Direct Numerical Simulation (DNS). The 'new' parameters obtained from the fit are the 'renormalized' parameters, as discussed in the previous section. With renormalized parameters, the STM is in better quantitative agreement with the DNS.

4.1 Dynamics

4.1.1 Introduction

Blocking refers to the formation of a quasi-stationary high-pressure system in the atmospheric mid-latitudes. This is associated with a reduction in the strength of the zonal circulation and a corresponding enhancement of the meridional motion, a situation which may persist on a time-scale of the order of a week or longer. In a pioneering study, Charney and DeVore (1979)—hereafter CdV—proposed a possible mechanism for blocking events in the atmosphere with their Multiple Equilibria hypothesis. They proposed that the atmosphere possesses a variety of steady states corresponding to the observed multiple weather regimes, the blocked and unblocked weather patterns being examples thereof. They used a severely truncated barotropic beta-plane model to make their case, finding two stable equilibrium states, which they identified with the above weather patterns, and one unstable state. One of the stable equilibria consists of strong zonal flow and weak wave activity, corresponding to the unblocked regime, while the other has weaker zonal flow and strong wave activity, corresponding to the blocked regime. A similar study was independently conducted by Wiin-Nielsen (1979) using spherical geometry; multiple states were also found in that study.

The physical mechanism which generates multiple equilibria, as proposed by CdV, can be described as follows. Meridional temperature gradients and the Coriolis effect create strong zonal (eastward) jets in mid-latitudes; this effect can be parameterized by an appropriate zonal forcing in a barotropic model. On the other hand, in the presence of topography, a stationary state is generated with the same pattern as the topography. This is effectively a drag on the zonal flow which opposes the zonal forcing. The stationary

state has a maximum amplitude at a critical value of the zonal wind; this critical value, also called the resonant value, is usually lower in value than the zonal forcing. If the flow is subcritical, then a tendency which increases the zonal flow will be accompanied by a tendency for the amplitude of the stationary state to increase, which will create greater drag on the flow, hence possibly offsetting the tendency for the zonal flow to increase. Hence, the flow may stay 'locked' near, and just below, the critical state. If the flow is sufficiently supercritical, however, the amplitude of the stationary state is too weak to cause sufficient drag on the flow, hence the flow will be pushed towards the forcing value. Thus, for some zonal forcing, dissipation, or topographic height parameter values, the flow will settle into either the state with winds near the zonal forcing value or to one with winds near the resonant wind value, depending on the initial conditions.

In severely truncated models (STMs) only a few dominant modes are retained. With this procedure, the hope is that some qualitative features of the full (high resolution) model can be captured by retaining only the 'essential' modes. The essential modes in the CdV problem are the zonal flow and the large scale topographic modes. On the other hand, as the problem is non-linear, one has to parameterize the effects of the discarded modes in some way. Egger (1981) attempted to do this by introducing a stochastic forcing in his STM. He obtained a probability distribution function with maxima corresponding to the stable equilibria found by CdV. Similar studies were conducted, for example, by Benzi et al. (1984), Speranza (1986), and Sura (2002). Another effect of the discarded modes is to facilitate the drain of energy from the retained modes. O'Brien and Branscome (1988), for example, used an artificial damping term to parameterize this effect in their severely truncated two-level baroclinic model. A less ad-hoc approach was taken by Rambaldi and Mo (1984) who constructed a STM which took into account the effects of non-linear interactions excluded by severe truncation.

Even though STMs are useful devices, they still need to stand the test of high resolution simulations. Such experiments have been run, for example, by Tung and Rosenthal (1985) who showed, with a channel model, that the range of parameters for which multiple equilibria are found is reduced when enough modes are retained. Holloway and Eert (1987)—hereafter HE, on the other hand, found that multiple equilibria appear over a wide and realistic range of parameters in a barotropic beta-plane model run at high resolution. The same conclusion was reached by Yoden (1985), using a similar model but with a different method for obtaining the equilibrium points. More recently, Tian et al. (2001) performed experiments on a rotating annulus and found two states resembling blocked and unblocked patterns in the atmosphere; numerical simulation, with a barotropic beta-plane model, of the experiment also yielded two equilibria. Moreover, they found that these states undergo two-way spontaneous transitions over time.

Another issue that arose with this work is the effect of baroclinic instability, a synoptic-scale atmospheric instability not captured by barotropic models. CdV proposed that the instability caused the atmosphere to intermittently switch from one state to the other. Baroclinic models have been investigated, for example, by Charney and Strauss (1980) and by Rheinhold and Pierrehumbert (1982). Both used severely truncated models and found multiple equilibria. However, Cehelsky and Tung (1987) claimed that when enough modes are taken into account in these models, the multiple equilibria do not appear. HE attempted to trigger transitions by introducing random torques in their barotropic model but were unsuccessful. The same was done by Tian et al. (2001), who observed two-way spontaneous transitions in their rotating annulus experiment but did not find any in their numerical simulation, suggesting that simple barotropic models are unable to cap-

ture this process. Of course, as has been pointed out by Tung and Rosenthal (1985), for example, the transitions observed in the atmosphere might be simply due to the different parameters changing; for instance, the zonal driving, which is due to differential heating, changes seasonally. A complementary point of view regarding the role of instabilities in the formation (as well maintenance and decay) of blocks is provided by three dimensional instability theory, as developed by Frederiksen (1982; 1983; 1992). In that study, it is found that baroclinic instability plays an important role in the development of patterns resembling those observed during blocking, particularly in the early stages of their development, with barotropic processes more important in the mature stage. Frederiksen's results are supported by the observational studies of Dole (1986), for example.

Concerns have also been raised whether resonance, which is a crucial element for the existence of multiple equilibria, is possible in spherical models of the atmosphere. High resolution experiments of this type, using barotropic models, have been carried out, for example, by Kallen (1985), Legras and Ghil (1985), and by Gravel and Derome (1993). In some of these experiments, the zonal wind forcing used was of sufficiently high value, e.g. 60 m s^{-1}, as to raise doubts about their realism. However, Yang et al. (1997)—hereafter YRK—showed, with a baroclinic model on a sphere, that multiple weather regimes exist for realistic values of parameters. Furthermore, they hypothesized that the zonal jet structure found in the atmosphere, which is simulated quite well in baroclinic models, plays a part in developing the resonant behaviour needed for the appearance of multiple equilibria in the CdV scenario by confining the Rossby waves in latitudinal bands.

As well as re-examining the theory of CdV, in this section, we seek to address a number of issues raised by previous investigations. These are as follows: (a) the effect of transient eddies on the flow; (b) the effect of a more complex—and more realistic—topography consisting of more than one mode on the system; (c) whether resonance is possible on a spherical (global) domain; and (d) whether the zonal jet structure found in the atmosphere can act as a waveguide as proposed by YRK.

4.1.2 Governing Equations

We use the generalized beta-plane barotropic vorticity equation:

$$\frac{\partial \zeta}{\partial t} = -J(\psi - Uy, \zeta + h + \beta y + k_0^2 U y) - \alpha\zeta - \nu\nabla^4\zeta, \tag{4.1}$$

as discussed by Frederiksen and O'Kane (2005) and in Section 2.8 and Appendix B of this thesis. The large-scale zonal flow, U, which is of particular interest in this study, has been separated from the rest of the flow, with the latter being rather loosely referred to as the 'small-scale' flow. The small-scale flow, minus small-scale zonal components, will at times also be referred to as the 'wavy' flow. Here $\zeta = \nabla^2\psi$, where ψ is the streamfunction and ζ is the vorticity, which correspond to the small-scale flow. J is the Jacobian operator, defined as $J(A, B) = \frac{\partial A}{\partial x}\frac{\partial B}{\partial y} - \frac{\partial B}{\partial x}\frac{\partial A}{\partial y}$. U is the large scale flow, defined as the average zonal flow over the domain. $h = f_0\frac{H}{H_s}$, where H is the topography; H_s is the scale height of atmosphere taken to be approximately 10 km; and f_0 is the Coriolis parameter at the location of the beta plane (which is assumed to be constant over the domain), defined as $f_0 = 2\sin\phi_0$, where ϕ_0 is the latitude at which the beta plane is located. α is the Ekman dissipation constant. ν is the parameter controlling the strength of the scale-selective dissipation, which is needed to limit the growth of the smallest scales retained in our model.

All the variables in this equation have been made dimensionless by scaling the lengths by $L_s = \frac{l}{2\pi}$ and the times by $T_s = \frac{1}{\Omega}$, where l is the size of the square domain that we are considering. The term containing k_0 is a quantitatively minor addition to the β-effect due to solid-body rotation (see Section 2.8 and Appendix B). It has little impact on our study of multiple equilibria, but is included here for completeness and to enable a one-to-one correspondence with the spherical case considered in Section 4.1.6. The corresponding equation for the large scale flow is

$$\frac{\partial U}{\partial t} = \alpha(\overline{U} - U) + \frac{1}{S}\int\int h\frac{\partial \psi}{\partial x}dS. \tag{4.2}$$

Here S is the area of the domain, and $\overline{U}$ is the prescribed value towards which the large scale flow is being relaxed. The latter is usually identified with the transfer of momentum from the tropics to the mid-latitudes.

We work in the spectral domain, which means that the fields (ψ, ζ, and h) are expanded in terms of complex Fourier series. For example,

$$\zeta(\mathbf{x}, t) = \sum_{\mathbf{k}} \zeta_{\mathbf{k}}(t)\exp(i\mathbf{k}\cdot\mathbf{x}), \tag{4.3}$$

where $\mathbf{x} = (x, y)$ are the coordinates in physical space, and $\mathbf{k} = (k_x, k_y)$ are the coordinates in wavenumber space. This choice of basis functions implies that, in physical space, our domain is doubly periodic. The choice of boundary conditions is not crucial for the arguments presented in Sections 4.1.3, 4.1.4, and 4.1.5. We shall address the relevance of the chosen boundary conditions in Section 4.1.7, where we attempt to make connections to realistic atmospheric flows. In the sum, for each value of $\mathbf{k}$ there is a corresponding $-\mathbf{k}$. Note that the Fourier (wave) amplitudes $\zeta_{\mathbf{k}}$, which together with U are the dynamical variables in our model, are in general complex; to ensure that the physical fields are real, we need to impose the condition $\zeta_{-\mathbf{k}} = \zeta^*_{\mathbf{k}}$ (the star, here, implies complex conjugation). We similarly expand the other fields ψ and h.

4.1.3 Severely Truncated Model

Before attempting a direct numerical simulation (DNS) of the above equations at high resolution, i.e., with numerous modes, it is worthwhile to consider a simplified system consisting of only the large scale flow and the topographic Rossby waves. This is a severely truncated model (STM). It is a useful approach as multiple equilibria, in the CdV scenario, arise from the existence of two competing forces: the zonal driving, due to a meridional temperature gradient, which pushes the flow eastward, and the topography, which generates a strong stationary field near the resonant wind value, giving the flow a strong meridional component. We assume that the topography is of the form $h = h_{\mathbf{k}}\exp(i\mathbf{k}\cdot\mathbf{x}) + h_{-\mathbf{k}}\exp(-i\mathbf{k}\cdot\mathbf{x})$; this corresponds to Fourier modes with wavenumbers $\mathbf{k}$ and $-\mathbf{k}$, or a superposition of two plane waves with the same wavenumber but exactly out of phase. We also assume that the 'wavy' field ψ is small so that we can ignore the non-linear term $J(\psi, \zeta)$; this assumption makes the problem analytically tractable, but we cannot ignore the non-linear effects altogether. The parametrization of non-linear effects is, in fact, the central theme of this thesis.

With the above assumptions, Eq. 4.1 becomes linear (see also Section 2.9.1)

$$\frac{\partial \zeta}{\partial t} = -\left(\beta + k_0^2 U\right)\frac{\partial \psi}{\partial x} - U\frac{\partial \zeta}{\partial x} - U\frac{\partial h}{\partial x} - \alpha\zeta. \tag{4.4}$$

Note that the scale selective operator in Eq. 4.1 is no longer relevant in this model. A discussion of an appropriate subgrid-scale parameterization for Eq. 4.4 is given in the second part of this chapter. The spectral forms of Eq. 4.4 and the form drag equation, Eq. 4.2, are obtained by expanding $\zeta = \zeta_{\mathbf{k}}(t)\exp(i\mathbf{k}\cdot\mathbf{x}) + \zeta_{-\mathbf{k}}(t)\exp(-i\mathbf{k}\cdot\mathbf{x})$, $\psi = \psi_{\mathbf{k}}(t)\exp(i\mathbf{k}\cdot\mathbf{x}) + \psi_{-\mathbf{k}}(t)\exp(-i\mathbf{k}\cdot\mathbf{x})$, and $h = h_{\mathbf{k}}\exp(i\mathbf{k}\cdot\mathbf{x}) + h_{-\mathbf{k}}\exp(-i\mathbf{k}\cdot\mathbf{x})$ and substituting in the respective physical space equations. We then obtain

$$\frac{\partial \zeta_{\mathbf{k}}}{\partial t} = -i\omega_{\mathbf{k}}^U \zeta_{\mathbf{k}} - ik_x h_{\mathbf{k}} U - \alpha_\zeta \zeta_{\mathbf{k}}, \tag{4.5}$$

$$\frac{\partial \zeta_{-\mathbf{k}}}{\partial t} = i\omega_{\mathbf{k}}^U \zeta_{-\mathbf{k}} + ik_x h_{-\mathbf{k}} U - \alpha_\zeta \zeta_{-\mathbf{k}}, \tag{4.6}$$

and

$$\frac{\partial U}{\partial t} = \frac{2k_x}{k^2} Im(\zeta_{\mathbf{k}} h_{\mathbf{k}}^*) + \alpha_U(\overline{U} - U), \tag{4.7}$$

where

$$\omega_{\mathbf{k}}^U = k_x\left(U - \frac{\beta + k_0^2 U}{k^2}\right) \tag{4.8}$$

is the Doppler-shifted Rossby-wave frequency, and $\mathbf{k} = (k_x, k_y)$. We have also defined $\alpha_\zeta = \alpha$ and $\alpha_U = \alpha$, for reasons to be apparent later.

It is illuminating to write equations (4.5), (4.6), and (4.7) in the following form:

$$\frac{\partial U}{\partial t} = \frac{2k_x}{k^2} Im(z_{\mathbf{k}}) + \alpha_U(\overline{U} - U) \tag{4.9}$$

$$\frac{\partial}{\partial t} Re(z_{\mathbf{k}}) = \omega_{\mathbf{k}}^U Im(z_{\mathbf{k}}) - \alpha_\zeta Re(z_{\mathbf{k}}) \tag{4.10}$$

$$\frac{\partial}{\partial t} Im(z_{\mathbf{k}}) = -\omega_{\mathbf{k}}^U Re(z_{\mathbf{k}}) - k_x |h_{\mathbf{k}}|^2 U - \alpha_\zeta Im(z_{\mathbf{k}}), \tag{4.11}$$

where

$$z_{\mathbf{k}} = \zeta_{\mathbf{k}} h_{\mathbf{k}}^*. \tag{4.12}$$

Here $Re(z_{\mathbf{k}})$ and $Im(z_{\mathbf{k}})$ are the real and imaginary parts of $z_{\mathbf{k}}$, respectively. $Im(z_{\mathbf{k}})$ is proportional to the topographic drag on the large-scale flow. The topographic drag grows as a result of the interaction between the topography and the large scale flow (Eq. 4.11), and the drag, in turn, acts on the large scale zonal flow (Eq. 4.9). The equilibrium points can be obtained by plotting $Im(z_{\mathbf{k}})$ against U, whose functional forms can be obtained from the steady-state versions of (4.9), (4.10), and (4.11):

$$Im(z_{\mathbf{k}}) = \frac{-k^2 \alpha_U}{2k_x}(\overline{U} - U), \tag{4.13}$$

and

$$Im(z_{\mathbf{k}}) = \frac{-k_x |h_{\mathbf{k}}|^2 \alpha_\zeta U}{(\alpha_\zeta)^2 + (\omega_{\mathbf{k}}^U)^2}. \tag{4.14}$$

Equation 4.13 comes from the form drag equation, (4.9), while Eq. 4.14 comes from (4.10)

and (4.11). The intersection of these two curves yields the equilibrium points. We also obtain an equation for $Re(z_{\mathbf{k}})$:

$$Re(z_{\mathbf{k}}) = \frac{-k_x |h_{\mathbf{k}}|^2 \omega_{\mathbf{k}}^U U}{(\alpha_\zeta)^2 + (\omega_{\mathbf{k}}^U)^2}, \tag{4.15}$$

which, however, does not help us in locating the positions of the equilibria. Equation (4.14) yields the resonance speed, U_{res}, at which the topographic drag becomes a maximum:

$$U_{res} = \frac{1}{(1 - \frac{k_0^2}{k^2})} \sqrt{\left(\frac{\alpha_\zeta}{k_x}\right)^2 + \left(\frac{\beta}{k^2}\right)^2}. \tag{4.16}$$

To determine the phase relationship between the streamfunction and topography in the presence of Ekman dissipation (the inviscid case is discussed in Section 2.9.1), we need to consider the steady state version of Eq. 4.5:

$$\psi_{\mathbf{k}} = \frac{k_x}{k^2} \left(\frac{i}{\alpha_\zeta + i\omega_{\mathbf{k}}^U}\right) h_{\mathbf{k}} U, \tag{4.17}$$

where we have used $\psi_{\mathbf{k}} = -\frac{\zeta_{\mathbf{k}}}{k^2}$. We can also write the streamfunction at steady state as

$$\psi_{\mathbf{k}} = (a + bi) h_{\mathbf{k}} = r \exp(i\theta) h_{\mathbf{k}}, \tag{4.18}$$

where

$$a = \frac{k_x U}{k^2} \left[\frac{\omega_{\mathbf{k}}^U}{(\alpha_\zeta)^2 + (\omega_{\mathbf{k}}^U)^2}\right], \tag{4.19}$$

$$b = -\frac{k_x U}{k^2} \left[\frac{\alpha_\zeta}{(\alpha_\zeta)^2 + (\omega_{\mathbf{k}}^U)^2}\right], \tag{4.20}$$

$$r = \sqrt{a^2 + b^2} = \frac{k_x U}{k^2} \frac{1}{\sqrt{(\alpha_\zeta)^2 + (\omega_{\mathbf{k}}^U)^2}}, \tag{4.21}$$

and

$$\tan\theta = \frac{b}{a} = -\frac{\alpha_\zeta}{\omega_{\mathbf{k}}^U}. \tag{4.22}$$

In physical space,

$$\psi = 2rRe\left\{h_{\mathbf{k}} \exp[i(\mathbf{k}\cdot\mathbf{x} + \theta)]\right\}. \tag{4.23}$$

Hence, in general, there is a phase difference between the streamfunction and the topography. The phase difference is determined from Eq. 4.22. Far away from resonance, $U \gg \frac{\beta + k_0^2}{k^2}$, and hence $\omega_{\mathbf{k}}^U$ is large, which implies that $\theta \to 0$. Thus, in that case, the streamfunction is in phase with the topography. On the other hand, near resonance, $U \approx \frac{\beta + k_0^2}{k^2}$, hence $\omega_{\mathbf{k}}^U$ is small, which implies that $|\theta| \to \frac{\pi}{2}$. Hence, in that case, the streamfunction is out of phase with the topography, being at most 90° out of phase.

As an example on finding the equilibrium points using the three-component system (STM), we use $H(x, y) = H_m \cos(3x)$, where $H_m = 1000$ m, which corresponds to a wavenumber $\mathbf{k} = (\pm 3, 0)$ topography, and from which we can easily work out the wave amplitude $h_{\mathbf{k}} = (\frac{H_m}{2}, 0)$; $\alpha^{-1} = 8.7$ days, $\overline{U} = 13.3$ m s^{-1}, $\beta = 2.0 \times 10^{-11}$ m^{-1} s^{-1} (corresponding to 30° latitude), and l (size of our square domain) = 6000 km. We have also set $k_0 = 0$ in (4.8), which corresponds to the standard beta-plane (see Frederiksen

and O'Kane (2005)). The resulting plots, for $Im(z_{\mathbf{k}})$, are shown as solid lines in Fig. 4.1 for $H_m = 1000$ m. We can see from these plots that multiple equilibria in the CdV model are associated with the resonance peak, at around 2 m s^{-1}, as predicted by (4.16), with the blocked state being close to, but just below, this peak, and a zonal forcing which pushes the flow towards a state where the drag is weak, near 13 m s^{-1}. The intermediate equilibrium is an unstable one. The dotted lines represent $Re(z_{\mathbf{k}})$. We can also obtain the equilibrium points algebraically by solving the cubic equation for U resulting from the elimination of $Im(z_{\mathbf{k}})$ between (4.13) and (4.14). We find that the three-component STM predicts multiple equilibria for the following range of values of H_m: 600 m$< H_m <$3000 m. In the next section, we discuss higher resolution DNS results depicted by asterisks in Fig. 4.1.

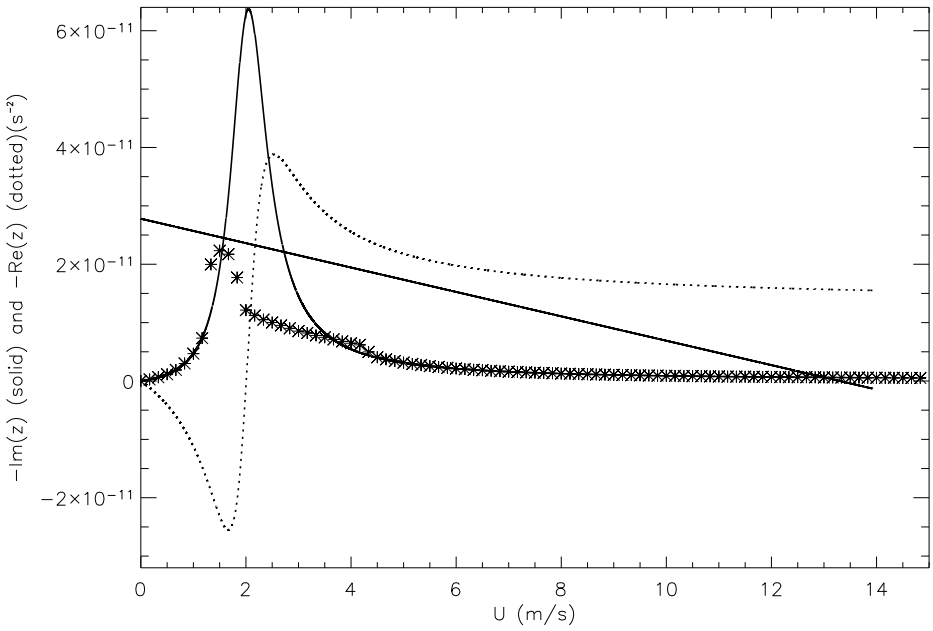

Figure 4.1: Resonance curves at equilibrium for the three-component model (solid line) and for the higher resolution DNS model (asterisks), with $H_m = 1000$ m. The straight line representing the form drag equation is common to both models. The dotted line represents the amplitude of the wave in phase with the topography.

4.1.4 Direct Numerical Simulations

We now carry a DNS of the spectral equations with the maximum circular truncation wavenumber of 16 (C16). We have found, through experimentation, that this truncation wavenumber is sufficient for exploring high resolution behaviour for our chosen parameters. Obviously, for different sets of parameters, this resolution may not be sufficient; for example, if the dissipation is much weaker. Unless otherwise stated, we keep the same set-up and parameters as stated in the previous section. In addition, we set the parameter $\nu = 6.06 \times 10^{13}$ m^4 s^{-1} in (4.1). These values are plausible for the atmosphere and were specified by HE, whose results we seek to confirm (although they did not specify the value of the parameter ν and scale height H_s used). In our experiments, unlike HE, we have not added modes of random amplitude to the sinusoidal topography; this enables us to have

the best possible comparison with the STM results.

The full spectral equations

$$\frac{\partial \zeta_{\mathbf{k}}}{\partial t} = \sum_{\mathbf{p}}\sum_{\mathbf{q}} \delta(\mathbf{k}+\mathbf{p}+\mathbf{q})\left[K(\mathbf{k},\mathbf{p},\mathbf{q})\zeta_{-\mathbf{p}}\zeta_{-\mathbf{q}} + A(\mathbf{k},\mathbf{p},\mathbf{q})\zeta_{-\mathbf{p}}h_{-\mathbf{q}}\right] + i\frac{k_x}{k^2}(\beta + k_0^2 U)\zeta_{\mathbf{k}} - ik_x U\zeta_{\mathbf{k}} - ik_x h_{\mathbf{k}} U - (\alpha + \nu k^4)\zeta_{\mathbf{k}}, \tag{4.24}$$

and

$$\frac{\partial U}{\partial t} = \alpha(\overline{U} - U) - \sum_{\mathbf{k}} \frac{ik_x \zeta_{\mathbf{k}} h_{\mathbf{k}}^*}{k^2}. \tag{4.25}$$

are stepped forward in time using a predictor-corrector algorithm. A more detailed description of the numerical methodology for the DNS is given in the thesis of O'Kane (2003). The interaction coefficients K and A are defined in Eqs. 2.52 and 2.51, respectively.

We start off the flow simulations with both a low initial $U = 2.0$ m s^{-1} and a high $U = 10.0$ m s^{-1} for a range of values of H_m: $0 < H_m \leq 2500$ m. The initial small-scale field is set to zero. The timestep is 1/60 day. We shall, at times, use a scaled time, αt, for convenience (when $\alpha t = 1$, $t = 8.7$ days). A bifurcation results as the parameter H_m is varied, as shown in Fig. 4.2. As H_m is increased from zero, the flows exhibit one (unblocked) equilibrium. Then as H_m reaches a critical value (around 1000 m), the flows suddenly exhibit two equilibria (blocked and unblocked). When H_m reaches another critical value (around 2300 m), the flows suddenly revert to one equilibrium (blocked). All the evolved final flow velocities are for $t = 167$ days. This curve confirms the result obtained by HE although the values for the topography are larger by roughly a factor of two. This might be due to a different scale height (not specified) used in that study. We can see that, at high resolution, the range of values of H_m for which multiple equilibria exist is reduced (now 1000 m< H_m <2300 m) although clearly this range remains significant.

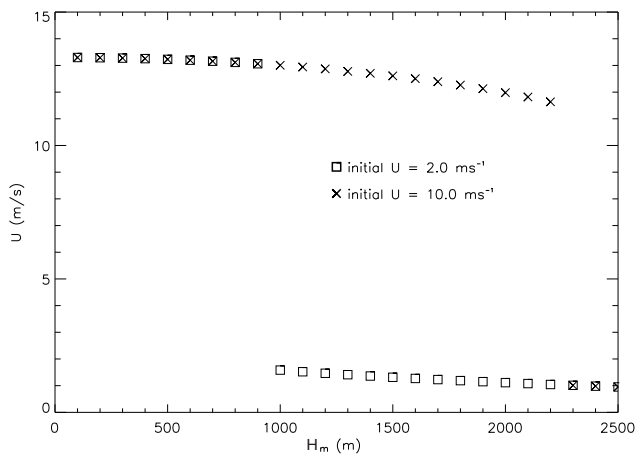

Figure 4.2: Equilibrium values of U for two flows with different initial conditions as a function of maximum topographic height H_m.

The first point to branch in Fig. 4.2, at $H_m = 1000$ m for initial $U = 2.0$ m s^{-1}, is interesting because it enables us to see how adding extra modes affects the low-order system described in Section 3. This is because the flows have been initialized with no energy in the small-scales; thus, in the initial stages the DNS behaves exactly like the

STM model (which has multiple states at this topographic height). When the other modes have picked up sufficient energy, as a result of non-linear interactions, the behaviour of the two systems starts to diverge. As can be seen in Fig. 4.3, the flow seems to settle in the blocked state until $\alpha t \approx 45$ and then suddenly makes a transition to the unblocked state. This brings up the question of whether all the flows in the blocked state eventually end up in the unblocked state. For this system at least, the answer is no: in the long run, the dual states seem to persist once the topography is high enough. We can see this in Fig. 4.4: when $H_m = 1100$ m, after $\alpha t \approx 60$, the flow develops an instability but remains in the blocked state. We have evolved the flow for as long as $\alpha t \approx 320$ but no transition was observed; it appears to have settled permanently in this unsteady equilibrium state.

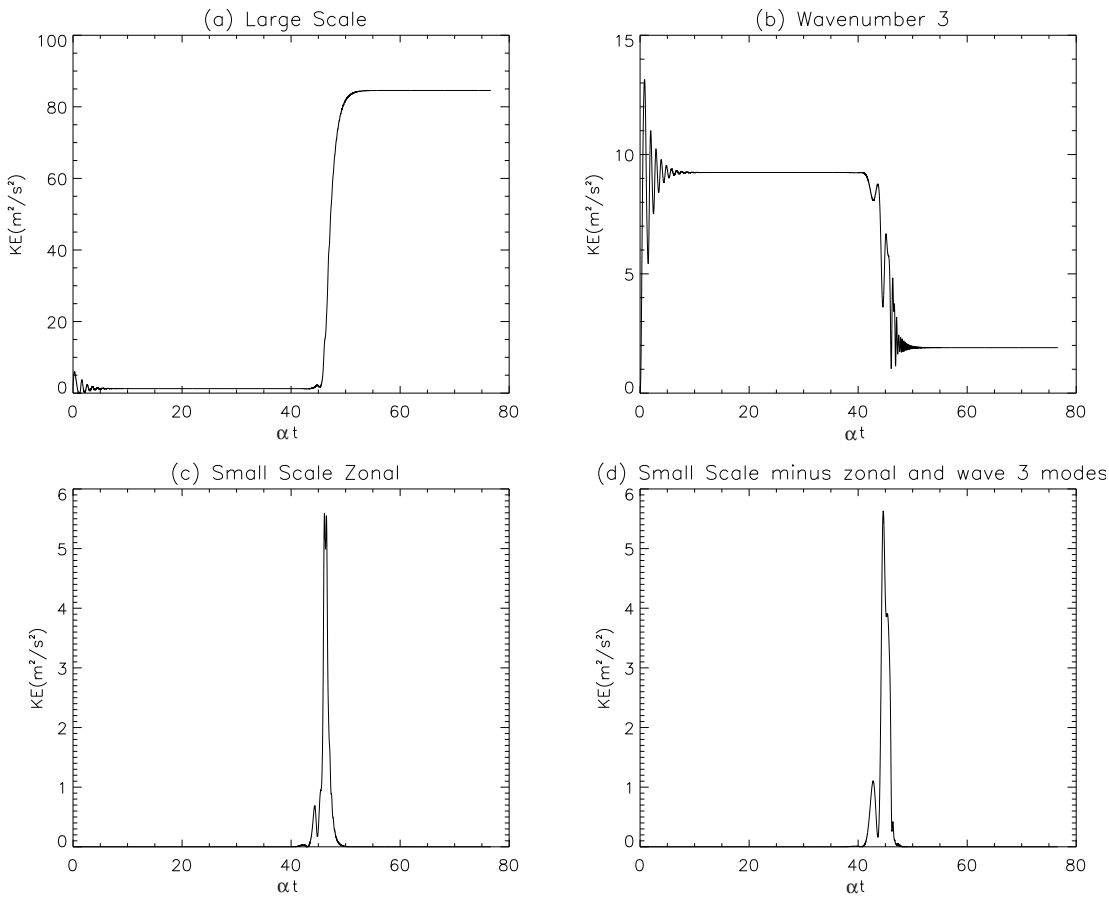

Figure 4.3: Kinetic energy time series of (a) large scale flow, (b) $k_x = \pm 3$, (c) $k_x = 0$, and (d) $k_x \neq 0, \pm 3$ modes for $H_m = 1000$ m

It is worthwhile to take a closer look at what happens to the different components of the flow for both $H_m = 1000$ m and $H_m = 1100$ m. The former being the case where the transient eddies actually 'destroy' the multiple states while the latter being a case where they are preserved. For $H_m = 1000$ m (Fig. 4.3), the small-scale flow is dominated by the $k_x = \pm 3, k_y = 0$ modes, as a result of interaction with the topography, until $\alpha t \approx 40$. When $40 < \alpha t < 50$, the flow suddenly jumps to the unblocked state; during this intermediate time, there is a dramatic drop in wavenumber 3 energy and a subsequent rise in the energies of the other modes while the large scale flow rapidly relaxes towards $\overline{U}$. For $\alpha t > 50$, the wavenumber 3 energy has settled to a lower—but not insignificant—value, and the other modes have vanished. It is important to note that the energy in

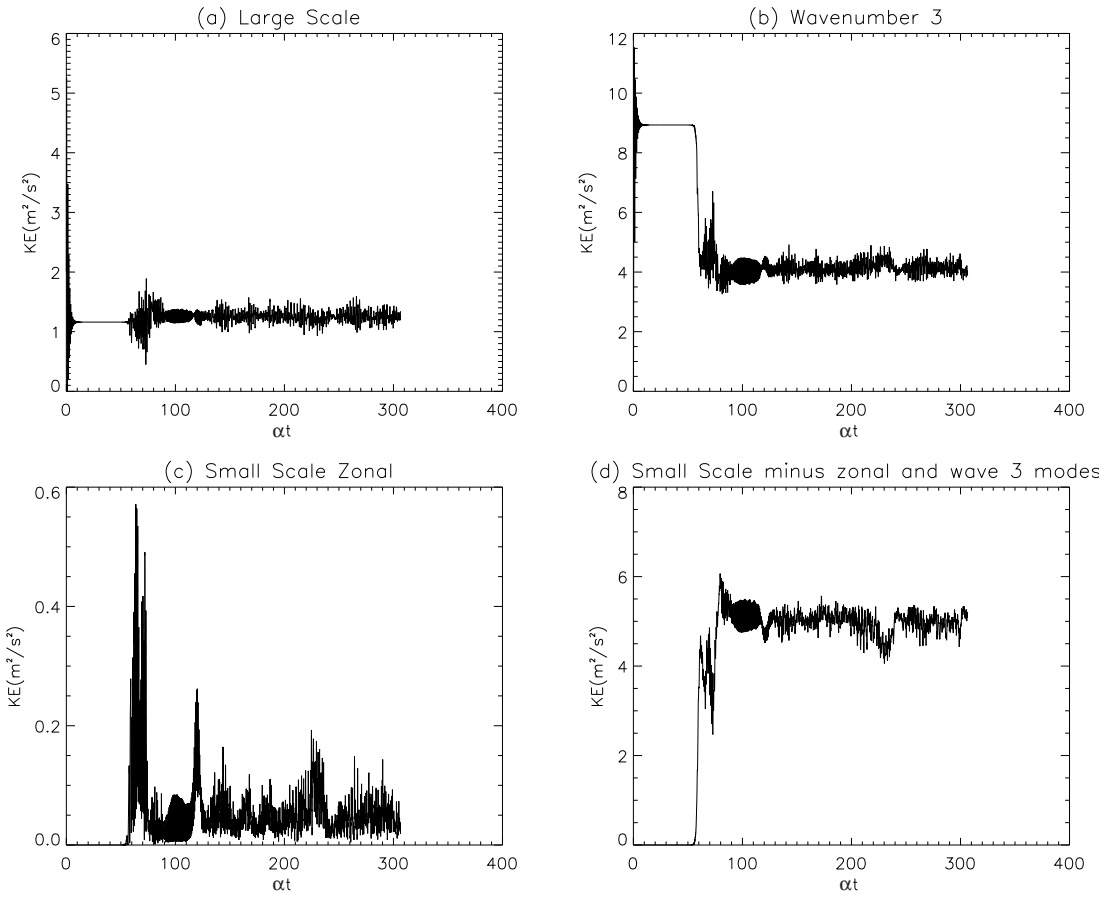

Figure 4.4: Kinetic energy time series of (a) large scale flow, (b) $k_x = \pm 3$, (c) $k_x = 0$, and (d) $k_x \neq 0, \pm 3$ modes for $H_m = 1100$ m

wavenumber 3 that remains in the unblocked state is not due to topographic drag in the flow, of which there is virtually none. We can see this in Fig. 4.5, which shows $Re(z_{\mathbf{k}})$ and $Im(z_{\mathbf{k}})$ ($z_{\mathbf{k}}$ has been defined in (4.12)). It is clear from equation (4.9) that $Im(z_{\mathbf{k}})$ represents the topographic drag on the flow; this drag disappears once the transient eddies have perturbed the system and the flow settles to a higher value of U. The remaining energy in wavenumber 3 is due to the real part of $z_{\mathbf{k}}$.

We have also shown, in Fig. 4.1, the resonance curve (asterisks) for the DNS. When compared to the resonance curve for the STM (solid curve), it is clear that the transient eddies have a damping effect on the stationary wave amplitude; hence, this topographic height represents the boundary at which multiple equilibria start to appear in the high-order system whereas for the low-order system the boundary is for smaller values of H_m. The resonance curve for the DNS has been calculated by evolving the small-scale flow, equation (4.24), with U kept constant, for a range of values of U ($0 \leq U \leq 15$ m s^{-1}). $Im(z_{\mathbf{k}})$, for $\mathbf{k} = (3, 0)$, was then averaged over a series of time-steps once the system had reached a steady state, for each value of U. It is also worthwhile noting that the resonant wind has shifted to a somewhat lower value as compared to the low-order system (STM). A similar effect is seen in the article by Speranza (1986), for example, which discusses the effects of wave-wave interactions on the low-order system.

For the case when $H_m = 1100$ m (Fig. 4.4), the flow is dominated by wavenumber 3 until $\alpha t \approx 60$ after which there is an analogous drop in that wavenumber's energy. The

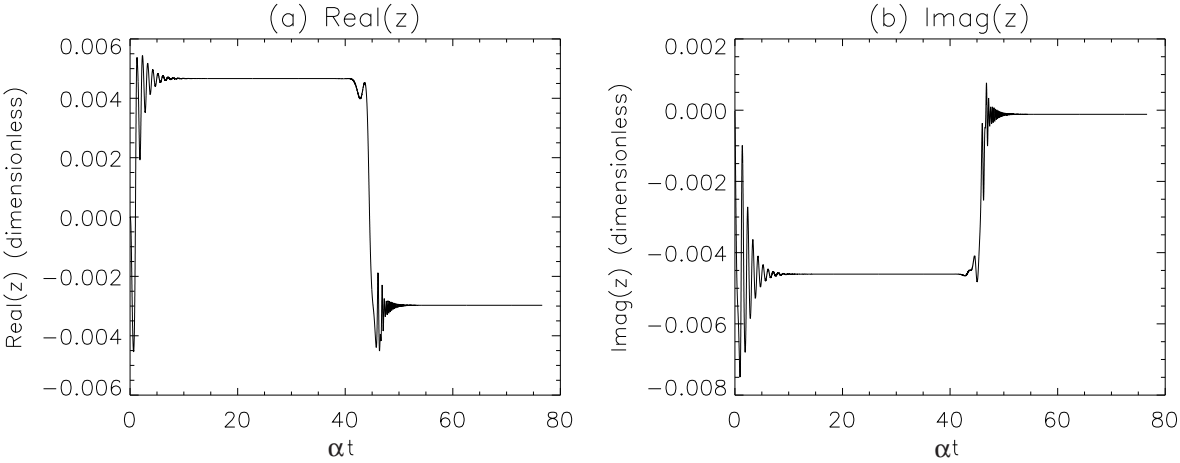

Figure 4.5: Time-evolution of (a) real part, and (b) imaginary part of z for $H_m = 1000$ m, obtained by DNS.

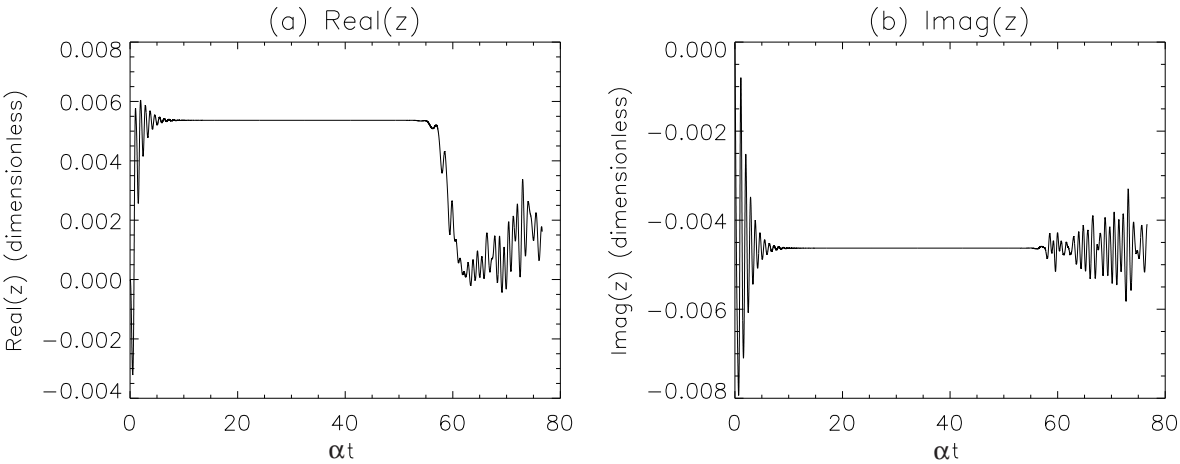

Figure 4.6: Same as in figure 4.5, but for $H_m = 1100$ m.

difference is that the extraction of energy from wavenumber 3 is not sufficient to allow the large scale flow to relax towards $\overline{U}$. The flow instead becomes dominated by transient eddies of various scales. In Fig. 4.6, the diagnostics $Re(z_{\mathbf{k}})$ and $Im(z_{\mathbf{k}})$ show that the mean drag remains more or less the same, even after instability sets in. The drop in wavenumber 3 energy is clearly due to the drop in the real part of $z_{\mathbf{k}}$.

It seems then that, with this simple model at least, the destabilizing effect of the transient eddies is not enough to limit the flow to just one equilibrium state (the unblocked state). Multiple equilibria as envisioned by CdV *can* appear in complex (multi-component) systems like the DNS. In the following sections we explore further a number of issues related to the behaviour of models exhibiting multiple equilibria.

4.1.5 Multi-mode Topographies

In this section, we take one step closer towards more realistic physical systems by considering topographies with more than one mode. How does the simple picture of dual equilibrium states, considered previously, change in this case? By extending the reasoning

of the previous sections, it might be possible to obtain more than one wavy equilibrium state. The reasoning is as follows. If there are several topographic modes of the right magnitudes, then each one could start to resonate at a particular (unique) value of U and therefore lock the flow near that state, leading to many wavy equilibria.

To investigate this possibility, we perform a high resolution experiment with topography of the form $H(x, y) = H_{m1}\cos(x)+H_{m2}\cos(2x)$, where $H_{m1} = 400$ m and $H_{m2} = 1200$ m. This topography consists of the zonal wavenumbers 1 and 2. The reason for this choice is the values of the resonance speeds as determined by equation (4.16): wavenumber 1 has a resonance speed of 18 m s^{-1} while for wavenumber 2 it is 4 m s^{-1}. Thus, for this case, the resonance speeds are well separated, and we have a better chance of observing distinct wavy equilibrium states. Since the resonance speeds fall as n^2, the equilibria tend to be clustered together for higher wavenumbers and hence harder to distinguish in terms of the value of the large-scale flow, U; this is what we wish to avoid. We also use $\overline{U} = 30$ m s^{-1}, $\alpha^{-1} = 18$ days, and $\nu = 3.03 \times 10^{14}$ m^4 s^{-1} in this section.

The results are shown as timeseries plots, after the flow has settled into a steady state, in Fig. 4.7. The large-scale flow has been initialized with three different values of U: 2, 18, and 30 m s^{-1}. The small-scales have been initialized with the same, non-zero, value in all three cases. As can be seen in Fig. 4.7, there are three distinct equilibrium states: the familiar unblocked state with strong zonal flow and relatively weak waves (dashed lines); the wavy state with a strong wavenumber 1 component and lower value of U (dotted lines); and the wavy state with a strong wavenumber 2 component with lowest value of U (solid lines). It is also clear that the latter has much stronger transient activity than the other states. This could be related to the higher values of the zonal wind possessed by the first two states, for, as we saw in the previous section, a high value of U seems to inhibit the growth of other modes in the system. In particular, this might account for the lack of transient activity in the 'wavenumber 1' state.

4.1.6 Global models

So far we have been considering blocking as a localized phenomenon. It is however of interest to consider whether we can use a global model to produce blocks in mid-latitudes. To accomplish this as realistically as possible, we need to use a spherical model. As mentioned in the introduction, most of the investigations using spherical models quoted in the literature, which have found multiple equilibria, required excessive zonal wind forcing not found in nature (greater than 50 m s^{-1}). In this section, we investigate why this is the case.

The generalized beta-plane equations are isomorphic to the spherical set of equations with appropriate replacements (see Section 2.8 and Appendix B). Thus we can immediately write the three-component system (STM) on the sphere:

$$\frac{\partial \zeta_{\mathbf{k}}}{\partial t} = -i\omega_{\mathbf{k}}^{U}\zeta_{\mathbf{k}} - imh_{\mathbf{k}}U - \alpha_{\zeta}\zeta_{\mathbf{k}}, \tag{4.26}$$

$$\frac{\partial \zeta_{-\mathbf{k}}}{\partial t} = i\omega_{\mathbf{k}}^{U}\zeta_{-\mathbf{k}} + imh_{-\mathbf{k}}U - \alpha_{\zeta}\zeta_{-\mathbf{k}}, \tag{4.27}$$

and

$$\frac{4}{3}\frac{\partial U}{\partial t} = \frac{2m}{n(n+1)}Im(\zeta_{\mathbf{k}}h_{\mathbf{k}}^{*}) + \alpha_{U}(\overline{U} - U), \tag{4.28}$$

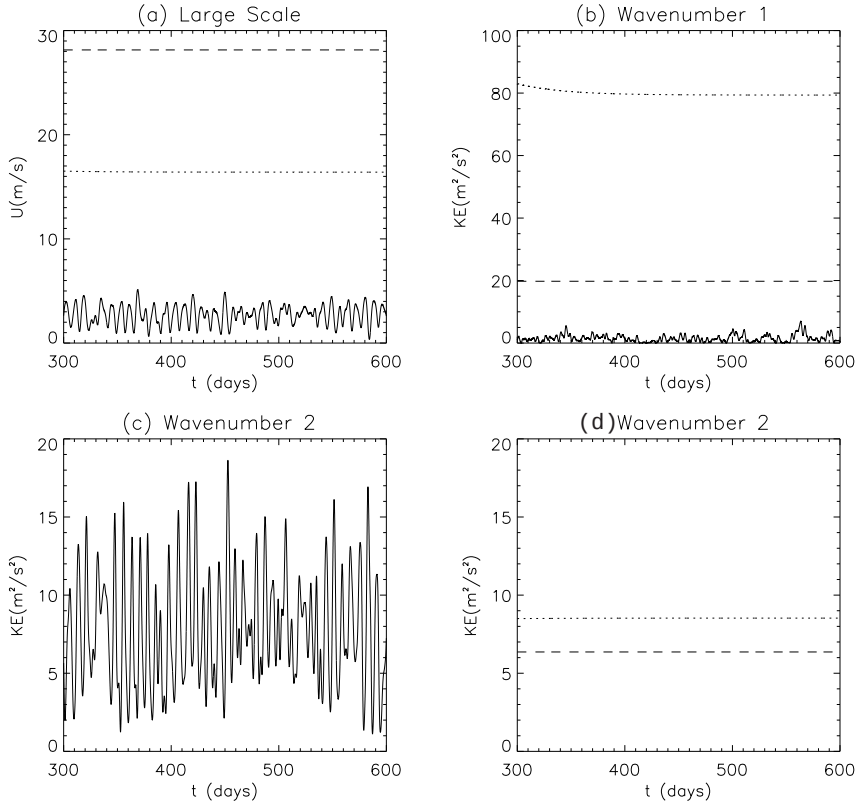

Figure 4.7: Time-evolution of (a) the large-scale flow, (b) wavenumber 1 kinetic energy, and (c) and (d) wavenumber 2 kinetic energy for flow with zonal wavenumbers 1 and 2 topographic components. The flows have three different initial conditions: the solid lines with $U = 2$ m s^{-1}, the short dashed lines with $U = 18$ m s^{-1}, and the long dashed lines with $U = 30$ m s^{-1}. Three distinct equilibrium states emerge as shown.

where

$$\omega_{\mathbf{k}}^{U} = m\left(U - \frac{2+2U}{n(n+1)}\right) \tag{4.29}$$

is, again, the Doppler-shifted Rossby-wave frequency, and $U = \frac{1}{2}\sqrt{\frac{3}{2}}\zeta_{01}$ is the zonal wind at the equator. $\overline{U}$ is defined similarly. Equations (4.26), (4.28), and (4.29) are analogous to (4.5), (4.7), and (4.8). Here we have chosen $\overline{\zeta}_{mn} = 0$ if $(m,n) \neq (0,1)$, which means we are only forcing the (0,1) mode. We have defined $\alpha_\zeta = \alpha$ and $\alpha_U = \frac{4}{3}\alpha$. The vector $\mathbf{k}$ has been defined as $\mathbf{k} = (m,n)$, with $-\mathbf{k} = (-m,n)$. Equations (4.28) and (4.7) differ by the constant factor multiplying the derivative $\frac{\partial U}{\partial t}$ in the former, but the steady state versions of these equations have exactly the same form. Hence, the steady-state expressions (4.13) to (4.16) are valid for the spherical case with the substitutions $k_x \to m$, $k^2 \to n(n+1)$, $\beta \to 2$, and $k_0^2 \to 2$.

The analog of the planar $(3,0)$ mode is the $(m,n) = (3,3)$ mode on the sphere. Using this mode we obtain, from 4.16), and using appropriate replacements, $U_{res} = 93$ m s^{-1}. If we define h with the variable Coriolis parameter (that is $h = 2\mu\frac{\Delta}{H}$—see Section 2.5), then this introduces a factor of μ. Hence, in that case, we need to use $(m,n) = (3,4)$ for h and ζ in our equations if the topography, H, consists of the wavenumber $(3,3)$. Using this mode, we find that the resonant speed reduces to 51 m s^{-1}; however, this is still

a substantial value. This might explain why spherical models need such unrealistically strong wind forcing for multiple equilibria to appear, for, as we saw in the planar case, the low-index state occurs near resonance while the high-index state occurs far away from resonance. This means that we need a forcing substantially greater than 51 m s^{-1} to observe the dual states. The difference in resonant speeds between the planar, regional model and the spherical, global model is partly due to geometry and partly due to domain size.

To see the effect of domain size, consider what happens if we 'scale-up' our localized beta-plane so that it 'covers' the whole globe but keep the original *dimensional* value of β. If we denote by U^{old}, the typical speed in the former (smaller) domain; U^{new}, the corresponding speed in the new (larger) domain; L_s^{old}, the length scaling in the old domain; and L_s^{new}, the scaling in the new domain, then it is easy to show that

$$U^{new} = \left(\frac{L_s^{new}}{L_s^{old}}\right)^2 U^{old}. \tag{4.30}$$

Let us choose the new (global) scaling such that the (non-dimensional) domain is still $[0, 2\pi] \times [0, 2\pi]$ but the (dimensional) surface area now being equal to $4\pi a^2$. This gives $L_s^{new} = \frac{a}{\sqrt{\pi}}$ while $L_s^{old} = \frac{3000}{\pi}$, in km, as in section 2. Using equation (4.30), this implies that the $U_{res}^{old} \approx 2$ m s^{-1} is 'equivalent' to $U_{res}^{new} \approx 28$ m s^{-1} in the new, 'global', domain. Thus, the low-index state would have zonal winds near this value; the high-index state would have values (talking the old 13.3 m s^{-1} as typical) near 188 m s^{-1}, which is unrealistic. On the face of it, this suggests that it might not be appropriate to consider multiple equilibria as arising from *global* resonance of Rossby waves.

4.1.7 Zonal jets and confinement of Rossby waves

We have seen in the previous section that if we simply scale up our regional model onto the globe, either in planar or spherical geometry, the parameters required to sustain multiple equilibria fall into an unrealistic range. On the other hand, if we view the multiple equilibria as a regional phenomenon, what is the mechanism responsible for confining the waves in a given region? YRK have suggested that the zonal jet structure found in the atmosphere, with strong westerlies at mid-latitudes and easterlies both equator-ward and pole-ward, results in confinement of the topographic waves generated in northern hemisphere mid-latitudes, and hence the possibility for *regional* resonance.

To test this idea further, we have scaled up our beta-plane model onto a global domain. This may result in some distortion of the flow outside the mid-latitude regions; however, the waveguide effect of the zonal jets ensures that the mid-latitude flow, which is primarily due to the interaction between the large scale zonal flow and topographic stationary waves in our model, is largely unaffected by this. To keep the non-dimensional form of the equations the same, we have placed the beta-plane at 60 degrees North. This ensures that the model domain remains a square. To obtain a jet structure reminiscent of that found in the real atmosphere or that obtained from more complex models, we have added a term of the form $\alpha\zeta_*(t)$ to the vorticity equation (4.1), where ζ_* is given by $\zeta_*(t) = 2A\cos(\mathbf{k}\cdot\mathbf{x})$, and we choose $\mathbf{k} = (0, \pm 2)$. A is an amplitude chosen so that in this case the maximum strength of the jet is 17.5 m s^{-1} (at 45 degrees). Together with a uniform relaxation, $U_* = 12.5$ m s^{-1}, over the whole domain, this gives a maximum wind of 30 m s^{-1} at 45 degrees and a minimum of -5 m s^{-1} at the equator and poles. We choose a relaxation time $\alpha^{-1} = 10$ days.

Fig. 4.8 demonstrates that the jet structure confines the topographic wave within latitudinal circles (in mid-latitudes). In this experiment, we have placed a conical mountain with a radius of 22.5^o and height $h_C = 3275$ m at 45° North, 180° East. The figure shows the eddy-streamfunction, which is the streamfunction with zonal components removed. Clearly the topographic wave is mainly confined in the region of the Westerly winds, which is between 22.5^o and 67.5^o North. The waves do not propagate outside of this region as the jet structure acts as a waveguide, confining them within this latitudinal band. To further demonstrate that the waveguide effect of the jet structure is responsible for this, we carry out experiments without such jets but with U_* simply relaxed to 30 m s^{-1} over the whole domain. The result is shown in Fig. 4.9. In this case, the topographic wave propagates over the whole domain as is evident in that figure.

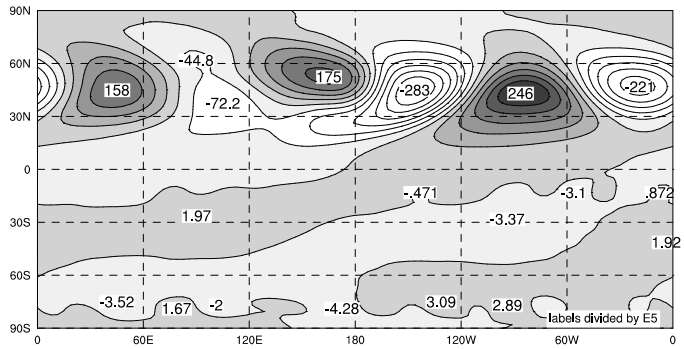

Figure 4.8: Eddy streamfunction contour plot showing topographic waves in 'blocked' state in the presence of latitudinally dependent jets for Northern Hemisphere conical mountain.

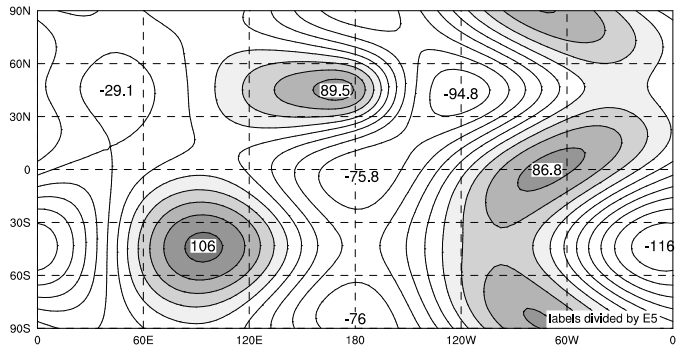

Figure 4.9: Eddy streamfunction contour plot showing topographic waves propagating throughout the domain when no latitudinally-dependent jet structure is imposed.

Having confirmed that the jet structure can effectively confine the topographic waves to localized regions and hence potentially lead to (local) resonance needed for multiple equilibria in the CdV scenario, we now investigate whether such multiple states do indeed occur. To achieve this with as much realism as possible, we use a representation of the Earth's topography as shown in Fig. 4.10. We have discovered robust multiple equilibria in the vicinity of the following values of parameters: A corresponding to a maximum of 50 m s^{-1} and $U_* = 40$ m s^{-1}, giving a maximum wind of 90 m s^{-1} at 45° and a minimum of -10 m s^{-1} at the equator and poles; $\alpha^{-1} = 20$ days; and $\nu = 6.06 \times 10^{14}$ m^4 s^{-1}. Fig. 4.11 shows the zonal winds averaged over a latitudinal band between 22.5^o and 67.5^o. The flows have been initialized with two different zonal winds: high (90 m s^{-1}) and

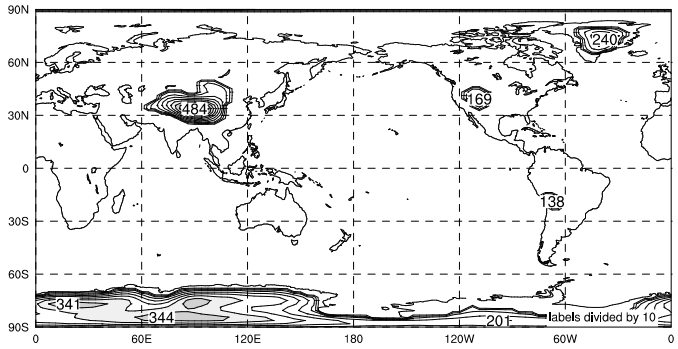

Figure 4.10: Global distribution of topography used in the experiment of Section 7. Only the highest elevations are shown.

low (2 m s^{-1}). We indicate with solid lines the flows in the (more interesting) Northern Hemisphere and with dotted lines the corresponding flows in the Southern Hemisphere. The Northern Hemisphere flow is clearly bimodal with a high wind state consisting of weak transients and a low wind state with stronger transients. The Southern Hemisphere flow also seems to have two very closely spaced equilibrium states. This is probably due to stationary waves excited by the relatively weaker topography that is present in the mid-latitudes of that hemisphere. Fig. 4.12 shows the timeseries plot of wavenumber 2 kinetic energy for the two states. Clearly it is much stronger in the blocked state than in the unblocked one. It is also clear that in the blocked state (upper curve), there are more interactions between different wavenumbers as is evident from the more complicated patterns of fluctuations than those in the unblocked state. This is consistent with the studies of the simpler models of the previous sections. Zonal wavenumber 2 is the dominant resonating mode in this experiment even though the topographic distribution is dominated by zonal wavenumber 1 rather than 2. The reason for this is that the resonant speed of the former is a formidable 116 m s^{-1}, as calculated from equation (4.16), which is probably not observable in the Earth's atmosphere. Figures 4.13 and 4.15 show the instantaneous zonal wind contours for the two states. The former shows the blocked state, with reduced winds and pronounced meanders in the Northern Hemisphere, while the latter shows the unblocked state with its stronger, more zonal winds in both hemispheres. Figures 4.14 and 4.16 show the corresponding contours of the eddy-streamfunction. Clearly the blocked state has 'stronger' highs and lows than the unblocked state, i.e., the stationary waves in the blocked state have a stronger amplitude. Another thing that is apparent from these contours is that there is a phase difference between the waves in the two states. The streamfunction contours in the unblocked state are roughly correlated with the topography while in the blocked state they are not; in fact, in the Northern Hemisphere mid-latitudes, in particular, they seem to be anti-correlated. This is quite consistent with the discussion of Section 4.1.3, where we saw that in the unblocked state the waves are in phase with the topography while in the blocked state they are out of phase. Although our global model is more complex than that described in Section 4.1.3, we can still see this behaviour. We can also deduce the positions of the centers of the 'blocks' (two of them) from these figures by locating the positions of the highs in the eddy-streamfunction contours or, alternatively, from the positions of maximum poleward deflection of the zonal wind contours. It is interesting that these positions, near 0° and 180° longitude, are at, or slightly to the west of the longitudinal positions of the observed North Atlantic and North Pacific blocks respectively.

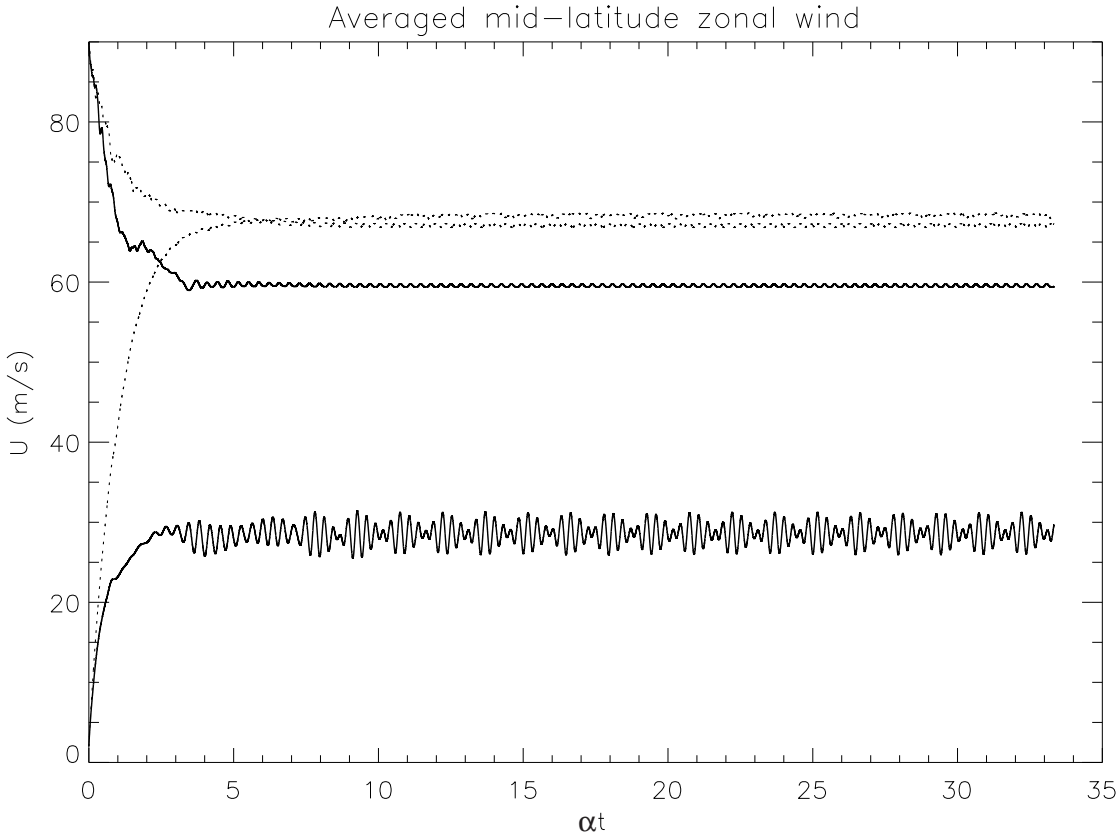

Figure 4.11: Zonal winds averaged over a mid-latitude band. The solid lines are for the Northern Hemisphere while the dotted lines are for the Southern Hemisphere. Two flows are shown, with different initial conditions. The Southern hemisphere flows converge to two very finely spaced equilibria while the Northern Hemisphere ones have two distinct equilibria.

The values of the winds used in this experiment are probably larger than what would be expected in the atmosphere. However, we should note that there are many unknowns and features that have only been crudely represented in our model such as the effect of zonally asymmetric heating, the precise latitudinal profile of the zonal jets, and the appropriate relaxation time for the jet structure as compared to the Ekman dissipation time-scale, to mention just a few. Ambiguous interpretations of the barotropic vorticity equation as the vertically-averaged flow or as the flow at a particular vertical level (Tung, 1985) means that the range of realistic parameters is potentially large, which could easily account for the higher than expected winds.

4.2 Parameterization of Non-linear Interactions

We found in Sections 4.1.3 and 4.1.4 that the severely truncated three-component system (STM) is a very useful device for understanding and predicting the behaviour of the DNS. However, we also found some significant differences between the two models. These differences arise because of the absence of non-linear interactions in the STM. In this section, we shall attempt to improve the performance of the STM, so that it is better able to simulate the broad results of the DNS while still maintaining its simple structure.

First of all we summarize the crucial differences between the models as depicted in

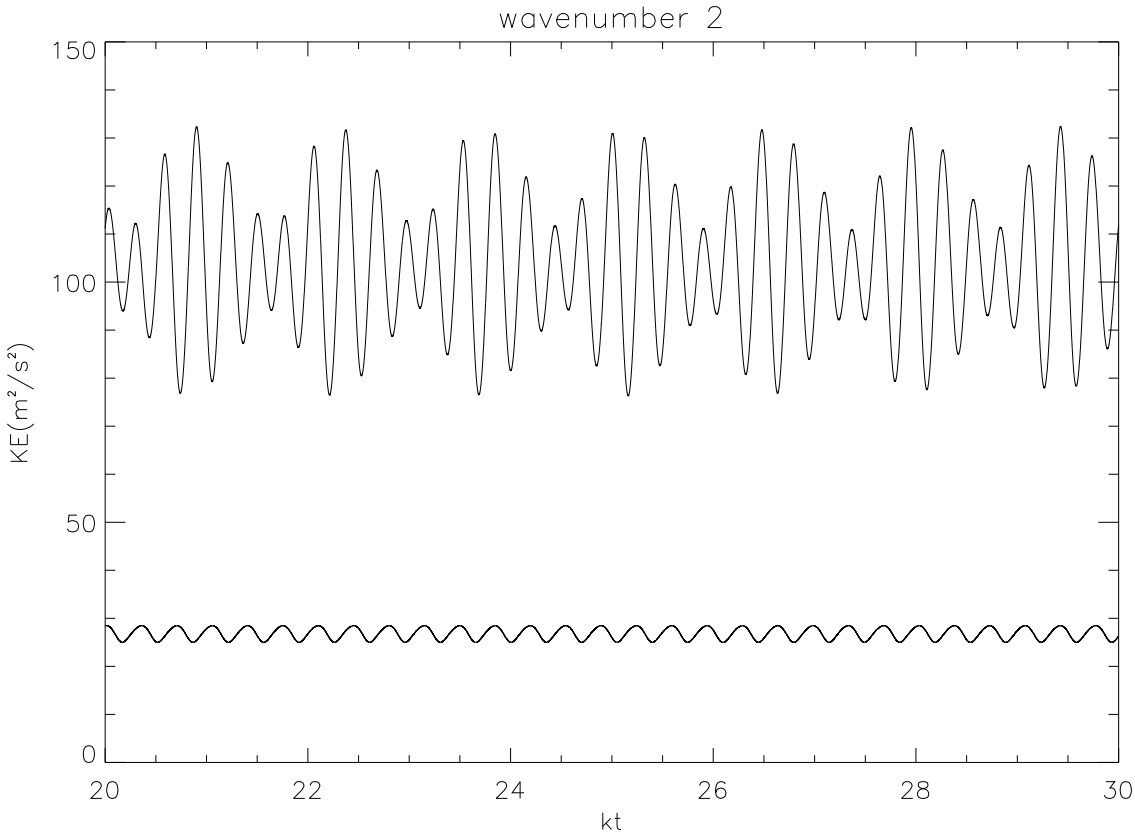

Figure 4.12: Time series of wavenumber 2 kinetic energy in a (statistically) steady state. The top curve is the 'blocked' flow while the bottom one is 'unblocked'.

Fig. 4.1. The drag, $Im(z_{\mathbf{k}})$, on the large scale flow in the three-component system has a higher peak, which is more than three times the corresponding drag in the C16 DNS. Moreover, the peak in the STM occurs for higher values of U than that for the C16 DNS. The differences between the two models are only apparent for $1 < U < 5$ ms^{-1}; outside of this range, the two models are in excellent agreement. The physical reason for this is not hard to understand. The stationary wave amplitude is only significant in the previously mentioned range; hence, it is only in this range that a topographic instability emerges once the amplitude reaches some critical value. Outside of this range, there is no other source of instability in this problem, hence the STM is sufficient for describing the system as other modes are not excited. The phenomenology of topographic turbulence also tells us that once transient eddies are excited, they will contribute to the drag on the large scale flow via the topography. Hence, the curve in Fig. 4.1 (from the C16 DNS) is the net result of two processes: the reduction of the drag due to non-linear instability of the stationary wave, and its enhancement due to interaction between transient eddies and topography. The net effect is clearly a reduction of the drag. The reduction of the topographic drag may be parameterized by imposing a stronger dissipation coefficient α (see Eq. 4.14). However, this alone will not shift the peak of the curve to lower values of U. To accomplish this we need to adjust the frequency $\omega_{\mathbf{k}}^U$ as well. It is convenient to think of the shift in $\omega_{\mathbf{k}}^U$ as arising due to a shift in β. Thus, a lower value of β will result in $\omega_{\mathbf{k}}^U$ vanishing at a lower value of U, and hence the peak of the curve will also shift in the same direction. This suggests that it may be possible to parameterize the effect of the non-linear interactions

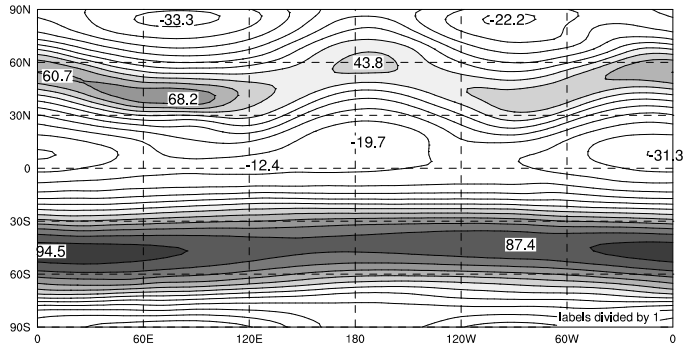

Figure 4.13: Zonal wind contour plot in 'blocked' state in the presence of latitudinally dependent jets with underlying topography of figure 4.10.

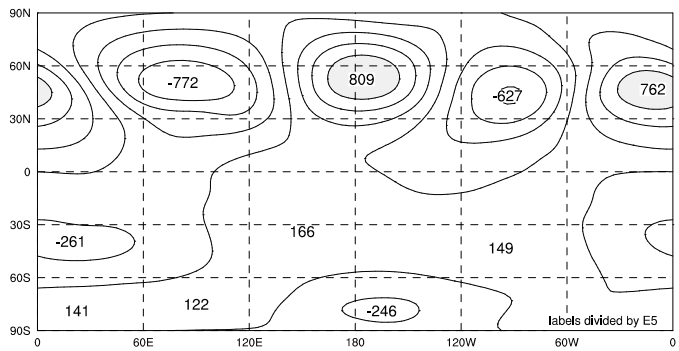

Figure 4.14: Eddy Streamfunction contour plot in 'blocked' state in the presence of latitudinally dependent jets with underlying topography of figure 4.10.

on the drag by increasing the dissipation coefficient, α, and reducing β.

It is possible to calculate effective coefficients α_r and β_r by inverting the three-component expressions, Eqs. 4.14 and 4.15, and using the values of $Re(z_{\mathbf{k}})$ and $Im(z_{\mathbf{k}})$ from the C16 DNS. Hence,

$$\alpha_r(U) = \frac{-k_x|h_{\mathbf{k}}|^2 U Im(z_{\mathbf{k}})}{|z|^2}. \tag{4.31}$$

and

$$\omega_r(U) = \frac{-k_x|h_{\mathbf{k}}|^2 U Re(z_{\mathbf{k}})}{|z|^2}. \tag{4.32}$$

Thus, with $\omega_r(U)$ from Eq. 4.32, we obtain from Eq. 4.8:

$$\beta_r(U) = k^2\left(U - \frac{\omega_r(U)}{k_x}\right) - k_0^2 U. \tag{4.33}$$

The effective parameters α_r and β_r are shown in Figs. 4.17 and 4.18, respectively, as functions of U. The effective dissipation coefficient, α_r, as expected, is stronger than the actual Ekman drag coefficient, α, by as much as a factor of 5 at $U = 2.3$ ms^{-1}. This can be regarded as the parameterization for the net effect of stationary wave amplitude reduction, due to non-linear instability, and its enhancement due to coupling between transient eddies and the topography. Clearly, the loss of amplitude is the dominant effect. The effective change in the Coriolis parameter, β_r, is on the other hand weaker, reducing

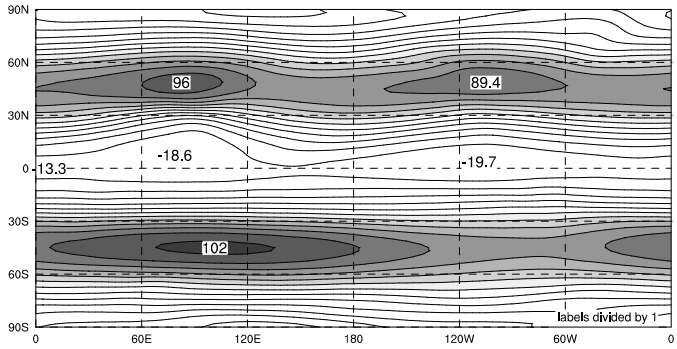

Figure 4.15: Zonal wind contour plot in 'unblocked' state in the presence of latitudinally dependent jets with underlying topography of figure 4.10.

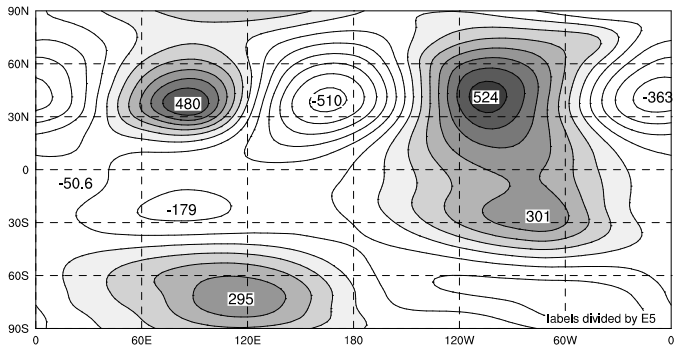

Figure 4.16: Eddy Streamfunction contour plot in 'unblocked' state in the presence of latitudinally dependent jets with underlying topography of figure 4.10.

to a minimum value about 2 times smaller than the actual value at 2.8 ms^{-1}. This can be regarded as a parameterization for the shift of resonance to lower values of U of the stationary wave.

The replacements $\alpha \to \alpha_r(U)$ and $\omega \to \omega_r(U)$ in Eqs. 4.14 will yield the drag $Im(z_{\mathbf{k}})$ in the STM identical to the drag in the C16 DNS. However, the use of U dependent parameters may not be a convenient solution to the problem. It is possible, instead, to treat the problem by least squares minimization as follows. We seek to minimize the function

$$f(\overline{\alpha}, \overline{\beta}) = \sum_{i=1}^{N} \left[y_i - Z_i(\overline{\alpha}, \overline{\beta}, U_i) \right]^2 , \tag{4.34}$$

where

$$Z(\overline{\alpha}, \overline{\beta}, U_i) = \frac{-k_x |h_{\mathbf{k}}|^2 \overline{\alpha} U_i}{\overline{\alpha}^2 + k_x^2 \left(U_i - \frac{\overline{\beta} + k_0^2 U_i}{k^2} \right)} . \tag{4.35}$$

Here, the y_is are the values of $Im(z_{\mathbf{k}})$ calculated from the C16 DNS at distinct values of U_i. Z is the functional form of the topographic drag as calculated from the STM. $\overline{\alpha}$ and $\overline{\beta}$ are parameters that minimize the total error. The function $f(\overline{\alpha}, \overline{\beta})$ has been minimized numerically using Brent's Principal Axis (PRAXIS) method (Brent, 1973). The non-dimensional values $\overline{\alpha} = 4.38 \times 10^{-2}$ and $\overline{\beta} = 0.15$ were found; these are consistent with the expectation that the actual value of $\alpha = 1.82 \times 10^{-2}$ would increase and that of $\beta = 0.26$ would decrease. The values of $-Im(z_{\mathbf{k}})$ using the STM, Eq. 4.14, with $\alpha \to \overline{\alpha}$ and $\beta \to \overline{\beta}$, and for comparison, those obtained from the C16 DNS, are shown in Fig.

4.19. Clearly, there is an underestimation of the drag at the peak ($1.5 \leq U \leq 2.5$), and mostly overestimation in other areas. This is the price we have to pay for working with U independent parameters. In many respects, however, the use of the parameters $\overline{\alpha}$ and $\overline{\beta}$ improves the profile of the drag. The difference in amplitude between the peaks of the three-component system and the C16 DNS is only about 25% as opposed to the factor of 3 difference when using the parameters α and β. The peak is also now correctly shifted to about 1.5 ms^{-1} from the original 2.0 ms^{-1} calculated with α and β.

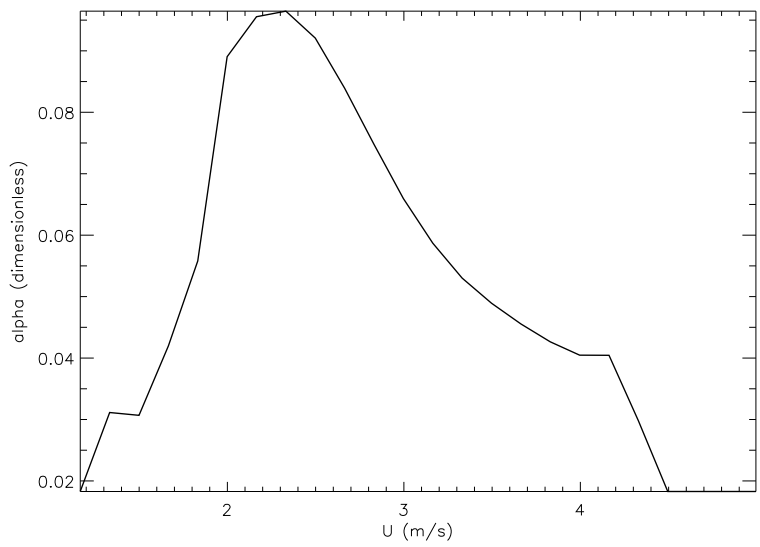

Figure 4.17: The effective dissipation coefficient $\alpha_r(U)$ in the three-component system (STM).

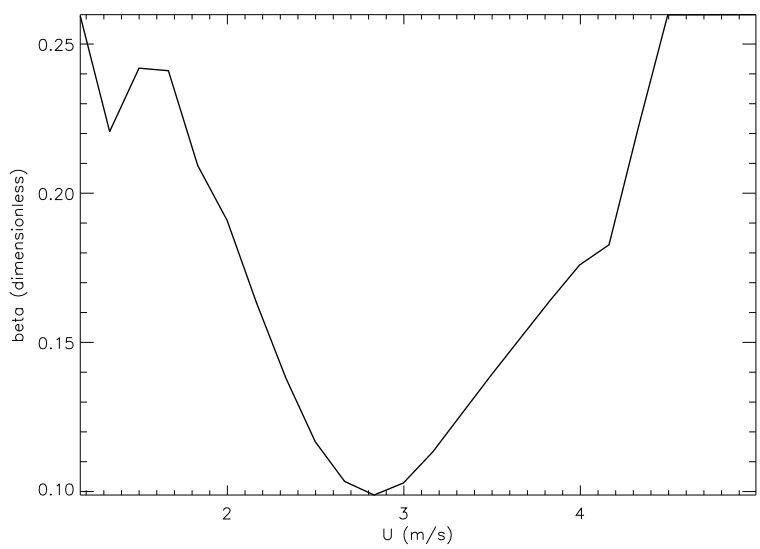

Figure 4.18: The effective variation of Coriolis parameter $\beta_r(U)$ in the three-component system (STM).

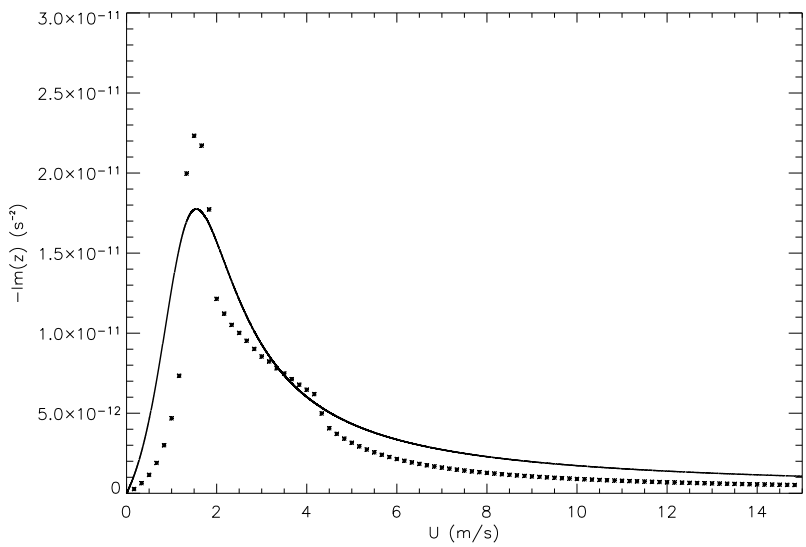

Figure 4.19: A comparison of the drag calculated with $\overline{\alpha}$ and $\overline{\beta}$ in the three-component system (STM) (solid curve) and the corresponding drag calculated in the C16 DNS (asterisks).

4.3 Summary and Conclusion

We have found that a severely truncated, regional barotropic beta-plane model of the atmosphere consisting of just the topographically-excited waves in a background flow possesses multiple equilibria for a wide range of physically-plausible parameters. Furthermore, when numerous other modes are introduced in the flow, multiple equilibria still exist albeit with a reduced range of parameters. We have also investigated how some of the flows at the parameter 'boundaries' spontaneously flip from the blocked state to the unblocked one as instabilities develop in the flow. We have discussed why some global models require excessive winds to maintain multiple equilibria and have investigated further the ideas of YRK that models with a realistic zonal jet structure can ameliorate this problem. By introducing mid-latitudinal jets in our (barotropic) model, we have indeed found that the zonal jet structure in global baroclinic models helps to confine the topographic Rossby waves within a given latitudinal band and that this can lead to resonance without the excessive winds needed in a simple global barotropic scenario, where the waves are allowed to travel over the whole domain. Although we have found multiple equilibrium states resembling the blocked and unblocked patterns in the atmosphere in this case, the winds needed in our experiments are still somewhat larger than observed ones. Nevertheless, contrary to objections raised by some previous studies, we have been able to show that multiple equilibria can appear in the presence of transient activity and realistic topographic distribution and may be confined in mid-latitude regions in global models. We have also investigated how the very severely truncated model (STM) may be improved by parameterizing the discarded non-linear interactions. We have found that increasing the value of the dissipation coefficient, α, and reducing the variation of the Coriolis parameter, β, leads to a STM that can predict the behaviour of the DNS much more accurately. We have solved for the effective α and β analytically, which gives exact agreement, but leads to zonal wind dependent parameters, and by a least squares algorithm, which only gives a very broad agreement, but has the advantage of leading to constant parameters. The effective parameters may be referred to as renormalized parameters, using the lan-

guage adopted in Section 3.3.2. The rest of this thesis will be devoted to more systematic methods of parameterizing non-linear interactions.

Chapter 5

Dynamical Subgrid-scale Parameterizations

5.1 Introduction

A turbulent flow consists of motions of a variety of spatial and temporal scales. Therefore, to numerically simulate such a flow, one needs a grid and timestep of sufficient fineness to resolve the smallest scales of motion. Such a simulation is called a Direct Numerical Simulation (DNS). Unfortunately, the computational cost of a DNS scales with the Reynolds number as Re^3 (Piomelli and Chasnov, 1996). Hence, very high Reynolds number flows, such as geophysical flows, are unattainable by DNS. A solution to this problem is to reduce the grid size (and timestep), and to parameterize the non-linear interactions between the resolved-scale motions and the subgrid-scale motions. This is the motivation for what are called dynamical subgrid-scale parameterizations. The resulting simulation, with subgrid-scale motions parameterized, is called a Large Eddy Simulation (LES). The coupling between resolved and subgrid scale motions leads to a subgrid flux of energy (or enstrophy), which, in the case of a positive flux (drain), can be parameterized by an eddy viscosity. Early attempts to calculate the eddy viscosity based on flow properties include the works of Smagorinsky (1963), Lilly (1966), Corby (1968), and Leith (1969) in the context of atmospheric flows. The work of Deardorff (1970), who considered channel flow using Smagorinsky's formulation, is generally regarded as the first attempt at an LES of turbulent flow for non-geophysical flows.

In general, it is not possible to deterministically parameterize subgrid-scale motions, as these are inherently chaotic. Instead, one can only hope to capture their statistics. In any case, if one tried to capture the detailed motions of the subgrid scales, then an inevitable error in such a procedure, however small, would propagate upscale and contaminate the resolved-scale motions, given enough time. As an example of this phenomenon, the atmosphere has been shown to be unpredictable after a period of about two weeks due to the saturation of errors (Charney et al., 1966). In the context of subgrid-scale parameterizations this has been noted by Herring (1979).

This leads one to the conclusion that any LES of turbulence must be inherently stochastic in nature. If we regard the statistical averages as time-averages over a characteristic eddy-turnover time of the subgrid-scales, then it may be possible to regard the large resolved scales as quasi deterministic since the small scales relax much faster than the large scales. However, in this thesis, we shall mainly consider flows at statistical steady state, and attempt to maintain the correct statistics at all scales of motion. The problem of time-dependent subgrid-scale parameterizations will not be considered although the methodology we employ could be extended to such cases by considering an evolving

ensemble of flows.

The structure of this chapter is as follows. Firstly, we shall look at subgrid-scale parameterization based on advection-diffusion tensors, which are currently popular in oceanic modelling. Then we shall look at parameterizations based on statistical closure theories, such as the DIA and EDQNM, mainly for atmospheric flows; we shall also briefly mention parameterizations based on Renormalization Group (RG) methods. This is followed by an examination of the parameterizations outlined by Frederiksen and Kepert (Frederiksen and Kepert, 2006), which are motivated by closure theories, but are implemented using DNS. This methodology will form the basis for the study outlined in Chapters 6, 7, and 8 on subgrid-scale parameterizations in various two-level quasi-geostrophic flows. Lastly, we compare the advective-tensor methodology with the DNS methodology to be used in this thesis. We shall attempt to justify why closure-motivated methodologies, our DNS methodology in particular, are needed to satisfactorily parameterize subgrid-scale turbulence.

5.2 Advective-Diffusive Tensor Parameterizations

In this section we review commonly used subgrid-scale parameterization schemes, particularly in oceanic modelling. In the atmosphere, the deformation scale is well resolved in general circulation simulations at standard resolutions, and thus the net subgrid flux of enstrophy is dissipative. This explains why hyperdiffusive (biharmonic or higher) operators are generally used to parameterize the subgrid flux of enstrophy with reasonable success. The usage of ad-hoc hyperdiffusive operators is however not without difficulties, as discussed by Frederiksen et al. (1996). The usage of overly strong dissipation may, surprisingly, increase the kinetic energy of the large scales; a possible explanation for this effect is proposed in that paper. This was partly the motivation for the investigation of self-consistent closure-based subgrid-scale parameterization schemes considered by Frederiksen and Davies (1997), which will be discussed further in the next section.

In the ocean, the deformation scale is an order of magnitude smaller, making it difficult to resolve with standard resolutions used for climatic studies. This means that there are significantly energetic eddies that are not resolved in such simulations, and hence their description as non-eddy-resolving. On the basis of QG turbulence phenomenology, discussed in Section 3.2.6, we expect there to be an overestimation of mean large-scale potential energy and a net injection of transient barotropic energy in such simulations if the subgrid fluxes are not parameterized. Andrews and McIntyre (1976) showed that part of the effect of the eddies on the mean flow is an extra circulation so that flow tracers are advected by a 'residual circulation', rather than the imposed circulation (in the absence of eddies). In the language adopted in Chapter 3, we may call the latter circulation the 'bare' circulation and the former, the 'renormalized' circulation. This work was further developed by Plumb (1979) (see also Plumb and Mahlman, 1987, and references therein), who showed that the eddy (subgrid) flux may be parameterized by a symmetric tensor, that diffuses the tracers, and an antisymmetric tensor that advects the tracers.

In oceanic modelling, the early approach was also to use diffusion operators in the horizontal and vertical (for example, Brian and Lewis, 1979). However, Redi (1982) proposed a diffusion operator that mixes tracers along isopycnals (constant-density surfaces), rather than horizontally and vertically. This corresponds to a (symmetric) diffusion tensor, which is diagonal in the isopycnal cordinate system, but is generally not diagonal in the z-coordinate system. This idea was further developed by Cox (1987) for use in ocean

models. Hirst and Cai (1994) investigated the effect of the Redi-Cox diffusion scheme, and found that it improves such features such as salinity structure, but has little effect on the large-scale currents. Gent and McWilliams (GM) (1990) and Gent et al. (1995) proposed a parameterization scheme based on an antisymmetric, and thus advective, tensor. This tensor modifies the circulation so that the large-scale potential energy is reduced to account for the energy extracted by the baroclinically-unstable eddies.

The advective-diffusive tensor parameterization of subgrid-scale eddies can be illustrated as follows. The discussion follows Griffies (1998) and Vallis (2006). The starting point is the averaged three-dimensional (continuously stratified) QGPV equation, without forcing and dissipation:

$$\frac{\partial \overline{q}}{\partial t} + \overline{\mathbf{u} \cdot \nabla q} = 0. \tag{5.1}$$

Here, the over-line refers to some kind of averaging procedure such as ensemble, time, or zonal averaging. This of course leads to a closure problem as the second term is non-linear in q. If in this second term we split u and q into mean and transient quantities

$$\begin{aligned} \mathbf{u} &= \overline{\mathbf{u}} + \mathbf{u}' \\ q &= \overline{q} + q', \end{aligned} \tag{5.2}$$

then it becomes

$$\overline{\mathbf{u} \cdot \nabla q} = \overline{\mathbf{u}} \cdot \nabla \overline{q} + \overline{\mathbf{u}' \cdot \nabla q'}. \tag{5.3}$$

This is because $\overline{q'}$ and $\overline{\mathbf{u}'}$ are zero by definition. We also assume that $\nabla \cdot \mathbf{u} = 0$ so that $\overline{\mathbf{u}' \cdot \nabla q'} = \nabla \cdot (\overline{\mathbf{u}' q'})$, and hence

$$\frac{\partial \overline{q}}{\partial t} + \overline{\mathbf{u}} \cdot \nabla \overline{q} = -\nabla \cdot \mathbf{Q}. \tag{5.4}$$

Here $Q = \overline{\mathbf{u}' q'}$ is the eddy flux of potential vorticity. The eddy flux is then parameterized in terms of a 'diffusion' tensor, $\mathbf{T}$ (Monin and Yaglom, 1975; Plumb and Mahlman, 1987), as follows:

$$\mathbf{Q} = -\mathbf{T} \nabla \overline{q}. \tag{5.5}$$

Here, $\mathbf{T}$ is a general tensor; no symmetry is assumed and its components depend on space and time in general. The tensor $\mathbf{T}$ has both diffusive and advective qualities, and hence it is better to call it an advection-diffusion tensor.

The tensor T_{ij} can be decomposed into symmetric, S_{ij}, and antisymmetric, A_{ij} parts as follows:

$$S_{ij} = \frac{1}{2} \left(T_{ij} + T_{ji} \right) \tag{5.6}$$

and

$$A_{ij} = \frac{1}{2} \left(T_{ij} - T_{ji} \right) \tag{5.7}$$

so that

$$T_{ij} = S_{ij} + A_{ij}. \tag{5.8}$$

These are associated with the 'diffusive' flux

$$\mathbf{Q_s} = -\mathbf{S} \nabla q \tag{5.9}$$

and the skew flux

$$\mathbf{Q_a} = -\mathbf{A}\nabla q. \tag{5.10}$$

It can be shown that $\mathbf{Q_s} \cdot \nabla q < 0$ under certain circumstances. This is done as follows. The symmetric tensor $\mathbf{S}$ can always be rotated so that is diagonal in some coordinate system. Further, to simplify the discussion, we assume that it is isotropic. Then we can write $S_{ij} = \kappa\delta_{ij}$, where κ is a scalar and δ_{ij} is the Kronecker Delta function, an isotropic second order tensor. Thus, we have

$$\begin{aligned} \mathbf{Q_s} \cdot \nabla q &= -\kappa\delta_{ij}\frac{\partial q}{\partial x_j}\frac{\partial q}{\partial x_i} \\ &= -\kappa\frac{\partial q}{\partial x_i}\frac{\partial q}{\partial x_i} \\ &= -\kappa\left(\nabla q\right)^2. \end{aligned} \tag{5.11}$$

Hence, $\mathbf{Q_s} \cdot \nabla q < 0$ if $\kappa > 0$. This means that the eddy flux will reduce the gradients of q, making it 'smoother'. Under these circumstances the eddy flux is referred to as a down-gradient flux.

Symmetric turbulent fluxes are widely used in numerical simulations of the atmosphere and ocean. The conventional scale-selective eddy viscosity formulation is one example of the use of such a tensor. Examples of more sophisticated forms are such as that proposed by Redi (1982) for oceanic simulations. Redi proposed that S_{ij} should be diagonal in the isopycnal coordinate system, with the S_{33} element being relatively small. This corresponds to down-gradient mixing along isopycnals. In the z-coordinate system, this corresponds to a non-diagonal but symmetric tensor (Griffies et al, 1998).

The skew flux is neither down-gradient nor up-gradient; that is, $\mathbf{Q_a} \cdot \nabla q = 0$. This can be shown as follows.

$$\begin{aligned} \mathbf{Q_a} \cdot \nabla q &= -A_{ij}\frac{\partial q}{\partial x_j}\frac{\partial q}{\partial x_i} \\ &= -A_{ji}\frac{\partial q}{\partial x_i}\frac{\partial q}{\partial x_j} \\ &= A_{ij}\frac{\partial q}{\partial x_j}\frac{\partial q}{\partial x_i} \\ &= 0. \end{aligned} \tag{5.12}$$

The third step in Eq. 5.12 follows since $A_{ij} = -A_{ji}$. Hence the skew flux has no effect on the gradients of q. A flux that has this property is a divergenceless advective flux. A divergenceless advective flux carries a tracer around in a fluid without changing its concentration. For this reason, the skew flux is sometimes known as the advective flux. Griffies (Griffies, 1998) makes the point that the skew flux and advective flux are really different, but they have the same divergence, and hence they have the same effect on the flow. This can be demonstrated as follows.

Let the eddy flux be parameterized by the skew flux so that

$$\frac{Dq}{Dt} = -\nabla \cdot \mathbf{Q_a} = \nabla\cdot\left(\mathbf{A}\nabla q\right) \equiv \frac{\partial}{\partial x_i}\left(A_{ij}\frac{\partial q}{\partial x_j}\right) \tag{5.13}$$

The divergence term can be written

$$\frac{\partial}{\partial x_i}\left(A_{ij}\frac{\partial q}{\partial x_j}\right) = \frac{\partial A_{ij}}{\partial x_i}\frac{\partial q}{\partial x_j} \tag{5.14}$$

since $A_{ij}\frac{\partial}{\partial x_i}\left(\frac{\partial q}{\partial x_j}\right) = 0$ due to the antisymmetry of A_{ij}. Additionally,

$$\frac{\partial}{\partial x_j}\left(\frac{\partial A_{ij}}{\partial x_i}q\right) = \frac{\partial A_{ij}}{\partial x_i}\frac{\partial q}{\partial x_j} \tag{5.15}$$

since $\frac{\partial}{\partial x_j}\left(\frac{\partial A_{ij}}{\partial x_i}\right) = 0$ again due to the antisymmetry of A_{ij}. Hence

$$\begin{aligned}\frac{\partial}{\partial x_i}\left(A_{ij}\frac{\partial q}{\partial x_j}\right) &= \frac{\partial}{\partial x_j}\left(\frac{\partial A_{ij}}{\partial x_i}q\right)\\ &= -\frac{\partial}{\partial x_j}\left(v_j^* q\right),\end{aligned} \tag{5.16}$$

where

$$v_j^* = -\frac{\partial A_{ij}}{\partial x_i} \tag{5.17}$$

is the turbulent advecting velocity, also known as the bolus velocity. It is straightforward to show that $\mathbf{v}^*$ is divergenceless since

$$\begin{aligned}\frac{\partial v_j^*}{\partial x_j} &= -\frac{\partial}{\partial x_j}\frac{\partial A_{ij}}{\partial x_i}\\ &= 0\end{aligned} \tag{5.18}$$

by the antisymmetry of A_{ij}. Finally, we have

$$\frac{Dq}{Dt} = -\frac{\partial}{\partial x_j}\left(v_j^* q\right) = -\frac{\partial Q_j}{\partial x_j} = -\nabla\cdot\mathbf{Q}_\mathbf{a}', \tag{5.19}$$

where $\mathbf{Q}_\mathbf{a}' = \mathbf{v}^* q$ is the advective flux. The divergence of the advective flux can be written as

$$\nabla\cdot\mathbf{Q}_\mathbf{a}' = \mathbf{v}^*\cdot\nabla q, \tag{5.20}$$

since $\nabla\cdot\mathbf{v}^* = \mathbf{0}$. As mentioned earlier, skew fluxes have been used by GM to parameterize baroclinic eddies. GM originally formulated their closure scheme in terms of the eddy flux of thickness (of an isopycnal), which was taken to be proportional to the mean thickness gradient. The bolus (eddy-induced) velocity obtained acts in such a way so as to reduce the potential energy of the fluid, which is what happens in baroclinic instability.

Further improvements to the GM parameterization were suggested by Treguier et al. (1997), who advocated the use of inhomogeneous mixing coefficients; a similar proposal was made by Visbeck et al. (1997). Treguier et al. (1997), Lee et al. (1997), and Treguier (1999) suggested that the eddy flux of potential vorticity should be used to construct the antisymmetric tensor (or eddy-induced velocity), rather than the eddy flux of thickness as originally proposed by GM. Roberts and Marshall (1998) proposed that biharmonic diffusion, instead of the original harmonic diffusion used by GM, should be used to capture enstrophy cascade at the smallest scales. Anisotropic tensors have been advocated by Smith and Gent (2004).

The GM parameterization scheme has been implemented in ocean circulation models, with substantial improvements to the large scale circulation noted (Danabasoglu and McWilliams, 1995; Boning et al., 1995; Hirst and McDougall, 1996). Encouraging results have also been noted by Duffy et al. (1995), England (1995), and England and Holloway (1996). On the other hand, Duffy et al. (1997) and England and Rahmstorf (1999), who studied tracer distributions, reported the shortcomings of the GM parameterization in capturing some large scale features of oceanic flows. Hallberg and Gnanadesikan (2006) compared high resolution (eddy resolving) and low resolution (non-eddy-resolving) simulations in the Southern Ocean, and concluded that the GM parameterization is inadequate for describing some features of the eddy-resolving circulation. It is difficult to pinpoint the origins of the discrepancies reported by these studies as the models employed are substantially complex. What is clear, however, is that current formulations do not adequately capture the turbulent transfers that are predicted by QG phenomenology (see Section 3.2.6). In particular, there is no mechanism in current formulations that captures the injection of barotropic energy from the unresolved baroclinic instability injection scales. This is a point alluded to by Wirth (2000), who studied a two-level QG model, and noted that a diffusive parameterization may only be appropriate for scales much larger than the Rhines scale, where the inverse cascade is 'arrested' (See Section 3.2.6). The rest of this chapter will be devoted to more fundamental subgrid-scale parameterization schemes that do capture the turbulent transfers correctly.

5.3 Closure-based Parameterizations

Since LESs are inherently stochastic, the natural starting point for subgrid-scale parameterization is statistical closure theory. We shall use the DIA closure for the barotropic vorticity equations, introduced in Section 3.3.2, to illustrate this approach, following Frederiksen and Davies (1997). The two-time covariance equation for the DIA is

$$\begin{aligned}\frac{\partial}{\partial t}C_{\mathbf{k}}(t,t) &= -2Re\int_{t_0}^{t} ds\eta_{\mathbf{k}}(t,s)C_{-\mathbf{k}}(t,s) + 2Re\int_{t_0}^{t} dsS_{\mathbf{k}}(t,s)R_{-\mathbf{k}}(t,s) \\ &- 2ReD^0_{\mathbf{k}}C_{\mathbf{k}}(t,t) + F^0_{\mathbf{k}}(t), \end{aligned} \tag{5.21}$$

where

$$\eta_{\mathbf{k}}(t,s) = -4\sum_{\mathbf{p}}\sum_{\mathbf{q}}\delta(\mathbf{k}+\mathbf{p}+\mathbf{q})K(\mathbf{k},\mathbf{p},\mathbf{q})K(-\mathbf{p},-\mathbf{q},-\mathbf{k})R_{-\mathbf{p}}(t,s)C_{-\mathbf{q}}(t,s) \tag{5.22}$$

and

$$S_{\mathbf{k}}(t,s) = 2\sum_{\mathbf{p}}\sum_{\mathbf{q}}\delta(\mathbf{k}+\mathbf{p}+\mathbf{q})K(\mathbf{k},\mathbf{p},\mathbf{q})K(-\mathbf{k},-\mathbf{p},-\mathbf{q})C_{-\mathbf{p}}(t,s)C_{-\mathbf{q}}(t,s). \tag{5.23}$$

Furthermore,

$$F^0_{\mathbf{k}}(t,t') = \langle f^0_{\mathbf{k}}(t)f^0_{-\mathbf{k}}(t')\rangle = F^0_{\mathbf{k}}(t)\delta(t-s) \tag{5.24}$$

for white noise forcing. Now imagine that a fictitious truncation is performed at some intermediate wavenumber $\mathbf{k}_*$, so that $\mathbf{k} \leq \mathbf{k}_*$. We can then split the non-linear terms in Eqs. 5.22 and 5.23 into two parts. One part consists of contributions from wavenumbers $\mathbf{p}$ and $\mathbf{q}$ such that both $\mathbf{p}$ and $\mathbf{q}$ are less than $\mathbf{k}_*$. This is called the resolved part, denoted by a superscript R. The other part consists of either $\mathbf{p}$ and $\mathbf{q}$ both greater than $\mathbf{k}_*$, or

one of $\mathbf{p}$ or $\mathbf{q}$ greater than $\mathbf{k}_*$. This is called the subgrid part, denoted by the superscript S. Note that the wavenumbers $\mathbf{p}$ and $\mathbf{q}$ are vectors, so strictly we have to define by what measure we regard one vector to be greater than the other. If we imagine the truncation to be circular, then the circle of radius k_* defines the boundary between resolved and subgrid wavenumbers. A position vector that lies within this boundary is resolved, and that which is outside is subgrid. With these considerations, we can write 5.22 and 5.23 as

$$\eta_{\mathbf{k}}(t,s) = \eta^R_{\mathbf{k}}(t,s) + \eta^S_{\mathbf{k}}(t,s) \tag{5.25}$$

and

$$S_{\mathbf{k}}(t,s) = S^R_{\mathbf{k}}(t,s) + S^S_{\mathbf{k}}(t,s), \tag{5.26}$$

Equation 5.21 can then be written as

$$\begin{aligned} \frac{\partial}{\partial t} C_{\mathbf{k}}(t,t) &= -2Re \int_{t_0}^{t} ds \eta^R_{\mathbf{k}}(t,s) C_{-\mathbf{k}}(t,s) + 2Re \int_{t_0}^{t} ds S^R_{\mathbf{k}}(t,s) R_{-\mathbf{k}}(t,s) \\ &- 2Re D^r_{\mathbf{k}} C_{\mathbf{k}}(t,t) + F^r_{\mathbf{k}}(t). \end{aligned} \tag{5.27}$$

Here,

$$D^r_{\mathbf{k}} = D^0_{\mathbf{k}} + D^d_{\mathbf{k}} \tag{5.28}$$

is the renormalized dissipation, and

$$F^r_{\mathbf{k}} = F^0_{\mathbf{k}} + F^b_{\mathbf{k}} \tag{5.29}$$

is the renormalized noise covariance. Additionally,

$$D^d_{\mathbf{k}} = \frac{1}{C_{\mathbf{k}}(t,t)} \int_{t_0}^{t} ds \eta^S_{\mathbf{k}}(t,s) C_{-\mathbf{k}}(t,s) \tag{5.30}$$

is the subgrid drain eddy dissipation, and

$$F^b_{\mathbf{k}} = 2Re \int_{t_0}^{t} ds S^S_{\mathbf{k}}(t,s) R_{-\mathbf{k}}(t,s) \tag{5.31}$$

is the subgrid eddy backscatter covariance. We can also define the eddy drain viscosity as

$$\nu^d_{\mathbf{k}} = \frac{D^d_{\mathbf{k}}}{k^2} \tag{5.32}$$

and the eddy backscatter viscosity as

$$\nu^b_{\mathbf{k}} = -\frac{F^b_{\mathbf{k}}}{2k^2 C_{\mathbf{k}}}. \tag{5.33}$$

The eddy drain and backscatter viscosities can be combined to define a net eddy viscosity

$$\nu^n_{\mathbf{k}} = \nu^d_{\mathbf{k}} + \nu^b_{\mathbf{k}}. \tag{5.34}$$

The net eddy viscosity parameterizes the net flux between the resolved and subgrid scales. It corresponds to a deterministic parameterization, and as such is closer in spirit to conventional ad-hoc eddy viscosities; however, it is calculated self-consistently from the statistics of the flow, and so is an improvement over ad-hoc methodologies.

The systematic approach to parameterizing the subgrid scales based on the statistics of the flow, as calculated by closure theory, can be traced back to the works of Leith (1971) and Kraichnan (1976). Leith used EDQNM closure theory to calculate a function similar to the net eddy viscosity for atmospheric two dimensional flows. Leith's dissipation function was used in the general atmospheric circulation models described by Boer et al. (1984) and Laursen and Eliasen (1989) with reported improvements in the simulations when compared to standard diffusion schemes. Kraichnan defined a net eddy viscosity using the test field model (a closure scheme), in both two and three dimensions. He noted that in both cases, the net eddy viscosity has a cusp (a sharp rise) near the truncation scale. Furthermore, in two dimensions, the net eddy viscosity is negative at the large scales, indicating an injection of energy. Kraichnan showed that at the large scales, far away from the truncation scale, the net eddy viscosity is virtually independent of wavenumber. Hence, at the large scales, the net eddy viscosity is simply an enhanced (or reduced) version of the molecular viscosity. Kraichnan's explanation for this is that at the large scales, the contribution from the subgrid scales is mostly in the form of non-local interactions. Since for any interacting triad $\mathbf{k} + \mathbf{p} + \mathbf{q} = \mathbf{0}$, we can see that if $\mathbf{k} \approx \mathbf{0}$ (large scale), then $\mathbf{p} \approx -\mathbf{q}$, and since at least one of $\mathbf{p}$ or $\mathbf{q}$ must be large (that is, a subgrid scale), we conclude that both $\mathbf{p}$ and $\mathbf{q}$ are large. Hence, the triad interaction involves a large scale mode interacting with two small-scale modes. Now, this is similar to the assumption made in deriving the molecular viscosity, namely, that the motions of interest are large compared to thermal fluctuations. Thus, at the large scales, the net eddy viscosity behaves just like molecular viscosity. However, near the truncation scale, there exist both local and non-local interactions, so the molecular viscosity concept breaks down, and a cusp is seen. In fact, the cusp is an indication that the net transfers are mainly local. We can imagine the following idealized situation. The enstrophy is injected at a single wavenumber, and passed downscale to the next wavenumber only. If there is an abrupt truncation below some wavenumber, then we expect to see a sharp rise in the spectrum only at that wavenumber; other wavenumbers, having passed on the enstrophy to neighboring wavenumbers, will remain unaffected. Hence, to maintain a constant transfer, all we need is a negative transfer at the truncation scale; this is the origin of the cusp seen in the net eddy viscosity. This view is strengthened by the fact that when a smoother filter, for example a Gaussian filter, instead of a sharp cut, is used to effect the truncation, the cusp is not seen (Leslie and Quarini, 1979).

Domaradzki and Rogallo(1990) made the point that it is important to distinguish between energy transfer (between modes) and triad interactions. Although energy transfer between modes is thought to be mostly local in the inertial range, and this is a crucial factor leading to the existence of k^{-3} (and $k^{-\frac{5}{3}}$) power laws in this range, this does not necessarily mean that all the triad interactions that lead to this transfer are purely local. For example, it is possible for one large-scale mode to interact with two small-scale modes of similar size in such a way that the energy (or enstrophy) is exchanged primarily between the two small-scale modes. This is a non-local triad interaction, but the transfer between the two small-scale modes may be quite local. Domaradzki and Rogallo's results suggest that the transfers occurring in three-dimensional turbulence are predominantly of this type. A similar conclusion was reached by Maltrud and Vallis (1993), who studied non-linear interactions in two-dimensional turbulence. It is important to note that when we refer to local transfers in this thesis, as we shall extensively in Chapters 6, 7, and 8, it is in the sense just discussed and not in the sense that the triad interactions involve wavevectors all of similar size, which is clearly not the case based on the above studies.

The net eddy viscosity, as calculated by Leith and Kraichnan, is a substantial improvement over ad-hoc eddy viscosities which are still commonly used in atmospheric and oceanic modelling. Further developments of these ideas were made by Basdevant et al. (1978), Chollet and Lesieur (1981) and Chollet (1984), which were based on the EDQNM closure theory. However, the net eddy viscosity parameterization also has a substantial deficiency in that it is deterministic. The net eddy viscosity only parameterizes the average net flux between the resolved and subgrid scales; therefore, there is an error associated with this process because only the average flux is being parameterized. This error will eventually contaminate the large resolved scales. This is not captured by a deterministic model, which would tend to overestimate the predictability of the large resolved scales. Therefore, a subgrid-scale parameterization scheme needs to be stochastic to take into account the noise (error) introduced by the subgrid scales. This was suggested by Leslie and Quarini (1979). Another way to look at this is from the point of view of closure theories, such as the DIA, which indicate that there is a two-way exchange of energy (enstrophy) between the resolved and subgrid-scales. The energy (enstrophy) input, the stochastic backscatter, has been shown to play an important role in the dynamics of the resolved scales, such as providing an instability mechanism for large-scale turbulence to grow (Leith, 1990; Piomelli et al, 1991).

As noted by Kraichnan (1970), closure theories, such as the DIA, have stochastic representations (see also Leith, 1971). In the stochastic representation, the Langevin equation is used instead of the covariance equation. The Langevin equation for the DIA is a stochastic equation that reproduces the statistics of the DIA closure, Eq. 3.51 (see Leith, 1971). This approach was pursued by Bertoglio (1985) and Chasnov (1991), who reported apparent improvements to their simulations. Pursuing the stochastic representation means that one needs to calculate both the drain dissipation and stochastic forcing covariance.

For atmospheric flows, this approach was taken by Frederiksen and Davies (1997). They calculated the drain dissipation, $D^d_{\mathbf{k}}$, and the stochastic backscatter, $F^b_{\mathbf{k}}$, using both EDQNM and DIA closure theories for the barotropic vorticity equation on the sphere. Both parameters displayed cusps near the truncation scale. The drain dissipation, as expected, was stronger than the net dissipation, and was slightly negative at the large scales. Frederiksen and Davies did not find any difference in the statistics of their LES when using either drain dissipation and backscatter or net dissipation alone.

5.4 Subgrid-scale Parameterizations using Renormalization Group Methods

Here we briefly mention that there exists another body of work devoted to the subgrid-scale parameterization problem based on the Renormalization Group (RG) method. The RG is a generic method of statistical physics that enables the dynamics of a (complex) physical system to be expressed in a scale-independent form. Hence, it promises to provide a systematic way of calculating the scale-independent eddy-viscosity in turbulent fluids. The application of RG methods to turbulent fluids was pioneered by Forster et al. (1977), and it was shown by Yakhot and Orszag (1986) that the methodology may be used to successfully calculate physical constants such as Kolmogorov's constant. The use of RG methods in the subgrid-scale parameterization problem was pioneered by Rose (1977), who obtained an eddy diffusivity for his passive scalar convection problem. Further developments to the field were made by McComb and co-workers (McComb, 1982, 1986; McComb

and Shanmugasundaram, 1983, 1985). Zhou et al. (1988) and Zhou and Vahala (1993) proposed how a cusp-like eddy viscosity may be obtained from this formalism. Extensive reviews of the subject are given by Zhou et al. (1997), Smith and Woodruff (1998), and the thesis of Kiyani (2006).

5.5 Subgrid-scale Parameterizations using DNS

Statistical closure schemes have primarily been implemented for homogeneous and isotropic turbulence although recently inhomogeneous turbulence for barotropic flows has also been treated (Frederiksen, 1999). However, DNS is still the primary tool in practical problems. It is therefore of interest to calculate the quantities $D_{\mathbf{k}}$ and $F_{\mathbf{k}}$ by DNS. Subgrid-scale parameterizations by DNS have been attempted with some success by Domaradzki et al. (1987), Lesieur and Rogallo (1989), and Chasnov (1991) for three-dimensional flows. Koshyk and Boer (1995) and Kaas et al. (1999) have attempted subgrid-scale parameterizations by DNS for atmospheric circulation models. The methodology that we employ in this thesis was outlined by Frederiksen and Kepert (2006). It is based on the idea that closure theories have stochastic representations (the Langevin equation). Unlike in closure based parameterizations, however, the damping and noise covariance parameters are determined from the statistics of DNS.

Here, for the purposes of clarity, we outline Frederiksen and Kepert's methodology in scalar form, which is appropriate in barotropic problems. Motivated by the stochastic representation of closure theory, we can write:

$$\left(\frac{\partial x(t)}{\partial t}\right)_S = m(t)x(t) + f(t). \tag{5.35}$$

Here, x is a general symbol for a resolved-scale mode. The mode might represent the spectral amplitude of vorticity ($\zeta_{\mathbf{k}}$) if the barotropic vorticity equation is considered. m is a dissipation coefficient (if negative), and f is stochastic forcing. Note that m and f, like x, are functions of wavenumber. Multiplying Eq. 5.35 by $x^*(t_0)$ and averaging, we have

$$\langle\left(\frac{\partial x(t)}{\partial t}\right)_S x^*(t_0)\rangle = m(t)\langle x(t)x^*(t_0)\rangle \tag{5.36}$$

because $\langle f(t)x^*(t_0)\rangle = 0$ by causality since it is assumed that $t > t_0$. In other words, a forcing at a given time cannot influence the flow at earlier times. Now at each time, t, we can find a value of m to satisfy Eq. 5.36; however, a time-dependent dissipation is inconvenient. Hence, a time-averaged dissipation, which is constant in time, is calculated instead. Taking the view that the most important contribution to the drain viscosity comes near the truncation scale, and that at these scales the characteristic eddy-turnover time, τ, is much shorter compared to the eddy-turnover times of the larger scales, it is sufficient to average only over the time-scale $t - t_0 = \tau$. In the continuum limit, the average takes the form of an integral, so

$$m = \frac{\int_{t_0}^{t} ds\langle\left(\frac{\partial x(s)}{\partial t}\right)_S x^*(t_0)\rangle}{\int_{t_0}^{t} ds\langle x(t)x^*(t_0)\rangle}. \tag{5.37}$$

The contribution of the stochastic forcing to the equal-time covariance, $F(t) = \langle f(t)x^*(t)\rangle + \langle f^*(t)x(t)\rangle$, is determined by multiplying Eq. 5.35 by $x^*(t)$, and its complex

conjugate by $x(t)$. After averaging and adding the resulting two equations we have,

$$\langle \left(\frac{\partial x(t)}{\partial t}\right)_S x^*(t)\rangle + \langle x(t) \left(\frac{\partial x(t)}{\partial t}\right)_S^* \rangle = m\langle x(t)x^*(t)\rangle + \langle x(t)x^*(t)\rangle m^* + F(t) \tag{5.38}$$

Hence, F can be determined, as m is given by Eq. 5.37, and the terms in angular brackets can be calculated from the statistics of DNS. Having determined F, the stochastic forcing, f, can then be constructed (see Appendix F). An implicit assumption in the calculations above is that the subgrid scales are transients. For a general problem with both mean and transient contributions to the subgrid tendency, it is not clear that Eq. 5.35 has the right form to parameterize the subgrid contribution. For example, Frederiksen (1999) devised a DIA-type closure scheme for inhomogeneous topographic turbulence. He found that the subgrid eddies damp the mean and transient fields differently. In that study, the total mean subgrid tendency, in the absence of topography, can be written as

$$\left(\frac{\partial\langle\zeta_{\mathbf{k}}(t)\rangle}{\partial t}\right)_S = -\int_{t_0}^{t} ds \eta_{\mathbf{k}}^S(t,s)\langle\zeta_{\mathbf{k}}(s)\rangle + j_{\mathbf{k}}(t), \tag{5.39}$$

where $\eta_{\mathbf{k}}^S$ is the same as that defined for the homogeneous DIA, and

$$j_{\mathbf{k}}(t) = \sum_{(\mathbf{p},\mathbf{q})} \sum_{\in S} K(\mathbf{k},\mathbf{p},\mathbf{q})\langle\zeta_{-\mathbf{p}}(t)\rangle\langle\zeta_{-\mathbf{q}}(t)\rangle \tag{5.40}$$

is the residual Jacobian. The transient subgrid tendency, on the other hand, is

$$\left(\frac{\partial\hat{\zeta}_{\mathbf{k}}(t)}{\partial t}\right)_S = -\int_{t_0}^{t} ds \left[\eta_{\mathbf{k}}^S(t,s) + \pi_{\mathbf{k}}^S(t,s)\right] \hat{\zeta}_{\mathbf{k}}(s) + \hat{f}_{\mathbf{k}}(t), \tag{5.41}$$

where $\pi_{\mathbf{k}}^S$ is an additional damping term that appears in the inhomogeneous DIA, and $\hat{f}_{\mathbf{k}}$ is defined as the stochastic backscatter. In this thesis, however, the main focus is on parameterizing the transient subgrid flux, and since we work exclusively at steady state, a simpler solution is to use a mean subgrid tendency, without breaking up this term into its constituents, namely, the mean dissipation term and the residual Jacobian. That is, for the general barotropic problem, with both mean and transient contributions to the tendency, we have

$$\left(\frac{\partial x(t)}{\partial t}\right)_S = m\hat{x}(t) + \hat{f}(t) + \bar{f}, \tag{5.42}$$

where

$$x(t) = \bar{x} + \hat{x}(t), \tag{5.43}$$

with $\bar{x}$ and $\hat{x}$ being mean and transient parts of x, respectively; similarly,

$$f(t) = \bar{f} + \hat{f}(t), \tag{5.44}$$

where

$$\bar{f} = \langle \left(\frac{\partial x(t)}{\partial t}\right)_S \rangle \tag{5.45}$$

is the mean subgrid tendency, which can be easily calculated from the statistics of DNS. We can also construct a deterministic parameterization scheme, analogous to the net viscosity

defined for barotropic flows in Eq. 5.34, as follows. Let

$$\left(\frac{\partial \hat{x}(t)}{\partial t}\right)_S = m_n \hat{x}(t). \tag{5.46}$$

Then multiplying Eq. 5.46 by $\hat{x}^*(t)$, and averaging, we have

$$m_n = \frac{\langle \left(\frac{\partial \hat{x}(t)}{\partial t}\right)_S \hat{x}^*(t)\rangle}{\langle \hat{x}(t)\hat{x}^*(t)\rangle}. \tag{5.47}$$

This definition of the coefficient m_n is equivalent to (minus) the net dissipation defined in Eq. 5.34.

Frederiksen and Kepert (2006) assumed that the subgrid tendency is purely transient ($\bar{f} = 0$), which is a good assumption for the flows that they considered. They looked at LES of barotropic flows with atmospheric parameters at the resolutions of T31 and T63. They found that the drain eddy viscosity and stochastic backscatter parameters were similar to those obtained with the closure based methodologies in Frederiksen and Davies (1997). In the two-level problem that we consider, however, there will be a mean subgrid tendency if the injection region due to baroclinic instability is not resolved, so we have to consider the more general case to account for this possibility. Thus, for the two-level problem, we parameterize the subgrid tendencies of the potential vorticity as

$$\begin{aligned}\left(\frac{\partial q^1_{\mathbf{k}}}{\partial t}\right)_S &= M_{11}(\mathbf{k})\hat{q}^1_{\mathbf{k}} + M_{12}(\mathbf{k})\hat{q}^2_{\mathbf{k}} + \hat{f}_1(\mathbf{k}) + \bar{f}_1(\mathbf{k})\\ \left(\frac{\partial q^2_{\mathbf{k}}}{\partial t}\right)_S &= M_{21}(\mathbf{k})\hat{q}^1_{\mathbf{k}} + M_{22}(\mathbf{k})\hat{q}^2_{\mathbf{k}} + \hat{f}_2(\mathbf{k}) + \bar{f}_2(\mathbf{k})\end{aligned} \tag{5.48}$$

Here $\hat{q}^i_{\mathbf{k}}$ are the transient potential vorticities; $M_{ij}(\mathbf{k})$ are 'damping' parameters; $\hat{f}_i(\mathbf{k})$ are the transient forcing functions; and $\bar{f}_i(\mathbf{k})$ are the mean forcing functions at each level. The mean subgrid forcing functions $\bar{f}_1$ and $\bar{f}_2$ are the resultants of the mean damping and the so-called residual Jacobian terms. Equation 5.48 can be written in compact matrix notation as

$$\left(\frac{\partial \mathbf{x}(t)}{\partial t}\right)_S = \mathbf{M}\hat{\mathbf{x}}(t) + \hat{\mathbf{f}}(t) + \bar{\mathbf{f}}, \tag{5.49}$$

where

$$\left(\frac{\partial \mathbf{x}(t)}{\partial t}\right)_S = \begin{pmatrix} \left(\frac{\partial q^1_{\mathbf{k}}}{\partial t}\right)_S \\ \left(\frac{\partial q^2_{\mathbf{k}}}{\partial t}\right)_S \end{pmatrix}. \tag{5.50}$$

and

$$\hat{\mathbf{x}} = \begin{pmatrix} \hat{q}^1_{\mathbf{k}} \\ \hat{q}^2_{\mathbf{k}} \end{pmatrix}. \tag{5.51}$$

The matrix $\mathbf{M}$ is computed from

$$\mathbf{M} = \left[\int_{t_0}^{t} ds \langle \left(\frac{\partial \hat{\mathbf{x}}(s)}{\partial t}\right)_S \hat{\mathbf{x}}^\dagger(t_0)\rangle\right]\left[\int_{t_0}^{t} ds \langle \hat{\mathbf{x}}(s)\hat{\mathbf{x}}^\dagger(t_0)\rangle\right]^{-1}. \tag{5.52}$$

The contribution of the noise to the equal-time covariance matrix

$$\mathbf{F} = \langle \hat{\mathbf{f}}(t)\hat{\mathbf{x}}^\dagger(t)\rangle + \langle \hat{\mathbf{x}}(t)\hat{\mathbf{f}}^\dagger(t)\rangle \tag{5.53}$$

may be obtained from the Lyapunov equation

$$\langle \left(\frac{\partial \hat{\mathbf{x}}(t)}{\partial t}\right)_S \hat{\mathbf{x}}^\dagger(t)\rangle + \langle \hat{\mathbf{x}}(t) \left(\frac{\partial \hat{\mathbf{x}}(t)}{\partial t}\right)_S^\dagger \rangle = \mathbf{M}\langle \hat{\mathbf{x}}(t)\hat{\mathbf{x}}^\dagger(t)\rangle + \langle \hat{\mathbf{x}}(t)\hat{\mathbf{x}}^\dagger(t)\rangle \mathbf{M}^\dagger + \mathbf{F}(t) \tag{5.54}$$

after computing $\mathbf{M}$. The random forcing, $\hat{\mathbf{f}}$, is obtained by assuming that

$$\langle \hat{\mathbf{f}}(t)\hat{\mathbf{f}}(t')\rangle = \mathbf{F}(t)\delta(t-t'). \tag{5.55}$$

The mean forcing, $\bar{\mathbf{f}}$, is simply computed from

$$\bar{\mathbf{f}} = \langle \left(\frac{\partial \mathbf{x}(t)}{\partial t}\right)_S \rangle. \tag{5.56}$$

The quantities in angular brackets are computed from the statistics of DNS. Chapters 6, 7, and 8 of this thesis are based on Eq. 5.49. The goal will be to calculate the matrices

$$\mathbf{M}(\mathbf{k}) = \begin{pmatrix} M_{11}(\mathbf{k}) & M_{12}(\mathbf{k}) \\ M_{21}(\mathbf{k}) & M_{22}(\mathbf{k}) \end{pmatrix}, \tag{5.57}$$

$$\mathbf{F}(\mathbf{k}) = \begin{pmatrix} F_{11}(\mathbf{k}) & F_{12}(\mathbf{k}) \\ F_{21}(\mathbf{k}) & F_{22}(\mathbf{k}) \end{pmatrix}, \tag{5.58}$$

and

$$\bar{\mathbf{f}}(\mathbf{k}) = \begin{pmatrix} \bar{f}_1(\mathbf{k}) \\ \bar{f}_2(\mathbf{k}) \end{pmatrix}. \tag{5.59}$$

for a variety of quasigeostrophic flows, both atmospheric and oceanic. Note that these matrices are in general complex. It will frequently be convenient to refer to the real and imaginary parts separately. Hence,

$$\mathbf{M} = \mathbf{M^r} + i\mathbf{M^i}, \tag{5.60}$$

$$\mathbf{F} = \mathbf{F^r} + i\mathbf{F^i}, \tag{5.61}$$

and

$$\bar{\mathbf{f}} = \bar{\mathbf{f}}^{\mathbf{r}} + i\bar{\mathbf{f}}^{\mathbf{i}}. \tag{5.62}$$

Additionally, note that we could define a dissipation matrix $\mathbf{D} = -\mathbf{M}$ to be consistent with previously used notation in the context of barotropic flows with dissipative subgrid fluxes. However, in the flows that we shall look at in subsequent chapters, the coefficients of the matrix $\mathbf{M}$ may be of either sign (the flux may be dissipative or injective), and hence that notation is not as useful. In subsequent chapters, we shall, rather loosely, refer to $\mathbf{M}$ as the dissipation matrix. We shall also frequently refer to $-\mathbf{M^r}$ since the diagonal elements of this matrix can then be compared to the barotropic dissipation of Frederiksen and Kepert (2006), for example. The net dissipation matrix, $\mathbf{M_n}$, is defined as

$$\mathbf{M_n} = \left[\langle \left(\frac{\partial \hat{\mathbf{x}}(t)}{\partial t}\right)_S \mathbf{x}^\dagger(t)\rangle\right] \left[\langle \mathbf{x}(t)\mathbf{x}^\dagger(t)\rangle\right]^{-1}. \tag{5.63}$$

We shall then denote the 'drain' dissipation matrix, defined in Eq. 5.52, by $\mathbf{M_d}$ to distinguish it from the net dissipation matrix $\mathbf{M_n}$ and the stochastic backscatter by $\mathbf{F_b}$.

5.6 Relationship between Turbulent Diffusion and Spectral Parameterizations

It is important to examine the relationship between the advective-diffusive flux parameterizations, described in Section 5.2, and the closure motivated spectral parameterizations described in Section 5.5. Firstly, we shall look at the simple case of a homogeneous, isotropic tensor. Then we shall look at the case of a homogeneous but anisotropic tensor. Finally, we shall consider the case of a spatially-varying (inhomogeneous) tensor. In all cases, we shall expand the three-dimensional potential vorticity, q, in Complex Fourier Series:

$$q(x, y, z, t) = \sum_{\mathbf{k}} q_{\mathbf{k}} \exp\left(i\mathbf{k} \cdot \mathbf{x}\right). \tag{5.64}$$

Here $q_{\mathbf{k}}$ is the wave amplitude corresponding to the three-dimensional wavenumber $\mathbf{k} = (k_x, k_y, k_z)$. Note that this choice of eigenfunctions, although convenient for our purposes, does not guarantee the 'rigid-lid' boundary conditions in the vertical, and hence any comparison with the two-level equations, for example, is purely heuristic.

Homogeneous and Isotropic Diffusive Tensor

This corresponds to $T_{ij} = \kappa\delta_{ij}$, where κ is a constant. Hence, writing the subgrid tendency as $\frac{\partial q}{\partial t}$, we have

$$\frac{\partial q}{\partial t} = \kappa \frac{\partial}{\partial x_i}\left(\frac{\partial q}{\partial x_i}\right). \tag{5.65}$$

Upon substituting Eq. 5.64 in Eq. 5.65, we obtain the spectral form

$$\frac{\partial q_{\mathbf{k}}}{\partial t} = -D(k) q_{\mathbf{k}}, \tag{5.66}$$

where

$$D(k) = \kappa k^2 \tag{5.67}$$

is the dissipation in spectral space. This is an enhanced (or reduced, if $\kappa < 0$) version of the molecular viscosity. However, as discussed in Section 5.3, the eddy dissipation does not depend on k^2 but on substantially higher powers of k. In other words, the dissipation is very scale-selective, as we expect it to be if a cascade is occurring. This can perhaps be ameliorated by specifying the eddy flux, $\mathbf{Q}$, to be

$$\mathbf{Q} = -(-1)^n \kappa \nabla \left(\nabla^{2n} q\right), \tag{5.68}$$

where $n = 0$ corresponds to the simple Laplacian operator for the dissipative term. The spectral space dissipation then becomes

$$D(k) = \kappa k^{2(n+1)}. \tag{5.69}$$

Experiments (Frederiksen and Davies, 1997; Frederiksen and Kepert, 2006) show that n should be at least 7 in atmospheric simulations using realistic resolutions.

Homogeneous and Anisotropic Diffusive Tensor

In this case T_{ij} is a constant (homogeneous) tensor. Then

$$\frac{\partial q}{\partial t} = T_{ij}\frac{\partial}{\partial x_i}\left(\frac{\partial q}{\partial x_i}\right) = S_{ij}\frac{\partial}{\partial x_i}\left(\frac{\partial q}{\partial x_i}\right) \tag{5.70}$$

because of the antisymmetry of A. The spectral form is

$$\frac{\partial q_{\mathbf{k}}}{\partial t} = -D(\mathbf{k})q_{\mathbf{k}}, \tag{5.71}$$

where

$$D(\mathbf{k}) = \sum_i \sum_j k_i S_{ij} k_j. \tag{5.72}$$

In Eq. 5.72 the summation symbols have been re-instated for clarity. In this case, then, the dissipation is anisotropic in spectral space. It is however in general not easy to reconstruct the matrix $\mathbf{S}$ from $D_{\mathbf{k}}$ using the spectral parameterizations.

Inhomogeneous Diffusive Tensor

This is the most general situation; that is, we have

$$\frac{\partial q}{\partial t} = \frac{\partial}{\partial x_i}\left(T_{ij}\frac{\partial q}{\partial x_j}\right). \tag{5.73}$$

As well as the potential vorticity, q, we now expand

$$T_{ij}(x, y, z) = \sum_{\mathbf{k}} T^{ij}_{\mathbf{k}} \exp\left(i\mathbf{k}\cdot\mathbf{x}\right). \tag{5.74}$$

Substituting Eqs. 5.64 and 5.74 in Eq. 5.73, we find, after some algebra, that

$$\frac{\partial q_{\mathbf{k}}}{\partial t} = -\sum_{\mathbf{m}}\sum_{\mathbf{n}} \delta(\mathbf{k}+\mathbf{m}+\mathbf{n})D(\mathbf{m},\mathbf{n})q_{-\mathbf{n}}. \tag{5.75}$$

Here,

$$\begin{aligned} D(\mathbf{m},\mathbf{n}) &= (m_i + n_i)\, T^{ij}_{-\mathbf{m}} n_j \\ &= \left(m_i T^{ij}_{-\mathbf{m}} n_j + n_i S^{ij}_{-\mathbf{m}} n_j\right) \\ &\equiv -\left(\mathbf{m}\cdot\mathbf{T}_{-\mathbf{m}}\cdot\mathbf{n} + \mathbf{n}\cdot\mathbf{S}_{-\mathbf{m}}\cdot\mathbf{n}\right) \end{aligned} \tag{5.76}$$

is the inhomogeneous dissipation. We have again used the antisymmetry property of $\mathbf{A}$ in Eq. 5.76, and $\mathbf{T_k} = \mathbf{S_k} + \mathbf{A_k}$ is the matrix of the wave amplitudes of $\mathbf{T}$ which is complex (not purely real) in general. This means that in contrast to the homogeneous case, the inhomogeneous dissipation has both real and imaginary components. We can use the delta function to remove one sum so that

$$\frac{\partial q_{\mathbf{k}}}{\partial t} = -\sum_{\mathbf{m}} D(\mathbf{m}, -\mathbf{k}-\mathbf{m})q_{\mathbf{k}+\mathbf{m}}. \tag{5.77}$$

Equation 5.77 can clearly be written in matrix form as the evolution equation for each wave amplitude is a sum of terms linear in other wave amplitudes. In this study, we assume that the flows are horizontally homogeneous (but possibly anisotropic). This means that the sum in Eq. 5.77 extends only over vertical wavenumbers. If there are only two vertical wavenumbers, as in a two-level system, then a 2×2 matrix will exist for each horizontal wavenumber. This is a form consistent with the parameterizations outlined in Section 5.5.

5.7 Discussion

The advective-diffusive tensor subgrid-scale parameterization methodology is widely employed in oceanography with reported improvements in large-scale circulation simulations. However, there are some conceptual and practical problems associated with this methodology. Firstly, the phenomenology of stratified quasi-geostrophic turbulence clearly shows (see Fig. 3.1) that the energy extracted from the large-scale flow, in the form of potential energy, ends up as kinetic energy near the deformation scale. This kinetic energy becomes barotropic, and then cascades up again towards the large scales where it is eventually dissipated. Hence, if the deformation scale is not resolved in a numerical model, then there should be an injection of energy from the subgrid scales accompanying the reduction in potential energy of the large scales. The advective tensor proposed by Gent and McWilliams is able to produce a reduction in potential energy, but there is no corresponding injection of kinetic energy. The Redi-Cox diffusion tensor is assumed to be downgradient so that it cannot inject energy, but only drain it. Even if an up-gradient 'diffusion' tensor is allowed, this would be numerically very unstable. The closure-motivated methodology outlined in Section 5.5 is able to inject energy through the stochastic backscatter term, and since this is accompanied by a drain dissipation, it turns out to be numerically stable, as will be shown in subsequent chapters.

Another problem, though not as serious, is that the eddy flux divergence term is assumed to be of the form $\nabla\cdot(\mathbf{T}\nabla q)$, which for a constant $\mathbf{T}$ corresponds to a Laplacian operator. In fact, the spectral space dissipation in the atmosphere has been shown to be much steeper than the k^2 dependence implied by a Laplacian operator. The dissipation in the ocean is probably shallower than that in the atmosphere (this will be backed-up by the results in subsequent chapters), but steeper than k^2. This can presumably be overcome by specifying the divergence of the diffusive eddy flux to be of the form $\nabla\cdot\left[\mathbf{S}\nabla\left(\nabla^{2n}q\right)\right]$; this is similar to the suggestion of Roberts and Marshall (1998).

Last, but not least, the advective-diffusive methodology as used in oceanography does not take into account the difference between mean-transient and transient-transient interactions (and this is related to the fact there is no injection of barotropic kinetic energy in those formulations). Rather, the assumption seems to be that there is a 'spectral gap' between the mean field and the eddies, with the mean field being confined to low wavenumbers and eddies to higher wavenumbers, and as such eddy-eddy interactions are not considered important. There could be reasonable justifications for this. For example, the beta effect will tend to inhibit eddy-eddy interactions at the large scales. Additionally, if the large-scale dissipation happens to be of sufficient magnitude, eddy-eddy interactions will be suppressed. It is one of the aims of this study to examine such issues.

However, we feel that a generic subgrid-scale parameterization scheme for geophysical flows should take into account eddy-eddy interactions, and our closure-motivated methodology is designed for this purpose. We do not explicitly parameterize the mean subgrid flux in this study; rather, as was described in Section 5.5, the mean field is adjusted based on

assumption of balance at steady state. The mean subgrid forcing is dynamically equivalent to the Gent-McWilliams skew flux because it reduces the mean potential energy of the flow; nonetheless, the self-consistently calculated matrices $\mathbf{M}$ and $\mathbf{F}$ parameterize effects of eddies that are not captured in any current subgrid-scale parameterization schemes. In subsequent chapters, the DNS based methodology will be used to parameterize subgrid-scale turbulence in both atmospheric and oceanic flows.

Chapter 6

Equivalent Layers

In this chapter, we shall relax the solid body rotation flow towards a prescribed mean value, consisting of oppositely directed flows of equal magnitude in the two layers. As there is no rotation, and the drag is the same in both layers, the kinetic energy is equally distributed across the layers, hence the term *Equivalent Layers*, as coined by Salmon (Salmon, 1978). The high degree of symmetry in this problem makes it a good starting point for analyzing subgrid-scale parameterizations in stratified flows.

The governing equations for the DNS are the spherical two layer QGPV equations without rotation:

$$\frac{\partial q_i}{\partial t} = -J(\psi_i, q_i) - D_i^0 \zeta_i + \kappa(q_i^{rel} - q_i) \ , \tag{6.1}$$

where i=1,2. The zonal wind is relaxed towards $u_i^{rel} = U_i^{rel} cos\phi$, where ϕ is the latitude, and $U_1^{rel} = -U_2^{rel}$ are the maximum winds (at the equator); q_i^{rel} are the potential vorticities corresponding to the zonal winds u_i^{rel}. The relaxation time scale is given by κ^{-1}. The bare dissipation operator, D_i^0, is

$$D_i^0 = \alpha + (-1)^p \nu^0 \nabla^{2p} \ . \tag{6.2}$$

Here, α is the linear friction coefficient, due to Ekman drag; ν^0 is an ad-hoc dissipation, chosen together with the order of the Laplacian operator, p, so that the inertial range of the energy spectrum follows the k^{-3} power law. The model is integrated in spectral space, as described in Appendix E, and taken to steady-state. An artificial truncation is performed at a wavenumber N_*, and the matrices $\mathbf{M}$, $\mathbf{F}$, and $\bar{\mathbf{f}}$ calculated to parameterize the non-linear tendency for wavenumbers less or equal to N_* (see Section 5.5 and Appendix F). The corresponding matrices $\mathbf{M}'$, $\mathbf{F}'$, and $\mathbf{f}'$ in the BTBC formulation are also calculated (see Appendix G). The LES at maximum wavenumber N_* is then performed using the parameterized form of the subgrid non-linear tendency, Eq. F.15, which appears as an additional term in the spectral form of Eq. 6.1. Both the stochastic parameterization, with $\mathbf{M_d}$ and $\mathbf{F_b}$, and the deterministic parameterization, with $\mathbf{M_n}$ only, are considered.

6.1 Atmospheric Flows

6.1.1 DNS at T126

For the atmosphere the following parameters have been chosen: the drag, α, in both layers has been set to a damping time of 12.5 days; the dissipation, $\nu^0 = 3.96 \times 10^{31}$ m^{8}s^{-1}; the order of the Laplacian operator $p = 4$; the relaxation time for the mean flow, κ, is 11.6 days;

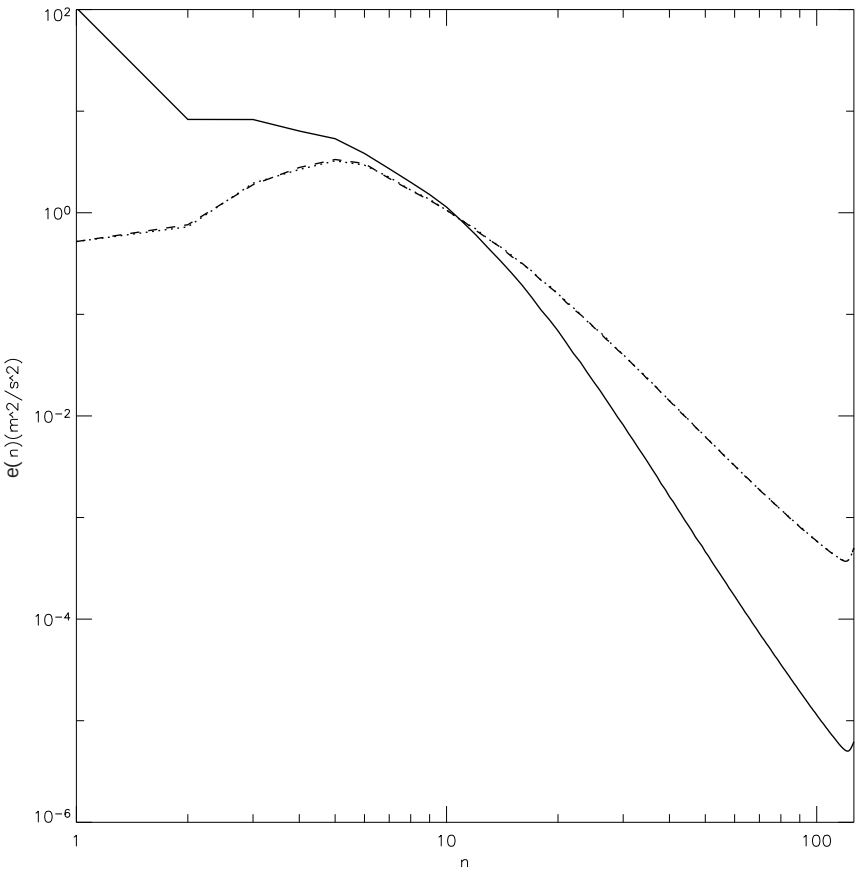

Figure 6.1: Energy spectra as functions of total wavenumber (n): potential energy (solid), Level 1 kinetic energy (dashed), and Level 2 kinetic energy (dotted) for the atmospheric equivalent layer DNS at T126.

the layer coupling constant, $F_a = 2.5 \times 10^{-12}$ m^{-2}, giving $\lambda_i \sim 500$ km; and the prescribed maximum mean flow is $U_1^{rel} = 7.5$ ms^{-1}, $U_2^{rel} =$ -7.5 ms^{-1}. The equations have been stepped forward in time for 520 days at steady state—after an initial spin-up period, with a timestep of 450 s, at the resolution of T126. The number of longitude by latitude grid points is 384 $\times$ 192. We can obtain a rough estimate for the wavenumber corresponding to the deformation scale, k_i, as follows: $\lambda_i \sim 500$ km corresponds to approximately $\frac{500}{6000} = \frac{1}{12}$ radians of longitude, taking the radius of the Earth to be approximately 6000 km. Then $k_i = \frac{1}{\lambda_i} = 12$. Hence, the deformation scale is somewhere around wavenumber 12.

Figs. 6.1 and 6.2 show, respectively, $e(n)$, the total, and, $E(m)$, the zonal wavenumber averaged energy spectra (see Eqs. E.41 and E.42 of Appendix E.4). Both potential and kinetic energy spectra are shown. The kinetic energies of Level 1 and Level 2 are the same in this problem, and ν^0 has been chosen so that the kinetic energy spectrum has an approximately n^{-3} dependence all the way to the truncation scale. There is, however, a slight lifting of the tail right at the trucation scale, evident in Fig. 6.1, which highlights the difficulties with working with an ad-hoc eddy hyperdiffusion. A principal aim of this study is to find a systematic method for overcoming such difficulties. The potential energy spectra have an approximately n^{-5} dependence; Merilees and Warn (1971) discuss this

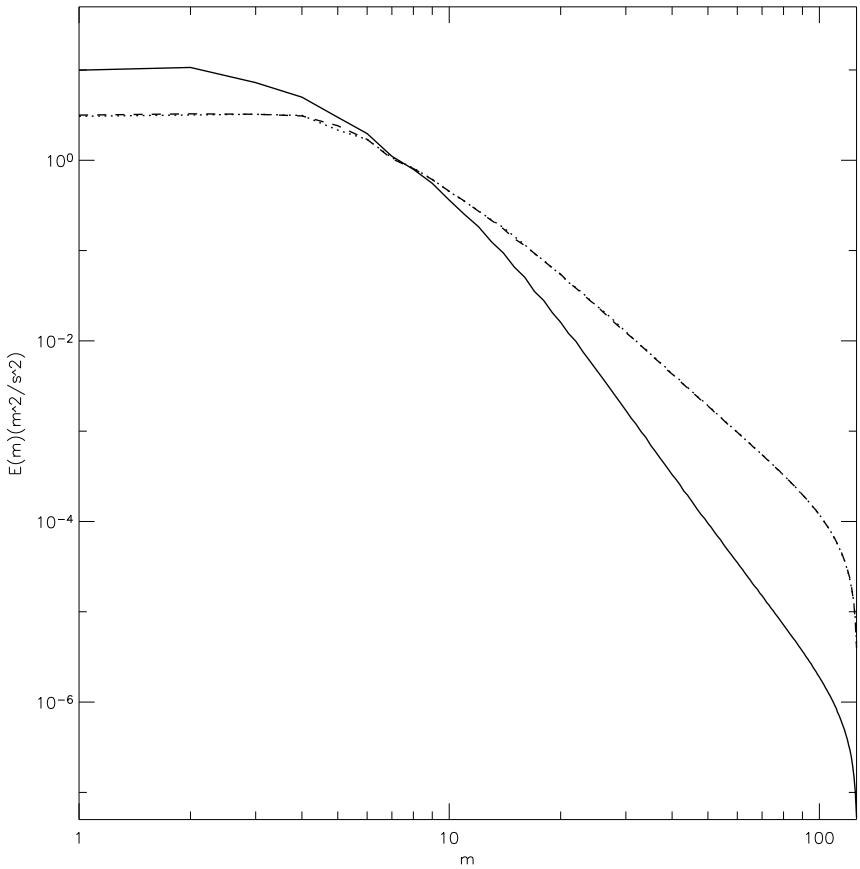

Figure 6.2: Energy spectra as functions of zonal wavenumber (m): potential energy (solid), Level 1 kinetic energy (dashed), and Level 2 kinetic energy (dotted) for the atmospheric equivalent layer DNS at T126.

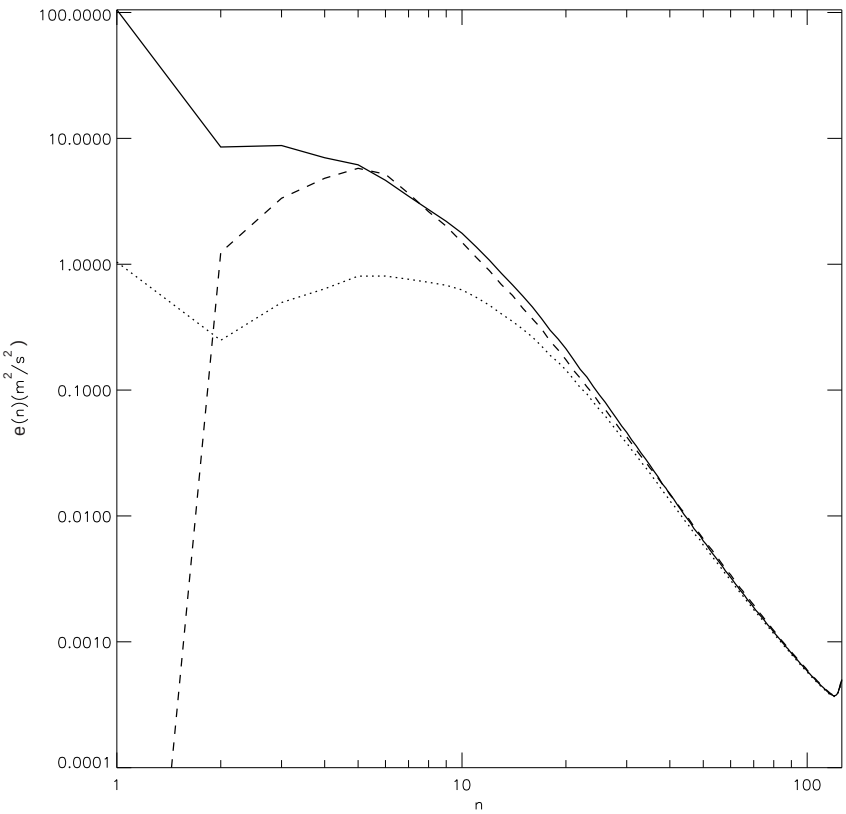

Figure 6.3: Energy spectra as functions of total wavenumber (n): total baroclinic energy (solid), barotropic kinetic energy (dashed), and baroclinic kinetic energy (dotted) for the atmospheric equivalent layer DNS at T126.

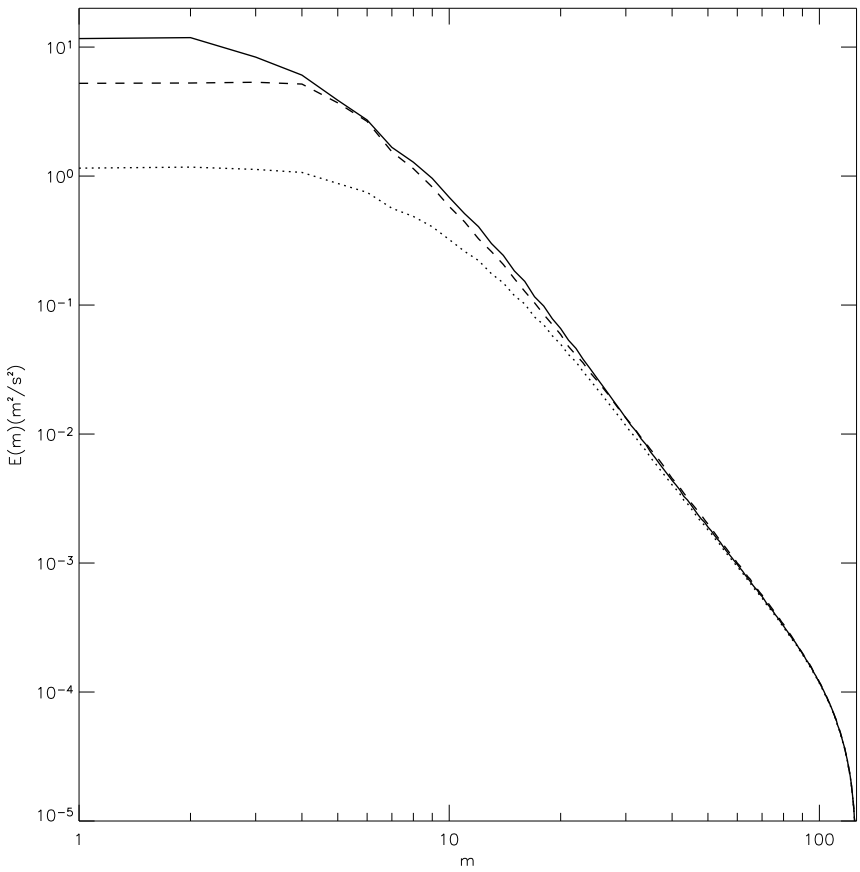

Figure 6.4: Energy spectra as functions of zonal wavenumber (m): total baroclinic energy (solid), barotropic kinetic energy (dashed), and baroclinic kinetic energy (dotted) for the atmospheric equivalent layer DNS at T126.

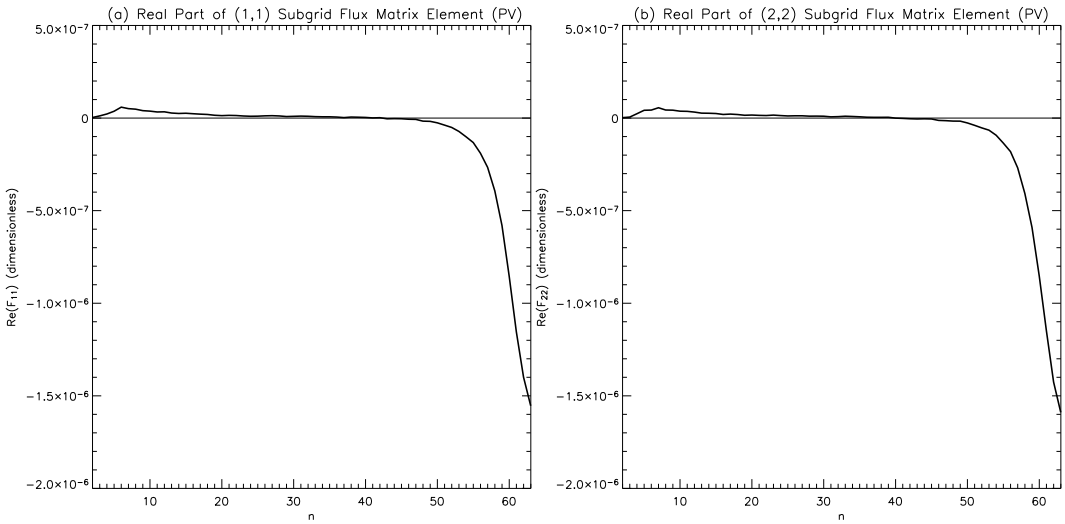

Figure 6.5: Diagonal elements of the real part of the isotropic subgrid flux matrix in the PV formulation: (a) $\mathcal{F}^r_{11}$; (b) $\mathcal{F}^r_{22}$.

phenomenon, which is related to coarse vertical resolution. Fig. 6.2 reveals an inertial range for values of m of about 10 to 100. Figs. 6.3 and 6.4 show the corresponding spectra in terms of barotropic and baroclinic energies. At the large scales ($m, n < 30$), the kinetic energy is dominated by barotropic energy. This is presumably due to barotropization of the flow. Transient kinetic energy produced near the deformation scale is preferentially cascaded upscale via the barotropic mode, as discussed in Section 3.2.6.

In Figs. 6.1 and 6.3, the $n = 1$ energy is dominated by the mean energy from the $(m, n) = (0, 1)$ (solid body rotation mode) relaxation specified for this flow. This is evident from the fact that the $n = 1$ barotropic energy is effectively zero. This is because we have mean $(m, n) = (0, 1)$ flows of equal magnitudes but opposite directions, which corresponds to $\psi_{01} = 0$, and hence no barotropic energy. The mean energy at wavenumber $(m, n) = (0, 1)$ is thus in the form of baroclinic energy. Some of this mean energy is converted into transient energy near the deformation scale, and finds its way upscale again, mainly in the form of barotropic energy, due to the inverse cascade process. At small scales ($m, n > 30$), the baroclinic energy is mostly kinetic, and furthermore, there is an equipartition between barotropic and baroclinic energies. This result can be anticipated from the phenomenology of QG turbulence for scales smaller than the deformation radius, discussed in Section 3.2.6. The equipartitioning of kinetic and potential energies for scales smaller than the deformation radius was first predicted by Charney (1971).

6.1.2 Subgrid-scale Parameterizations at T63

An artificial truncation was performed at $N_* = 63$, and the matrices $\mathbf{M}$, $\mathbf{F}$, and $\overline{\mathbf{f}}$ calculated. Given that the deformation scale is somewhere around $n = 12$, a truncation at T63 is more than sufficient to resolve the deformation scale. This is typical of truncations in atmospheric circulation models with modern computational capabilities (Hamilton, 2006). Given that the energy containing eddies are well resolved, we do not expect a substantial contribution from the mean subgrid tendency, $\overline{\mathbf{f}}$, and this is indeed found to be the

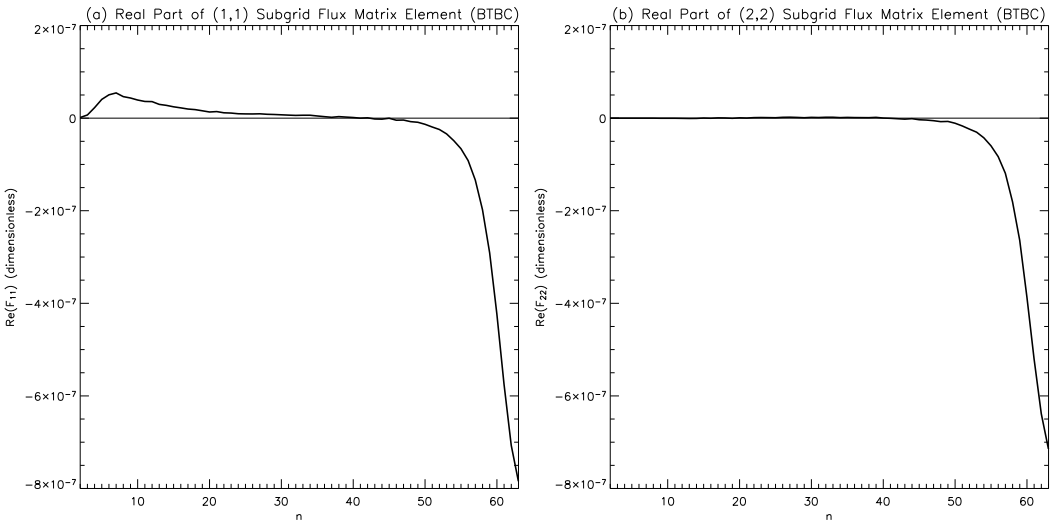

Figure 6.6: Diagonal elements of the real part of the isotropic subgrid flux matrix in the BTBC formulation: (a) $\mathcal{F}^r_{11}$; (b) $\mathcal{F}^r_{22}$.

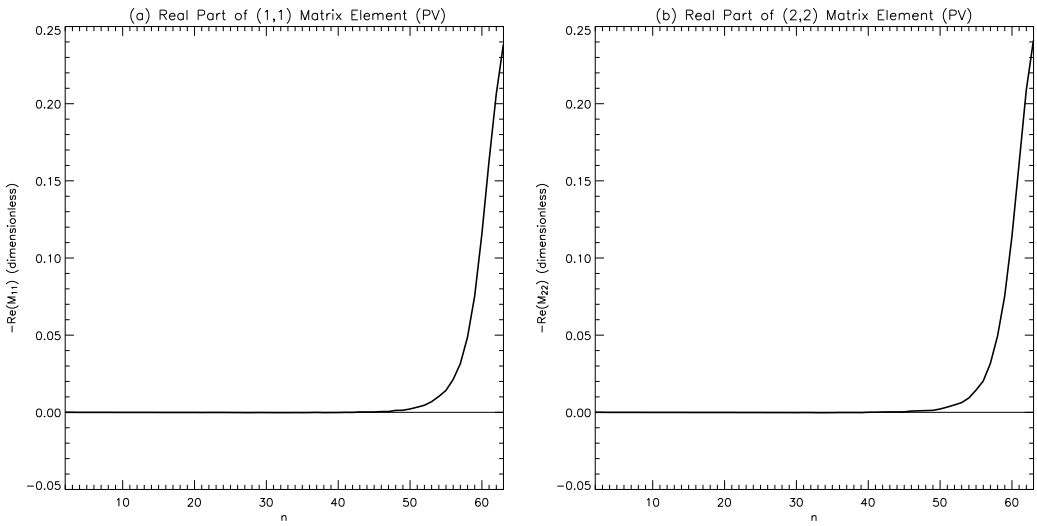

Figure 6.7: Diagonal elements of the real part of the isotropic net dissipation matrix in the PV formulation: (a) $-M^r_{11}$; (b) $-M^r_{22}$.

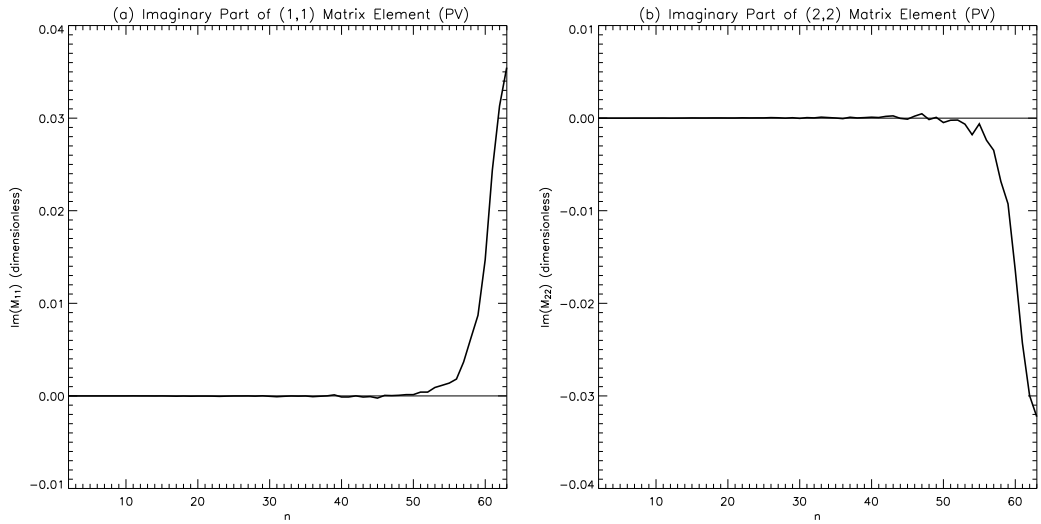

Figure 6.8: Diagonal elements of the imaginary part of the isotropic net dissipation matrix in the PV formulation: (a) M_{11}^i; (b) M_{22}^i.

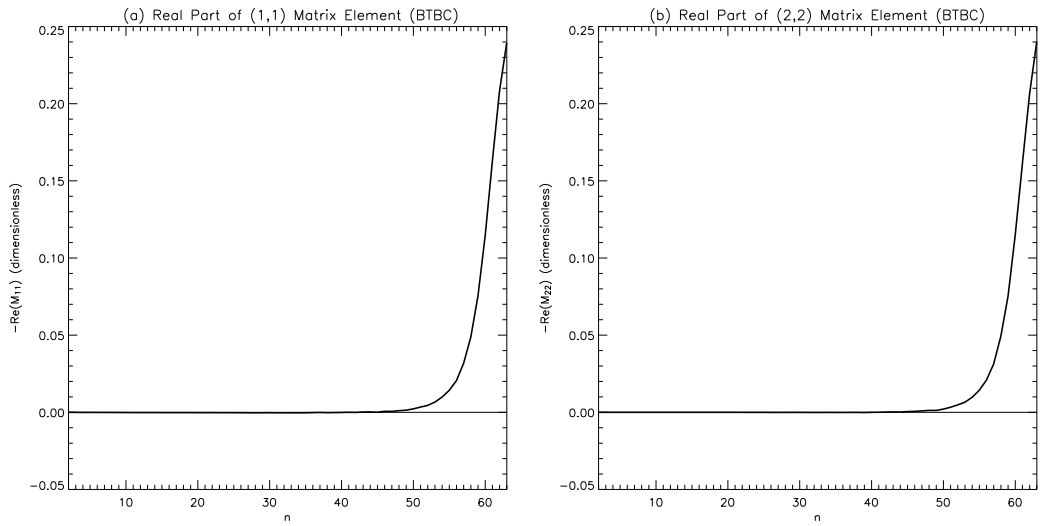

Figure 6.9: Diagonal elements of the real part of the isotropic net dissipation matrix in the BTBC formulation: (a) $-M_{11}^r$; (b) $-M_{22}^r$.

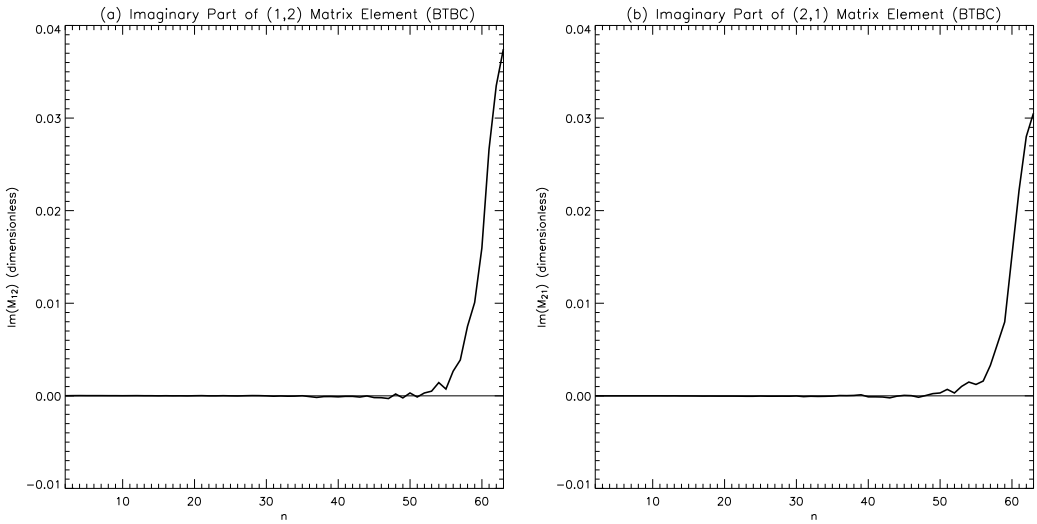

Figure 6.10: Off-diagonal elements of the imaginary part of the isotropic net dissipation matrix in the BTBC formulation: (a) M^i_{12}; (b) M^i_{21}.

case. Further, based on the phenomenology of QG turbulence, we expect the net subgrid transfer to be dominated by a negative flux of enstrophy for wavenumbers $m, n >> k_i$. This corresponds to a positive dissipation coefficient (or a matrix dissipation with positive eigenvalues). Finally, at these scales, the two layers behave as if they were uncoupled, and hence the off-diagonal elements of the matrices in PV space vanish. Unless stated otherwise, all the matrix coefficients presented are isotropized; that is, they have been averaged over the zonal wavenumber m as described in Appendix F.

Figure 6.5 shows the diagonal elements of subgrid flux matrix $\mathcal{F} = \langle \left(\frac{\partial \hat{\mathbf{x}}(t)}{\partial t}\right)_S \hat{\mathbf{x}}^\dagger(t)\rangle + \langle \hat{\mathbf{x}}(t) \left(\frac{\partial \hat{\mathbf{x}}(t)}{\partial t}\right)_S^\dagger \rangle$ in the PV formulation, with $\left(\frac{\partial \hat{\mathbf{x}}(t)}{\partial t}\right)_S$ and $\hat{\mathbf{x}}$ defined in Eqs. 5.50 and 5.51. $\mathcal{F}$ represents the contribution of the subgrid terms to the potential vorticity equal-time covariance matrix tendency. The off-diagonal elements are over two orders of magnitude smaller, and are not shown. The Level 1 subgrid flux is the same as the Level 2 subgrid flux in this problem, and they are both negative near the truncation scale, indicating a negative flux of potential enstrophy due to unresolved subgrid scales. The corresponding matrix, $\mathcal{F}'$ in the BTBC formulation is shown in Fig. 6.6. The off-diagonal elements turn out be zero in the BTBC formulation due to the symmetry of the equivalent layer problem. The diagonal elements describe (twice) the contribution of the subgrid modes to the barotropic ($\mathcal{F}'_{11}$ element) and baroclinic ($\mathcal{F}'_{22}$ element) enstrophy. The barotropic and baroclinic fluxes are roughly equal in this problem. They are both negative near the truncation scale, implying negative fluxes of barotropic and baroclinic enstrophies. This is compatible with the phenomenology of QG turbulence for $n >> k_i$ (See Section 3.2.6). Interestingly, the barotropic flux has a slight positive region, at the large scales, for $n < 40$. This is absent in the baroclinic flux. In this region, which in fact corresponds to the negative viscosity region typical of two-dimensional fluids, there is an injection of barotropic energy to large scales.

Fig 6.7 shows the diagonal elements of the real part of the net dissipation matrix $-\mathbf{M}^{\mathbf{r}}_{\mathbf{n}}$. The net dissipation coefficients have the typical cusp near the truncation scale ($n > 50$).

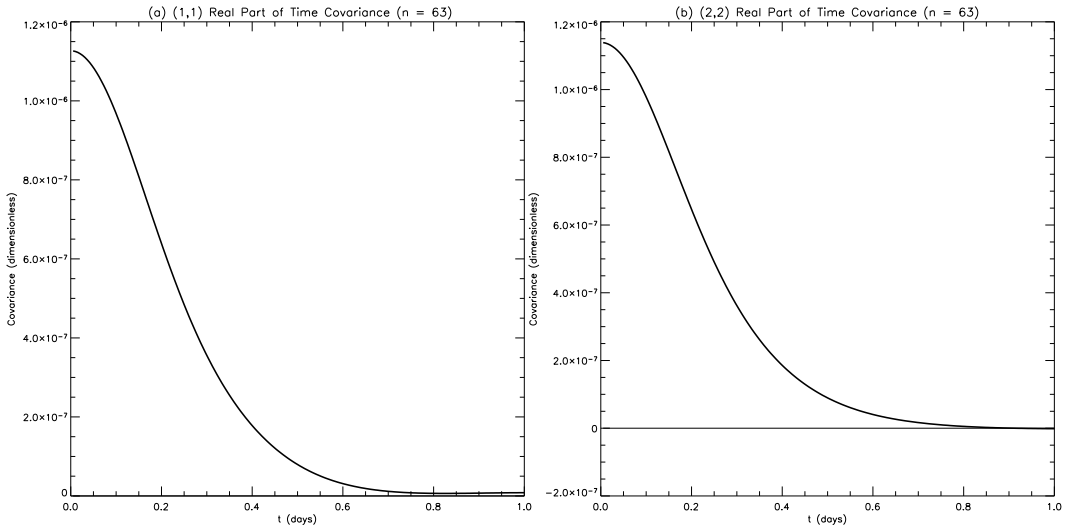

Figure 6.11: Time covariances of the subgrid tendency matrix in the PV formulation: (a) Level 1; (b) Level 2.

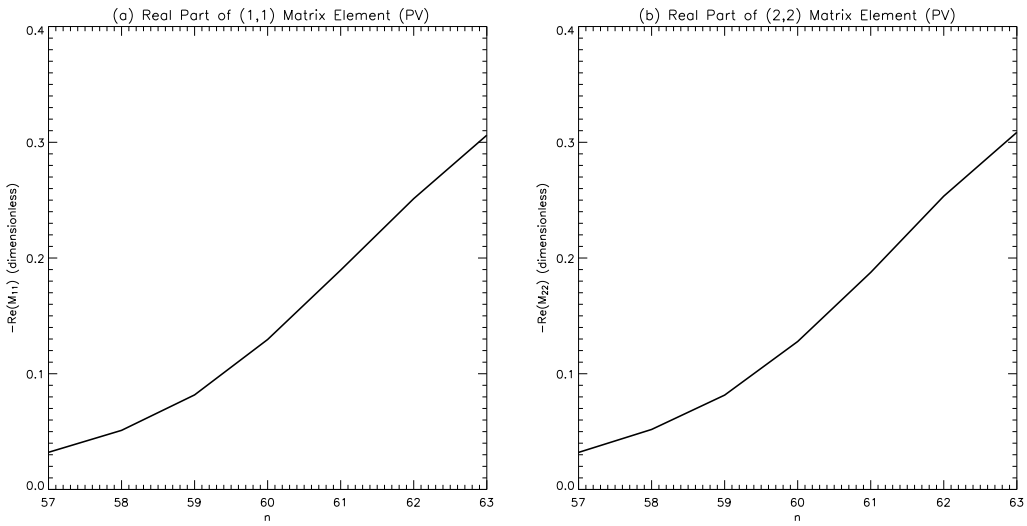

Figure 6.12: Diagonal elements of the real part of the isotropic drain dissipation matrix in the PV formulation: (a) $-M^r_{11}$; (b) $-M^r_{22}$.

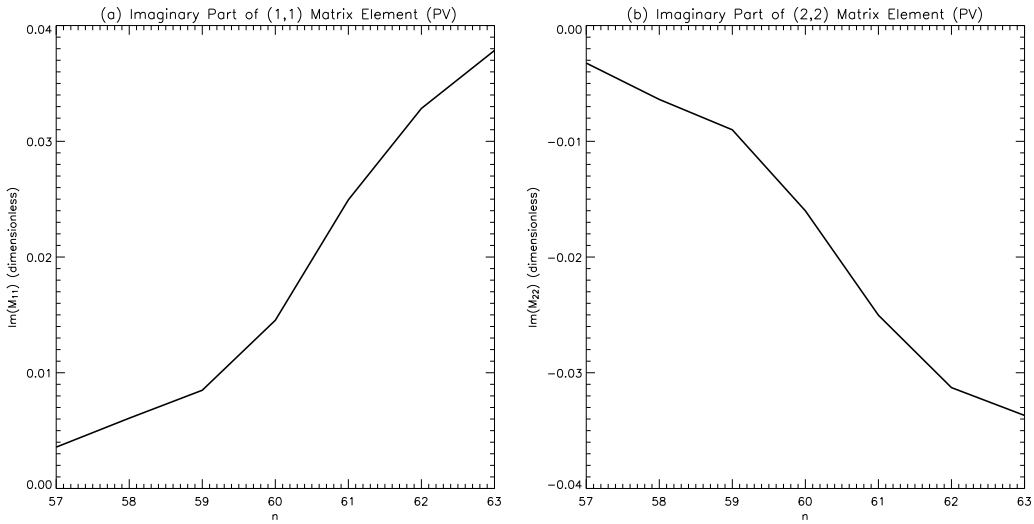

Figure 6.13: Diagonal elements of the imaginary part of the isotropic drain dissipation matrix in the PV formulation: (a) M^i_{11}; (b) M^i_{22}.

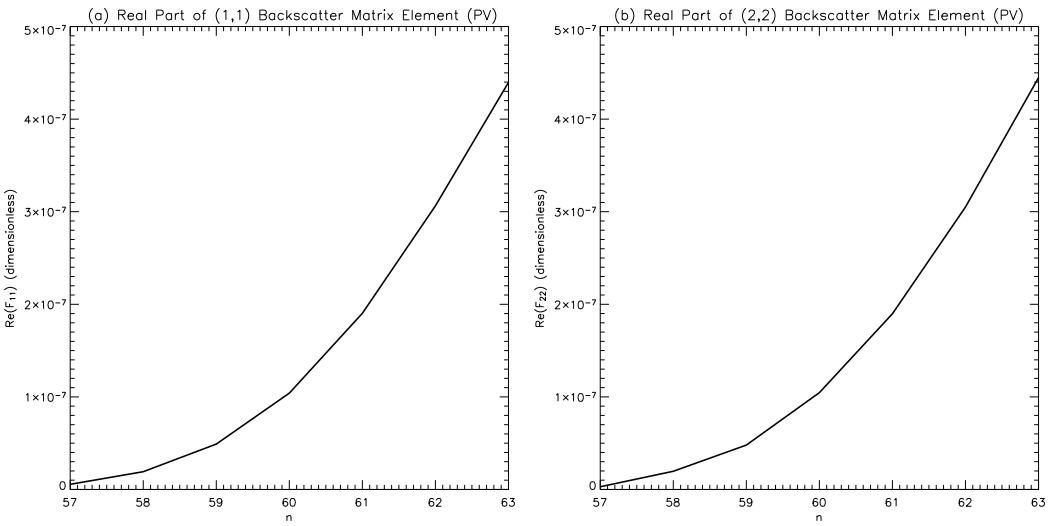

Figure 6.14: Diagonal elements of the isotropic backscatter matrix in the PV formulation: (a) F^r_{11}; (b) F^r_{22}.

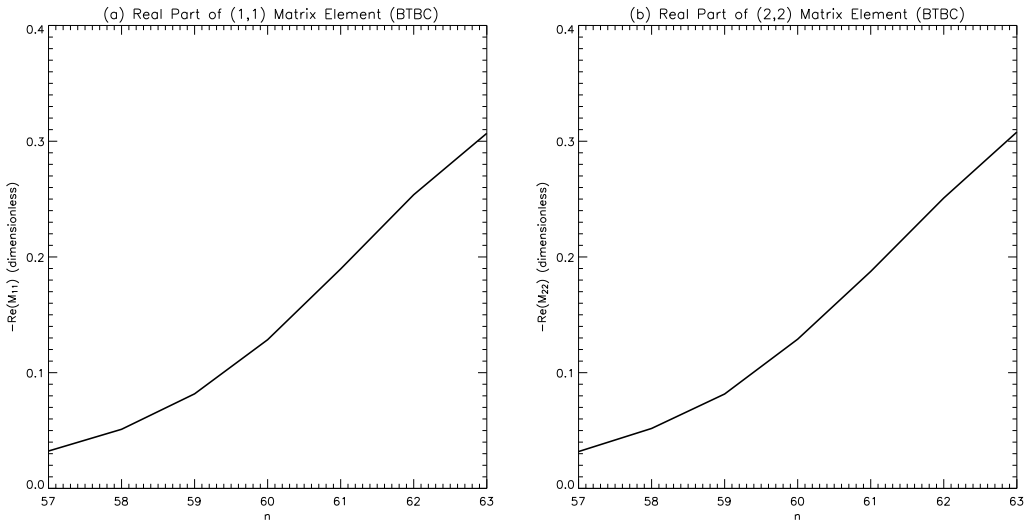

Figure 6.15: Diagonal elements of the real part of the isotropic drain dissipation matrix in the BTBC formulation: (a) $-M^r_{11}$; (b) $-M^r_{22}$.

Otherwise, not only is the net dissipation flat far away from the truncation scale, as predicted by Kraichnan (1976), it is also practically zero. This says that the turbulent fluxes at these resolutions are dominated by local transfers. The diagonal elements of the imaginary part of the net 'dissipation' matrix, $\mathbf{M^i_n}$, are shown in Fig. 6.8. The (diagonal) elements of $\mathbf{M^i_n}$ are equal in magnitude, but of opposite sign. Furthermore, they are at least five times as small as $-\mathbf{M^r_n}$, and are hence probably not very significant dynamically. The corresponding net dissipation matrices $-\mathbf{M'^r_n}$ and $\mathbf{M'^i_n}$ in the BTBC formulation are shown in Figs. 6.9 and 6.10, respectively. $-\mathbf{M'^r_n}$ is effectively equal to $-\mathbf{M^r_n}$ in this case; $\mathbf{M'^i_n}$ is, however, purely *off-diagonal*, with the M'^i_{12} element slightly larger than the M'^i_{21} element. Clearly, however, $-\mathbf{M'^r_n}$ is the dominant matrix.

The drain dissipation, $\mathbf{M_d}$, and stochastic backscatter, $\mathbf{F_b}$, matrices have been calculated by integrating over a timescale $\tau = 0.125$ day. Fig. 6.11 shows the time covariance $\langle \left(\frac{\partial \hat{q}^i_{mn}(t)}{\partial t}\right)_S \left(\frac{\partial \hat{q}^i_{mn}(t_0)}{\partial t}\right)^*_S \rangle$ as a function of time, t, at $n = 63$. The subgrid tendency decorrelates after a period of about 0.8 day. There is some arbitrariness about the choice of τ. The reason for this is that the decorrelation time is in general wavenumber dependent; however, we use the same τ on all wavenumbers for the purpose of simplicity. In general, nevertheless, the most significant contribution comes from the cusp near the truncation scale, and hence we choose a typical decorrelation time near that scale. Experience has shown that choosing τ to be too large can sometimes lead to the unwanted effect of negative eigenvalues of the matrix $\mathbf{F}$ just before the cusp. These negative values are usually small in magnitude, and presumably arise when errors in estimating $\mathbf{M}$ are of the same order as the true value of $\mathbf{M}$, which can happen just before the cusp, where the $\mathbf{M}$ is small. We should stress, however, that the eigenvalues of $\mathbf{F}$ are *never* found to be negative at the cusp itself. It is generally found that the longer the integration time, the more prominent is the cusp; that is, the peak at the truncation scale rises, and the contribution just before the cusp falls. This is the reason for choosing τ somewhat smaller than the decorrelation time. Even with this choice, we cannot avoid slightly negative values of the eigenvalues of

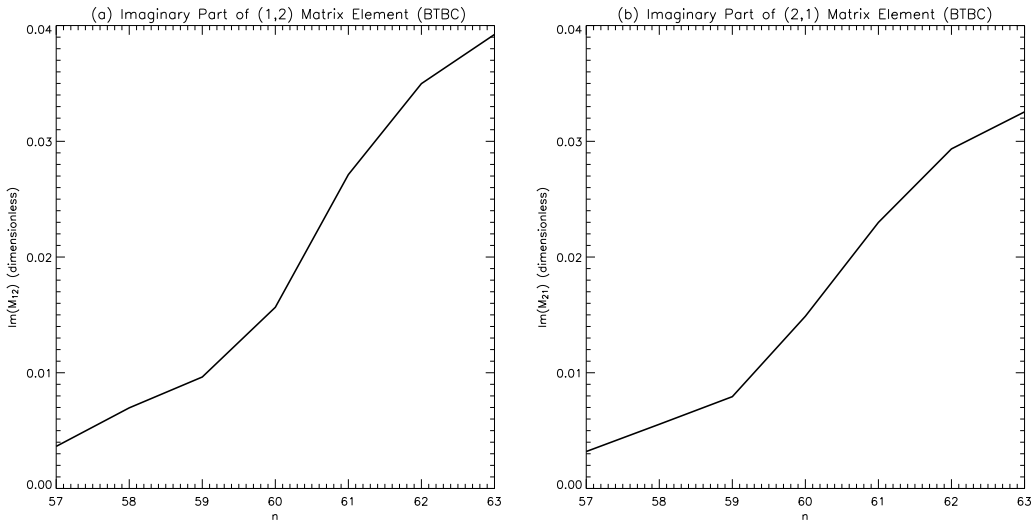

Figure 6.16: Off-diagonal elements of the imaginary part of the isotropic drain dissipation matrix in the BTBC formulation: (a) M^i_{12}; (b) M^i_{21}.

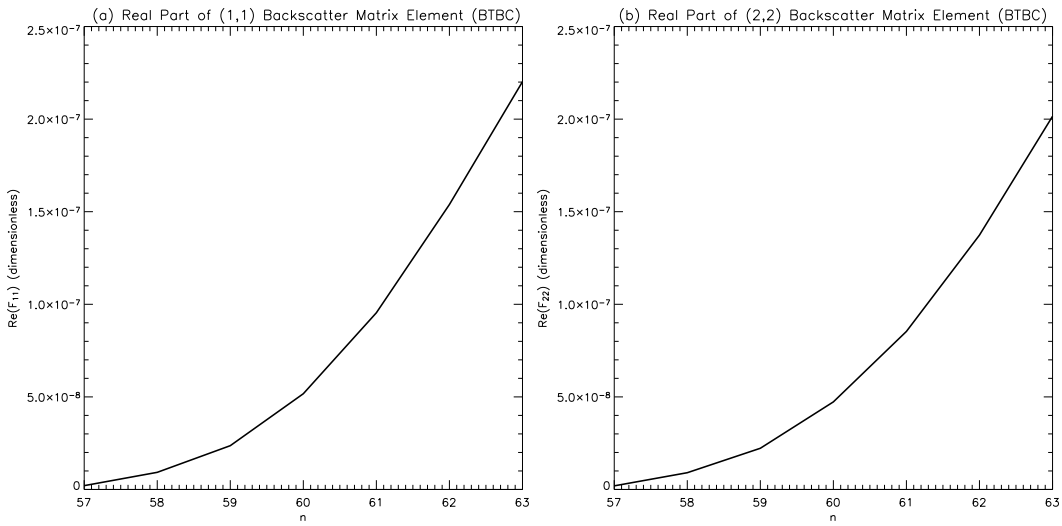

Figure 6.17: Diagonal elements of the isotropic backscatter matrix in the BTBC formulation: (a) F^r_{11}; (b) F^r_{22}.

$\mathbf{F}$ below some wavenumber. This is remedied by defining

$$\mathbf{M} = \begin{cases} \mathbf{M_d} & \text{if } n > n_c; \\ \mathbf{M_n} & \text{otherwise} \end{cases} \tag{6.3}$$

and

$$\mathbf{F} = \begin{cases} \mathbf{F_b} & \text{if } n > n_c; \\ \mathbf{0} & \text{otherwise,} \end{cases} \tag{6.4}$$

where n_c is some cut-off wavenumber, usually several wavenumbers below the truncation scale. In other words we use the drain dissipation and backscatter near the truncation scale, and the net dissipation alone away from the truncation scale. This is reasonable as the stochastic backscatter is much more scale-selective than the net eddy dissipation.

The diagonal elements of $-\mathbf{M_d^r}$ and $\mathbf{M_d^i}$ are shown in Figs. 6.12 and 6.13, respectively. The cutoff wavenumber has been chosen to be $n_c = 57$. $-\mathbf{M_d^r}$ is in this case only slightly stronger than $-\mathbf{M_n^r}$, and is an order of magnitude greater than $\mathbf{M_d^i}$. Otherwise, the drain and net dissipations are qualitatively similar. The diagonal elements of the backscatter matrix, $\mathbf{F_b^r}$ are shown in Fig. 6.14. The corresponding matrices $-\mathbf{M_d'^r}$, $\mathbf{M_d'^i}$, and $\mathbf{F_b'^r}$ in the BTBC formulation are shown in Figs. 6.15, 6.16, and 6.17, respectively.

6.1.3 LES at T63

Large eddy simulations at T63 using bare parameters (no subgrid-scale parameterization), net dissipation (deterministic parameterization), and drain dissipation and backscatter (stochastic parameterization) were performed. Figs. 6.18 and 6.19 show, respectively, the n and m averaged kinetic energy spectra for Level 1 using bare parameters. We shall be using the Level 1 kinetic energy spectra to test the performance of the LES for the rest of this thesis. Without any subgrid-scale parameterizations, the kinetic energy spectra start deviating from the high resolution spectra (also shown in both figures) at wavenumbers somewhat above $m, n = 20$. The tail of the specta lift due to insufficient drain of enstrophy near the truncation scale. Below this wavenumber, however, the spectra are in reasonably good agreement, except for what looks like some sampling error. Hence, for this flow at least, the large scale features are largely unaffected by subgrid-scale effects. This is consistent with the phonomenology of QG turbulence, for if the truncation is performed within the inertial range, the turbulent transfers are to a large extent local, and hence the loss of the extra sink of enstrophy due to the absence of subgrid scales will manifest itself locally. Note that, as discussed in Section 5.3, this does not necessarily imply that the triad interactions are purely local; indeed, several studies (see Section 5.3) point to the fact that they are quite non-local. However, both the severe cusp and the localness of the deviation of the spectra, upon using bare parameters, point to the fact that the transfer of enstrophy is local. Figs. 6.20 and 6.21 show the LES at T63 using the net dissipation (deterministic) parameterization scheme. There is excellent agreement between the deterministic LES and the high resolution DNS throughout the inertial range. The slight large scale deviations look like sampling errors. Similarly, upon using the stochastic parameterization scheme for $n > 57$, we obtain very good agreement between the LES and DNS. This is shown in Figs. 6.22 and 6.23.

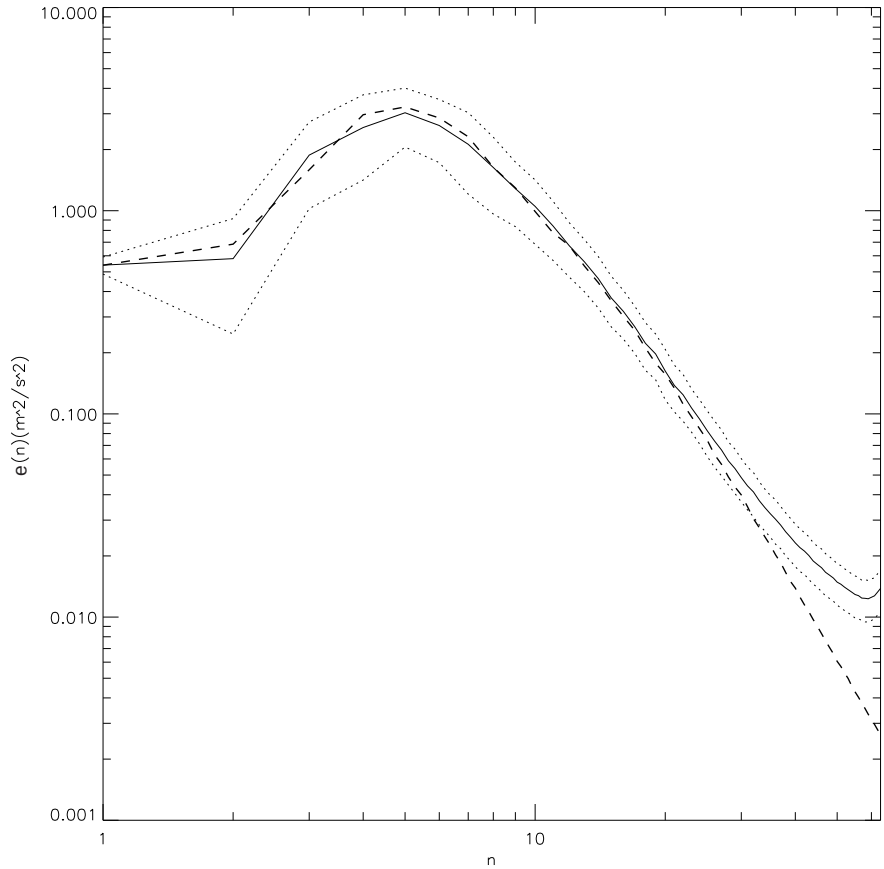

Figure 6.18: Energy spectra (Level 1) as functions of total wavenumber (n): kinetic energy for LES with bare parameters (solid); LES kinetic energy plus and minus standard deviation (dotted); and T126 DNS kinetic energy (dashed).

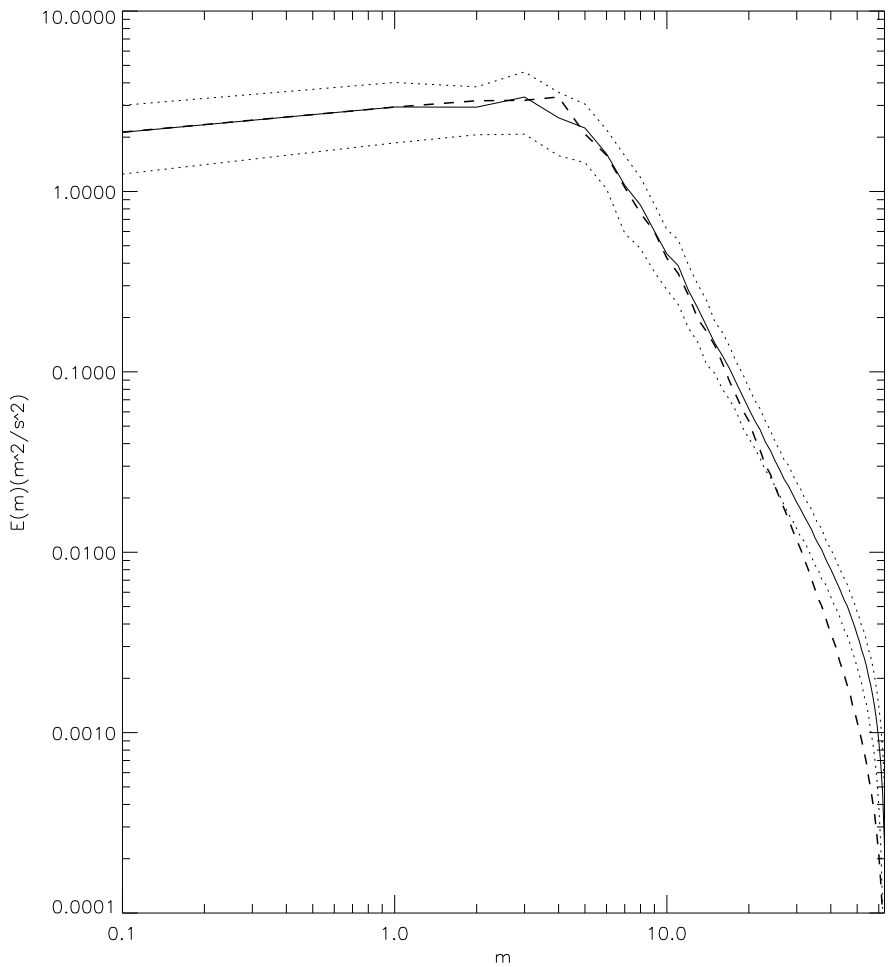

Figure 6.19: Energy spectra (Level 1) as functions of zonal wavenumber (m): kinetic energy for LES with bare parameters (solid); LES kinetic energy plus and minus standard deviation (dotted); and T126 DNS kinetic energy (dashed).

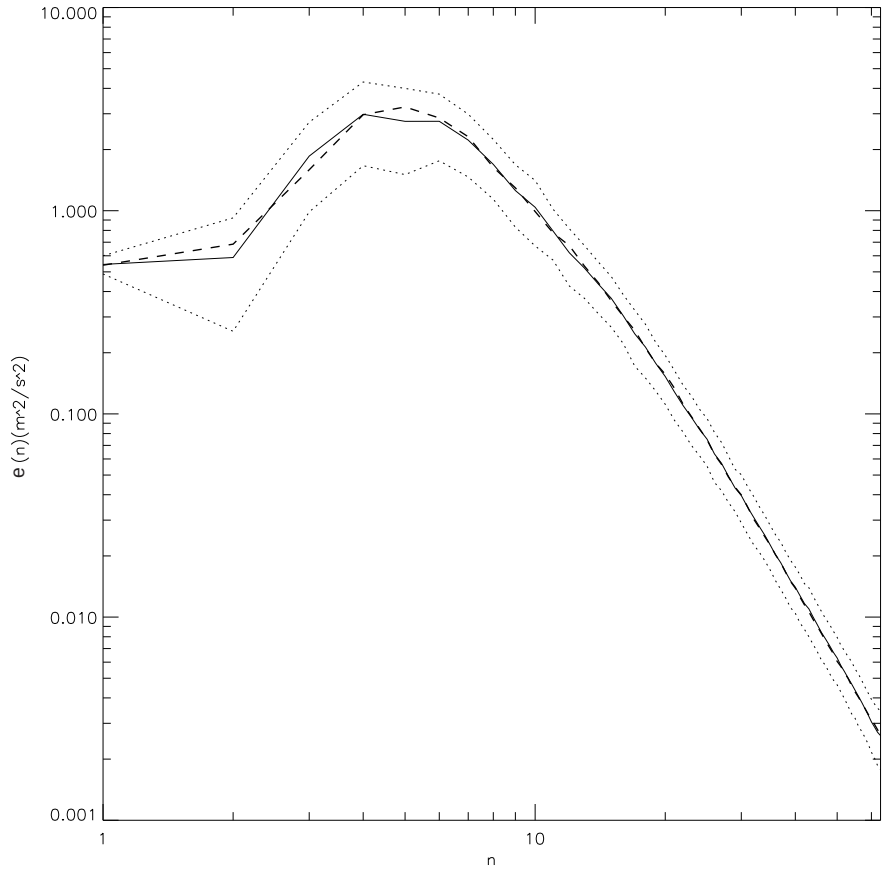

Figure 6.20: Energy spectra (Level 1) as functions of total wavenumber (n): kinetic energy for LES with renormalized net dissipation (solid); LES kinetic energy plus and minus standard deviation (dotted); and T126 DNS kinetic energy (dashed).

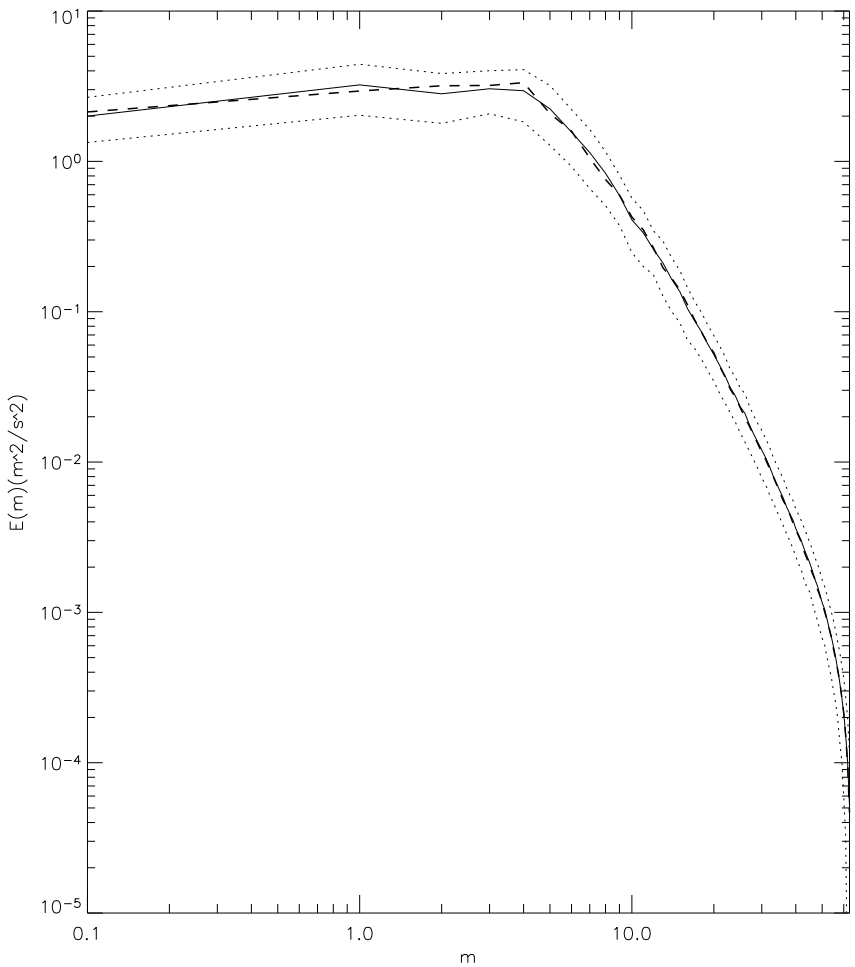

Figure 6.21: Energy spectra (Level 1) as functions of zonal wavenumber (m): kinetic energy for LES with renormalized net dissipation (solid); LES kinetic energy plus and minus standard deviation (dotted); and T126 DNS kinetic energy (dashed).

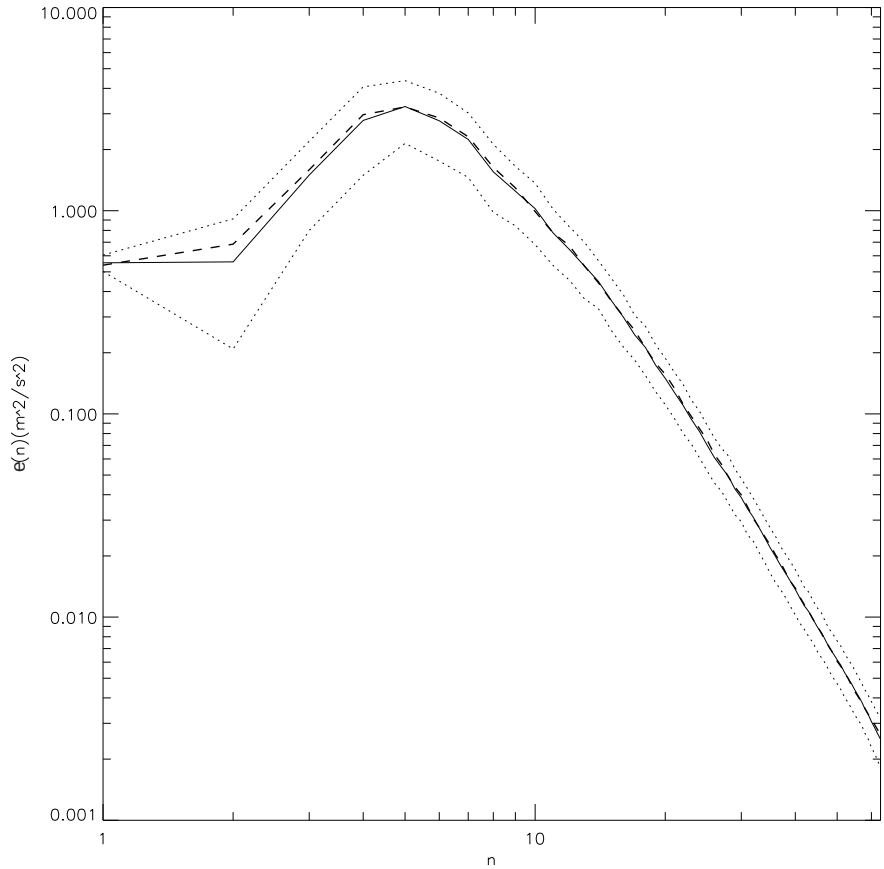

Figure 6.22: Energy spectra (Level 1) as functions of total wavenumber (n): kinetic energy for LES with renormalized drain dissipation and stochastic backscatter(solid); LES kinetic energy plus and minus standard deviation (dotted); and T126 DNS kinetic energy (dashed).

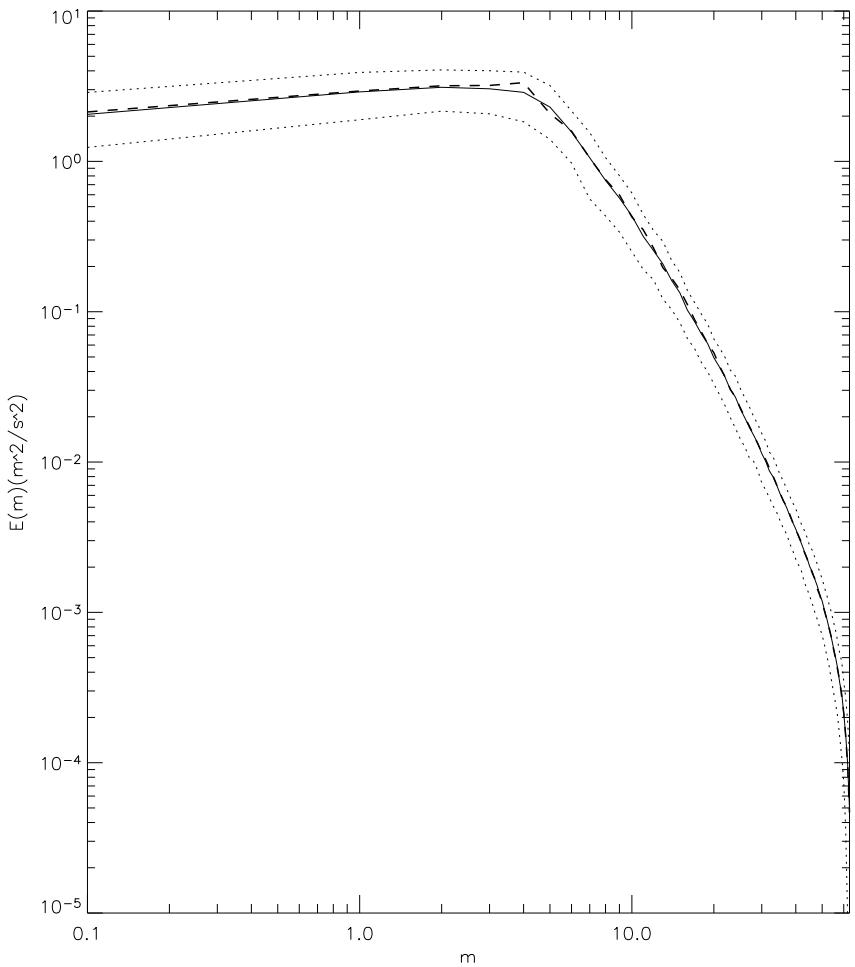

Figure 6.23: Energy spectra (Level 1) as functions of zonal wavenumber (m): kinetic energy for LES with renormalized drain dissipation and stochastic backscatter (solid); LES kinetic energy plus and minus standard deviation (dotted); and T126 DNS kinetic energy (dashed).

6.2 Oceanic Flows

6.2.1 DNS at 252

Oceanic simulations are much more computationally demanding in comparison to atmospheric simulations mainly because the internal radius of deformation, λ_i, for the ocean is small, being the order of 50 km. This means that we need at least ten times the resolution used in atmospheric simulations to fully resolve the oceanic baroclinic eddies. To address this problem, we have chosen, as a first step, to perform a high resolution simulation at the resolution of T252, which should be sufficient to resolve the baroclinically-unstable eddies for our chosen coupling constant, F_o. The following parameters have been chosen: the coupling constant, $F_o = 2.4 \times 10^{-10}\mathrm{m}^{-2}$, which corresponds to $\lambda_i = 50$ km; the drag, α, in both layers has been set to a damping time of 20 days; the viscosity, $\nu^0 = 1.68 \times 10^8$ $\mathrm{m}^4\mathrm{s}^{-1}$; the order of the Laplacian operator, p, is 2; the relaxation time for the mean flow, κ, is 1.16 days; the mean zonal wind is again relaxed towards $u_i^{rel} = U_i^{rel} cos\phi$, where ϕ is the latitude, and $U_1^{rel} = -U_2^{rel}$ are the maximum winds (at the equator); the maximum zonal winds are $U_1^{rel} = 0.1875$ ms^{-1}, $U_2^{rel} = -0.1875$ ms^{-1}. The equations have been stepped forward in time for 104 days at steady state—after an initial spin-up period, with a timestep of 600 s. The number of longitude by latitude grid points is 768×384. Using the same reasoning as in Section 6.1.1, the wavenumber corresponding to the deformation scale is around 120.

Figs. 6.24 and 6.25 show the kinetic and potential energy spectra. An inspection of the kinetic energy spectra reveals what appears to be an inertial range for (m, n) between about 40 to somewhat over 100. The slope of the inertial range is around -2.2, which is steeper than the $-\frac{5}{3} = -1.67$ slope predicted for an energy cascade in QG turbulence. Nonetheless, if we accept that the deformation scale is around wavenumber 120, then at least a proportion of the kinetic energy at larger scales, including the peak, which is in the range $20 < n < 30$, must be due to an inverse cascade. This view is strengthened by Figs. 6.26 and 6.27, which show the corresponding spectra in the BTBC formulation. The previously mentioned peak is seen to be dominated by barotropic kinetic energy. The baroclinic kinetic energy is much broader, and more significantly, is peaked at around $n = 100$. This situation is thus completely different to the atmospheric case discussed in the previous section. In that problem, the truncation was always within the forward (enstrophy) cascade inertial range. In the oceanic problem considered here, however, realistic truncations at T126 and T63 are probably within the inverse cascade region, or within the injection region. Ad-hoc hyperdiffusion schemes are unlikely to be of much use in those regions. The methodology for subgrid-scale parameterizations, outlined in Section 5.5, is completely general however, and should be applicable in those regions.

6.2.2 Subgrid-scale Parameterizations at T126

An artificial truncation at $N_* = 126$ is then performed, and the matrices $\mathbf{M_n}$, $\mathbf{M_d}$, $\mathbf{F_b}$, and $\bar{\mathbf{f}}$ calculated. At T126, the most baroclinically-unstable wavenumbers are well resolved, and thus $\bar{\mathbf{f}}$, as expected, is small. The real and imaginary parts of the subgrid flux matrix, $\mathcal{F}$, are shown in Figs. 6.28 and 6.29, respectively. It is easier to relate these fluxes to the phenomenology of QG turbulence when they are in the BTBC form. The real and imaginary parts of the fluxes in BTBC form are shown in Figs. 6.30 and 6.31, respectively. They are clearly not as scale selective as in the atmospheric case. The real part is diagonal and the imaginary part is off-diagonal. This arises because of the

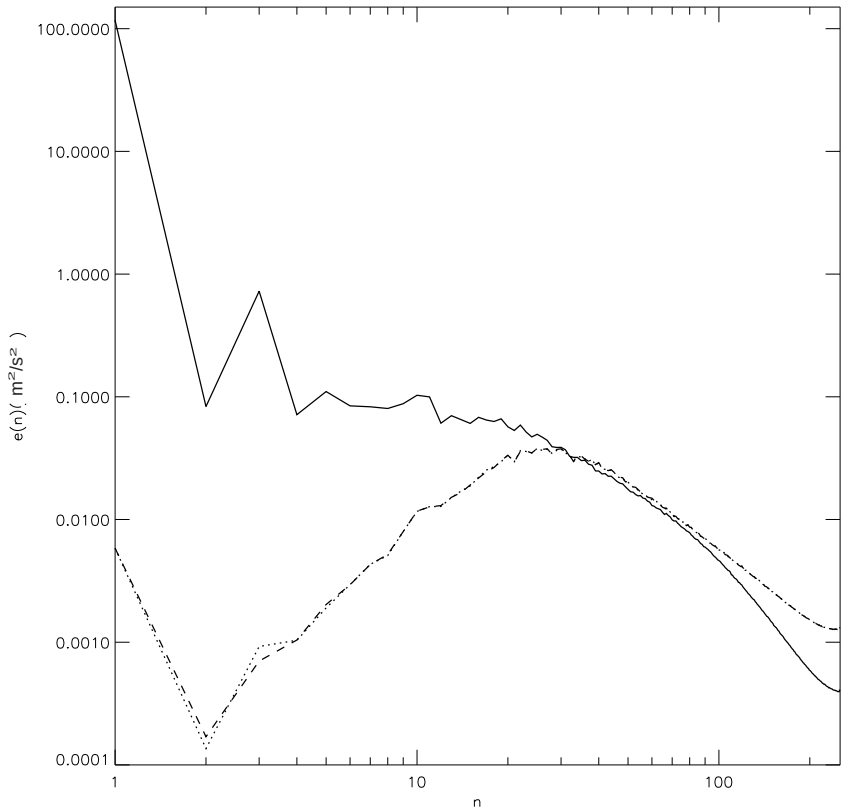

Figure 6.24: Energy spectra as functions of total wavenumber (n): potential energy (solid), Level 1 kinetic energy (dashed), and Level 2 kinetic energy (dotted) for the oceanic equivalent layer DNS at T252.

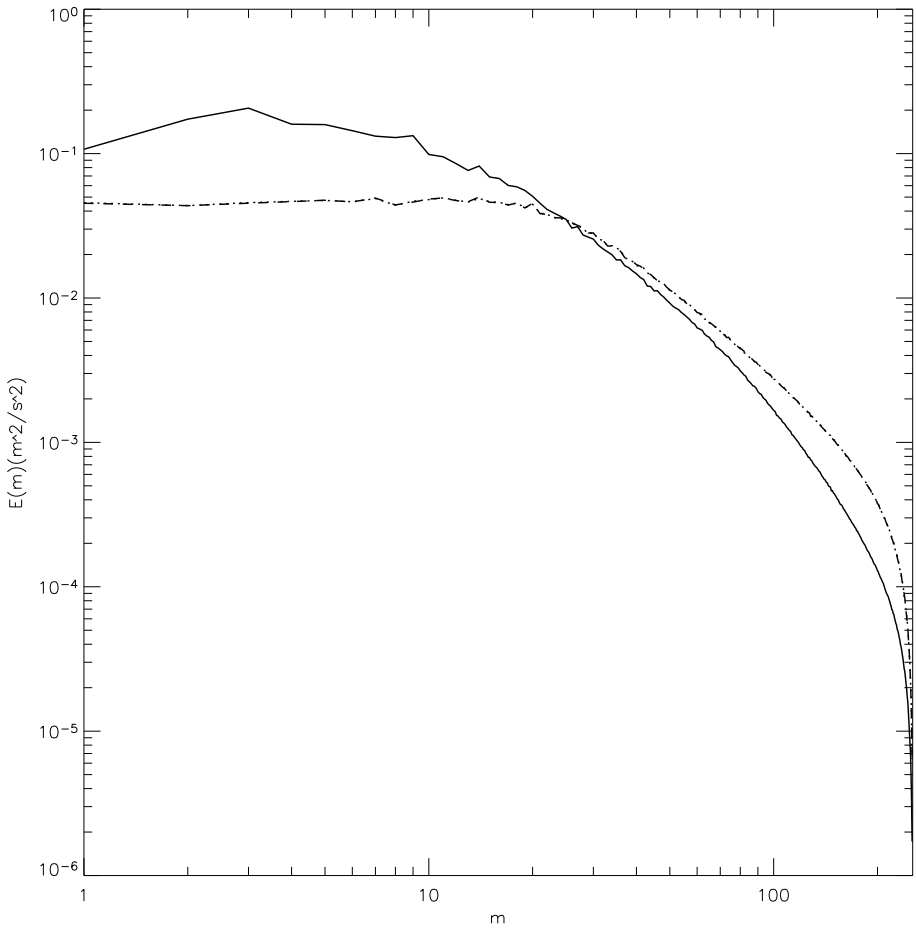

Figure 6.25: Energy spectra as functions of zonal wavenumber (m): potential energy (solid), Level 1 kinetic energy (dashed), and Level 2 kinetic energy (dotted) for the oceanic equivalent layer DNS at T252.

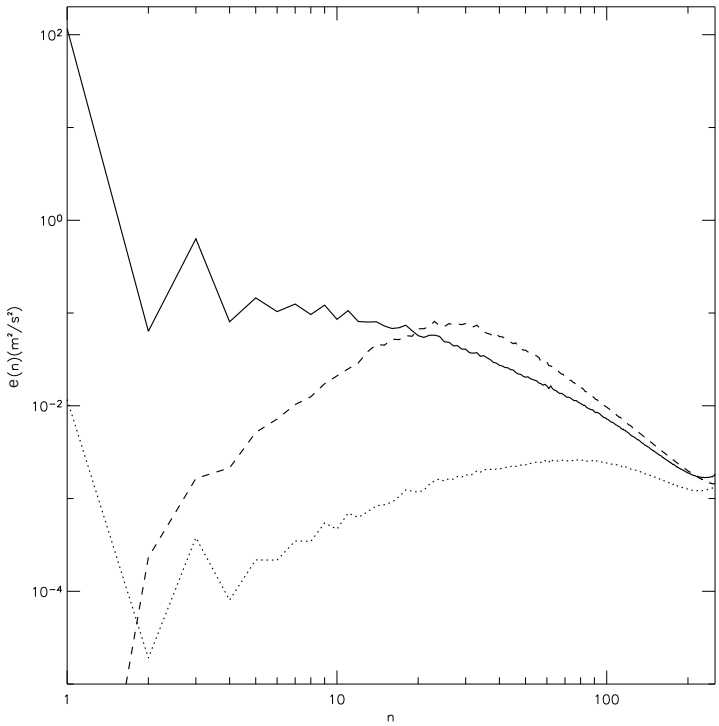

Figure 6.26: Energy spectra as functions of total wavenumber (n): total baroclinic energy (solid), barotropic kinetic energy (dashed), and baroclinic kinetic energy (dotted) for the oceanic equivalent layer DNS at T252.

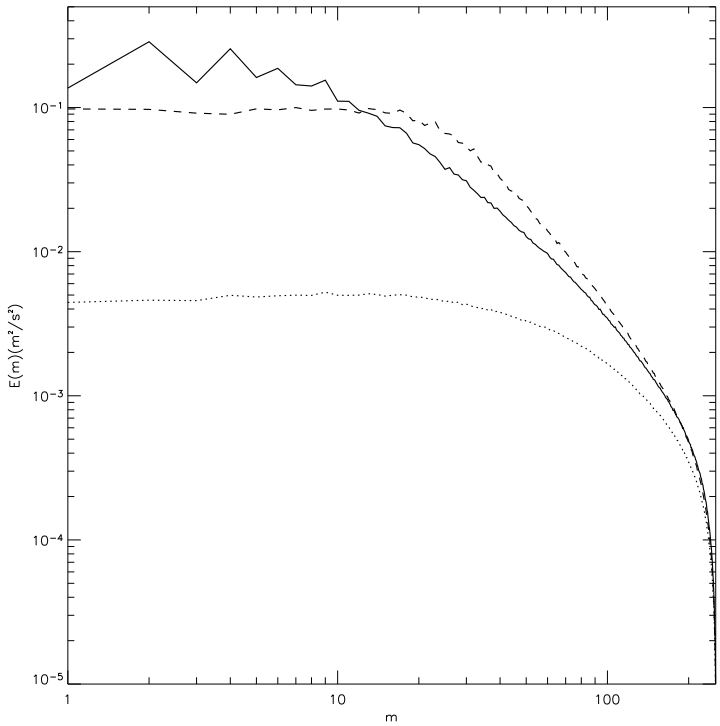

Figure 6.27: Energy spectra as functions of zonal wavenumber (m): total baroclinic energy (solid), barotropic kinetic energy (dashed), and baroclinic kinetic energy (dotted) for the oceanic equivalent layer DNS at T252.

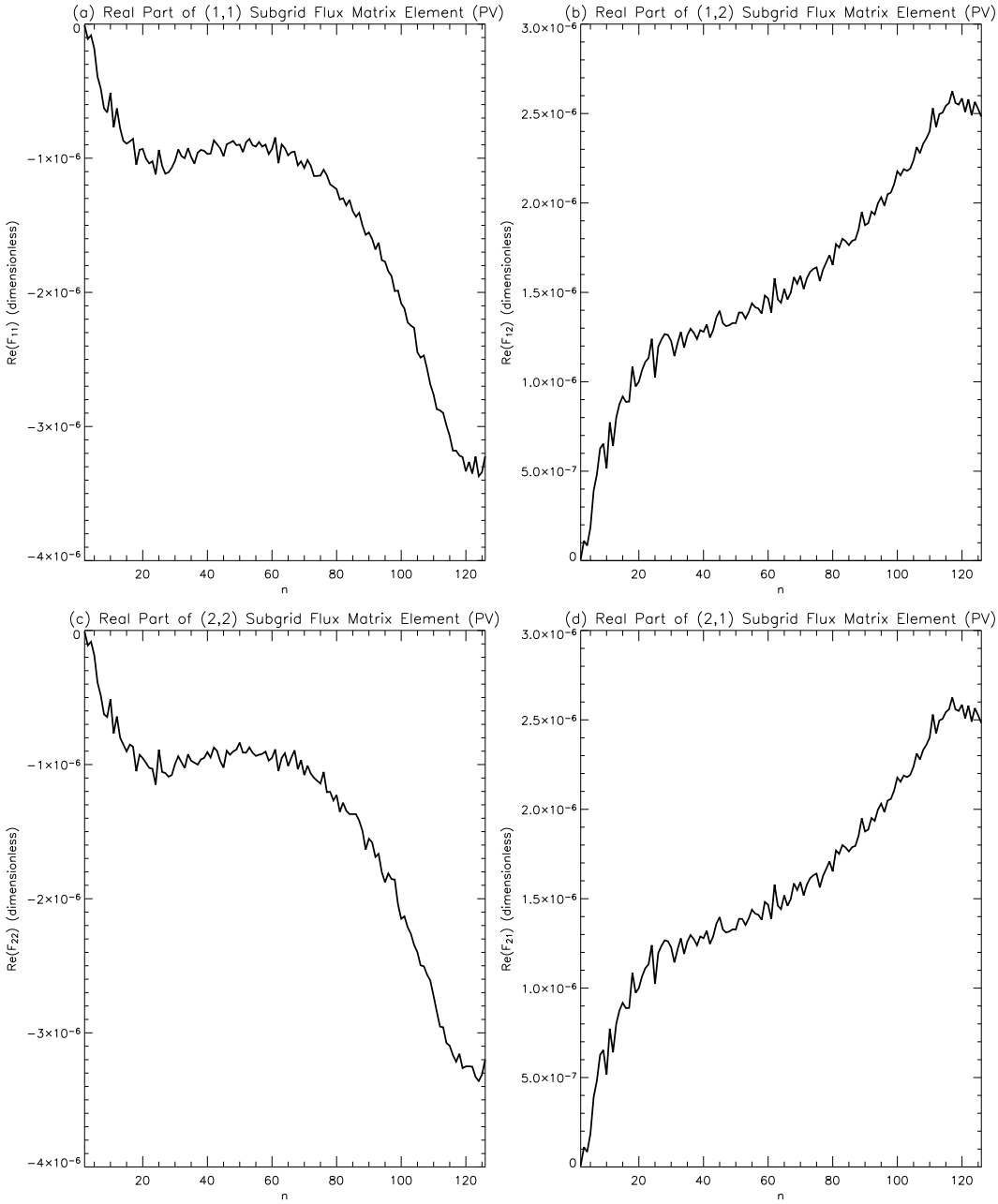

Figure 6.28: Elements of the real part of the isotropic subgrid flux matrix in the PV formulation: (a) $\mathcal{F}^r_{11}$; (b) $\mathcal{F}^r_{12}$; (c) $\mathcal{F}^r_{22}$; and (d) $\mathcal{F}^r_{21}$ (T126) .

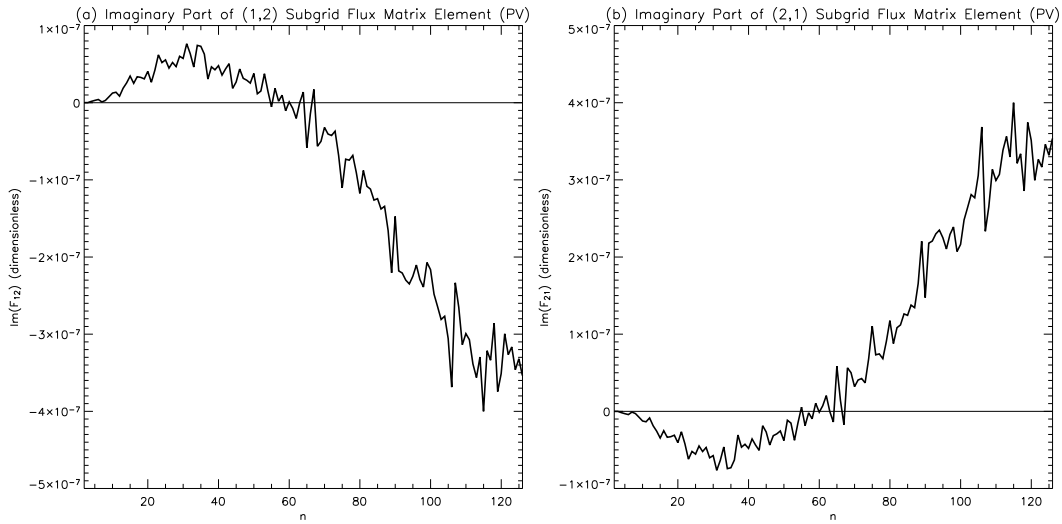

Figure 6.29: Off-diagonal elements of the imaginary part of the isotropic subgrid flux matrix in the PV formulation: (a) $\mathcal{F}^i_{12}$; (b) $\mathcal{F}^i_{21}$ (T126) .

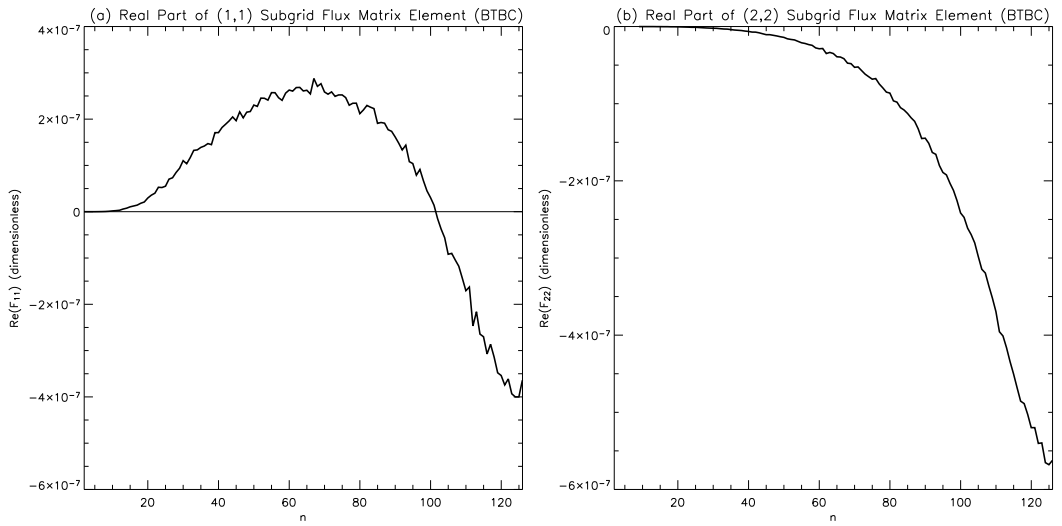

Figure 6.30: Diagonal elements of the real part of the isotropic subgrid flux matrix in the BTBC formulation: (a) $\mathcal{F}^r_{11}$; (b) $\mathcal{F}^r_{22}$ (T126).

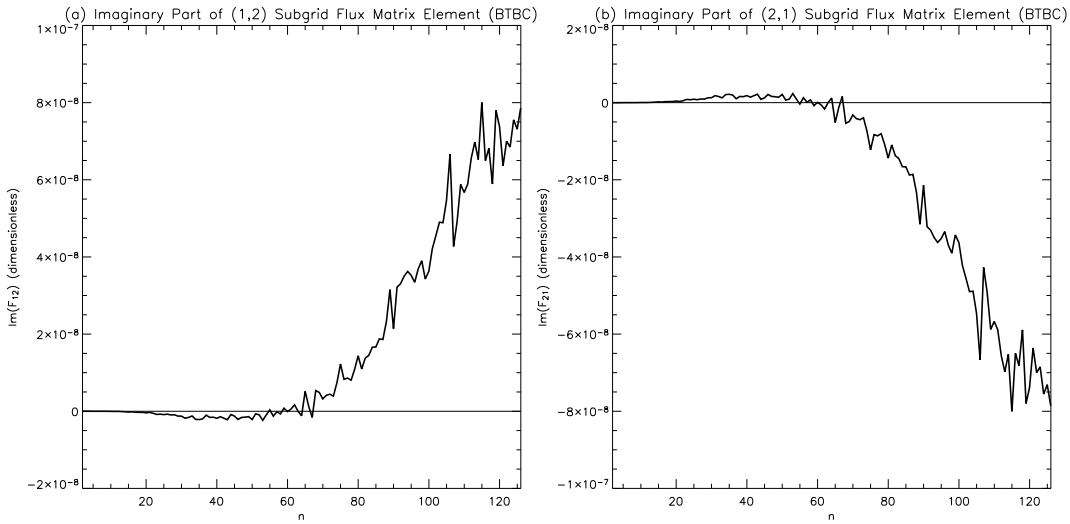

Figure 6.31: Off-diagonal elements of the imaginary part of the isotropic subgrid flux matrix in the BTBC formulation: (a) $\mathcal{F}^i_{12}$; (b) $\mathcal{F}^i_{21}$ (T126).

symmetry of the equivalent layer problem, as will be discussed further in what follows. The diagonal elements are more relevant as they describe the barotropic and baroclinic enstrophy (energy) fluxes. The barotropic flux has a strong injection region for $n < 100$. In this region, barotropic energy is injected from the subgrid scales. We can see that this must be so since the energy flux $\mathcal{E} = \frac{\mathcal{Z}}{n(n+1)}$, where $\mathcal{Z}$ is the enstrophy flux. Hence, the barotropic energy flux will be dominated by the injection region for which $n < 100$ since $\mathcal{E}$ will preferentially select the lower wavenumber contributions of the enstrophy flux. The baroclinic flux of enstrophy, on the other hand, is always negative, and furthermore, the corresponding energy flux has no injection region, but is only dissipated.

The coefficients of the net dissipation matrix $-\mathbf{M}^{\mathbf{r}}_{\mathbf{n}}$ are shown in Fig. 6.32. The diagonal elements of this matrix have the typical cusp near the truncation scale, and are positive, indicating a horizontal drain of (potential) enstrophy. The off-diagonal elements, on the other hand, are negative. The diagonal elements are also somewhat larger than the off-diagonal elements, but certainly not large enough to neglect the off-diagonal elements as was done in the atmospheric case. In this problem, the full matrix structure is needed to correctly parameterize the transfers. At the largest scales, there is a very slight kink; this is probably not dynamically significant, but is a result of numerical errors due to the very small contribution to the subgrid tendency at those scales. This can lead to the matrices becoming ill-conditioned there. The contribution to the subgrid tendency at those scales is so small that it can be neglected altogether. The imaginary part of the net 'dissipation' matrix is shown in 6.33. Clearly, sampling errors are significant here. This is because the elements of this matrix are roughly an order of magnitude less than the elements of $-\mathbf{M}^{\mathbf{r}}_{\mathbf{n}}$, and hence are more affected by sampling error than the latter. However, one can still discern a pattern near the truncation scale. The diagonal elements are roughly equal, but of opposite sign; the off-diagonal elements are also roughly equal, and of opposite sign. In fact, this pattern is replicated in all of the equivalent layer problems we have examined.

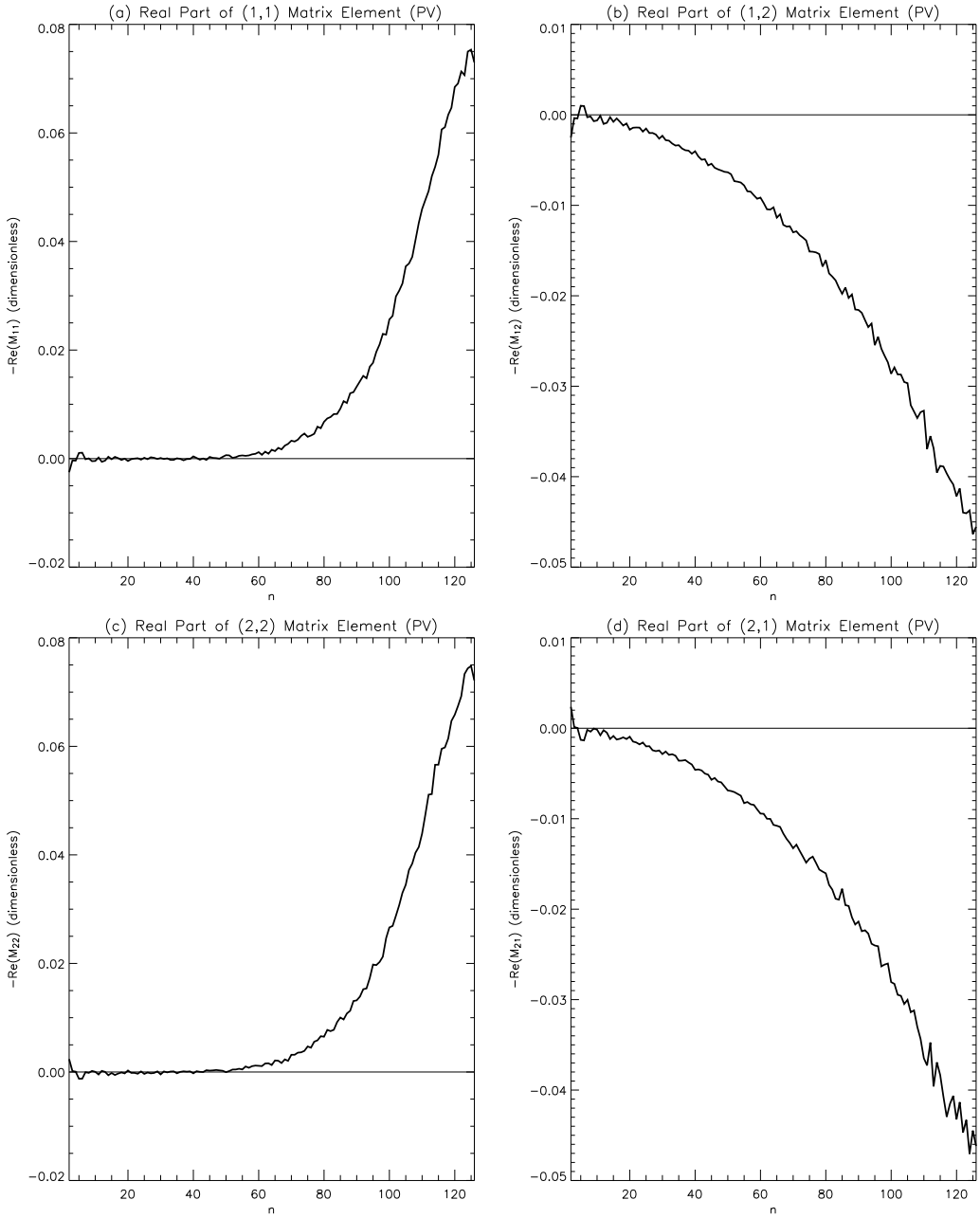

Figure 6.32: Real part of the isotropic net dissipation matrix in the PV formulation: (a) $-M^r_{11}$; (b) $-M^r_{12}$; (c) $-M^r_{22}$; (d) $-M^r_{21}$ (T126).

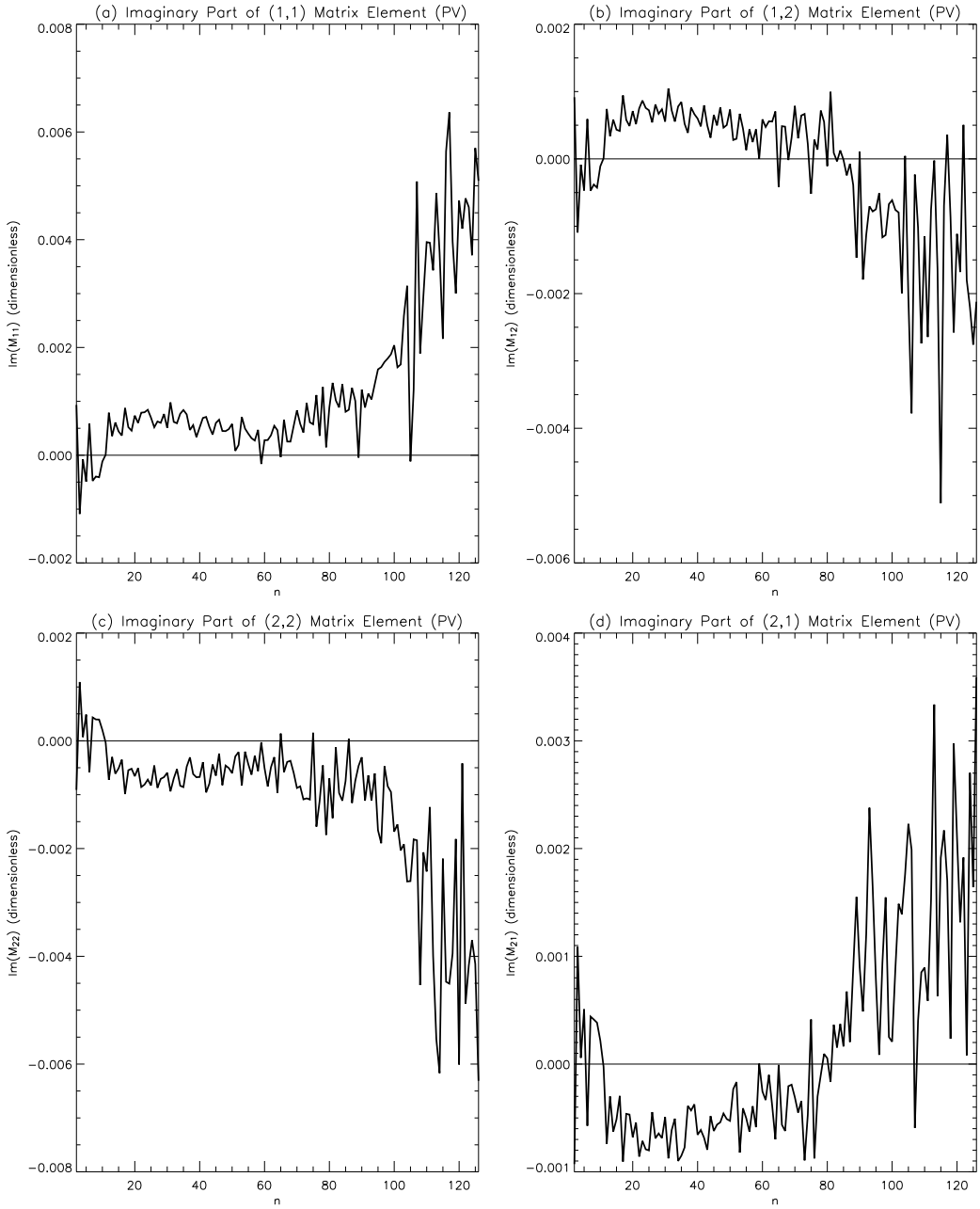

Figure 6.33: Imaginary part of the isotropic net dissipation matrix in the PV formulation: (a) M^i_{11}; (b) M^i_{12}; (c) M^i_{22}; (d) M^i_{21} (T126).

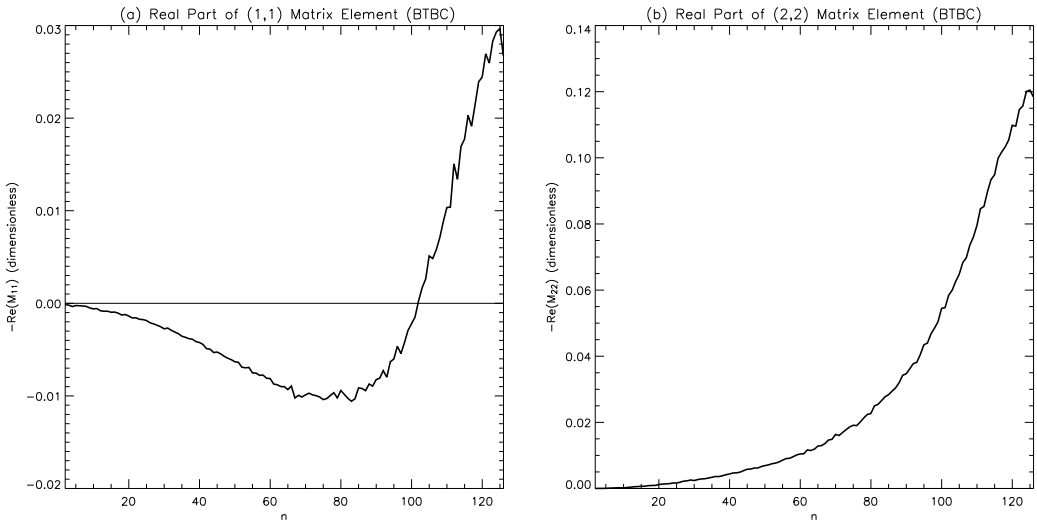

Figure 6.34: Real part of the isotropic net dissipation matrix in the BTBC formulation: (a) $-M^r_{11}$; (b) $-M^r_{22}$ (T126).

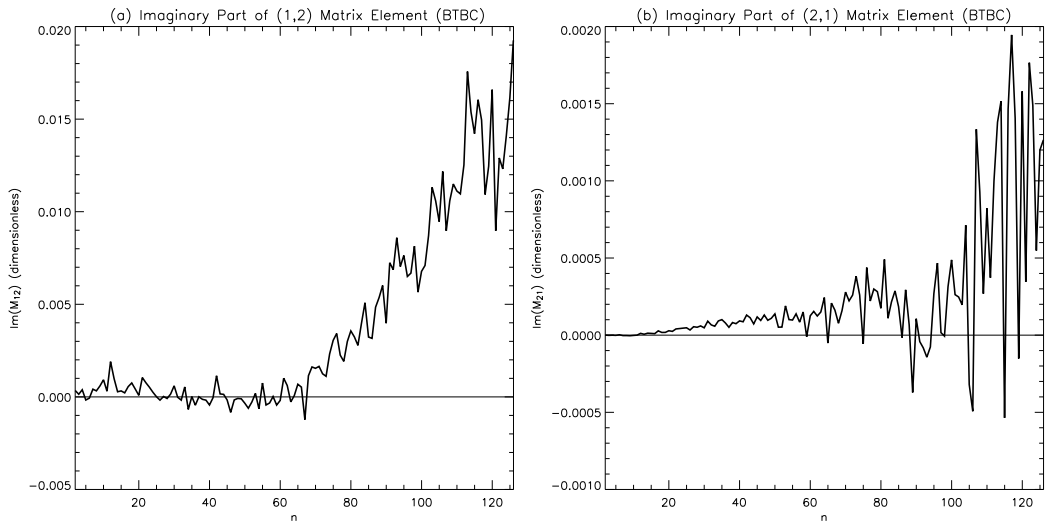

Figure 6.35: Imaginary part of the isotropic net dissipation matrix in the BTBC formulation: (a) M^i_{12}; (b) M^i_{21} (T126).

That is, the real part of the net dissipation matrix $-\mathbf{M_n^r}$ has the form

$$-\mathbf{M_n^r} = \begin{pmatrix} \alpha & -\beta \\ -\beta & \alpha \end{pmatrix}, \tag{6.5}$$

in the PV formulation, where α and β are real (and it should be remembered, wavenumber dependent). The eigenvalues of this matrix are $\alpha - \beta$ with eigenvector

$$\begin{pmatrix} 1 \\ 1 \end{pmatrix},$$

and $\alpha + \beta$ with eigenvector

$$\begin{pmatrix} 1 \\ -1 \end{pmatrix}.$$

As eigenvectors are arbitrary up to a constant, we can multiply the second eigenvector by $c = 1 + \frac{2F}{n(n+1)}$ to obtain the following transformation matrix

$$\begin{pmatrix} 1 & c \\ 1 & -c \end{pmatrix}.$$

This matrix is precisely the inverse of the matrix needed to transform from PV coordinates to BTBC coordinates (see Appendix G), thus the real part of the dissipation matrix will be diagonal in the BTBC formulation:

$$-\mathbf{M_n'^r} = \begin{pmatrix} \alpha - \beta & 0 \\ 0 & \alpha + \beta \end{pmatrix}. \tag{6.6}$$

Note that this also means the baroclinic transfer is purely dissipative (positive) while the barotropic transfer may be dissipative or injective. The imaginary part of the dissipation matrix, $\mathbf{M_n^i}$ has the generic form

$$\mathbf{M_n^i} = \begin{pmatrix} \gamma & -\delta \\ \delta & -\gamma \end{pmatrix}, \tag{6.7}$$

in the PV formulation, where γ and δ are both positive. Upon applying the matrix transformation given by Eq. G.12, one obtains

$$\mathbf{M_n'^i} = \begin{pmatrix} 0 & \gamma + \delta \\ \gamma - \delta & 0 \end{pmatrix}. \tag{6.8}$$

in the BTBC formulation. Thus the imaginary part of the dissipation matrix is off-diagonal in the BTBC formulation. Note that this also means the off-diagonal element representing transfer from baroclinic to barotropic mode will always be positive while the opposite transfer may be of either sign. These are important results because they simplify the matrix structure of the parameterizations in the BTBC formulation. The BTBC variables are thus the natural variables to study the equivalent layer problem; hence their widespread use in this thesis.

The real part of the net dissipation matrix, $-\mathbf{M_n'^r}$, in the BTBC formulation is shown in Fig. 6.34. It is diagonal for the reasons given above. The barotropic element, although positive (dissipative) near the truncation scale, has a significant negative (injective) contri-

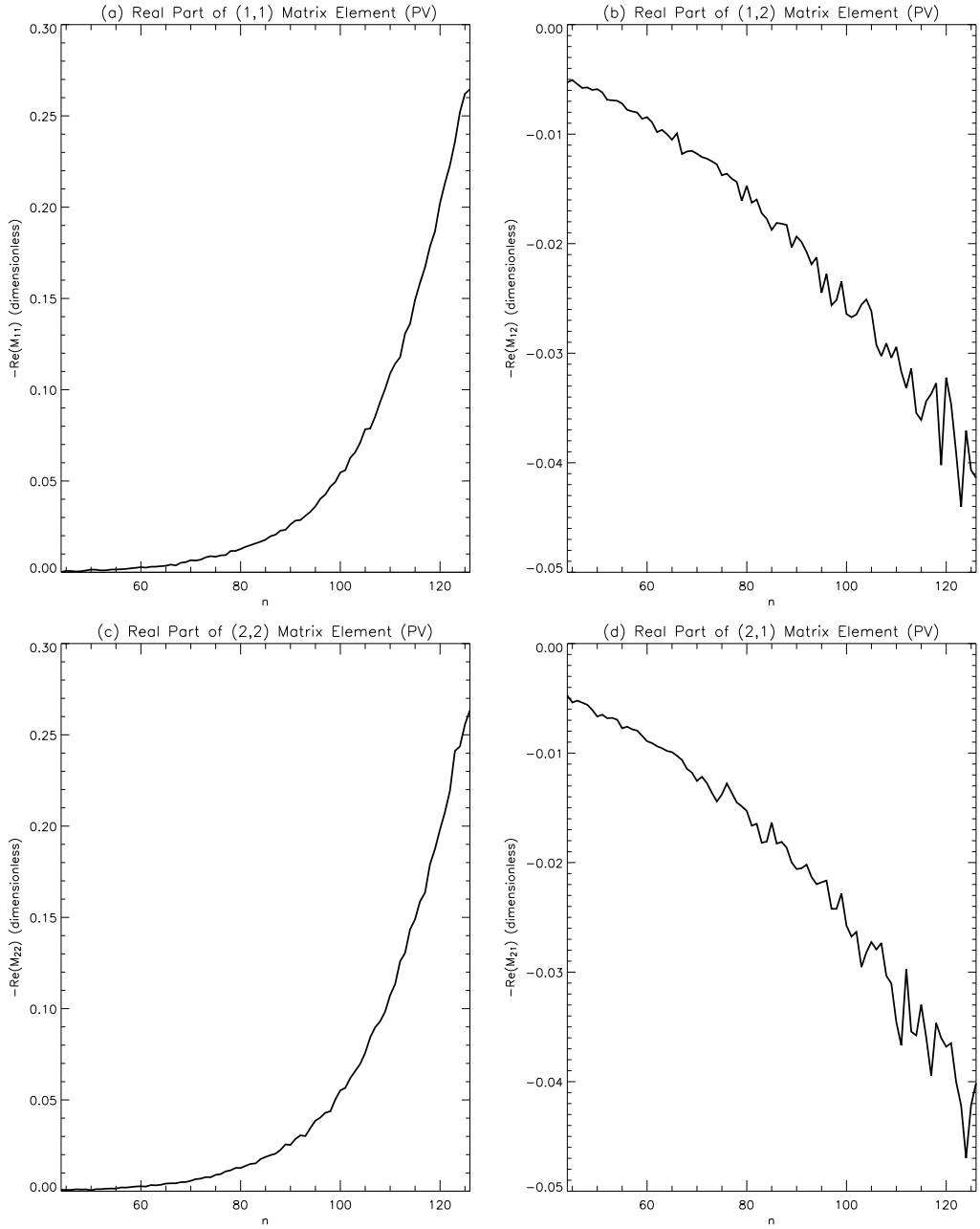

Figure 6.36: Real part of the isotropic drain dissipation matrix in the PV formulation: (a) $-M^r_{11}$; (b) $-M^r_{12}$; (c) $-M^r_{22}$; (d) $-M^r_{21}$ (T126).

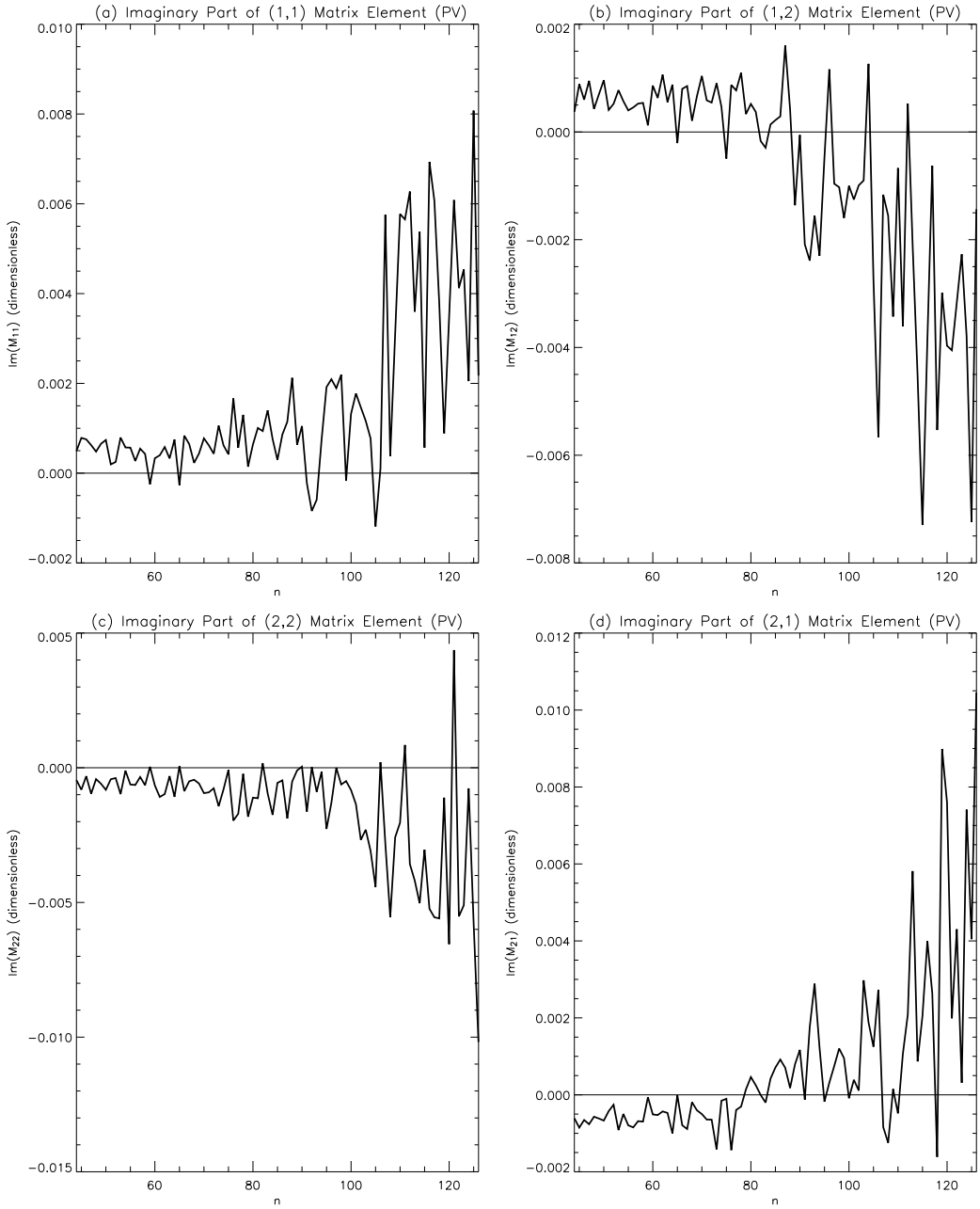

Figure 6.37: Imaginary part of the isotropic drain dissipation matrix in the PV formulation: (a) M^i_{11}; (b) M^i_{12}; (c) M^i_{22}; (b) M^i_{21} (T126).

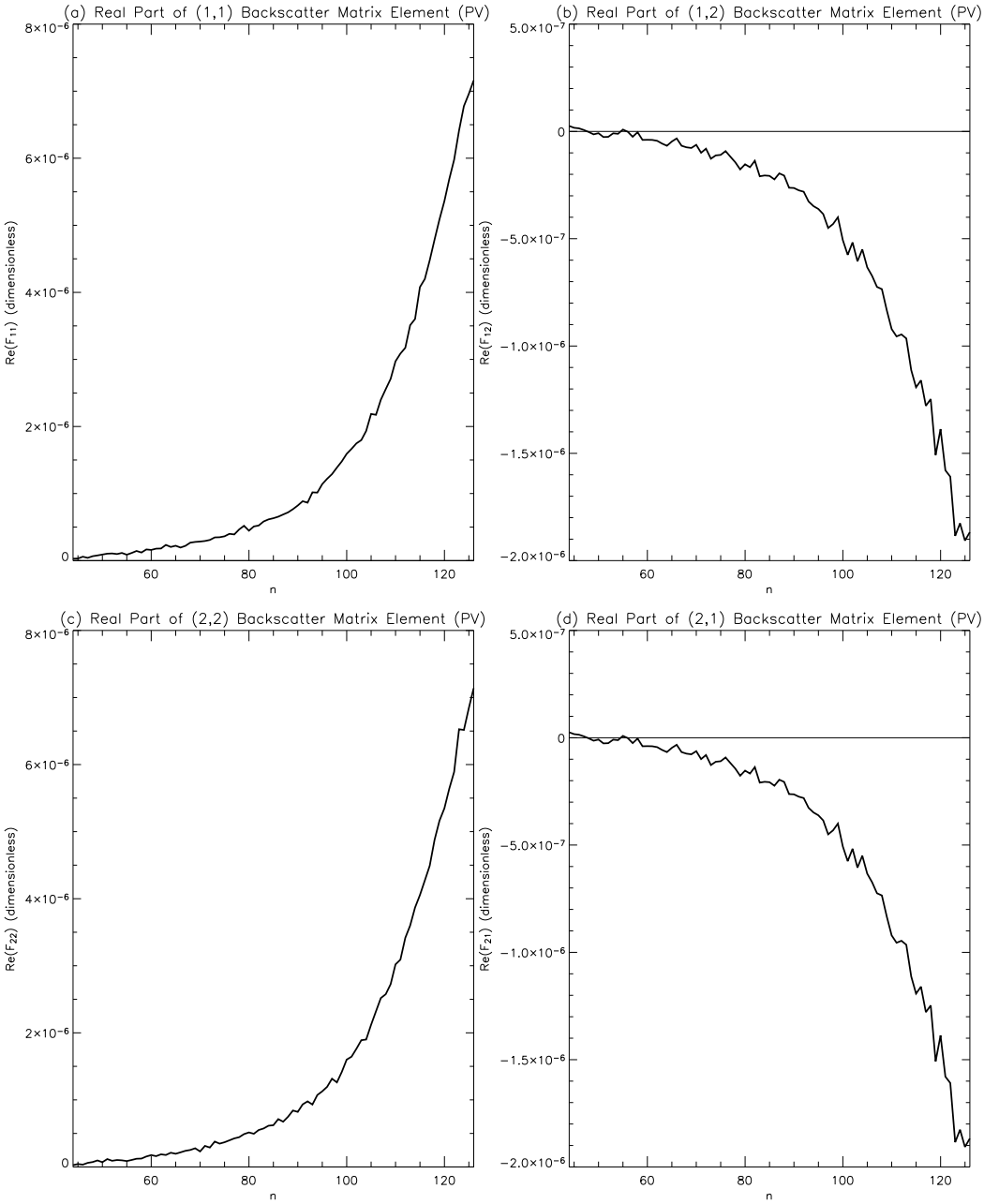

Figure 6.38: Real part of the isotropic stochastic backscatter matrix in the PV formulation: (a) F^r_{11}; (b) F^r_{12}; (c) F^r_{22}; (d) F^r_{21} (T126).

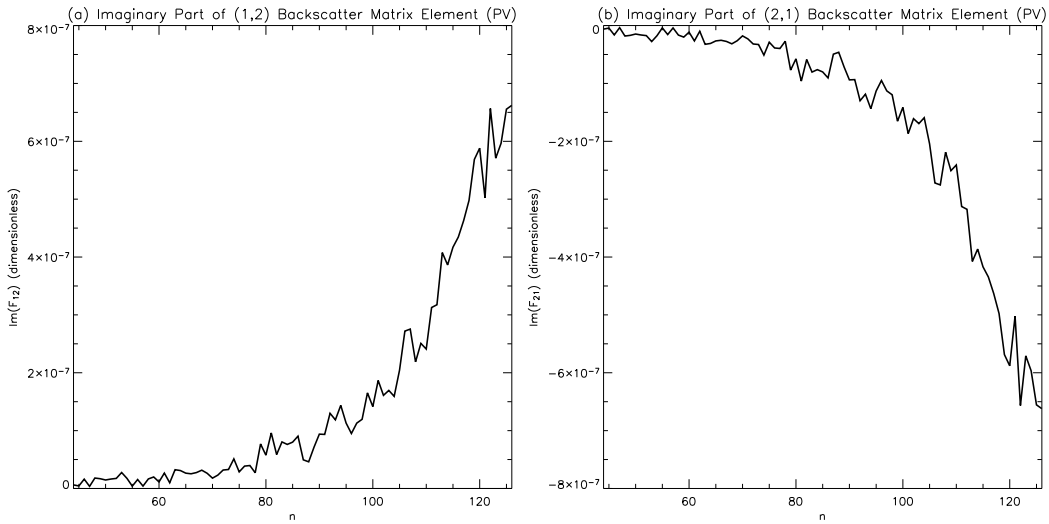

Figure 6.39: Imaginary part of the isotropic stochastic backscatter matrix in the PV formulation: (a) F^i_{12}; (b) F^i_{21} (T126).

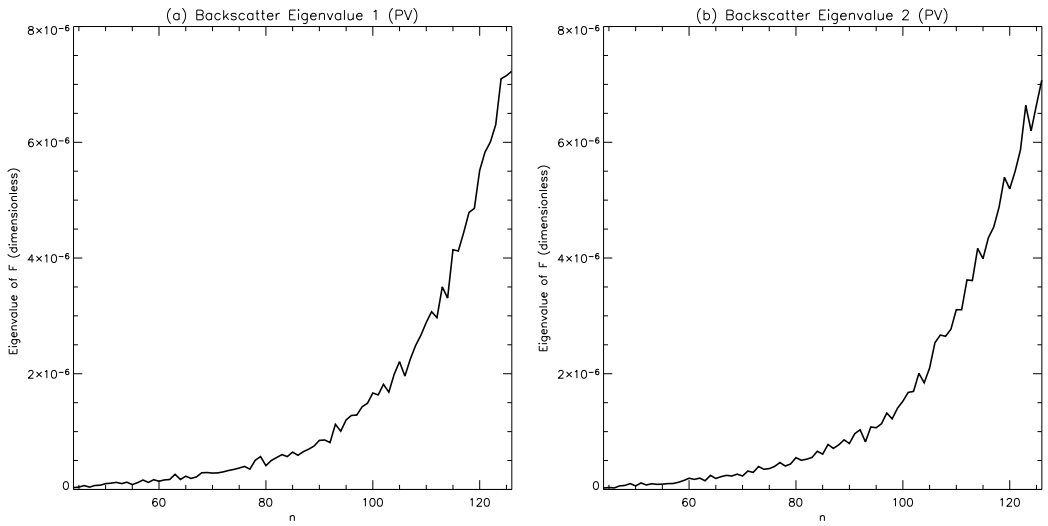

Figure 6.40: Eigenvalues of the isotropic stochastic backscatter matrix in the PV formulation (T126).

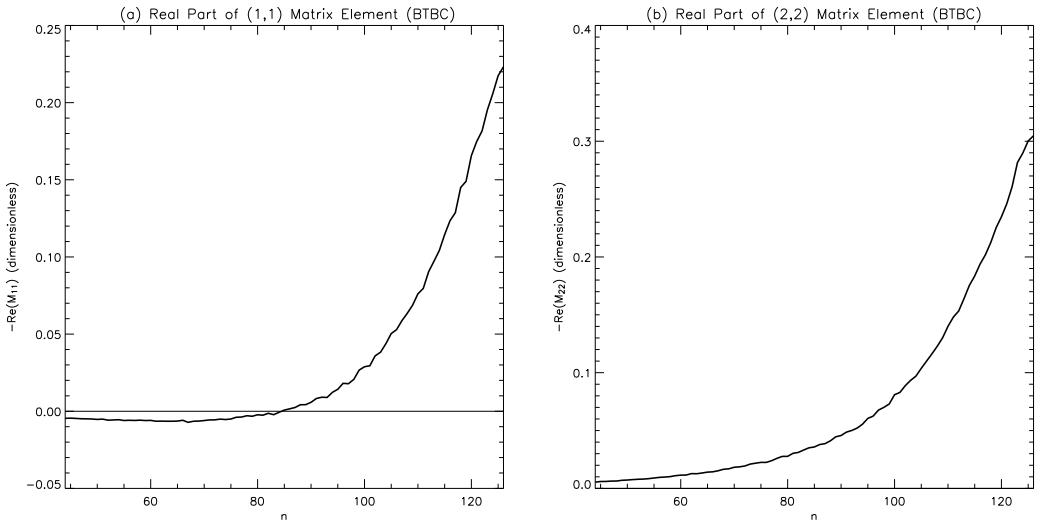

Figure 6.41: Real part of the isotropic drain dissipation matrix in the BTBC formulation: (a) $-M^r_{11}$; (b) $-M^r_{22}$ (T126).

bution below n about 100. The baroclinic component is always dissipative, and is almost four times as large as the barotropic component. The imaginary part of the net dissipation matrix, $\mathbf{M'^i_n}$, is shown in 6.35; it is purely off-diagonal as discussed above. The M^i_{12} element is an order of magnitude greater than the M^i_{21} element, implying a greater contribution to the barotropic tendency than the baroclinic tendency. The $\mathbf{M'^i_n}$ matrix also has a surprisingly clear 'signal' compared to the corresponding matrix in PV space, highlighting the importance of studying both formulations. Overall, however, the most significant element is the baroclinic element of $-\mathbf{M'^r_n}$.

The drain dissipation $\mathbf{M_d}$ and backscatter $\mathbf{F_b}$ matrices have been calculated using a decorrelation time τ of 1 day. A cutoff wavenumber of $n_c = 44$ has been imposed. The $-\mathbf{M^r_d}$ matrix is shown in Fig. 6.36. The diagonal elements are enhanced by a factor of at least three over the corresponding $-\mathbf{M^r_n}$ diagonal elements near the truncation scale. The off-diagonal elements are however relatively unchanged in magnitude, except perhaps for the introduction of additional sampling error due to the averaging procedure (over time lags) in calculating $\mathbf{M_d}$. The imaginary part $\mathbf{M^i_d}$, shown in Fig. 6.37, still has large sampling error, and is insignificant compared to $-\mathbf{M^r_d}$. The real and imaginary parts of the backscatter matrix, $\mathbf{F^r_b}$ and $\mathbf{F^i_b}$, are shown in Figs 6.38 and 6.39. The diagonal elements of $\mathbf{F^r_b}$ are dominant, being greater in magnitude than the off-diagonal elements by a factor of almost four. The off-diagonal elements of $\mathbf{F^r_b}$ are also negative. The diagonal elements of $\mathbf{F^i_b}$ are zero since $\mathbf{F_b}$ always has real diagonal elements by definition. The off-diagonal elements are equal in magnitude, but of opposite signs. Furthermore, they are smaller than the off-diagonal elements of $\mathbf{F^r_b}$ by a factor of about three, and hence overall do not play a very big role in the dynamics of the flow. The eigenvalues of $\mathbf{F_b}$ are shown in Fig. 6.40. The eigenvalues are of similar size to the diagonal elements of $\mathbf{F^r_b}$.

The corresponding matrices $\mathbf{M'_d}$ and $\mathbf{F'_b}$ in the BTBC formulation have also been calculated. The dissipation matrix $-\mathbf{M'^r_d}$ is shown in Fig. 6.41. The barotropic element is now almost an order of magnitude greater than the corresponding element in $-\mathbf{M'^r_n}$ near the truncation scale. It is also less negative at the large scales. The baroclinic element

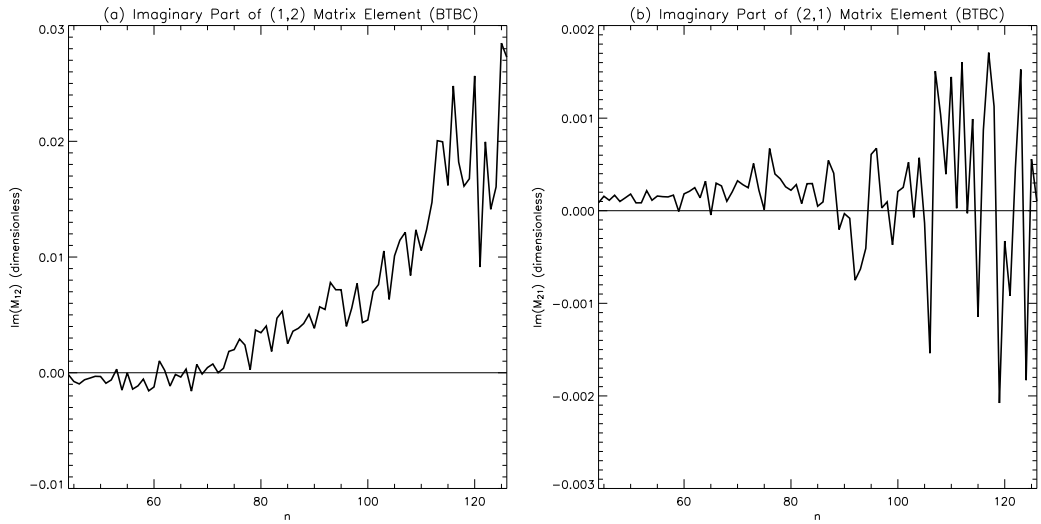

Figure 6.42: Imaginary part of the isotropic drain dissipation matrix in the BTBC formulation: (a) M_{12}^i; (b) M_{21}^i (T126).

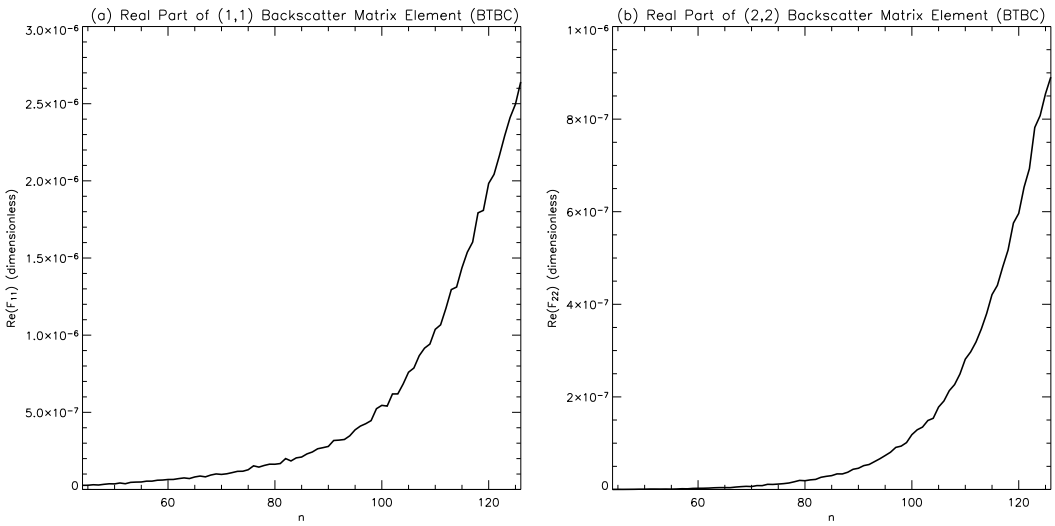

Figure 6.43: Real part of the isotropic stochastic backscatter matrix in the BTBC formulation: (a) F_{11}^r; (b) F_{22}^r (T126).

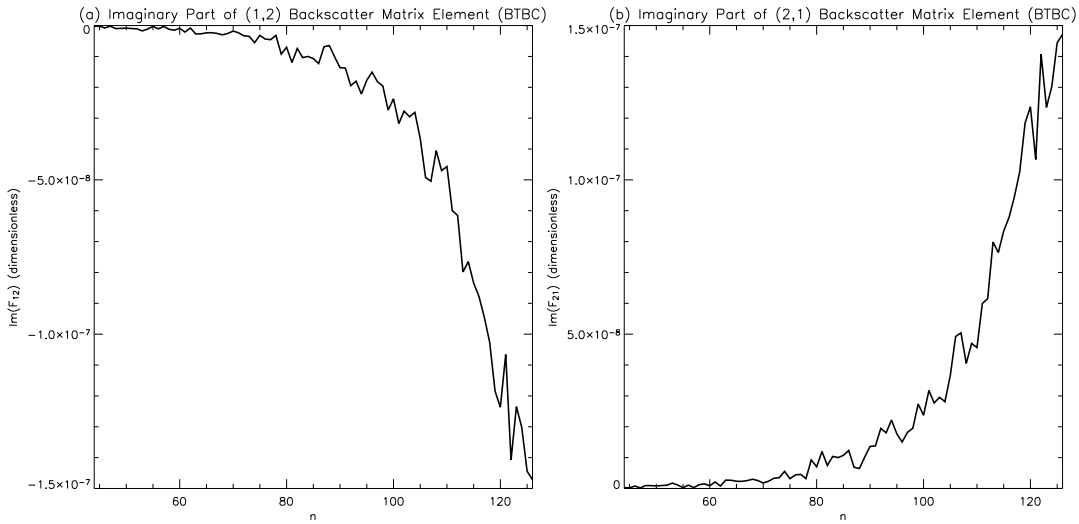

Figure 6.44: Imaginary part of the isotropic stochastic backscatter matrix in the PV formulation: (a) F^i_{12}; (b) F^i_{21} (T126).

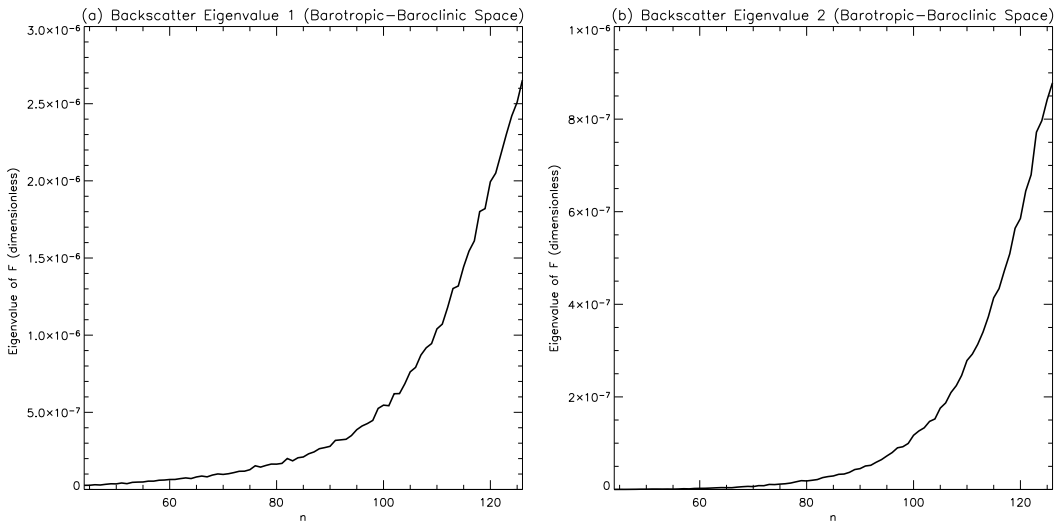

Figure 6.45: Eigenvalues of the isotropic stochastic backscatter matrix in the PV formulation (T126).

is larger than the corresponding element in $-\mathbf{M}_{\mathbf{n}}^{\prime\mathbf{r}}$ roughly by a factor of three. The two elements of $-\mathbf{M}_{\mathbf{d}}^{\prime\mathbf{r}}$ are now of comparable magnitudes. The imaginary matrix $\mathbf{M}_{\mathbf{d}}^{\prime\mathbf{i}}$ is shown in Fig. 6.42. There is not much difference in terms of magnitude compared to the corresponding $\mathbf{M}_{\mathbf{n}}^{\prime\mathbf{i}}$ matrix. The real and imaginary parts of the backscatter matrix, $\mathbf{F}_{\mathbf{b}}^{\prime\mathbf{r}}$ and $\mathbf{F}_{\mathbf{b}}^{\prime\mathbf{i}}$, are shown in Figs. 6.43 and 6.44, respectively. The real part is dominant, being an order of magnitude greater than the imaginary part. This is reflected in the eigenvalues of $\mathbf{F}_{\mathbf{b}}^{\prime}$, shown in Fig. 6.45, which are effectively the same as the diagonal elements of $\mathbf{F}_{\mathbf{b}}^{\prime\mathbf{r}}$.

6.2.3 LES at T126

A large eddy simulation has been performed at T126, using the stochastic parameterization for $n > 44$, and the deterministic parameterization for $n < 44$. The results, after running the LES for 104 days, are shown in Figs. 6.46 and 6.47. Clearly, there is significant sampling error due to the relatively short integration time. However, the agreement between the LES and higher resolution DNS is satisfactory; the LES spectrum is in broad agreement with the DNS. The next step is to investigate a truncation at the lower resolution of T63. We now have an LES at T126 which is able to broadly reproduce the features of the DNS at T252. The advantage, of course, is that at T126 we can afford to run the simulation for much longer, and hence we can reduce sampling errors, which in general will be worse at T63 than at T126 due to larger eddy turnover times. We run the LES at T126 for 2700 days, using a timestep of 1200 s. Note that, as far as subgrid-scale parameterizations at T63 are concerned, the LES at T126 will be considered to be the control run, and not the T252 run. Hence, for example, when we refer to 'bare' parameters at T63, we are referring to the parameters used in the T126 LES; these parameters are, however, 'renormalized' relative to the T252 DNS. Nevertheless, in practice, there is very little difference between the bare parameters for the T252 DNS and those for the T126 LES at T63 because most of the renormalization is confined near the truncation scale due to the scale-selectiveness of the subgrid fluxes.

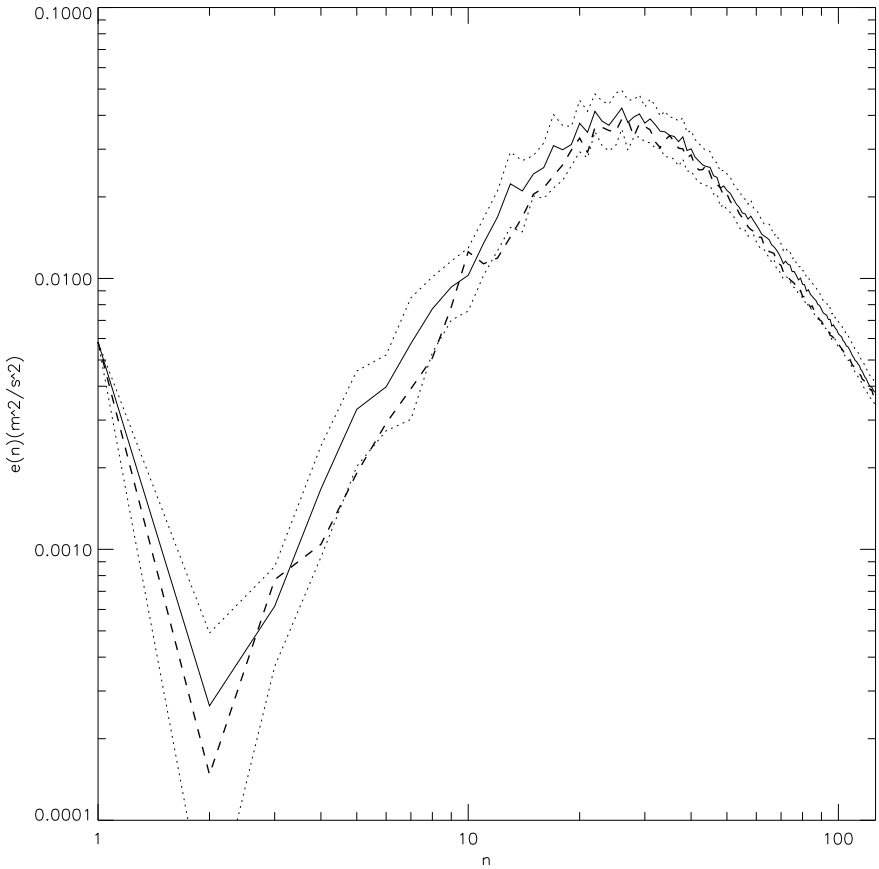

Figure 6.46: Energy spectra (Level 1) as functions of total wavenumber (n): kinetic energy for T126 LES with renormalized drain dissipation and backscatter (solid); LES kinetic energy plus and minus standard deviation (dotted); and T252 DNS kinetic energy (dashed).

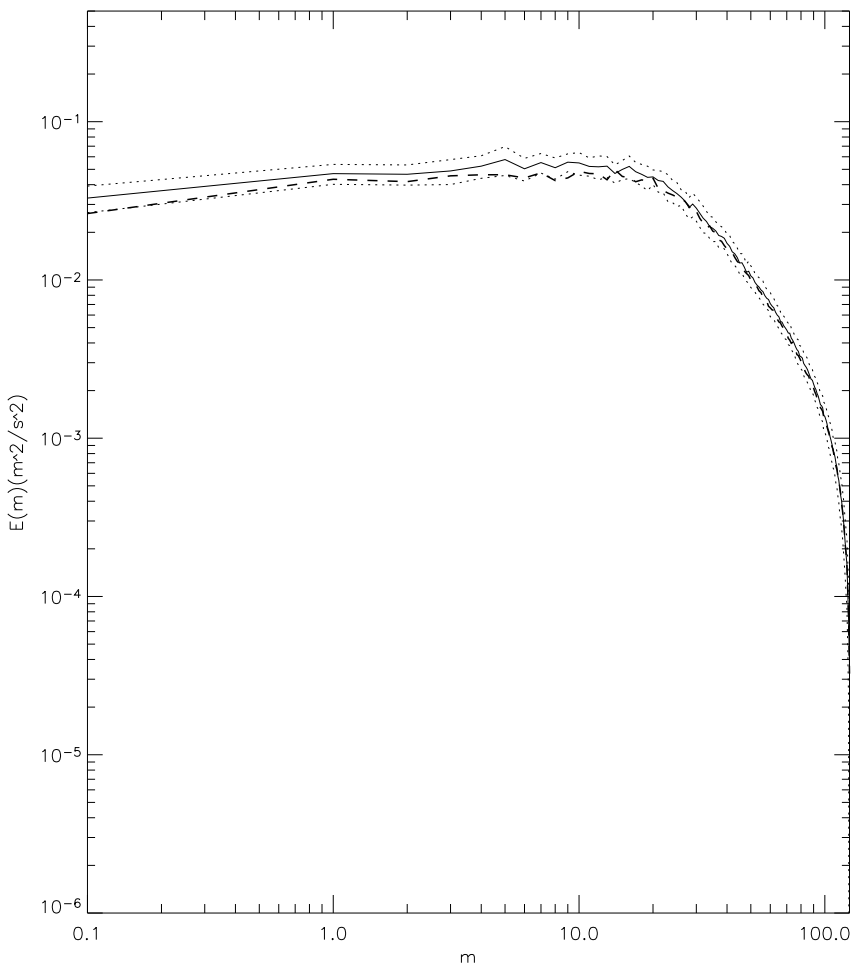

Figure 6.47: Energy spectra (Level 1) as functions of zonal wavenumber (m): kinetic energy for T126 LES with renormalized drain dissipation and backscatter (solid); LES kinetic energy plus and minus standard deviation (dotted); and T252 DNS kinetic energy (dashed).

6.2.4 Subgrid-scale Parameterizations at T63

An artifical truncation at $N_* = 63$ is performed in the long (2700 day) LES at T126. The matrices $\mathbf{M_n}$, $\mathbf{M_d}$, $\mathbf{F_b}$, and $\bar{\mathbf{f}}$ are then calculated. Figures 6.48 and 6.49 show, respectively, the real and imaginary parts of subgrid enstrophy flux matrix, $\mathcal{F}$, in PV space. The fluxes are qualitatively similar to those at T126; however, they are generally greater by a factor of at least two. Clearly, then, both truncations cannot be in the strict inertial range since in that case the fluxes would be equal. The fluxes at T63 are also significantly less scale-selective than at T126. In fact, Fig. 6.48 shows that there is a flat region of the flux for wavenumbers $20 < n < 50$, possibly indicating that non-local transfers are more significant in this region (see discussion in Section 5.3). Figures 6.50 and 6.51 show the corresponding fluxes in BTBC space. Similarly to the T126 case, the barotropic (diagonal) flux has a prominent energy injection region for $n < 50$, and the baroclinic (diagonal) flux is always dissipative. The barotropic flux is in this case, however, greater than the baroclinic flux.

Figure 6.52 shows the real part of the net dissipation matrix, $-\mathbf{M_n^r}$, at T63. This is qualitatively similar to the corresponding matrix at T126. The diagonal elements are positive and the off-diagonal elements are negative. The diagonal elements are slightly larger than the off-diagonal elements. There are some differences, however. The elements of $-\mathbf{M_n^r}$ at T63 are roughly half the the size of the corresponding elements at T126. Additionally, at T63, the matrix elements are less scale-selective. This is especially apparent in the off-diagonal elements, which actually flatten in the last ten wavenumbers or so near the truncation scale.

The imaginary matrix $\mathbf{M_n^i}$ is shown in Fig. 6.53. In terms of magnitude, its elements are roughly five times smaller than those of the real part, and thus may not be as significant dynamically. When compared to the corresponding matrix at T126, its diagonal elements have the opposite sign near the truncation scale. However, they satisfy the symmetry property implied by Eq. 6.7 with $\gamma \to -\gamma$, so we still expect the form implied by Eq. 6.8 for $\mathbf{M_n^{\prime i}}$. The corresponding matrices in the BTBC formulation are shown in Figs. 6.54 and 6.55. The real part, $-\mathbf{M_n^{\prime r}}$, is qualitatively similar to the corresponding matrix at T126 in these sense that the baroclinic element is larger and is always positive, while the barotropic element is negative except near the truncation scale. The imaginary part, $\mathbf{M_n^{\prime i}}$, is again qualitatively similar to the corresponding matrix at T126. The M_{12}^i element is larger than the M_{21}^i element, although not by as big margin as at T126. The barotropic contribution from the off-diagonal elements is still dominant. However, overall, the baroclinic contribution from the diagonal element of $\mathbf{M_n^{\prime r}}$ dominates.

The matrices $\mathbf{M_d}$ and $\mathbf{F_b}$ are calculated using a decorrelation time τ of 4 days. The time covariance $\langle \left(\frac{\partial \hat{q}^i_{mn}(t)}{\partial t}\right)_S \left(\frac{\partial \hat{q}^j_{mn}(t_0)}{\partial t}\right)^*_S \rangle$ as a function of time is shown in Fig. 6.56. This shows that 4 days is a more than sufficient integration time as the time covariance drops to zero after about 2 days. The scale selectiveness of the backscatter is not as severe as in the atmospheric case; nonetheless, very slightly negative eigenvalues of $\mathbf{F_b}$ are seen for $n < 17$, and hence we choose $n_c = 17$ as the cutoff wavenumber. The real part of the drain dissipation matrix, $-\mathbf{M_d^r}$, is shown in Fig. 6.57. The qualitative structure of this matrix is very similar to that of the corresponding net dissipation matrix, $-\mathbf{M_n^r}$. The diagonal elements are positive while the off-diagonal elements are negative and smaller in magnitude. The diagonal elements are boosted by a factor of about four when compared to the net dissipation matrix. The off-diagonal elements are also slightly larger (about 1.5 times as much) than those of the net dissipation matrix. This is somewhat different from the T126 case, where the off-diagonal elements were not affected much by the integration

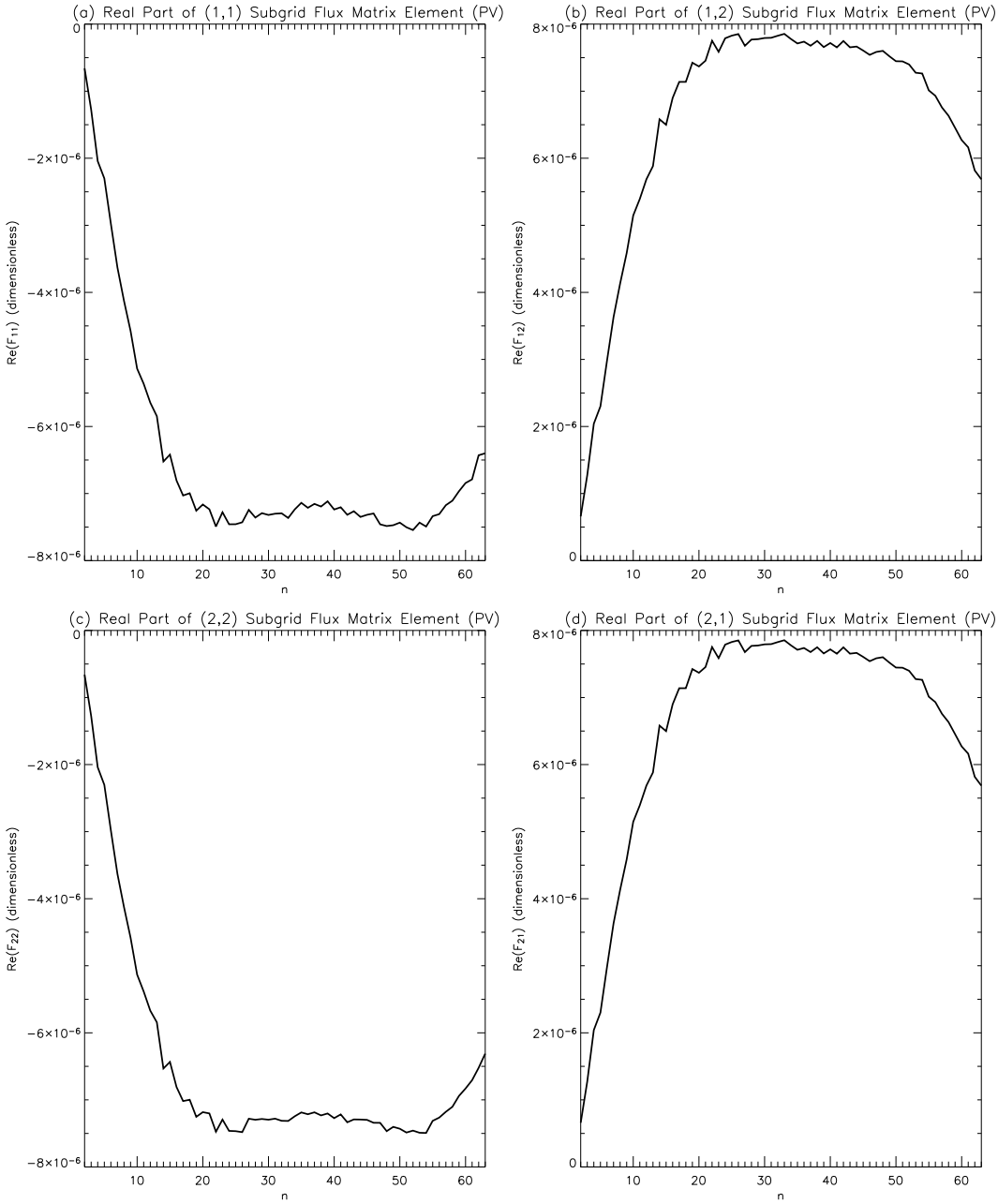

Figure 6.48: Elements of the real part of the isotropic subgrid flux matrix in the PV formulation: (a) $\mathcal{F}^r_{11}$; (b) $\mathcal{F}^r_{12}$; (c) $\mathcal{F}^r_{22}$; and (d) $\mathcal{F}^r_{21}$ (T63) .

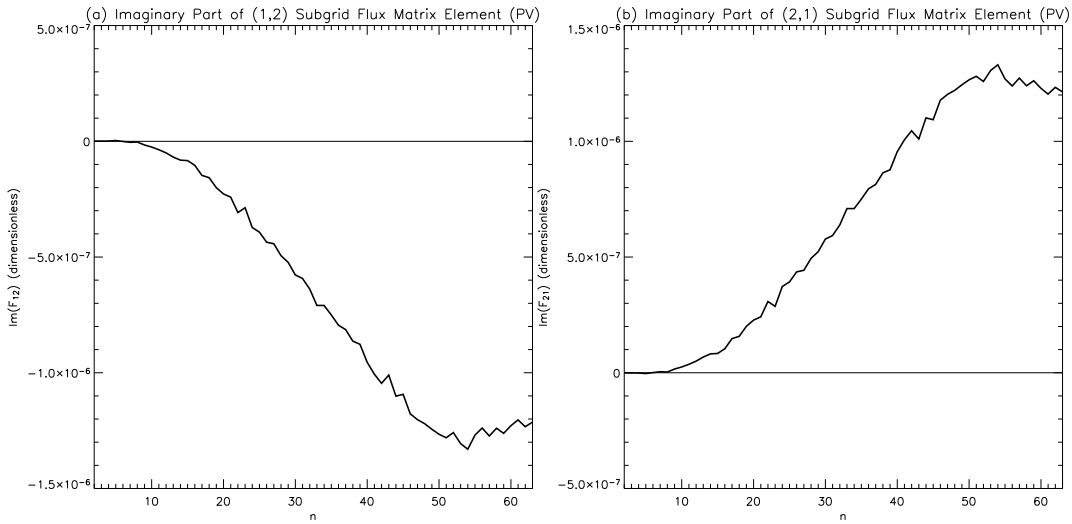

Figure 6.49: Off-diagonal elements of the imaginary part of the isotropic subgrid flux matrix in the PV formulation: (a) $\mathcal{F}^r_{12}$; (b) $\mathcal{F}^r_{21}$ (T63) .

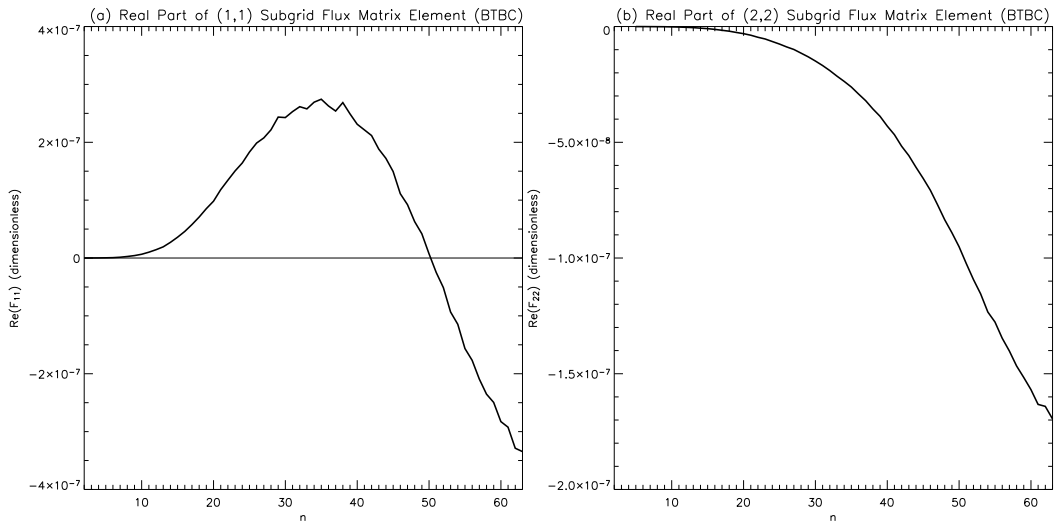

Figure 6.50: Diagonal elements of the real part of the isotropic subgrid flux matrix in the BTBC formulation: (a) $\mathcal{F}^r_{11}$; (b) $\mathcal{F}^r_{22}$ (T63).

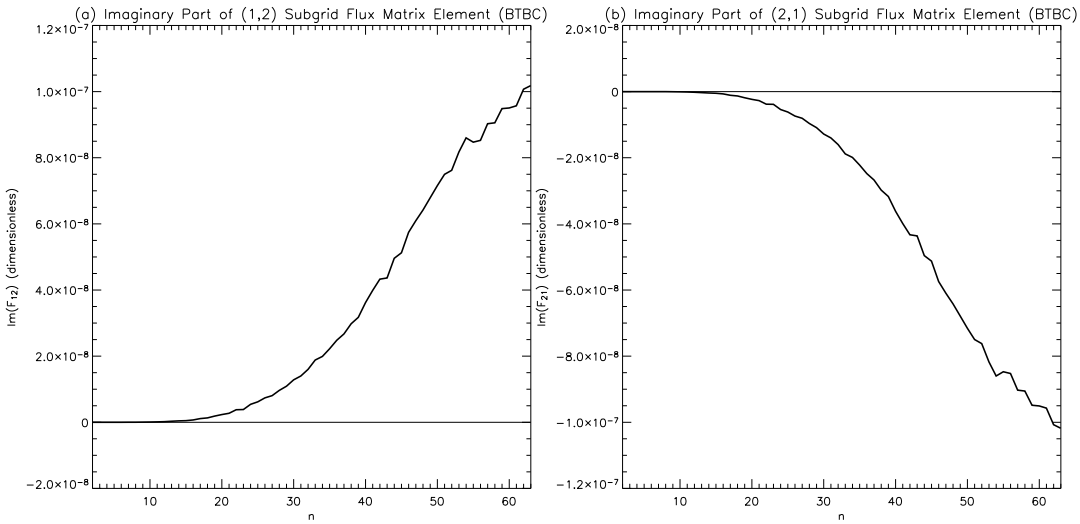

Figure 6.51: Off-diagonal elements of the imaginary part of the isotropic subgrid flux matrix in the BTBC formulation: (a) $\mathcal{F}^i_{12}$; (b) $\mathcal{F}^i_{21}$ (T63).

over different time-lags. Additionally, the drain dissipation matrix elements are more scale selective than the corresponding net dissipation matrix elements.

The imaginary part of the drain dissipation matrix, $\mathbf{M^i_d}$ is shown in Fig. 6.58. Qualitatively, there is not much difference with the corresponding net dissipation matrix, $\mathbf{M^i_n}$, except the point where the elements change sign is shifted to higher wavenumbers. The elements of this matrix are however much smaller than those of $-\mathbf{M^r_d}$. The real and imaginary parts of the backscatter matrix, $\mathbf{F^r_b}$ and $\mathbf{F^i_b}$, are shown in Figs. 6.59 and 6.60, respectively. Both have the same qualitative structure as at T126. That is, the real part, $\mathbf{F^r_b}$, has positive diagonal elements and negative off-diagonal elements of smaller magnitude. The imaginary part, $\mathbf{F^r_b}$, has elements on the off-diagonal with even smaller magnitude; they are also opposite in sign. The magnitudes of the elements of the backscatter at T63 are larger than at T126. The eigenvalues of the backscatter matrix are shown in 6.61. As at T126, they are dominated by the contribution from the diagonal elements of $\mathbf{F^r_b}$.

The matrices $\mathbf{M'_d}$ and $\mathbf{F'_b}$ in BTBC space have also been calculated. Figure 6.62 shows the real part of the dissipation matrix, $-\mathbf{M'^r_d}$. This is qualitatively similar to the corresponding matrix at T126. The baroclinic element is positive at all wavenumbers while the brotropic element is slighly negative for n less than about 40. The magnitudes are roughly half of those for the corresponding T126 matrix. The imaginary part, $\mathbf{M'^i_d}$, is shown in Fig. 6.63. It is very similar to the corresponding matrix at T126. The M^i_{12} element is almost an order of magnitude larger than the M^i_{21} element; however, overall, the real part dominates. The real and imaginary parts of the backscatter matrix, $\mathbf{F'^r_b}$ and $\mathbf{F'^i_b}$, are shown in Figs. 6.64 and 6.65, respectively. These are qualitatively similar to the corresponding T126 matrices. The diagonal elements of $\mathbf{F'^r_b}$ are both positive while the off-diagonal elements of $\mathbf{F'^i_b}$ are of opposite sign, and an order of magnitude less. The eigenvalues of $\mathbf{F'_b}$ are of course dominated by the diagonal elements of the real part $\mathbf{F'^r_b}$, and are shown in Fig. 6.66.

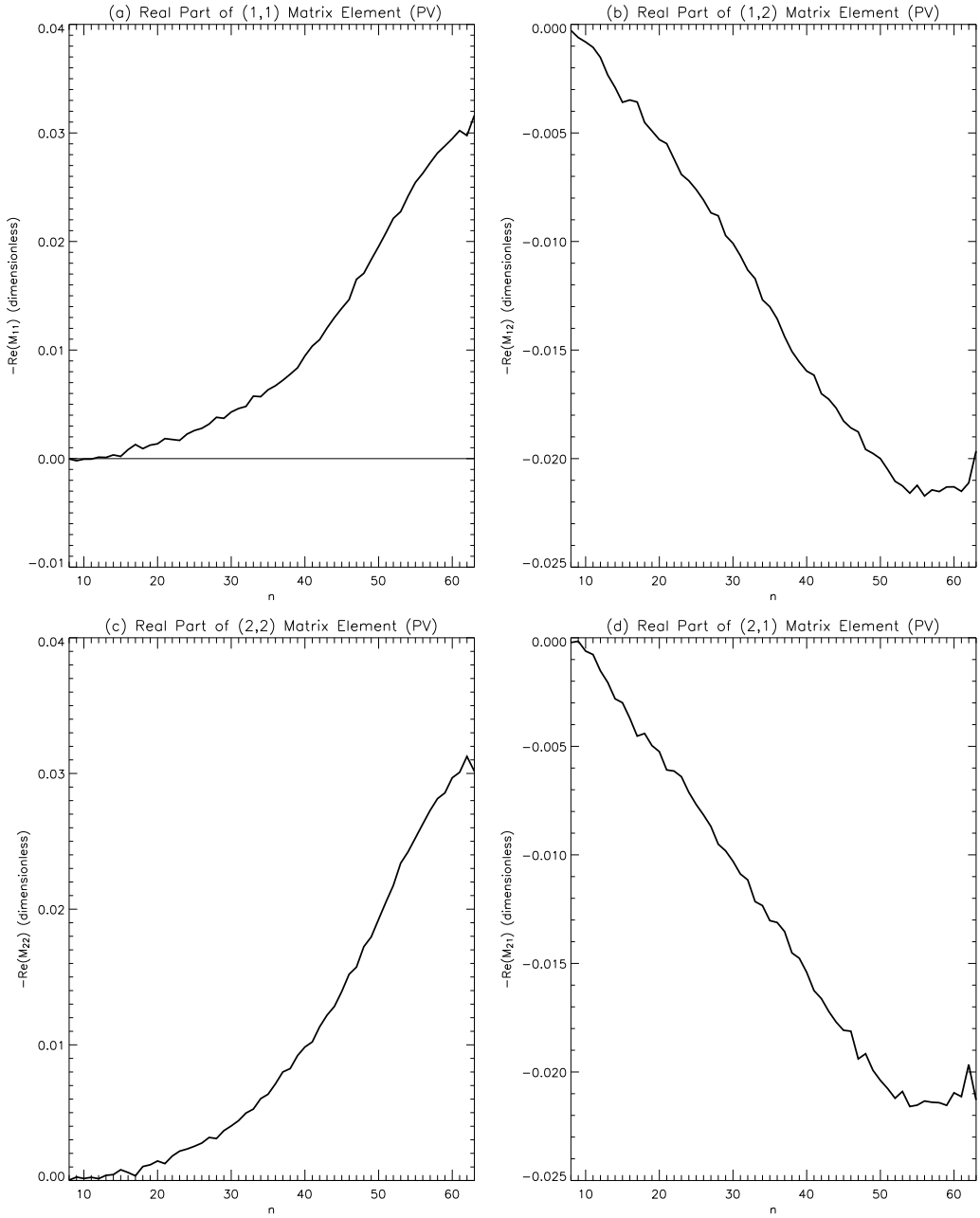

Figure 6.52: Real part of the isotropic net dissipation matrix in the PV formulation: (a) $-M^r_{11}$; (b) $-M^r_{12}$; (c) $-M^r_{22}$; (d) $-M^r_{21}$ (T63).

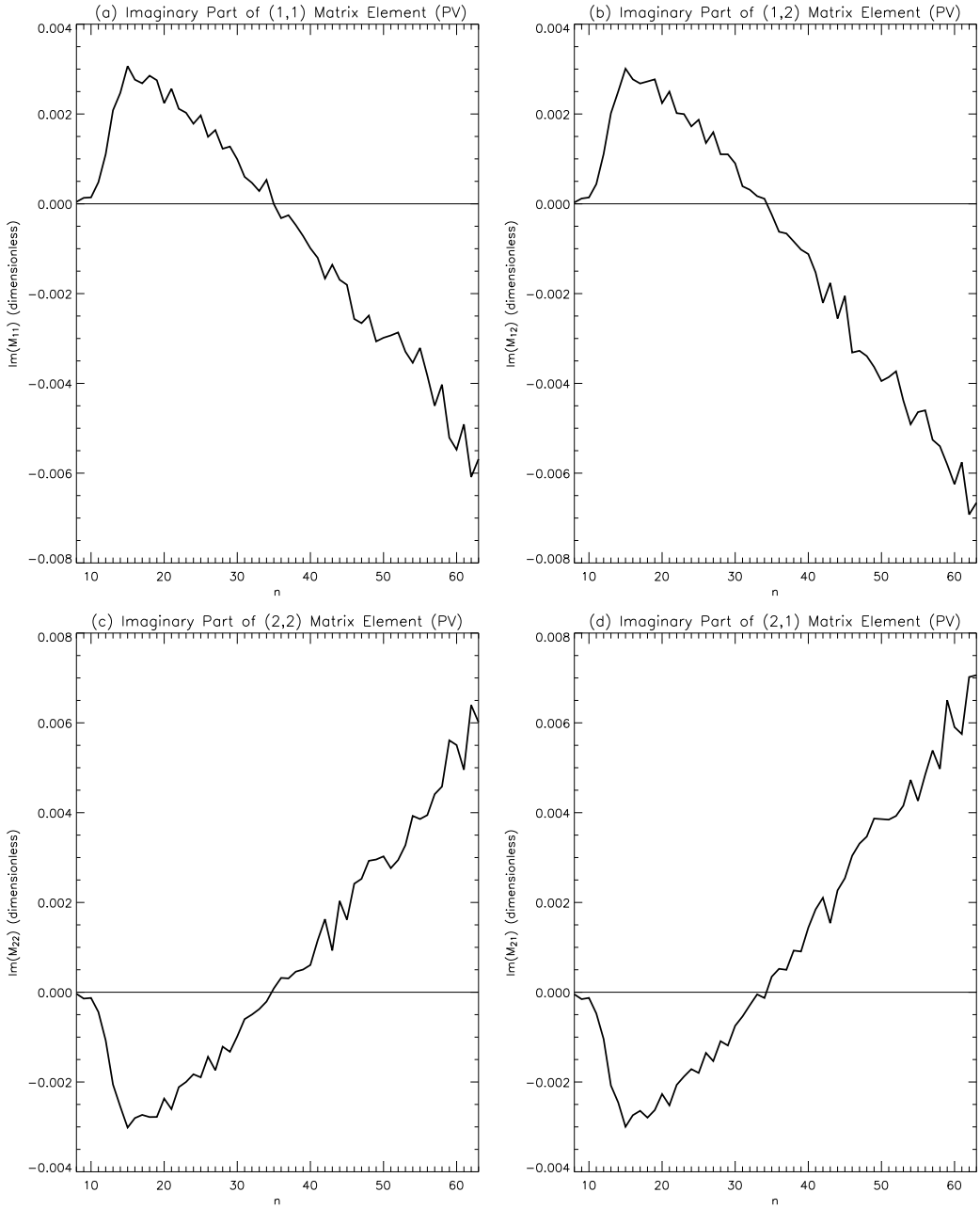

Figure 6.53: Imaginary part of the isotropic net dissipation matrix in the PV formulation: (a) M_{11}^i; (b) M_{12}^i; (c) M_{22}^i; (d) M_{21}^i (T63).

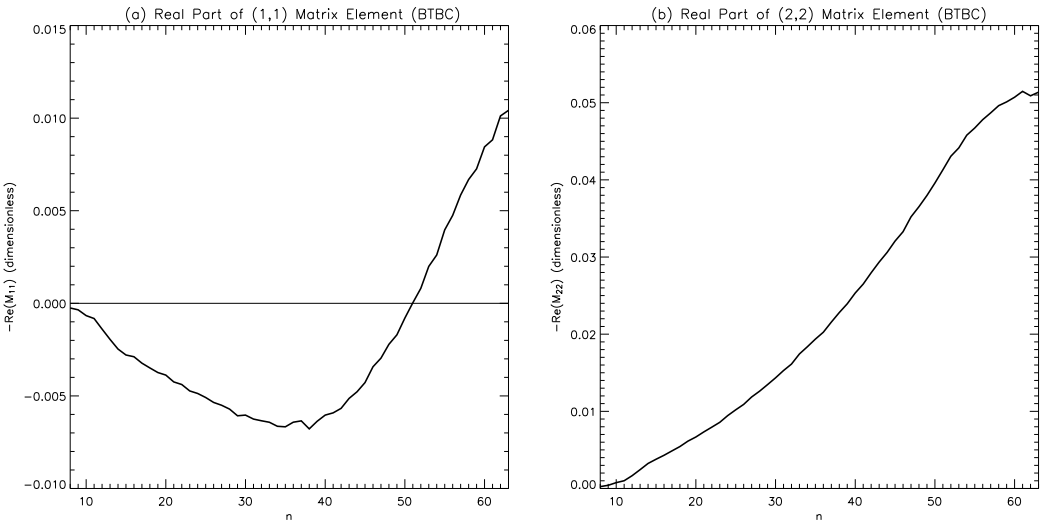

Figure 6.54: Real part of the isotropic net dissipation matrix in the BTBC formulation: (a) $-M^r_{11}$; (b) $-M^r_{22}$ (T63).

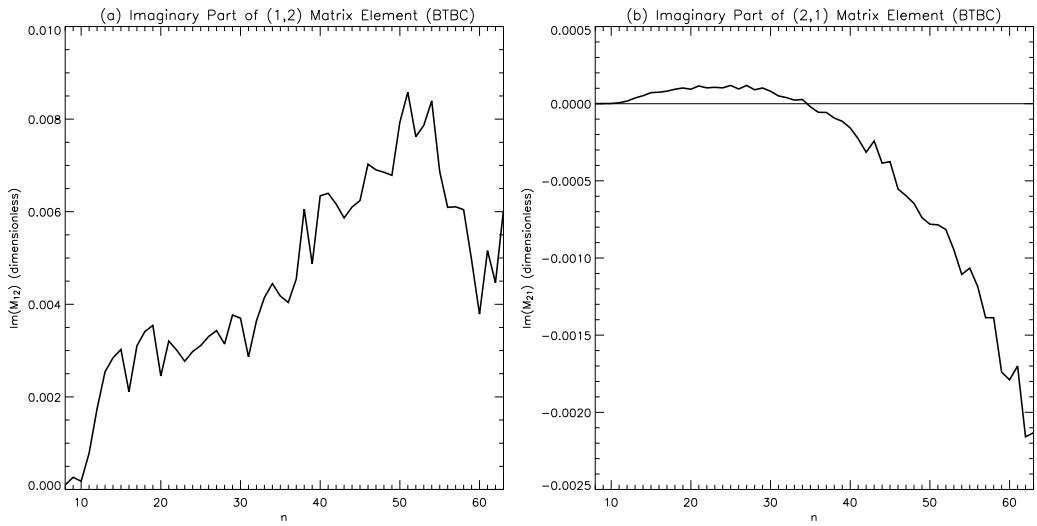

Figure 6.55: Imaginary part of the isotropic net dissipation matrix in the BTBC formulation: (a) M^i_{12}; (b) M^i_{21} (T63).

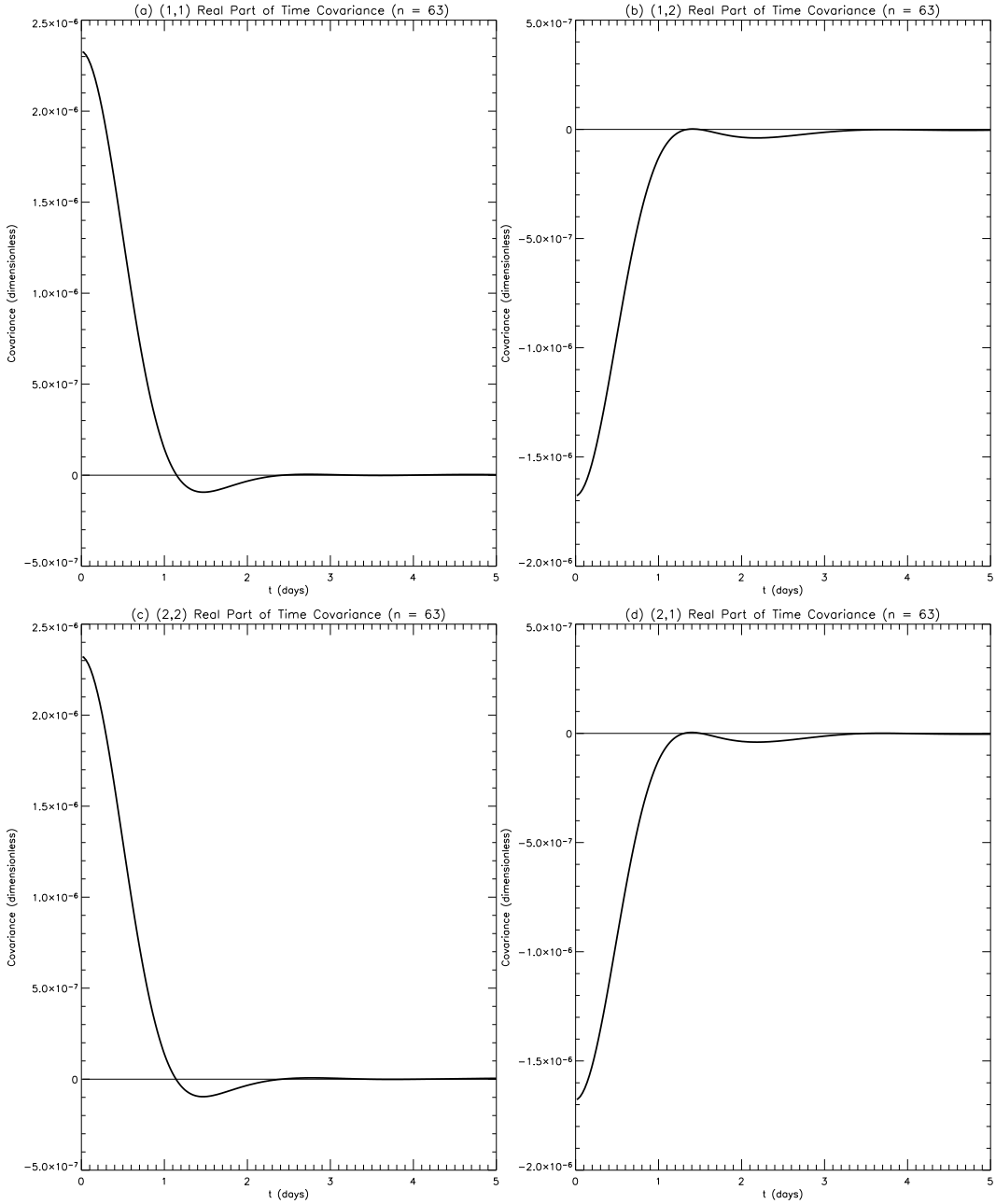

Figure 6.56: Time covariances of the subgrid tendency matrix in the PV formulation: (a) Level 1; (b) Level 2; (c)Level 1/Level 2; (d)Level 2/Level 1 ($n = 63$).

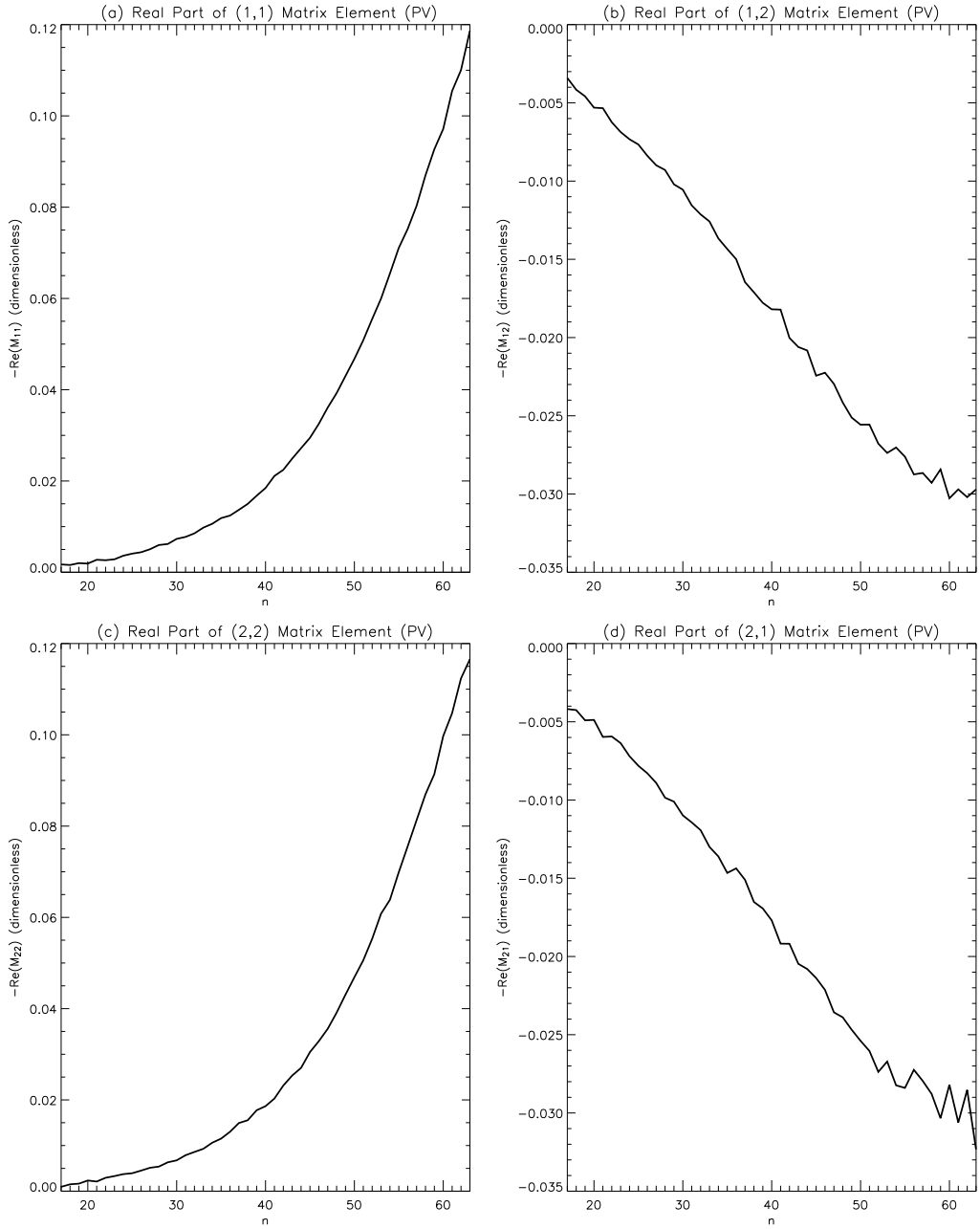

Figure 6.57: Real part of the isotropic drain dissipation matrix in the PV formulation: (a) $-M^r_{11}$; (b) $-M^r_{12}$; (c) $-M^r_{22}$; (d) $-M^r_{21}$ (T63).

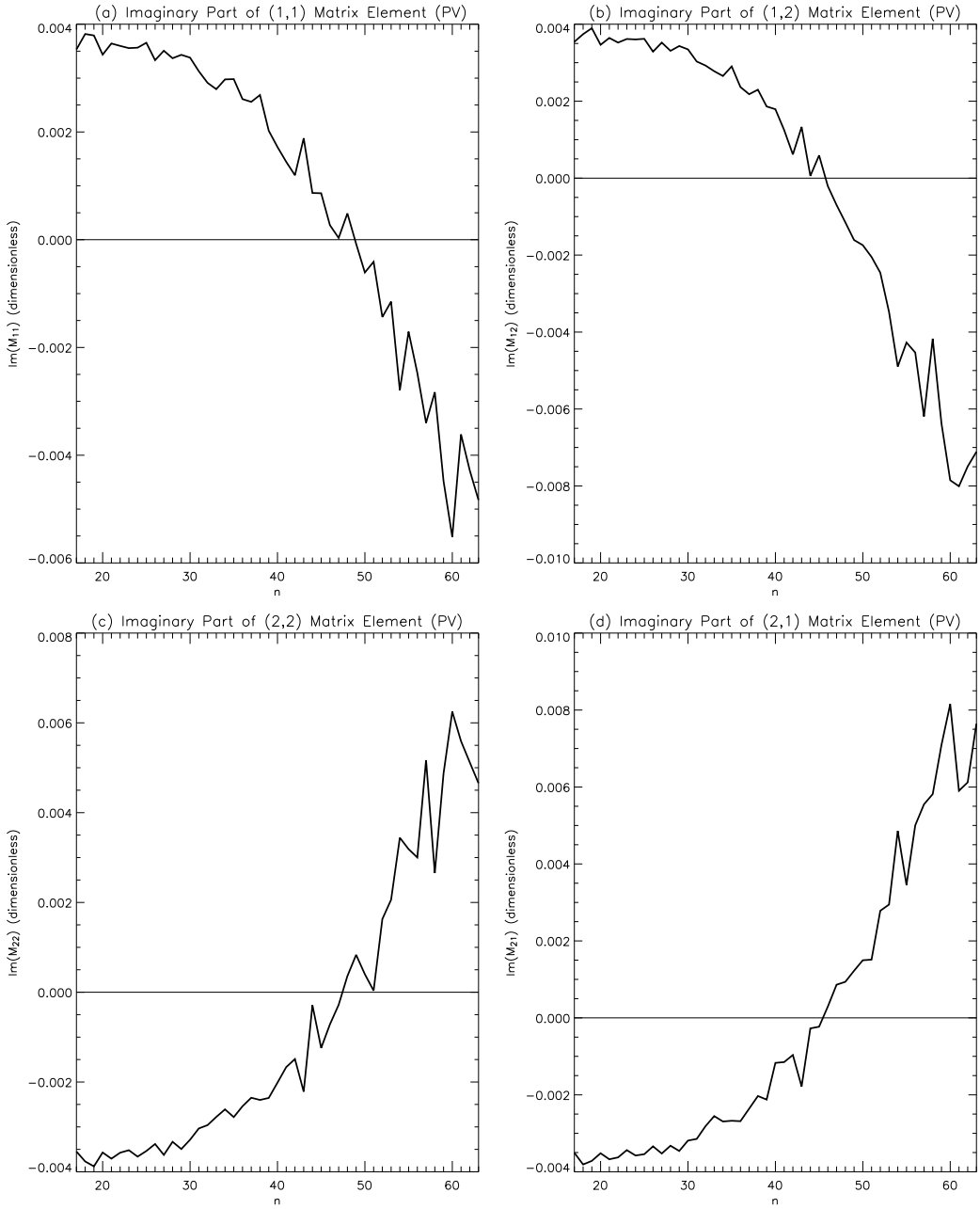

Figure 6.58: Imaginary part of the isotropic drain dissipation matrix in the PV formulation: (a) M^i_{11}; (b) M^i_{12}; (c) M^i_{22}; (b) M^i_{21} .

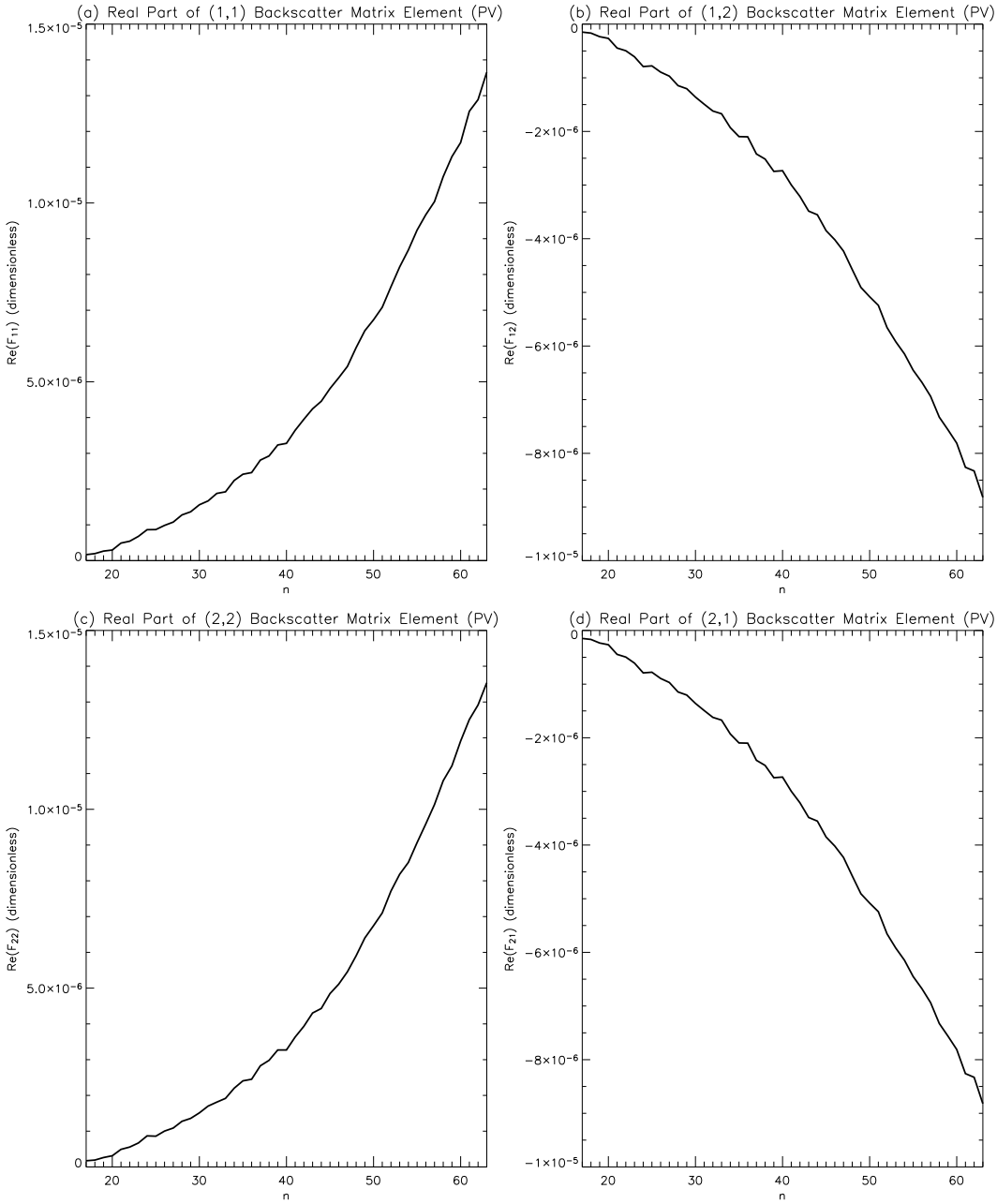

Figure 6.59: Real part of the isotropic stochastic backscatter matrix in the PV formulation: (a) F^r_{11}; (b) F^r_{12}; (c) F^r_{22}; (d) F^r_{21} (T63).

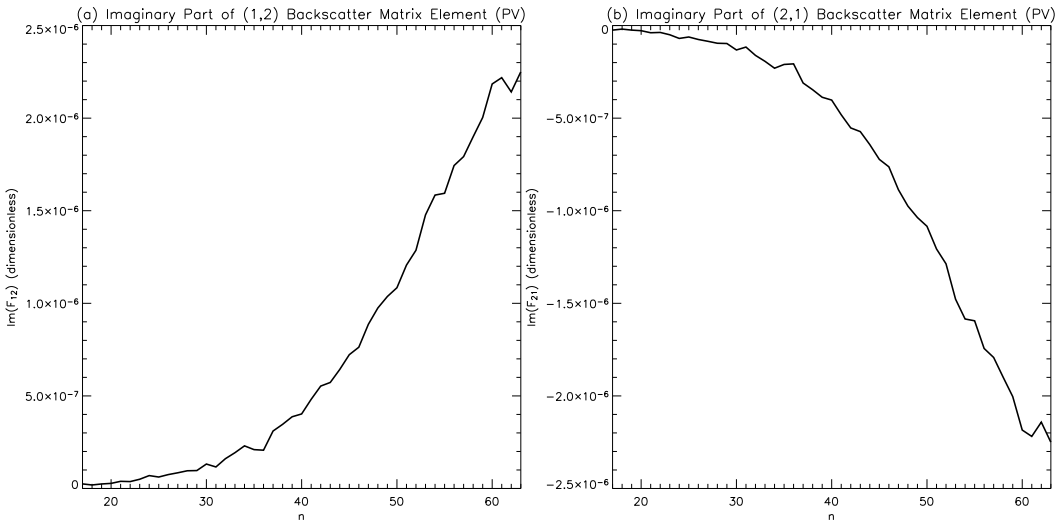

Figure 6.60: Imaginary part of the isotropic stochastic backscatter matrix in the PV formulation: (a) F^i_{12}; (b) F^i_{21}.

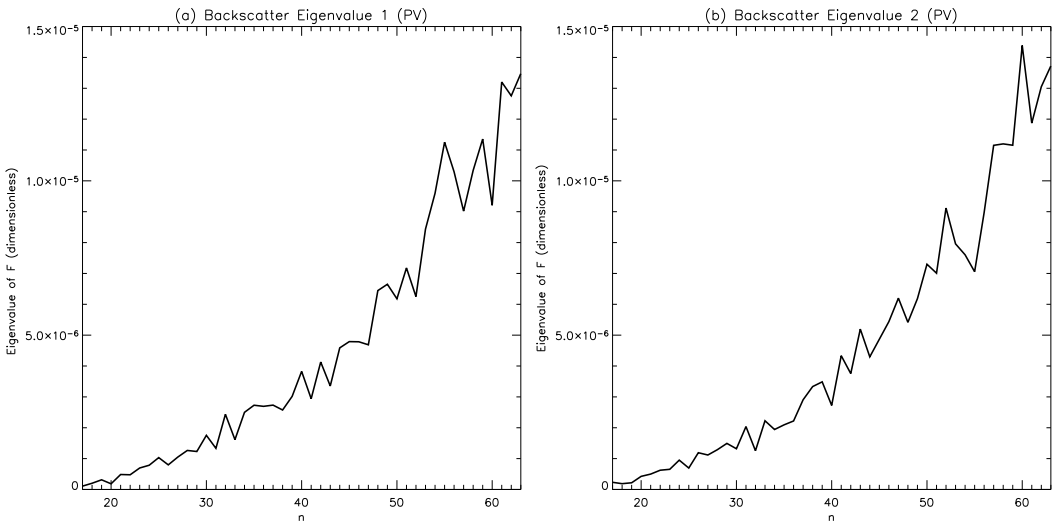

Figure 6.61: Eigenvalues of the isotropic stochastic backscatter matrix in the PV formulation (T63).

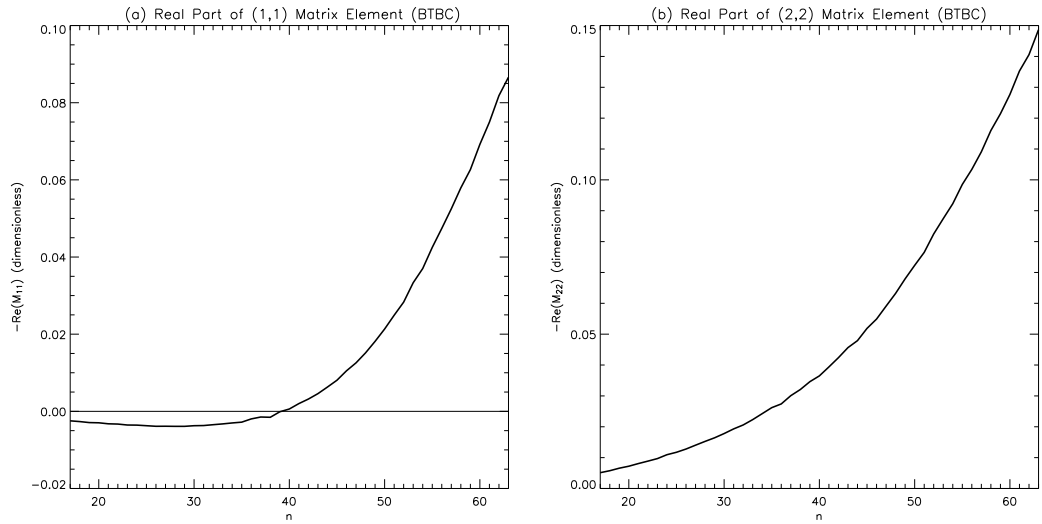

Figure 6.62: Diagonal elements of the real part of the isotropic drain dissipation matrix in the BTBC formulation: (a) $-M^r_{11}$; (b) $-M^r_{22}$ (T63).

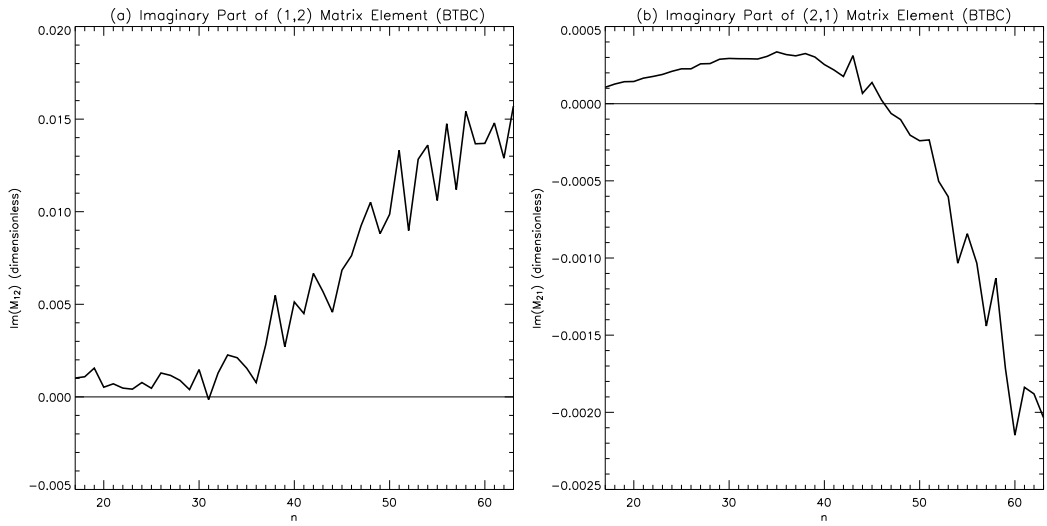

Figure 6.63: Off-diagonal elements of the imaginary part of the isotropic drain dissipation matrix in the BTBC formulation: (a) M^i_{12}; (b) M^i_{21} (T63).

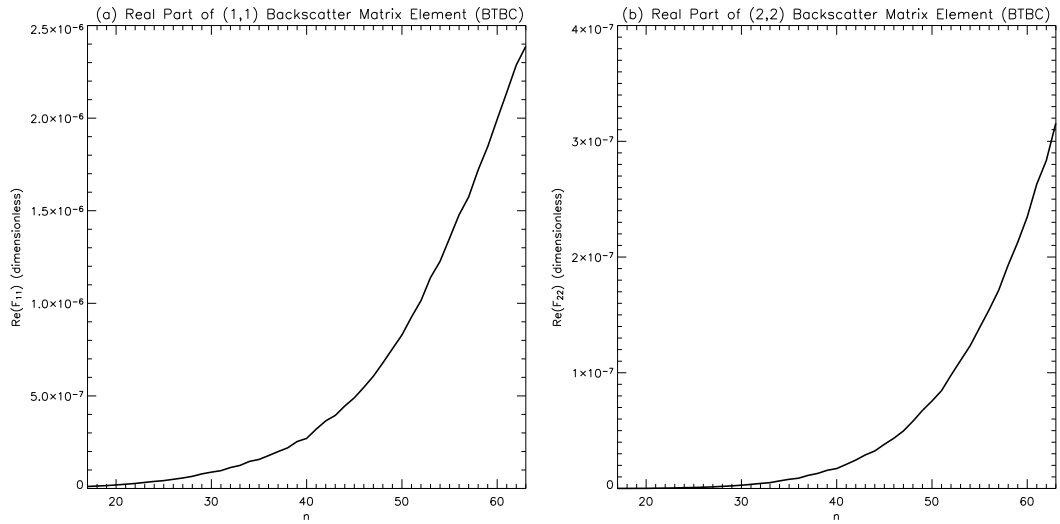

Figure 6.64: Diagonal elements of the real part of the isotropic stochastic backscatter matrix in the BTBC formulation: (a) F_{11}^r; (b) F_{22}^r (T63).

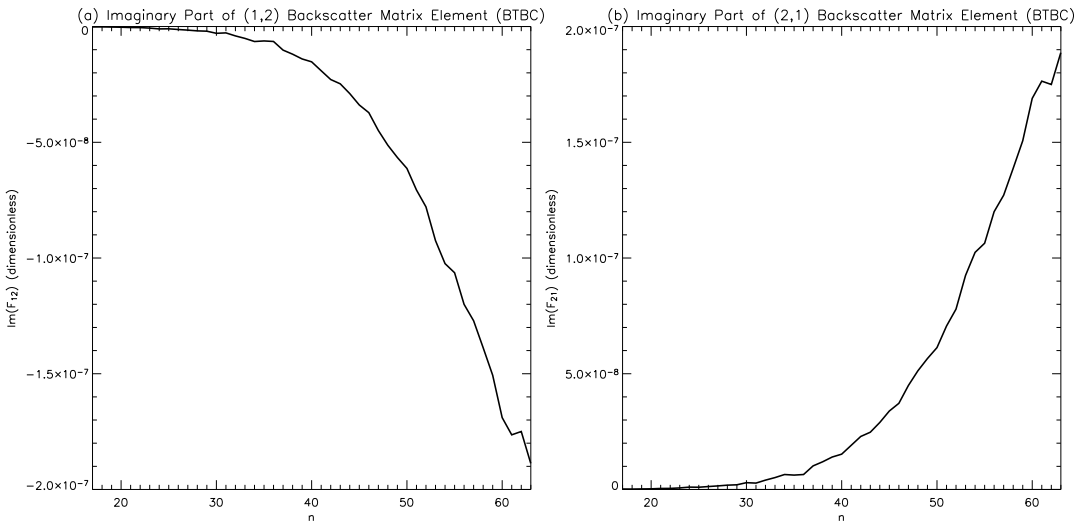

Figure 6.65: Off-diagonal elements of the imaginary part of the isotropic stochastic backscatter matrix in the BTBC formulation: (a) F_{12}^i; (b) F_{21}^i (T63).

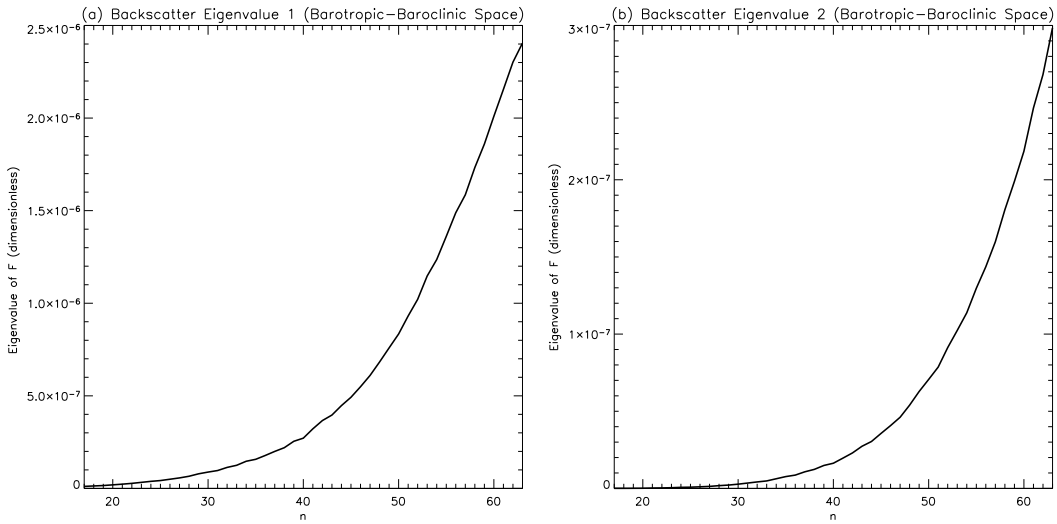

Figure 6.66: Eigenvalues of the isotropic stochastic backscatter matrix in the BTBC formulation (T63).

6.2.5 LES at T63

The LES at T63 is performed using bare parameters, the deterministic parameterization in the form of the net dissipation matrix, and the stochastic parameterization. The results of the LES with bare parameters are shown in Figs. 6.67 and 6.68. Clearly, with bare parameters, the T63 simulation bears no resemblance to the T126 LES. The tail rises dramatically for the total wavenumber kinetic energy spectrum, and the zonal wavenumber spectrum is unrealistically flat at the small scales. This is in contrast to what happened in the atmospheric case. There, the truncation is performed deep in the inertial range, and the spectrum is mainly affected near the truncation scale; the large scale spectrum remains relatively unaffected. In the oceanic spectrum considered here, the truncation is probably performed near the injection scale, and without subgrid-scale parameterizations, this leads to extreme problems at all scales. The large scale energy is underestimated and the small scale energy is grossly overestimated. This highlights the difficulty in oceanic subgrid-scale parameterizations. Frederiksen et al. (1996) proposed an explanation for the observed drop in large scale energy when the small scale energy rises. This is related to the simultaneous conservation of energy and enstrophy. We have also attempted to perform the LES with the net dissipation matrix alone—the deterministic parameterization. Unfortunately, the simulation becomes numerically too unstable, and the result blows up. This could be related to the partly negative dissipation on the barotropic mode; negative dissipations are known to be numerically unstable. However, when the LES is performed with the stochastic parameterization, there is no numerical instability evident. The results are shown in Figs. 6.69 and 6.70. There is in general excellent agreement between the LES at T63 and at T126.

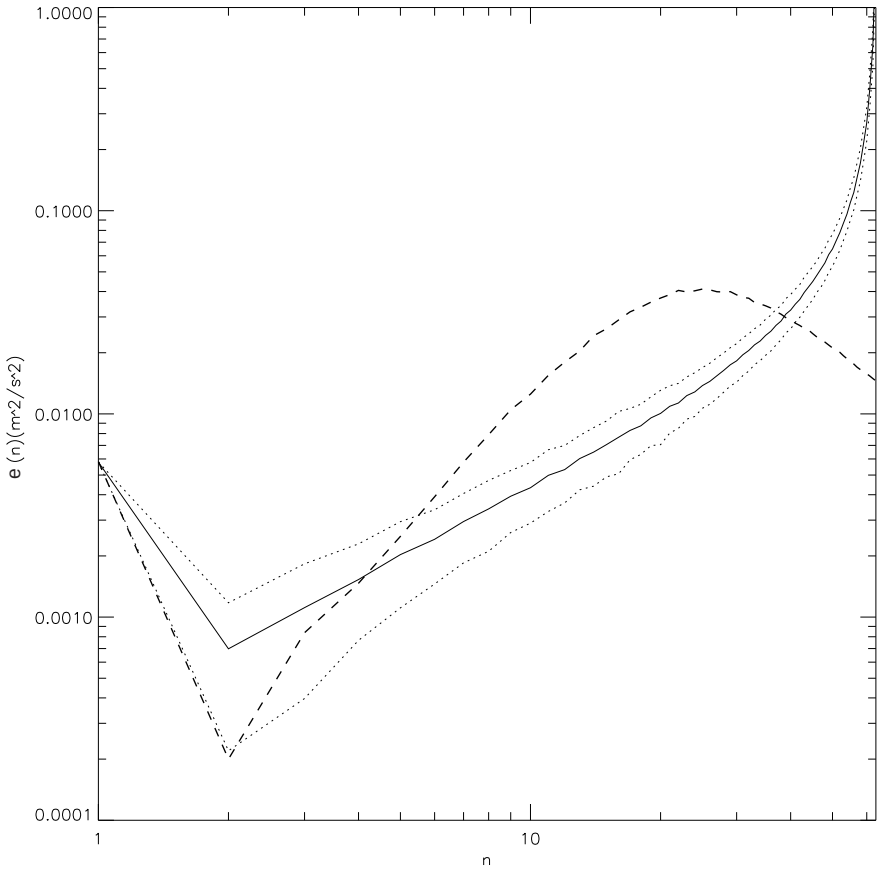

Figure 6.67: Energy spectra (Level 1) as functions of total wavenumber (n): kinetic energy for T63 LES with bare dissipation (solid); LES kinetic energy plus and minus standard deviation (dotted); and T126 LES kinetic energy spectrum (dashed).

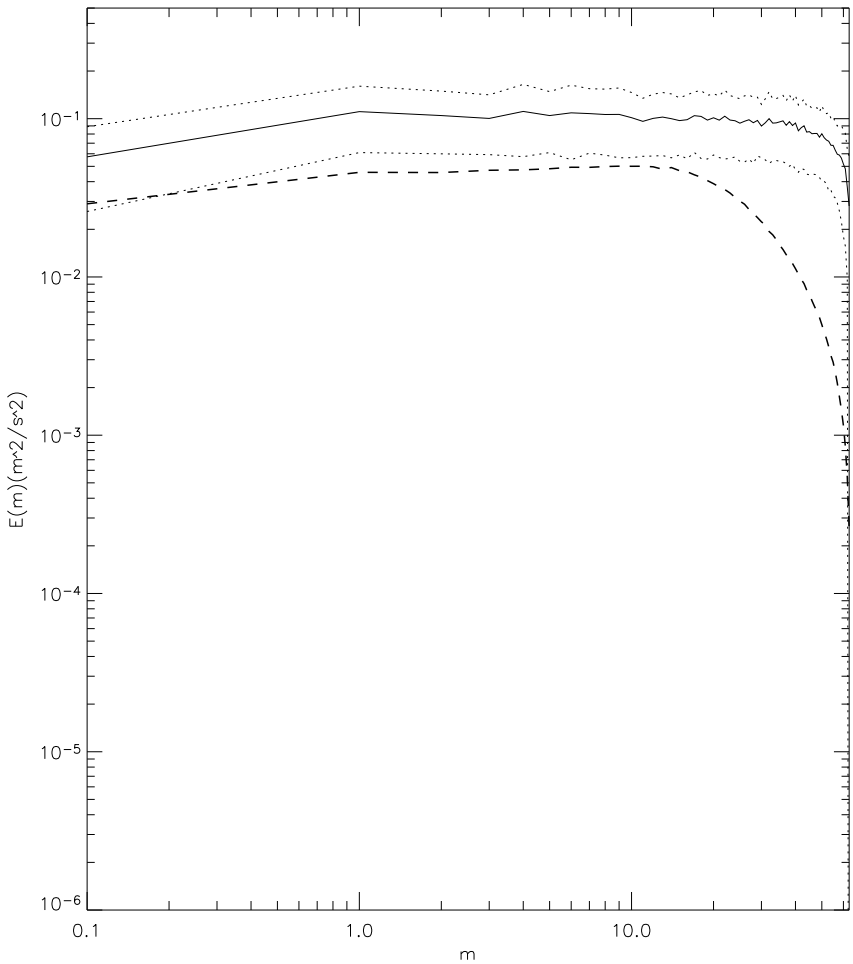

Figure 6.68: Energy spectra (Level 1) as functions of zonal wavenumber (m): kinetic energy for T63 LES with bare dissipation (solid); LES kinetic energy plus and minus standard deviation (dotted); and T126 LES kinetic energy spectrum (dashed).

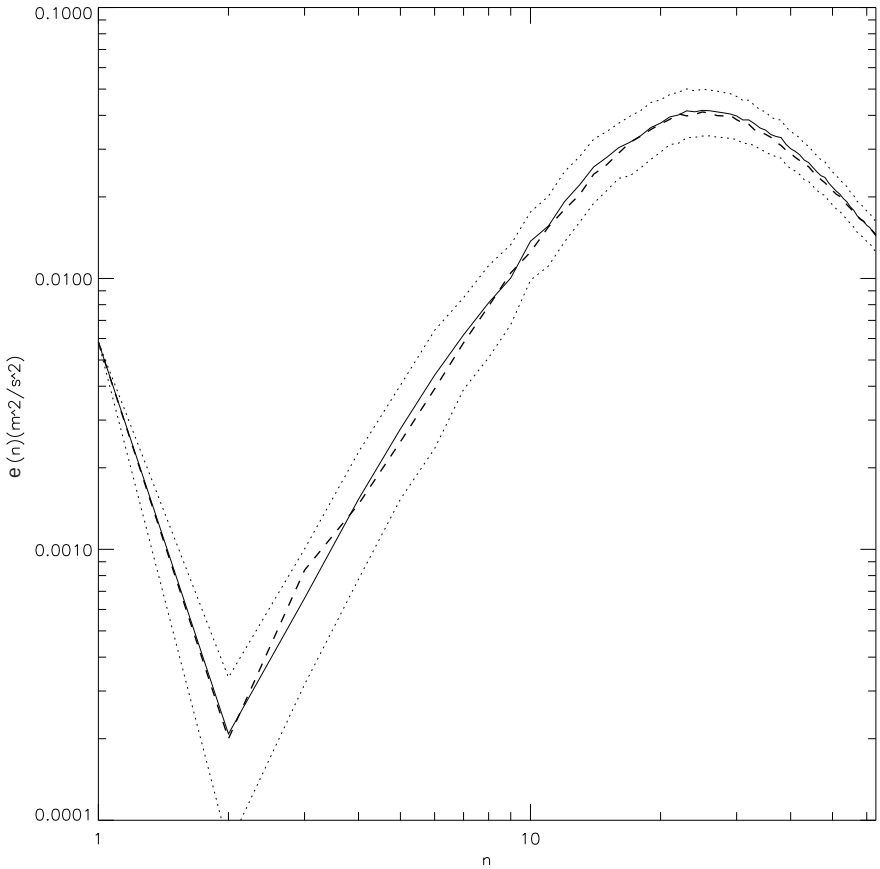

Figure 6.69: Energy spectra (Level 1) as functions of total wavenumber (n): kinetic energy for T63 LES with renormalized drain dissipation and backscatter (solid); LES kinetic energy plus and minus standard deviation (dotted); and T126 LES kinetic energy (dashed).

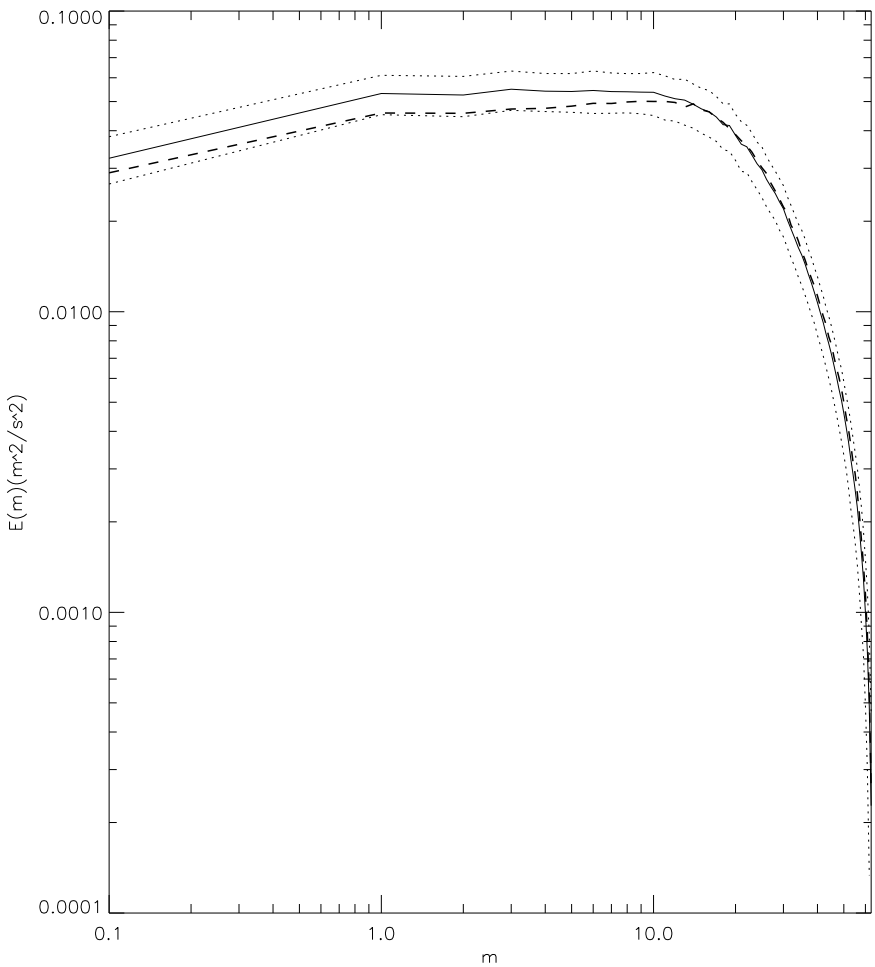

Figure 6.70: Energy spectra (Level 1) as functions of zonal wavenumber (m): kinetic energy for T63 LES with renormalized drain dissipation and backscatter (solid); LES kinetic energy plus and minus standard deviation (dotted); and T126 LES kinetic energy (dashed).

6.3 Discussion

The equivalent layer problem is a good starting point for exploring subgrid-scale parameterizations in stratified flows. The level-symmetry in this problem leads to the net dissipation matrix, $\mathbf{M_n}$, acquiring a simple form when expressed in barotropic-baroclinic (BTBC) variables. $\mathbf{M'_n}$ has purely real diagonal elements, and purely imaginary off-diagonal elements in the BTBC formulation. A similar structure is acquired by $\mathbf{M'_d}$ and $\mathbf{F'_b}$. In most of the problems we have described, the imaginary parts of the matrices are significantly smaller than the real parts, and hence, in the BTBC formulation, the matrices are approximately diagonal. This is not true in general; in some more severely truncated problems (that have been considered, but are not described in this thesis), the coupling between resolved barotropic and subgrid baroclinic modes, for example, is quite strong and cannot be ignored. However, for realistic atmospheric and oceanic truncations at T63, or greater, this coupling is very weak, and so the equivalent layer flows are quasi diagonal as far as subgrid-scale parameterizations are concerned.

In atmospheric flows at the relatively high resolution of T63, a further simplification occurs, namely, that the level-coupling is very weak, and so the problem is diagonal in PV level coordinates as well. This can be anticipated from the phenomenology of QG turbulence for wavenumbers much greater than the deformation scale, which is the case in our simulations since the deformation scale is around wavenumber 12. For such wavenumbers, QG turbulence phenomenology predicts that the turbulent transfers are controlled by barotropic-like triads, and hence the vertical coupling vanishes. In other words, at these scales, the flow behaves as if it consists of two uncoupled layers. The off-diagonal elements of the matrices then vanish. The diagonal elements of these matrices all display prominent cusps near the truncation scale. The net dissipation matrix, $\mathbf{M_n}$, is practically zero until $n \sim 50$, after which it rises sharply to the truncation scale at $n = 63$. The drain dissipation matrix, $\mathbf{M_d}$, and the stochastic backscatter matrix, $\mathbf{F_b}$, are more scale-selective, not being significant until $n \sim 57$, after which they rise more sharply to effectively greater values than the net dissipation matrix elements. The degree to which the elements of $\mathbf{M_d}$ and $\mathbf{F_b}$ rise depends on the whether we have sufficiently integrated over the decorrelation time. Unfortunately, errors in estimating $\mathbf{M_d}$, whether due to sampling or specification of scale-independent decorrelation time, can lead to slightly negative eigenvalues for $\mathbf{F_b}$, at around the point where the cusp starts to appear. We therefore specify a deterministic parameterization, using $\mathbf{M_n}$, for $n < n_c$. In practice, this may not be necessary as the net dissipation below n about 50 is negligibly small in the atmospheric case. In the atmosphere, there is not much difference in the results of the LES using either the purely deterministic formulation or the stochastic formulation near the truncation scale. Both give excellent agreement between the LES and the higher resolution DNS. It was found to be sufficient to employ the m averaged (isotropized) matrices. This is because the flow is to a large extent isotropic near the truncation scale.

In the ocean, vertical coupling is important, and we have to consider the full matrix structure of the parameterizations. The generic structure of the matrices in the PV formulation, based on realistic truncations at T63 and T126 is as follows. The elements of the matrices rise (or fall) to a cusp near the truncation scale, just as in the atmospheric case. However, the scale-selectiveness is not as severe as in the atmosphere. This implies that, at T63 at least, the non-linear transfers may not be as local in oceanic simulations as they are in the corresponding atmospheric simulations at the same resolution. In the atmosphere, the truncation is 'deep' in the forward cascade inertial range; it is not clear

that this is the case in the ocean, and hence the difference in the two simulations. The imaginary components of the matrices have been found to be relatively small, and are therefore of secondary importance. For the real parts of the matrices, the structure is that the diagonal elements are somewhat larger than off-diagonal elements. Additionally, for both $\mathbf{M_d}$ and $\mathbf{F_b}$, the diagonal elements are positive while the off-diagonal elements are negative. The backscatter eigenvalues also have less tendency to become negative compared to the atmospheric case because they are less scale-selective; that is, they do not vanish until at the very largest scales. The off-diagonal elements are also not much different in $\mathbf{M_d}$ as compared to $\mathbf{M_n}$; that is, the off-diagonal elements decorrelate faster than the diagonal elements.

As discussed above, the matrices in this problem take on simpler and more illuminating forms in the BTBC formulation. The oceanic net dissipation matrix then simply becomes a diagonal matrix with purely real elements. A positive value for a diagonal element of $-\mathbf{M_n'^r}$ implies a negative flux of energy or enstrophy, and a negative value implies a positive flux. The barotropic dissipation is found to be negative except near the truncation scale, where it rises to a cusp. The baroclinic dissipation is found to be positive at all scales. Hence, the subgrid contribution to the barotropic mode is injective at the large scales while for the baroclinic mode it is always dissipative. Moreover, near the truncation scale, the baroclinic dissipation is greater than the barotropic dissipation. In terms of the drain and backscatter matrices, the barotropic drain dissipation becomes less negative at the largest scales and more positive at the truncation scale. The baroclinic dissipation also becomes more positive. The barotropic backscatter is found to be greater than the baroclinic backscatter. We have also found that the deterministic parameterization does not work in the oceanic LES due to the development of numerical instability. This is probably related to the fact that the barotropic mode is being acted on by a partly negative dissipation. The problem disappears once the stochastic formulation is employed, and a good agreement between low resolution and high resolution simulations results. The stochastic formulation does not employ dissipations as negative as the deterministic formulation; instead, random forcing is used to inject energy (or enstrophy). This turns out to be a more numerically stable configuration. Again, as in the atmospheric case, it was found to be sufficient to employ the isotropized matrices to run the LES. This is despite the fact that the truncation scales are closer to the deformation scale than in the atmospheric case.

The mean subgrid forcing, $\bar{\mathbf{f}}$, has turned out to be negligible in this problem. In the atmospheric case, the baroclinically-unstable eddies are well resolved, and hence there is practically no difference in mean potentially energy between the LES and DNS. Since the only significant contribution to $\bar{\mathbf{f}}$ is expected to come from the loss of potential energy to baroclinically-unstable eddies, it is reasonable that $\bar{\mathbf{f}}$ should be small. In the oceanic case, the T126 truncation probably resolves most of the baroclinically-unstable eddies as well; in the T63 truncation we do expect some conversion of potential energy into subgrid eddy kinetic energy. However, the only source of mean potential energy is the $(m, n) = (0, 1)$ mode, and the potential energy of this mode is so large compared to the eddy kinetic energy (see Fig. 6.24) that the change in potential energy is negligible. Hence the contribution from $\bar{\mathbf{f}}$ to the dynamics is negligibly small. Note that this will not be true in general when there are other spectral sources of potential energy, as for the problem in Chapter 8 for example. In the next two chapters, we shall build on the insight gained from studying this highly symmetrical problem to study more complex, and hence less symmetrical, problems.

Chapter 7

Simple Flows with Differential Rotation

In this chapter, we shall attempt to increase the realism of the flow by introducing differential rotation. We shall also be using different drag coefficients in the two layers. This means, of course, that the level-symmetry of the previous chapter will be broken, and the matrices in BTBC formulation will not be purely diagonal or off-diagonal. This leads to a conceptually harder problem. Differential rotation also tends to stabilize the large eddies; that is, the inverse cascade is 'arrested', and instead there is an enhanced zonalization of the flow. This is called the Rhines effect (Rhines, 1977; Vallis and Maltrud, 1993; Frederiksen et al, 1996). This will have some effect on the subgrid scale parameterizations, particularly for oceanic flows, where there is a more significant contribution from the subgrid scales on the large scales, as was seen in the previous chapter. The governing equations for the DNS are the spherical two layer QGPV equations, including rotation:

$$\frac{\partial q_i}{\partial t} = -J(\psi_i, q_i) - 2\frac{\partial \psi_i}{\partial \lambda} - D_i^0 \zeta_i + \kappa(q_i^{rel} - q_i) \ , \tag{7.1}$$

where i=1,2. The zonal wind is relaxed towards $u_i^{rel} = U_i^{rel} cos\phi$, where ϕ is the latitude, and U_1^{rel}, U_2^{rel} are the maximum winds (at the equator); q_i^{rel} are the potential vorticities corresponding to the zonal winds u_i^{rel}. The relaxation time scale is given by κ. The bare dissipation operator, D_i^0, is

$$D_i^0 = \alpha_i + (-1)^p \nu_i^0 \nabla^{2p} \ . \tag{7.2}$$

Here, α_i are the linear friction coefficients, due to Ekman drag; ν_i^0 are ad-hoc viscosities, chosen together with the order of the Laplacian operator, p, so that the inertial range of the energy spectrum follows the k^{-3} power law all the way to the truncation scale. The model is integrated in spectral space, as described in Appendix E, and taken to steady-state. An artificial truncation is performed at a wavenumber N_*, and the matrices $\mathbf{M}$, $\mathbf{F}$, and $\bar{\mathbf{f}}$ calculated to parameterize the non-linear tendency for wavenumbers less than N_* (see Section 5.5 and Appendix F). The LES at maximum wavenumber N_* is then performed using the parameterized form of the subgrid non-linear tendency, Eq. F.15, which appears as an additional term in the spectral form of Eq. 6.1. Both the stochastic parameterization, with $\mathbf{M_d}$ and $\mathbf{F_b}$, and the deterministic parameterization, with $\mathbf{M_n}$ only, are considered.

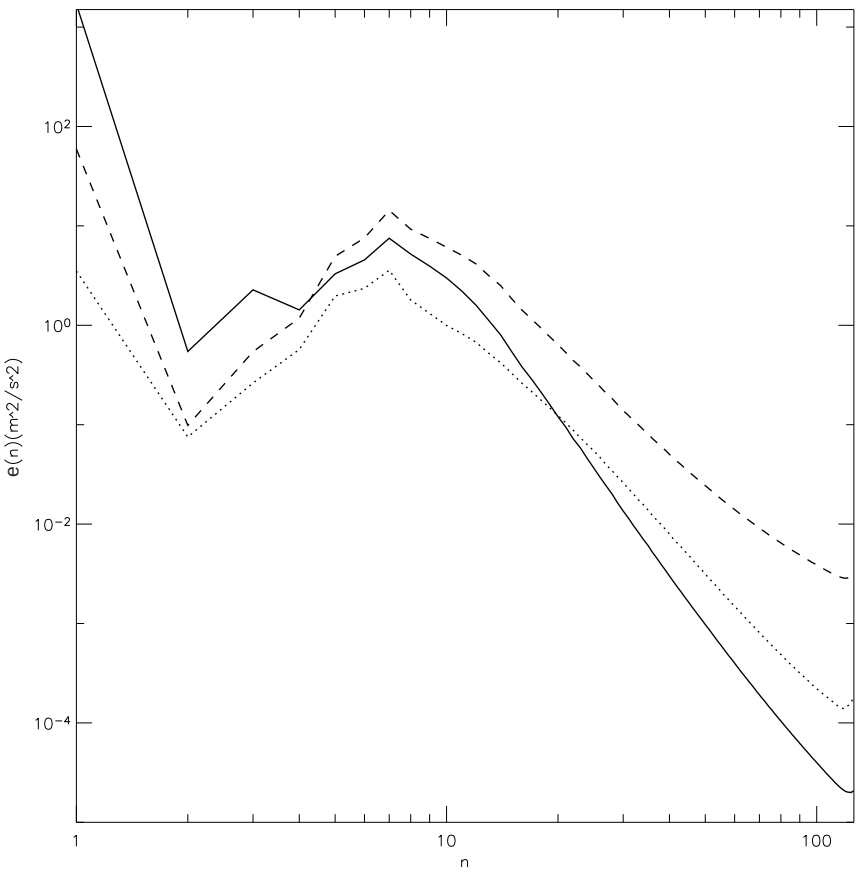

Figure 7.1: Energy spectra as functions of total wavenumber (n): potential energy (solid), Level 1 kinetic energy (dashed), and Level 2 kinetic energy (dotted) for the atmospheric DNS (with rotation) at T126.

7.1 Atmospheric Flows

7.1.1 DNS at T126

For the atmosphere the following parameters have been chosen: the drag, α_i, has been set to a damping time of 20 days for Layer 1 (top), and 5 days for Layer 2 (bottom); the hyperviscosity $\nu_i^0 = 1.98 \times 10^{32}$ m^{8}s^{-1} in both layers; the order of the Laplacian operator $p = 4$; the relaxation time for the mean flow, κ, is 11.6 days; the layer coupling constant, $F_a = 2.5 \times 10^{-12}$ m^{-2}, giving $\lambda_i \sim 500$ km; and the prescribed maximum mean flow is $U_1^{rel} = 30$ ms^{-1} and $U_2^{rel} = 15$ ms^{-1}. The equations have been stepped forward in time for 520 days at steady state—after an initial spin-up period, with a timestep of 450 s, at the resolution of T126. Given that the layer coupling constant is the same as that used in the atmospheric equivalent layer problem of the previous chapter, we still expect that the deformation scale corresponds to approximately wavenumber 12. The beta effect will change the spectral location of maximum baroclinic instability somewhat, however, as discussed in Section 2.9.2.

Figs. 7.1 and 7.2 show, respectively, $e(n)$, the total, and, $E(m)$, the zonal wavenumber averaged energy spectra (see Eqs. E.41 and E.42 of Appendix E.4). Both potential and

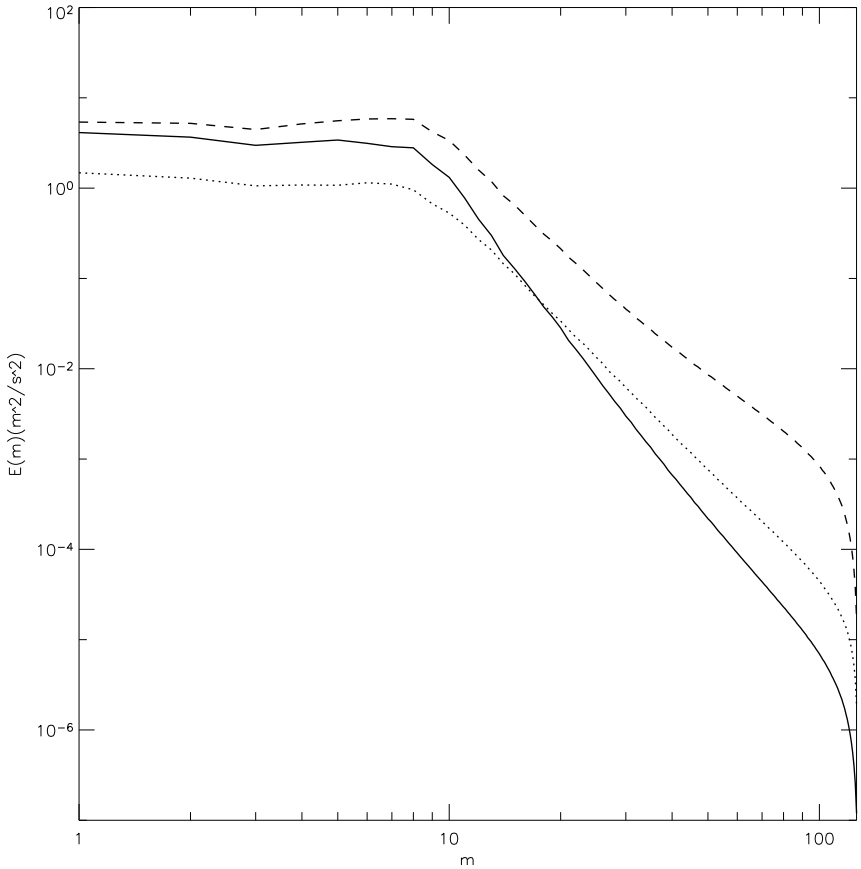

Figure 7.2: Energy spectra as functions of zonal wavenumber (m): potential energy (solid), Level 1 kinetic energy (dashed), and Level 2 kinetic energy (dotted) for the atmospheric DNS (with rotation) at T126.

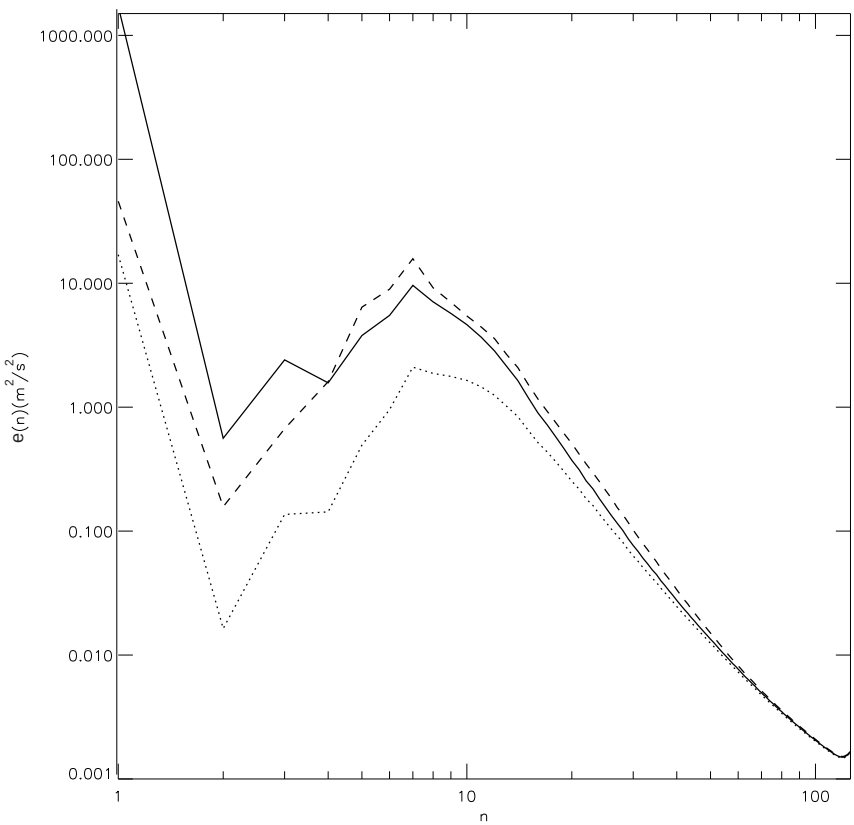

Figure 7.3: Energy spectra as functions of total wavenumber (n): total baroclinic energy (solid), barotropic kinetic energy (dashed), and baroclinic kinetic energy (dotted) for the atmospheric DNS (with rotation) at T126.

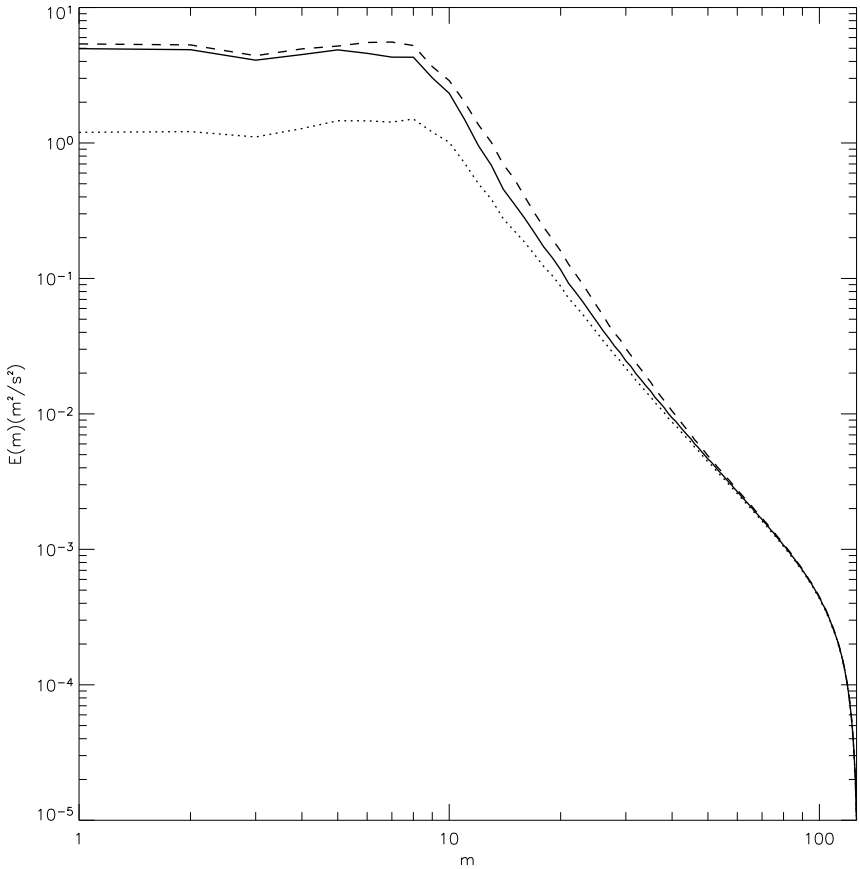

Figure 7.4: Energy spectra as functions of zonal wavenumber (m): total baroclinic energy (solid), barotropic kinetic energy (dashed), and baroclinic kinetic energy (dotted) for the atmospheric DNS (with rotation) at T126.

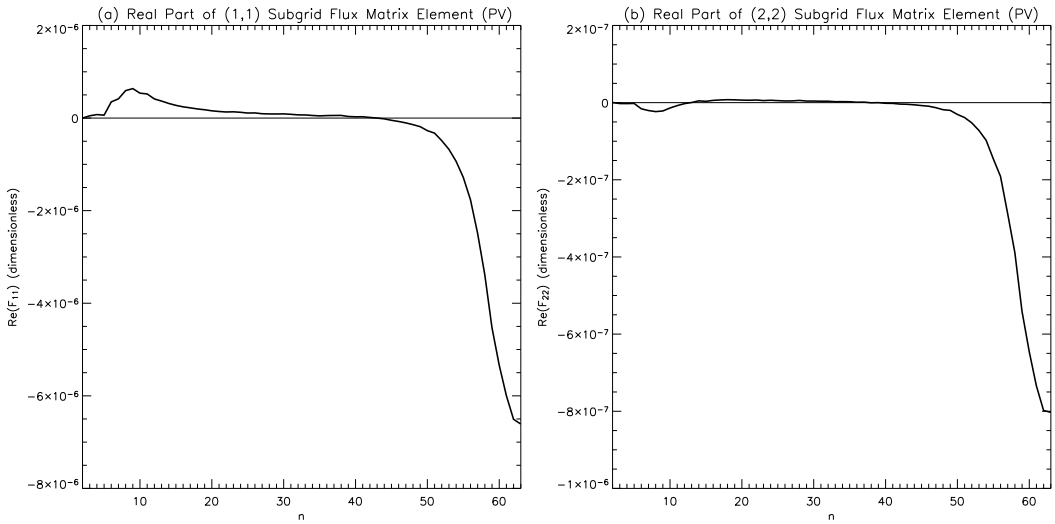

Figure 7.5: Diagonal elements of the real part of the isotropic subgrid flux matrix in the PV formulation: (a) $\mathcal{F}^r_{11}$; (b) $\mathcal{F}^r_{22}$.

kinetic energy spectra are shown. The kinetic energy of Level 1 is greater than that of Level 2 in this problem, and ν_i^0 have been chosen so that the kinetic energy spectrum has an approximately n^{-3} dependence all the way to the truncation scale. The tail of spectrum does lift somewhat at the small scales, especially for Level 1, which has more energy (enstrophy) than Level 2; this again highlights the difficulties with working with an ad-hoc eddy hyperdiffusion. The potential energy spectra are steeper as was found in the previous chapter, and as discussed by Merilees and Warn (1971). Figs. 7.1 and 7.2 reveal what looks like an inertial range for Level 1 between wavenumbers 15 – 50; this is quite steep, however, having a slope of about -3.7. Level 2 has a longer 'inertial range' which extends almost all the way to the truncation scale with a slightly steeper slope. Figs. 7.3 and 7.4 show the corresponding spectra in terms of barotropic and baroclinic energies. At larger scales ($m, n < 50$), the kinetic energy is dominated by barotropic energy, which is presumably due to barotropization of the flow.

In Figs. 7.1 and 7.3, the $n = 1$ energy is dominated by the mean energy from the $(m, n) = (0, 1)$ (solid body rotation mode) relaxation specified for this flow. The mean energy has both barotropic and baroclinic components in contrast to the equivalent layer problem, which had only baroclinic mean energy. It is the baroclinic (potential) energy, however, that feeds the baroclinically unstable eddies; the barotropic energy in the $(m, n) = (0, 1)$ mode is approximately conserved in the absence of topography. At small scales ($m, n > 60$), the baroclinic energy is mostly kinetic, and furthermore, there is an equipartition between barotropic and baroclinic energies as found for the equivalent layer case.

7.1.2 Subgrid-scale Parameterizations at T63

An artificial truncation was performed at $N_* = 63$, and the matrices $\mathbf{M}$, $\mathbf{F}$, and $\bar{\mathbf{f}}$ calculated. Most of the properties of the turbulent fluxes at these scales, stated for the equivalent layer problem, still hold. The deformation scale is somewhere around $n = 12$,

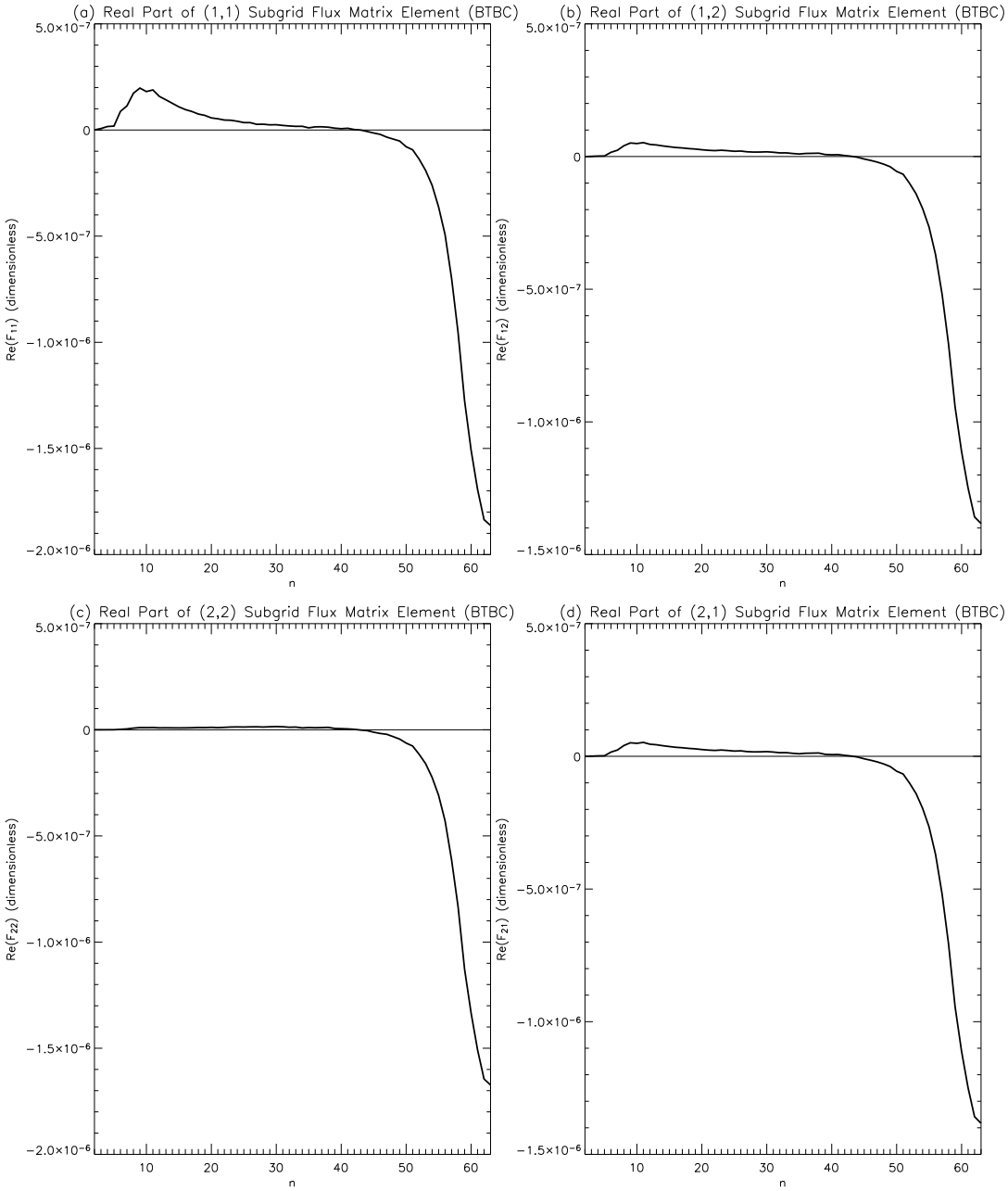

Figure 7.6: Elements of the real part of the isotropic subgrid flux matrix in the BTBC formulation: (a) $\mathcal{F}^r_{11}$; (b) $\mathcal{F}^r_{12}$; (c) $\mathcal{F}^r_{22}$; and (d) $\mathcal{F}^r_{21}$.

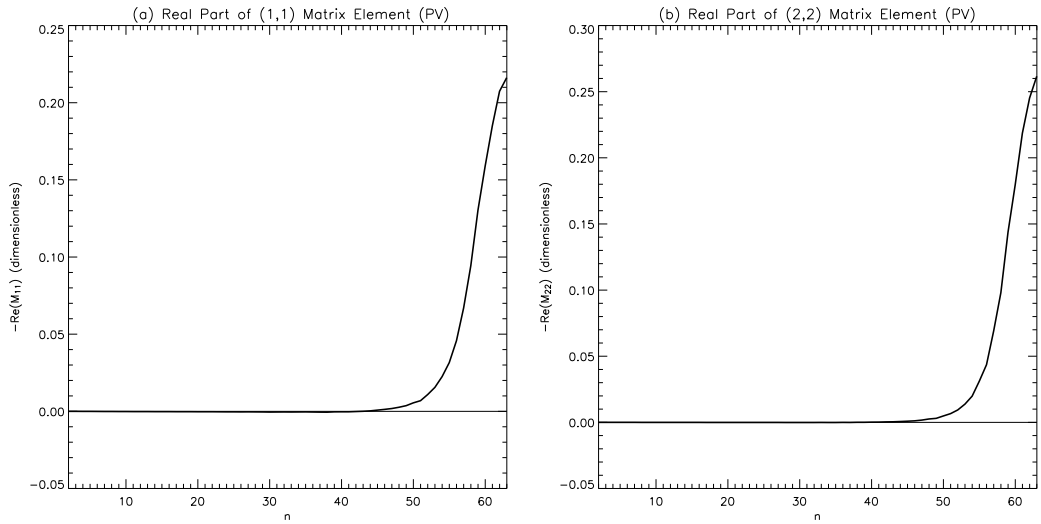

Figure 7.7: Diagonal elements of the real part of the isotropic net dissipation matrix in the PV formulation: (a) $-M^r_{11}$; (b) $-M^r_{22}$.

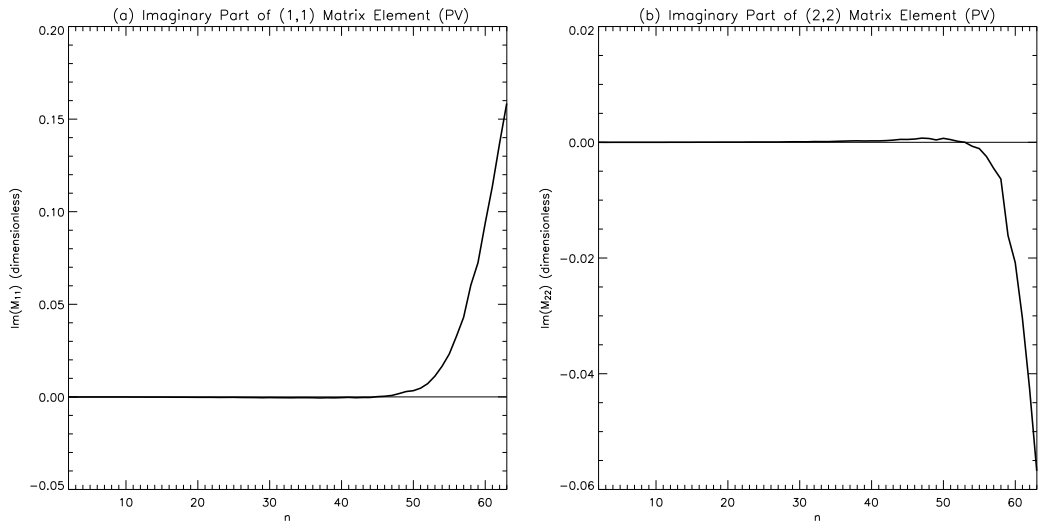

Figure 7.8: Diagonal elements of the imaginary part of the isotropic net dissipation matrix in the PV formulation: (a) M^i_{11}; (b) M^i_{22}.

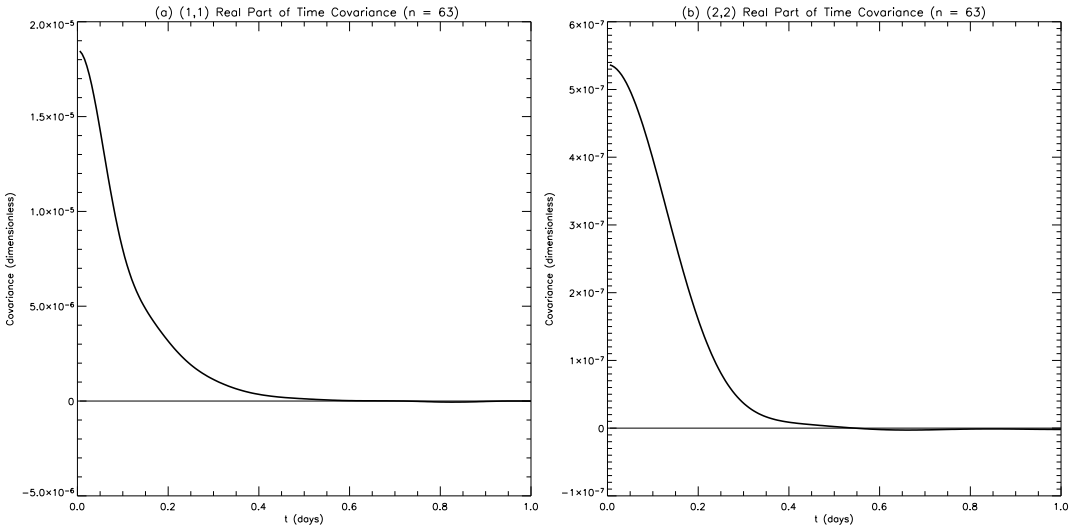

Figure 7.9: Time covariances of the subgrid tendency matrix in the PV formulation: (a) Level 1; (b) Level 2.

so that a truncation at T63 is more than sufficient to resolve it, and hence we do not expect a substantial contribution from the mean subgrid tendency, $\overline{\mathbf{f}}$; the net subgrid transfer is dominated by a negative flux of enstrophy for wavenumbers $m, n >> k_i$, which corresponds to a positive dissipation coefficient (or a matrix dissipation with positive eigenvalues); the two layers behave as if they were uncoupled, and hence the off-diagonal elements of the matrices in PV space vanish. Unless otherwise stated, all the matrix coefficients presented are isotropic; that is, they have been averaged over the zonal wavenumber m as described in Appendix F.

Figure 7.5 shows the diagonal elements of the subgrid flux matrix $\mathcal{F} = \langle \left(\frac{\partial \hat{\mathbf{x}}(t)}{\partial t}\right)_S \hat{\mathbf{x}}^\dagger(t) \rangle + \langle \hat{\mathbf{x}}(t) \left(\frac{\partial \hat{\mathbf{x}}(t)}{\partial t}\right)_S^\dagger \rangle$ in the PV formulation, with $\left(\frac{\partial \hat{\mathbf{x}}(t)}{\partial t}\right)_S$ and $\hat{\mathbf{x}}$ defined in Eqs. 5.50 and 5.51. This matrix represents the contribution of the subgrid terms to the equal-time potential vorticity covariance matrix tendency. As in the equivalent layer problem, the fluxes in both levels are negative near the truncation scale, indicating a drain of potential enstrophy; they are also extremely scale selective. The main difference in this case, however, is that the Level 1 flux is over an order of magnitude greater than the Level 2 flux. The corresponding fluxes in BTBC space are shown in Fig. 7.6. The barotropic and baroclinic enstrophy fluxes are roughly equal, just as in the equivalent layer problem, in spite of the fact that the fluxes in each level are vastly different. There is also an energy injection region for $n < 40$, peaked at $n = 10$, for the barotropic flux, which is again similar to the equivalent layer case. The baroclinic flux also has a very slight injection region for $n < 40$, but this seems much more flat as well as being significantly less in magnitude. There are also significant off-diagonal fluxes; these are related to the degree of correlation between the barotropic and baroclinic modes.

Fig 7.7 shows the diagonal elements of the real part of the net dissipation matrix $-\mathbf{M}_\mathbf{n}^\mathbf{r}$; the off-diagonal elements are dominated by sampling noise, being at least two orders of magnitude less than the diagonal elements, and are not shown. The net dissipation coefficients have the typical cusp near the truncation scale ($n > 50$). Otherwise, not only

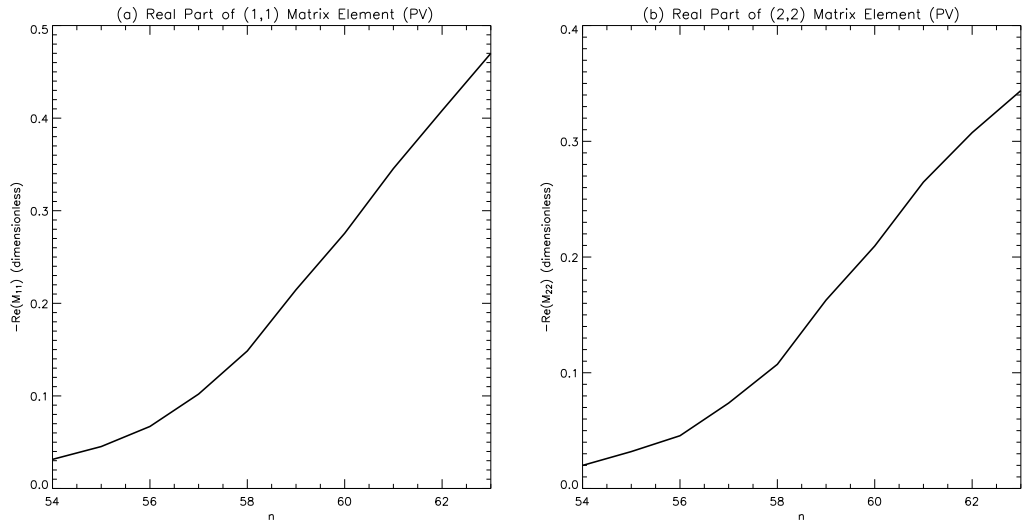

Figure 7.10: Diagonal elements of the real part of the isotropic drain dissipation matrix in the PV formulation: (a) $-M^r_{11}$; (b) $-M^r_{22}$.

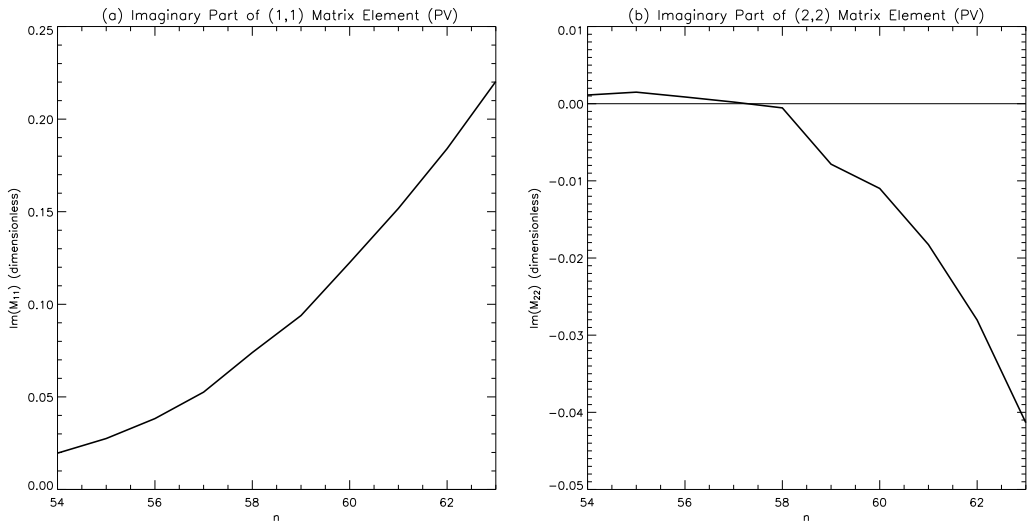

Figure 7.11: Diagonal elements of the imaginary part of the isotropic drain dissipation matrix in the PV formulation: (a) M^i_{11}; (b) M^i_{22}.

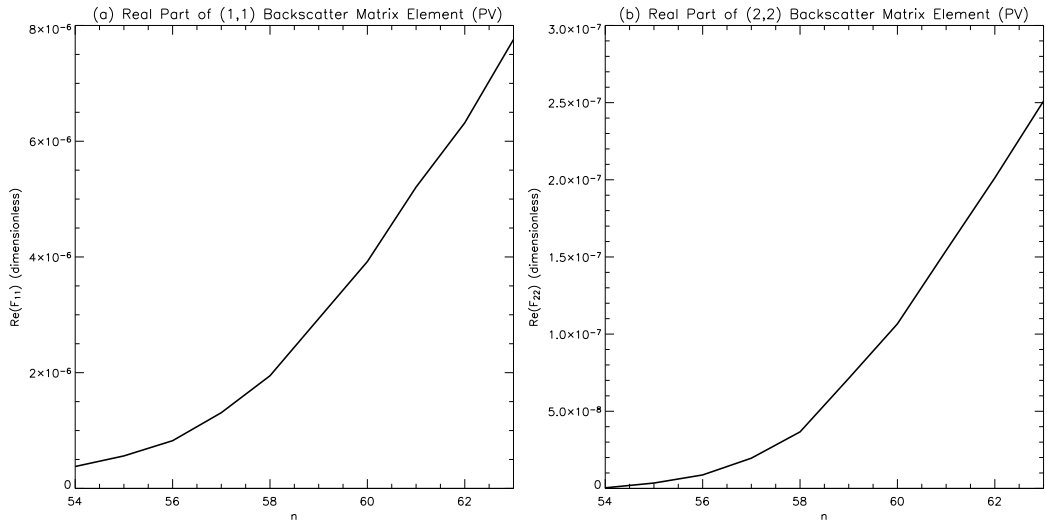

Figure 7.12: Diagonal elements of the isotropic backscatter matrix in the PV formulation: (a) F^r_{11}; (b) F^r_{22}.

is the net dissipation flat far away from the truncation scale, as predicted by Kraichnan (1976), it is also practically zero. Even though the two levels have different fluxes, the diagonal elements of $-\mathbf{M^r_n}$ are similar in size, with the dissipation in Level 2 marginally greater. The diagonal elements of the imaginary part of the net 'dissipation' matrix, $\mathbf{M^i_n}$, are shown in Fig. 7.8. The M^i_{11} element is about three times greater than the M^i_{22} element near the truncation scale; however, M^i_{11} is positive while M^i_{22} is negative, just as in the equivalent layer problem. Furthermore, unlike in the equivalent layer problem, M^i_{11} is of similar size to the elements of $-\mathbf{M^r_n}$, and cannot seemingly be ignored. However, since the problem is quasi diagonal, the only contribution to the enstrophy flux comes from the real part of the diagonal elements; hence, the diagonal elements of $\mathbf{M^i_n}$ do not contribute to the subgrid enstrophy flux. If we only seek to parameterize the subgrid enstrophy flux, then the diagonal elements of $-\mathbf{M^r_n}$ are sufficient for this purpose.

The drain dissipation, $\mathbf{M_d}$, and stochastic backscatter, $\mathbf{F_b}$, matrices have been calculated by integrating over a timescale $\tau = 0.125$ day. Fig. 7.9 shows the time covariance $\langle \left(\frac{\partial \hat{q}^i_{mn}(t)}{\partial t}\right)_S \left(\frac{\partial \hat{q}^i_{mn}(t_0)}{\partial t}\right)^*_S \rangle$ as a function of time, t, at $n = 63$. The subgrid tendency decorrelates after a period of about 0.4 day. We choose a cutoff wavenumber $n_c = 54$ so that the stochastic parameterization is applied only for $n > n_c$. The diagonal elements of $\mathbf{M^r_d}$ and $\mathbf{M^i_d}$ are shown in Figs. 7.10 and 7.11, respectively. The Level 1 contribution of $-\mathbf{M^r_d}$ is in this case twice as strong as that of $-\mathbf{M^r_n}$; the Level 2 dissipation, on the other hand, has only received a slight boost from the integration (over different time-lags) compared to the corresponding element of $-\mathbf{M^r_n}$. The result is that the Level 1 drain dissipation is slightly larger than the Level 2 drain dissipation. The Level 1 contribution from $\mathbf{M^i_d}$ has been enhanced slightly over the corresponding $\mathbf{M^i_n}$ element; the Level 2 contribution is relatively unchanged, however. The diagonal elements of the backscatter matrix, $\mathbf{F^r_b}$ are shown in Fig. 7.12. The Level 1 backscatter is over an order of magnitude greater than the Level 2 backscatter. This suggests that in general the backscatter depends upon the total flux; the greater the flux, the greater the backscatter. The net dissipation, however, may be quite independent of the total flux.

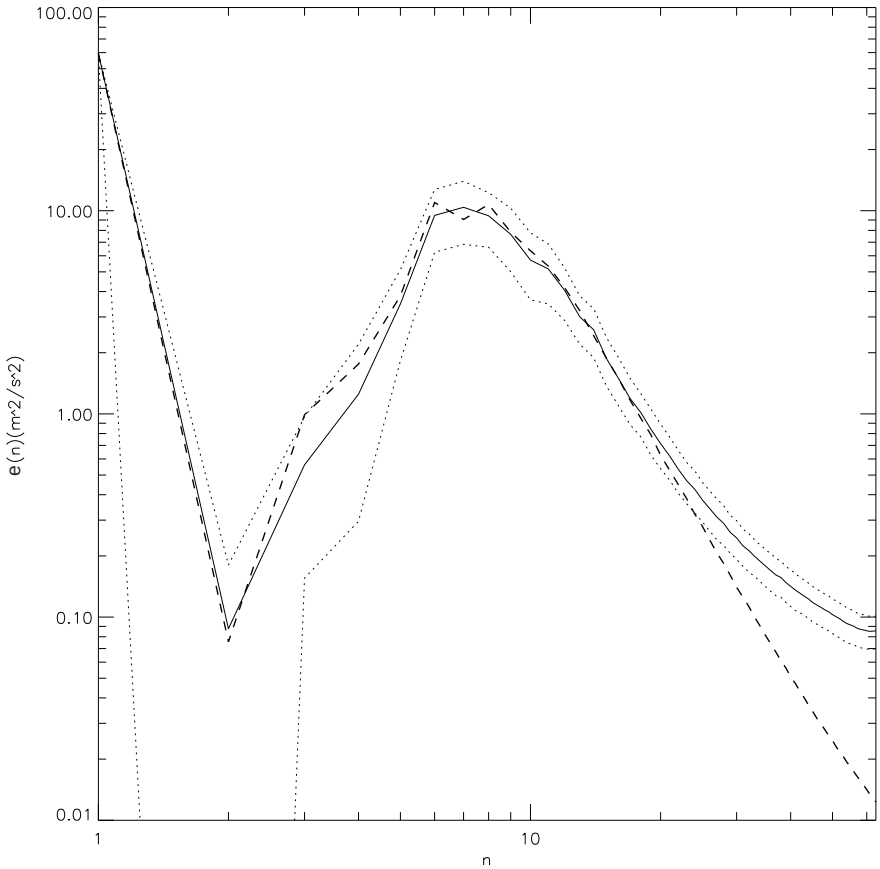

Figure 7.13: Energy spectra (Level 1) as functions of total wavenumber (n): kinetic energy for LES with bare parameters (solid); LES kinetic energy plus and minus standard deviation (dotted); and T126 DNS kinetic energy (dashed).

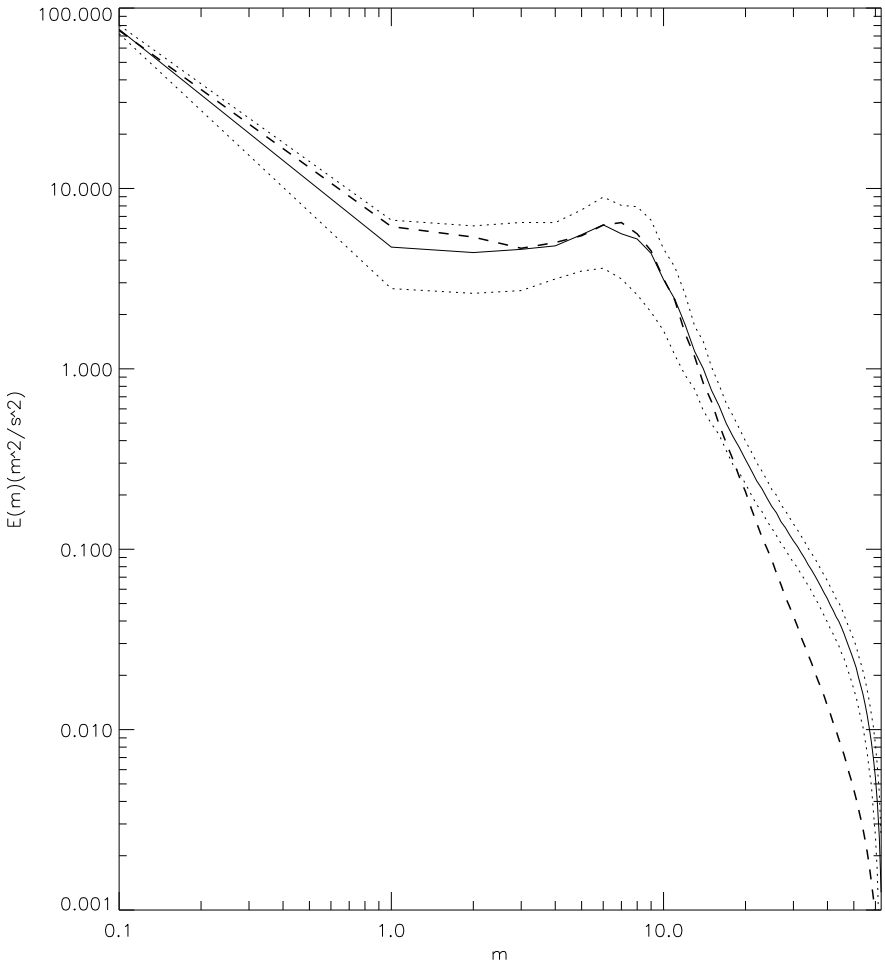

Figure 7.14: Energy spectra (Level 1) as functions of zonal wavenumber (n): kinetic energy for LES with bare parameters (solid); LES kinetic energy plus and minus standard deviation (dotted); and T126 DNS kinetic energy (dashed).

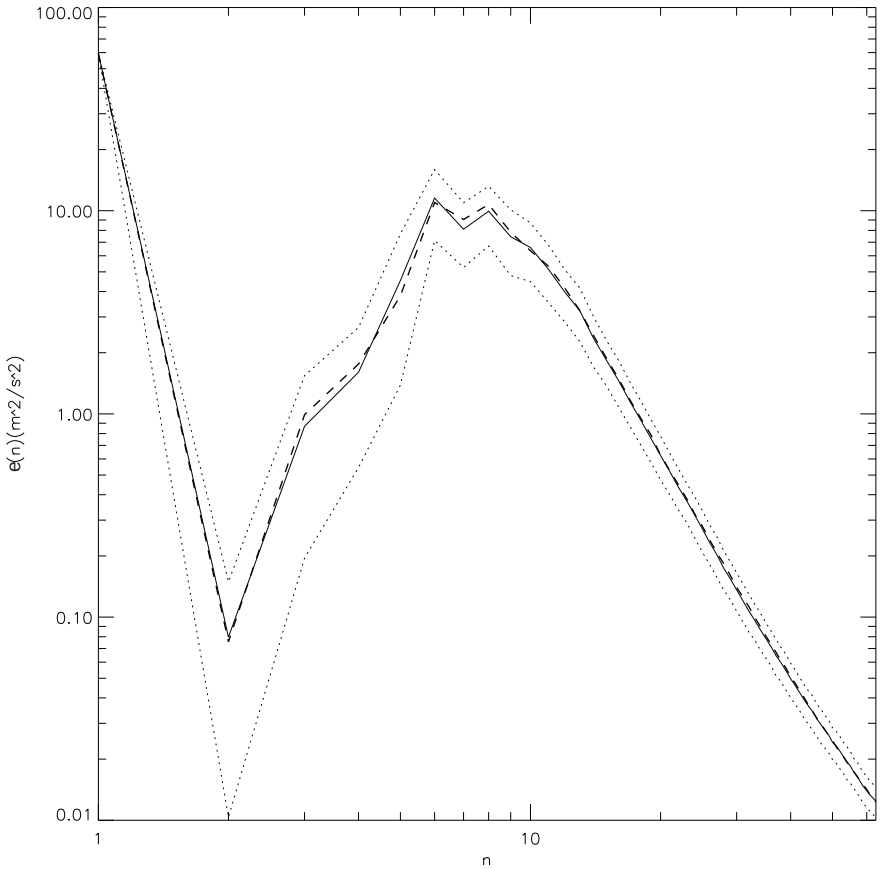

Figure 7.15: Energy spectra (Level 1) as functions of total wavenumber (n): kinetic energy for LES with renormalized drain dissipation and stochastic backscatter(solid); LES kinetic energy plus and minus standard deviation (dotted); and T126 DNS kinetic energy (dashed).

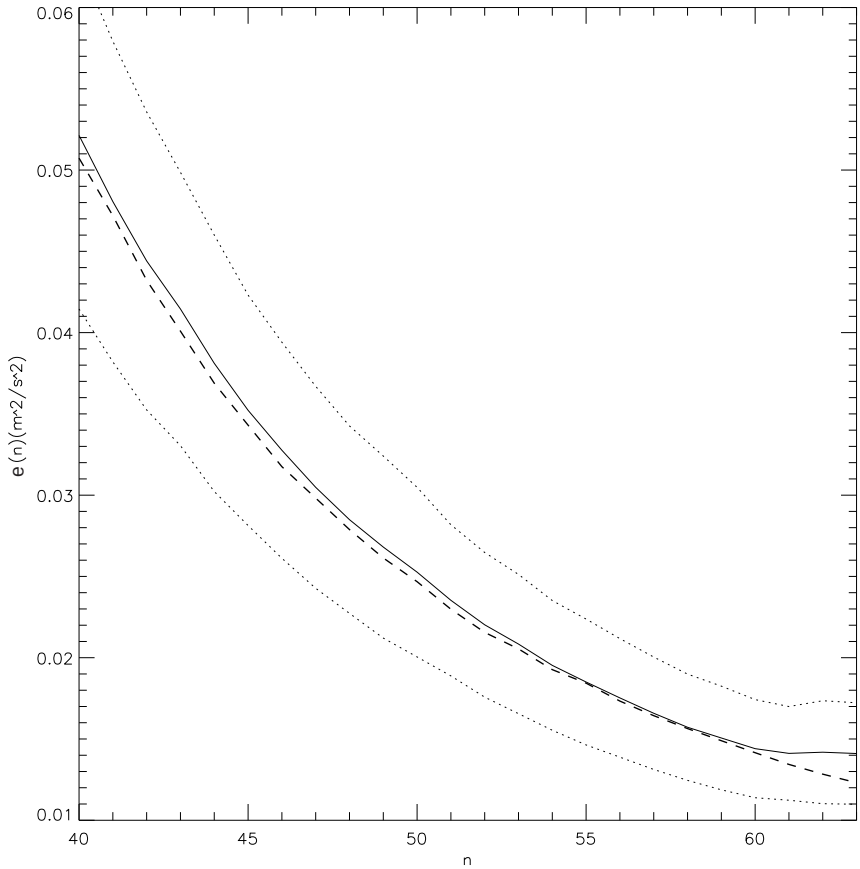

Figure 7.16: Energy spectra (Level 1) as functions of total wavenumber (n): kinetic energy for LES with renormalized net dissipation (solid); LES kinetic energy plus and minus standard deviation (dotted); and T126 DNS kinetic energy (dashed).

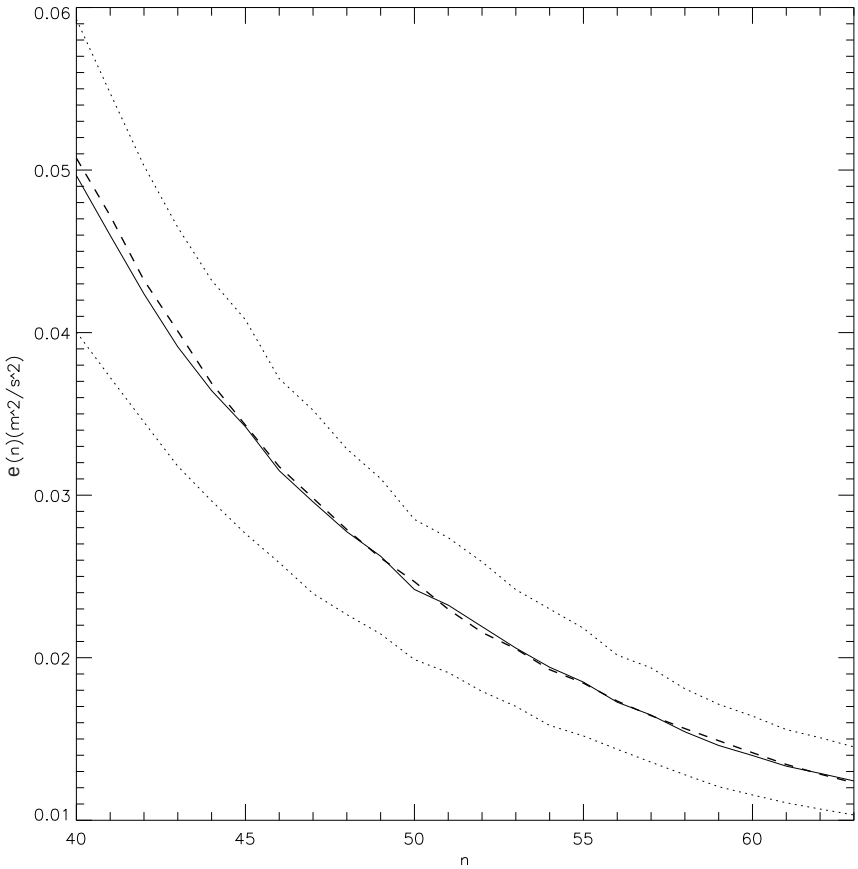

Figure 7.17: Energy spectra (Level 1) as functions of total wavenumber (n): kinetic energy for LES with renormalized drain dissipation and stochastic backscatter (solid); LES kinetic energy plus and minus standard deviation (dotted); and T126 DNS kinetic energy (dashed).

7.1.3 LES at T63

Large eddy simulations at T63 using bare parameters (no subgrid-scale parameterization), net dissipation (deterministic parameterization), and drain dissipation and backscatter (stochastic parameterization) were performed. Figs. 7.13 and 7.14 show the kinetic energy spectra as functions of n and m, respectively, for Level 1 using bare parameters. As in the equivalent layer problem, the deviation of the spectra associated with a reduced sink of enstrophy is confined to wavenumbers of about $m, n > 20$ or so. A suggestion of why this is the case was offered in the previous chapter. Upon using the LES with both the deterministic and stochastic parameterization schemes, a very good agreement is obtained between the LES and DNS at T126. The result using the stochastic parameterization is shown in Fig. 7.15. Broadly, there is not much difference between the two parameterization schemes; however, a closer inspection of the spectra near the truncation scale reveals some differences. Figs. 7.16 and 7.17 show, respectively, the kinetic energy spectra as functions of n obtained from the LES with deterministic and stochastic parameterizations, respectively, for values of n between 40 and 63. We can see that a closer agreement is obtained between LES and DNS at T126 upon using the stochastic parameterization. In particular, the deterministic parameterization has a tendency to lift the tail of the LES right at the truncation scale ($n > 60$); this is not seen in the LES with stochastic parameterization. The kink near the truncation scale is not an anomaly arising in this particular simulation, but has been observed in several experiments when using the net dissipation alone. It highlights the fact that the stochastic parameterization is numerically more stable.

7.2 Oceanic Flows

7.2.1 DNS at 252

In this section, we perform a high resolution oceanic DNS at T252 with the aim of calculating the subgrid-scale parameters $\mathbf{M}$ and $\mathbf{F}$ at T126. The mean subgrid-scale forcing, $\bar{\mathbf{f}}$, is again expected to be small for the reasons given in Chapter 6. The T252 DNS should be sufficient for resolving the baroclinically unstable eddies for our chosen coupling constant, F_o. The following parameters have been chosen: the coupling constant, $F_o = 2.4 \times 10^{-10}\text{m}^{-2}$, which corresponds to $\lambda_i = 50$ km; the drag, α_i, for Level 1 corresponds to a damping time of 40 days, and for Level 2 it is 10 days; the viscosity, $\nu_i^0 = 4.6 \times 10^{12}$ m^{4}s^{-1} for both levels; the order of the Laplacian operator, p, is 2; the relaxation time for the mean flow, κ, is 1.16 days; the mean zonal current is again relaxed towards $u_i^{rel} = U_i^{rel} cos\phi$, where ϕ is the latitude, and U_1^{rel} and U_2^{rel} are the maximum currents (at the equator); the maximum zonal currents are $U_1^{rel} = 1.0$ ms^{-1} and $U_2^{rel} = 0.5$ ms^{-1}. The equations have been stepped forward in time for 104 days at steady state—after an initial spin-up period, with a timestep of 600 s. The number of longitude by latitude grid points is 768 $\times$ 384. Using the same reasoning as in Section 6.1.1, the wavenumber corresponding to the deformation scale is around 120.

Figs. 7.18 and 7.19 show the kinetic and potential energy spectra. An inspection of the kinetic energy spectra reveals what appears to be an inertial range for (m, n) somewhere between about 50 and 100. The slope of this 'inertial range' is around -1.9, which is close to the $-\frac{5}{3}$ = -1.67 slope predicted for an energy cascade in QG turbulence. As in the atmospheric case, the constant slope region is more pronounced for the bottom level. The eddy kinetic energy is an order of magnitude less than the corresponding eddy kinetic

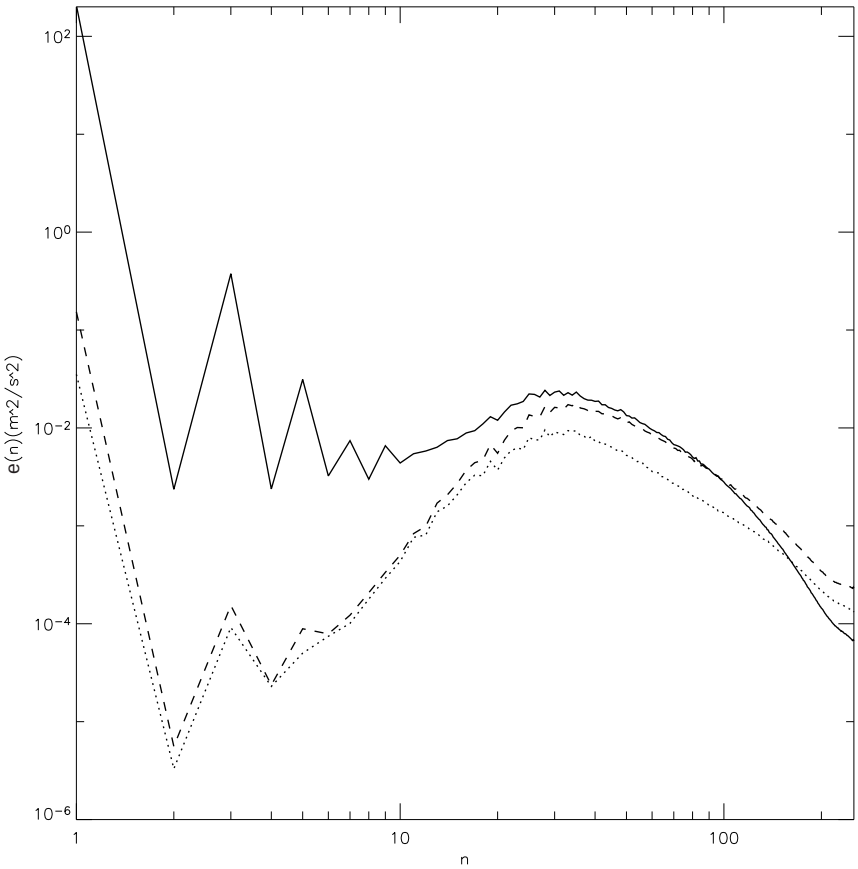

Figure 7.18: Energy spectra as functions of total wavenumber (n): potential energy (solid), Level 1 kinetic energy (dashed), and Level 2 kinetic energy (dotted) for the oceanic DNS (with rotation) at T252.

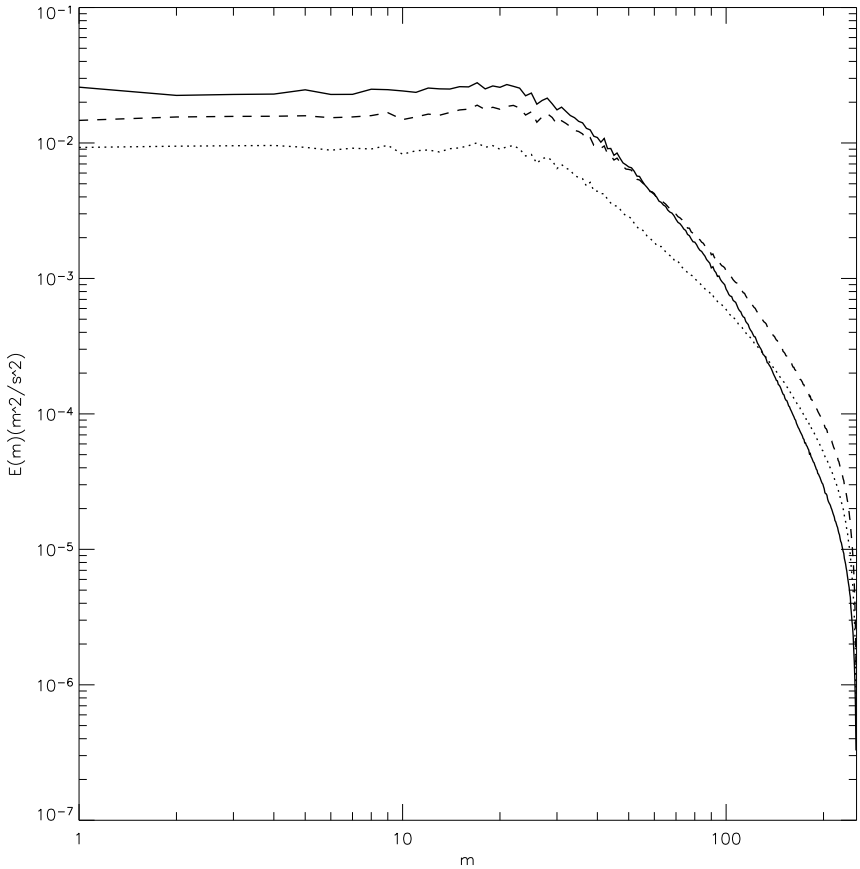

Figure 7.19: Energy spectra as functions of zonal wavenumber (m): potential energy (solid), Level 1 kinetic energy (dashed), and Level 2 kinetic energy (dotted) for the oceanic DNS (with rotation) at T252.

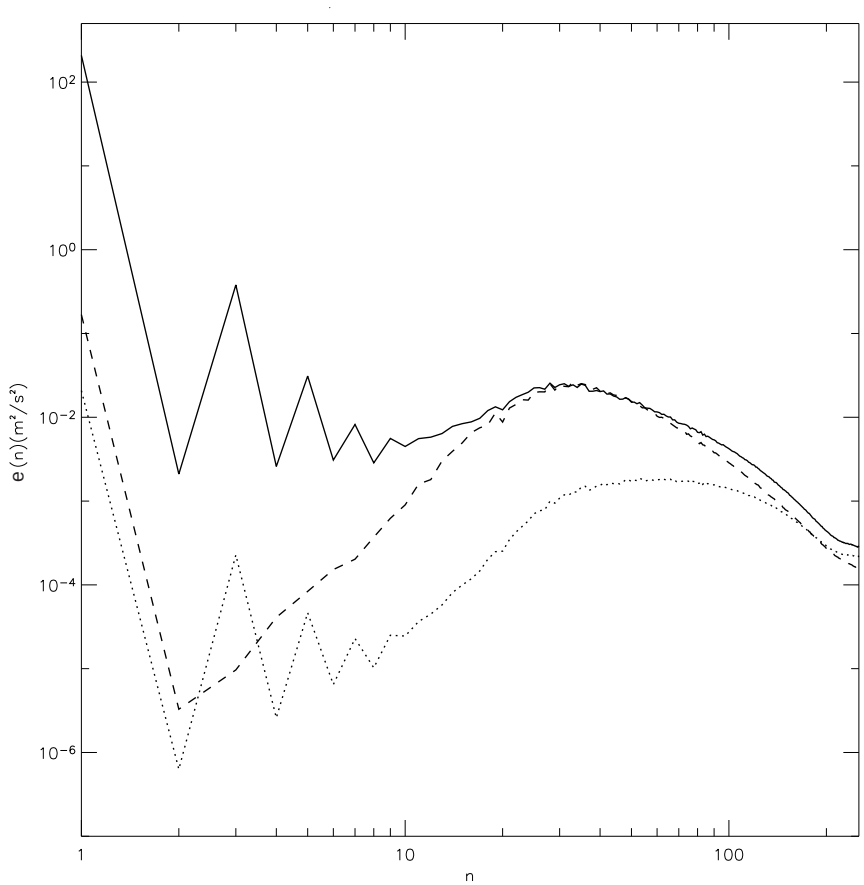

Figure 7.20: Energy spectra as functions of total wavenumber (n): total baroclinic energy (solid), barotropic kinetic energy (dashed), and baroclinic kinetic energy (dotted) for the oceanic DNS (with rotation) at T252.

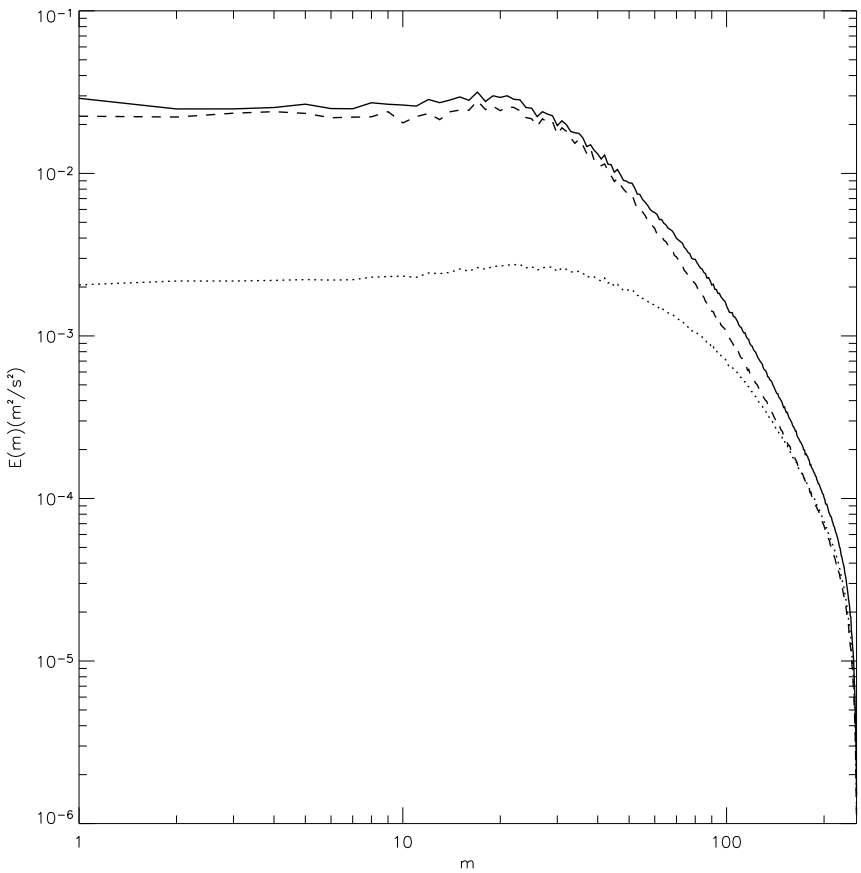

Figure 7.21: Energy spectra as functions of zonal wavenumber (m): total baroclinic energy (solid), barotropic kinetic energy (dashed), and baroclinic kinetic energy (dotted) for the oceanic DNS at T252.

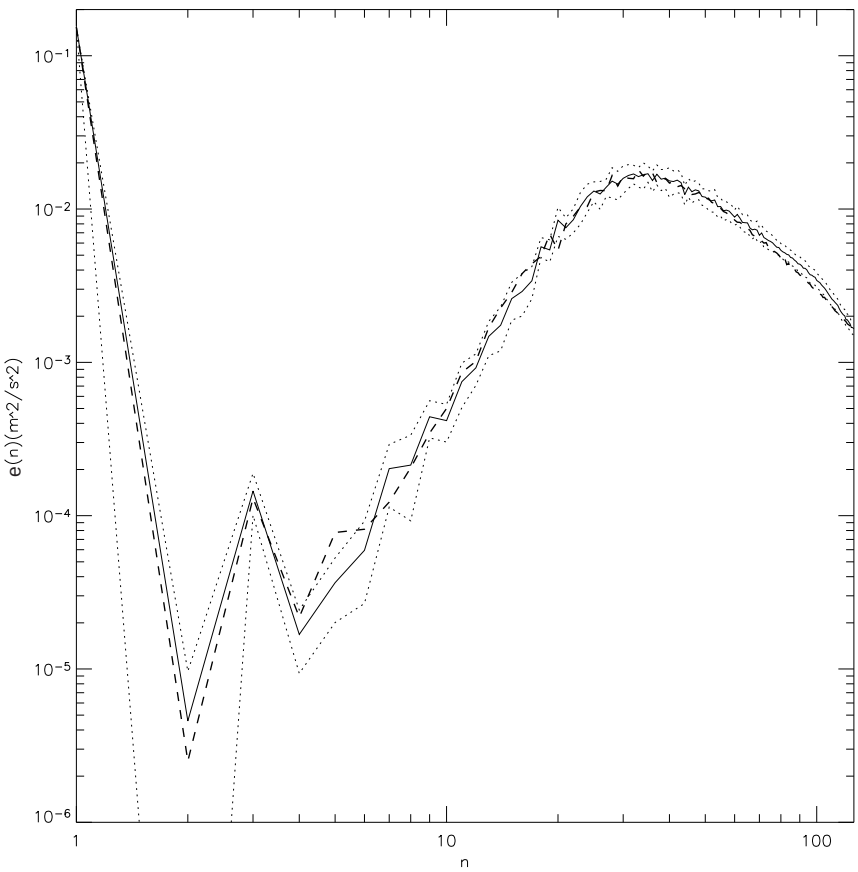

Figure 7.22: Energy spectra (Level 1) as functions of total wavenumber (n): kinetic energy for T126 LES with renormalized drain dissipation and backscatter (solid); LES kinetic energy plus and minus standard deviation (dotted); and T252 DNS kinetic energy (dashed).

energy in the equivalent layer problem. This is despite the fact that the mean shear at the equator is larger in this problem (0.5 ms^{-1}) compared to the equivalent layer problem (0.375 ms^{-1}). This is presumably because the beta effect tends to stabilize the flow. The distribution of barotropic and baroclinic energy is shown in Figs. 7.20 and 7.21. Again, the large scale kinetic energy is dominated by the barotropic energy. The peak of the baroclinic kinetic energy is much broader than that of the barotropic kinetic energy, as in the equivalent layer problem. The equipartition of barotropic and baroclinic energy is not as exact as for the atmospheric case, for the small scales, because the smallest scales resolved are not sufficiently far away from the deformation scale. The $n = 1$ potential energy, which is mostly $(m, n) = (0, 1)$ mean potential energy is again much larger than the kinetic energy at all scales, and hence we expect the mean subgrid forcing at any scale of truncation not to be dynamically important in this problem.

7.2.2 Subgrid-scale Parameterizations and LES T126

An artificial truncation at $N_* = 126$ is then performed, and the matrices $\mathbf{M_n}$, $\mathbf{M_d}$, and $\mathbf{F_b}$ calculated using a decorrelation time τ of 1 day. A cutoff wavenumber of $n_c = 48$ has been

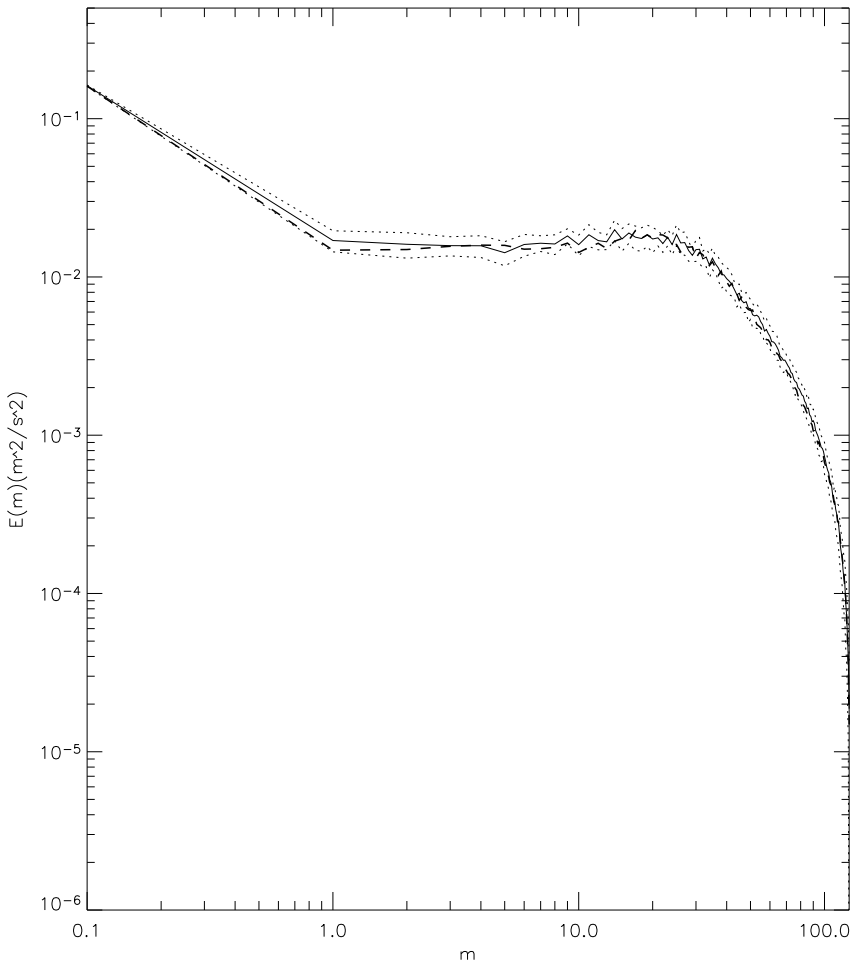

Figure 7.23: Energy spectra (Level 1) as functions of zonal wavenumber (m): kinetic energy for T126 LES with renormalized drain dissipation and backscatter(solid); LES kinetic energy plus and minus standard deviation (dotted); and T252 DNS kinetic energy (dashed).

imposed. The subgrid matrix parameters are qualitatively very similar to those at T63, albeit with more sampling error, and hence we shall postpone their detailed description until we discuss subgrid-scale parameterizations at T63. A large eddy simulation has been performed at T126, using the stochastic parameterization for $n > 48$, and the deterministic parameterization for $n < 48$. The results, after running the LES for 104 days, are shown in Figs. 7.22 and 7.23. Clearly, there is some sampling error. However, the agreement between the LES and higher resolution DNS is quite satisfactory; the LES spectrum is in broad agreement with the DNS. The next step is to investigate truncations at the lower resolution of T63. We now have an LES at T126 which is able to broadly reproduce the features of the DNS at T252. The advantage, as discussed in the previous chapter, is that at T126 we can afford to run the simulation for much longer, and hence we can reduce sampling errors, which in general will be worse at T63 than at T126 due to larger eddy turnover times. We run the LES at T126 for 2700 days, using a timestep of 1200 s.

7.2.3 Subgrid-scale Parameterizations at T63

An artifical truncation at $N_* = 63$ is performed in the long (2700 day) LES at T126. The matrices $\mathbf{M_n}$, $\mathbf{M_d}$, and $\mathbf{F_b}$ are then calculated. Figures 7.24 and 7.25 show the real and imaginary parts, respectively, of the subgrid flux matrix $\mathcal{F}$. The diagonal flux is slightly greater for Level 1 than for Level 2. Both are dissipative at all scales. The real parts of the off-diagonal fluxes are roughly the size of the $\mathcal{F}^r_{11}$ element, but are of the opposite sign. A comparison with the equivalent layer case reveals that the fluxes at large wavenumbers are reduced in this problem; that is, the fluxes are more scale selective. This is presumably due to the beta effect. The corresponding fluxes in BTBC space are shown in Figs. 7.26 and 7.27. The baroclinic enstrophy flux is slightly greater than the barotropic enstrophy flux near the truncation scale. The barotropic flux has a strong energy injection for wavenumbers $n < 50$ while the baroclinic flux is dissipative at all wavenumbers. The off-diagonal fluxes, with real and imaginary parts, are also significant in size; they are related to the degree of correlation between barotropic and baroclinic modes, but do not contribute to the energy and enstrophy directly.

Figure 7.28 shows the real part of the net dissipation matrix, $-\mathbf{M^r_n}$, at T63. The $-M^r_{11}$ diagonal element is completely negative; it is however, an order of magnitude smaller than the $-M^r_{22}$ diagonal element; the $-M^r_{22}$ element is positive at all wavenumbers. The $-M^r_{12}$ element is negative and is even slightly greater than the $-M^r_{22}$ element. The other off-diagonal element, $-M^r_{21}$ is mostly negative, except near the truncation scale. The imaginary part of the net 'dissipation' matrix is shown in 7.29. This matrix is structurally similar to the corresponding equivalent layer matrix. All the elements seem to have roughly the same magnitude near the truncation scale. The M^i_{11} and M^i_{21} elements are larger than the corresponding $-\mathbf{M^r_n}$ elements. Hence, unlike in the equivalent layer case, we cannot claim that the $\mathbf{M^i_n}$ matrix is dynamically insignificant.

The matrices $\mathbf{M_d}$ and $\mathbf{F_b}$ are calculated using a decorrelation time τ of 4 days. The time covariance $\langle \left(\frac{\partial \hat{q}^i_{mn}(t)}{\partial t}\right)_S \left(\frac{\partial \hat{q}^j_{mn}(t_0)}{\partial t}\right)^*_S \rangle$ as a function of time is shown in Fig. 7.30. This shows that 4 days is a more than sufficient integration time as the time covariance drops to zero after about 2 days. In this case it is found that the eigenvalues of $\mathbf{F_b}$ are positive for all wavenumbers. The real part of the drain dissipation matrix, $-\mathbf{M^r_d}$, is shown in Fig. 7.31. The $-M^r_{11}$ diagonal element is quite different to the corresponding $-\mathbf{M^r_n}$ element. It rises to a positive value near the truncation scale; furthermore, the magnitude near the truncation scale is ten times that for the $-\mathbf{M^r_n}$ element. The $-M^r_{22}$ diagonal element is

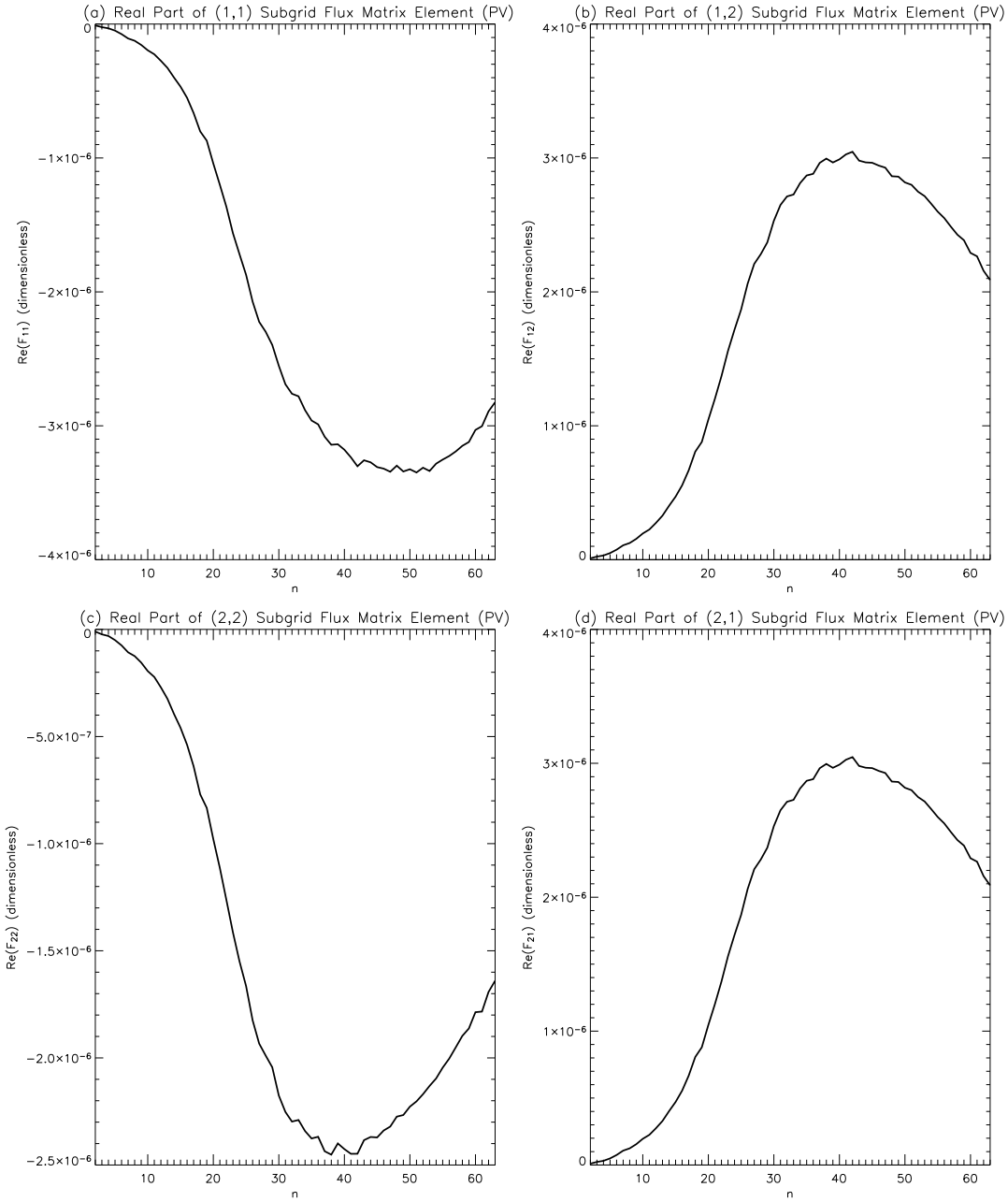

Figure 7.24: Elements of the real part of the isotropic subgrid flux matrix in the PV formulation: (a) $\mathcal{F}^r_{11}$; (b) $\mathcal{F}^r_{12}$; (c) $\mathcal{F}^r_{22}$; and (d) $\mathcal{F}^r_{21}$ (T63) .

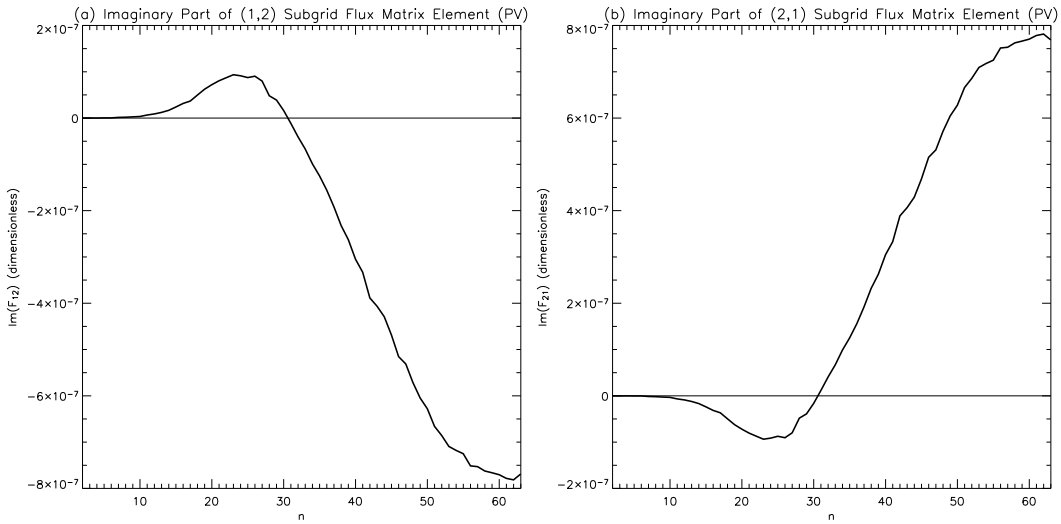

Figure 7.25: Off-diagonal elements of the imaginary part of the isotropic subgrid flux matrix in the PV formulation: (a) $\mathcal{F}^i_{12}$; (b) $\mathcal{F}^i_{21}$ (T63) .

almost three times as great as the corresponding $-\mathbf{M^r_n}$ element; otherwise, it is qualitatively similar. The off-diagonal elements are qualitatively similar to the corresponding $-\mathbf{M^r_n}$ elements.

The imaginary part of the drain dissipation matrix, $\mathbf{M^i_d}$ is shown in Fig. 7.32. The M^i_{11} diagonal element has significantly reduced near the truncation scale so that the contribution in the intermediate wavenumbers looks more significant than that near the truncation scale. The M^i_{22} diagonal element is slightly enhanced over the corresponding $\mathbf{M^i_n}$ element. The off-diagonal elements are similar, both qualitatively and quantitatively, to the corresponding $\mathbf{M^i_n}$ elements. All elements of $-\mathbf{M^r_d}$, with the exception of $-M^r_{21}$, are now greater than the elements of $\mathbf{M^i_d}$; hence the real part of the drain dissipation matrix is now more significant than the imaginary part. The real and imaginary parts of the backscatter matrix, $\mathbf{F^r_b}$ and $\mathbf{F^i_b}$, are shown in Figs. 7.33 and 7.34, respectively. The real part, $\mathbf{F^r_b}$, has positive diagonal elements and negative off-diagonal elements of smaller magnitude. The F_{22} element is about the same size as the off-diagonal elements. The imaginary part, $\mathbf{F^i_b}$, has elements in the off-diagonal with smaller magnitude than the corresponding elements of $\mathbf{F^r_b}$; they are also opposite in sign. The eigenvalues of the backscatter matrix are shown in Fig. 7.35. One eigenvalue is greater than the other by an order of magnitude. The corresponding eigenvectors are not shown, but they are relatively independent of wavenumber; the matrix, $\mathbf{P}$, of eigenvectors is approximately

$$\mathbf{P} = \begin{pmatrix} 0.8 & -0.6 \\ 0.6 & 0.8 \end{pmatrix} \tag{7.3}$$

near the truncation scale.

7.2.4 LES at T63

The LES at T63 is performed using bare parameters, the deterministic parameterization in the form of the net dissipation matrix, and the stochastic parameterization. The results

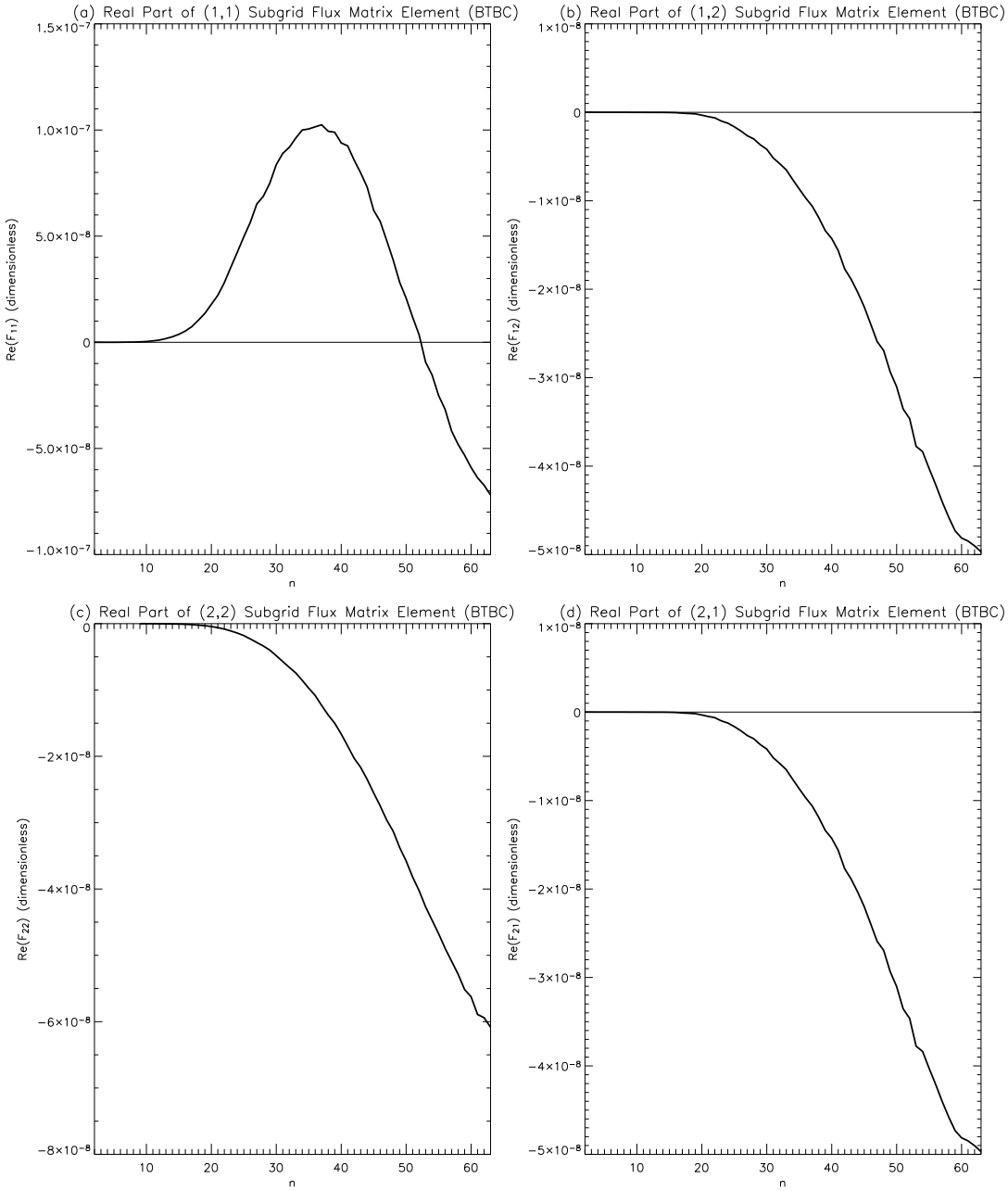

Figure 7.26: Elements of the real part of the isotropic subgrid flux matrix in the BTBC formulation: (a) $\mathcal{F}^r_{11}$; (b) $\mathcal{F}^r_{12}$; (c) $\mathcal{F}^r_{22}$; and (d) $\mathcal{F}^r_{21}$ (T63).

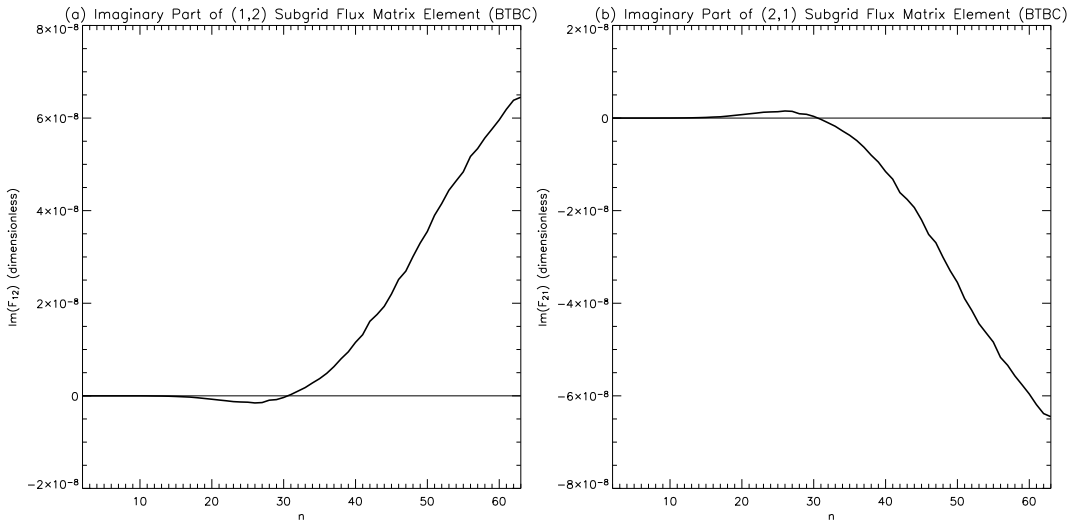

Figure 7.27: Off-diagonal elements of the imaginary part of the isotropic subgrid flux matrix in the BTBC formulation: (a) $\mathcal{F}^i_{12}$; (b) $\mathcal{F}^i_{21}$ (T63).

of the LES with bare parameters are shown in Figs. 7.36 and 7.37. Clearly, with bare parameters, the T63 simulation bears no resemblance to the T126 LES. The tail rises dramatically for the total wavenumber kinetic energy spectrum, and the zonal wavenumber spectrum is unrealistically flat at the small scales. We have also attempted to perform the LES with the net dissipation matrix alone—the deterministic parameterization. As in the equivalent layer case, the deterministic parameterization causes serious numerical instabilities to appear, with the result eventually blowing up. Figs. 7.38 and 7.39 show the results of the LES upon using the stochastic parameterization. There is in general excellent agreement between the LES at T63 and at T126, except at the largest scales where the subgrid flux is very small, and thus dominated by errors in estimating $\mathbf{M}$ and $\mathbf{F}$. The energy at $(m, n) = (0, 1)$ is dominated by the mean energy of the imposed relaxation, and is thus relatively independent of the subgrid-scale parameterizations.

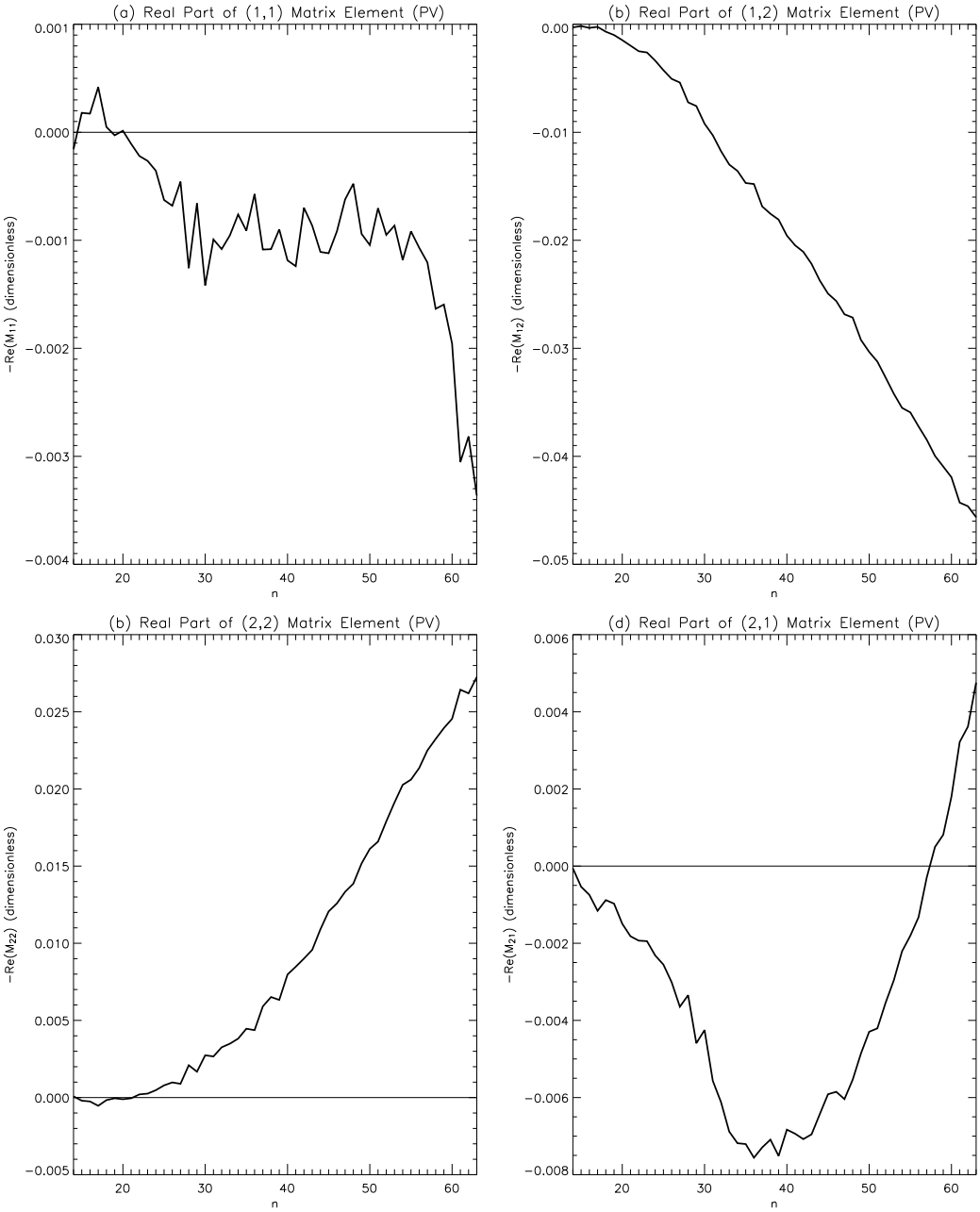

Figure 7.28: Real part of the isotropic net dissipation matrix in the PV formulation: (a) $-M^r_{11}$; (b) $-M^r_{12}$; (c) $-M^r_{22}$; (d) $-M^r_{21}$ (T63).

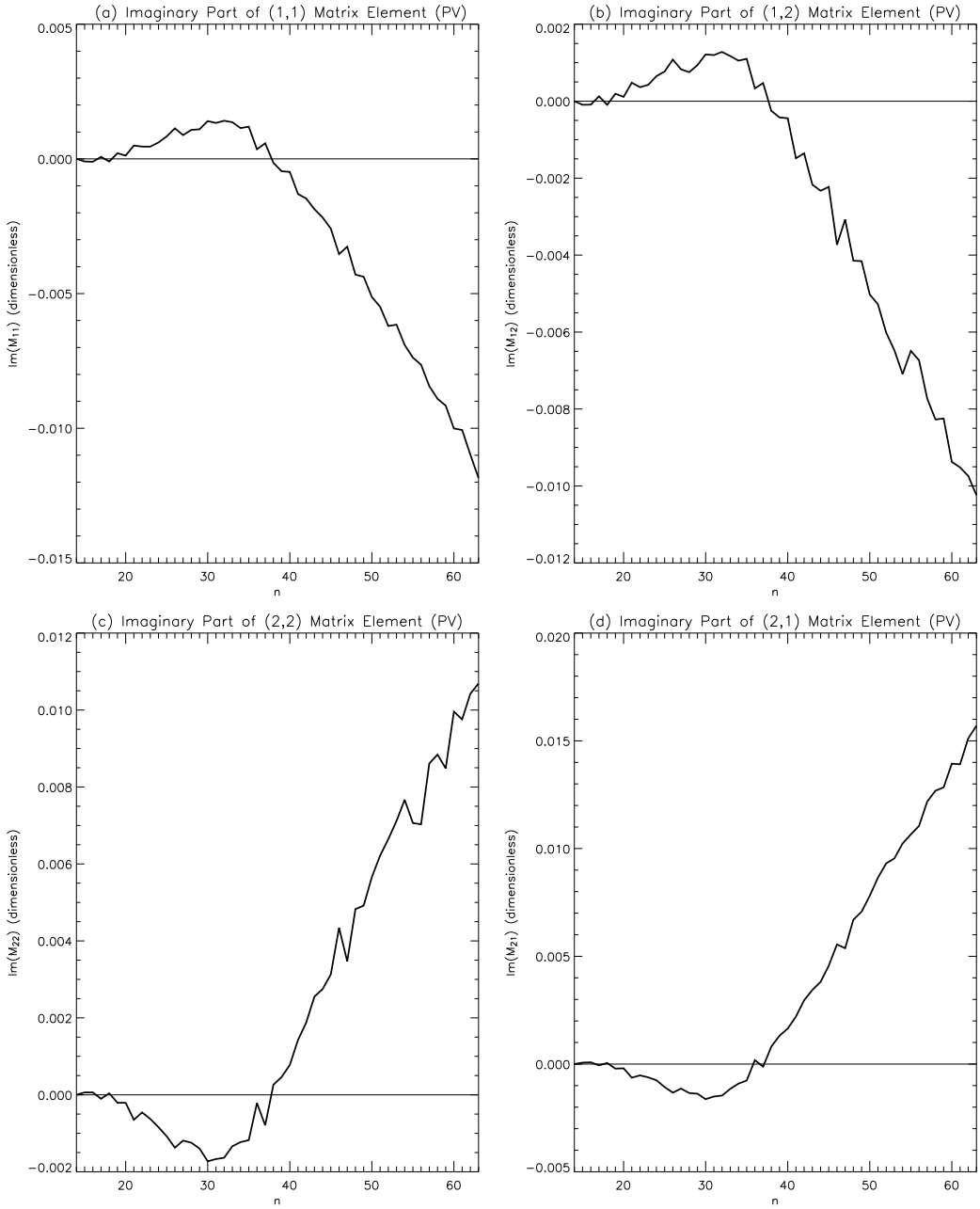

Figure 7.29: Imaginary part of the isotropic net dissipation matrix in the PV formulation: (a) M^i_{11}; (b) M^i_{12}; (c) M^i_{22}; (d) M^i_{21} (T63).

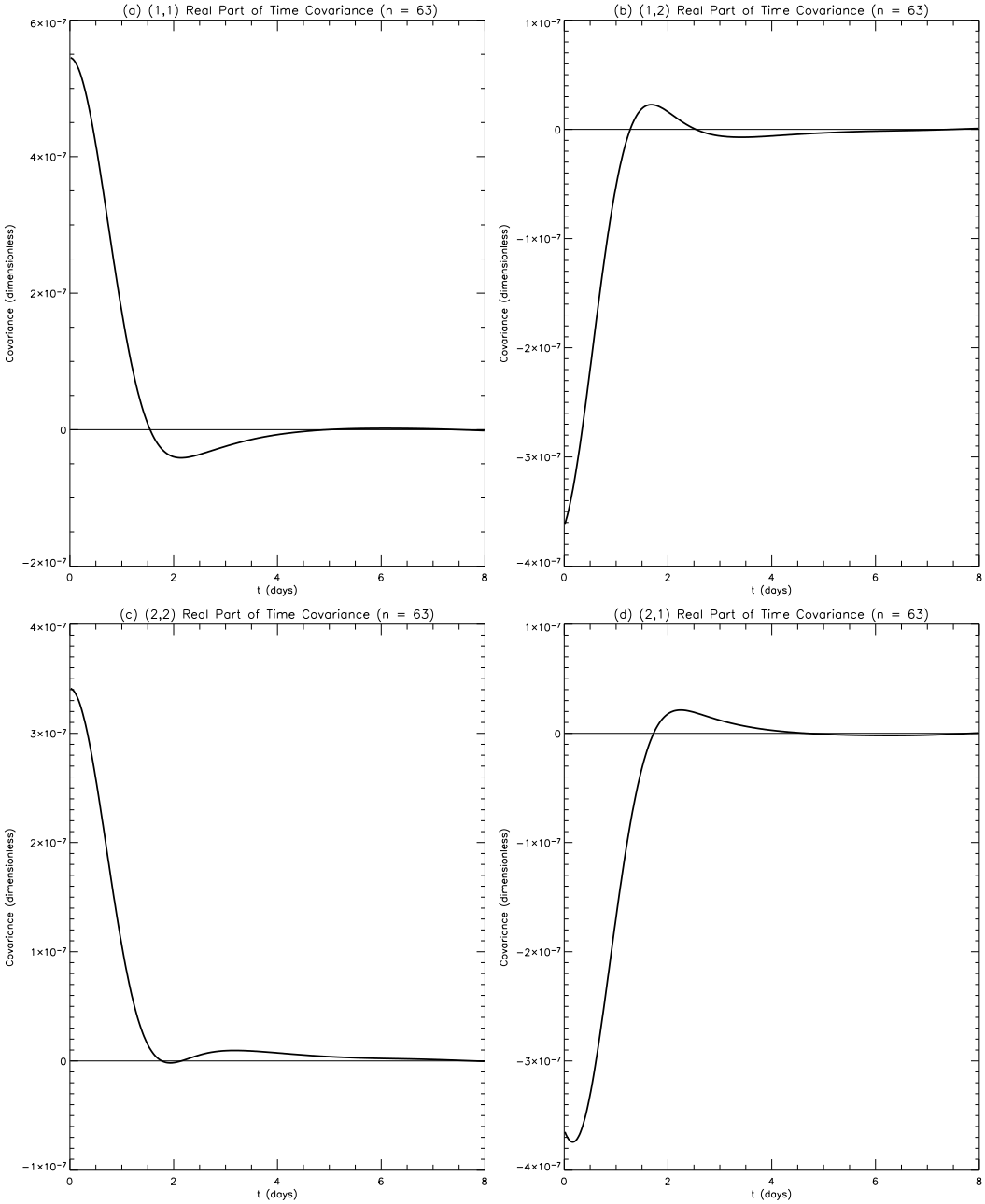

Figure 7.30: Time covariances of the subgrid tendency matrix in the PV formulation: (a) Level 1; (b) Level 2; (c)Level 1/Level 2; (d)Level 2/Level 1 ($n = 63$).

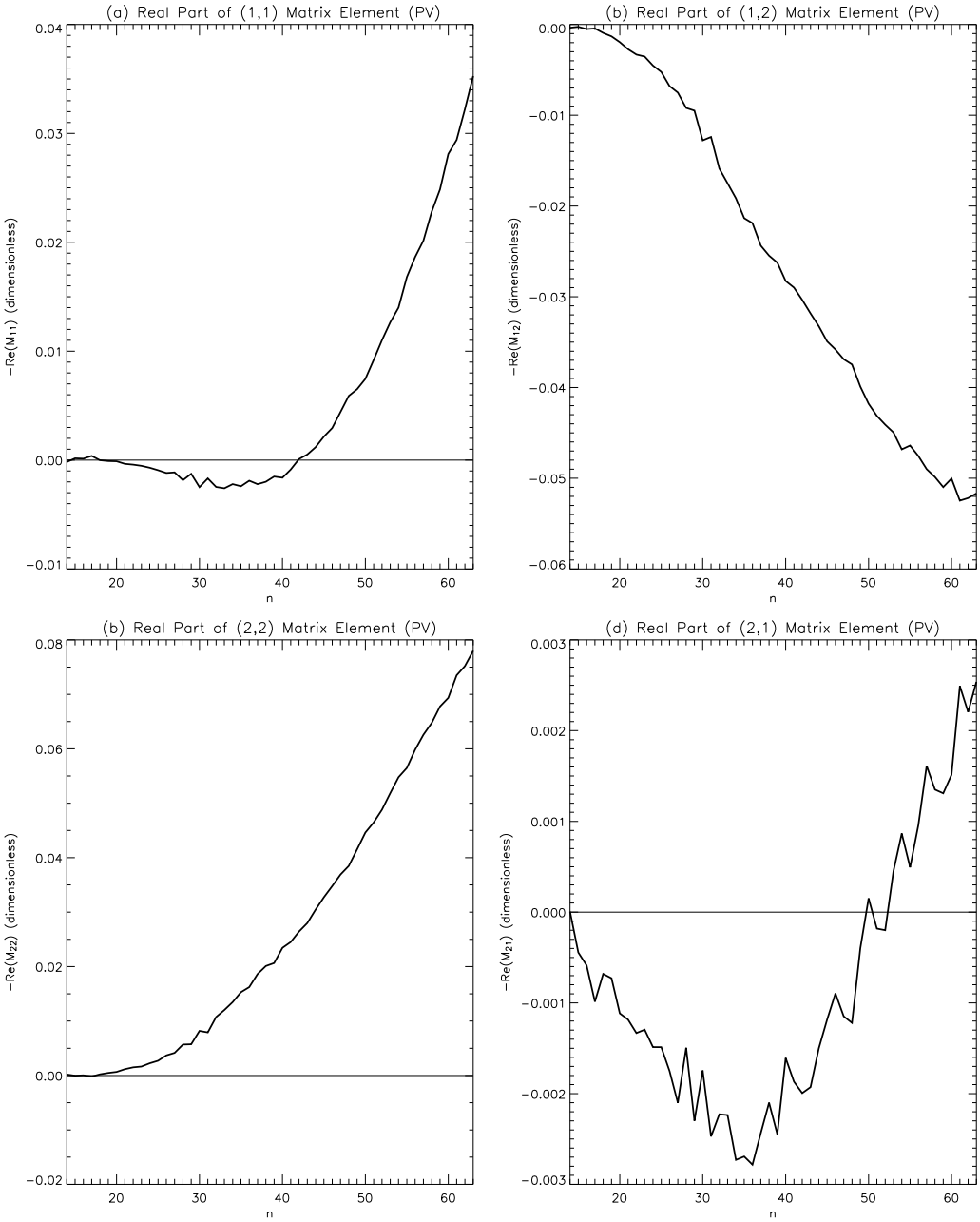

Figure 7.31: Real part of the isotropic drain dissipation matrix in the PV formulation: (a) $-M^r_{11}$; (b) $-M^r_{12}$; (c) $-M^r_{22}$; (d) $-M^r_{21}$ (T63).

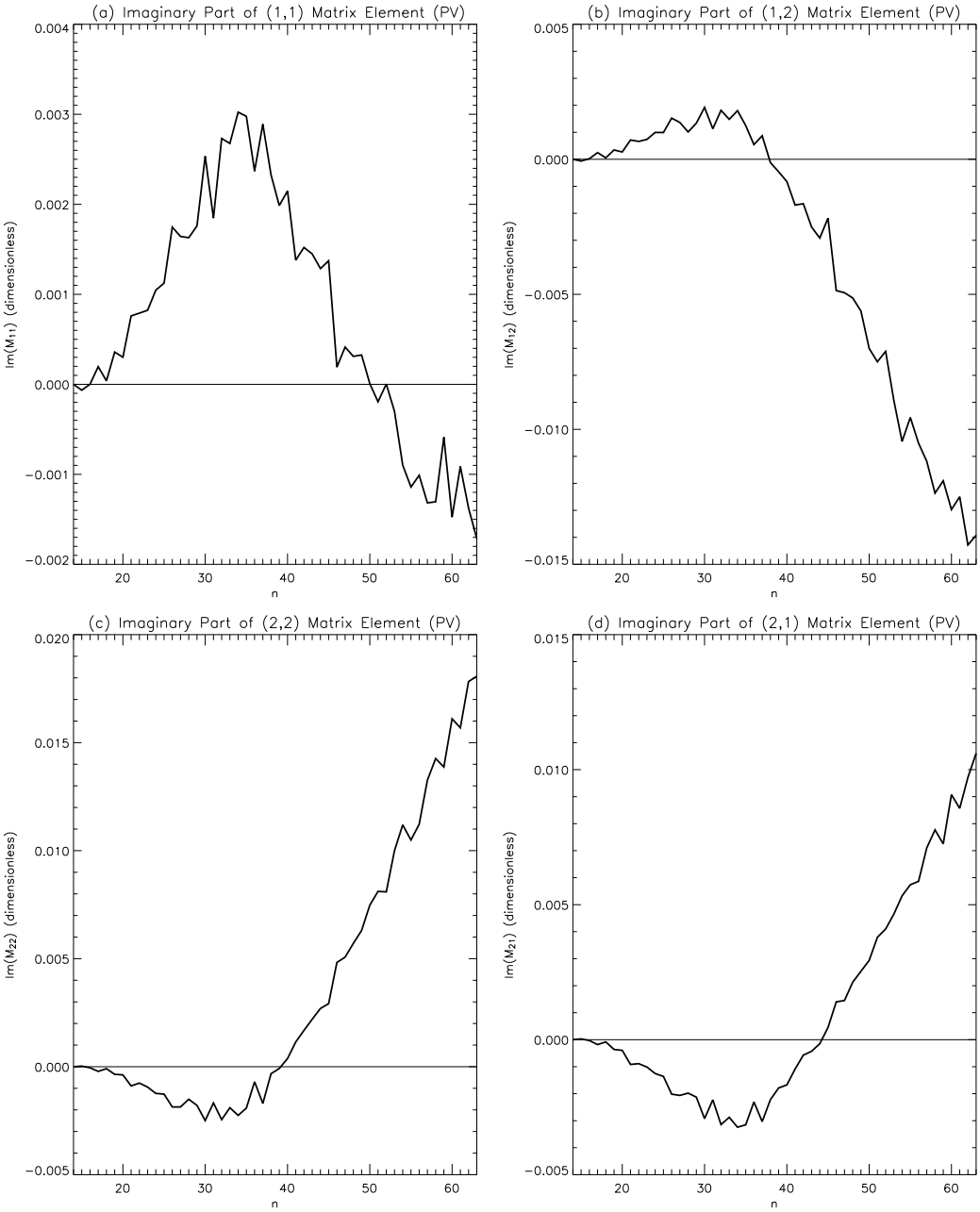

Figure 7.32: Imaginary part of the isotropic drain dissipation matrix in the PV formulation: (a) M^i_{11}; (b) M^i_{12}; (c) M^i_{22}; (b) M^i_{21} .

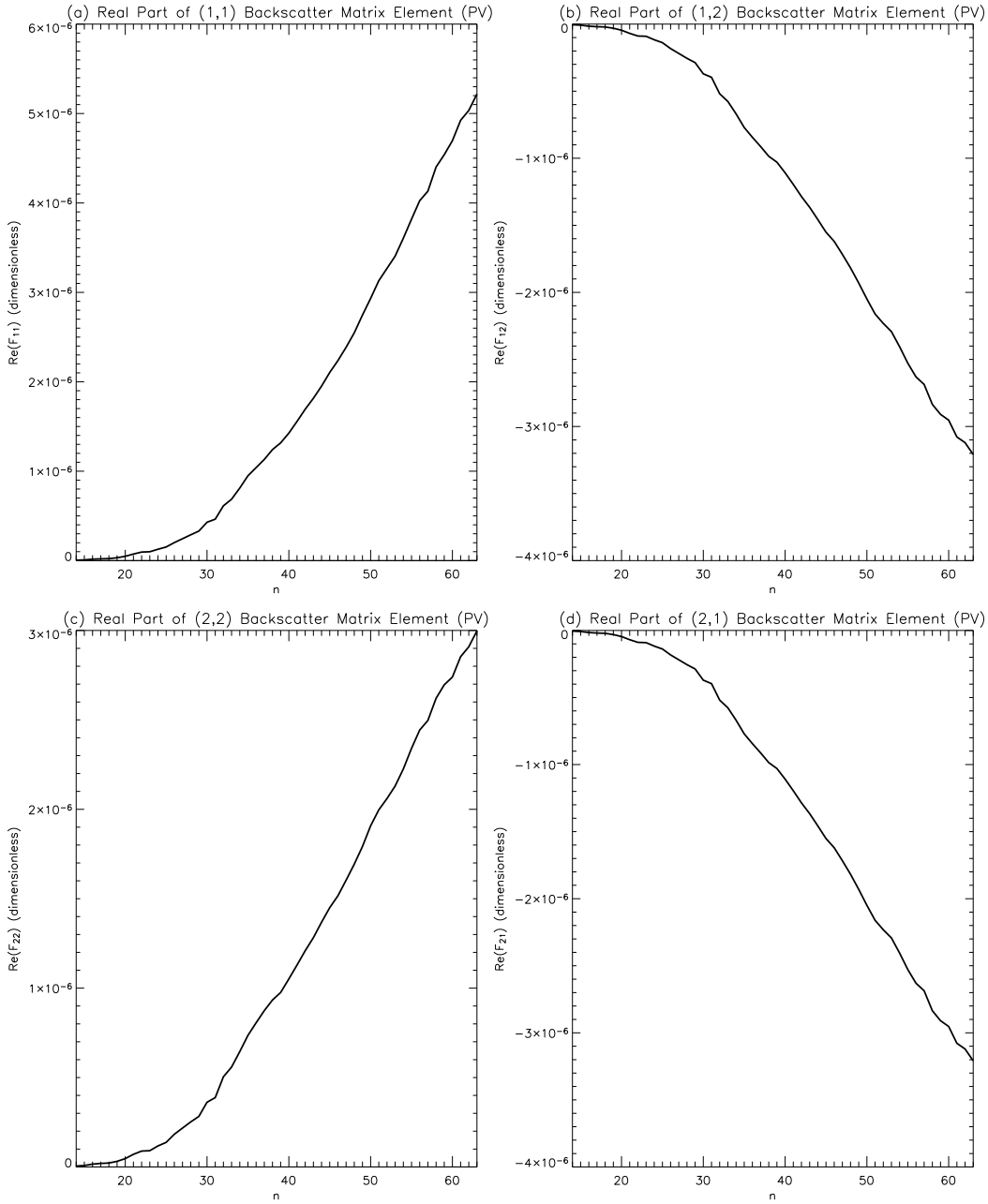

Figure 7.33: Real part of the isotropic stochastic backscatter matrix in the PV formulation: (a) F^r_{11}; (b) F^r_{12}; (c) F^r_{22}; (d) F^r_{21} (T63).

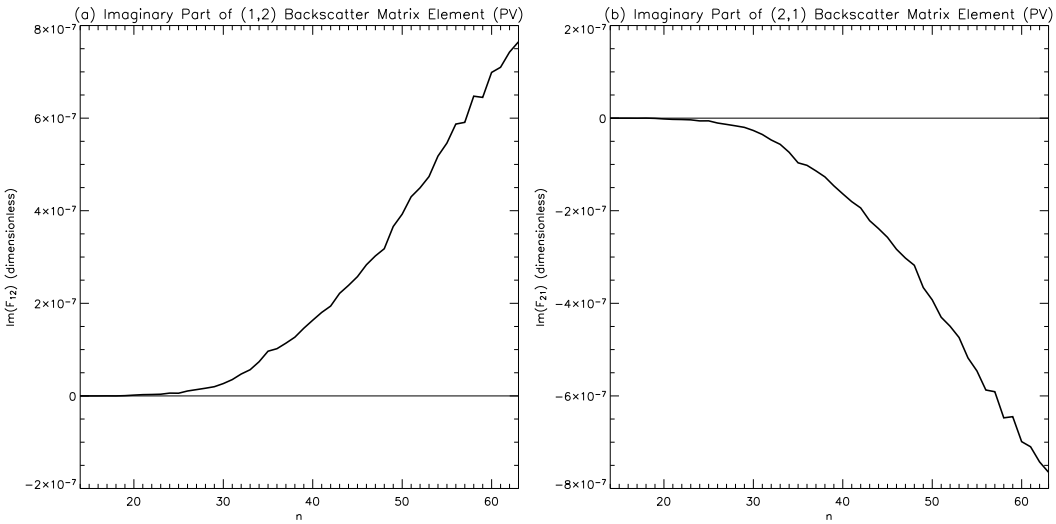

Figure 7.34: Imaginary part of the isotropic stochastic backscatter matrix in the PV formulation: (a) F^i_{12}; (b) F^i_{21}.

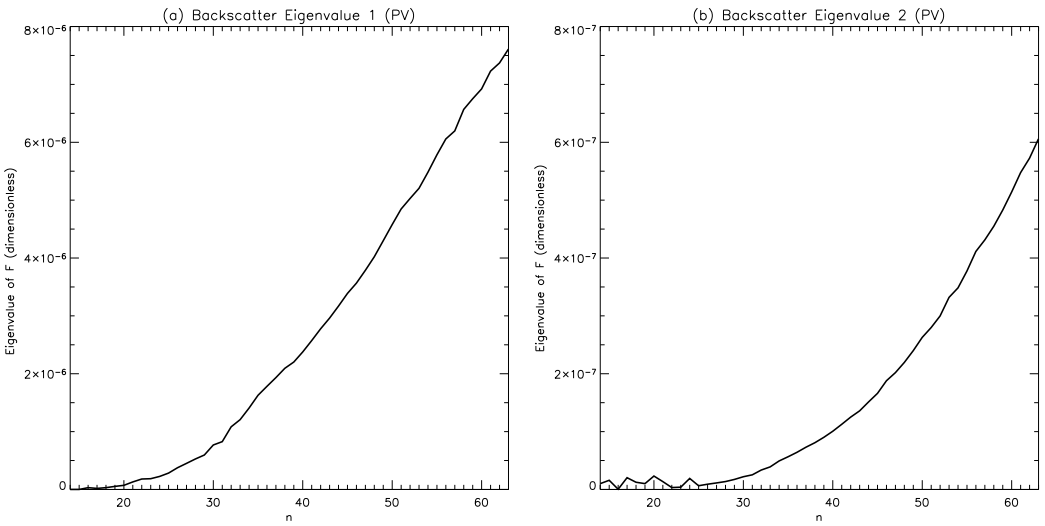

Figure 7.35: Eigenvalues of the isotropic stochastic backscatter matrix in the PV formulation (T63).

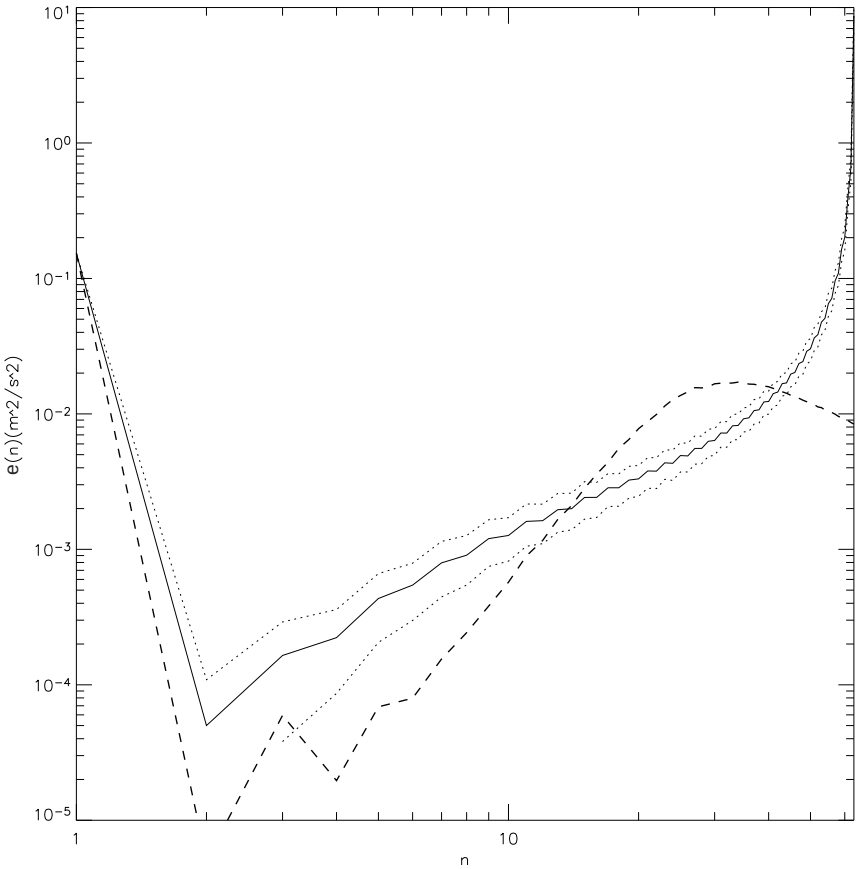

Figure 7.36: Energy spectra (Level 1) as functions of total wavenumber (n): kinetic energy for T63 LES with bare dissipation (solid); LES kinetic energy plus and minus standard deviation (dotted); and T126 LES kinetic energy (dashed).

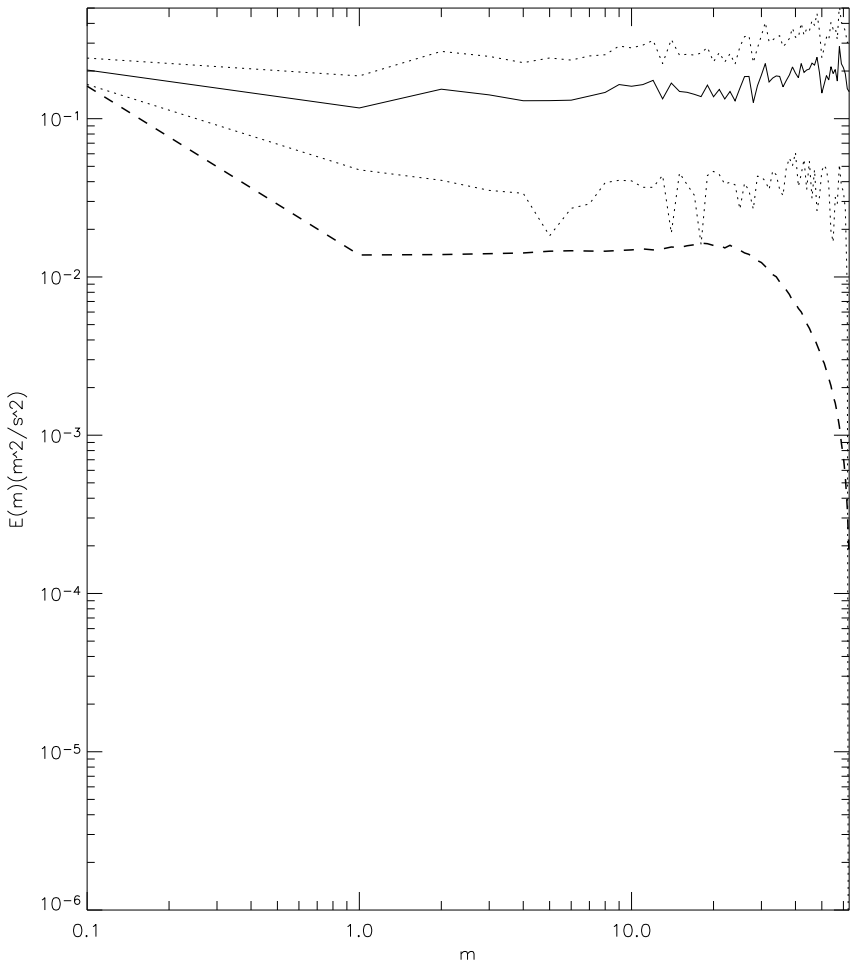

Figure 7.37: Energy spectra (Level 1) as functions of zonal wavenumber (m): kinetic energy for T63 LES with bare dissipation (solid); LES kinetic energy plus and minus standard deviation (dotted); and T126 LES kinetic energy (dashed).

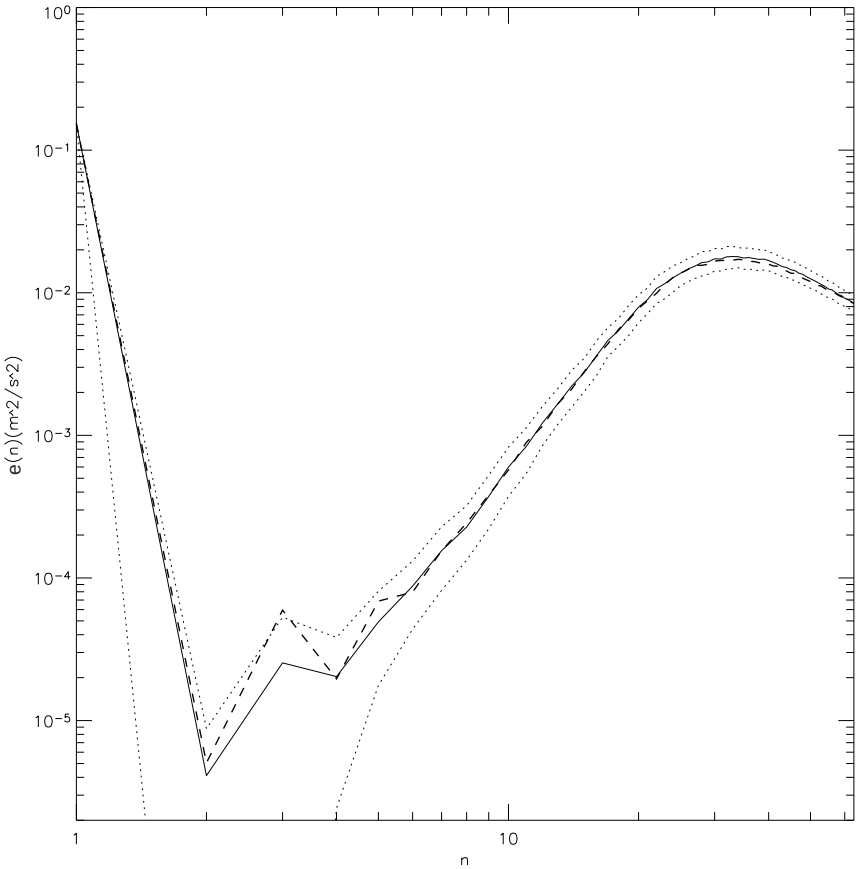

Figure 7.38: Energy spectra (Level 1) as functions of total wavenumber (n): kinetic energy for T63 LES with renormalized drain dissipation and backscatter (solid); LES kinetic energy plus and minus standard deviation (dotted); and T126 LES kinetic energy (dashed).

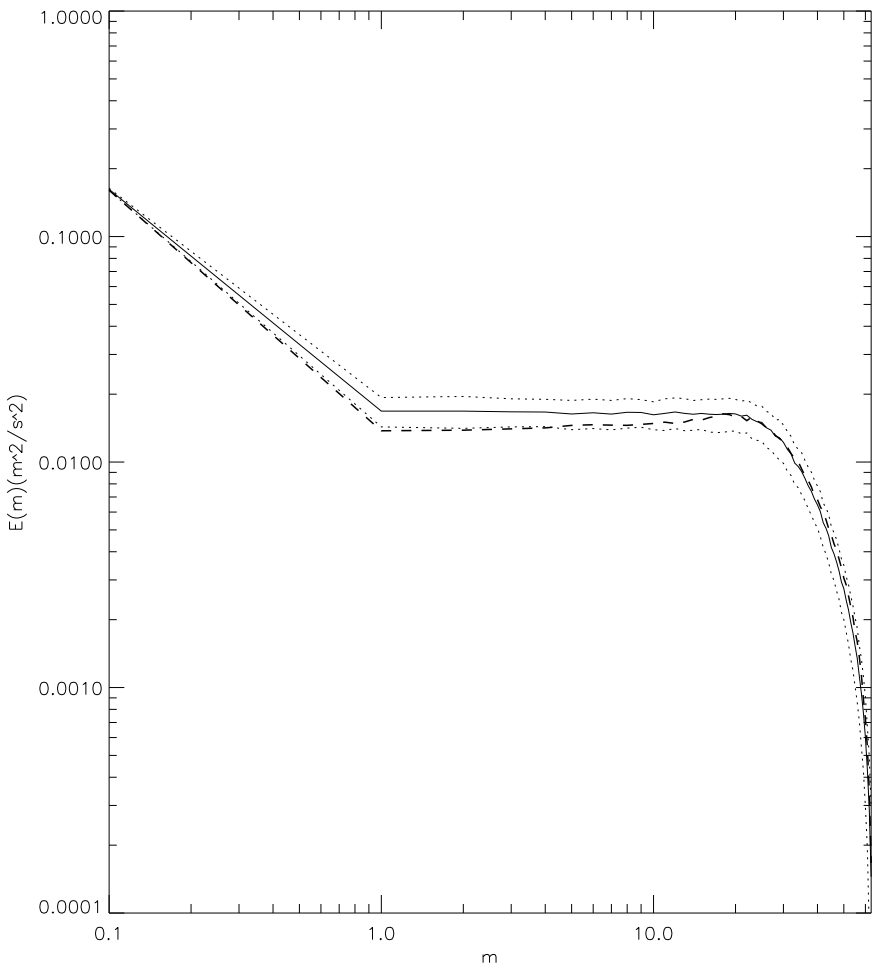

Figure 7.39: Energy spectra (Level 1) as functions of zonal wavenumber (m): kinetic energy for T63 LES with renormalized drain dissipation and backscatter (solid); LES kinetic energy plus and minus standard deviation (dotted); and T126 LES kinetic energy (dashed).

7.3 Discussion

The beta effect has been found to stabilize the large scale eddies as predicted by the phenomenology of QG turbulence. In general, the eddy kinetic energy produced for a given mean shear is reduced when compared to the equivalent layer case, which had no beta effect. This means that the eddies are baroclinically more stable—even in a linear sense—with the beta effect operating. The non-linear interactions are also suppressed, particularly the long range interactions between the large and small scales. This is apparent from the shapes of the subgrid fluxes; when compared to the equivalent layer case, the large scale contribution is significantly diminished. This is more noticeable in the oceanic simulations, which have a large separation between the large and injection scales.

The flux in the top level is greater than the flux in the bottom level in this problem. It is found that the flux of enstrophy plays an important role in determining the relative magnitudes of the subgrid matrix parameters. In the atmosphere, where the matrices are practically diagonal because the truncation scale is much greater than the deformation scale, the stochastic backscatter in the top level is found to be as much as an order of magnitude greater than that in the bottom level as a result of the greater flux there. The drain dissipation parameters, on the other hand, turn out to be relatively close in magnitude. In the atmospheric LES it is again found that, broadly, the deterministic and stochastic parameterizations perform comparably well. However, a closer inspection of the LES near the truncation scale reveals that the stochastic parameterization performs marginally better. Specifically, the deterministic parameterization tends to slightly lift the tail of the spectrum right at the truncation scale. This is particularly evident for the top level, which has a strong flux. The stochastic parameterization does not display this phenomenon when implemented in the LES.

For oceanic simulations, where the full matrix structure of the parameters needs to be considered, the structure of these matrices is as follows. The elements of the drain dissipation matrix have in general larger real than imaginary components, with the exception of the M_{21} element. Both the diagonal elements are positive near the truncation scale, with the top level contribution being slightly negative at the large scales. This is because the barotropic mode is predominantly the top level in this problem; that is $\psi = \frac{1}{2}(\psi_1 + \psi_2) \approx \frac{1}{2}\psi_1$, if $\psi_1 \gg \psi_2$. In terms of magnitude, the top level diagonal contribution tends to be less than that for the bottom level. The off-diagonal elements are dominated by the top level contribution (M_{12} element), which is negative at all wavenumbers, and comparable in size to the diagonal elements. The bottom level off-diagonal contribution (M_{21} element) is in general the smallest element, and its real part is negative except near the truncation scale. In fact, for this element, it is the imaginary part that is dominant, and this has a similar structure to the real part. The backscatter matrix is dominated by the F_{11} element; the other elements are somewhat smaller and have similar sizes. Structurally, the diagonal elements are positive while the real parts of the off-diagonal elements are negative; the imaginary parts of the off-diagonal elements are generally smaller in size. The deterministic formulation again displayed the difficulty identified in the previous chapter; namely, that the diagonal barotopic dissipation matrix element in the BTBC formulation ($-M^r_{11}$) is significantly negative. In this case, this matrix element was found to be negative at all scales at T63. In comparison, the corresponding matrix element in the stochastic formulation (the drain dissipation matrix element) was found to be only slightly negative at the large scales, but significantly, was positive near the truncation scale. The two matrix elements are shown side-by-side for comparison in Fig. 7.40. In the stochastic

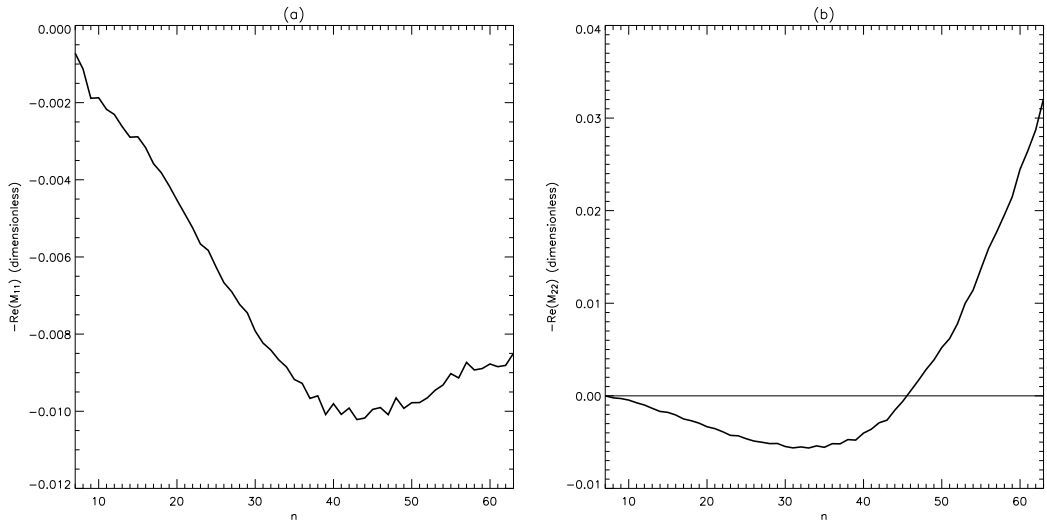

Figure 7.40: A comparison of diagonal barotropic dissipation coefficients ($-M^r_{11}$) for: (a) net dissipation ($-\mathbf{M^r_n}$); (b) drain dissipation ($-\mathbf{M^r_d}$) matrices in the BTBC formulation (T63).

formulation, the injection of barotropic energy from the subgrid scales, due to the inverse cascade, is captured by the stochastic forcing, rather than by the negative dissipation of the deterministic formulation. This is a more numerically stable configuration.

In running the oceanic LES, it as found that, as for the equivalent layer problem, it is impossible to use the deterministic parameterization because it is too numerically unstable. The stochastic parameterization generally gives good agreement with the higher resolution simulation. Furthermore, it is sufficient to use the isotropized (m averaged) matrix parameters in this problem despite the fact that the beta effect induces large scale anisotropy in the form of westward travelling Rossby waves. In the next chapter, instead of the $(m, n) = (0, 1)$ (solid body rotation) relaxation imposed in this and the previous chapter, we shall examine more complicated sources of baroclinic mean energy, namely, meridionally confined jets and currents.

Chapter 8

Flows with Jets and Differential Rotation

In this chapter we shall continue to analyze two-layer flows in the presence of differential rotation. However, the mean field imposed here is of a more complicated nature than the $(m, n) = (0, 1)$ relaxation of the previous two chapters. We impose mean fields corresponding to the zonal circulation found in the atmosphere, with strong mid-latitude jet streams. For the ocean, we impose a strong current at 60° South, which roughly corresponds to the Atlantic Circumpolar Current (ACC). Spectrally, these mean fields corresponding to forcing on the modes $(m, n) = (0, n)$, where n is typically confined to small wavenumbers (we have chosen $n < 15$). Importantly, n is no longer just one as in the previous two chapters. This means that there are several spectral sources of mean baroclinic energy which can be used to generate transient energy. Hence, the assumption that the change in potential energy is small compared to the total potential energy cannot be used in general to justify the exclusion of the mean subgrid forcing as was done in the previous two chapters. This makes the problem harder as we have to parameterize both the mean and transient fluxes. The motivation, of course, is that this situation is closer to what happens in real geostrophic flows. The governing equations for the DNS are again the spherical two layer QGPV equations, including differential rotation:

$$\frac{\partial q_i}{\partial t} = -J(\psi_i, q_i) - 2\frac{\partial \psi_i}{\partial \lambda} - D_i^0 \zeta_i + \kappa(q_i^{rel} - q_i) \ , \tag{8.1}$$

where i=1,2. The zonal wind is relaxed towards u_i^{rel}; q_i^{rel} in Eq. 8.1 is the potential vorticity corresponding to the imposed wind $\mathbf{u_i^{rel}} = (u_i^{rel}, 0)$. The other terms in Eq. 8.1 are the same as defined in previous chapters.

8.1 Atmospheric Flows

For the atmosphere the following parameters have been chosen: the drag, α_i, has been set to a damping time of 20 days for Layer 1 (top), and 5 days for Layer 2 (bottom); the hyperviscosity $\nu_i^0 = 3.9 \times 10^{32}$ m^{8}s^{-1} in both layers; the order of the Laplacian operator $p = 4$; the relaxation time for the mean flow, κ, is 11.6 days; the layer coupling constant, $F_a = 2.5 \times 10^{-12}$ m^{-2}, giving $\lambda_i \sim 500$ km. The latitudinal profile of the jets u_i^{rel} is shown in Fig. 8.1. The equations have been stepped forward in time for 1000 days at steady state—after an initial spin-up period, with a timestep of 450 s; the resolution is T126 with 384×192 grid points. The deformation scale corresponds to approximately wavenumber 12 as in the previous two chapters.

Figures 8.2 and 8.3 show the contours of the mean zonal wind $(\overline{u_i}(\lambda, \phi))$ for the top

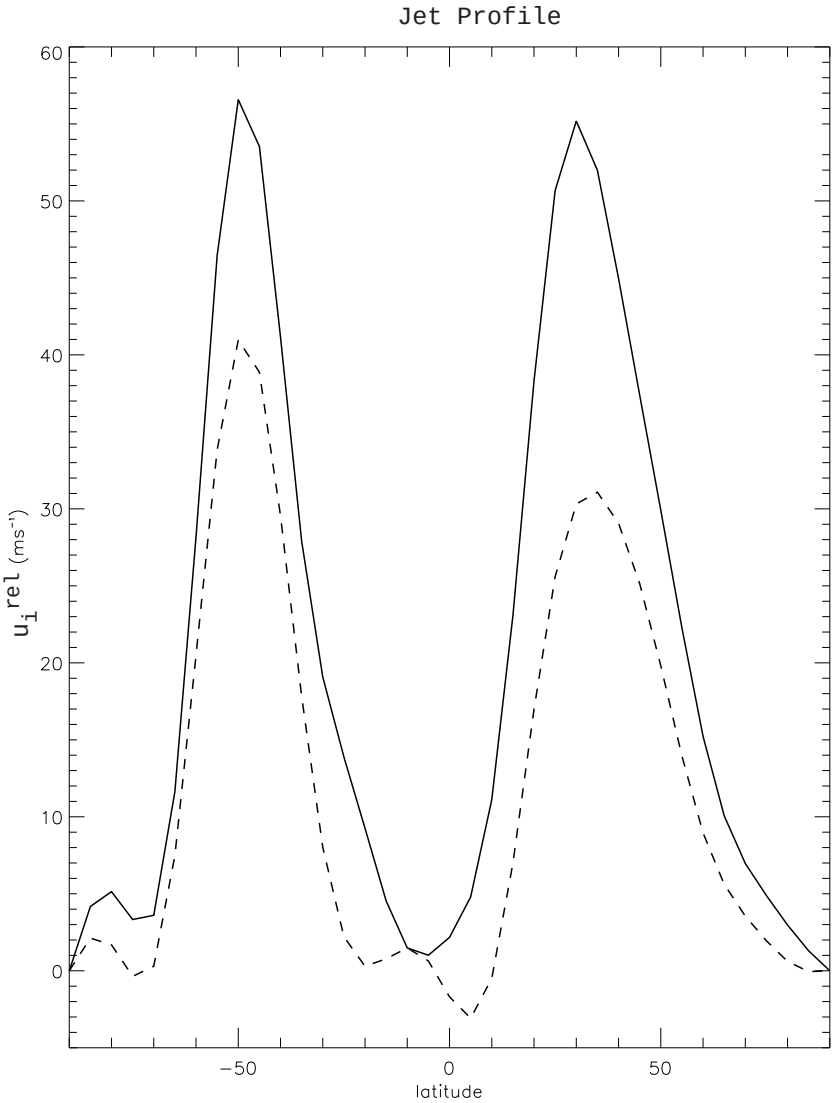

Figure 8.1: The imposed zonal wind u_i^{rel} for the atmosphere: Level 1 (solid) and Level 2 (dashed).

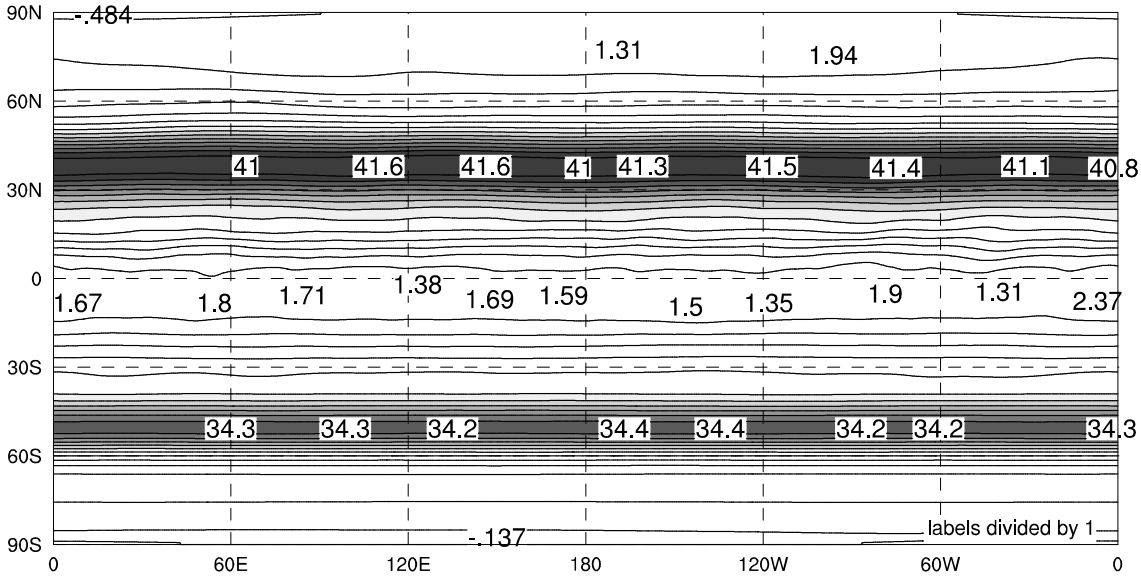

Figure 8.2: Time-averaged zonal current for atmospheric DNS (with rotation and jets) at T126 (Level 1).

and bottom levels, respectively. The mean flow is dominated by the jet streams in both hemispheres; the jet streams are sheared in the vertical as can clearly be seen by comparing the winds in the two figures. Figs. 8.4 and 8.5 show, respectively, $e(n)$, the total, and, $E(m)$, the zonal wavenumber averaged energy spectra (see Eqs. E.41 and E.42 of Appendix E.4). As for the problem in the previous chapter, the flows have different kinetic energies in the two layers. The ad-hoc hyperdiffusion coefficients have been chosen so that the spectra have an approximate n^{-3} dependence all the way to the truncation scale. This works quite well in Level 2, which has a constant slope region for wavenumbers (m, n) between 15 and 80. It works less well for the top layer which starts to lift its tail after $n = 50$ or so, which is evident in Fig. 8.4. This phenomenon was also observed in the problem of the previous chapter. All the spectra have a kink right at the truncation scale. This was also observed when using the deterministic LES of the previous chapter; it is a problem that can be cured by using the stochastic parameterization, as was demonstrated in Chapter 7. Most of the energy in the largest scales in Fig. 8.4 is in the form of mean energy. Figure 8.6 shows the relative distribution of mean and transient kinetic energies for Level 1 as functions of n . For $n < 5$, the kinetic energy is mostly mean while for $n > 15$ it is mostly transient. The distribution of (total) barotropic and baroclinic energy is shown in Figs. 8.7 and 8.8. As in the previous two chapters, the large scale energy is mostly in the form of barotropic energy. Equipartition of barotropic and baroclinic energies is observed for $n > 50$ or so.

8.1.1 Subgrid-scale Parameterizations at T63

The subgrid potential enstrophy flux matrix, which represents the contribution of the subgrid terms to the equal-time potential vorticity covariance matrix tendency, $\mathcal{F} = \langle \left(\frac{\partial \hat{\mathbf{x}}(t)}{\partial t}\right)_S \hat{\mathbf{x}}^\dagger(t) \rangle + \langle \hat{\mathbf{x}}(t) \left(\frac{\partial \hat{\mathbf{x}}(t)}{\partial t}\right)_S^\dagger \rangle$ in the PV formulation, with $\left(\frac{\partial \hat{\mathbf{x}}(t)}{\partial t}\right)_S$ and $\hat{\mathbf{x}}$ defined in Eqs. 5.50 and 5.51, is very similar to that of the previous chapter, and is thus not shown. The off-diagonal fluxes are negligibly small. The diagonal fluxes are dominated by the Level 1 flux, which is an order of magnitude greater than the Level 2 flux. The

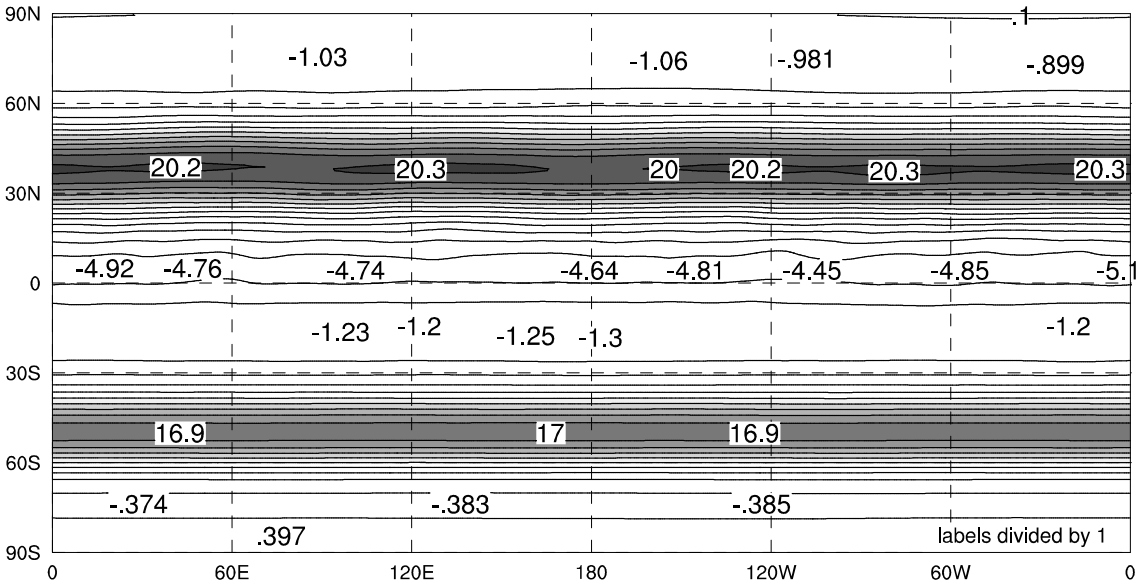

Figure 8.3: Time-averaged zonal current for atmospheric DNS (with rotation and jets) at T126 (Level 2).

diagonal elements of the real part of the net dissipation matrix, $-\mathbf{M_n^r}$, are shown in Fig. 8.9. The diagonal contributions to both levels are effectively the same, and display the typical cusp profiles as for the simpler problems of the previous two chapters. The imaginary components of this matrix, $\mathbf{M_n^i}$, are shown in Fig. 8.10. Both elements seem to be somewhat smaller than the corresponding $-\mathbf{M_n^r}$ elements. The M_{11}^i element seems to dip near the truncation scale, and is smaller than the $-M_{22}^i$ element. this seems to be contrary to what was found in the previous chapter, where the M_{11}^i element was in general larger. A contour plot of the full anisotropic (m and n dependent) matrix shows that it can be quite anisotropic (see Appendix H). In fact, M_{11}^i is negative for high values of m, near $n = 63$. This explains why the isotropized elements dip near the truncation scale. This shows that it can be hard to make a generic statement about the form of $-\mathbf{M_n^i}$; however, the diagonal elements of this matrix do not contribute to the enstrophy flux, so if the energy and enstrophy are the only flow quantities that we seek to maintain, we can ignore $\mathbf{M_n^i}$ altogether in atmospheric problems.

The drain dissipation, $\mathbf{M_d}$, and stochastic backscatter, $\mathbf{F_b}$, matrices have been calculated by integrating over a timescale $\tau = 0.125$ day. The time covariance matrix $\langle \left(\frac{\partial \hat{q}_{mn}^i(t)}{\partial t}\right)_S \left(\frac{\partial \hat{q}_{mn}^i(t_0)}{\partial t}\right)_S^* \rangle$ as a function of time, t, at $n = 63$, is shown in Fig. 8.11. The decorrelation time is around 0.2 days. The cutoff wavenumber is $n_c = 55$, below which, the deterministic parameterization is used. The diagonal elements of the real part of the drain dissipation matrix, $-\mathbf{M_d^r}$, are shown in Fig. 8.12. The Level 1 contribution, $-M_{11}^r$, is enhanced by a factor of nearly three over the corresponding $-\mathbf{M_n^r}$ element. The Level 2 contribution, $-M_{22}^r$, is not enhanced by as much, with the result that $-M_{11}^r$ is now slightly greater than $-M_{22}^r$. This is a pattern also seen in the simpler problem of the previous chapter. The imaginary components, $\mathbf{M_d^i}$, are shown in Fig. 8.13. The M_{11}^i element is slightly enhanced over the corresponding $\mathbf{M_n^i}$ element; however, it is still not rising to a cusp, and we suspect that it is also as anisotropic. The M_{22}^i element is relatively unchanged over the corresponding $\mathbf{M_n^i}$ element. The diagonal elements of the stochastic backscatter matrix, $\mathbf{F_b^r}$, are shown in Fig. 8.14. The Level 1 backscatter is over an order

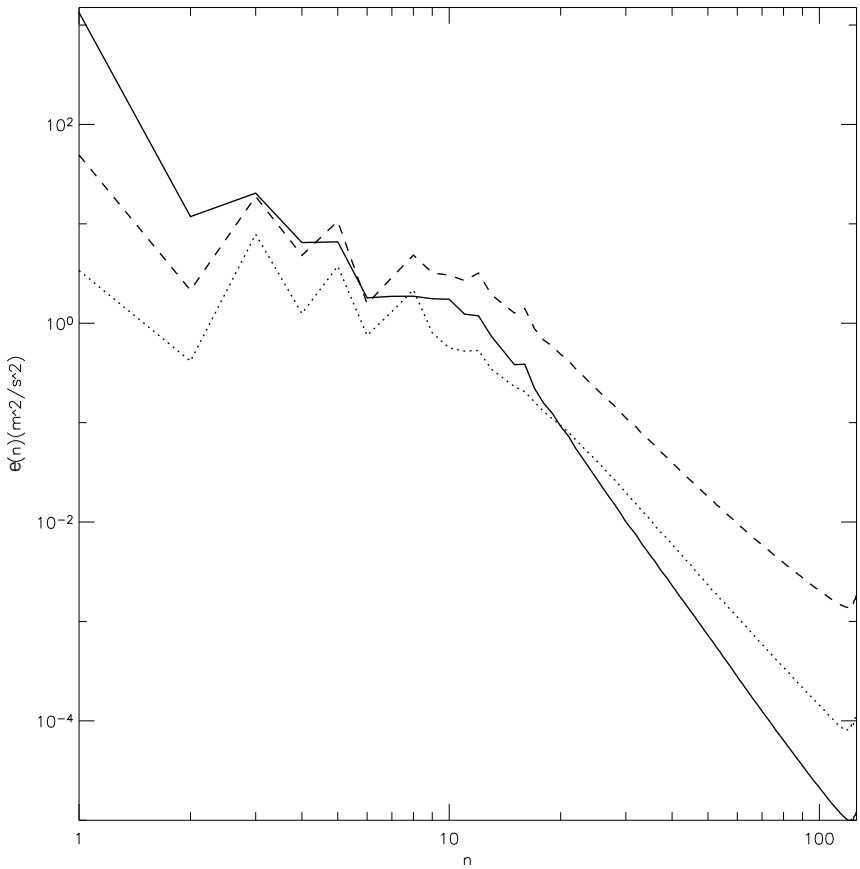

Figure 8.4: Energy spectra as functions of total wavenumber (n): potential energy (solid), Level 1 kinetic energy (dashed), and Level 2 kinetic energy (dotted) for the atmospheric DNS (with rotation and jets) at T126.

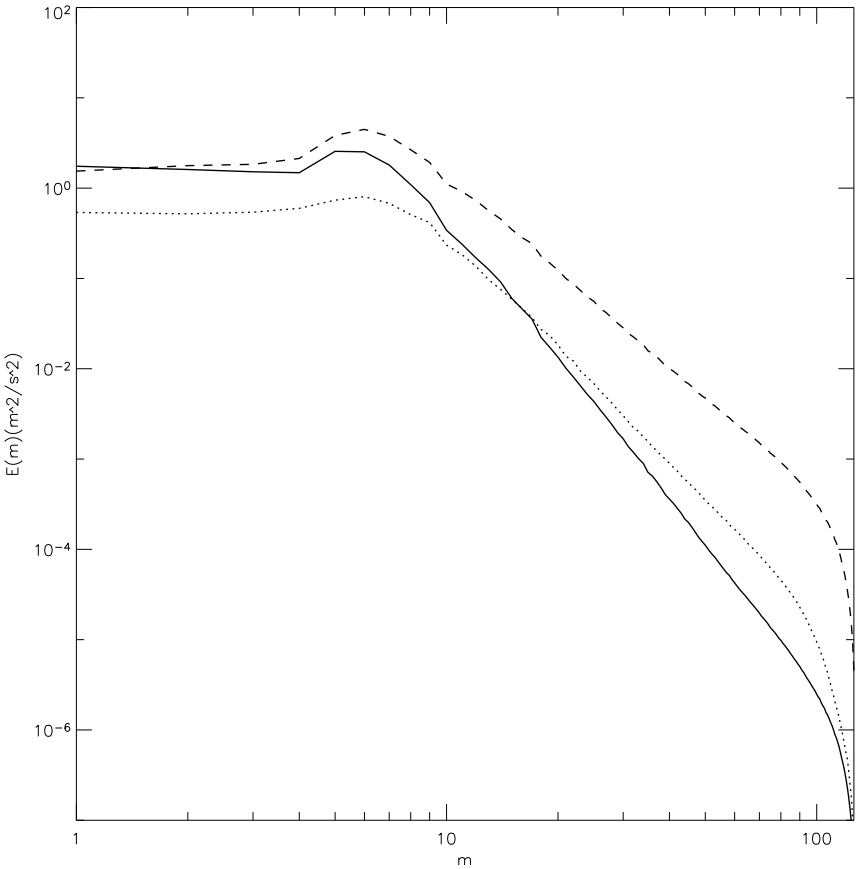

Figure 8.5: Energy spectra as functions of zonal wavenumber (m): potential energy (solid), Level 1 kinetic energy (dashed), and Level 2 kinetic energy (dotted) for the atmospheric DNS (with rotation and jets) at T126.

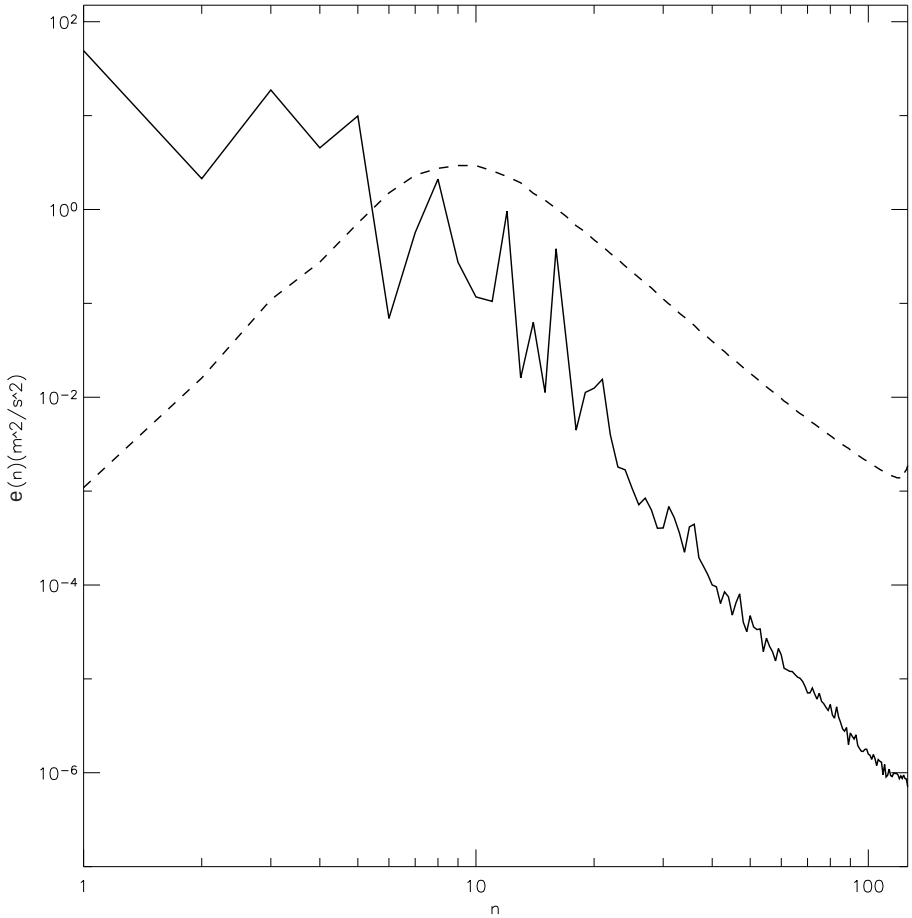

Figure 8.6: Relative distribution of mean and transient energy for the atmospheric DNS (with rotation and jets) at T126. Mean kinetic energy as a function of total wavenumber (n) (solid) and transient kinetic energy (dashed) for Level 1.

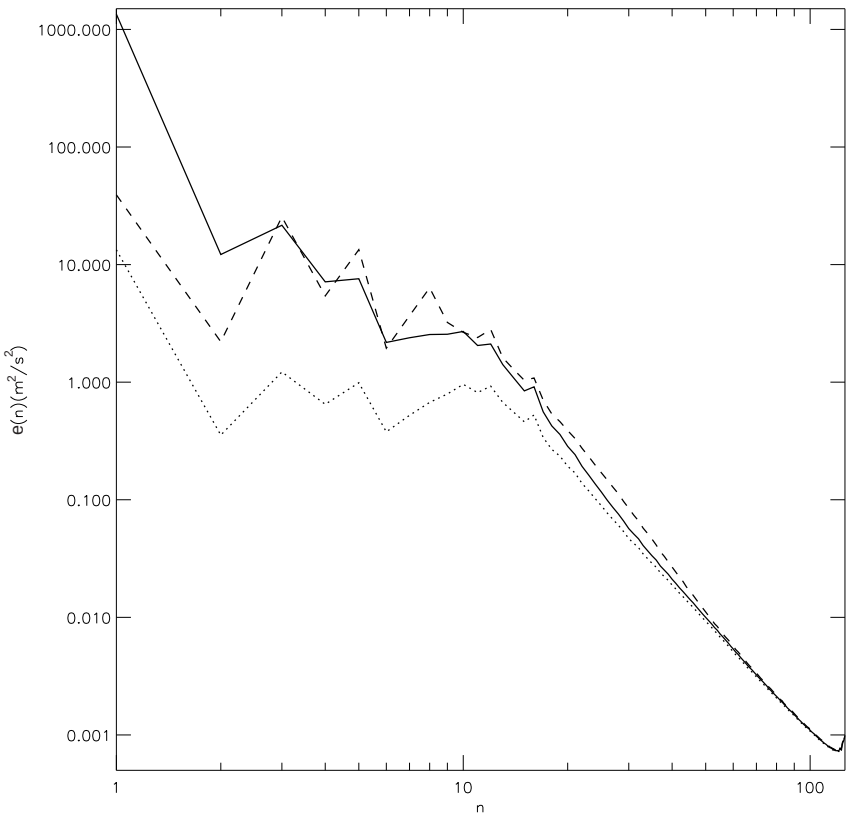

Figure 8.7: Energy spectra as functions of total wavenumber (n): total baroclinic energy (solid), barotropic kinetic energy (dashed), and baroclinic kinetic energy (dotted) for the atmospheric DNS (with rotation and jets) at T126.

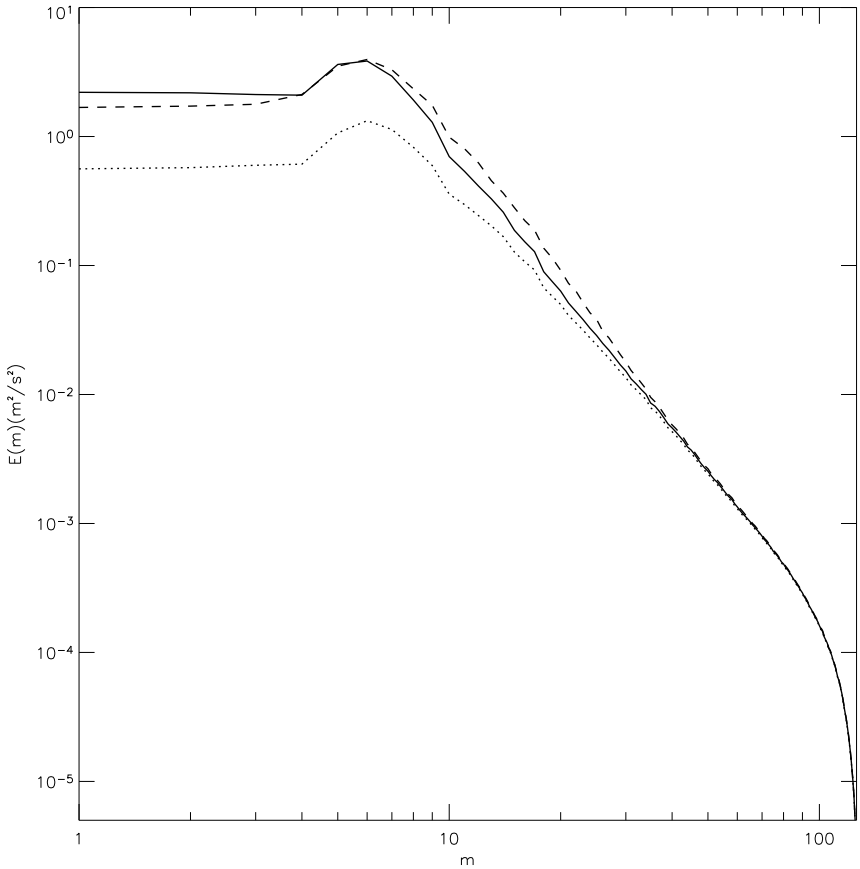

Figure 8.8: Energy spectra as functions of zonal wavenumber (m): total baroclinic energy (solid), barotropic kinetic energy (dashed), and baroclinic kinetic energy (dotted) for the atmospheric DNS (with rotation and jets) at T126.

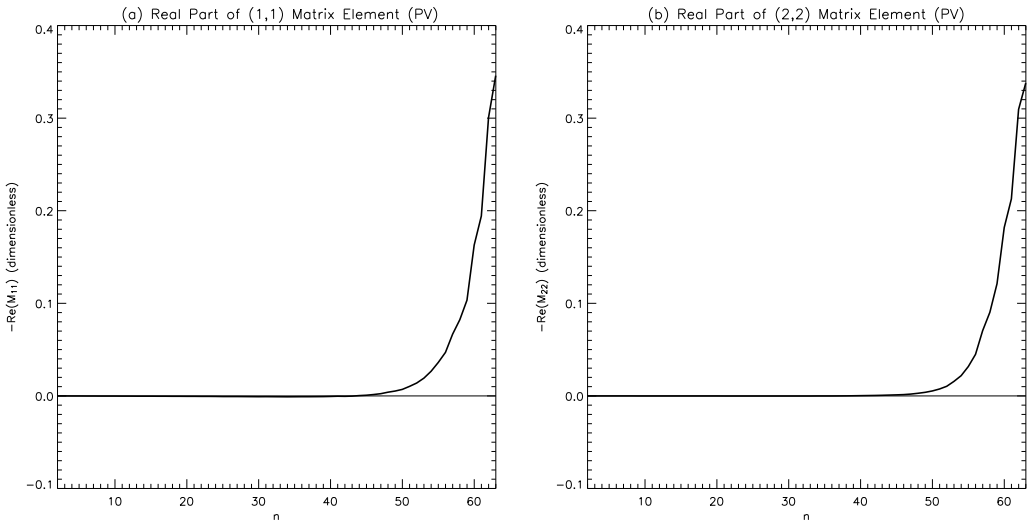

Figure 8.9: Diagonal elements of the real part of the isotropic net viscosity matrix in the PV formulation: (a) $-M^r_{11}$; (b) $-M^r_{22}$.

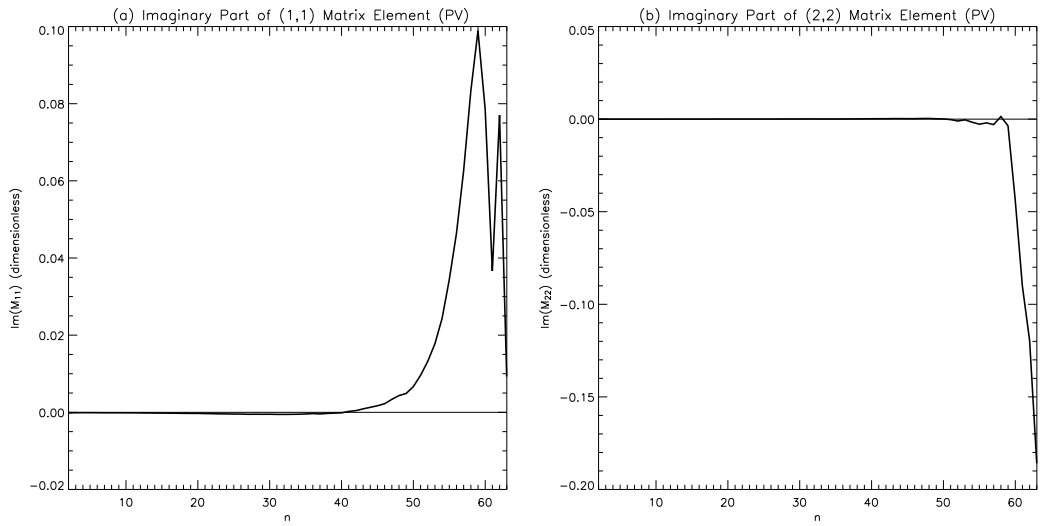

Figure 8.10: Diagonal elements of the imaginary part of the isotropic net viscosity matrix in the PV formulation: (a) M^i_{11}; (b) M^i_{22}.

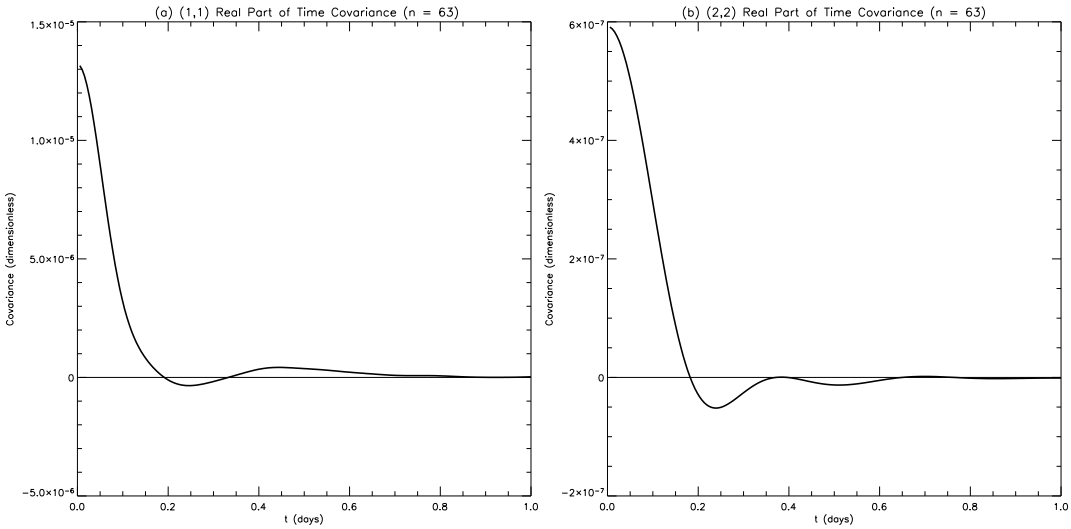

Figure 8.11: Time covariances of the subgrid tendency matrix in the PV formulation: (a) Level 1; (b) Level 2.

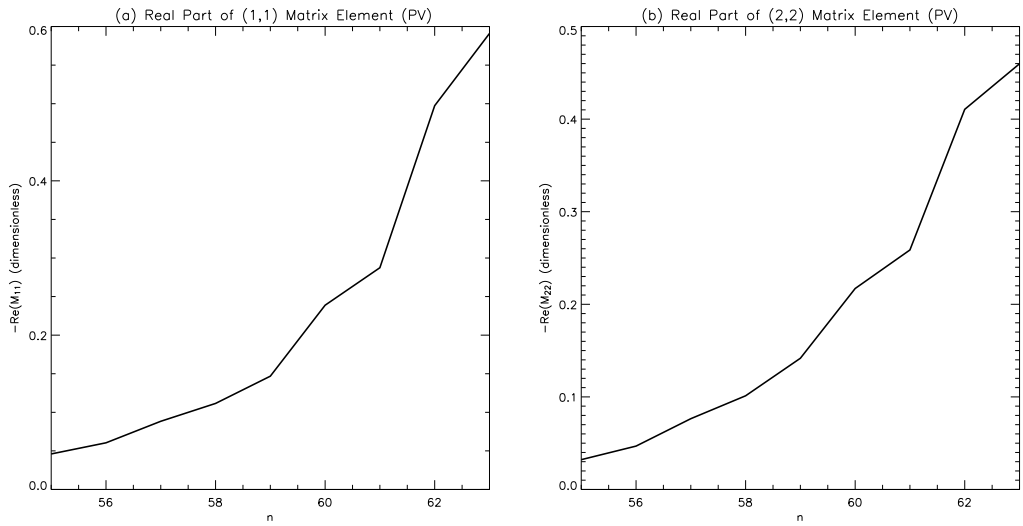

Figure 8.12: Diagonal elements of the real part of the isotropic drain viscosity matrix in the PV formulation: (a) $-M^r_{11}$; (b) $-M^r_{22}$.

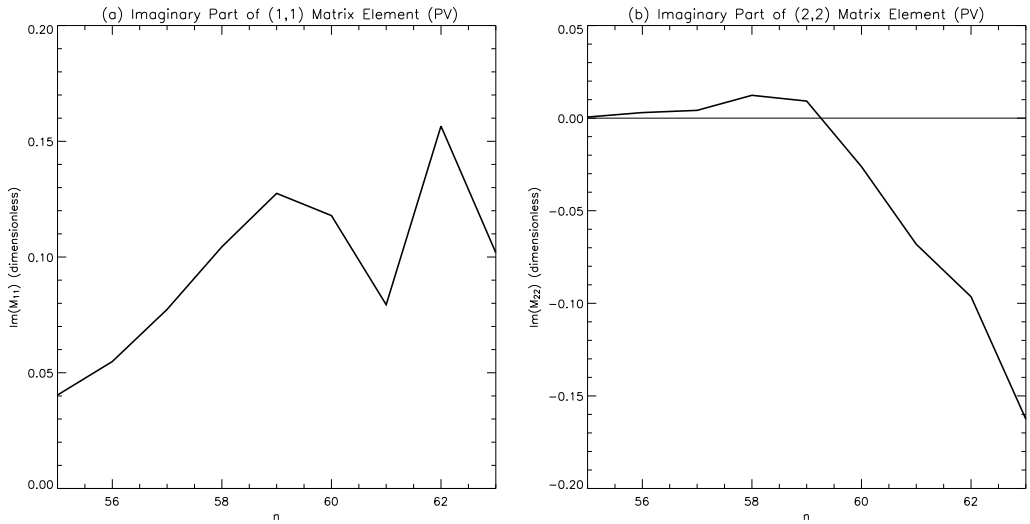

Figure 8.13: Diagonal elements of the imaginary part of the isotropic drain viscosity matrix in the PV formulation: (a) M^i_{11}; (b) M^i_{22}.

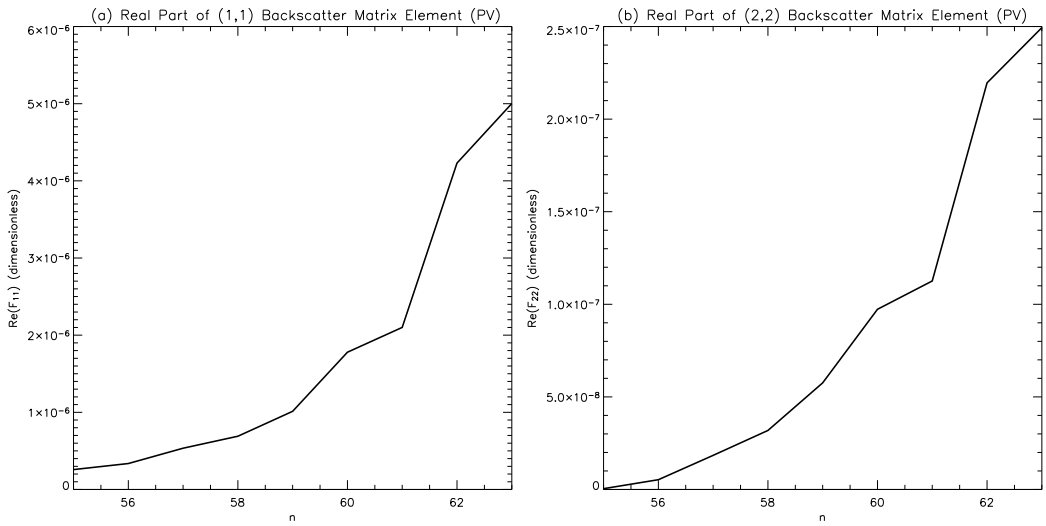

Figure 8.14: Diagonal elements of the isotropic backscatter matrix in the PV formulation: (a) F^r_{11}; (b) F^r_{22}.

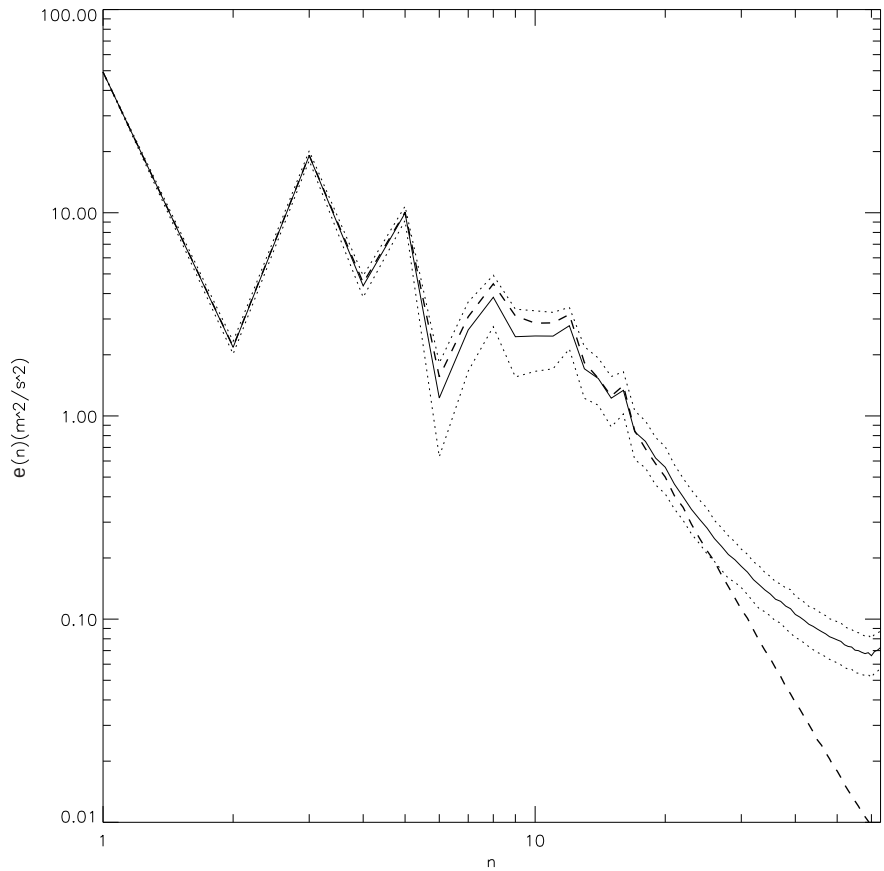

Figure 8.15: Energy spectra (Level 1) as functions of total wavenumber (n): kinetic energy for LES with bare parameters (solid); LES kinetic energy plus and minus standard deviation (dotted); and T126 DNS kinetic energy (dashed).

of magnitude greater than the Level 2 backscatter, just as in the simpler problem of the previous chapter.

8.1.2 LES at T63

The LES at T63 was performed using bare parameters, the deterministic parameterization, and the stochastic parameterization. The results of the LES using bare parameters are shown in Figs. 8.15 and 8.16. As was found in the previous chapters, the lack of subgrid-scale paramterization in atmospheric flows where the truncation is well in the inertial range affects the spectra mainly locally . In other words, the LES deviates; its tail rises due to an insubstantial sink of enstrophy, but this deviation is mainly confined to wavenumbers $n > 20$ or so. The change in the large scales is minimal. However, there does seem to be a slight underestimation of the energy in the range $5 < n < 15$ (in the n spectra), which is consistent with the findings of Frederiksen et al. (1996). The performance of the LES with both deterministic and stochastic parameterizations is very similar, with perhaps a slight kink visible for the deterministic parameterization (not shown), for the reasons given in the previous chapter. Both parameterizations, however, result in good agreement between

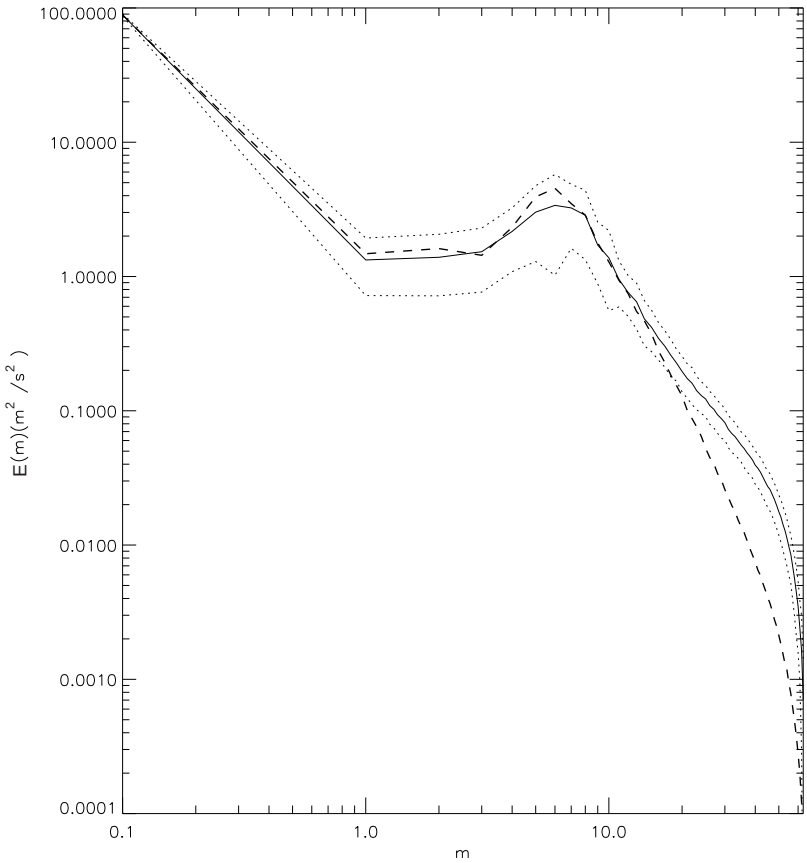

Figure 8.16: Energy spectra (Level 1) as functions of zonal wavenumber (n): kinetic energy for LES with bare parameters (solid); LES kinetic energy plus and minus standard deviation (dotted); and T126 DNS kinetic energy (dashed).

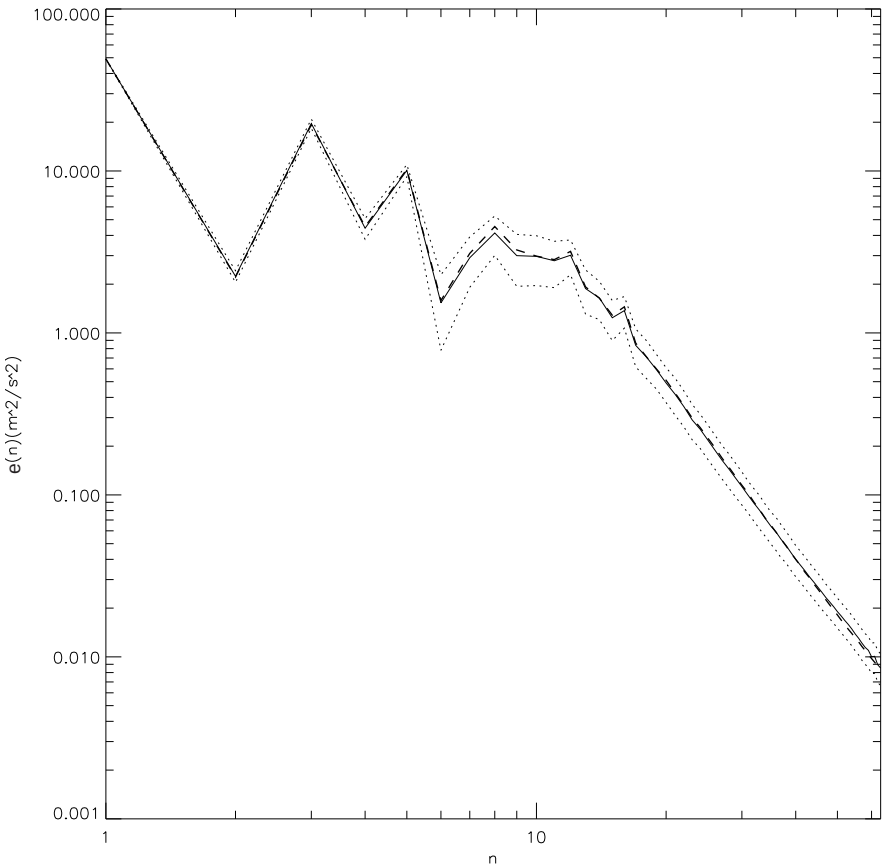

Figure 8.17: Energy spectra (Level 1) as functions of total wavenumber (n): kinetic energy for LES with renormalized drain viscosity and stochastic backscatter(solid); LES kinetic energy plus and minus standard deviation (dotted); and T126 DNS kinetic energy (dashed).

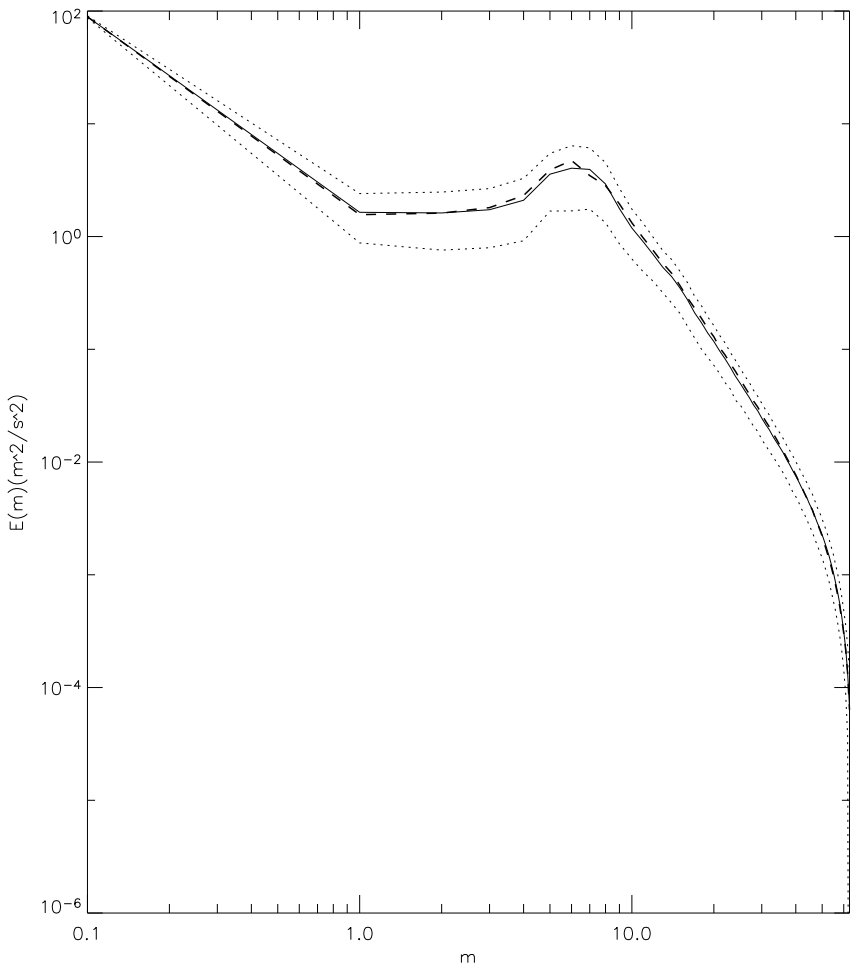

Figure 8.18: Energy spectra (Level 1) as functions of zonal wavenumber (n): kinetic energy for LES with renormalized drain viscosity and stochastic backscatter (solid); LES kinetic energy plus and minus standard deviation (dotted); and T126 DNS kinetic energy (dashed).

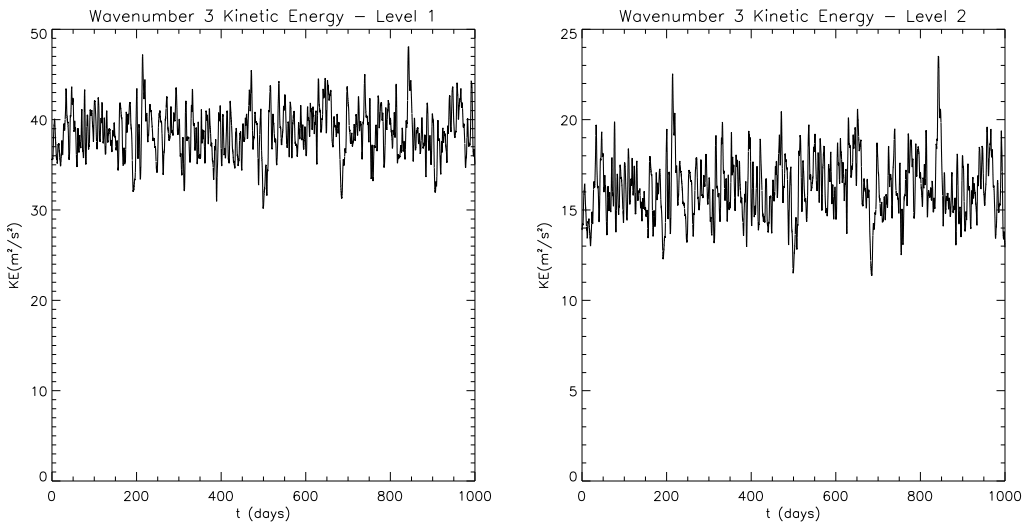

Figure 8.19: Time-series of the wavenumber 3 kinetic energy of the atmospheric DNS (with rotation and jets) at T126.

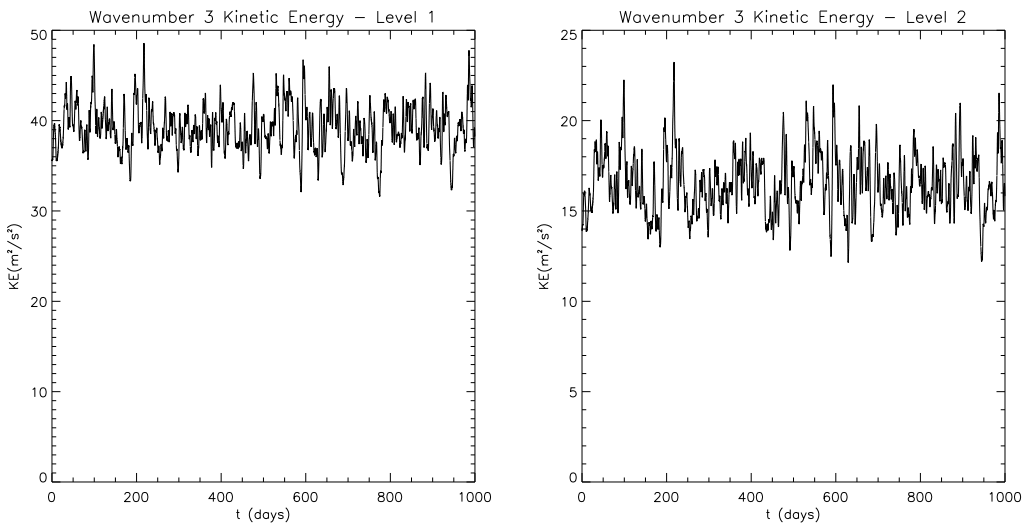

Figure 8.20: Time-series of the wavenumber 3 kinetic energy of the atmospheric LES (with rotation and jets) at T63 using the drain viscosity and stochastic backscatter parametrization.

the LES and DNS at T126. The results for the stochastic parameterization are shown in Figs. 8.17 and 8.18. We also show the time evolution of the $n = 3$ (averaged over m) kinetic energy of the DNS at T126 in Fig. 8.19, and for comparison the corresponding diagnostic for the T63 LES with stochastic parameterization in Fig. 8.20 (the choice of $n = 3$ is arbitrary). Visually, at least, there is no significant difference between the time evolution of the LES and DNS; the mean energy and its fluctuations are comparable in both cases.

8.2 Oceanic Parameters

In this section, we relax the flow towards a meridionally confined current centered at 60^oS, which is a crude model of the ACC. The following parameters have been chosen: the coupling constant, $F_o = 2.4 \times 10^{-10}\text{m}^{-2}$, which corresponds to $\lambda_i = 50$ km; the drag, α_i, for Level 1 corresponds to a damping time of 40 days, and for Level 2 it is 10 days; the viscosity, $\nu_i^0 = 4.6 \times 10^{12}$ m^4s^{-1} for both levels; the order of the Laplacian operator, p, is 2; the relaxation time for the mean flow, κ, is 116 days. The latitudinal profile of the currents u_i^{rel} are shown in Fig. 8.21; they are centered at 60^oS. The equations have been stepped forward in time for 104 days at steady state—after an initial spin-up period, with a timestep of 600 s; the resolution is T252 with 768×384 grid points. The deformation scale corresponds to approximately wavenumber 120 as in the previous two chapters.

The mean currents $\overline{u_i}$ generated are shown in Fig. 8.22. The maximum (zonally averaged) current (at 60^oS) is about 2.5 ms^{-1} for the top level and 2.0 ms^{-1} for the bottom level. The currents $\overline{u_i}$, without zonal averaging, are shown as contour plots in Figs. 8.23 and 8.24. The simulated currents are somewhat larger than observed ACC values, but are sufficient for our purposes. In any case, it is thought that bottom topography plays an important role in the dynamics of the ACC (McWilliams et al., 1978; Treguier and McWilliams, 1990; Wolff et al., 1991), particularly in providing form drag, but this is absent in our model.

The energy spectra as functions of n and m are shown in Fig. 8.25 and 8.26, respectively. A comparison with the corresponding m averaged spectra of the previous chapters reveals that the large scale potential energy is not as great here, being an order of magnitude less. Moreover, for $5 < n < 15$, a region with comparable mean and transient energies (see Fig. 8.27), the potential energy is only slightly greater than the kinetic energy. Hence, for this problem we can expect the subgrid mean forcing, $\overline{\mathbf{f}}$, to be dynamically important as the loss of potential energy to baroclinically unstable eddies is significant compared to the total available potential energy. The zonal energy plot reveals a very sharp drop in the energies for large m; this probably related to the fact that the energy containing eddies are within the region of the current core (45^oS to 75^oS), and hence most of the transient energy is 'trapped' in this region; outside of this region, there is very little activity. The energy is however calculated over the whole domain. The distribution of mean and transient energy for Level 1 kinetic energy spectrum as a function of n is shown in Fig. 8.27. This reveals that for $n < 5$, the energy is predominantly in the form of mean flow while for $n > 15$, or so, the energy is predominantly in the form of transients. The distribution of (total) barotropic and baroclinic energies is shown in Figs. 8.28 and 8.29, respectively. The now familiar phenomenon of barotropization is apparent for scales greater than $m, n = 100$ or so; at these scales, the energy is predominantly barotropic. Again, we see that the peaks of the barotropic and baroclinic energies are at different spectral locations. The baroclinic spectrum, which is much broader in comparison, is peaked at wavenumbers around 80

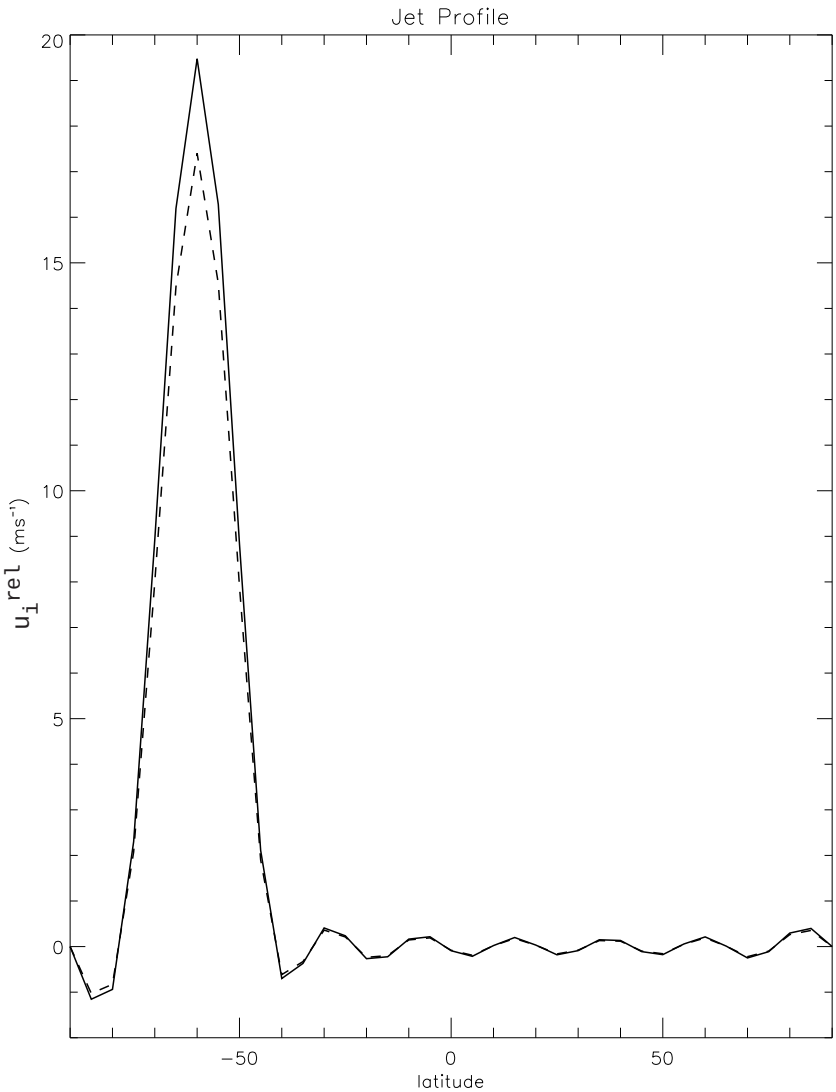

Figure 8.21: The imposed zonal currents u_i^{rel} for the ocean: Level 1 (solid) and Level 2 (dashed).

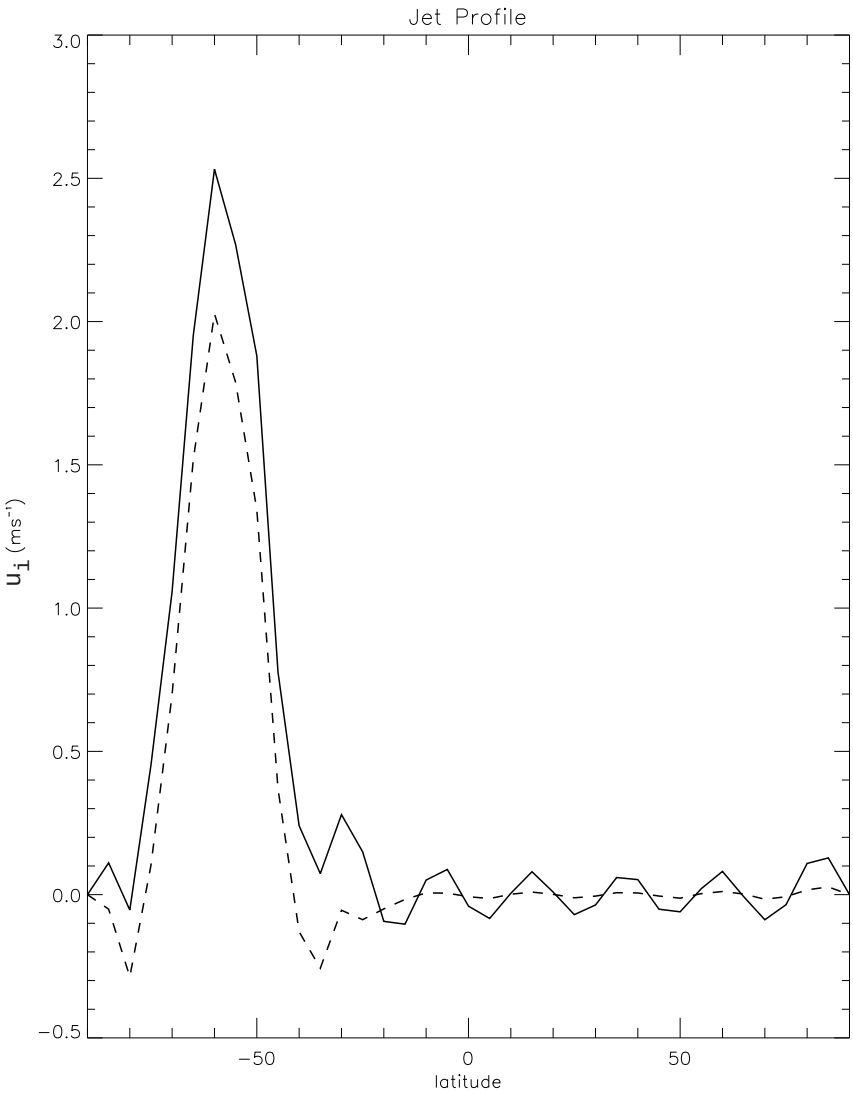

Figure 8.22: Zonal currents u_i for the ocean: Level 1 (solid) and Level 2 (dashed).

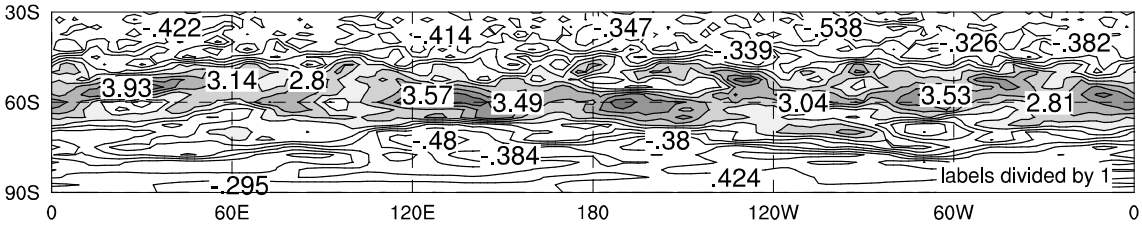

Figure 8.23: Time-averaged zonal wind for the oceanic DNS (with rotation and jets) at T252 (Level 1).

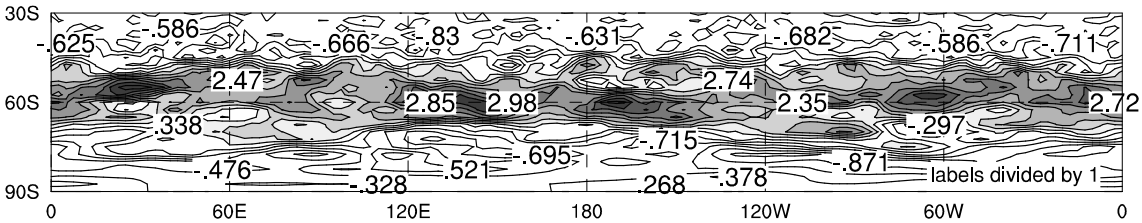

Figure 8.24: Time-averaged zonal wind for the oceanic DNS (with rotation and jets) at T252 (Level 2).

while the barotropic spectrum is peaked for wavenumbers between 20 and 30 (the peaks at larger scales correspond to predominantly mean fields).

8.2.1 Subgrid-scale Parameterizations and LES at T126

The matrices $\mathbf{M_n}$, $\mathbf{M_d}$, $\mathbf{F_b}$, and $\bar{\mathbf{f}}$ are calculated at T126. The decorrelation time, τ, is 1 day. The LES is initially run for 104 days, with a timestep of 600 s, using the stochastic parameterization for $n > n_c$. We impose a cutoff wavenumber of $n_c = 66$, below which the deterministic parameterization is used. The results are shown in Fig. 8.30 and 8.31. The agreement between the LES and DNS at 252 is not perfect; however, it is broadly satisfactory, and a significant improvement over using bare parameters. For the n spectra (Fig. 8.30), there is an overestimation for $n > 60$, and an underestimation for $n < 60$. For the m spectra (Fig. 8.31), the agreement is quite good for $m < 40$, after which there is an overestimation of kinetic energy. We now have a simulation at T126 which is in good agreement with the T252 DNS for larger scales ($n < 60$ or so), but with somewhat poorer agreement at smaller scales. The LES at T126 is then run for 2700 days, using a timestep of 1200 s, for the purpose of exploring subgrid-scale parameterizations at T63. The reason for this two-step procedure, as explained in previous chapters, is that $N_* = 63$ is a realistic and interesting truncation scale; however, it is hard to obtain good samples directly from the computationally demanding T252 simulation, hence the two-step procedure. The latitudinal profile of the mean zonal currents are shown in Fig. 8.32. The mean zonal currents are somewhat overestimated compared to the currents obtained with the higher resolution DNS at T252 (Fig. 8.22).

8.2.2 Subgrid-scale Parameterizations at T63

The subgrid flux matrix, $\mathcal{F}$, at the artificial truncation wavenumber $N_* = 63$ is shown in Figs. 8.33 and 8.34. The fluxes are qualitatively similar to the ones obtained for the simple rotating flow of the previous chapter. The difference is that the fluxes are much

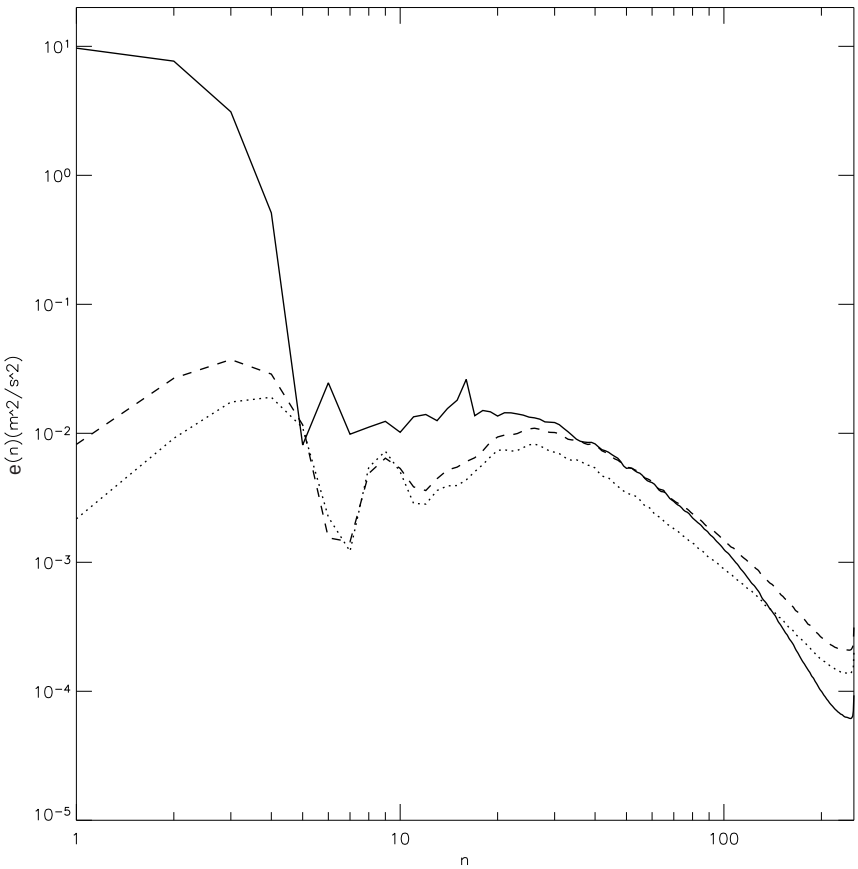

Figure 8.25: Energy spectra as functions of total wavenumber (n): potential energy (solid), Level 1 kinetic energy (dashed), and Level 2 kinetic energy (dotted) for the oceanic DNS (with rotation and jets) at T252.

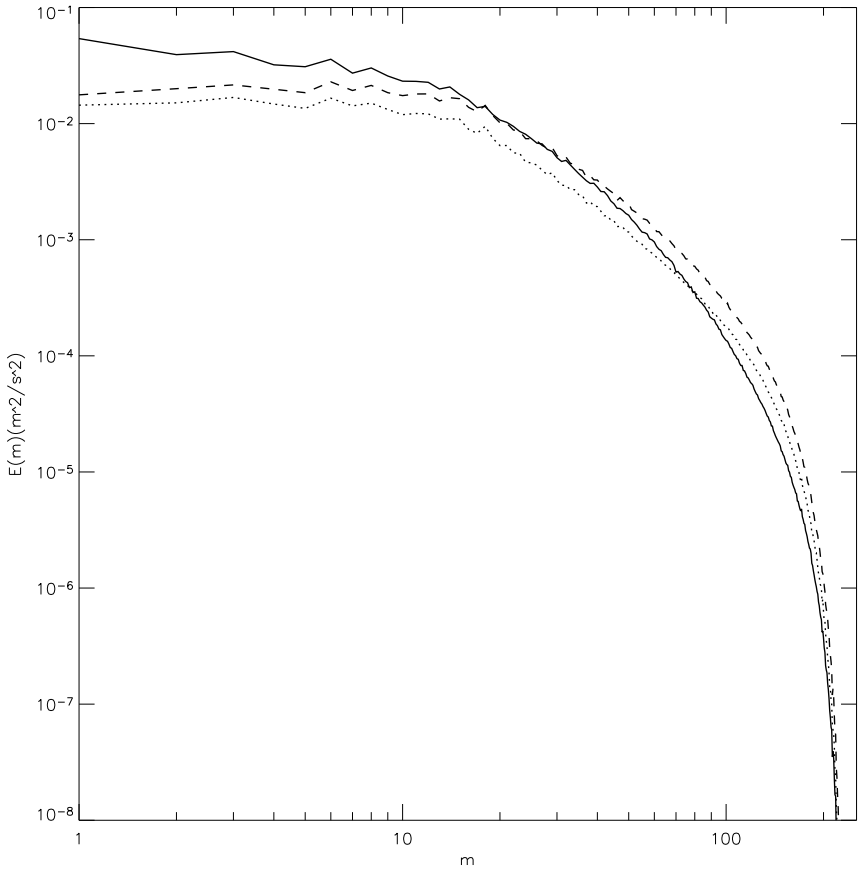

Figure 8.26: Energy spectra as functions of zonal wavenumber (m): potential energy (solid), Level 1 kinetic energy (dashed), and Level 2 kinetic energy (dotted) for the oceanic DNS (with rotation and jets) at T252.

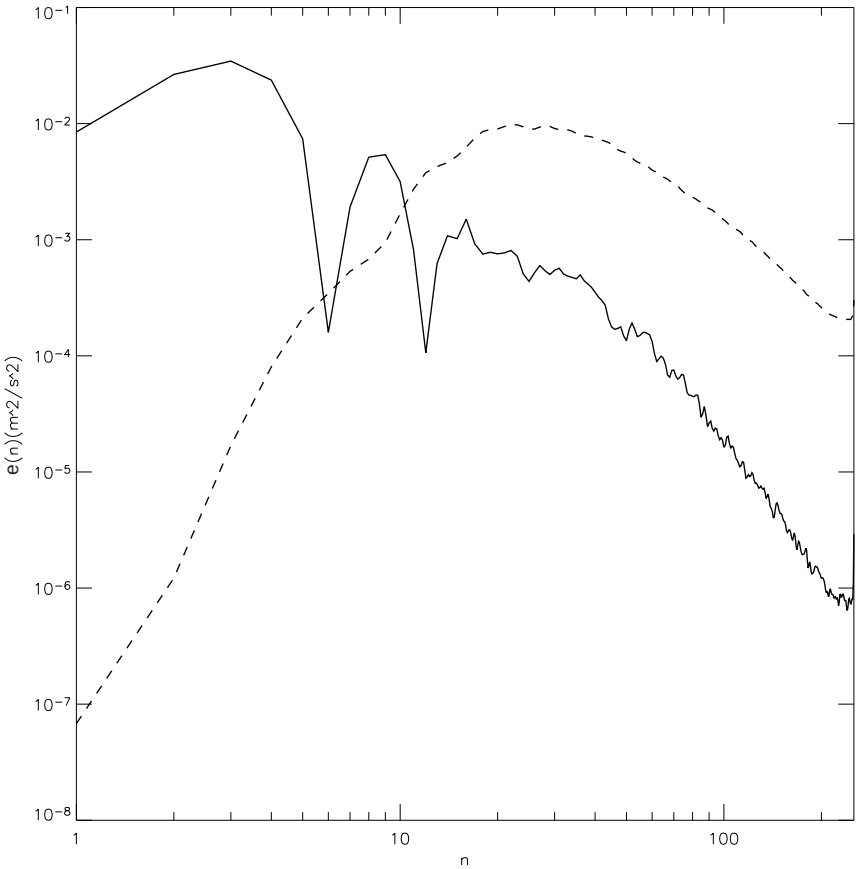

Figure 8.27: Relative distribution of mean and transient energy for the oceanic DNS (with rotation and jets) at T252. Mean kinetic energy as a function of total wavenumber (n) (solid) and transient kinetic energy (dashed) for Level 1.

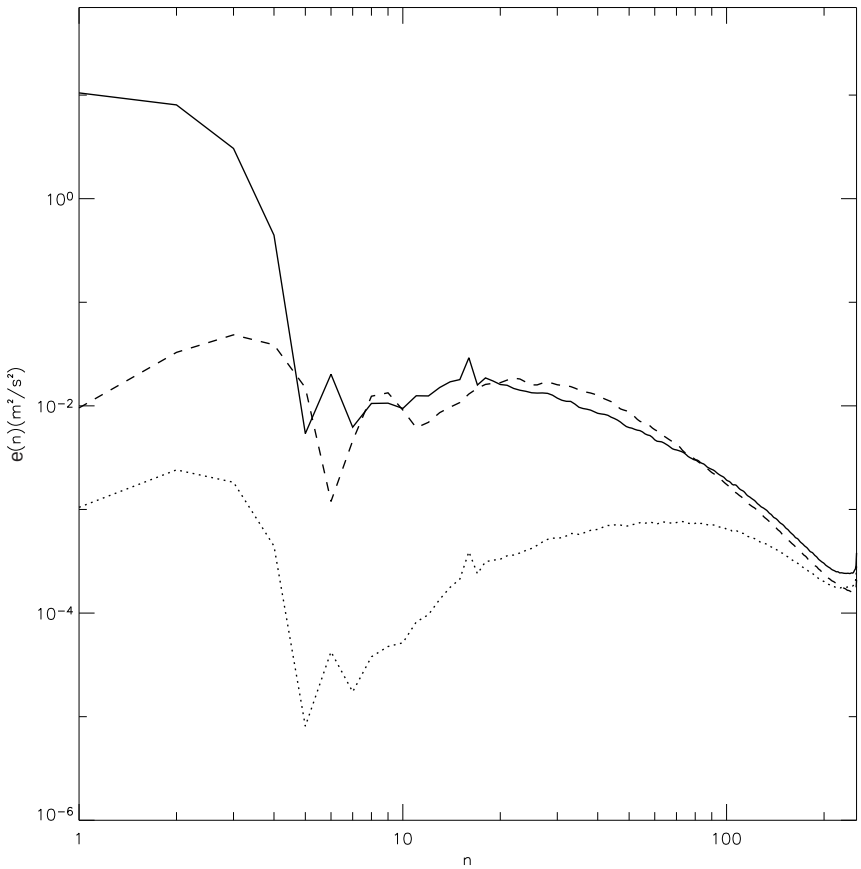

Figure 8.28: Energy spectra as functions of total wavenumber (n): total baroclinic energy (solid), barotropic kinetic energy (dashed), and baroclinic kinetic energy (dotted) for the oceanic DNS (with rotation) at T252.

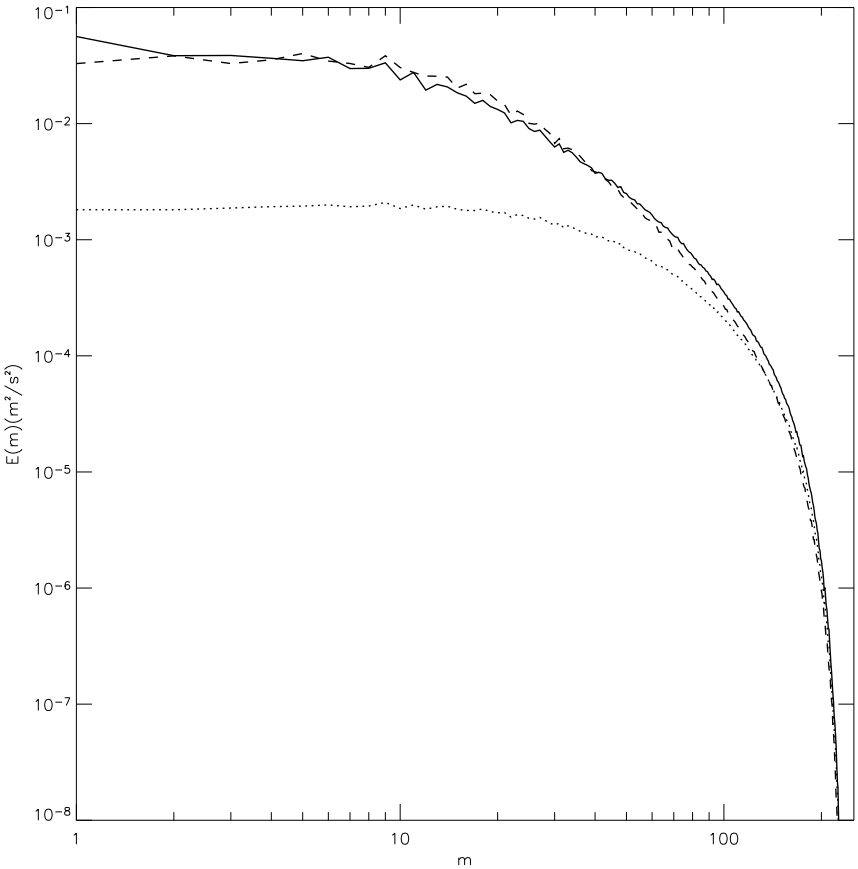

Figure 8.29: Energy spectra as functions of zonal wavenumber (m): total baroclinic energy (solid), barotropic kinetic energy (dashed), and baroclinic kinetic energy (dotted) for the oceanic DNS (with rotation and jets) at T252.

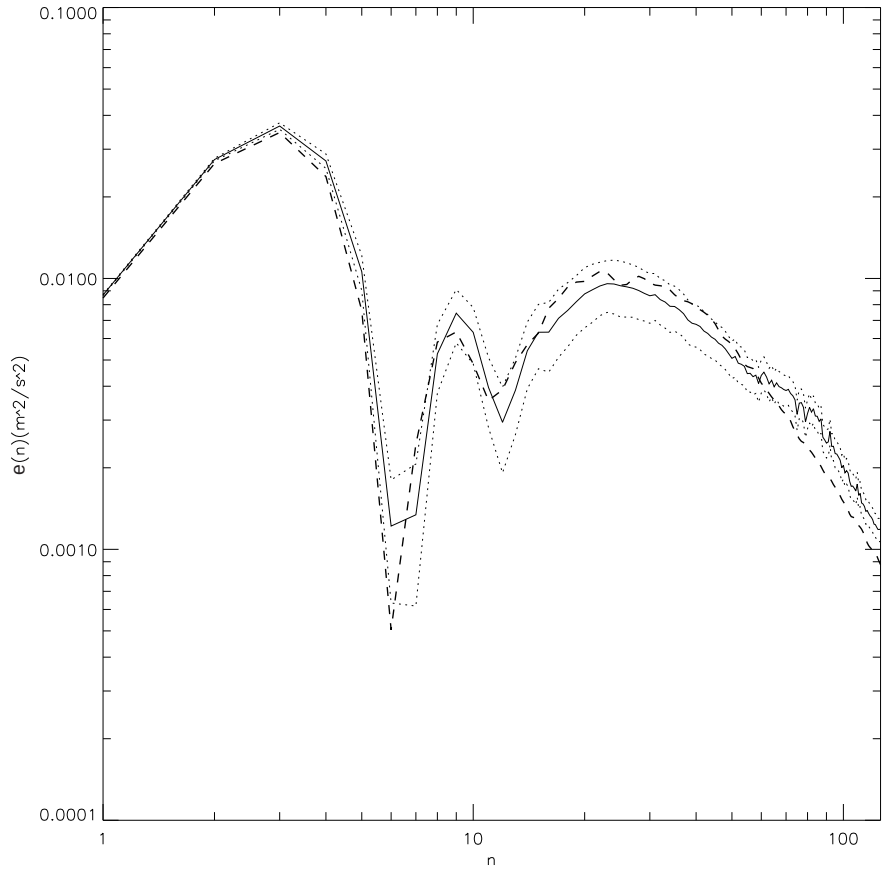

Figure 8.30: Energy spectra (Level 1) as functions of total wavenumber (n): kinetic energy for T126 LES with renormalized drain dissipation and backscatter (solid); LES kinetic energy plus and minus standard deviation (dotted); and T252 DNS kinetic energy (dashed).

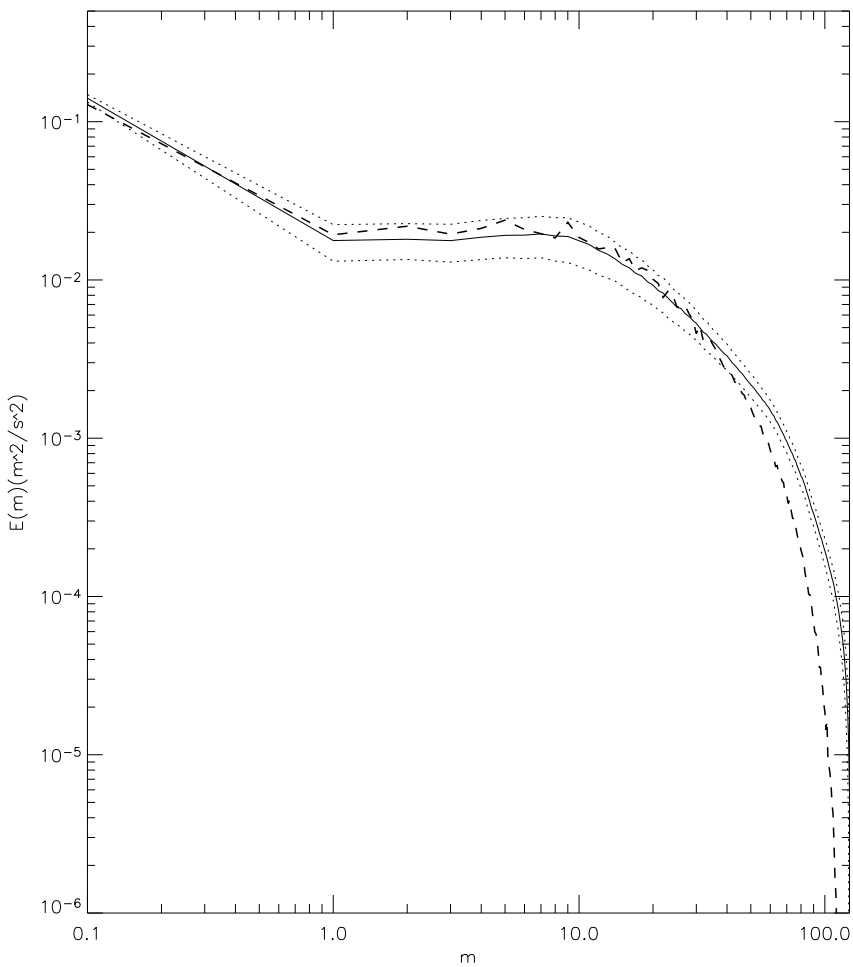

Figure 8.31: Energy spectra (Level 1) as functions of zonal wavenumber (m): kinetic energy for T126 LES with renormalized drain dissipation and backscatter (solid); LES kinetic energy plus and minus standard deviation (dotted); and T252 DNS kinetic energy (dashed).

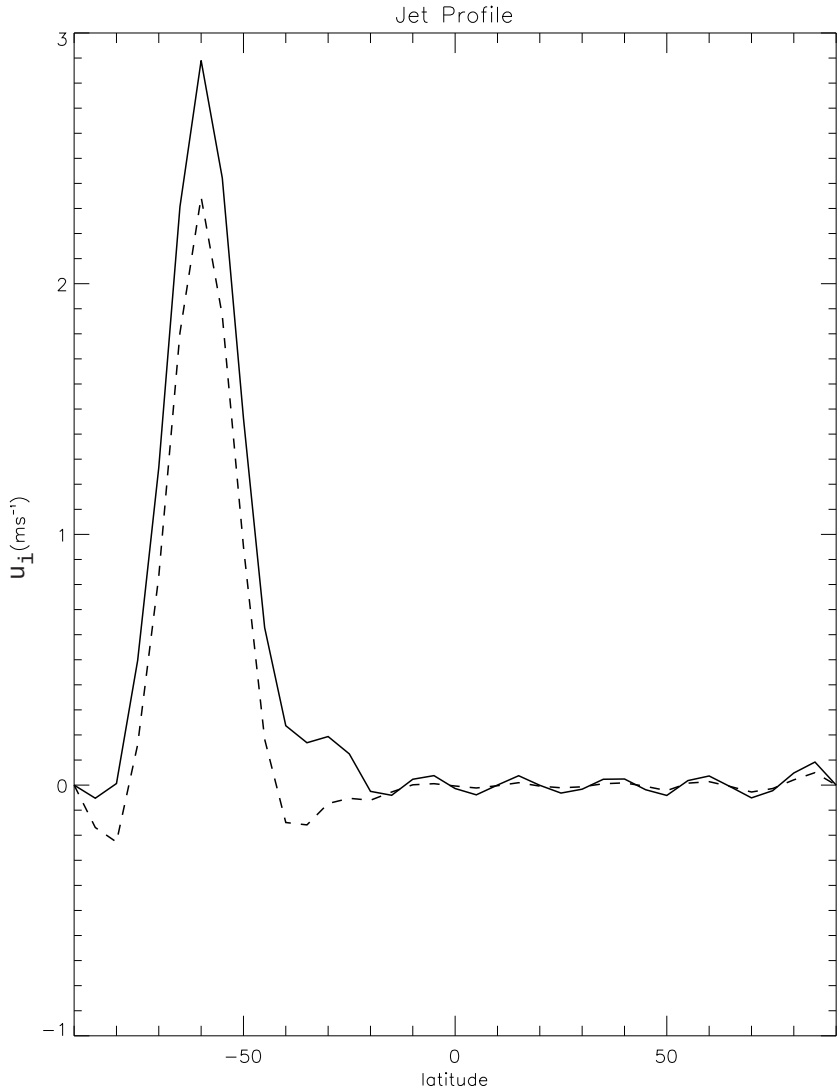

Figure 8.32: Zonal currents u_i for the ocean obtained from the T126 LES: Level 1 (solid) and Level 2 (dashed).

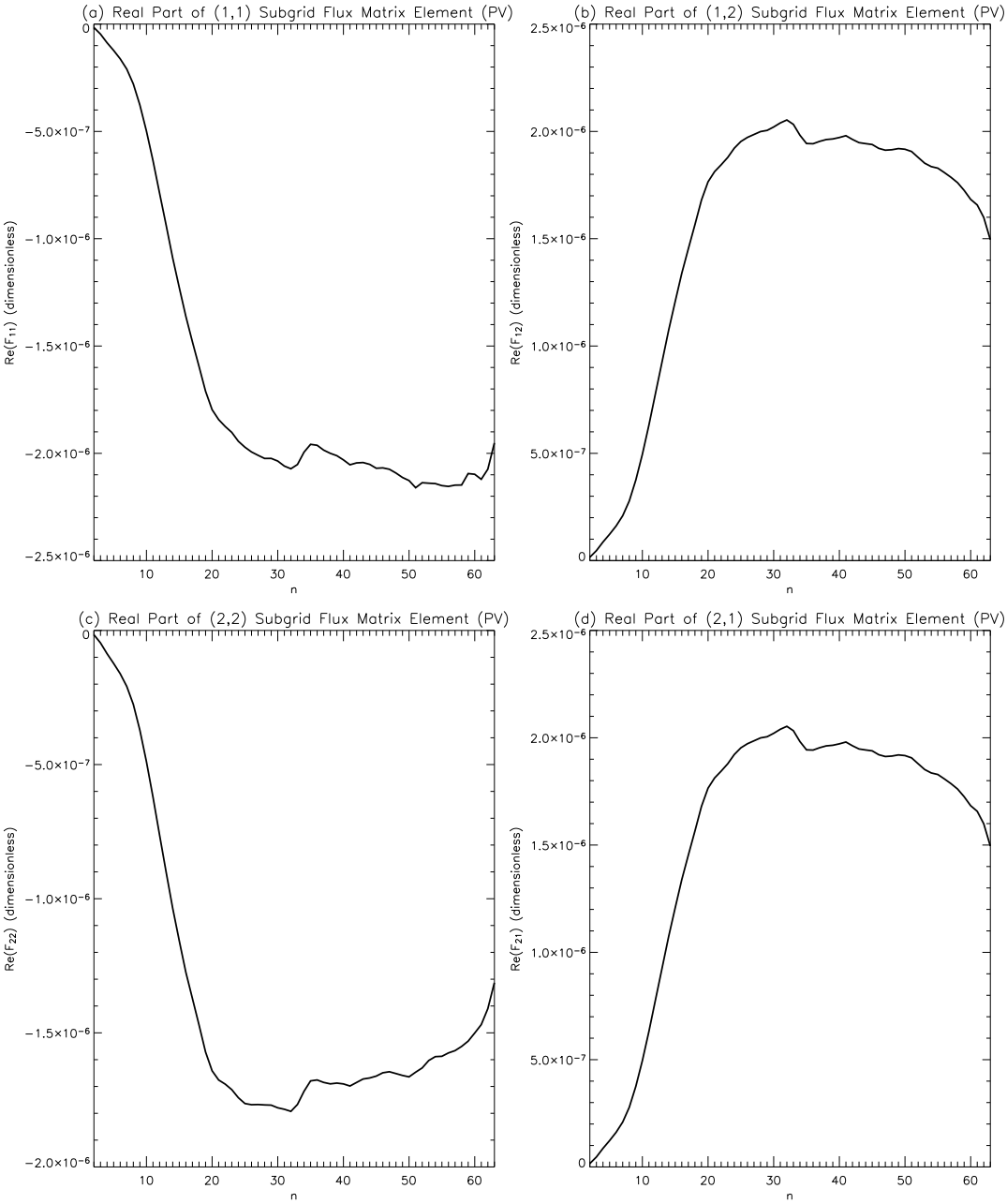

Figure 8.33: Elements of the real part of the isotropic subgrid flux matrix in the PV formulation: (a) $\mathcal{F}^r_{11}$; (b) $\mathcal{F}^r_{12}$; (c) $\mathcal{F}^r_{22}$; and (d) $\mathcal{F}^r_{21}$ (T63) .

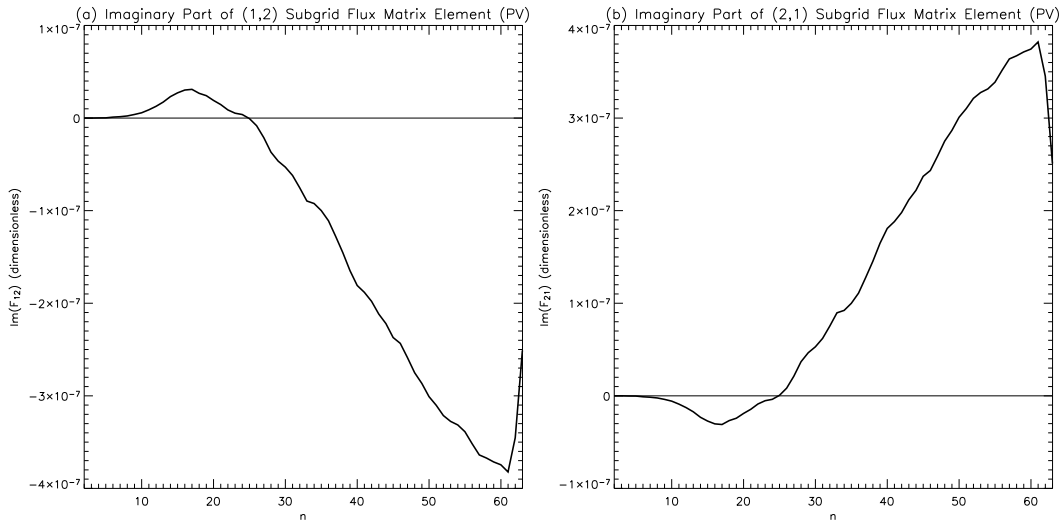

Figure 8.34: Off-diagonal elements of the imaginary part of the isotropic subgrid flux matrix in the PV formulation: (a) $\mathcal{F}^i_{12}$; (b) $\mathcal{F}^i_{21}$ (T63) .

broader near the truncation scale; in fact, in that respect, they are more similar to the ones obtained for the equivalent layer problem. The imaginary parts of the off-diagonal elements (Fig. 8.34) seem to dip right before $n = 63$; this is a sign that the fluxes are probably not very isotropic. The corresponding fluxes in the BTBC formulation are shown in Figs. 8.35 and 8.36. Again, the fluxes are qualitatively similar to those obtained in the previous chapters. The barotropic flux is more or less the same as the baroclinic flux near the truncation scale. However, for $n < 52$, the barotropic flux is positive, peaking at around wavenumber 35. This corresponds to a positive energy flux at these wavenumbers as discussed in previous chapters.

The matrices $\mathbf{M_d}$, $\mathbf{F_b}$, and $\bar{\mathbf{f}}$ have been calculated using a decorrelation time τ of 2 days. The time covariance $\langle \left(\frac{\partial \hat{q}^i_{mn}(t)}{\partial t}\right)_S \left(\frac{\partial \hat{q}^j_{mn}(t_0)}{\partial t}\right)^*_S \rangle$ as a function of time is shown in Fig. 8.37. Clearly, 2 days is a sufficient time for the subgrid tendency to decorrelate in this problem, as evident from that figure. As alluded to above, the fluxes in this problem are not isotropic as for the previous simpler problems. Here, we have a 'band' of strong eddy activity for latitudes between 45^oS and 75^oS, but very little activity outside of this region. Hence, the fluxes in spectral space are significantly anisotropic. It is prudent, then, to work with fully m and n dependent matrix parameters instead of the isotropized parameters used so far. Figures 8.38 to 8.51 show the contour plots of the two dimensional wavenumber dependent matrices $\mathbf{M_d}$ and $\mathbf{F_b}$. Most of the elements have a cusp-like profile; however, there is anisotropy (m dependence) evident, albeit in varying degrees, in all of them.

The diagonal elements of $-\mathbf{M^r_d}$ are shown in Figs. 8.38 and 8.39. Both have positive (dissipative) peaks near the truncation scale, with the Level 2 contribution being twice that of the Level 1 contribution. This is similar to what was found in the simpler problem of the previous chapter. The peaks are quite anisotropic, being centered in the wavenumber region $20 < m < 40$ for n near the truncation scale. The off-diagonal elements of $-\mathbf{M^r_d}$ are shown in Figs. 8.40 and 8.41. The Level 1 contribution ($-M_{12}$ element) has the highest peak of all the elements of $-\mathbf{M^r_d}$ and the Level 2 contribution ($-M_{21}$ element) has the lowest. In this case, both elements are negative near the truncation scale. The $-M_{21}$

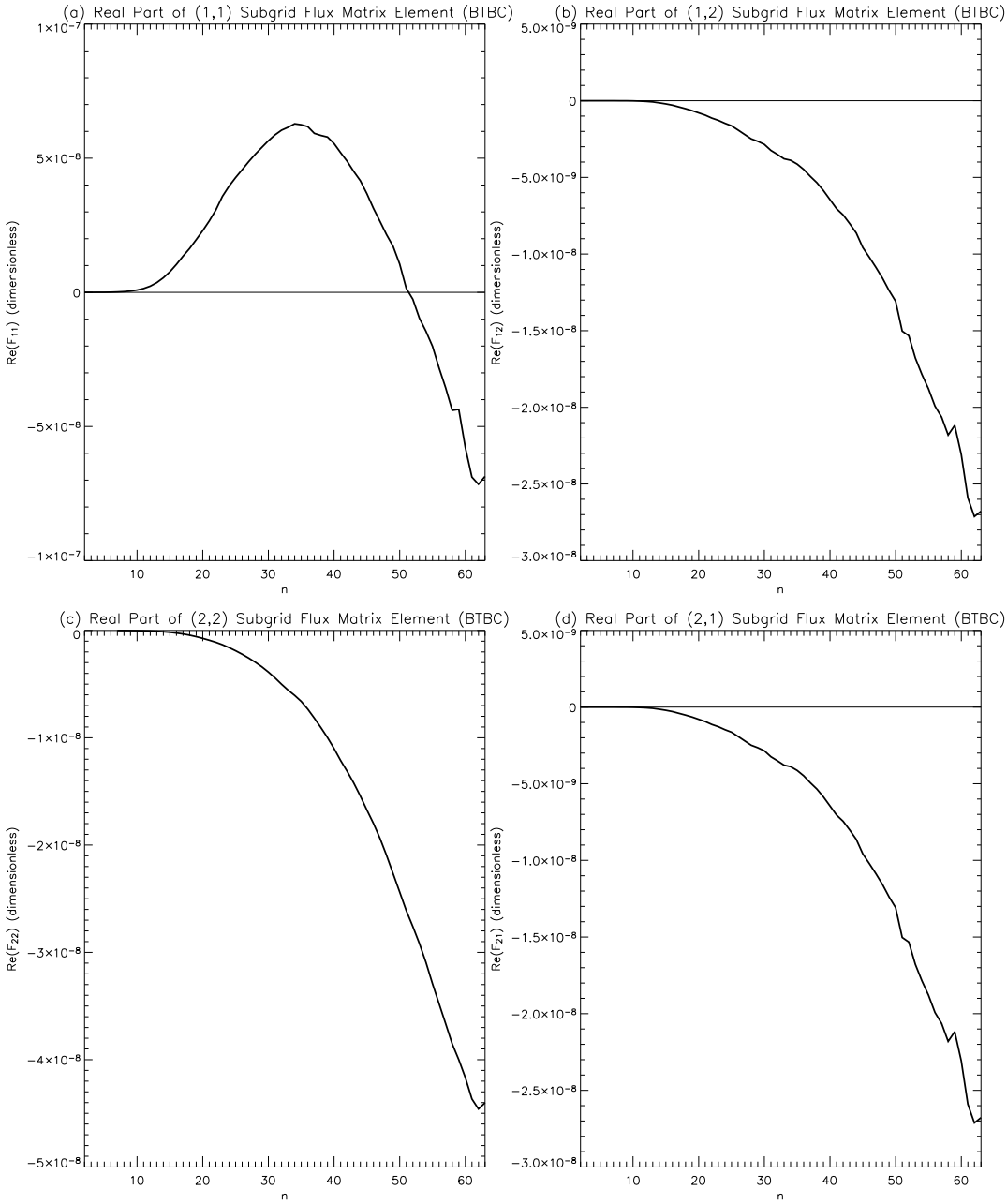

Figure 8.35: Elements of the real part of the isotropic subgrid flux matrix in the BTBC formulation: (a) $\mathcal{F}^r_{11}$; (b) $\mathcal{F}^r_{12}$; (c) $\mathcal{F}^r_{22}$; and (d) $\mathcal{F}^r_{21}$ (T63).

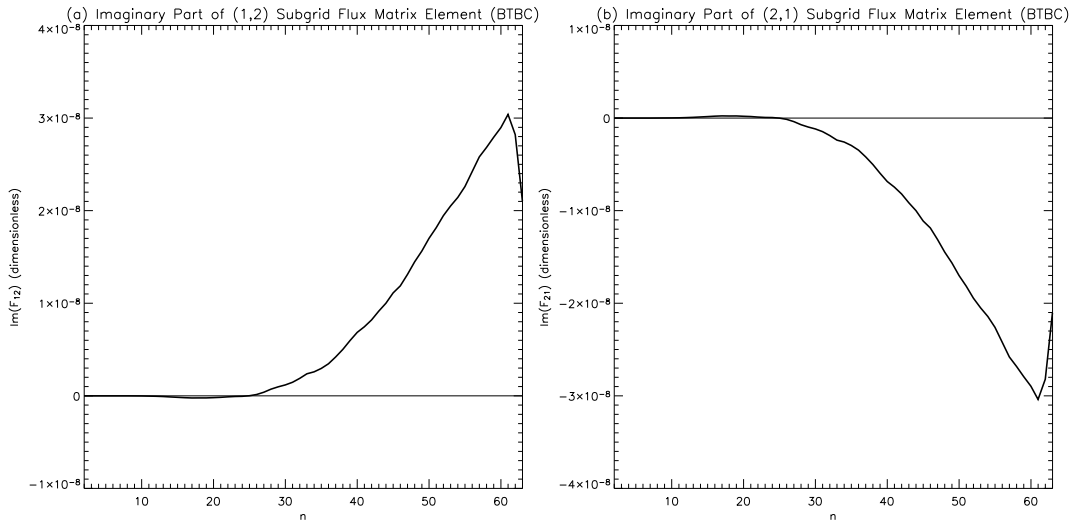

Figure 8.36: Off-diagonal elements of the imaginary part of the isotropic subgrid flux matrix in the BTBC formulation: (a) $\mathcal{F}^i_{12}$; (b) $\mathcal{F}^i_{21}$ (T63).

element, being so much smaller than the other elements, is more susceptible to sampling errors, hence its 'grainy' appearance. The diagonal elements of the imaginary part, $\mathbf{M^i_d}$, are shown in Figs. 8.42 and 8.43. The peaks of these elements are roughly half the peaks of the corresponding $-\mathbf{M^r_d}$ elements. The peaks are both positive, and interestingly, occur just below the maximum n value, and are also centered in the region $20 < m < 40$. The off-diagonal elements are shown in Figs. 8.44 and 8.45. The M^i_{12} element has a negative peak near the truncation scale, which as for the diagonal elements of $\mathbf{M^i_d}$, occurs just before the highest value of n. This peak is, however, only about half the value of the corresponding $-\mathbf{M^r_d}$ element. The M^i_{21} element has a positive peak near the truncation scale, which again occurs just before the maximum value of n. M^i_{21} and $-M^r_{21}$ are similar in size near the truncation scale.

The backscatter matrix elements are shown in Figs. 8.46 to 8.51. The pattern is similar to the one obtained in the simpler rotating flow of the previous chapter. The F^r_{11} element (Fig. 8.46) is slightly larger than the rest of the elements of $\mathbf{F^r_b}$ (Figs. 8.47 to 8.49), which are all similar in size. The diagonal elements of $\mathbf{F^r_b}$ are positive while the off-diagonal elements are negative. The off-diagonal elements of $\mathbf{F^i_b}$ (Figs. 8.50 and 8.51) are about four times as small as the corresponding real parts of $\mathbf{F^i_b}$, and are hence less significant. All of the backscatter elements are significantly anisotropic near the truncation scale, being peaked between wavenumber $20 < m < 40$, which roughly corresponds to the peaks of $-\mathbf{M^r_d}$.

The mean subgrid forcing, $\overline{\mathbf{f}}$, elements are shown in Fig. 8.52. Only $m = 0$ elements are shown. The dominant contribution to $\overline{\mathbf{f}}$ comes from the conversion of mean baroclinic potential energy from the forced large scale $m = 0$ modes ($n \leq 15$). It is this subgrid contribution that the Gent-McWilliams skew flux attempts to parameterize (see Section 5.2). However, as discussed in Section 5.7, the focus of this study is on the parameterization of the transient subgrid flux. Since the simulation is at steady state, we can account for the mean subgrid tendency by simply adding $\overline{\mathbf{f}}$ to the tendency in the T63 LES, as discussed

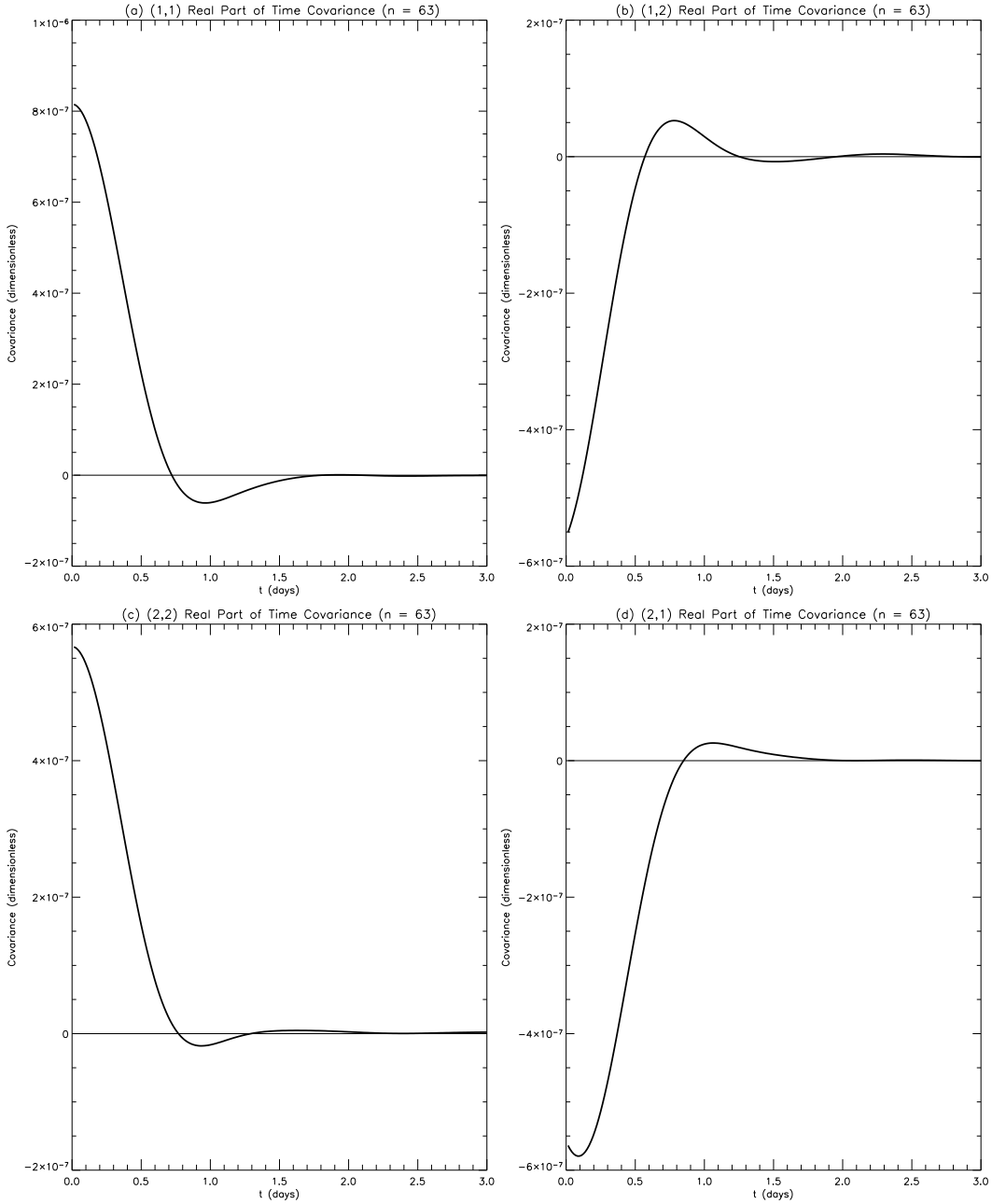

Figure 8.37: Time covariances of the subgrid tendency matrix in the PV formulation: (a) Level 1; (b) Level 2; (c)Level 1/Level 2; (d)Level 2/Level 1 ($n = 63$).

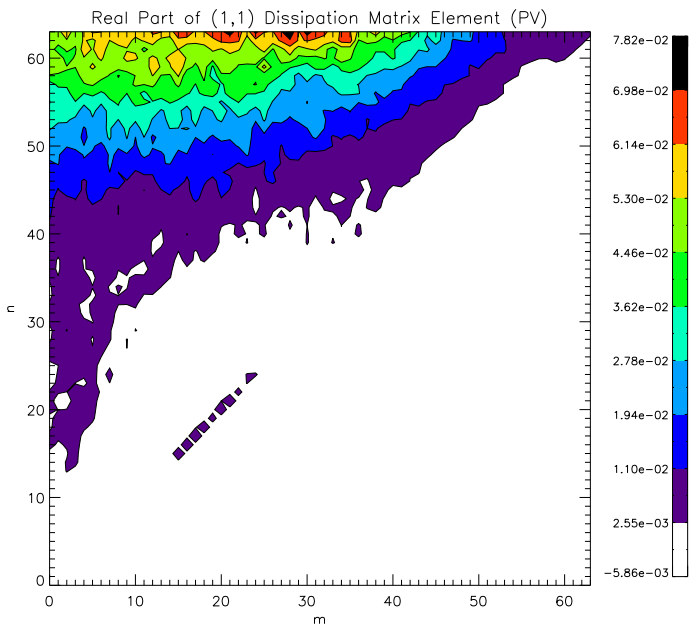

Figure 8.38: The $-M^r_{11}$ anisotropic matrix element of the drain dissipation matrix in the PV formulation (T63).

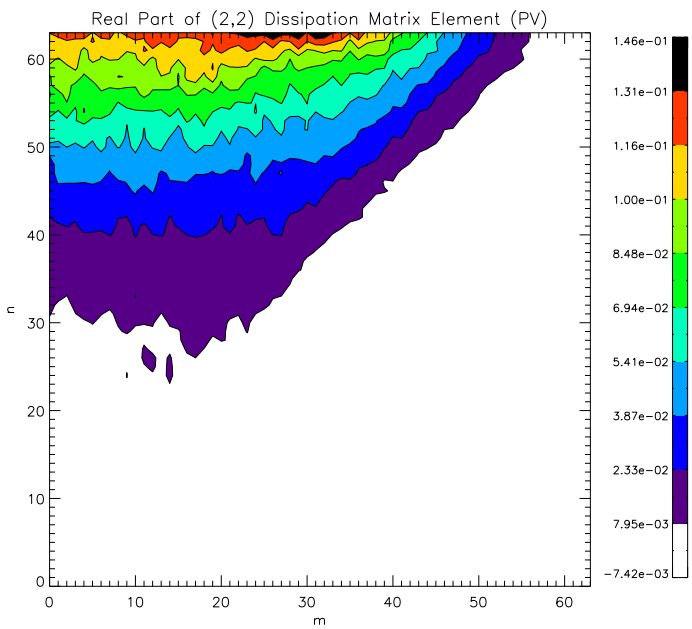

Figure 8.39: The $-M^r_{22}$ anisotropic matrix element of the drain dissipation matrix in the PV formulation (T63).

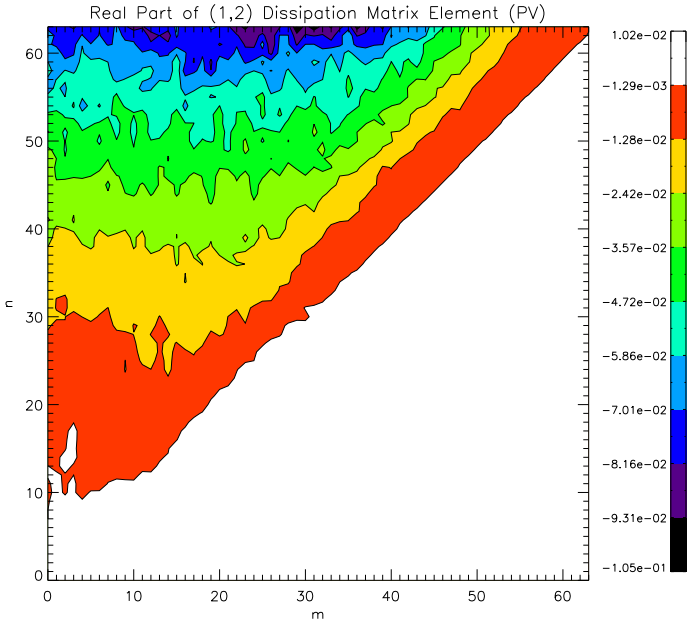

Figure 8.40: The $-M_{12}^{r}$ anisotropic matrix element of the drain dissipation matrix in the PV formulation (T63).

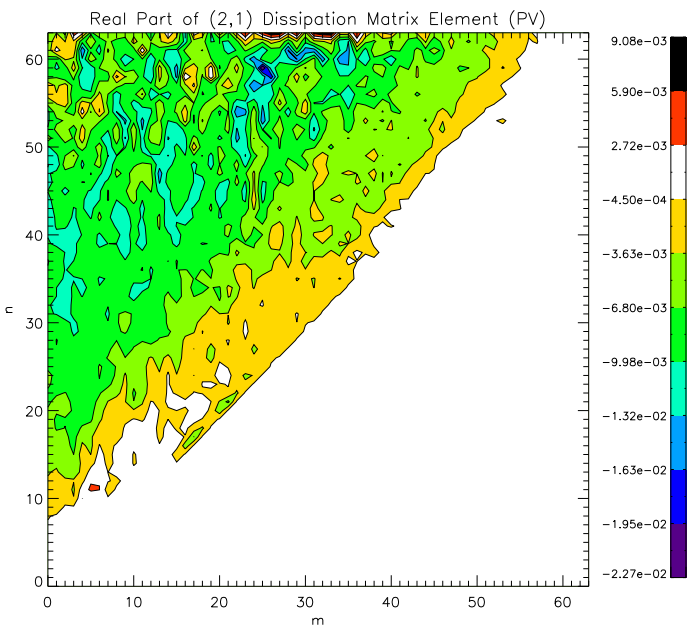

Figure 8.41: The $-M_{21}^{r}$ anisotropic matrix element of the drain dissipation matrix in the PV formulation (T63).

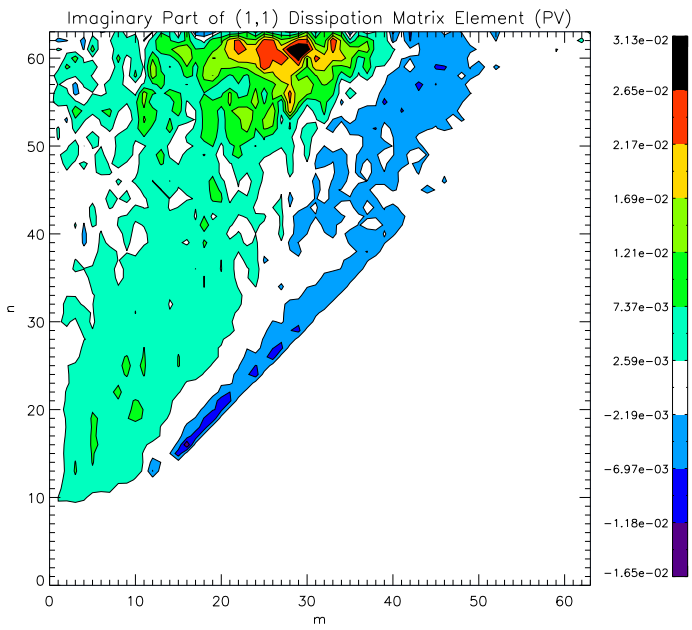

Figure 8.42: The M^i_{11} anisotropic matrix element of the drain dissipation matrix in the PV formulation (T63).

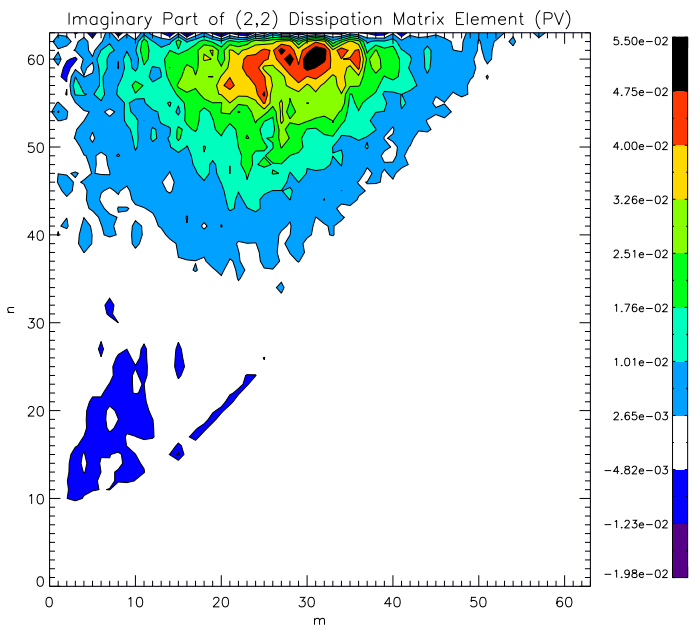

Figure 8.43: The M^i_{22} anisotropic matrix element of the drain dissipation matrix in the PV formulation (T63).

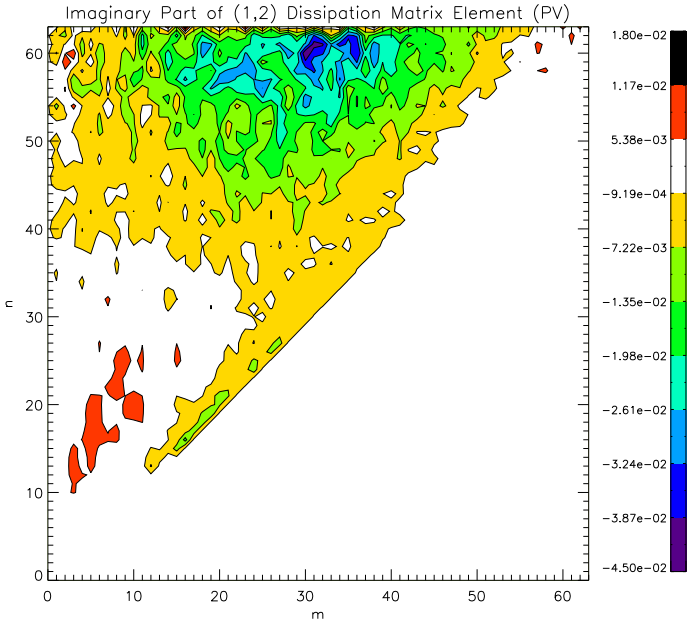

Figure 8.44: The M^i_{12} anisotropic matrix element of the drain dissipation matrix in the PV formulation (T63).

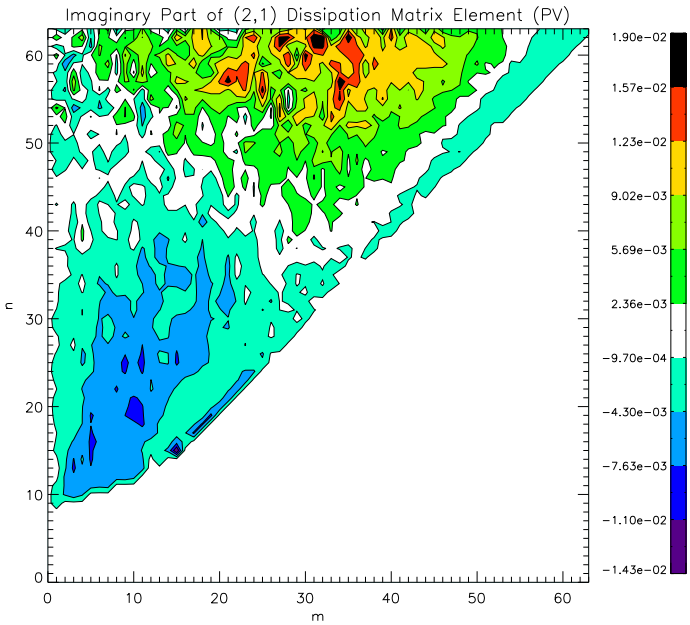

Figure 8.45: The M^i_{21} anisotropic matrix element of the drain dissipation matrix in the PV formulation (T63).

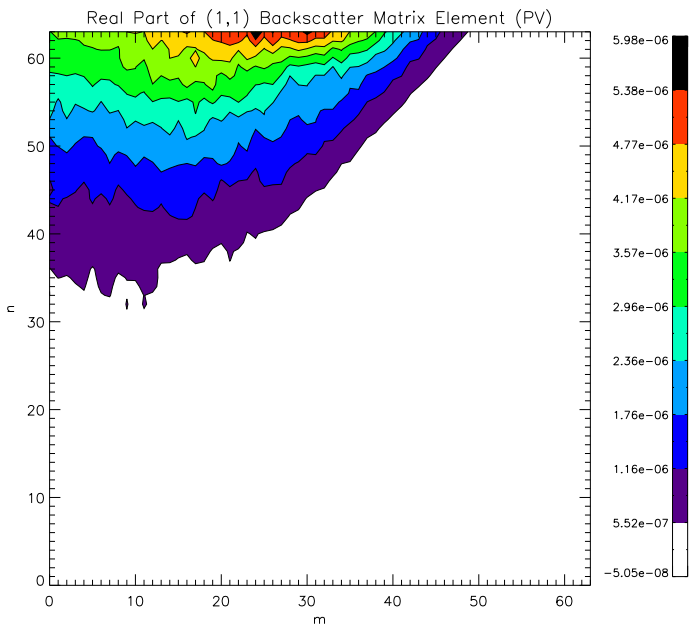

Figure 8.46: The F_{11}^r anisotropic matrix element of the drain dissipation matrix in the PV formulation (T63).

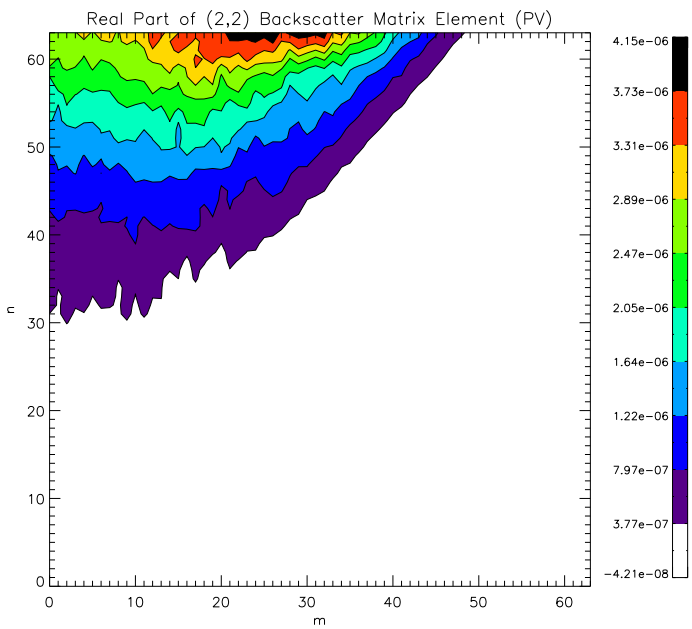

Figure 8.47: The F_{22}^r anisotropic matrix element of the drain dissipation matrix in the PV formulation (T63).

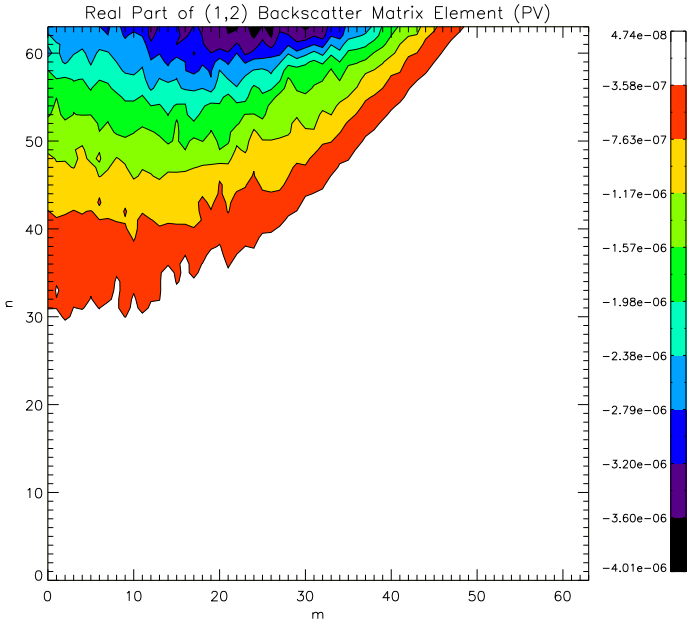

Figure 8.48: The F^T_{12} anisotropic matrix element of the drain dissipation matrix in the PV formulation (T63).

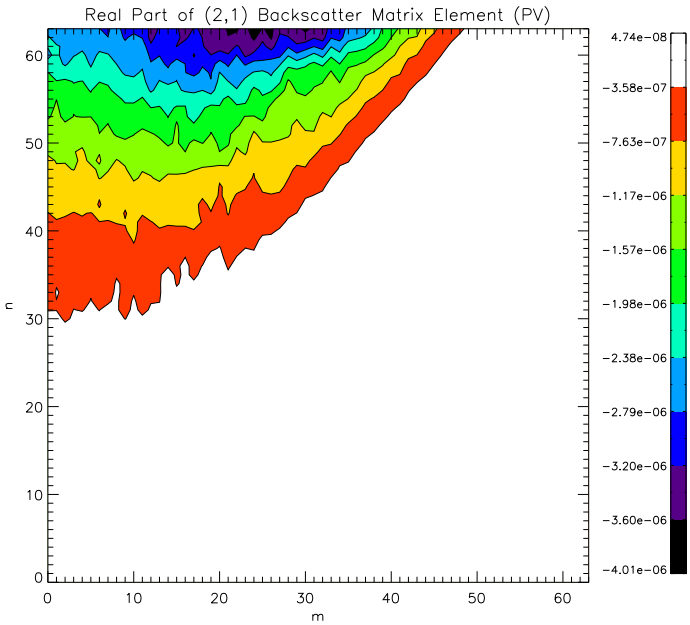

Figure 8.49: The F^T_{21} anisotropic matrix element of the drain dissipation matrix in the PV formulation (T63).

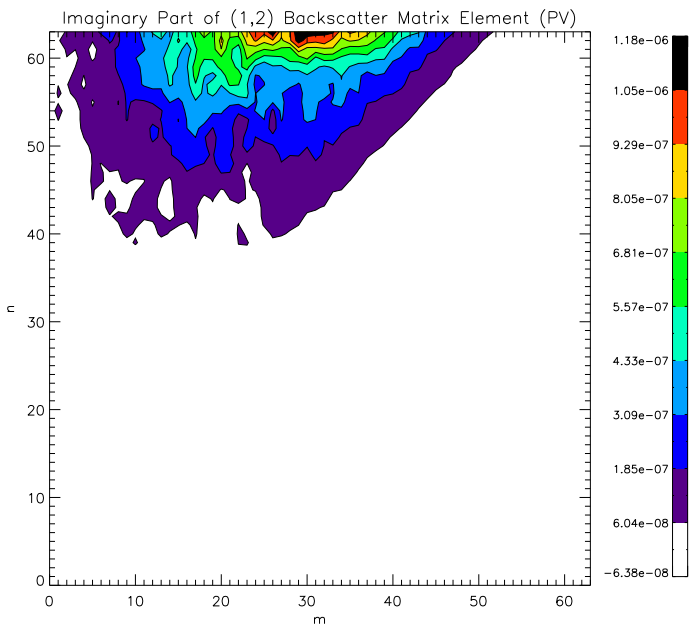

Figure 8.50: The F^i_{12} anisotropic matrix element of the drain dissipation matrix in the PV formulation (T63).

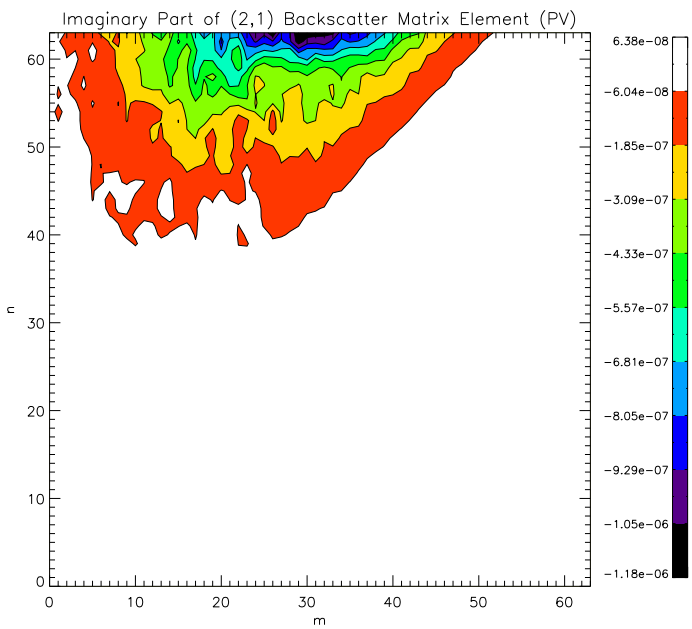

Figure 8.51: The F^i_{21} anisotropic matrix element of the drain dissipation matrix in the PV formulation (T63).

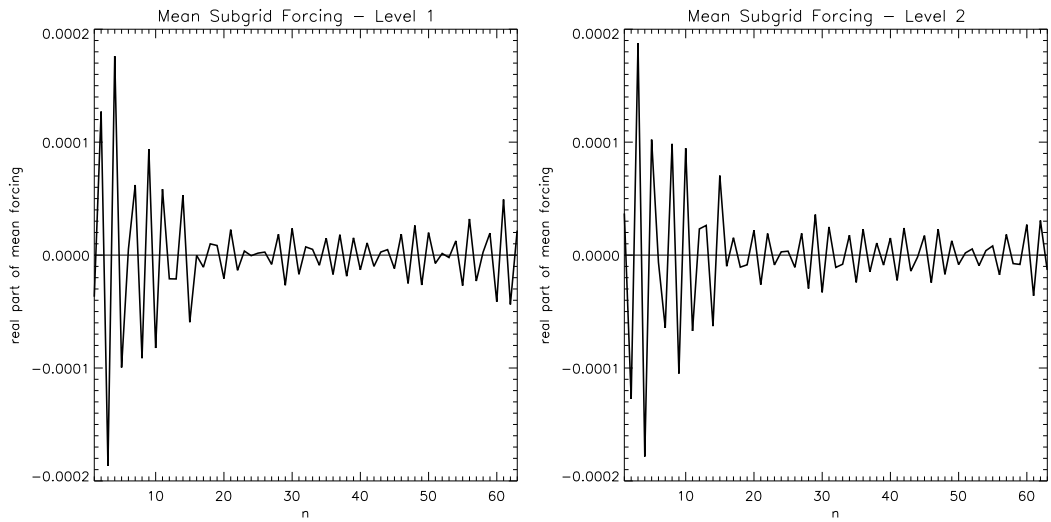

Figure 8.52: The mean subgrid forcing, $\bar{\mathbf{f}}$, vector elements (T63).

in Sections 5.5 and Appendix F. We can define

$$\mathbf{q^{eddy}} = \frac{1}{\kappa}\bar{\mathbf{f}} \tag{8.2}$$

so that the effective relaxation in Eq. 8.1 is modified in the LES to $\kappa\left[\left(q_i^{rel} + q_i^{eddy}\right) - q_i\right]$. Figure 8.53 shows the zonal current, u_i^{eddy}, corresponding to q_i^{eddy}. There is a strong contribution in the vicinity of the current core (60^oS). The effect of the forcing on each level at this location is to enhance the current, with the bottom level being enhanced more than the top level. This sets up a negative shear which reduces the potential energy of the flow. There also seems to be a reduction of the flow, at around 80^oS, with the top level being reduced more than the bottom level, but this is outside the region of the current core. The ratio measuring the strength the eddy-induced zonal current compared to the total current is $\left|\frac{u_1^{eddy}-u_2^{eddy}}{u_1^{rel}-u_2^{rel}}\right| \approx 0.1$ at this, relatively high, resolution. Generally, it increases with reduced resolution as more baroclinically unstable modes are unresolved.

8.2.3 LES at T63

Large eddy simulations were performed at T63 using bare parameters and the stochastic parameterization. The results for the bare parameter LES are shown in Figs. 8.54 and 8.55, respectively. As in the simpler oceanic problems of the previous chapter, there is a dramatic rise of the tail for the n spectrum and an unnatural flatness for the m spectrum. The potential energy n spectrum is also displayed in 8.56 for the purpose of examining the large scale potential energy. There seems to be a reduction of potential energy for $n < 4$ and a gain for larger wavenumbers. The results of the LES with stochastic parameterization are shown in Figs. 8.57 and 8.58. The LES at T63 is seen to be in reasonably good agreement with the LES at T126. There is some drift, however, notably an overestimation for wavenumbers $n > 30$. There is also a slight overestimation for the largest scales, which consist mainly of mean energy. For the m spectra, the drift is seen for

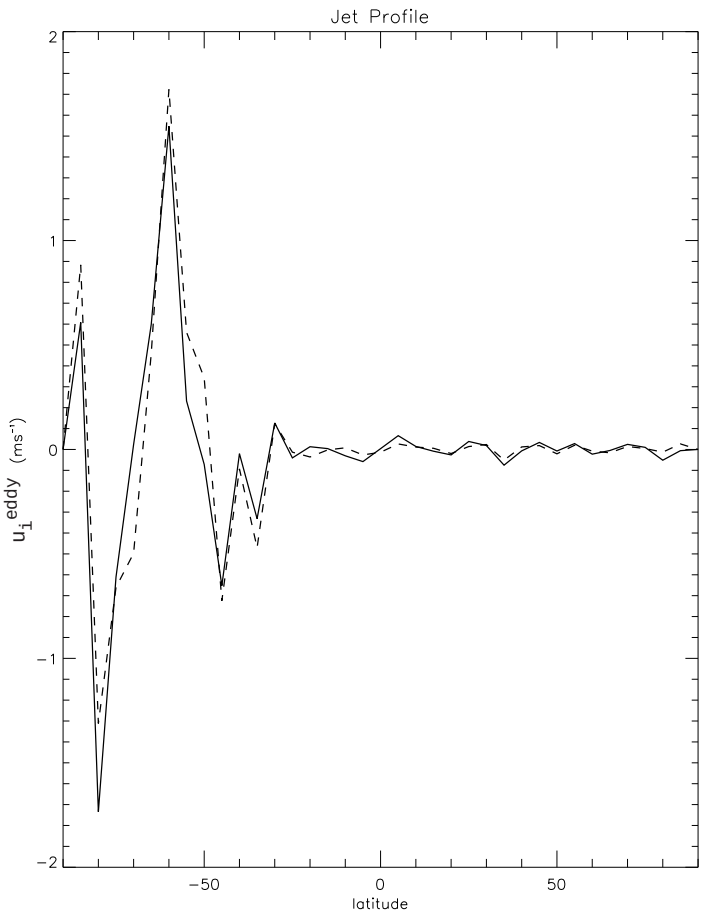

Figure 8.53: The subgrid-eddy induced zonal current relaxation field, u_i^{eddy}, zonally averaged (T63): Level 1 (solid) and Level 2 (dashed).

wavenumbers m somewhat greater than 10. A similar pattern of error was observed for the T126 LES when compared with the T252 DNS (see Figs. 8.30 and 8.31). This error could be related to insufficient sampling, but at this stage we cannot confirm that this is indeed the case. Notwithstanding the errors, it is clear that the parameterization improves the simulation tremendously. In fact, as can be seen from the bare parameter results, without the parameterization, the T63 LES bears no resemblance to the T126 LES. We again mention that this is quite different from the atmospheric simulations at this resolution, in which the parameterization is only important in maintaining the spectrum relatively near the truncation scale.

Figure 8.59 shows the kinetic energy time-series for (m averaged) wavenumber $n = 3$, for the T126 LES. As for the atmospheric case, the aim is to examine the time evolution of some large scale motion, and the choice of $n = 3$ is arbitrary. The corresponding diagnostic for the T63 LES is shown in Fig. 8.60. As can be deduced from the kinetic energy n spectrum (Fig. 8.57) for Level 1, there is a slight overestimation of the mean kinetic energy for the T63 LES. There is also a corresponding underestimation for Level 2 (spectra not shown), which can be seen in Figs. 8.59 and 8.60. As far as the amplitudes of the fluctuations are concerned, the T63 LES underestimates the amplitudes slightly. The lower resolution LES, then, appears to stabilize the system more than it should. One would imagine that this effect is proportional to the integration time, τ, since longer integration times generally lead to enhanced values of $\mathbf{M_d}$ and $\mathbf{F_b}$, and this tends to 'clamp down' the system more. Of course, as one reduces the integration time, $\mathbf{M_d} \to \mathbf{M_n}$ and $\mathbf{F_b} \to \mathbf{0}$, and as discussed in previous chapters, this makes the system so 'loose' that it blows up numerically. One would imagine then that an optimal integration time could be found such that the system has the right amount of fluctuation energy. This is however not pursued in this thesis. Finally, we compare the zonally averaged currents for the LES at T63 and T126 in Fig. 8.61. The agreement is in general good except at the core (60^oS), where the T63 LES overestimates the current by about 0.3 ms^{-1}, which is an error of about 10%.

8.2.4 Subgrid-scale Parameterizations at T15

The generic problem of oceanic subgrid-scale parameterizations is how to parameterize both the mean-transient and transient-transient interactions in a turbulent flow in which, firstly, the transient energy injection is not resolved, and secondly, the transient injection is fed by the resolved mean field. The truncations in the oceanic problems that we have examined so far are only partly representative of this generic problem. The reason is that in truncating the flow at T63, which is the minimum resolution that we have used thus far, we have retained a large portion of the baroclinically-unstable waves. Hence, we are only partially addressing the generic problem in which, ideally, no baroclinically unstable waves are retained. The question that we seek to answer now is whether the truncation at T63 is representative of the dynamics to be found in all realistic oceanic simulations. Is there anything new to be learned by performing a more severe truncation? The difficulty with more severe truncations is that we are further away from the inertial range, and hence the features of the flow are not as universal as in the inertial range. Thus, the subgrid-scale parameters may vary greatly in size and structure from flow to flow. Nonetheless, we shall proceed with an artificial truncation at $N_* = 15$. At this resolution, we expect most of the baroclinically unstable waves to be unresolved.

The subgrid fluxes, represented by the matrix $\mathcal{F}$, in PV space, are visually quite similar

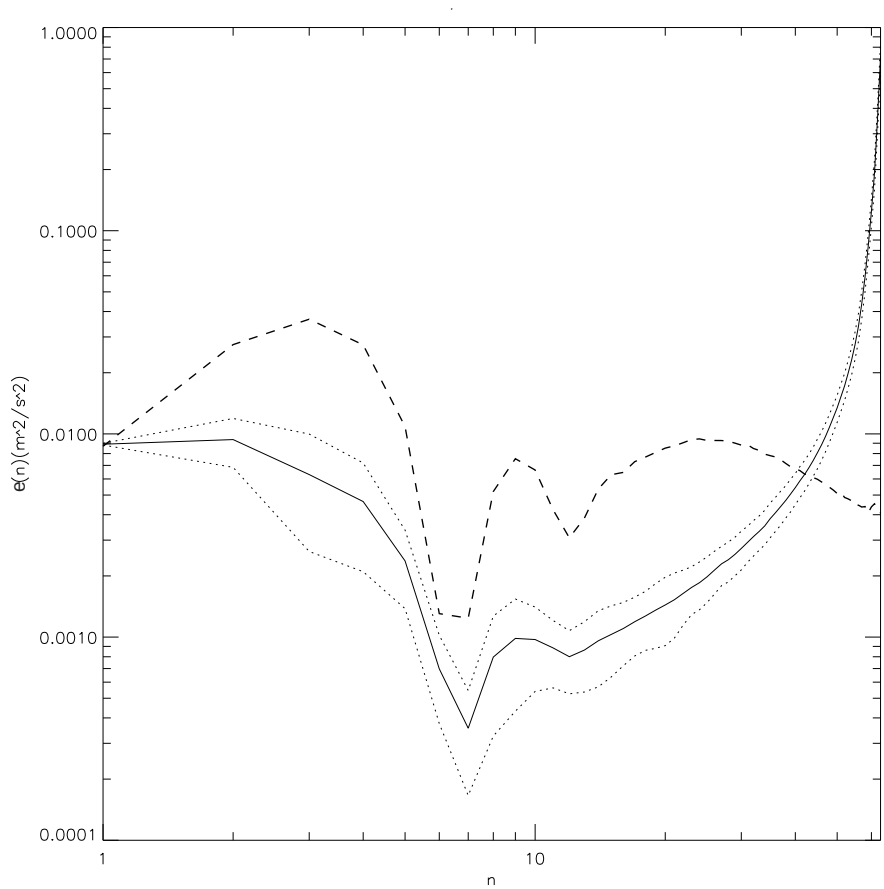

Figure 8.54: Energy spectra (Level 1) as functions of total wavenumber (n): kinetic energy for T63 LES with bare dissipation (solid); LES kinetic energy plus and minus standard deviation (dotted); and T126 LES kinetic energy (dashed).

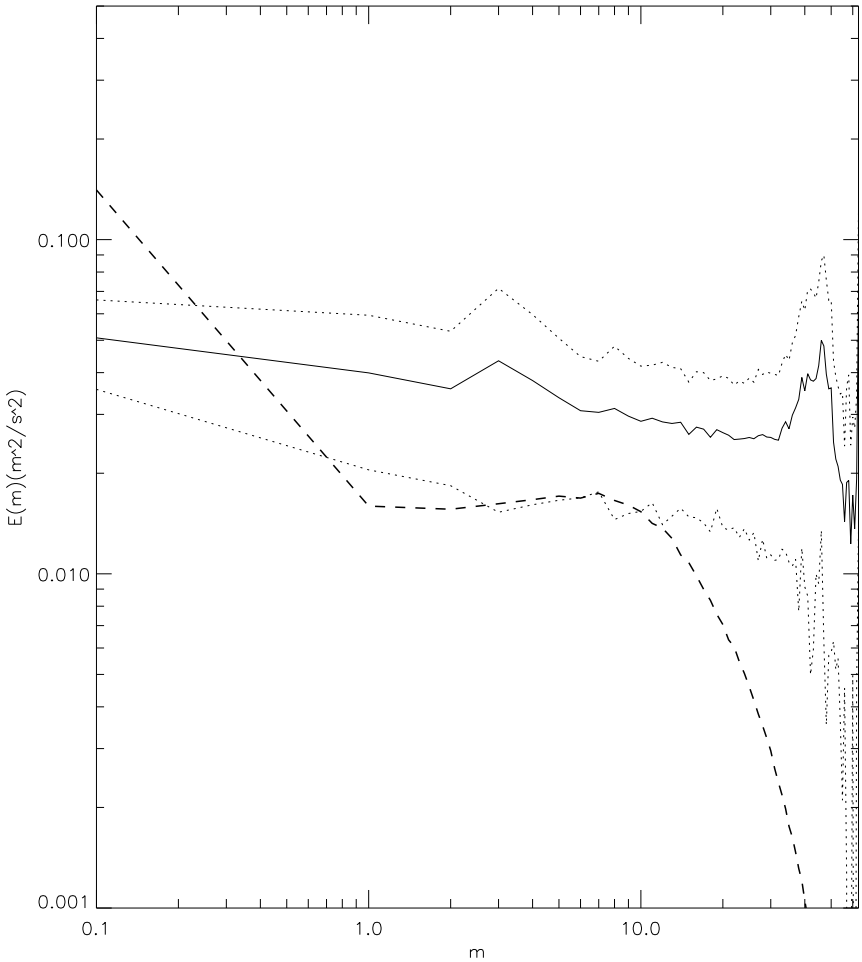

Figure 8.55: Energy spectra (Level 1) as functions of zonal wavenumber (m): kinetic energy for T63 LES with bare dissipation (solid); LES kinetic energy plus and minus standard deviation (dotted); and T126 LES kinetic energy (dashed).

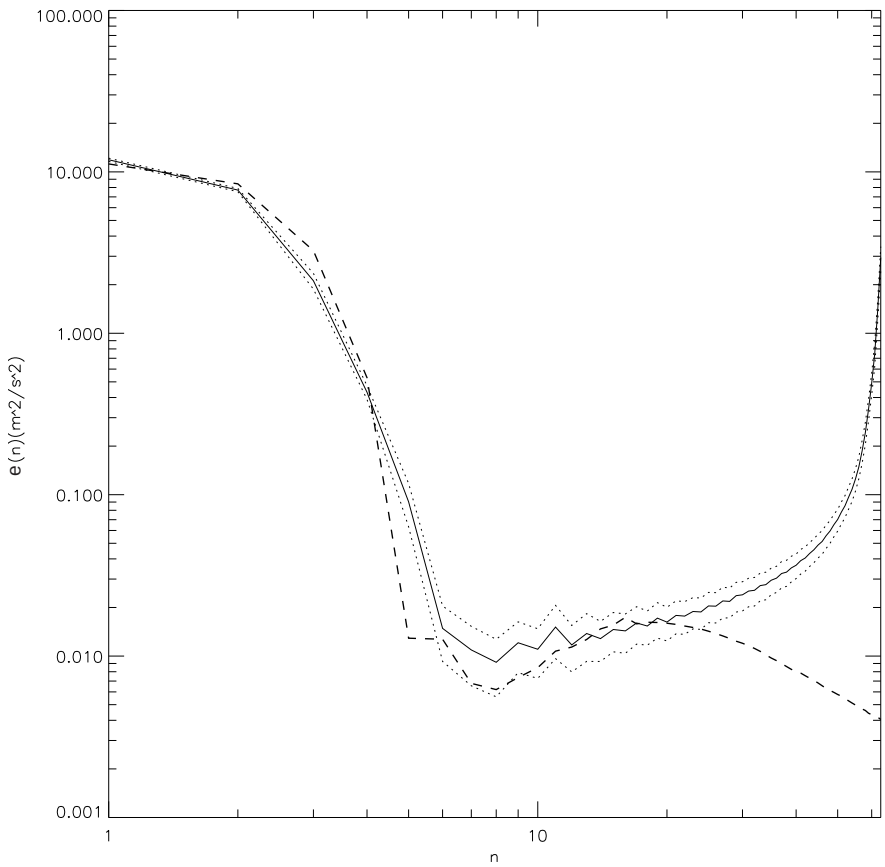

Figure 8.56: Energy spectra (Level 1) as functions of total wavenumber (n): potential energy for T63 LES with bare dissipation (solid); LES kinetic energy plus and minus standard deviation (dotted); and T126 LES potential energy (dashed).

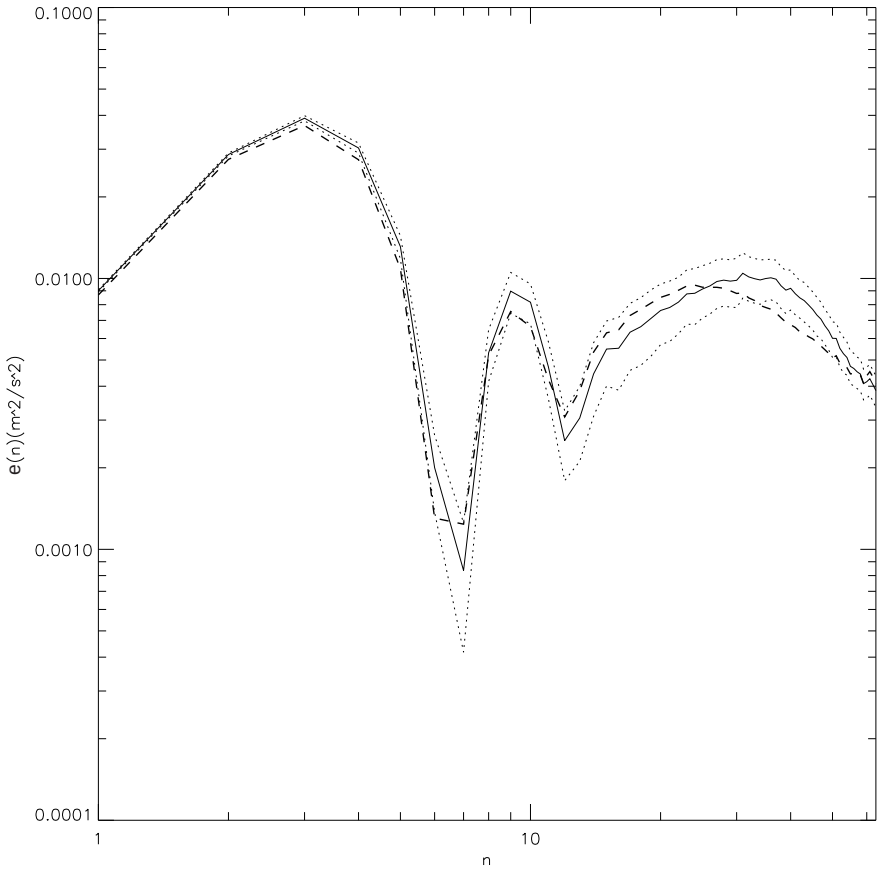

Figure 8.57: Energy spectra (Level 1) as functions of total wavenumber (n): kinetic energy for T63 LES with renormalized drain dissipation and backscatter (solid); LES kinetic energy plus and minus standard deviation (dotted); and T126 LES kinetic energy (dashed).

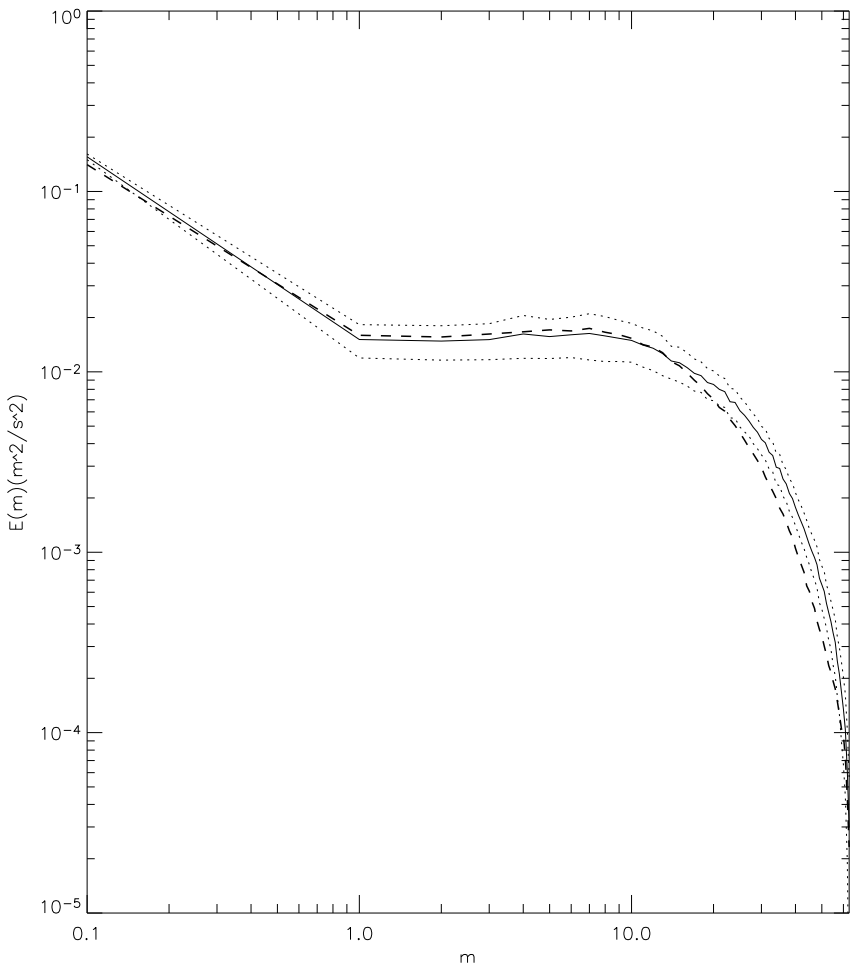

Figure 8.58: Energy spectra (Level 1) as functions of zonal wavenumber (m): kinetic energy for T63 LES with renormalized drain dissipation and backscatter (solid); LES kinetic energy plus and minus standard deviation (dotted); and T126 LES kinetic energy (dashed).

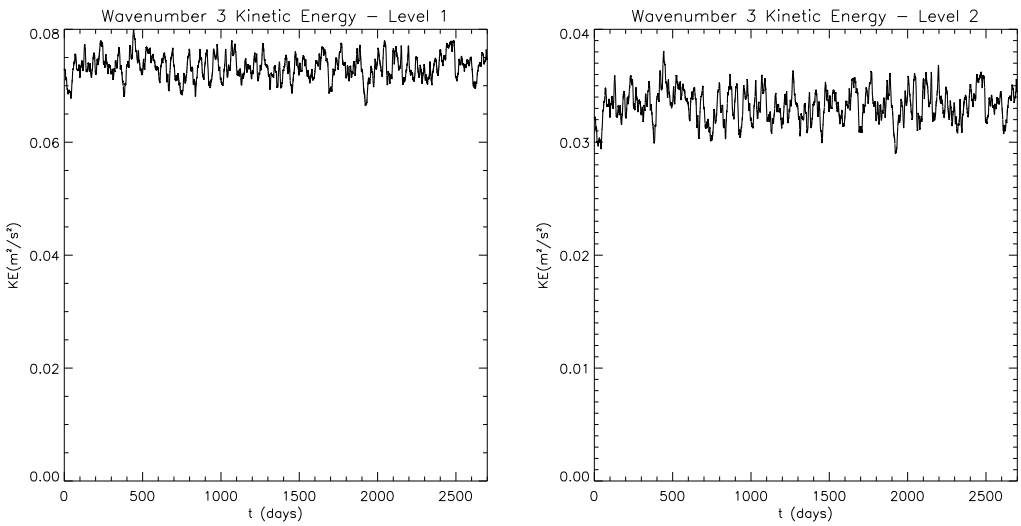

Figure 8.59: Time-series of the wavenumber 3 kinetic energy of the oceanic LES (with rotation and jets) at T126.

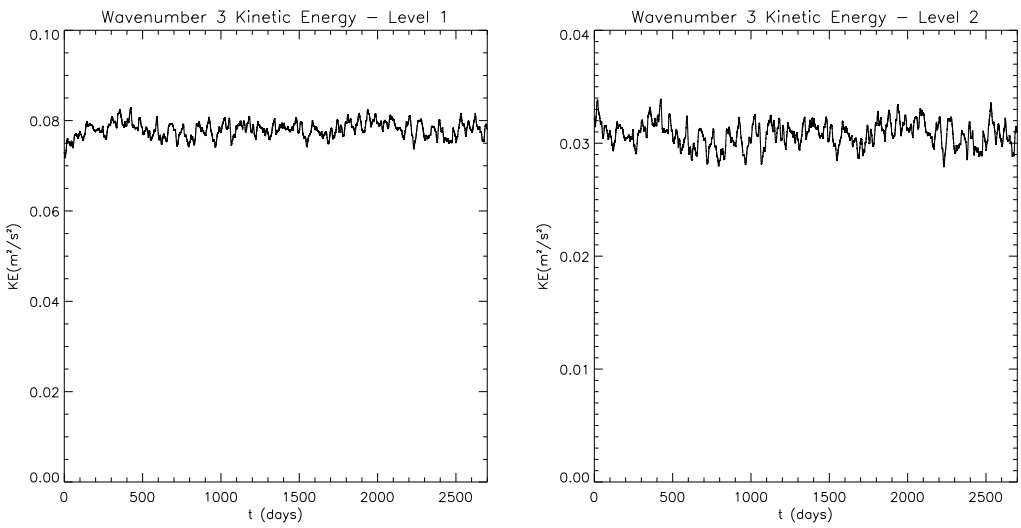

Figure 8.60: Time-series of the wavenumber 3 kinetic energy of the oceanic LES (with rotation and jets) at T63 using the drain dissipation and stochastic backscatter parametrization.

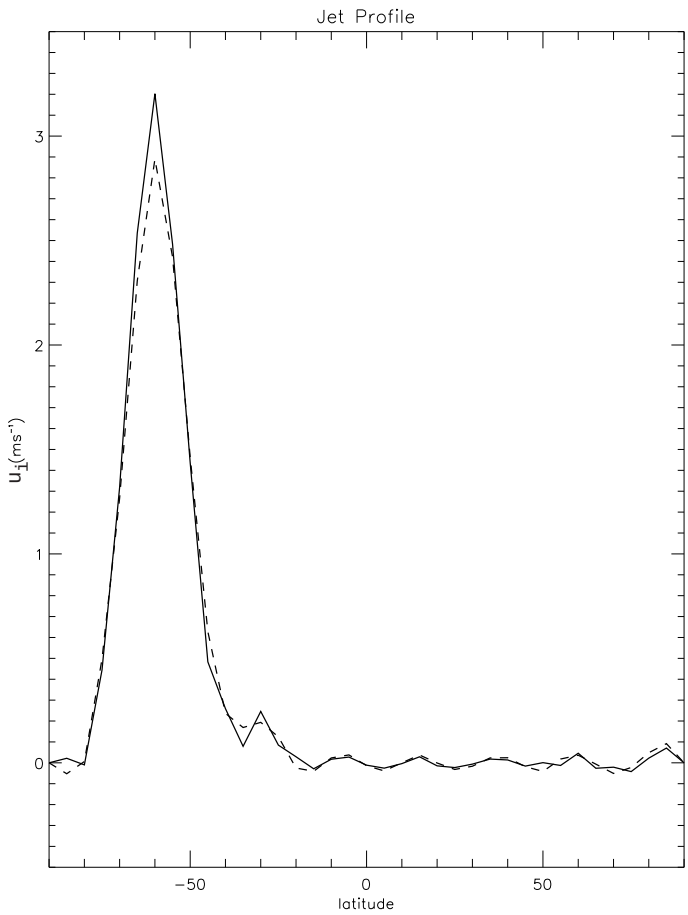

Figure 8.61: The zonally averaged current u_1 (top level) using the LES at T63 (solid) and the corresponding diagnostic for the LES at T126 (dashed).

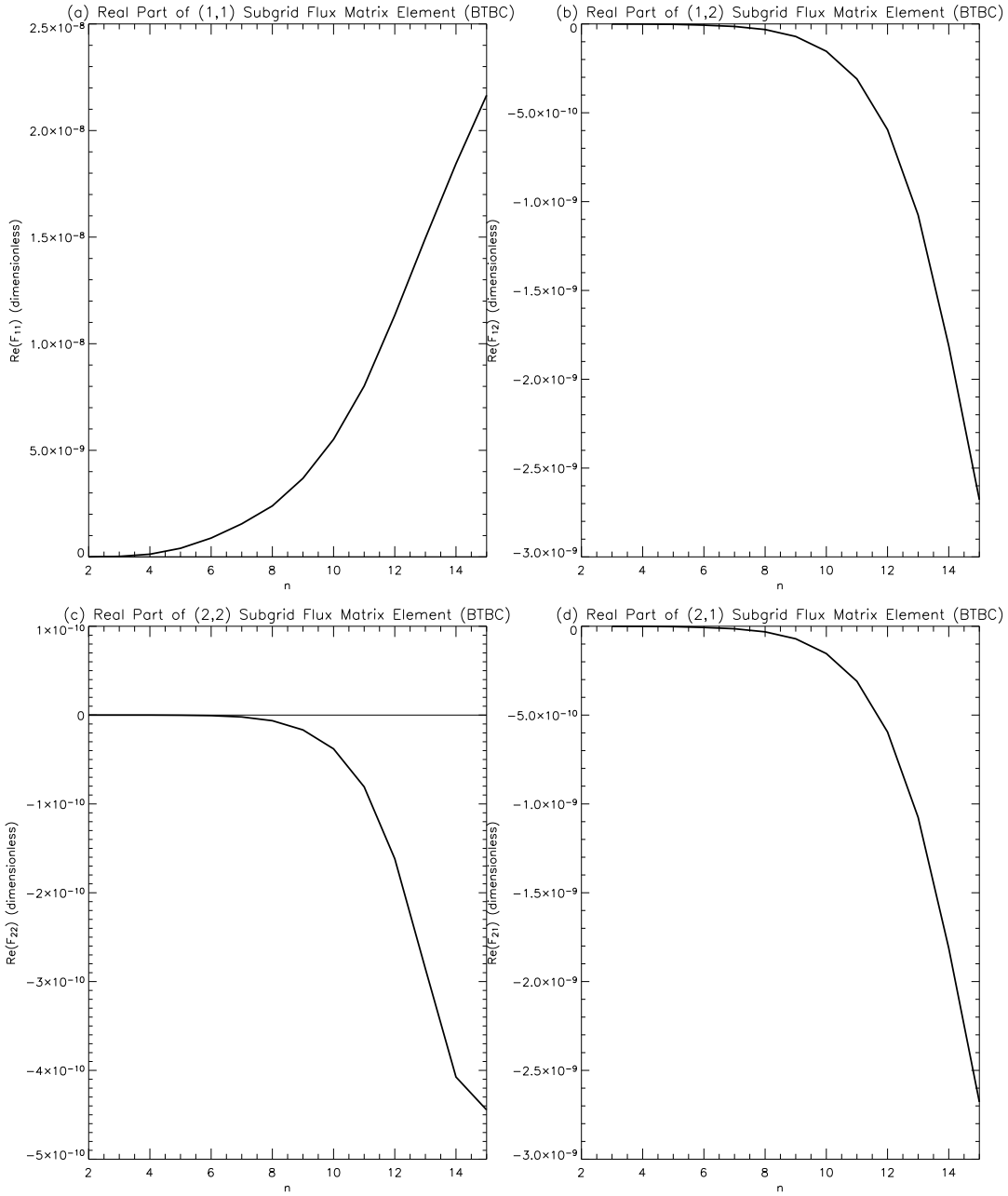

Figure 8.62: Elements of the real part of the isotropic subgrid flux matrix in the BTBC formulation: (a) $\mathcal{F}^r_{11}$; (b) $\mathcal{F}^r_{12}$; (c) $\mathcal{F}^r_{22}$; and (d) $\mathcal{F}^r_{21}$ (T15).

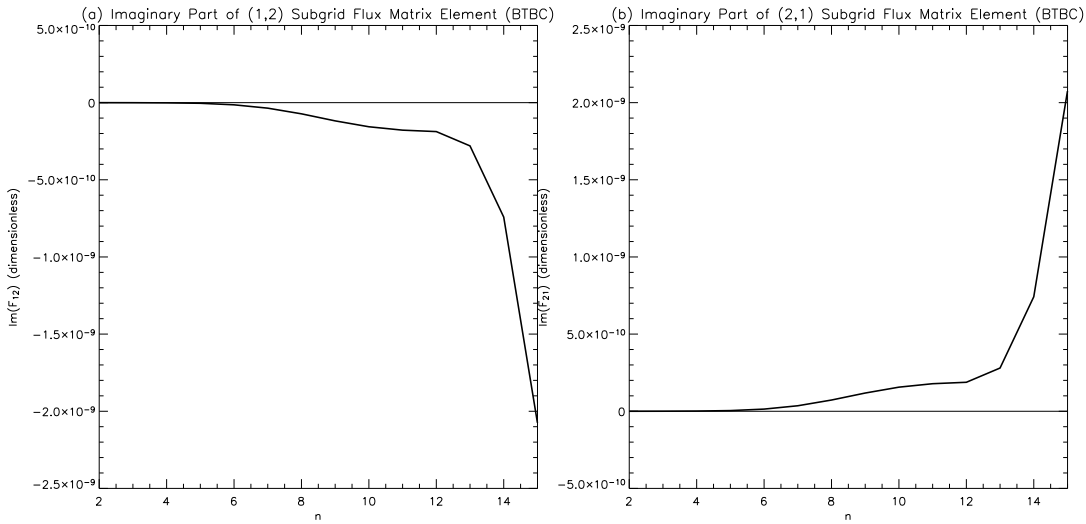

Figure 8.63: Off-diagonal elements of the imaginary part of the isotropic subgrid flux matrix in the BTBC formulation: (a) $\mathcal{F}^i_{12}$; (b) $\mathcal{F}^i_{21}$ (T15).

to the corresponding fluxes at T63, except for the fact the former seem, surprisingly, more scale selective. These fluxes are not shown; instead we display the fluxes in BTBC space, in Figs. 8.62 and 8.63, where the differences between the two types of truncation are more apparent. The barotropic energy flux is more striking as it is quite different to the corresponding flux at T63. Instead of distinct injection and dissipation regions, there is only one dissipation region, which rises to a cusp near the truncation scale. Hence, clearly, at T15 we are in the spectral region where the barotropic energy is inversely cascaded from the unresolved injection scale. This may also explain why the fluxes seem more scale selective, namely, that the energy injection region is sufficiently far away, and a pure cascade is operating. The baroclinic flux is completely dissipative, which supports the claim of QG phenomenology that these fluxes are oppositely directed in spectral space. Interestingly, it is more than two orders of magnitude smaller than the barotropic flux, which suggests that there is hardly any injection of *transient* baroclinic energy at large scales. This again supports the idea that this is a truly non-eddy-resolving truncation.

The matrices $\mathbf{M_d}$, $\mathbf{F_b}$, and $\bar{\mathbf{f}}$ are calculated using a decorrelation time of 16 days. This is more than sufficient to capture the decorrelation time of the subgrid tendency (not shown), which is about 10 days. The matrix elements $\mathbf{M_d}$ and $\mathbf{F_b}$ are highly anisotropic as expected. They are shown in Appendix I. The mean subgrid forcing, $\bar{\mathbf{f}}$, is shown in Fig. 8.64. Structurally, this is similar to the corresponding vector elements at T63 (see Fig. 8.52), but in terms of magnitude, the T15 elements are as much as an order of magnitude greater at the largest scales ($n < 5$). This is consistent with the fact that at T15, there are more unresolved baroclinically unstable modes, and hence the difference in potential energy between high resolution and low resolution simulations is greater. The corresponding eddy-induced ('bolus') relaxation current, u_i^{eddy}, in physical space is shown as a function of latitude, after zonal averaging, in Fig. 8.65. A comparison with the corresponding parameters at T63 (see Fig. 8.53) reveals that although the actual magnitudes of u_i^{eddy} are not that different, the *shears* in u_i^{eddy} are different for the two truncations. The ratio measuring the strength the residual circulation compared to the

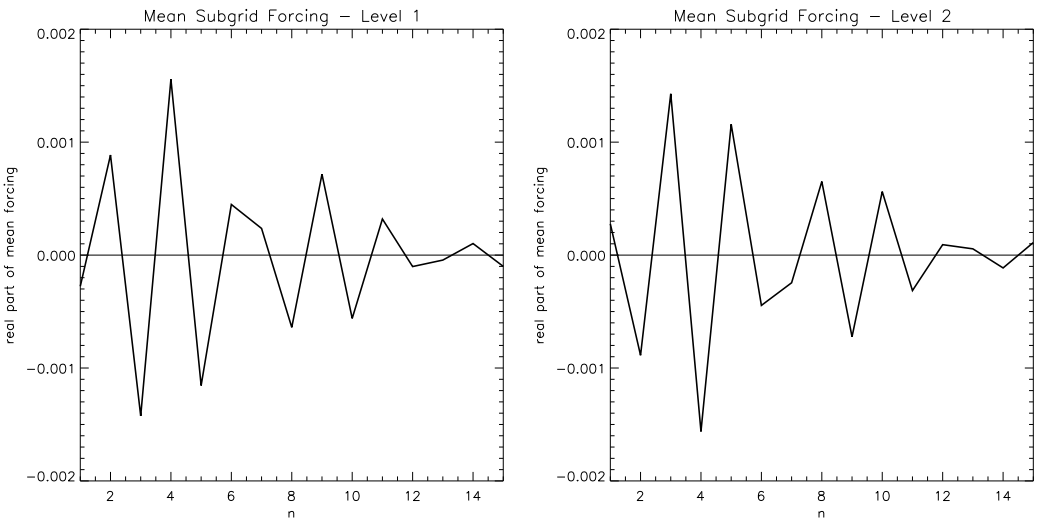

Figure 8.64: The mean subgrid forcing, $\overline{\mathbf{f}}$, vector elements (T15).

total circulation is $\left|\frac{u_1^{eddy}-u_2^{eddy}}{u_1^{rel}-u_2^{rel}}\right| \approx 0.5$ while at T63 it is only 0.1.

8.2.5 LES at T15

Large eddy simulations were performed with bare parameters and with the stochastic parameterizations. Figures 8.66, 8.67, and 8.68 show the results of the LES with bare parameters. The n spectrum demonstrates that there is an overestimation of Level 1 kinetic energy in the part of the spectrum dominated by mean fields and an underestimation near the truncation scale, which is dominated by transients. That the mean fields are being overestimated and the transients underestimated is also confirmed by the m spectrum which displays overestimation for $m = 0$ (dominated by mean fields) and underestimation for the rest (mostly transients). The potential energy n spectrum shows that potential energy is being overestimated at most scales, except near the truncation scale. It is not hard to interpret these results using QG phenomenology. There are hardly any baroclinically unstable modes at T15 hence there is no conversion of mean large scale potential energy into transient kinetic energy, which explains the overestimation of large scale mean energy and underestimation of transient kinetic energy seen in the spectra of the LES with bare parameters. The results of the LES using the stochastic parameterization are shown in Figs. 8.69 and 8.70. The agreement between the LES at T15 and T126 is excellent.

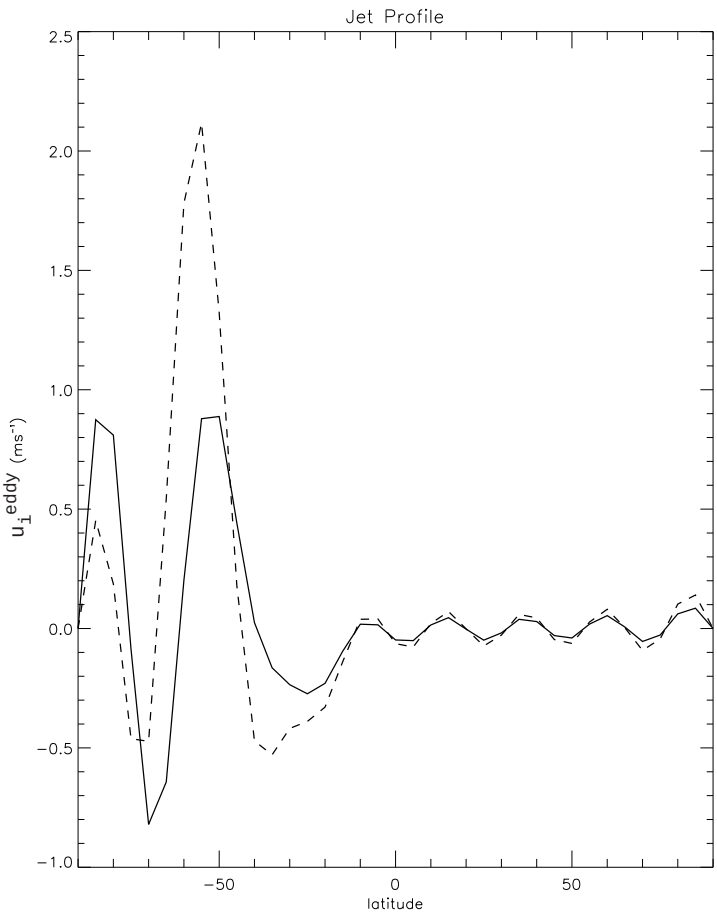

Figure 8.65: The subgrid-eddy induced zonal current relaxation field, u_i^{eddy}, zonally averaged (T15): Level 1 (solid) and Level 2 (dashed).

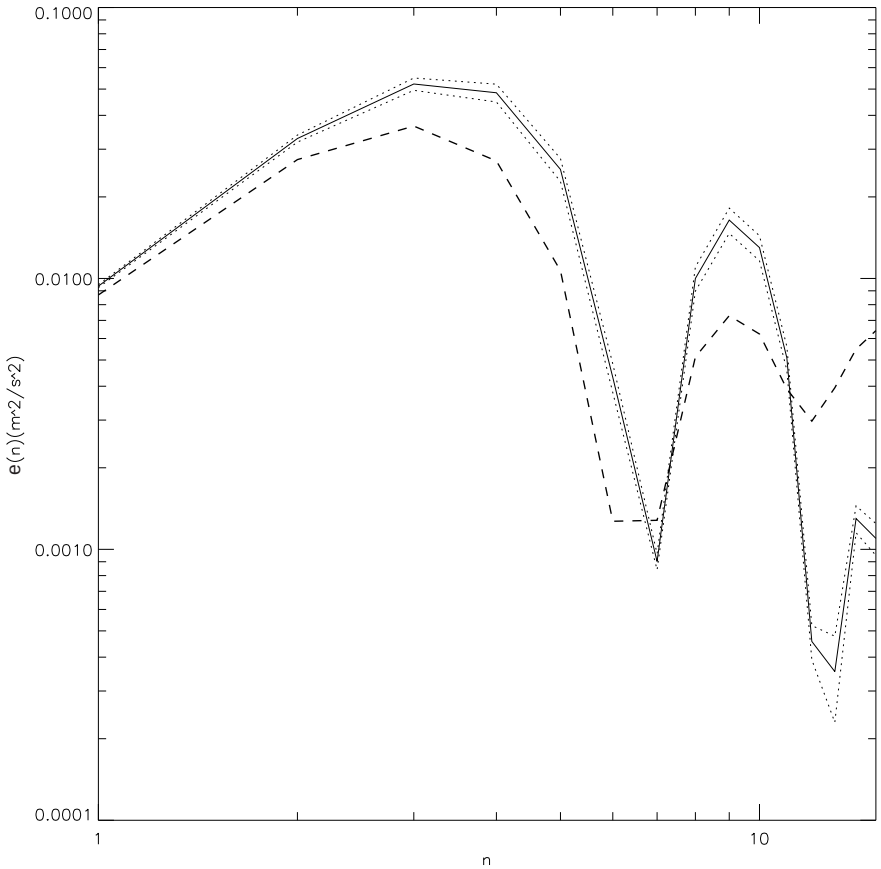

Figure 8.66: Energy spectra (Level 1) as functions of total wavenumber (n): kinetic energy for T15 LES with bare dissipation (solid); LES kinetic energy plus and minus standard deviation (dotted); and T126 LES kinetic energy (dashed).

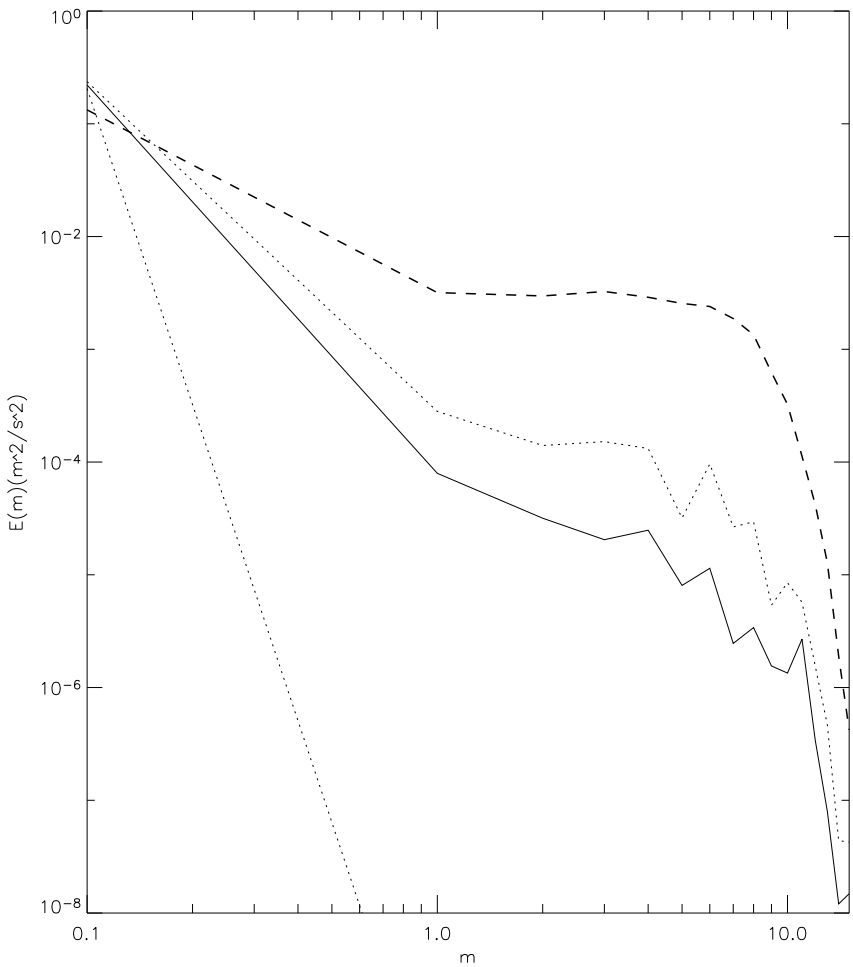

Figure 8.67: Energy spectra (Level 1) as functions of zonal wavenumber (m): kinetic energy for T15 LES with bare dissipation (solid); LES kinetic energy plus and minus standard deviation (dotted); and T126 LES kinetic energy (dashed).

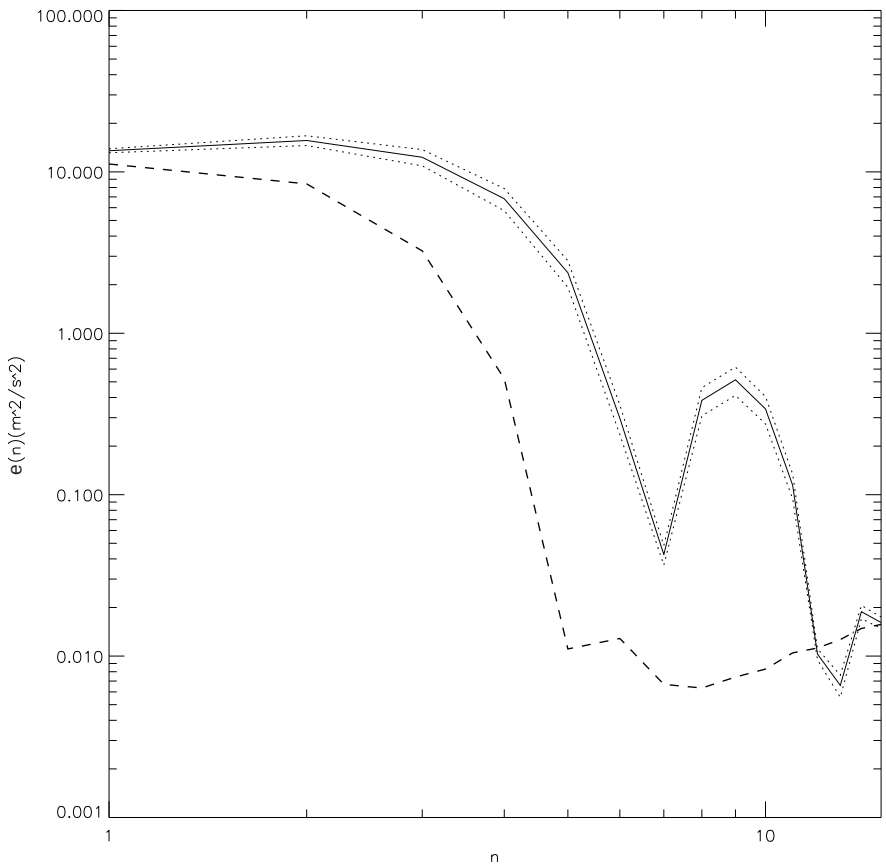

Figure 8.68: Energy spectra (Level 1) as functions of total wavenumber (n): potential energy for T15 LES with bare dissipation (solid); LES kinetic energy plus and minus standard deviation (dotted); and T126 LES potential energy (dashed).

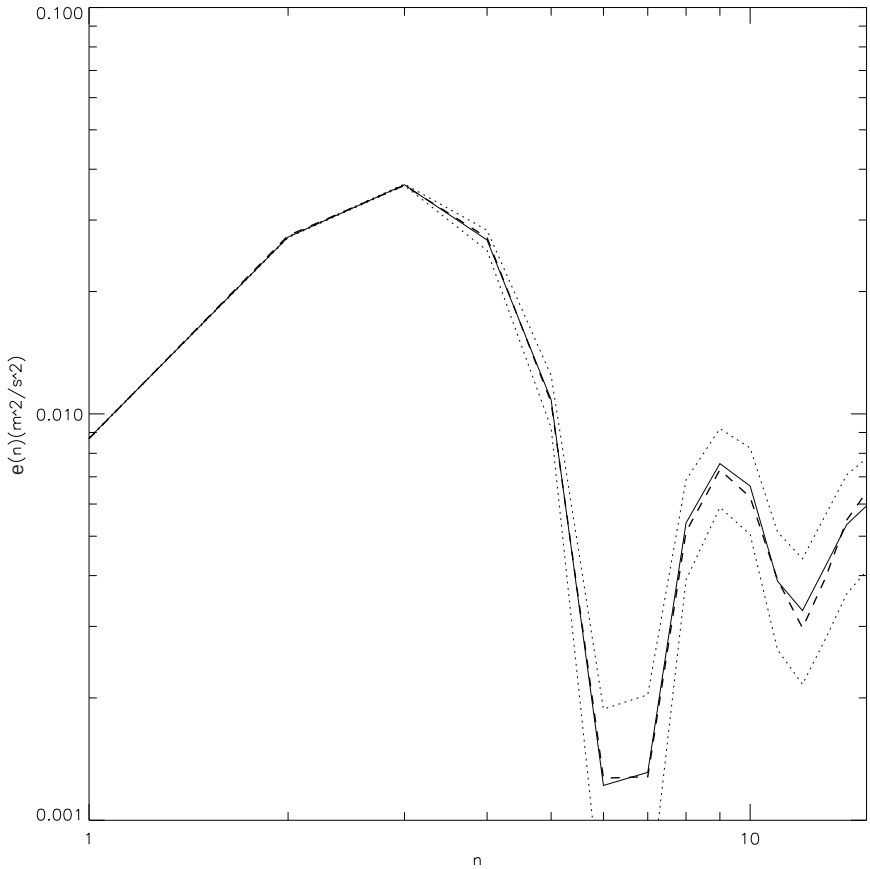

Figure 8.69: Energy spectra (Level 1) as functions of total wavenumber (n): kinetic energy for T15 LES with renormalized drain dissipation and backscatter (solid); LES kinetic energy plus and minus standard deviation (dotted); and T126 LES kinetic energy (dashed).

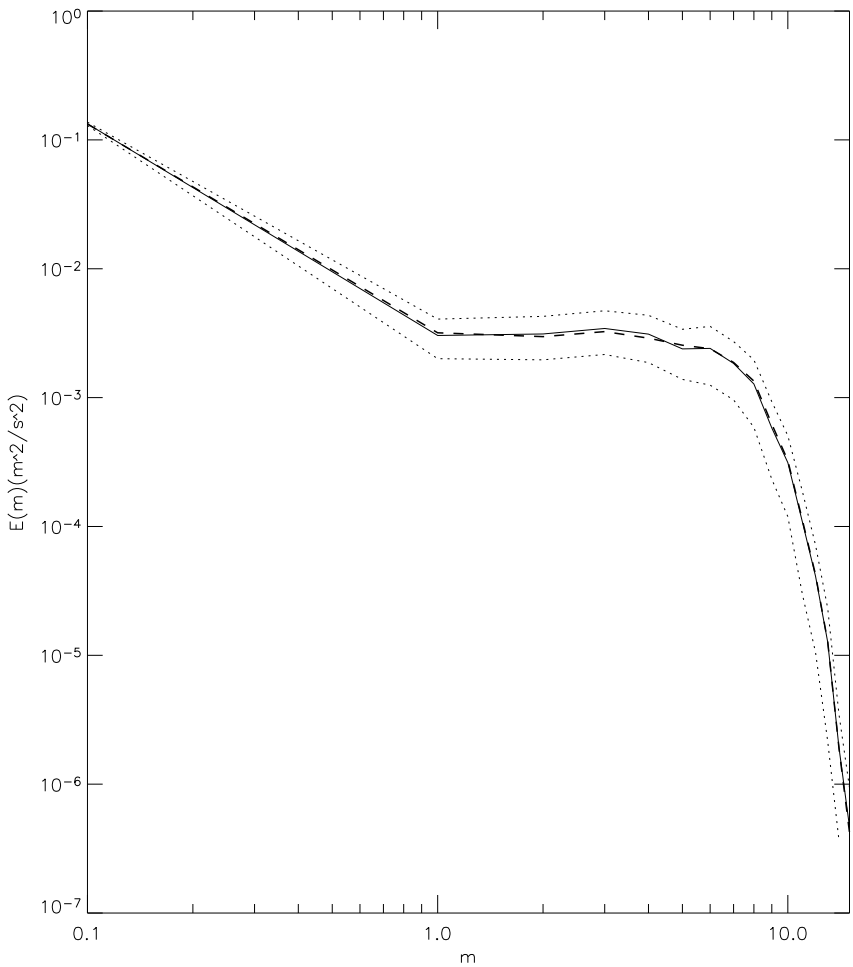

Figure 8.70: Energy spectra (Level 1) as functions of zonal wavenumber (m): kinetic energy for T15 LES with renormalized drain dissipation and backscatter (solid); LES kinetic energy plus and minus standard deviation (dotted); and T126 LES kinetic energy (dashed).

8.3 Discussion

In this chapter, we have increased the complexity of the mean-transient interaction by introducing zonal jets and currents. This corresponds to mean fields for a range of modes with wavenumbers $1 \leq n \leq 15$ and $m = 0$. For atmospheric flows, the matrix parameters calculated at T63 were found to have similar forms to those of the previous chapter. That is, the isotropized matrices $\mathbf{M_d}$ and $\mathbf{F_b}$ had very scale selective cusps; the matrices were also again found to be nearly diagonal. Furthermore, F^r_{11} was found to be an order of magnitude greater than F^r_{22} as in the previous problem, and presumably for similar reasons. The M^i_{11} element of the $\mathbf{M^i_n}$ matrix was found to be different to the corresponding element of the simpler problem in Chapter 7. An inspection of the full anisotropic matrices $\mathbf{M_n}$ (and indeed, $\mathbf{M^i_d}$) as a function of two dimensional wavenumber (m, n) revealed $\mathbf{M^i_n}$ to be significantly anisotropic, hence the unexpected result. It should be remembered that the diagonal elements of $\mathbf{M^i_n}$ do not contribute to the enstrophy flux, and so do not have any direct effect on the energy and enstrophy spectra. Intriguingly, the elements of $\mathbf{M^r_n}$ also seem to have some anisotropy, and yet when the isotropized parameters are used, excellent results are obtained. When running the LES, we have again found that errors induced in the spectrum due to the use of bare parameters are only confined to relatively large wavenumbers. An examination of the time evolution of large scale kinetic energy revealed that there are no significant differences in the amplitudes of the fluctuations nor their frequency between the LES and higher resolution DNS.

For oceanic simulations, the most significant difference in this chapter is that the subgrid mean forcing was found to be a relatively important term dynamically. This is because the change in potential energy of the large scale modes was a significant fraction of the available energy. At T63, the ratio $\left|\frac{u_1^{eddy}-u_2^{eddy}}{u_1^{rel}-u_2^{rel}}\right|$ was found to be around 0.1 near the core of the current. The matrix elements $\mathbf{M_d}$ and $\mathbf{F_b}$ were found to be more anisotropic than the corresponding elements of the simpler problems, without currents, considered in previous chapters. Otherwise, they were qualitatively similar to those found for the simple flow of Chapter 7. The deterministic parameterization displayed the same problem as that in previous chapters; namely, that the barotropic element is injective, and hence numerically unstable when modelled as a dissipation alone. Figure 8.71 shows the isotropized diagonal barotropic matrix elements $(-M^r_{11})$ of the net, $-\mathbf{M^r_n}$, and drain, $-\mathbf{M^r_d}$, dissipation matrix elements in the BTBC formulation at T63. The matrix element in the deterministic formulation is completely negative at all scales, but the corresponding element in the stochastic formulation is only slightly negative at the large scales, and, importantly, is positive near the truncation scale. The barotropic injection of energy from the subgrid scales, due to the inverse cascade, in the stochastic formulation is accomplished by the stochastic forcing. This is a more numerically stable configuration.

The LES at T63 (and indeed at T126) did not perform as well as the corresponding simulations in the simpler problems of earlier chapters. The reason for this is not completely clear. However, the LES with stochastic parameterization did manage to broadly reproduce the features of higher resolution simulations. On the other hand, the LES with bare parameters produced results that had no resemblance to the LES at T126. The amplitudes of the fluctuations were found to be slightly smaller than the corresponding amplitudes for the T126 LES. It was proposed that this is due to the 'clamping' effect of the strong $\mathbf{M_d}$ and $\mathbf{F_b}$ parameters. Since the magnitudes of $\mathbf{M_d}$ and $\mathbf{F_b}$ depend on τ, the decorrelation time, it is likely that reducing τ will result in the amplitudes of the

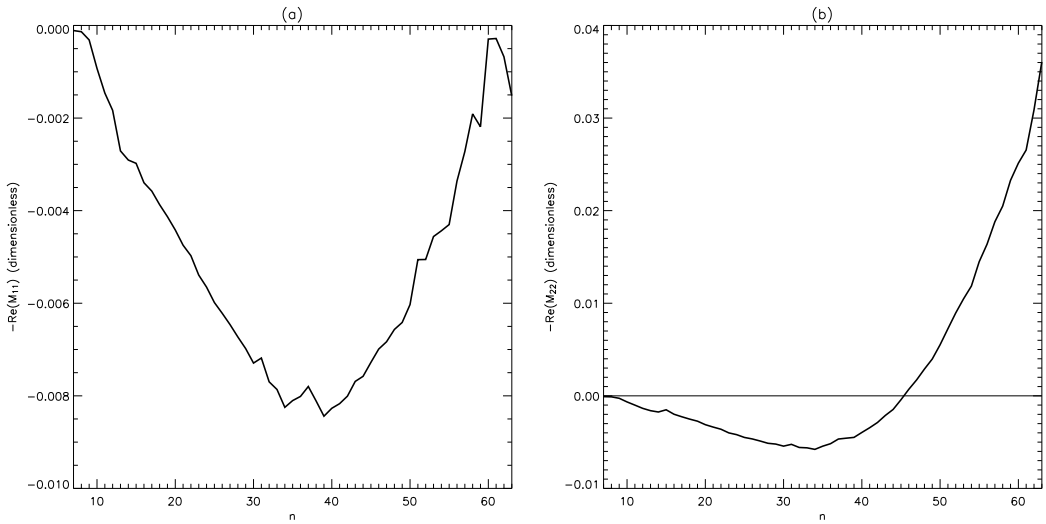

Figure 8.71: A comparison of diagonal barotropic dissipation coefficients ($-M^r_{11}$) for: (a) net dissipation ($-\mathbf{M^r_n}$); (b) drain dissipation ($-\mathbf{M^r_d}$) matrices in the BTBC formulation (T63).

fluctuations being closer to those of the T126 LES.

The results of the LES as well as the form of the fluxes at T63 suggest that this resolution is near to the injection region of the spectrum, so that a significant range of baroclinically unstable waves are retained by this truncation. It is not clear whether all realistic oceanic simulations at T63 will share this feature. The idealized problem of oceanic subgrid-scale parameterizations assumes that the mean fields are completely resolved while the transients (eddies) are completely unresolved. The truncation at T15 was found to be closer to this idealized problem. The subgrid flux was found to be completely positive for the barotropic mode, and practically zero for the baroclinic mode. The matrix elements $\mathbf{M_d}$ and $\mathbf{F_b}$ at T15 were found to be highly anisotropic, especially the dissipation matrix $\mathbf{M_d}$. The backscatter matrix, $\mathbf{F_b}$, seemed to have a clearer signal, with the F^r_{11} element being dominant, which is somewhat similar to what was found at T63. The backscatter matrix element F^r_{11} represents mainly the injection of barotropic energy into the system, and this is the main transfer as there is hardly any baroclinic flux. The mean subgrid forcing was found to yield the ratio $\left|\frac{u_1^{eddy}-u_2^{eddy}}{u_1^{rel}-u_2^{rel}}\right|$ of about 0.5, a substantial fraction of the total mean forcing. The LES at T15 was found to be in excellent agreement with the LES at T126.

Chapter 9

Conclusion

In this chapter, we broadly summarize the main results of this thesis and discuss their implications in a broader sense. Firstly, we shall discuss the study of multiple equilibria in Chapter 4. This can be divided into two parts, namely, the basic dynamics of multiple equilibria, and the parameterization of non-linear interactions. The latter is part of the central theme of this thesis. Multiple equilibrium states have been found to be ubiquitous for barotropic flows over topography, for some range of parameters. Furthermore, the parameters used were plausible atmospheric parameters, with a possible exception being the strength of the zonal wind, which was at least a factor of 2 too large in some experiments. Multiple equilibria were found in severely truncated models, in models with single-mode topography, in models with multiple topographic modes, in spherical models, and in models with fairly realistic zonal jets and topographic distribution. In the latter models, it was also found that the location of 'blocks' is close to the locations with observed frequent blocking events.

The main controversial issue regarding the theory of multiple equilibria in the atmosphere, as proposed by Charney and DeVore (1979), has been the values of the parameters needed to observe these states in numerical models, especially the zonal winds (Tung, 1985). In this regard, our experiments have been unable to settle the issue. It appears to be the case that for QG barotropic models, at least, the zonal winds required to observe multiple equilibrium states are somewhat too large. Having said this, it is not completely clear that other parameters used in the model, such as the topographic vorticity, h, and the Ekman drag, α, are 'correct' either. For example, there is a wide range of values α commonly used, ranging from 5 to 20 days damping time. Furthermore, stationary heating patterns, such as land-ocean temperature gradients, also contribute to the stationary wave field; this has, however, not been included in our studies, nor in other studies that we know of. With such large uncertainty in the values of parameters to be used in barotropic models, it is perhaps tolerable to have zonal winds being a factor of 2 or more outside the observed range.

Notwithstanding the difficulties with the interpretation of the results, the problem of multiple equilibria does provide a good example of the generic problem of parameterizing nonlinear interactions in severely truncated models (STMs). Multiple equilibria, as discussed in this thesis, arise due to the fact that the topographic stationary wave amplitude has a sharp (resonant) response at some value of the zonal wind. Hence, if the zonal wind is forced towards some value, greater than the resonant value, two stable attractors of the flow may emerge: one with zonal winds near the resonant value and large stationary wave amplitude; the other with zonal winds near the forcing value and weak stationary wave amplitude. Thus, this problem is intrinsically a two-mode problem, with the zonal flow and stationary wave being the two modes. A two-mode system of equations (which

turns out to be three equations because our basis functions are complex) can be obtained from the barotropic vorticity equation by ignoring non-linear interactions, and choosing the topography to be of single mode. It is at first a bit surprising how well this STM performs in comparison to a DNS of the fully non-linear equations of motion.

The good performance of the STM is probably due to the fact the phenomena under investigation (multiple equilibria as described in this thesis) are essentially linear phenomena. That is, non-linear interactions are not needed for their appearance. The non-linear interactions will change the amplitudes of the mean fields somewhat, but the mean fields interact in qualitatively the same way in a fully non-linear simulation. We have also investigated how to improve the performance of the STM, so that it is also quantitatively closer to the DNS. By curve fitting, we have found that adjusting α, the dissipation coefficient, and β, the variation of the Coriolis parameter, is sufficient to give a better comparison between the two models. This adjustment of parameters was referred to as renormalization in this thesis. In general, renormalized parameters enable a low-order system to reproduce more faithfully the dynamics of a higher-order system.

This study lends encouragement to the endeavour of modelling complex multi-component dynamics with low-order models. Such models may not be sufficient to make accurate predictions, but are useful for investigating the basic dynamics of complex phenomena. They can also be used in exploratory studies. A good example of this is in locating the multiple equilibria at some value of the parameters in a high resolution model. It would be computationally very expensive to search through parameter space for the location of multiple equilibria using a high resolution model. However, with a STM, such as the three-component system, this task is trivial. Having roughly identified the locations in parameter space of the multiple equilibria, one can then embark on a more focussed investigation to pinpoint the location of multiple equilibria with a high resolution model. This method was used to produce some of the results in Chapter 4.

Having established a heuristic parameterization scheme for the reduced model of Chapter 4, we then proceeded with the more ambitious task of parameterizing non-linear interactions in large eddy simulations, which are simulations at fairly high resolutions, but not high enough to capture all the scales of motion. In such simulations, clearly, one must also parameterize the transient-transient interactions, as these are the predominant interactions near the truncation scale when the truncation wavenumber is fairly high. The problem of parameterizing the unresolved fluxes in a large eddy simulation is called the subgrid-scale parameterization problem. The main focus of this thesis was on parameterizing the transient fluxes in a statistical sense, so that the energy and enstrophy spectra (which are effectively statistical variances) are the same regardless of resolution. In fact, this is the only sense in which these fluxes can be parameterized, as subgrid-scale motions are not deterministic in any practical sense. The methodology used was originally proposed by Frederiksen and Kepert (2006), and demonstrated for barotropic flows.

In a stratified flow, such as the two-level model that we worked with, the subgrid fluxes of energy and enstrophy are parameterized by matrix dissipation and backscatter coefficients, of the same order as the number of levels in the model (two in this case). The reason for the matrix representation is that in general the flow is vertically inhomogeneous; however, it is assumed to be sufficiently horizontally homogeneous, at least near the truncation scale. The matrices then couple the vertical modes only. In some problems, oceanic problems in particular, the fluxes also have mean components that need to be accounted for in the LES. One advantage of Frederiksen and Kepert's methodology is that it enables one to model both the drain flux and the backscatter flux separately, unlike

many other parameterization schemes that treat the net flux only, and are thus completely deterministic. A deterministic parameterization will in general model the net flux, but will not model the injection of noise into the system from the subgrid scales. The other advantage of this methodology is that it is DNS based, and so it has wide applicability.

On applying the methodology to atmospheric problems at the typical resolution of T63, it was found that vertical coupling was sufficiently small at this resolution, so that, practically, the matrix formulation was not needed. One can instead treat the problem as two uncoupled barotropic problems, as far as subgrid-scale parameterizations are concerned. Both the dissipation and backscatter parameters had typical prominent cusps near the truncation scale. It was also found that the backscatter was proportional to the flux in a given level, so that the more energetic (or rather enstrophetic) top level had a backscatter over an order of magnitude greater than that of the bottom level in the problems that we looked at. The drain dissipation parameters were, however, roughly the same, notwithstanding the flux difference. The deterministic parameterization, employing a net dissipation parameter, and the stochastic parameterization, employing drain dissipation and backscatter parameters, were also compared. Both parameterizations were found to perform extremely well. However, a more precise comparison near the truncation scale revealed that the stochastic parameterization tends to clamp down the system harder, and hence can overcome the slight lifting of the tail seen in some deterministic simulations. It was also found that the errors due to the use of bare parameters were confined mainly in the small scales in atmospheric simulations. This was hypothesized to be the case because a T63 truncation for the atmosphere, with an energy injection region around wavenumber 10, is well in the inertial range, and hence the enstrophy transfers are quite local there.

The more novel application of this methodology, and forming the core of this thesis, was in oceanic problems. There, the radius of deformation is usually too small, being the order of 50 km, to be resolved by simulations at typical resolutions of T63. The theory is then that the baroclinically unstable eddies, which correspond spectrally to the injection region, are not well resolved. If that is the case then two effects ensue. Firstly, the mean potential energy is overestimated as there are no baroclinically-unstable eddies to extract the potential energy in the model. Secondly, the transient energy flux is underestimated because there is an inverse cascade of energy emanating from the unresolved injection region. In fact, in our experiments, it was found that this idealized situation corresponds more closely to the T15 truncation in Chapter 8. At higher resolutions, baroclinically unstable eddies are retained, at least partially, and the separation between modes in the injection region and those outside of this region is not as clean. Nonetheless, the idea that there is a reduction of potential energy and an injection of barotropic kinetic energy seemed to hold, although there was an accompanying flux of enstrophy, both barotropic and baroclinic, due to resolved baroclinically unstable modes.

The problem of simulating the correct mean potential energy has been tackled with some success by the use of skew fluxes, as originally proposed by Gent and McWilliams (1990). The fluxes are associated with an eddy-induced circulation that acts in precisely such a way so as to lower the mean, mainly large scale, potential energy. However, the handling of the transient fluxes, which are important mostly near the truncation scale, is less satisfactory. The standard approach has been to use Laplacian, or in some cases higher order, operators, which are purely dissipative. This seems puzzling in the light of QG turbulence phenomenology which predicts that there should be an injection of energy from the subgrid scales if baroclinically unstable waves are not well resolved. Therefore, the parameterization of transient subgrid fluxes in current oceanic models seems to be

incomplete.

We have applied Frederiksen and Kepert's methodology to oceanic simulations (LESs) at T63. As alluded to above, we found that there is a strong positive energy flux in the barotropic mode, which cannot be possibly modelled by Laplacian operators. Indeed, the LES run with the deterministic parameterization, which is in some respects similar to a hyperdiffusion operator, was found to be too numerically unstable to be of any use. The stochastic parameterization, in most cases, performed extremely well compared to the higher resolution simulation. We have also calculated the mean subgrid flux in Chapter 8, and found that the flux induces a mean flow which acts in such a way so as to lower the mean potential energy of the flow.

In many respects, the oceanic problem is harder than the atmospheric one, not least because we are not guaranteed to be in the inertial range at the truncation scale. This means that the parameters calculated at T63, say, may not have the same form at other truncation scales, and for other flow configurations, as is the case, by and large, in the atmospheric problem. It also means that, unlike in the atmospheric problem, the consequences of not parameterizing the fluxes properly lead to the simulation drifting away from the true solution at all scales. It seems, then, that the best way to apply this methodology to a variety of problems is to perform the calculations of the parameters for each particular problem, rather than to try to obtain a generic form (of the wavenumber dependence) of the parameters, and hope that a scaling factor can be found for a specific problem.

A good example of this approach is when the system was truncated from T252 down to T63 in the previous chapters. The T252 simulation is very computationally demanding, and hence very long runs are impractical. However, to sample the T63 simulation properly, which is needed to calculate the parameters accurately, long runs are needed. A way out of this conundrum was provided by the fact that the turbulent fluxes are fairly local at these resolutions (as can be guessed from their fairly scale selective nature), and hence it was sufficient to work at T126 to calculate the parameters at T63. The T126 simulation is clearly less demanding than at T252, and hence longer runs can be performed. However, we still needed to maintain roughly the same spectra at T126 as at T252. We therefore performed a short run at T252, and calculated the parameters at T126 based on this run. The resulting parameters at T126 do not maintain the spectra faithfully at all scales, due to sampling errors, but they broadly reproduce the correct flow statistics, and importantly, if the flow features under investigation are large scale, requiring long sampling times, the computational cost saving is considerable.

The methodology for subgrid-scale parameterizations used in this thesis is quite general. We have shown that it works extremely well in quasigeostrophic two-level problems. The next step would be to look at multi-level quasigeostrophic problems, problems with topography, and primitive equation models. It would also be desirable to extend this methodology to grid-point modelling.

Appendix A

The Spherical QGPV Equations

We can write down the three-dimensional QGPV equation

$$\frac{\partial q}{\partial t} + J(\psi, q) = 0, \tag{A.1}$$

where

$$q = \nabla^2\psi + f + \frac{\partial}{\partial z}\left(\frac{f_0^2}{N^2}\frac{\partial \psi}{\partial z}\right), \tag{A.2}$$

in spherical coordinates (λ, μ, z, t) with the replacements $x \to \lambda$ and $y \to \mu$ in the equations of motion. Here, λ is the longitude and

$$\mu = \sin\phi, \tag{A.3}$$

where ϕ is the latitude. The Jacobian operator is thus

$$J(\psi, \chi) = \frac{\partial \psi}{\partial \lambda}\frac{\partial \chi}{\partial \mu} - \frac{\partial \psi}{\partial \mu}\frac{\partial \chi}{\partial \lambda}. \tag{A.4}$$

The Laplacian operator in spherical coordinates is

$$\nabla^2\chi = \frac{\partial}{\partial \mu}\left[(1-\mu^2)\frac{\partial \chi}{\partial \mu}\right] + \frac{1}{1-\mu^2}\frac{\partial^2 \chi}{\partial \lambda^2}. \tag{A.5}$$

Here, χ is a general scalar function. We also retain the full, sinusoidal, variation of the Coriolis parameter; that is

$$f = 2\mu. \tag{A.6}$$

However, the f_0 in the vertical derivative in Eq. A.2 is a constant; this means that the layer coupling parameter, F, remains a constant after vertical discretization as in the planar case. We have scaled the lengths and times in Eq. A.1 by a, the radius, and Ω, the angular velocity of the Earth, respectively. The inclusion of topography and vertical discretization into the two-level equations then follow exactly as in the beta-plane approximation (planar geometry). We do not expect the spherical QGPV equations to realistically simulate large scale motion outside of the mid-latitudes. However, we are mainly interested in the parameterization of subgrid-scales, that is, mainly small-scale motions. The advantage of working in spherical geometry is that the results can be readily applied to more complex models, like GCMs of the atmosphere, which tend to be spherical. This approach was taken by Frederiksen et al. (2003).

In spherical geometry, the decomposition is done in terms of spherical harmonics, so

$$\chi(\lambda,\mu,t) = \sum_{mn} \chi_{mn}(t) P_n^m(\mu) \exp(im\lambda), \tag{A.7}$$

where m and n are the zonal and total wavenumbers respectively. $P_n^m(\mu)$ are orthonormal Legendre polynomials satisfying

$$\int_{-1}^{1} d\mu P_n^m(\mu) P_{n'}^m(\mu) = \delta(n-n'). \tag{A.8}$$

We also have

$$\frac{1}{(2\pi)} \int_0^{2\pi} d\lambda \exp\left[-i(m-m')\right] = \delta(m-m'). \tag{A.9}$$

It is then straightforward to show that the inverse transform to Eq. A.7 is

$$\chi_{mn}(t) = \frac{1}{(2\pi)} \int_0^{2\pi} \int_{-1}^{1} d\lambda d\mu P_n^m(\mu) \exp\left(-im\lambda\right) \chi(\lambda,\mu,t). \tag{A.10}$$

The condition for the reality of the physical-space fields, χ, analogous to Eq. 2.47 is

$$\chi_{-mn} = \chi_{mn}^*. \tag{A.11}$$

The relationship between spectral vorticity, ζ_{mn}, and streamfunction, ψ_{mn}, is

$$\zeta_{mn} = -n(n+1)\psi_{mn}. \tag{A.12}$$

Using Eqs. A.7-A.12, we obtain a spectral equation for the barotropic vorticity equation on the sphere of the same form as Eqs. 2.48:

$$\frac{\partial \zeta_{mn}}{\partial t} = i \sum_{pq} \sum_{rs} \delta(m+p+r) \left[K_{nqs}^{mpr} \zeta_{-pq} \zeta_{-rs} + A_{nqs}^{mpr} \zeta_{-pq} h_{-rs} \right] - i\omega_{mn} \zeta_{mn}, \tag{A.13}$$

where

$$\omega_{mn} = -\frac{2m}{n(n+1)}, \tag{A.14}$$

$$A_{nqs}^{mpr} = -\frac{1}{q(q+1)} I_{nqs}^{mpr}, \tag{A.15}$$

and

$$\begin{aligned} K_{nqs}^{mpr} &= \frac{1}{2}\left[A_{nqs}^{mpr} + A_{nsq}^{mrp}\right] \\ &= \frac{1}{2}\left[\frac{1}{s(s+1)-q(q+1)}\right] I_{nqs}^{mpr}; \end{aligned} \tag{A.16}$$

$$I_{nqs}^{mpr} = \int_{-1}^{1} d\mu P_n^m(\mu) \left[p P_q^p(\mu) \frac{d}{d\mu} P_s^r(\mu) - r P_s^r(\mu) \frac{d}{d\mu} P_q^p(\mu) \right]. \tag{A.17}$$

The spherical interaction coefficients $\delta(m+p+r)K_{nqs}^{mpr}$ and $\delta(m+p+r)A_{nqs}^{mpr}$ satisfy the

selection rules (Frederiksen and Sawford, 1980):

$$m + p + r = 0, \tag{A.18}$$

$$n + q + s = \text{odd integer, and} \tag{A.19}$$

$$|q - s| < n < q + s. \tag{A.20}$$

The two-level spherical equations can also be written in the compact form of Eq. 2.53 with the spherical interaction coefficients above generalized to include the vertical indices.

Appendix B

Generalized Beta Plane

In general, the barotropic vorticity equation on the beta plane can be written as

$$\frac{\partial Z}{\partial t} + J(\Psi, \nabla^2\Psi + \beta y + h) = 0, \tag{B.1}$$

where we changed the notation slightly from Eq. 2.45 for convenience. Ψ and $Z = \nabla^2\Psi$ are the streamfunction and vorticity for the flow. It is frequently convenient to split the 'wavy part' of the flow, ψ, from the background flow $\bar{\psi}$; that is

$$\Psi = \psi + \bar{\psi} \tag{B.2}$$

and

$$Z = \zeta + \bar{Z}. \tag{B.3}$$

In fact, the choice of doubly periodic boundary conditions implied by Eq. 2.46 is more sensible for the wavy part of the flow, rather than for the total flow. The simplest choice for the background flow is a flow uniform in space, but which is allowed to vary in time. Hence, defining

$$\bar{\psi} = -Uy, \tag{B.4}$$

we obtain a uniform zonal flow as desired, but $\bar{Z} = 0$ by this definition, so we have

$$\frac{\partial \zeta}{\partial t} + J(\psi - Uy, \zeta + \beta y + h) = 0. \tag{B.5}$$

We also need an evolution equation for the background flow, which cannot be derived from the vorticity equation, but needs to be deduced by other means; this will be discussed later. On the sphere, the 'wave' with $(m, n) = (0, 1)$ is analogous to a uniform flow on the beta plane because then $\psi = \psi_{01}\sqrt{\frac{3}{2}}\mu \propto \sin\phi$ and hence the zonal wind, $u \propto \cos\phi$, which is always positive in the range $-90^o < \phi < 90^o$ with a maximum at the equator ($\phi = 0$). This mode is called the solid body rotation mode because a spherical solid body in rotation about the vertical axis will have a zonal velocity which varies with the latitude in precisely this way. Hence, we define

$$\bar{\psi} = -U\mu, \tag{B.6}$$

and

$$\bar{Z} = 2U\mu, \tag{B.7}$$

where, U is the equatorial velocity. On the sphere (See Appendix A), all lengths are scaled by a, the Earth's radius and Ω, its angular velocity (that is, $a = \Omega = 1$). Thus,

$$\frac{\partial Z}{\partial t} + J(\psi - U\mu, \zeta + h + 2\mu + 2U\mu) = 0 \tag{B.8}$$

is the barotropic vorticity equation on the sphere. This can be written in spectral space as

$$\frac{\partial \zeta_{mn}}{\partial t} = i \sum_{pq} \sum_{rs} \delta(m+p+r) \left(K_{nqs}^{mpr} \zeta_{-pq} \zeta_{-rs} + A_{nqs}^{mpr} \zeta_{-pq} h_{-rs} \right) - i\omega_{mn}^{U} \zeta_{mn} - imh_{mn}U, \tag{B.9}$$

and

$$\frac{\partial U}{\partial t} = \frac{3}{4} \frac{2m}{n(n+1)} Im \left(\zeta_{mn} h_{-mn} \right). \tag{B.10}$$

Here,

$$\omega_{mn}^{U} = m \left[U - \frac{2+2U}{n(n+1)} \right] \tag{B.11}$$

is the Doppler shifted Rossby wave frequency. In deriving Eqs. B.9 to B.11, we have explicitly calculated the following interaction coefficients in terms of m and n: $K_{n,1,n}^{m,0,-m} = -\frac{1}{2}\sqrt{\frac{3}{2}}[\frac{1}{2} - \frac{1}{n(n+1)}]m$, $A_{n,1,n}^{m,0,-m} = -\frac{1}{2}\sqrt{\frac{3}{2}}m$, and $A_{1,n,n}^{0,m,-m} = \sqrt{\frac{3}{2}}\frac{m}{n(n+1)}$. The wavenumbers (m,n), (p,q), and (r,s) do not include the wavenumber $(0,1)$. Now, it can easily be shown (Frederiksen and O'Kane, 2005) that the set of equations

$$\frac{\partial \zeta}{\partial t} + J(\psi - Uy, \zeta + h + \beta y + k_0^2 U y) \tag{B.12}$$

and

$$\frac{\partial U}{\partial t} = \frac{1}{S} \int_S h \frac{\partial \psi}{\partial x} dS, \tag{B.13}$$

where S is the area of the domain $S = [0, 2\pi] \times [0, 2\pi] = (2\pi)^2$, in the Cartesian plane transform into the following set in spectral space:

$$\frac{\partial \zeta_{\mathbf{k}}}{\partial t} = \sum_{\mathbf{p}} \sum_{\mathbf{q}} \delta(\mathbf{k}+\mathbf{p}+\mathbf{q}) \left[K(\mathbf{k},\mathbf{p},\mathbf{q}) \zeta_{-\mathbf{p}} \zeta_{-\mathbf{q}} + A(\mathbf{k},\mathbf{p},\mathbf{q}) \zeta_{-\mathbf{p}} h_{-\mathbf{q}} \right] - i\omega_{\mathbf{k}}^{U} \zeta_{\mathbf{k}} - ik_x h_{\mathbf{k}} U \tag{B.14}$$

and

$$\frac{\partial U}{\partial t} = \frac{2k_x}{k^2} Im \left(\zeta_{\mathbf{k}} h_{-\mathbf{k}} \right), \tag{B.15}$$

where

$$\omega_{\mathbf{k}}^{U} = k_x \left(U - \frac{\beta + k_0^2 U}{k^2} \right) \tag{B.16}$$

is the Doppler shifted Rossby wave frequency on the plane. Equation B.12 is called the generalized beta-plane equation and Eq. B.13 is called the Form Drag equation. They lead to the set of planar equations B.14 to B.16 in spectral space becoming isomorphic to the spherical set B.9 to B.11 with the replacements $k_x \to m$, $\beta \to 2$, $k_0^2 \to 2$, $\mathbf{k} \to (m,n)$, $-\mathbf{k} \to (-m,n)$, and $k^2 \to n(n+1)$. The interaction coefficients $K(\mathbf{k},\mathbf{p},\mathbf{q}) \to i\delta(m+p+r)K_{nqs}^{mpr}$ and $A(\mathbf{k},\mathbf{p},\mathbf{q}) \to i\delta(m+p+r)A_{nqs}^{mpr}$. We also need $h_{\mathbf{k}} \to \frac{3}{4}h_{mn}$ in the form drag equation only. On the other hand, Eq. B.5 and B.13 (standard beta plane equations) do not lead to a set isomorphic to the spherical equations due to the absence of the $k_0^2 U y$ term.

Appendix C

The Forward and Inverse Cascades of Two-dimensional Turbulence

First, we need to write the conservation laws for an inviscid two-dimensional fluid in terms of the energy and enstrophy spectral components. In two-dimensions, $\mathbf{u}$ is related to the streamfunction as given by Eqs. 2.5 and 2.6. Hence, from the definition of the energy E, Eq. 3.3, we have

$$E = \int_V \nabla\psi \cdot \nabla\psi dV. \tag{C.1}$$

From the definition of the enstrophy, Eq. 3.6, we have

$$Z = \int_V \zeta^2 dV = \int_V \left(\nabla^2\psi\right)^2 dV. \tag{C.2}$$

Expanding the streamfunction as a complex Fourier series we have

$$\psi(x, y, t) = \sum_{\mathbf{k}} \psi_{\mathbf{k}}(t) \exp i\mathbf{k} \cdot \mathbf{x}, \tag{C.3}$$

where $\psi_{\mathbf{k}}$ is the wave amplitude corresponding to the two-dimensional wavenumber $\mathbf{k}$. Using Eq. C.3 in Eqs. C.1 and C.2 we have

$$E = \sum_{\mathbf{k}} E_{\mathbf{k}} \tag{C.4}$$

and

$$Z = \sum_{\mathbf{k}} Z_{\mathbf{k}}, \tag{C.5}$$

which says that the energy and enstrophy (in physical space) are sums of their respective spectral components. Here,

$$E_{\mathbf{k}} = k^2 \psi_{\mathbf{k}} \psi_{-\mathbf{k}} \tag{C.6}$$

and

$$Z_{\mathbf{k}} = k^4 \psi_{\mathbf{k}} \psi_{-\mathbf{k}} = k^2 E_{\mathbf{k}}. \tag{C.7}$$

The spectral form of the energy and enstrophy conservation laws is thus

$$\frac{\partial}{\partial t} \sum_{\mathbf{k}} E_{\mathbf{k}} = 0 \tag{C.8}$$

and

$$\frac{\partial}{\partial t}\sum_{\mathbf{k}} Z_{\mathbf{k}} = 0. \tag{C.9}$$

Not only is the total energy and enstrophy conserved, but each triad interaction involving wavenumbers $\mathbf{k}$, $\mathbf{p}$, and $\mathbf{q}$ such that $\mathbf{k}+\mathbf{p}+\mathbf{q}=\mathbf{0}$ conserves energy and enstrophy in detail (Lesieur, 1997). That is,

$$\frac{\partial}{\partial t}\left(E_{\mathbf{k}}+E_{\mathbf{p}}+E_{\mathbf{q}}\right)=0 \tag{C.10}$$

and

$$\frac{\partial}{\partial t}\left(Z_{\mathbf{k}}+Z_{\mathbf{p}}+Z_{\mathbf{q}}\right)=0. \tag{C.11}$$

The argument for the forward and inverse cascades of two-dimensional turbulence discussed here was given by Vallis (2006); a somewhat similar argument was also discussed by Salmon (1998). The starting point is the generalization of Eqs. C.8 and C.9 for a continuous wavenumber distribution:

$$\frac{\partial}{\partial t}\int E(k)dk = 0 \tag{C.12}$$

and

$$\frac{\partial}{\partial t}\int k^2 E(k)dk = 0. \tag{C.13}$$

The centroid of the energy distribution is defined as

$$k_e = \frac{\int kE(k)dk}{\int E(k)dk}. \tag{C.14}$$

The function

$$I(t) = \int (k-k_e)^2\, E(k)dk, \tag{C.15}$$

is also defined, where both k_e and $E(k)$ are functions of time. Now imagine that initially the energy is contained in only a single wavenumber, $k=k_e$, then $I(t=0)=0$. When $t>0$, other wavenumbers will be excited and then $I(t)>0$ as $I(t)$ is always positive. In general, we have

$$\frac{\partial I}{\partial t} > 0. \tag{C.16}$$

Now,

$$\begin{aligned} I(t) &= \int k^2E(k)dk + k_e^2\int E(k)dk - 2k_e\int kE(k)dk \\ &= \int k^2E(k)dk - k_e^2\int E(k)dk \\ &= Z - k_e^2 E. \end{aligned} \tag{C.17}$$

The second line in Eq. C.17 follows from replacing $\int kE(k)dk$ in the last term of the first line with $k_e\int E(k)dk$; this follows from Eq. C.14. Since E and Z are invariants, we have

$$\frac{\partial k_e^2}{\partial t} = -\frac{1}{E}\frac{\partial I}{\partial t} < 0. \tag{C.18}$$

So the centroid wavenumber (squared) of the energy distribution diminishes as the flow evolves. In other words, energy moves towards smaller wavenumbers (larger scales).

To deduce the direction of enstrophy transfer using the same arguments is not as straightforward; instead, a trick must be used. A new variable $\xi = \frac{1}{k}$ is defined. In terms of this new variable, the energy is

$$E = \sum_{\xi} \xi^2 Z_\xi \rightarrow \int \xi^2 Z(\xi) d\xi. \tag{C.19}$$

Defining the enstrophy centroid

$$\xi_z = \frac{\int \xi Z(\xi) d\xi}{\int Z(\xi) d\xi}. \tag{C.20}$$

and the function

$$I(t) = \int (\xi - \xi_z)^2 Z(\xi) d\xi, \tag{C.21}$$

where $\frac{\partial I}{\partial t} > 0$, we have, similarly to the energy energy transfer arguments,

$$\begin{aligned} I(t) &= \int \xi^2 Z(\xi) d\xi - \xi_z^2 \int Z(\xi) d\xi \\ &= E - \xi_z^2 Z. \end{aligned} \tag{C.22}$$

Since E and Z are invariants, we have

$$\frac{\partial \xi_z^2}{\partial t} = -\frac{1}{Z} \frac{\partial I}{\partial t} < 0. \tag{C.23}$$

So the enstrophy centroid moves towards smaller values of ξ. But since $\xi = \frac{1}{k}$, this corresponds to an enstrophy transfer towards larger values of k (the small scales).

Appendix D

Quadratic Invariants of Stratified QG Turbulence

Here, we consider the effects of stratification. We shall use the two-level QGPV equations without rotation, which can be written as

$$\frac{\partial q_i}{\partial t} + \nabla \cdot (q_i \mathbf{u}) = 0, \tag{D.1}$$

where

$$q_i = \nabla^2 \psi_i + (-1)^i F(\psi_1 - \psi_2), \tag{D.2}$$

and $i = 1, 2$. Our first goal is to find the quadratic invariants analogous to the energy and enstrophy defined for two-dimensional turbulence. The energy equation can be obtained as follows.

Multiply Eq. D.1 by ψ_i, then

$$\psi_i \frac{\partial q_i}{\partial t} + \psi_i \nabla \cdot (q_i \mathbf{u}) = 0. \tag{D.3}$$

Now, the second term in Eq. D.3 can be written as a divergence because

$$\nabla \cdot (\psi q \mathbf{u}) = \psi \nabla \cdot (q \mathbf{u}) + q \mathbf{u} \cdot \nabla \psi, \tag{D.4}$$

and furthermore $\mathbf{u} \cdot \nabla \psi = 0$ by the definition of the streamfunction (see Eqs. 2.5 and 2.6). Hence,

$$\psi_i \nabla (q_i \mathbf{u}) = \nabla \cdot (\psi q \mathbf{u}). \tag{D.5}$$

To handle the first term, we use the definition of q_i, Eq. D.2, so

$$\psi_i \frac{\partial q_i}{\partial t} = \frac{1}{2} \frac{\partial}{\partial t} (\psi_i q_i) = \frac{\partial}{\partial t} \left[\psi_i \nabla^2 \psi_i + (-1)^i F \psi_i (\psi_1 - \psi_2) \right]. \tag{D.6}$$

Now, $\nabla \cdot (\psi \nabla \psi) = \psi \nabla \cdot \nabla \psi + \nabla \psi \cdot \nabla \psi$ and $\nabla \cdot \nabla \psi = \nabla^2 \psi$ by definition, so

$$\psi_i \nabla^2 \psi_i = \nabla \cdot (\psi_i \nabla \psi_i) - \nabla \psi_i \cdot \nabla \psi_i. \tag{D.7}$$

Using Eq. D.7 in eq. D.6, substituting the result, as well as Eq. D.5, in Eq. D.1, and integrating over the domain, we have

$$\frac{1}{2} \frac{\partial}{\partial t} \int_A [\nabla \psi_1 \cdot \nabla \psi_1 - \nabla \cdot (\psi_1 \nabla \psi_1) + F \psi_1 (\psi_1 - \psi_2)] dA - \int_A \nabla \cdot (\psi_1 q_1 \mathbf{u}) dA = 0 \tag{D.8}$$

and

$$\frac{1}{2}\frac{\partial}{\partial t}\int_A [\nabla\psi_2\cdot\nabla\psi_2 - \nabla\cdot(\psi_2\nabla\psi_2) - F\psi_2(\psi_1-\psi_2)]dA - \int_A \nabla\cdot(\psi_2 q_2.\mathbf{u})dA = 0 \tag{D.9}$$

The integrals of divergence terms disappear by the divergence theorem as we assume that there is no flow in or out of the boundaries. Adding Eqs. D.8 and D.10, we obtain

$$\frac{\partial E}{\partial t} = 0, \tag{D.10}$$

where

$$E = K_1 + K_2 + P \tag{D.11}$$

is the total energy. Here,

$$K_1 = \frac{1}{2}\int_A \nabla\psi_1\cdot\nabla\psi_1 dA \tag{D.12}$$

is the Level 1 kinetic energy,

$$K_2 = \frac{1}{2}\int_A \nabla\psi_2\cdot\nabla\psi_2 dA \tag{D.13}$$

is the Level 2 kinetic energy, and

$$P = \frac{1}{2}\int_A \frac{1}{2}k_i^2(\psi_1-\psi_2)^2 dA \tag{D.14}$$

is the potential energy. The deformation scale is $k_i = \frac{1}{\sqrt{2F}}$.

Since $\frac{Dq_i}{Dt} = 0$, it follows immediately that

$$\frac{\partial Z_i}{\partial t} = 0, \tag{D.15}$$

where

$$Z_i = \int_A q_i^2 dA \tag{D.16}$$

is the potential vorticity of the layer of fluid. Equation D.15 says that the potential enstrophy of each fluid layer is conserved, and hence the average potential enstrophy is also conserved; that is

$$\frac{\partial Z}{\partial t} = 0, \tag{D.17}$$

where $Z = \frac{1}{2}(Z_1 + Z_2)$.

In terms of mean and shear streamfunctions, the energy

$$E = K_+ + K_- + P, \tag{D.18}$$

where

$$K_+ = \int_A \nabla\psi\cdot\nabla\psi dA \tag{D.19}$$

is the barotropic kinetic energy,

$$K_- = \int_A \nabla\tau\cdot\nabla\tau dA \tag{D.20}$$

is the baroclinic kinetic energy, and

$$P = \int_A k_i^2 \tau^2 dA \tag{D.21}$$

is the potential energy. The average potential enstrophy is

$$Z = \int_A \left(\nabla^2 \psi\right)^2 + \left(\nabla^2 \tau - k_i^2 \tau\right)^2 dA. \tag{D.22}$$

To obtain the corresponding spectral space quantities, we expand $\psi(x, y, t) = \sum_{\mathbf{k}} \psi_{\mathbf{k}}(t) \exp i\mathbf{k} \cdot \mathbf{x}$ and $\tau(x, y, t) = \sum_{\mathbf{k}} \tau_{\mathbf{k}}(t) \exp i\mathbf{k} \cdot \mathbf{x}$ to obtain $E = \sum_{\mathbf{k}} E_{\mathbf{k}}$ and $Z = \sum_{\mathbf{k}} Z_{\mathbf{k}}$ as the conserved quantities; that is

$$\frac{\partial}{\partial t} \sum_{\mathbf{k}} E_{\mathbf{k}} = 0 \tag{D.23}$$

and

$$\frac{\partial}{\partial t} \sum_{\mathbf{k}} Z_{\mathbf{k}} = 0. \tag{D.24}$$

Here

$$E_{\mathbf{k}} = E_{\mathbf{k}}^+ + E_{\mathbf{k}}^-, \tag{D.25}$$

$$E_{\mathbf{k}}^+ = k^2 \psi_{\mathbf{k}} \psi_{-\mathbf{k}} = \frac{\zeta_{\mathbf{k}}^0 \zeta_{-\mathbf{k}}^0}{k^2} \tag{D.26}$$

is the spectral barotropic kinetic energy, and

$$E_{\mathbf{k}}^- = \left(k^2 + k_i^2\right) \tau_{\mathbf{k}} \tau_{-\mathbf{k}} = \frac{\zeta_{\mathbf{k}}^1 \zeta_{-\mathbf{k}}^1}{k^2 + k_i^2} \tag{D.27}$$

is the spectral total baroclinic energy. The total baroclinic energy consists of

$$K_{\mathbf{k}}^+ = k^2 \tau_{\mathbf{k}} \tau_{-\mathbf{k}} = k^2 \frac{\zeta_{\mathbf{k}}^1 \zeta_{-\mathbf{k}}^1}{\left(k^2 + k_i^2\right)^2}, \tag{D.28}$$

the spectral baroclinic kinetic energy, and

$$P_{\mathbf{k}} = k_i^2 \tau_{\mathbf{k}} \tau_{-\mathbf{k}} = k_i^2 \frac{\zeta_{\mathbf{k}}^1 \zeta_{-\mathbf{k}}^1}{\left(k^2 + k_i^2\right)^2}, \tag{D.29}$$

the spectral potential energy. In Eqs. D.26 to D.29, we have used the definitions $\zeta_{\mathbf{k}}^0 = -k^2 \psi_{\mathbf{k}}$ and $\zeta_{\mathbf{k}}^1 = -(k^2 + k_i^2)\psi_{\mathbf{k}}$ of Section 2.6. The spectral average potential enstrophy is

$$Z_{\mathbf{k}} = k^2 E_{\mathbf{k}}^+ + \left(k^2 + k_i^2\right) E_{\mathbf{k}}^-. \tag{D.30}$$

It is convenient to think of $\psi_{\mathbf{k}}$ and $\tau_{\mathbf{k}}$ as vertical modes. Why is this the case? Consider the continuously stratified three-dimensional QGPV equation

$$\frac{\partial q}{\partial t} + J(\psi, q) = 0. \tag{D.31}$$

If we expand q as a complex Fourier series in *vertical* wavenumber:

$$q(x, y, z, t) = \sum_k q_k(x, y, t) \exp(ikz), \tag{D.32}$$

and substitute in Eq. D.31, we obtain, after some algebra,

$$\frac{\partial q_k}{\partial t} + \sum_p \sum_q \delta(k + p + q) J(\psi_{-p}, q_{-q}) = 0. \tag{D.33}$$

Note that the vertical wavenumbers must satisfy the same selection rule $k + p + q = 0$ as for horizontal wavenumbers. The connection between Eq. D.33 and the two-level QGPV equations in the BTBC formulation becomes clearer if we remove one sum by using the delta function so that

$$\frac{\partial q_k}{\partial t} + \sum_p J(\psi_{-p}, q_{p+k}) = 0. \tag{D.34}$$

Now we can see that Eq. D.34 is very similar in form to the two-level QGPV equations, Eqs. 2.42 and 2.43 with $h = f = 0$, if we truncate k and p to only two modes. The comparison is heuristic only, and not exact, because the choice of vertical eigenfunctions, Eq. D.32, does not satisfy the rigid-lid boundary conditions from which the two-level equations are derived. The crucial point, however, is that there is an isomorphism between the two-dimensional vorticity equation and the *three-dimensional* QGPV equation. If we vertically discretize the three-dimensional QGPV equation into a set of coupled horizontal equations, then the isomorphism between the two sets can be recovered if we write the coupled horizontal equations in terms of new variables, such as the mean and shear variables for the two-level system, and identify the new variables with vertical modes.

It is not hard to deduce that $k = 0$ in Eq. D.32 corresponds to the barotropic mode as this motion has no z-dependence. Higher values of k correspond to more degrees of freedom in the vertical; for example, $k = \pm 1$ corresponds to the first baroclinic mode. For the two-level model, there are only two vertical modes: $k = 0$ and $k = \pm 1$. As far as the selection rule is concerned, there are only two possibilities. First, that k, p, and q are all zero. This is called a barotropic triad. It consists of three interacting barotropic modes. Second, that one of k, p, or q is zero, one is $+1$, and the other one is -1. This is called a baroclinic triad. It consists of one barotropic mode interacting with two baroclinic modes. This is indeed the structure implied by the spectral form of the two-level QGPV equations in spectral form (Eqs. 2.42 and 2.43 with $h = \beta = 0$).

Given that the two-level QGPV equations conserve energy and potential enstrophy, we expect a forward cascade of potential enstrophy and an inverse cascade of energy to occur, using similar arguments to those in Section 3.2.4. However, given that the QGPV equations are inherently three-dimensional, with vertical as well as horizontal modes, the cascades occur in *three-dimensional* wavenumber. Hence, for example, not only does energy cascade to lower horizontal wavenumber, but it also cascades to lower vertical wavenumber, which is towards the barotropic mode (which has $k = 0$). So quasigeostrophic flows tend to become barotropic at the large scales.

The spectral form of the QGPV equations, Eqs. 2.53, reveals that the non-linear interactions occur in triads. This is a consequence of the quadratic non-linearity (the $\mathbf{u} \cdot \nabla q$ term) in the physical-space equations of motion. Since the non-linear terms just redistribute energy in the system, and do not create or remove it, it is not hard to see that each triad interaction must conserve energy in detail. Any triad interaction that does

not conserve energy cannot be allowed to occur. This is the interpretation of the delta function in the interaction coefficients; only triads interactions with wavenumbers $\mathbf{k}, \mathbf{p}, \mathbf{q}$ satisfying $\mathbf{k} + \mathbf{p} + \mathbf{q} = \mathbf{0}$ are energy conserving and will be allowed to occur. In fact, this argument extends to any other quadratic invariant of the system, such as the potential enstrophy (Lesieur, 1997).

Now, the two-level QGPV equations in spectral form, Eq. 2.53, contain two types of triad: the barotropic triad $\left\{\zeta^0_{\mathbf{k}}, \zeta^0_{\mathbf{p}}, \zeta^0_{\mathbf{q}}\right\}$ and the baroclinic triad $\left\{\zeta^0_{\mathbf{k}}, \zeta^1_{\mathbf{p}}, \zeta^1_{\mathbf{q}}\right\}$, following the notation of Section 2.7. Both triads must conserve energy and potential enstrophy in detail if $\mathbf{k} + \mathbf{p} + \mathbf{q} = \mathbf{0}$. Hence,

$$\frac{\partial}{\partial t}\left(E^+_{\mathbf{k}} + E^+_{\mathbf{p}} + E^+_{\mathbf{q}}\right) = 0 \tag{D.35}$$

and

$$\frac{\partial}{\partial t}\left(Z^+_{\mathbf{k}} + Z^+_{\mathbf{p}} + Z^+_{\mathbf{q}}\right) = 0 \tag{D.36}$$

for the barotropic triad. Similarly,

$$\frac{\partial}{\partial t}\left(E^+_{\mathbf{k}} + E^-_{\mathbf{p}} + E^-_{\mathbf{q}}\right) = 0 \tag{D.37}$$

and

$$\frac{\partial}{\partial t}\left(Z^+_{\mathbf{k}} + Z^-_{\mathbf{p}} + Z^-_{\mathbf{q}}\right) = 0 \tag{D.38}$$

for the baroclinic triad. Here,

$$Z^+_{\mathbf{k}} = k^2 E^+_{\mathbf{k}} \tag{D.39}$$

and

$$Z^-_{\mathbf{k}} = \left(k^2 + k_i^2\right) E^-_{\mathbf{k}}. \tag{D.40}$$

The barotropic triad in the two-level QGPV equations is thus formally the same as the triad in the two-dimensional vorticity equation since Eqs. D.35 and D.36 can be written as

$$\frac{\partial}{\partial t}\left(k^2\psi_{\mathbf{k}}\psi_{-\mathbf{k}} + p^2\psi_{\mathbf{p}}\psi_{-\mathbf{p}} + q^2\psi_{\mathbf{q}}\psi_{-\mathbf{q}}\right) = 0 \tag{D.41}$$

and

$$\frac{\partial}{\partial t}\left(k^4\psi_{\mathbf{k}}\psi_{-\mathbf{k}} + p^4\psi_{\mathbf{p}}\psi_{-\mathbf{p}} + q^4\psi_{\mathbf{q}}\psi_{-\mathbf{q}}\right) = 0. \tag{D.42}$$

However, the baroclinic triad is

$$\frac{\partial}{\partial t}\left[k^2\psi_{\mathbf{k}}\psi_{-\mathbf{k}} + \left(p^2 + k_i^2\right)\tau_{\mathbf{p}}\tau_{-\mathbf{p}} + \left(q^2 + k_i^2\right)\tau_{\mathbf{q}}\tau_{-\mathbf{q}}\right] = 0 \tag{D.43}$$

and

$$\frac{\partial}{\partial t}\left[k^4\psi_{\mathbf{k}}\psi_{-\mathbf{k}} + \left(p^2 + k_i^2\right)^2\tau_{\mathbf{p}}\tau_{-\mathbf{p}} + \left(q^2 + k_i^2\right)^2\tau_{\mathbf{q}}\tau_{-\mathbf{q}}\right] = 0, \tag{D.44}$$

which reflects the fact that the baroclinic triad makes stratified quasigeostrophic phenomenology 'richer' (Vallis, 2006) than plain two-dimensional turbulence phenomenology as it involves interaction between barotropic and baroclinic (vertical) modes. It is illuminating to write Eqs. D.43 and D.44 as

$$\frac{\partial}{\partial t}\left(k'^2\psi_{\mathbf{k}'}\psi_{-\mathbf{k}'} + p'^2\psi_{\mathbf{p}'}\psi_{-\mathbf{p}'} + q'^2\psi_{\mathbf{q}'}\psi_{-\mathbf{q}'}\right) = 0 \tag{D.45}$$

and

$$\frac{\partial}{\partial t}\left(k'^4\psi_{\mathbf{k}'}\psi_{-\mathbf{k}'} + p'^4\psi_{\mathbf{p}'}\psi_{-\mathbf{p}'} + q'^4\psi_{\mathbf{q}'}\psi_{-\mathbf{q}'}\right) = 0. \tag{D.46}$$

Here $\mathbf{k}', \mathbf{p}', \mathbf{q}'$ are three-dimensional wavenumbers defined so that

$$k'^2 = k^2 + k_i^2 \tag{D.47}$$

and

$$\begin{aligned} \psi_{(\mathbf{k},0)} &= \psi_{\mathbf{k}}, \\ \psi_{(\mathbf{k},k_i)} &= \tau_{\mathbf{k}}. \end{aligned} \tag{D.48}$$

and similarly for the wavenumbers $\mathbf{p}'$ and $\mathbf{q}'$. Now let us analyze Eqs. D.45 and D.46 for different wavenumber regimes. For scales comparable to the deformation scale, Eqs. D.45 and D.46 are formally identical to those corresponding to two-dimensional turbulence, with the replacements $\mathbf{k}' \to \mathbf{k}$, $\mathbf{p}' \to \mathbf{p}$, and $\mathbf{q}' \to \mathbf{q}$. Hence we expect the baroclinic triads to cascade energy towards lower wavenumbers and enstrophy towards higher wavenumbers. These wavenumbers are three-dimensional, however, so in particular, we expect that the energy will not only be cascaded upscale, but also towards the barotropic mode, which has the lowest vertical wavenumber. This is called barotropization of the flow.

For scales much smaller than the deformation scale, $\mathbf{k}' \approx \mathbf{k}$, $\mathbf{p}' \approx \mathbf{p}$, and $\mathbf{q}' \approx \mathbf{q}$, so that the baroclinic triad conservation laws, Eqs. D.45 and D.46 become identical, and not just isomorphic, to the barotropic triad conservation laws given by Eqs. D.41 and D.42. Thus, we expect that at small scales, the enstrophy is cascaded downscale and energy is cascaded upscale in *two-dimensional* wavenumber just as in two-dimensional turbulence. Stratification effects, such as barotropization, are not expected to occur at these scales. Of course, if the scales considered are too small, then three-dimensional effects become important, and the quasi-geostrophic approximation is no longer valid.

To analyze the case when the scales are much than the deformation scale, $\mathbf{k}, \mathbf{p}, \mathbf{q} \ll k_i$, we need to go back to the original equations, Eqs. D.43 and D.44. We can neglect k^2, p^2, and q^2, so that Eqs. D.43 and D.44 collapse into

$$\frac{\partial}{\partial t}\left(\tau_{\mathbf{p}}\tau_{-\mathbf{p}} + \tau_{\mathbf{q}}\tau_{-\mathbf{q}}\right) = 0. \tag{D.49}$$

Hence for scales much larger than the deformation scale, there is no simultaneous conservation laws for energy and potential enstrophy for the *baroclinic* triad. This means that the baroclinic triads at these scales can cascade energy downscale. The barotropic triads, however, always cascade energy upscale. Whether there is a net upscale or downscale cascade of energy will depend on the details of the problem at hand. In addition, Eq. D.49 implies that there is no exchange of energy between barotropic and baroclinic modes at these scales. Hence, barotropization cannot occur.

Appendix E

Numerical Integration of the Two-level Spherical QGPV Model

The two-level QGPV equations in spherical coordinates can be written as

$$\frac{\partial q_i}{\partial t} = \left(\frac{\partial q_i}{\partial t}\right)_N + \left(\frac{\partial q_i}{\partial t}\right)_L, \tag{E.1}$$

where $i = 1, 2$;

$$\left(\frac{\partial q_i}{\partial t}\right)_N = -J\left(\psi_i, q_i\right) \tag{E.2}$$

is the non-linear tendency, and

$$\left(\frac{\partial q_i}{\partial t}\right)_L = -2\frac{\partial \psi_i}{\partial \lambda} + f_i - \alpha\nabla^2\psi_i + (-1)^p \nu_i^0 \nabla^{2p}\left(\nabla^2\psi_i\right) \tag{E.3}$$

is the linear tendency. In Eq. E.3, the first term on the right hand side is the Coriolis force (differential rotation); the second term, f_i, is a parameterization for some kind of forcing, such heating or subgrid-scale processes; the third term represents Ekman drag; and the last term is a hyperdiffusion operator, with p an integer, which is a parameterization for subgrid-scale dissipation. The Jacobian operator in Eq. E.2 is defined as

$$J(A, B) = \frac{1}{\cos\phi}\left(\frac{\partial A}{\partial \lambda}\frac{\partial B}{\partial \phi} - \frac{\partial B}{\partial \lambda}\frac{\partial A}{\partial \phi}\right), \tag{E.4}$$

where λ is the longitude and ϕ is the latitude. The reduced potential vorticity, q_i, is defined as

$$q_i = \nabla^2\psi_i + (-1)^i F\left(\psi_1 - \psi_2\right). \tag{E.5}$$

The Laplacian operator in spherical coordinates is

$$\nabla^2\psi = \frac{1}{\cos^2\phi}\left[\frac{\partial^2\psi}{\partial\lambda^2} + \cos\phi\frac{\partial}{\partial\phi}\left(\cos\phi\frac{\partial\psi}{\partial\phi}\right)\right]. \tag{E.6}$$

The model is spectral in the sense that it is the spectral amplitudes that are stepped forward in time. So, for example,

$$\psi_i(\lambda, \phi, t) = \sum_{mn} \psi_{mn}^i(t) P_n^m(\sin\phi)\exp\left(im\lambda\right). \tag{E.7}$$

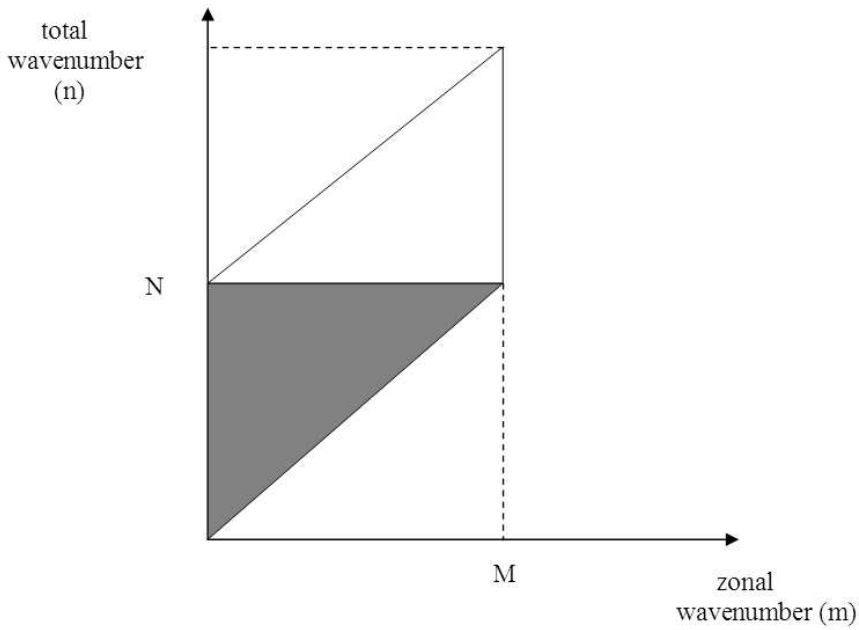

Figure E.1: Spectral truncation scheme on the sphere. The shaded area represents wavenumbers retained in the model.

Knowing ψ^i_{mn}, one can work out the spectral amplitudes for the other flow variables, such as ζ^i_{mn} from the fact that $\zeta_i = \nabla^2\psi_i$, and q^i_{mn} from the relationship given by Eq. E.5. The truncation in Eq. E.7 is triangular. The code is actually rhomboidal, but has been converted into a triangular one by zeroing the 'upper' triangle of the rhomboid. This depicted in E.1. The standard notation for triangular truncation at total wavenumber N is TN. so for example, T126 implies triangular truncation with maximum total wavenumber 126.

The spectral form of Eq. E.1 is

$$\frac{\partial q^i_{mn}}{\partial t} = \left(\frac{\partial q^i_{mn}}{\partial t}\right)_N + \left(\frac{\partial q^i_{mn}}{\partial t}\right)_L, \tag{E.8}$$

where m and n are zonal and total wavenumbers, respectively. The detailed forms of $\left(\frac{\partial q^i_{mn}}{\partial t}\right)_N$ and $\left(\frac{\partial q^i_{mn}}{\partial t}\right)_L$ will be discussed in subsequent sections. Timestepping of Eq. E.8 is done by the leap-frog method. The leap-frog method is however known to lead to splitting of the solutions due to the presence of a numerical mode. This is remedied by the introduction of a Modified Euler Backward timestepping scheme (Kurihara, 1965) after every 96 steps. The Modified Euler Backward scheme is also used for the first timestep. The viscous terms are known to lead to instability of the solutions if implemented by using the standard leap-frog scheme. This is overcome by evaluating the viscous terms using a lagged field; that is, the viscous terms at time t_i are evaluated using the vorticity (or potential vorticity) at time t_{i-1} when using the leap-frog method.

E.1 Non-Linear Tendency

In general, the non-linear tendency can be written in terms of interaction coefficients as in Eq. 2.53 for example. However, this has been found to be numerically inefficient due to the large number of interaction coefficients, especially at high resolution (Orszag, 1970b). Instead, at each timestep, the spectral amplitudes ($q^i_{mn}(t)$ and $\psi^i_{mn}(t)$) are transformed into physical space ($q_i(\lambda, \phi, t)$ and $\psi_i(\lambda, \phi, t)$), and evaluated using Eq. E.2. The resulting tendency $\left(\frac{\partial q_i}{\partial t}\right)_N$ is then transformed back into spectral space. This is know as the Grid Transform method. The discussion that follows is based on that given by Bourke (1972).

Using Eq. E.4 and the definitions

$$U_i = u_i \cos\phi, \tag{E.9}$$

$$V_i = v_i \cos\phi, \tag{E.10}$$

where u_i and v_i are the zonal and meridional winds given by

$$u_i = -\frac{\partial \psi_i}{\partial \phi} \tag{E.11}$$

and

$$v_i = \frac{1}{\cos\phi}\frac{\partial \psi_i}{\partial \lambda}, \tag{E.12}$$

and the fact that $\nabla \cdot \mathbf{u_i} = 0$, we can write Eq. E.2 as

$$\left(\frac{\partial q_i}{\partial t}\right)_N = -\frac{1}{\cos^2\phi}\left[\frac{\partial}{\partial \lambda}\left(U_i q_i\right) + \cos\phi \frac{\partial}{\partial \phi}\left(V_i q_i\right)\right]. \tag{E.13}$$

The terms $U_i q_i$ and $V_i q_i$ in Eq. E.13 are then expanded in terms of complex Fourier series along latitudinal circles:

$$U_i q_i = \sum_m A_m(\phi) \exp\left(im\lambda\right) \tag{E.14}$$

and

$$V_i q_i = \sum_m B_m(\phi) \exp\left(im\lambda\right). \tag{E.15}$$

Substituting Eqs. E.14 and E.15 in Eq. E.13, and then taking the inverse transform (as given by Eq. A.10), one obtains

$$\left(\frac{\partial q^i_{mn}}{\partial t}\right)_N = -\int_{\frac{\pi}{2}}^{\frac{\pi}{2}} \frac{1}{\cos^2\phi}\left[imA_m(\phi) + \frac{\partial B_m(\phi)}{\partial \phi}\right] P^m_n\left(\sin\phi\right)\cos\phi d\phi, \tag{E.16}$$

which can be written as

$$\left(\frac{\partial q^i_{mn}}{\partial t}\right)_N = -\int_{\frac{\pi}{2}}^{\frac{\pi}{2}} \frac{1}{\cos^2\phi}\left[imA_m(\phi)P^m_n\left(\sin\phi\right) - B_m(\phi)\cos\phi\frac{\partial}{\partial \phi}P^m_n\left(\sin\phi\right)\right]\cos\phi d\phi, \tag{E.17}$$

upon integrating the second term in Eq. E.16 by parts (Bourke, 1972).

The procedure for calculating the non-linear term can then be summarized as follows. At each timestep, U_i, V_i, and q_i are calculated from the spectral coefficients $U^i_{\mathbf{k}}$, $V^i_{\mathbf{k}}$, and $q^i_{\mathbf{k}}$ using a spectral (spherical harmonic) transform (see Eq. A.7). The coefficients A_m and B_m are then calculated from Eqs. E.14 and E.15 using an inverse (complex) Fourier

transform for each value of the latitude, ϕ. Finally, the spectral non-linear tendency can be calculated from Eq. E.17 by numerical quadrature.

E.2 Linear Tendency

The spectral form of the linear term is given by

$$\left(\frac{\partial q^i_{\mathbf{k}}}{\partial t}\right)_L = -2V^i_{mn} + f^i_{mn} - \left(\alpha + \nu^0_i [n(n+1)]^p\right) \zeta^i_{mn}, \tag{E.18}$$

where

$$V^i_{mn} = im\psi^i_{mn} = -im\frac{\zeta^i_{mn}}{n(n+1)} \tag{E.19}$$

is the spectral component of V_i; ψ^i_{mn} is the spectral component of ψ_i; and

$$\zeta^i_{mn} = -n(n+1)\psi^i_{mn} \tag{E.20}$$

is the spectral component of the relative vorticity $\zeta_i = \nabla^2\psi_i$. f^i_{mn} is the spectral component of the forcing, f_i.

E.3 Specification of forcing terms

The forcing function f^i_{mn} can be either deterministic or stochastic, or both, depending on what is being modelled. Numerically, these are handled differently; hence, we split

$$f^i_{mn} = \bar{f}^i_{mn} + \hat{f}^i_{mn}. \tag{E.21}$$

The deterministic 'forcing', $\bar{f}^i_{mn}$, in this study is a relaxation of the zonal wind towards some prescribed value; this is frequently referred to as a source term. Furthermore, the value at the top level is different to the value at the bottom level; hence, a vertical shear is imposed on the flow. This is a parameterization for the meridional heating gradients in the atmosphere, which, together with the Coriolis effect, are responsible for the formation of mid-latitude jet streams with vertical gradients. In the ocean, we can regard this to be a parameterization for the wind stress. Computationally, this is achieved by specifying

$$\bar{f}^i_{mn} = \kappa\left[\left(q^i_{mn}\right)^{rel} - q^i_{mn}\right] \tag{E.22}$$

which is a source term consisting of forcing and dissipation terms. Here κ is a relaxation inverse time-scale; $\left(q^i_{mn}\right)^{rel}$ is a prescribed value of the potential vorticity. For the simple case of solid-body-rotation relaxation, we can calculate $\left(q^i_{mn}\right)^{rel}$ from the zonal wind as follows. Since,

$$\left(q^i_{mn}\right)^{rel} = \left(\zeta^i_{mn}\right)^{rel} + (-1)^{(i-1)}F\left(\left(\zeta^1_{mn}\right)^{rel} - \left(\zeta^2_{mn}\right)^{rel}\right), \tag{E.23}$$

and $\left(\zeta^i_{mn}\right)^{rel}$ can be calculated from the relation

$$\left(\zeta^i_{mn}\right)^{rel} = 2\sqrt{\frac{2}{3}}U^{rel}_i, \tag{E.24}$$

where U_i^{rel} is the zonal wind at the equator.

The random forcing, $\hat{f}_{mn}^i$, is used to stochastically simulate the injection of energy from some unresolved process. In this study, we shall only use the random forcing to simulate stochastic backscatter from the subgrid scales. We assume that the noise being modelled is white; we also assume, for the time being, that the noise at the top level, $\hat{f}_{mn}^1$, is not correlated with the noise at the bottom level, $\hat{f}_{mn}^2$. The modification to level-correlated noise will be considered in Appendix F. For a white noise process, we have

$$\langle \hat{f}_{mn}(t)\hat{f}_{-mn}(s)\rangle = F_{mn}(t)\delta(t-s), \tag{E.25}$$

where $F_{mn}(t)$ is the contribution of the random forcing to the equal-time covariance tendency. The finite-difference form of the delta function for the leap-frog method is defined as

$$\delta(t-s) = \begin{cases} \frac{1}{2\Delta t} & \text{if } |t-s| < \Delta t; \\ 0 & \text{otherwise.} \end{cases} \tag{E.26}$$

The random noise is then defined as

$$\hat{f}_{mn}(t) = \sqrt{\frac{F_{mn}}{2\Delta t}}\, w_{mn}(t), \tag{E.27}$$

where w_{mn} is a random Gaussian variable such that

$$\langle w_{mn}\rangle = 0 \tag{E.28}$$

and

$$\langle w_{mn} w_{-mn}\rangle = 1. \tag{E.29}$$

The random Gaussian variables are generated by

$$w_{mn} = \sqrt{-2\ln A_{mn}^r}\exp\left(i\phi_{mn}^r\right), \tag{E.30}$$

where

$$A_{mn}^r = r_1 \tag{E.31}$$

and

$$\phi_{mn}^r = 2\pi r_2. \tag{E.32}$$

r_1 and r_2 are random numbers, uniform in the interval $[0,1]$. They are generated by the call to the subroutine *random_number(ranf)*, where *ranf* is a random number seed. This subroutine is part of the *FORTRAN 90* standard library package. To prevent too much splitting of the solutions, the random forcing at timestep t_i, $h_{mn}(t_i)$, is assumed to be correlated with the random forcing at the next timestep, namely, $h_{mn}(t_{i+1})$. This can be achieved by specifying

$$h_{mn}(t_i) = \frac{1}{\sqrt{2}}\left[\hat{f}_{mn}(t_i) + \hat{f}_{mn}(t_{i-1})\right]. \tag{E.33}$$

Note that the actual random forcing applied is as given by Eq. E.33, and we have suppressed vertical labels in Eqs. E.25 to E.33, but it is to be understood that these equations apply to both levels.

E.4 Diagnostics

The main diagnostics that are used are those of energy, both kinetic and potential, in the PV and BTBC formulations. In the PV formulation, we calculate

$$K^1_{mn} = \frac{1}{8}\frac{|\zeta^1_{mn}|^2}{n(n+1)}, \tag{E.34}$$

the Level 1 kinetic energy,

$$K^2_{mn} = \frac{1}{8}\frac{|\zeta^2_{mn}|^2}{n(n+1)}, \tag{E.35}$$

the Level 2 kinetic energy, and

$$P_{mn} = \frac{1}{8}F\frac{|\zeta^1_{mn} - \zeta^2_{mn}|^2}{[n(n+1)]^2}, \tag{E.36}$$

the potential energy. These expressions follow from the analogs of the physical-space expressions in Eqs. D.12, D.13, and D.14 in spherical geometry. Additionally, the energy diagnostics are defined per unit area, $4\pi^2$, and mass, $\frac{M}{2}$, of each layer of fluid, where M is the total mass of fluid. In BTBC space, we calculate

$$K^+_{mn} = \frac{1}{4}\frac{|\zeta^+_{mn}|^2}{n(n+1)}, \tag{E.37}$$

the barotropic kinetic energy,

$$K^-_{mn} = \frac{1}{4}\frac{|\zeta^-_{mn}|^2}{n(n+1)}, \tag{E.38}$$

the baroclinic kinetic energy, and

$$P_{mn} = \frac{1}{4}2F\frac{|\zeta^-_{mn}|^2}{[n(n+1)]^2}, \tag{E.39}$$

the potential energy. These follow from the analogs of Eqs. D.19, D.20, and D.21 in spherical geometry, and are defined per unit area and mass as the corresponding expressions in PV space above. We also use the total baroclinic energy

$$E^-_{mn} = \frac{1}{4}\left[n(n+1) + 2F\right]\frac{|\zeta^-_{mn}|^2}{[n(n+1)]^2}. \tag{E.40}$$

It is convenient to define the energy diagnostics above, collectively denoted by E_{mn}, in terms of total wavenumber, n, only by summing over the zonal wavenumber, m. Hence

$$e(n) = E_{0n} + \sum_{m=1}^{m=\mathcal{M}(n)} 2E_{mn}. \tag{E.41}$$

Similarly, a diagnostic dependent on m only can be defined as

$$E(m) = \sum_{n=N-\mathcal{N}(m)+1}^{n=N} E_{mn}. \tag{E.42}$$

Here, $\mathcal{M}(n)$ is the number of ms for a given n, and $\mathcal{N}(m)$ is the number of ns for a given m (see Fig. E.1).

Appendix F

Numerical Implementation of Subgrid-scale Parameterizations

The methodology for subgrid-scale parameterizations using DNS, outlined in Section 5.5, is implemented as follows. A simulation with maximum (total) truncation wavenumber N is performed. The parameters in this simulation, such as κ and U_i^{rel} (in the case of solid-body-rotation forcing), are adjusted so that reasonable values of large-scale (mean and transient) kinetic and potential energies are obtained. Additionally, the parameters ν_i^0 are adjusted so that the kinetic energy spectrum has an approximately k^{-3} dependence all the way to the maximum (total) wavenumber N. In fact, observations (Nastrom and Gage, 1985) suggest that in the atmosphere, at high resolution, corresponding to scales below about 600 km, a $k^{-\frac{5}{3}}$ energy spectrum exists. It is not completely clear that the $k^{-\frac{5}{3}}$ spectrum can be simulated by a simple two-level model, although such a claim was indeed made by Tung and Orlando (2003). For the purposes of this thesis, however, we have taken the view that the spectrum is k^{-3} all the way to N. This does not in any way invalidate any of the arguments regarding subgrid-scale parameterizations. The statistics of the model, denoted by angular brackets, are calculated by taking the flow to steady state, through a long integration, and then taking time-averages. So, for example,

$$\langle x \rangle = \frac{\sum_{t=t_{min}}^{t=t_{max}} x_t}{(t_{max} - t_{min} + 1)}. \tag{F.1}$$

Here, x_t is the value of the variable x, at time t. x could represent, for example, the vorticity, ζ_{mn}^i, or (twice) the enstrophy, $\zeta_{mn}^i \zeta_{-mn}^i$. In the averaging period $[t_{min}, t_{max}]$, the flow is in a steady state.

The code has also been designed so that it calculates the subgrid tendency at an 'artificial' cutoff wavenumber N_*, where $n \leq N_*$. That is, for $m, n \leq N_*$, which are the 'resolved' scales,

$$\left(\frac{\partial q_{mn}^i}{\partial t}\right)_S = \frac{\partial q_{mn}^i}{\partial t} - \left(\frac{\partial q_{mn}^i}{\partial t}\right)_R. \tag{F.2}$$

Here $\left(\frac{\partial q_{mn}^i}{\partial t}\right)_R$ is calculated by a 'masking' procedure so that the non-linear terms ($U_i q_i$ and $V_i q_i$) in Eqs. E.14 and E.15 are evaluated using a 'masked' field. So, for example,

$$\left(\psi_{mn}^i\right)_M = \begin{cases} \psi_{mn}^i & \text{if } m, n < N_*; \\ 0 & \text{otherwise.} \end{cases} \tag{F.3}$$

$\left(q_{mn}^i\right)_M$, $\left(U_{mn}^i\right)_M$, and $\left(V_{mn}^i\right)_M$ can then be evaluated from Eq. F.3. With this definition

of $\left(\frac{\partial q^i_{mn}}{\partial t}\right)_R$, the tendency $\left(\frac{\partial q^i_{mn}}{\partial t}\right)_S$ calculated in Eq. F.2 is then the 'subgrid' tendency, for it represents the contribution to the tendency due to interaction between modes such that at least one of the modes has wavenumber greater than N_*. At each timestep the fields q^i_{mn} and $\left(\frac{\partial q^i_{mn}}{\partial t}\right)_S$ are written to a file. Note that only fields with 'resolved' scale wavenumbers are stored.

We now have all the information required to calculate the matrices $\mathbf{M}$, $\mathbf{F}$, and $\bar{\mathbf{f}}$ to maintain the spectra if a spectral truncation is performed at the wavenumber N_*. First, we calculate the mean field, $\bar{q}^i_{mn}$, by averaging over the time interval $[t_{min}, t_{max}]$, and define the transient field

$$\hat{q}^i_{mn} = q^i_{mn} - \bar{q}^i_{mn}. \tag{F.4}$$

Similarly,

$$\widehat{\left(\frac{q^i_{mn}}{\partial t}\right)}_S = \left(\frac{q^i_{mn}}{\partial t}\right)_S - \overline{\left(\frac{q^i_{mn}}{\partial t}\right)_S}. \tag{F.5}$$

Following the notation of Section 5.5, we can write

$$\mathbf{x} = \begin{pmatrix} q^1_{mn} \\ q^2_{mn} \end{pmatrix} \tag{F.6}$$

and

$$\left(\frac{\partial \mathbf{x}}{\partial t}\right)_S = \begin{pmatrix} \left(\frac{\partial q^1_{mn}}{\partial t}\right)_S \\ \left(\frac{\partial q^2_{mn}}{\partial t}\right)_S \end{pmatrix} \tag{F.7}$$

so that

$$\hat{\mathbf{x}} = \mathbf{x} - \bar{\mathbf{x}} \tag{F.8}$$

and

$$\left(\frac{\partial \hat{\mathbf{x}}}{\partial t}\right)_S = \left(\frac{\partial \mathbf{x}}{\partial t}\right)_S - \left(\frac{\partial \bar{\mathbf{x}}}{\partial t}\right)_S. \tag{F.9}$$

The matrix $\mathbf{M}$ can then be calculated from Eq. 5.52, which has been rewritten here in a slightly different form for clarity:

$$\mathbf{M} = \langle \left[\int_{t_0}^{t} ds \left(\frac{\partial \hat{\mathbf{x}}(s)}{\partial t}\right)_S \hat{\mathbf{x}}^\dagger(t_0)\right] \rangle \langle \left[\int_{t_0}^{t} ds \hat{\mathbf{x}}(t) \hat{\mathbf{x}}^\dagger(t_0)\right]^{-1} \rangle. \tag{F.10}$$

The terms inside the angular brackets are matrices whose elements are in the form of integrals. The integrals are evaluated using the trapezoidal rule over some time interval $\tau = t - t_0$, long enough to capture several eddy turnover times of the scales with wavenumbers close to N_*. This forms one member of the ensemble. To obtain other members, we integrate over $\tau = (t+1) - (t_0+1)$, $\tau = (t+2) - (t_0+2)$, and so on. That is, in general,

$$\langle \int_{t_0}^{t} F(s) ds \rangle = \frac{1}{N} \sum_{i=1}^{N} \int_{t_0+i\Delta t}^{t+i\Delta t} F(s) ds, \tag{F.11}$$

where $N = T - \tau$, and T is the total number of timesteps for which the data has been stored within the steady state. $F(s)$ is a general symbol for a term such as $\left(\frac{\partial \hat{\mathbf{x}}(s)}{\partial t}\right)_S \hat{\mathbf{x}}^\dagger(t_0)$.

The final step is to preform the matrix operations to solve for $\mathbf{M}$ in Eq. F.10. Denoting

$$\mathbf{A} = \langle \int_{t_0}^{t} ds \hat{\mathbf{x}}(t) \hat{\mathbf{x}}^{\dagger}(t_0) \rangle \tag{F.12}$$

and

$$\mathbf{B} = \langle \int_{t_0}^{t} ds \left(\frac{\partial \hat{\mathbf{x}}(s)}{\partial t} \right)_S \hat{\mathbf{x}}^{\dagger}(t_0) \rangle, \tag{F.13}$$

we have $\mathbf{M} = \mathbf{B}\mathbf{A}^{-\mathbf{1}}$, which can be written as

$$\mathbf{A}^{\dagger}\mathbf{M}^{\dagger} = \mathbf{B}^{\dagger}. \tag{F.14}$$

The LAPACK routine *zgesv* solves for $\mathbf{X}$ in the system of equations $\tilde{\mathbf{A}}\mathbf{X} = \tilde{\mathbf{B}}$. Thus, setting $\tilde{\mathbf{A}} = \mathbf{A}^{\dagger}$ and $\tilde{\mathbf{B}} = \mathbf{B}^{\dagger}$, we can solve for $\mathbf{M}^{\dagger}$, and hence $\mathbf{M}$. Having found $\mathbf{M}$, we can then find $\mathbf{F}$, using Eq. 5.54, by straightforward matrix multiplication and addition. We now have the complete set of matrices $\mathbf{M}$, $\mathbf{F}$, and $\bar{\mathbf{f}}$. Using these matrices, we can truncate the system at wavenumber N_* while maintaining the same spectrum for $N < N_*$. We call all simulations employing $\mathbf{M}$, $\mathbf{F}$, and $\bar{\mathbf{f}}$, at a maximum resolution N_*, Large Eddy Simulations (LES).

In the LES, the non-linear terms are calculated in exactly the same way as in the DNS. However, we have additional terms in the linear tendency, namely

$$\left(\frac{\partial q^i_{mn}}{\partial t} \right)_S = \sum_j M^{ij}_{mn} \hat{q}^j_{mn} + \hat{f}^i_{mn} + \bar{f}^i_{mn}, \tag{F.15}$$

which parameterize the subgrid non-linear tendency. Here, the transient field $\hat{q}^i_{mn} = q^i_{mn} - \bar{q}^i_{mn}$, where $\bar{q}^i_{mn}$ is obtained by averaging over the the time interval $[t_{min}, t_{max}]$, as described above. The 'diffusive' term $\sum_j M^{ij}_{mn} \hat{q}^i_{mn} \equiv \mathbf{M}\hat{\mathbf{q}}$ is calculated by straightforward matrix multiplication, using a time-lagged value of q^i_{mn}, for computational stability. The mean subgrid tendency, $\bar{f}_{mn}$, is also straightforward to compute. The random forcing term, $\hat{f}^i_{mn}$, however, requires some discussion.

The covariance matrix $\mathbf{F}$ is in general non-diagonal. This means that the forcing on Level 1 should be correlated with the forcing on Level 2. Now, it can easily be shown from Eq. 5.54 that $\mathbf{F}$ is a Hermitian matrix; that is, $\mathbf{F} = \mathbf{F}^{\dagger}$. Hence, $\mathbf{F}$ has real eigenvalues, and can always be diagonalized. Thus, the matrix

$$\mathbf{G} = \mathbf{P}^{-\mathbf{1}}\mathbf{F}\mathbf{P} \tag{F.16}$$

is a diagonal matrix whose elements are the eigenvalues of $\mathbf{F}$, and $\mathbf{P}$ is a unitary matrix whose columns consist of the eigenvectors of $\mathbf{F}$. If we assume that the noise is white (see Eqs. 5.55 and E.25) then the random forcing vector $\hat{\mathbf{f}}$ in the QGPV equation can be written as

$$\hat{\mathbf{f}} = \frac{1}{\sqrt{2\Delta t}} \mathbf{P}\mathbf{g}. \tag{F.17}$$

Here,

$$\langle \mathbf{g}\mathbf{g}^{\dagger} \rangle = \mathbf{G} \tag{F.18}$$

and

$$\langle \hat{\mathbf{f}}\hat{\mathbf{f}}^{\dagger} \rangle = \frac{\mathbf{F}}{2\Delta t}. \tag{F.19}$$

Equation F.17 satisfies Eq. F.16 because, from Eq. F.17, $\mathbf{g} = \sqrt{2\Delta t}\mathbf{P}^\dagger\hat{\mathbf{f}}$, since $\mathbf{P}$ is a unitary matrix, and hence,

$$\begin{aligned}\mathbf{G} = \langle \mathbf{g}\mathbf{g}^\dagger \rangle &= 2\Delta t \mathbf{P}^\dagger \langle \hat{\mathbf{f}}\hat{\mathbf{f}}^\dagger \rangle \mathbf{P} \\ &= \mathbf{P}^\dagger \mathbf{F} \mathbf{P} \\ &= \mathbf{P}^{-1} \mathbf{F} \mathbf{P},\end{aligned}$$

where the last step follows because $\mathbf{P}$ is unitary, and hence its Hermitian conjugate is the same as its inverse. The matrix $\mathbf{G}$ has the form

$$\mathbf{G} = \begin{pmatrix} \lambda_1 & 0 \\ 0 & \lambda_2 \end{pmatrix}, \tag{F.20}$$

where λ_1 and λ_2 are eigenvalues of $\mathbf{F}$. Note that all the matrices above are functions of wavenumber. Reverting back to the notation used in Eq. F.15, we have

$$\hat{f}^i_{mn} = \frac{1}{\sqrt{2\Delta t}} \sum_j P^{ij}_{mn} g^j_{mn}, \tag{F.21}$$

where

$$g^i_{mn} = \sqrt{\lambda^i_{mn}} w^i_{mn} \tag{F.22}$$

and w^1_{mn} and w^2_{mn} are random Gaussian variables as defined as in Eqs. E.28 to E.32. To minimize splitting of the solutions, the random forcing imposed on the model is made slightly red over the timestep as discussed in Appendix E (Eq. E.33).

The truncation will frequently be performed at a scale small enough to regard the turbulence as isotropic. In that case, the matrices $\mathbf{M}$ and $\mathbf{F}$ do not depend on both m and n, the zonal and total wavenumbers, respectively, but only on n. The, reduced, isotropized matrices may be obtained from the full matrices by averaging over m; thus

$$\mathbf{M}(n) = \frac{1}{\mathcal{M}(n)} \sum_{m=0}^{m=\mathcal{M}(n)} \mathbf{M}(m,n) \tag{F.23}$$

and

$$\mathbf{F}(n) = \frac{1}{\mathcal{M}(n)} \sum_{m=0}^{m=\mathcal{M}(n)} \mathbf{F}(m,n). \tag{F.24}$$

Here, $\mathcal{M}(n)$ is the number of ms for a given n (see Fig. E.1). The mean subgrid forcing, $\overline{\mathbf{f}}$, is in general not expected to be isotropic, and is thus not averaged over when running the LES. It is expected that the dominant contribution to $\overline{\mathbf{f}}$ comes from the conversion of mean large-scale zonal energy into transient energy, which is very anisotropic.

Appendix G

Matrix Parameters in Barotropic-Baroclinic Space

Although the numerical code steps forward the potential vorticity field, and hence the matrix parameters $\mathbf{M}$, $\mathbf{F}$, and $\mathbf{f}$ are expressed in this space (PV space), it is frequently convenient to express the parameters in the barotropic-baroclinic (BTBC space) for diagnostic purposes. This is because the BTBC formulation brings out the isomorphism between two-dimensional and quasi-geostrophic flows more clearly, as discussed in Section 3.2.6.

In spectral space

$$\begin{aligned} q^1_{mn} &= \zeta^1_{mn} + \frac{F}{n(n+1)}\left(\zeta^1_{mn} - \zeta^2_{mn}\right) \\ q^2_{mn} &= \zeta^2_{mn} - \frac{F}{n(n+1)}\left(\zeta^1_{mn} - \zeta^2_{mn}\right). \end{aligned} \tag{G.1}$$

Hence

$$\begin{aligned} \zeta^+_{mn} &= \frac{1}{2}\left(\zeta^1_{mn} + \zeta^2_{mn}\right) = \frac{1}{2}\left(q^1_{mn} + q^2_{mn}\right) \\ \zeta^-_{mn} &= \frac{1}{2}\left(\zeta^1_{mn} - \zeta^2_{mn}\right) = \frac{1}{2c}\left(q^1_{mn} - q^2_{mn}\right), \end{aligned} \tag{G.2}$$

where

$$c = 1 + \frac{2F}{n(n+1)}. \tag{G.3}$$

This can be written more concisely in matrix form as

$$\mathbf{z} = \mathbf{T}\mathbf{q}, \tag{G.4}$$

where

$$\mathbf{z} = \begin{pmatrix} \zeta^+_{mn} \\ \zeta^-_{mn} \end{pmatrix}, \tag{G.5}$$

$$\mathbf{q} = \begin{pmatrix} q^1_{mn} \\ q^2_{mn} \end{pmatrix}, \tag{G.6}$$

and

$$\mathbf{T} = \frac{1}{2}\begin{pmatrix} 1 & 1 \\ \frac{1}{c} & -\frac{1}{c} \end{pmatrix}. \tag{G.7}$$

The matrix $\mathbf{T}$ transforms a vector $\mathbf{q}$ (PV space) into a vector $\mathbf{z}$ (BTBC space). The inverse

transform is given by the matrix

$$\mathbf{T^{-1}} = \begin{pmatrix} 1 & c \\ 1 & -c \end{pmatrix}. \tag{G.8}$$

Now, let

$$\frac{\partial \mathbf{q}}{\partial t} = \mathbf{M}\hat{\mathbf{q}} + \hat{\mathbf{f}} + \bar{\mathbf{f}}, \tag{G.9}$$

where $\frac{\partial \mathbf{q}}{\partial t}$ is the subgrid tendency. Multiplying Eq. G.9 from the left by $\mathbf{T}$, we have

$$\frac{\partial}{\partial t}\mathbf{T}\mathbf{q} = \mathbf{T}\mathbf{M}\hat{\mathbf{q}} + \mathbf{T}\hat{\mathbf{f}} + \mathbf{T}\bar{\mathbf{f}}. \tag{G.10}$$

Using Eq. G.4 and its inverse, $\mathbf{q} = \mathbf{T^{-1}}\mathbf{z}$, we have

$$\frac{\partial \mathbf{z}}{\partial t} = \mathbf{M}'\hat{\mathbf{z}} + \hat{\mathbf{f}}' + \bar{\mathbf{f}}', \tag{G.11}$$

where

$$\mathbf{M}' = \mathbf{T}\mathbf{M}\mathbf{T^{-1}}, \tag{G.12}$$

$$\hat{\mathbf{f}}' = \mathbf{T}\hat{\mathbf{f}}, \tag{G.13}$$

and

$$\bar{\mathbf{f}}' = \mathbf{T}\bar{\mathbf{f}}'. \tag{G.14}$$

We can also use Eq. G.13 to construct the covariance matrix $\mathbf{F}'$ as follows. Since $\mathbf{F}' = \hat{\mathbf{f}}'\left(\hat{\mathbf{f}}'\right)^{\dagger}$ and $\mathbf{F} = \hat{\mathbf{f}}\left(\hat{\mathbf{f}}\right)^{\dagger}$, we have, from Eq. G.13,

$$\begin{aligned} \mathbf{F}' &= \mathbf{T}\hat{\mathbf{f}}\left(\hat{\mathbf{f}}\right)^{\dagger}\mathbf{T}^{\dagger} \\ &= \mathbf{T}\mathbf{F}\mathbf{T}^{\dagger}. \end{aligned} \tag{G.15}$$

The matrices $\mathbf{M}'$, $\mathbf{F}'$, and $\bar{\mathbf{f}}'$, are expressed in BTBC space, and although not directly used in the LES, are very useful diagnostics, and will be referred to extensively in this study.

Appendix H

Matrix Parameters for Atmospheric LES at T63

The following figures show the anisotropic elements of the matrix $\mathbf{M_n}$, as contours, calculated for the atmospheric flow described in Section 8.1.1.

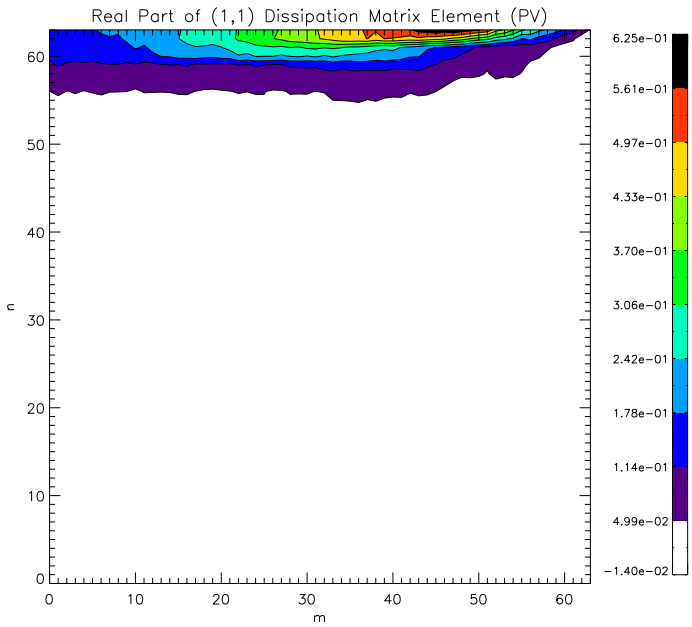

Figure H.1: The $-M^r_{11}$ anisotropic matrix element of the net dissipation matrix in the PV formulation (T63).

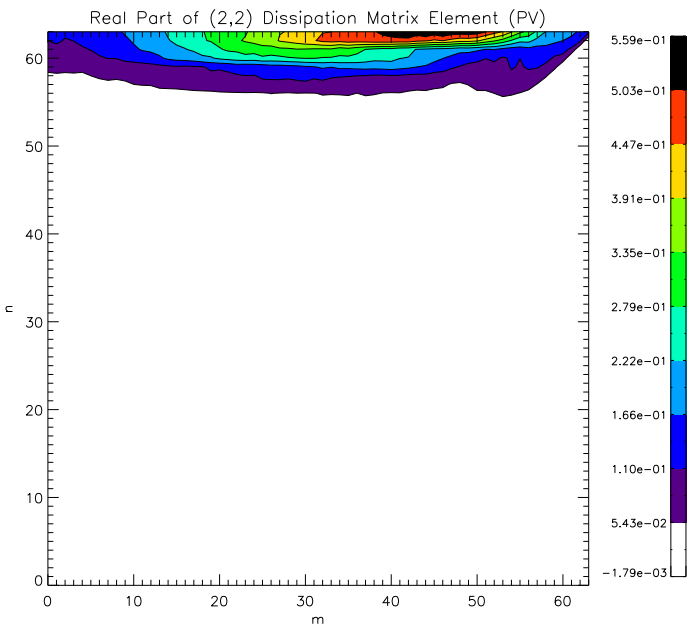

Figure H.2: The $-M^r_{22}$ anisotropic matrix element of the net dissipation matrix in the PV formulation (T63).

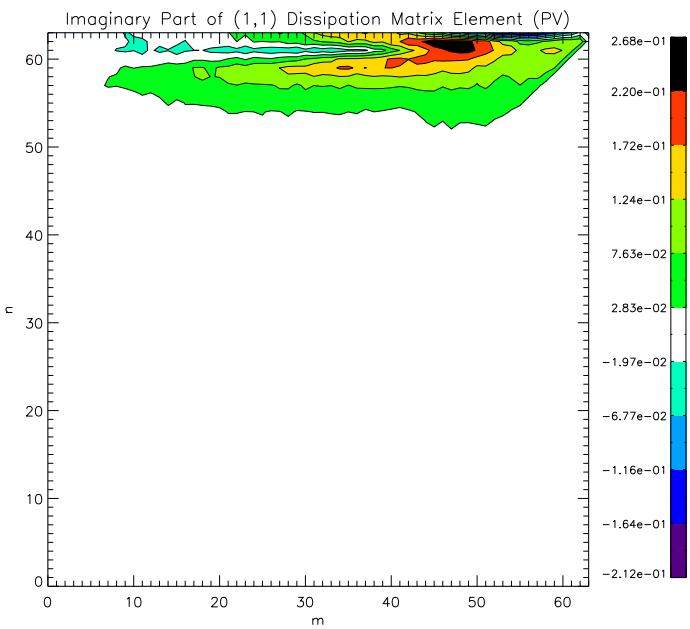

Figure H.3: The M^i_{11} anisotropic matrix element of the net dissipation matrix in the PV formulation (T63).

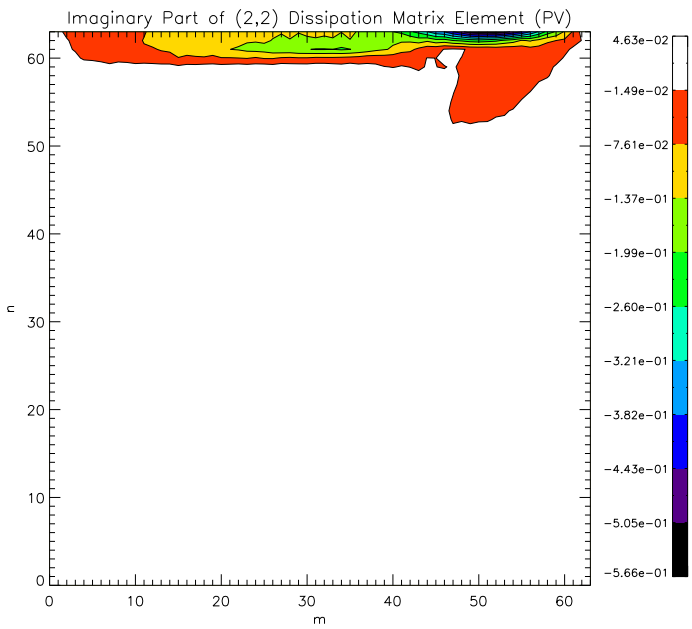

Figure H.4: The M^i_{22} anisotropic matrix element of the net dissipation matrix in the PV formulation (T63).

Appendix I

Matrix Parameters for Oceanic LES at T15

The following figures show the anisotropic matrix elements $\mathbf{M_d}$ and $\mathbf{F_b}$, as contours, calculated for the oceanic flow described in Section 8.2.4.

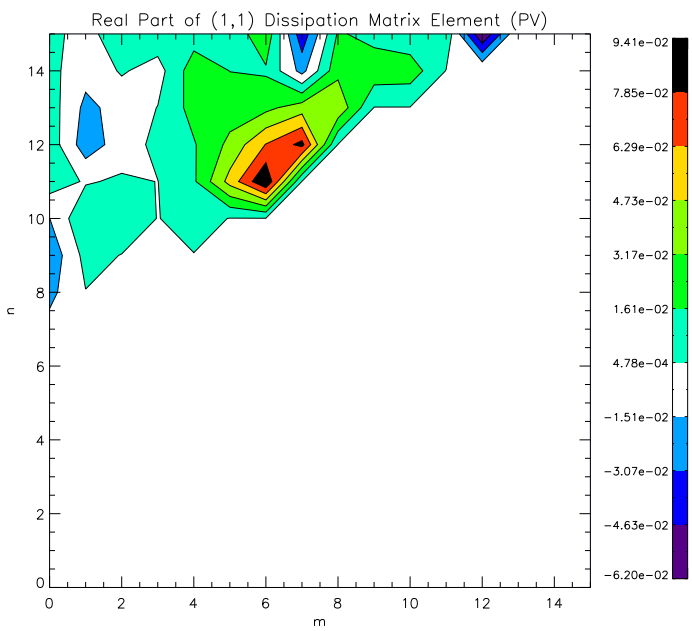

Figure I.1: The $-M^r_{11}$ anisotropic matrix element of the drain dissipation matrix in the PV formulation (T15).

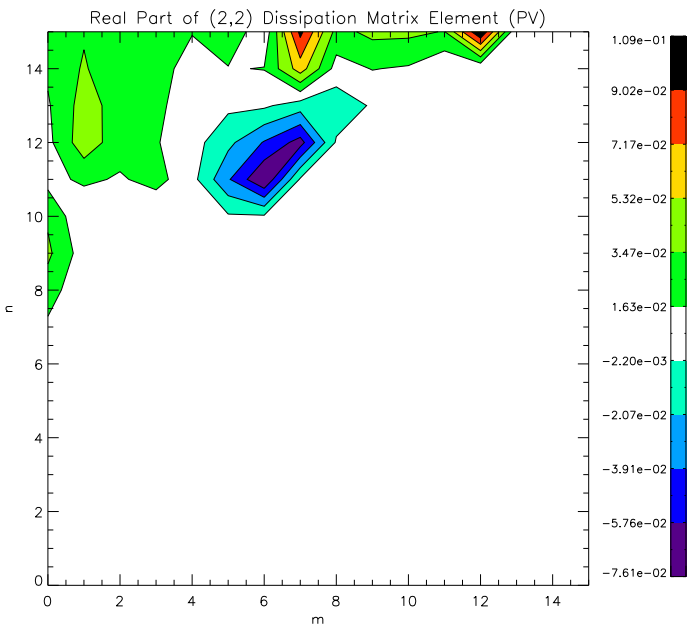

Figure I.2: The $-M^r_{22}$ anisotropic matrix element of the drain dissipation matrix in the PV formulation (T15).

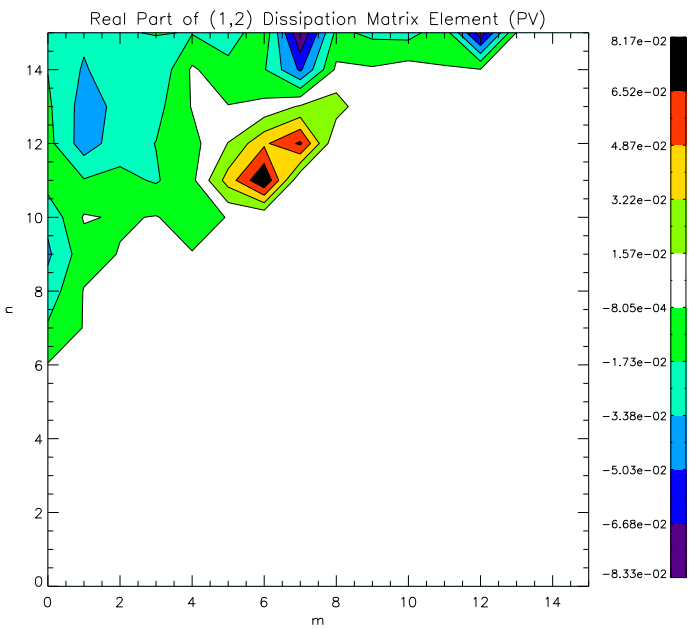

Figure I.3: The $-M^r_{12}$ anisotropic matrix element of the drain dissipation matrix in the PV formulation (T15).

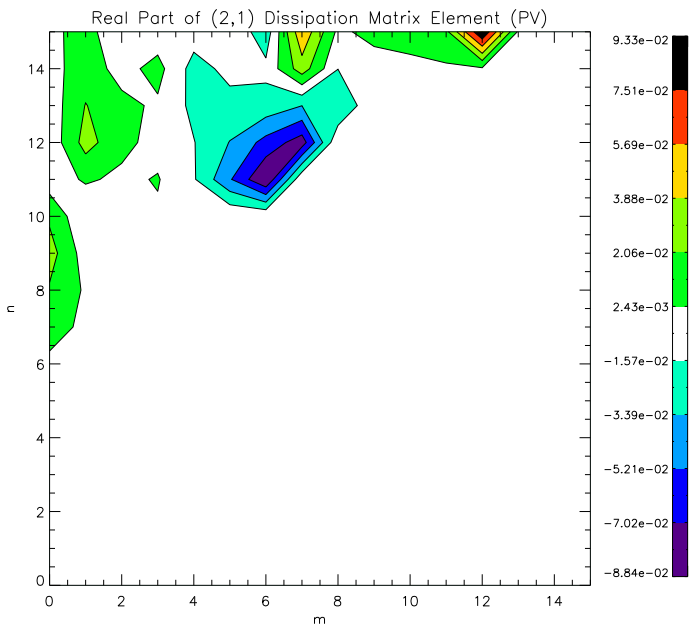

Figure I.4: The $-M_{21}^{r}$ anisotropic matrix element of the drain dissipation matrix in the PV formulation (T15).

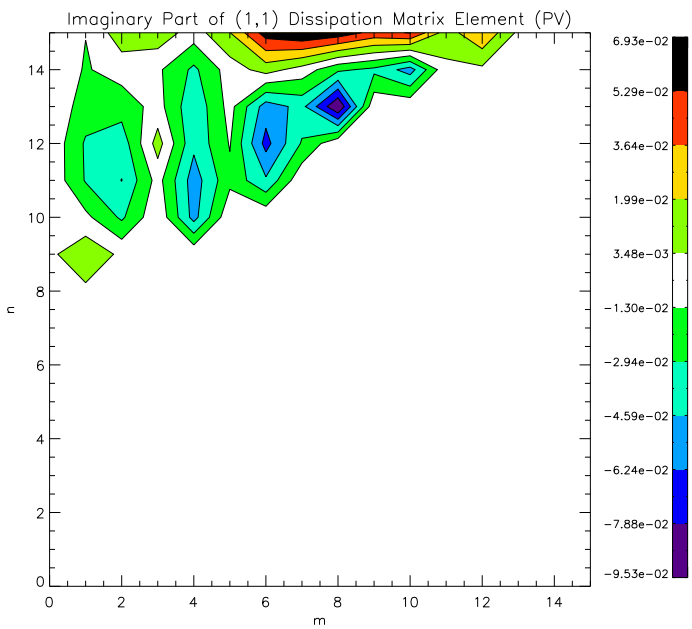

Figure I.5: The M_{11}^{i} anisotropic matrix element of the drain dissipation matrix in the PV formulation (T15).

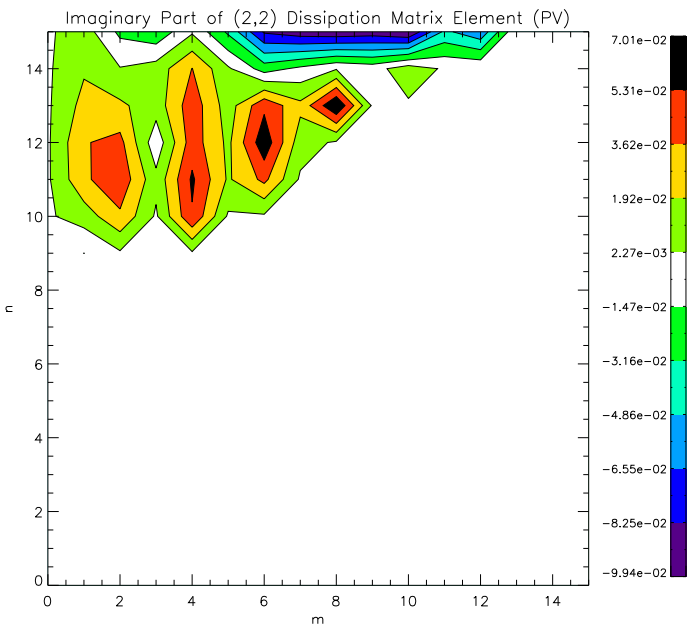

Figure I.6: The M^i_{22} anisotropic matrix element of the drain dissipation matrix in the PV formulation (T15).

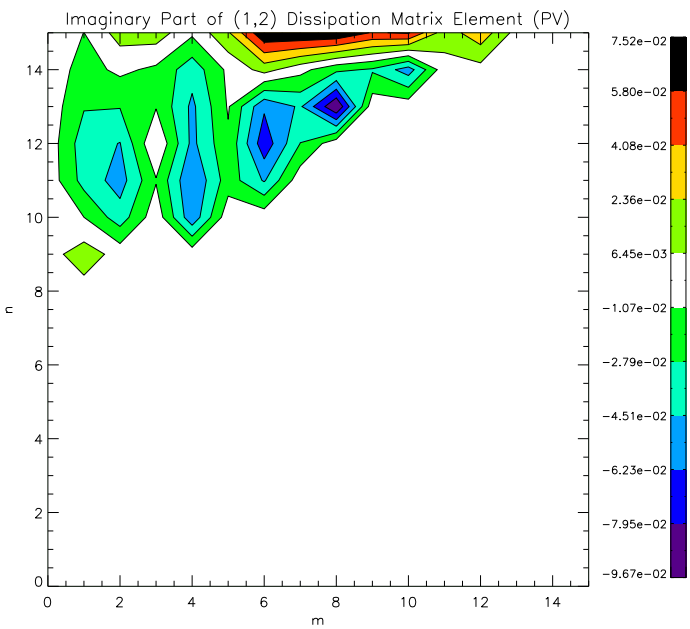

Figure I.7: The M^i_{12} anisotropic matrix element of the drain dissipation matrix in the PV formulation (T15).

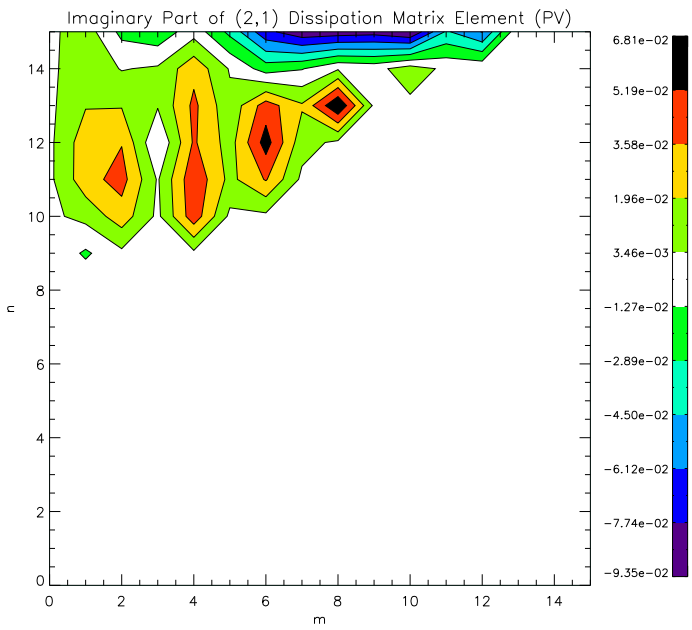

Figure I.8: The M^i_{21} anisotropic matrix element of the drain dissipation matrix in the PV formulation (T15).

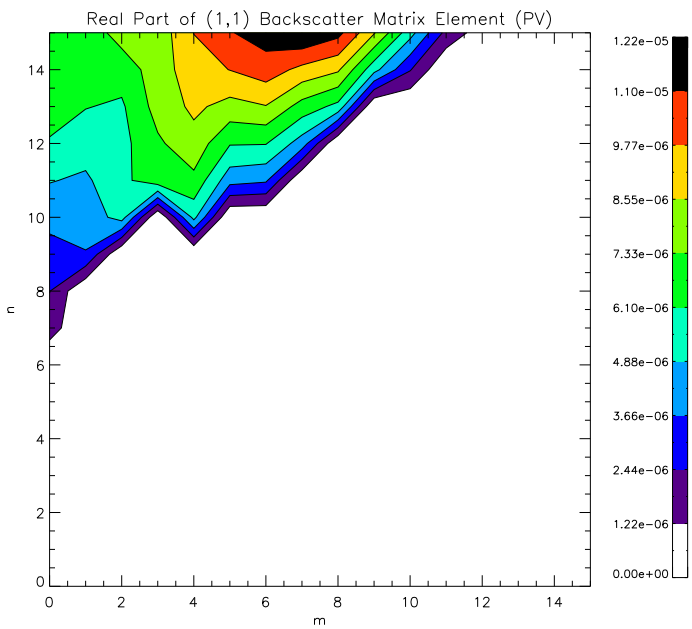

Figure I.9: The F^r_{11} anisotropic matrix element of the drain dissipation matrix in the PV formulation (T15).

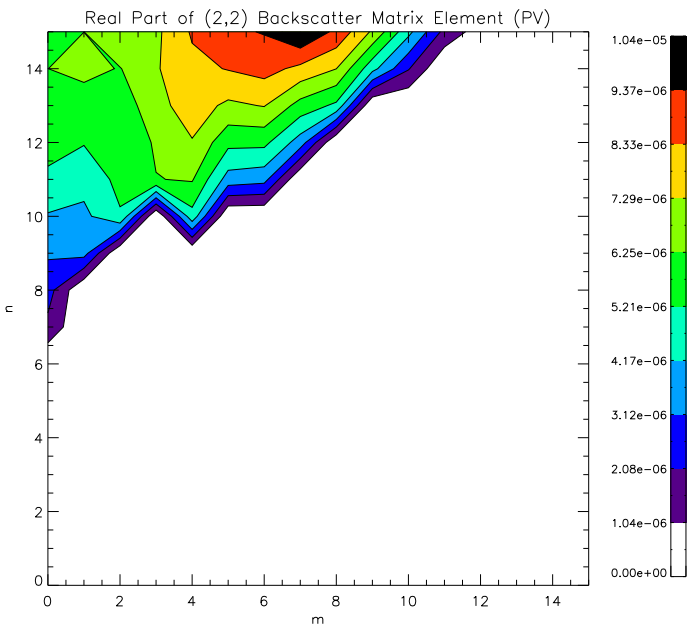

Figure I.10: The F^r_{22} anisotropic matrix element of the drain dissipation matrix in the PV formulation (T15).

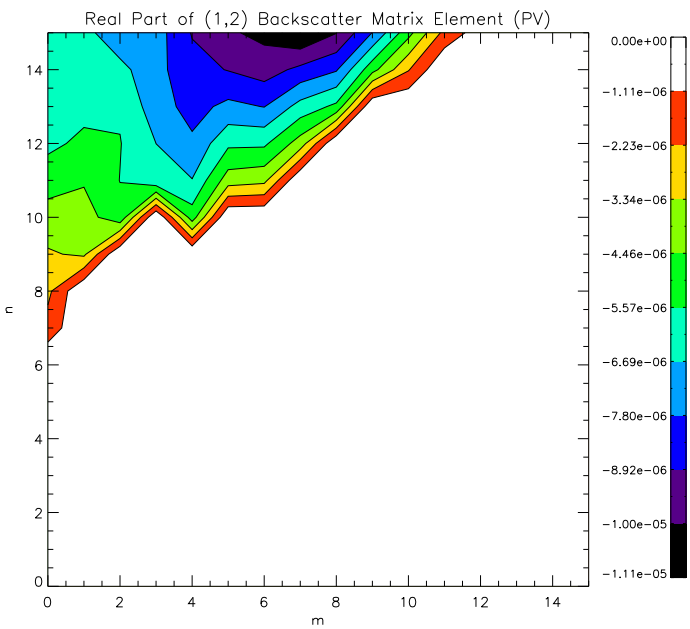

Figure I.11: The F^r_{12} anisotropic matrix element of the drain dissipation matrix in the PV formulation (T15).

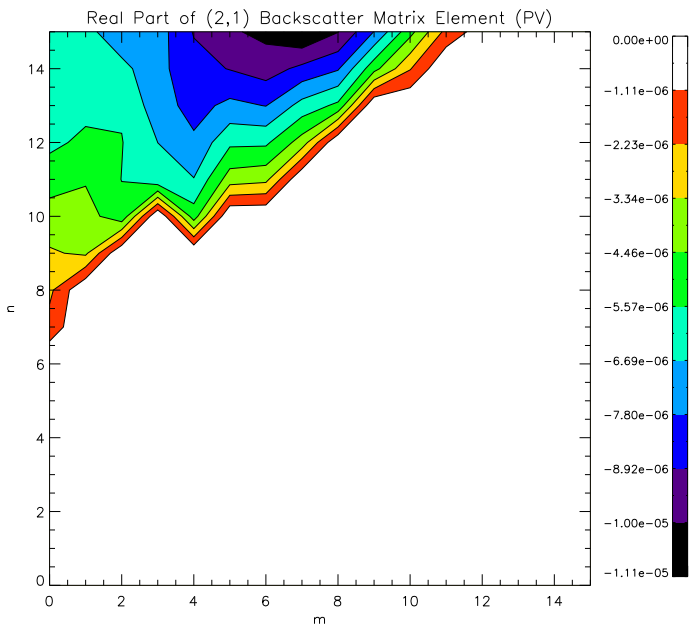

Figure I.12: The F_{21}^{r} anisotropic matrix element of the drain dissipation matrix in the PV formulation (T15).

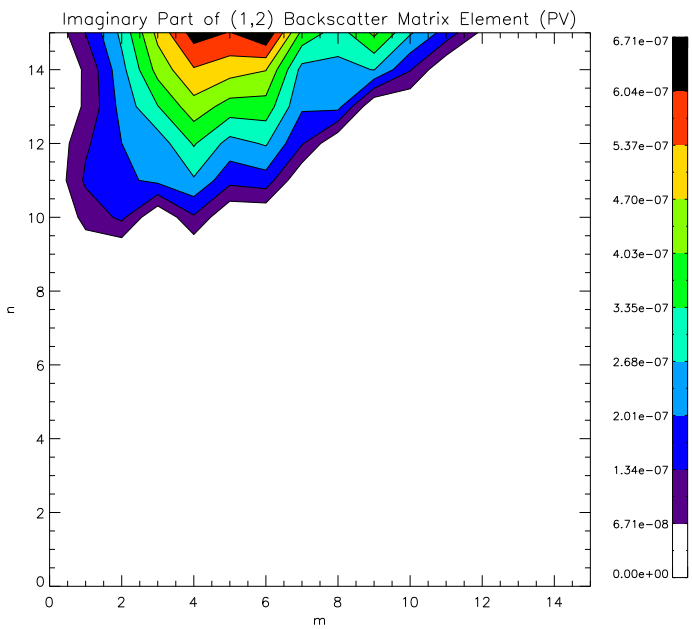

Figure I.13: The F_{12}^{i} anisotropic matrix element of the drain dissipation matrix in the PV formulation (T15).

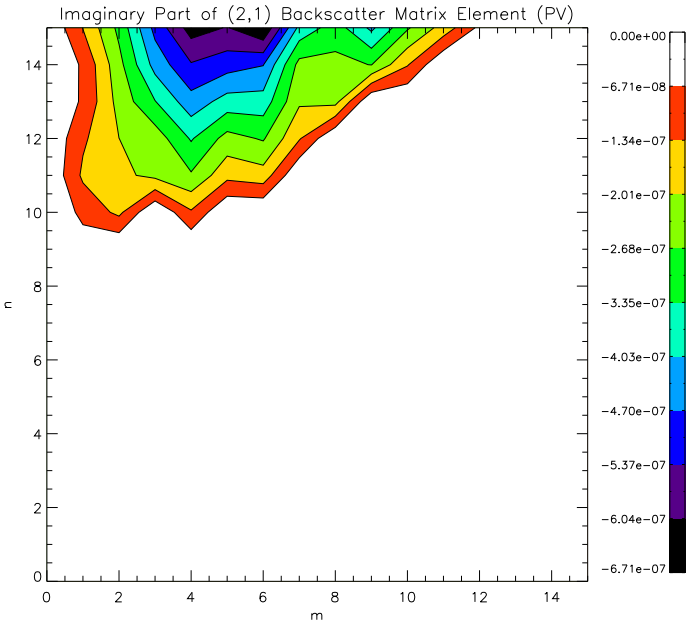

Figure I.14: The F_{21}^{i} anisotropic matrix element of the drain dissipation matrix in the PV formulation (T15).

Bibliography

[1] Andrews, D.G., and M.E. McIntyre, 1976: Planetary waves in horizontal and vertical shear: The generalized Eliassen-Palm relation and the mean zonal acceleration. *J. Atmos. Sci.*, **33**, 2031–2048.

[2] Basdevant, C., M. Lesieur, and R. Sadourny, 1978: Subgrid-scale modeling of enstrophy transfer in two-dimensional turbulence. *J. Atmos. Sci.*, **35**, 1028–1042.

[3] Batchelor, G.K., 1969: Computation of the energy spectrum in homogeneous two-dimensional turbulence. *Phys. Fluids*, **12**, II 233–238.

[4] Benzi, R., A.R. Hansen, and A. Sutera, 1984: On stochastic perturbation of simple blocking models. *Quart. J. Roy. Meteor. Soc.*, **110**, 393–409.

[5] Boer, G.J., N.A. McFarlane, R. Laprise, J.D. Henderson, and J.P. Blanchet, 1984: The Canadian Climate Centre spectral atmospheric general circulation model. *Atmos. Ocean*, **22**, 397–429.

[6] Boning, C.W., W.R. Holland, F.O. Bryan, G. Danabasoglu, and J.C. McWilliams, 1995: An overlooked problem in model simulations of the thermohaline circulation and heat transport in the Atlantic ocean. *J. Climate*, **8**, 515–523.

[7] Bourke, W., 1972: An efficient, one-Level, primitive-equation spectral model. *Mon. Weath. Rev.*, **100**, 683–689.

[8] Bretherton, F.P., and D.B. Haidvogel, 1976: Two-dimensional turbulence above topography. *J. Fluid. Mech.*, **78**, 129–154.

[9] Brent, R.P., 1973: *Algorithms for Minimization without Derivatives.* Prentice-Hall.

[10] Bryan, K., and L.J. Lewis, 1979: A water mass model of the global ocean. *J. Geophys. Res.*, **84**, 2503–2517.

[11] Cehelsky, P., and K.K. Tung, 1987: Theories of multiple equilibria and weather regimes—A critical reexamination. Part II: Baroclinic two-layer models. *J. Atmos. Sci.*, **44**, 3282–3303 (1987).

[12] Charney, J.G., 1947: The dynamics of long waves in a baroclinic Westerly current. *J. Meteor.*, **4**, 135–162.

[13] Charney, J.G., R.G. Fleagle, H. Riehl, V.E. Lally, and D.Q. Wark, 1966: The feasibility of a global observation and analysis experiment. *Bull. Amer. Meteor. Soc.*, **47**, 200–220.

[14] Charney, J.G., 1971: Geostrophic Turbulence. *J. Atmos. Sci.*, **28**, 1087–1095.

[15] Charney, J.G., and J.G. DeVore, 1979: Multiple flow equilibria in the atmosphere and blocking. *J. Atmos. Sci.*, **36**, 1205–1216.

[16] Charney, J.G., and D.M. Strauss, 1980: Form drag instability, multiple equilibria and propagating planetary waves in baroclinic, orographically forced, planetary wave systems. *J. Atmos. Sci.*, **37**, 1157–1176.

[17] Chasnov, J.R., 1991: Simulation of the Kolmogorov inertial subrange using an improved subgrid model. *Phys. Fluid A*, **3**, 188–200.

[18] Corby, G., 1968: *General circulation research. Aims and basic model.* British Meteorological Office manuscript, Bracknell, Berkshire, England.

[19] Cox, M.D., 1987: Isopycnal diffusion in a z-coordinate ocean model. *Ocean Modeling*, **74**, 1–5.

[20] Danabasoglu, G., and J.C. McWilliams, 1995: Sensitivity of the global ocean circulation to parameterizations of mesoscale tracer transports. *J. Phys. Oceanogr.*, **8**, 2967–2987.

[21] Deardorff, J.W., 1970: A numerical study of three-dimensional turbulent channel flow at large Reynolds numbers. *J. Fluid Mech.*, **41**, 453–480.

[22] Dickinson, R.E., 1978: Rossby waves – long-period oscillations of oceans and atmospheres, *Ann. Rev. Fluid Mech.*, **10**, 159–195

[23] Dole, R., 1986: The life cycles of persistent anomalies and blocking over the North Pacific. *Anomalous Atmospheric Flows and Blocking*, R. Benzi, B. Saltzman, and A. Wiin-Nielsen, Eds. *Adv. Geophys.*, **29**, 31–69.

[24] Domaradzki, J.A., R.W. Metcalfe, R.S. Rogallo, and J.J. Riley, 1987: Analysis of subgrid-scale eddy viscosity with use of results from direct numerical simulations. *Phys. Rev. Lett.*, **58**, 547–550.

[25] Domaradzki, J.A., and R.S. Rogallo, 1990: Local energy transfer and nonlocal interactions in homogeneous, isotropic turbulence. *Phys. Fluids A*, **2**, 413–426.

[26] Duffy, P.B., P. Elgroth, A.J. Bourgeois, and K. Caldeira, 1995: Effect of improved subgrid scale transport of tracers on uptake of bomb radiocarbon in ghe GFDL ocean general circulation model. *Geophys. Res. Lett.*, **22**, 1065–1068.

[27] Duffy, P.B., K. Caldeira, J. Selvaggi, and M.I. Hoffert, 1997: Effects of subgrid-scale mixing parameterizations on simulated distributions of natural ^{14}C, temperature, and salinity in a three-dimensional ocean General Circulation Model. *J. Phys. Oceanogr.*, **27**, 498–523.

[28] Eady, E.T., 1949: Long waves and cyclone waves. *Tellus*, **1**, 33–52.

[29] Egger, J., 1981: Stochastically driven large-scale circulations with multiple equilibria. *J. Atmos. Sci.*, **38**, 2606–2618.

[30] England, M.H., 1995: Using chlorofluorocarbons to assess ocean climate models. *Geophys. Res. Lett.*, **22**, 3051–3054.

[31] England, M.H, and G. Holloway, 1996: Simulations of CFC-11 outflow and seawater age in the deep North Atlantic. *Applications of Trace Substance Measurements to Oceanographic Problems*, P. Schlosser, W. Smethie, and J. Toggweiler, Eds., Amer. Geophys. Union.

[32] England, M.H., and S. Rahmstorf, 1999: Sensitivity of ventilation rates and radiocarbon uptake to subgrid-scale mixing in ocean models. *J. Phys. Oceanogr.*, **29**, 2802–2828.

[33] Fjortoft, R., 1953: On the changes in the spectral distribution of kinetic energy for 2D non-divergent flows. *Tellus*, **5**, 225–230.

[34] Forster, D., D.R. Nelson, and M.J. Stephen, (1977): Large-distance and long-time properties of randomly stirred fluids. *Phys. Rev. A*, **16**, 732–749.

[35] Frederiksen, J.S., and B.L. Sawford, 1980: Statistical dynamics of two-dimensional inviscid flow on the sphere. *J. Atmos. Sci.*, **37**, 717–732.

[36] Frederiksen, J.S., 1982: A unified three-dimensional instability theory of the onset of blocking and cyclogenesis. *J. Atmos. Sci.*, **39**, 969–982.

[37] Frederiksen, J.S., 1982: Eastward and westward flows over topography in nonlinear and linear barotropic models. *J. Atmos. Sci.*, **39**, 2477–2489.

[38] Frederiksen, J.S., 1983: A unified three-dimensional instability theory of the onset of blocking and cyclogenesis. II. Teleconnection patterns. *J. Atmos. Sci.*, **40**, 2593–2609.

[39] Frederiksen, J.S., 1992: Towards a unified instability theory of large-scale atmospheric disturbances. *Trends in Atmospheric Science*, **1**, 239–261.

[40] Frederiksen, J.S., M.R. Dix, and S.M. Kepert, 1996: Systematic energy errors and the tendency toward canonical equilibrium in atmospheric circulation models. *J. Atmos. Sci.*, **53**, 887–904.

[41] Frederiksen, J.S., and A.G. Davies, 1997: Eddy viscosity and stochastic backscatter parameterizations on the sphere for atmospheric circulation models. *J. Atmos. Sci.*, **54**, 2475–2492.

[42] Frederiksen, J.S., 1999: Subgrid-scale parameterizations of eddy-topographic force, eddy viscosity, and stochastic backscatter for flow over topography. *J. Atmos. Sci.*, **56**, 1481–1494.

[43] Frederiksen, J.S., M.R. Dix, and A.G. Davies, 2003: The effects of closure-based eddy diffusion on the climate and spectra of a GCM. *Tellus A*, **55**, 31–44.

[44] Frederiksen, J.S., 2003: Renormalized closure theory and subgrid-scale parameterizations for two-dimensional turbulence. *Nonlinear Dynamics: From Lasers to Butterflies*. R. Ball and N. Akhmediev Eds. World Scientific, 225–256.

[45] Frederiksen, J.S., and T.J. O'Kane, 2005: Inhomogeneous closure and statistical mechanics for Rossby wave turbulence over topography. *J. Fluid. Mech.*, **539**, 137–165.

[46] Frederiksen, J.S., and S.M. Kepert, 2006: Dynamical subgrid-scale parameterizations from direct numerical simulations. *J. Atmos. Sci.*, **63**, 3006–3019.

[47] Frisch, U., 1995: *Turbulence : the legacy of A. N. Kolmogorov*. Cambridge University Press.

[48] Gall, R., 1976: A comparison of linear baroclinic instability theory with the eddy statistics of a general circulation model. *J. Atmos. Sci.*, **33**, 349–373.

[49] Gent, P.R., and J.C. McWilliams, 1990: Isopycnal mixing in ocean circulation models. *J. Phys. Oceanogr.*, **20**, 150–155.

[50] Gent, P.R., J. Willebrand, T.J. McDougall, and J.C. McWilliams, 1995: Parameterizing eddy-induced tracer transports in ocean circulation models. *J. Phys. Oceanogr.*, **25**, 463–474.

[51] Gravel, S., and J. Derome, 1993: A study of multiple equilibria in a β-plane and a hemispheric model of a barotropic atmosphere. *Tellus*, **45A**, 81–98.

[52] Griffies, S.M., A. Gnanadesikan, R.C. Pacanowski, V.D. Larichev, J.K. Dukowicz, and R.D. Smith, 1998: Isoneutral diffusion in a z-coordinate ocean model. *J. Phys. Oceanogr.*, **28**, 805–830.

[53] Griffies, S.M., 1998: The GentMcWilliams skew flux. J. Phys. Oceanogr., **28**, 831–841.

[54] Halberg, R., and A. Gnanadesikan, 2006: The role of eddies in determining the structure and response of the wind-driven Southern Hemisphere overturning: Results from the Modeling Eddies in the Southern Ocean (MESO) Project. *J. Phys. Oceanogr.*, **36**, 2232–2252.

[55] Haltiner, G.J., and R.T. Williams, 1980: *Numerical prediction and dynamic meteorology.* Wiley.

[56] Hamilton, K., 2006: High resolution global modelling of the atmospheric circulation. *Adv. Atm. Sci.*, **23**, 842–856.

[57] Hart, J.E., 1981: Wavenumber selection in nonlinear baroclinic instability. *J. Atmos. Sci.*, **38**, 400–408.

[58] Herring. J.R., 1979: Subgrid scale modeling – An introduction and overview. *Turbulent Shear Flows 1.* F. Durst, B. Launder, F. Schmidt, J. Whitelaw, Eds. Springer-Verlag.

[59] Hirst, A.C., and W. Cai, 1994: Sensitivity of a world ocean GCM to changes in subsurface mixing parameterization. *J. Phys. Oceanogr.*, **24**, 1256–1279.

[60] Hirst, A.C., and T.J. McDougall, 1996: Meridional overturning and dianeutral transport in a z-coordinate ocean Model including eddy-induced advection. *J. Phys. Oceanogr.*, **28**, 1205–1223.

[61] Holloway, G., 1986: Eddies, waves, circulation, and mixing: statistical geofluid mechanics. *Ann. Rev. Fluid Mech.*, **18**, 91–147.

[62] Holloway, G., and J. Eert, 1987: Intransitive multiple equilibria in eddy-active barotropic flows. *J. Atmos. Sci.*, **44**, 2001–2005.

[63] Holton, J.R., 1992: *An Introduction to Dynamic Meteorology.* Academic Press.

[64] Jensen, R.V., 1981: Functional integral approach to classical statistical dynamics. *J. Stat. Phys.*, **25**, 183–210.

[65] Kaas, E., A. Guldberg, W. May, and M. Deque, 1999: Using tendency errors to tune the parameterization of unresolved dynamical scale interactions in atmosperic general circulation models. *Tellus A*, **51**, 612–629.

[66] Kallen, E., 1985: On hysteresis-like effects in orographically forced models. *Tellus*, **37A**, 249–257.

[67] Kiyani, K., 2005: *An assessement of renormalization methods in the statistical theory of isotropic turbulence.* PhD Thesis, Edingburgh University, UK.

[68] Koshyk, J.N., and G.J. Boer, 1995: Parameterization of dynamical subgrid-scale processes in a spectral GCM. *J. Atmos. Sci.*, **52**, 965–976.

[69] Kraichnan, R.H., 1959: The structure of isotropic turbulence at very high Reynolds numbers. *J. Fluid Mech.*, **5**, 497–543

[70] Kraichnan, R.H., 1964: Kolmogorov's hypothesis and Eulerian turbulence theory. *Phys. Fluids*, **7**, 1723–1734.

[71] Kraichnan, R.H., 1967: Inertial ranges in two-dimensional turbulence. *Phys. Fluids*, **10**, 1417–1423.

[72] Kraichnan, R.H., 1971: Inertial-range transfer in two- and three-dimensional turbulence. *J. Fluid. Mech.*, **47**, 525–535.

[73] Kraichnan, R.H., 1970: Convergents to turbulence functions. *J. Fluid Mech.*, **41**, 189–217.

[74] Kraichnan, R.H., 1976: Eddy viscosity in two and three Dimensions. J. Atmos. Sci., **33**, 1521–1536.

[75] Kurihara, Y., 1965: On the use of implicit and iterative methods for the time integration of the wave equation. *Mon. Weath. Rev*, **93**, 33–46.

[76] Laursen, L., and E. Eliasen, 1989: On the effects of the damping mechanisms in an atmospheric circulation model. *Tellus A*, **41**, 385–400.

[77] Lee. M.M., D.P. Marshall, and R.G. Williams, 1997: On the eddy transfer of tracers: advective or diffusive? *J. Mar. Res.*, **55**, 483–505

[78] Legras, B., and M. Ghil, 1985: Persistent anomalies, blocking and variations in atmospheric predictability. *J. Atmos. Sci.*, **42**, 433–471.

[79] Leith, C.E., 1968: Diffusion approximation fro two-dimensional turbulence. *Phys. Fluids*, **11**, 671–672.

[80] Leith, C.E., 1969: Two dimensional eddy viscosity coefficients. *Proc. Symp. Numerical Weather Prediction*, Tokyo, Japan Meteorological Agency, 141–144. Also in *Numerical simulation of turbulent flow. Properties of weather under unusual conditions.* New York, Interscience, 267–271.

[81] Leith, C.E., 1971: Atmospheric predictability and two-Dimensional Turbulence. *J. Atmos. Sci.*, **28**, 145–161.

[82] Leith, C.E., 1990: Stochastic backscatter in a subgrid-scale model: Plane shear mixing layer. *Phys. Fluids A*, **2**, 297–299.

[83] Lesieur, M., 1989: Large-eddy simulation of passive scalar diffusion in isotropic turbulence. *Phys. Fluids A*, **1**, 718–722.

[84] Lesieur, M., 1997: *Turbulence in Fluids.* Kluwer Academic Publishers.

[85] Leslie, D.C., and G.L. Quarini, 1979: The application of turbulence theory to the formulation of subgrid modelling procedures. *J. Fluid Mech.*, **91**, 65–91.

[86] Lilly, D.K., 1966: On the application of the eddy viscosity concept in the inertial subrange of turbulence. NCAR Manuscript 123.

[87] Maltrud, M.E., and G.K. Vallis, 1993: Energy and enstrophy transfer in numerical simulations of two-dimensional turbulence. *Phys. Fluids A*, **5**, 1760–1775.

[88] Marshall, J., C. Hill, L. Perelman, and A. Adcroft, 1997: Hydrostatic, quasi-hydrostatic, and nonhydrostatic ocean modeling. *J. Geophys. Res.*, **102**, 5733–5752.

[89] McComb, W.D., 1982: Reformulation of the statistical equations for turbulent shear flow. *Phys. Rev. A*, **26**, 1078–1094.

[90] McComb, W.D., and V. Shanmugasundaram, 1983: Fluid turbulence and the renormalization group: A preliminary calculation of the eddy viscosity. *Phys. Rev A*, **28**, 2588–2590.

[91] McComb, W.D., and V. Shanmugasundaram, 1985: Renormalization group calculation of the eddy viscosity for isotropic turbulence. J. Phys. A: Math. Gen., **18**, 2191–2198.

[92] McComb, W.D., 1986: Application of renormalization group (RG) methods to the subgrid modeling problems. *Direct and Large Eddy Simulation of Turbulence.*, U. Schumann and R. Friedrich, Eds. Notes on Numerical and Fluid Mechanics, Vol. 15. Vieweg, Braunschweig.

[93] McComb, W.D., 1990: *The Physics of Fluid Turbulence.* Oxford University Press.

[94] McWilliams, J.C., W.R. Holland, and J.H.S. Chow, 1978: A description of numerical Antarctic circumpolar currents. *Dyn. Atm. Oceans*, **2**, 213–291.

[95] Merilees, P.E., and Warn, T., 1971: The Resolution implications of geostrophic turbulence. J. Atmos. Sci. **29**, 990–991.

[96] Monin, A.S., and A.M. Yaglom, 1975: *Statistical Fluid Dynamics: Vol. 2.* MIT Press.

[97] Nastrom, G.D., and K.S. Gage, 1985: A climatology of atmospheric wavenumber spectra of wind and temperature observed by commercial aircraft. *J. Atmos. Sci.*, **42**, 950–960.

[98] O'Brien, E., and L.E. Branscome, 1988: Modes of variability in a low-order two-level model. *Tellus*, **40A**, 358–374.

[99] O'Kane, T.J., 2003: *The statistical dynamics of geophysical flows: An investigation of two-dimensional turbulent flow over topography.* PhD Thesis, Monash University, Australia.

[100] Orszag, S.A., 1970a: Analytical theories of turbulence. *J. Fluid Mech.*, **41**, 363–386.

[101] Orszag, S.A., 1970b: Transform method for the calculation of vector-coupled sums: Application to the spectral form of the vorticity equation. *J. Atmos. Sci.*, **27**, 890–895.

[102] Orszag, S.A., 1977: Statistical theories of turbulence. *Fluid Dynamics 1973, Les Houches Summer School of Theoretical Physics.* Gordan and Breech.

[103] Piomelli, U., 1991: Subgrid-scale backscatter in turbulent and transitional flows. *Phys. Fluids A*, **3**, 1766–1771.

[104] Piomelli, U., and J.R. Chasnov, 1996: Large eddy simulations: theory and applications. *Transition and Turbulence Modeling.* M. Hallback, D. Henningson, A. Johansson, and P. Alfredsson, Eds. Kluwer Academic Publishers.

[105] Phythian, R., 1977: The functional formalism of classical statistical dynamics. *J. Phys. A: Math.*, **10**, 777–789.

[106] Platzman, G.W., 1968: The Rossby wave. *Quart. J. Roy. Meteorol. Soc.*, **94**, 225–248

[107] Plumb, R.A., 1979: Eddy fluxes of conserved quantities by small-amplitude waves. *J. Atmos. Sci.*, **36**, 1699–1704.

[108] Plumb, R.A., and J.D. Mahlman, 1987: The zonally averaged transport characteristics of the GFDL General Circulation/Transport Model. *J. Atmos. Sci.*, **44**, 298–327.

[109] Rambaldi, S., and K.C. Mo, 1984: Forced Stationary Solutions in a Barotropic Channel: Multiple Equilibria and Theory of Nonlinear Resonance. *J. Atmos. Sci.*, **41**, 3135–3146.

[110] Redi, M.H., 1982: Oceanic isopycnal mixing by coordinate rotation. *J. Phys. Oceanogr.*, **12**, 1154–1158.

[111] Reinhold, B.B., and R.T. Pierrehumbert, 1982: Dynamics of weather regimes: quasi-Stationary waves and blocking. *Mon. Weath. Rev.*, **110**, 1105–1145.

[112] Rhines, P.B., 1969: Slow oscillations in an ocean of varying depth. Part 1. Abrupt topography. *J. Fluid Mech.*, **37**, 161–189.

[113] Rhines, P.B., 1975: Waves and turbulence on a beta-plane. *J. Fluid. Mech*, **69**, 417–443.

[114] Rhines, P.B., 1977: The dynamics of unsteady currents. *The Sea Vol. 6.* John Wiley and Sons.

[115] Roberts, M., and D. Marshall, 1998: Do we require adiabatic dissipation schemes in eddy-resolving ocean models? *J. Phys. Oceanogr.*, **28**, 2050–2063.

[116] Rose, H.A., 1977: Eddy-diffusivity, eddy noise, and subgrid-scale modelling. *J. Fluid Mech.*, **81**, 719–734.

[117] Rossby, C.G., 1939: Relation between variations in the intensity of the zonal circulation of the atmosphere and the displacements of the semi-permanent centers of action. *J. Mar. Res.*, **2**, 38–55.

[118] Rossby, C.G., 1945: On the propagation of frequncies and energies in certain types of oceanic and atmospheric waves. *J. Meteor.*, **2**, 187–204.

[119] Salmon, R., G. Holloway, and M.C. Hendershott, 1976: The equilibrium statistical mechanics of simple quasi-geostrophic models. *J. Fluid Mech.*, **75**, 691–703.

[120] Salmon, R., 1978: Two-layer quasi-geostrophic turbulence in a simple special case. *Geophys. Astrophys. Fluid Dynamics*, **10**, 25–52

[121] Salmon, R., 1980: Baroclinic instability and geostrophic turbulence. *Geophys. Astrophys. Fluid Dynamics*, **15**, 167–211.

[122] Salmon, R., 1998: *Lectures on Geophysical Fluid Dynamics.* Oxford University Press.

[123] Smagorinsky, J., 1963: General circulation experiments with the primitive equations. 1. The basic experiment. *Mon. Wea. Rev*, **91**, 99–165.

[124] Smith, L.M., and S.L. Woodruff, 1998: Renormalization-group analysis of turbulence. *Ann. Rev. Fluid Mech.*, **30**, 275–310.

[125] Smith, R.D., and P.R. Gent, 2004: Anisotropic GentMcWilliams parameterization for ocean models. *J. Phys. Oceanogr.*, **34**, 2541–2564.

[126] Speranza, A., 1986: Deterministic and statistical properties of northern hemisphere, mid-latitude circulation: minimal theoretical models. *Anomalous Atmospheric Flows and Blocking*, R. Benzi, B. Saltzman, and A. Wiin-Nielsen, Eds. *Adv. Geophys.*, **29**, 199–225.

[127] Sukoriansky, S., N. Dikovskaya, and B. Galperin, 2006: On the 'arrest' of inverse cascade and the Rhines scale. *J. Atmos. Sci.*, **64**, 3312–3327.

[128] Sura, P., 2002: Noise-Induced Transitions in a Barotropic β-Plane Channel. *J. Atmos. Sci.*, **59**, 97–110.

[129] Tennekes, H., 1985: A comparative pathology of atmospheric turbulence in two and three dimensions. *Turbulence and Predictability in Geophysical Fluid Dynamics and Climate Dynamics.* M. Ghil, R. Benzi, and G. Parisi, Eds. North-Holland.

[130] Tian, Y., E.R. Weeks, K. Ide, J.S. Urbach, C.N. Baroud, M. Ghil, and H.L. Swinney, 2001: Experimental and numerical studies of an eastward jet over topography. *J. Fluid. Mech.*, **438**, 129–157.

[131] Treguier, A.M., and J.C. McWilliams, 1990: Topographic influences on wind-driven, stratified flow in a β-plane channel: An idealized model for the Antarctic circumpolar current. *J. Phys. Oceanogr.*, **20**, 321–343.

[132] Tregueier, A.M., I.M. Held, and V.D. Larichev, 1997: Parameterization of quasi-geostrophic eddies in primitive equation ocean models. *J. Phys. Oceanogr.*, **27**, 567–580

[133] Tung, K.K., and A.J. Rosenthal, 1985: Theories of multiple equilibria-A critical reexamination. Part I: Barotropic models. *J. Atmos. Sci.*, **42**, 2804–2819.

[134] Tung, K.K., and W.W. Orlando, 2003: The k^{-3} and $k^{-5/3}$ energy spectrum of atmospheric turbulence: quasigeostrophic two-level model simulation. *J. Atmos. Sci.*, **60**, 824–835.

[135] Vallis, G.K., 1992: Problems and phenomenology in two-dimensional turbulence. *Nonlinear Phenomena in Atmospheric and Oceanic Sciences*, G. Carnevale and R. Pierrehumbert, Eds., Springer-Verlag.

[136] Vallis, G.K., and M.E. Maltrud, 1993: Generation of mean flows and jets on a beta plane and over topography. *J. Phys. Oceanogr.*, **23**, 1346–1362.

[137] Vallis, G.K., 2006: *Atmospheric and Oceanic Fluid Dynamics: Fundamentals and Large-scale Circulation.* Cambridge University Press.

[138] Veronis, G., 1966: Rossby waves with bottom topography. *J. Mar. Res.*, **24**, 338–348.

[139] Washington, W., and C.L. Parkinson, 1986: *An introduction to three-dimensional climate modeling.* Oxford University Press.

[140] Wiin-Nielsen, A., 1979: Steady states and stability properties of a low-order barotropic system with forcing and dissipation. *Tellus*, **31**, 375–386.

[141] Wirth, A., 2000: The parameterization of baroclinic instability in a simple model. *J. Mar. Res.*, **58**, 571–583.

[142] Wolff, J.O., E. Maier-Reimer, and D.J. Olbers, 1991: Wind-driven flow over topography in a zonal β-plane channel: A quasi-geostrophic model of the Antarctic circumpolar current. *J. Phys. Oceanogr.*, **21**, 236–264.

[143] Wyld, H.W., 1961: Formulation of the theory of turbulence in an incompressible fluid. *Ann. Phys.*, **14**, 143–165.

[144] Yakhot, V., and S.A. Orszag, 1986: Renormalization-group analysis of turbulence. *Phys. Rev. Lett.*, **57**, 1722–1724.

[145] Yang, S., B. Reinhold, and E. Kallen, 1997: Multiple weather regimes and baroclinically forced spherical resonance. *J. Atmos. Sci.* **54**, 1397–1409.

[146] Yoden, S., 1985: Bifurcation properties of a quasi-geostrophic, barotropic, low-order model with topography. *J. Meteor. Soc. Japan*, **63**, 535–546.

[147] Zidikheri, M.J., J.S. Frederiksen, and T.J. O'Kane, 2007: Multiple equilibria and atmospheric blocking. *Frontiers in Turbulence and Coherent Structures*, J. Denier and J.S. Frederiksen, Eds. World Scientific Lecture Notes in Complex Systems – Vol. 6, 59–85.

[148] Zhou, Y., G. Vahala, and M. Hossain, 1988: Renormalization-group theory for the eddy viscosity in subgrid modeling. *Phys. Rev A*, **37**, 2590–2598.

[149] Zhou, Y., and G. Vahala, 1993: Reformulation of recursive-renormalization-group-based subgrid modeling of turbulence. *Phys. Rev. E*, **47**, 2503–2519.

[150] Zhou, Y., W.D. McComb, and G. Vahala, 1997: Renormalization Group (RG) in turbulence: Historical and comparative Perspective. ICASE Report No.97-36, NASA, Langley.